TOPICAL MEETING ON LASER AND OPTICAL REMOTE SENSING:
INSTRUMENTATION AND.. (U) OPTICAL SOCIETY OF AMERICA
WASHINGTON D C J W QUINN AUG 88 ARO-25000.1-GS-CF

ARO 25000.1-GS-CF

(2)

AD-A200 275

TOPICAL MEETING ON

LASER AND OPTICAL REMOTE SENSING: INSTRUMENTATION AND TECHNIQUES

DTIC
S ELECTE
OCT 1 8 1988
a D

**TECHNICAL
DIGEST SERIES
VOLUME 18**

SEPTEMBER 28–OCTOBER 1, 1987
NORTH FALMOTH,
MASSACHUSETTS

88 1017 054

REPORT DOCUMENTATION PAGE

1a. REPORT SECURITY CLASSIFICATION Unclassified	1b. RESTRICTIVE MARKINGS

2a. SECURITY CLASSIFICATION AUTHORITY	3. DISTRIBUTION / AVAILABILITY OF REPORT
2b. DECLASSIFICATION / DOWNGRADING SCHEDULE	Approved for public release; distribution unlimited.

4. PERFORMING ORGANIZATION REPORT NUMBER(S)	5. MONITORING ORGANIZATION REPORT NUMBER(S) ARO 25000.1-GS-CF

6a. NAME OF PERFORMING ORGANIZATION Optical Soc of America	6b. OFFICE SYMBOL (If applicable)	7a. NAME OF MONITORING ORGANIZATION U. S. Army Research Office

6c. ADDRESS (City, State, and ZIP Code) Washington, D C 20036	7b. ADDRESS (City, State, and ZIP Code) P. O. Box 12211 Research Triangle Park, NC 27709-2211

8a. NAME OF FUNDING / SPONSORING ORGANIZATION U. S. Army Research Office	8b. OFFICE SYMBOL (If applicable)	9. PROCUREMENT INSTRUMENT IDENTIFICATION NUMBER DAAL03-87-G-0092

8c. ADDRESS (City, State, and ZIP Code)	10. SOURCE OF FUNDING NUMBERS			
P. O. Box 12211 Research Triangle Park, NC 27709-2211	PROGRAM ELEMENT NO.	PROJECT NO.	TASK NO.	WORK UNIT ACCESSION NO.

11. TITLE (Include Security Classification)

Topical Meeting on Laser and Optical Remote Sensing: Instrumentation and Techniques

12. PERSONAL AUTHOR(S)
Jarus W. Quinn, Executive Director

13a. TYPE OF REPORT Final	13b. TIME COVERED FROM 6/1/87 TO 5/31/88	14. DATE OF REPORT (Year, Month, Day) August 1988	15. PAGE COUNT 376

16. SUPPLEMENTARY NOTATION The view, opinions and/or findings contained in this report are those
of the author(s) and should not be construed as an official Department of the Army position,
policy, or decision, unless so designated by other documentation.

17.	COSATI CODES		18. SUBJECT TERMS (Continue on reverse if necessary and identify by block number)
FIELD	GROUP	SUB-GROUP	Remote Sensing, Optical Remote Sensing, Optical Systems,
			Scattering, Turbulence, Lidars, Lasers, Atmospheric Gases

19. ABSTRACT (Continue on reverse if necessary and identify by block number)

The meeting on Laser and Optical Remote Sensing: Instrumentation and Techniques
was held as scheduled. Summaries of the papers were published in the Technical
Digest Series, Volume 18 by the Optical Society of America.

20. DISTRIBUTION / AVAILABILITY OF ABSTRACT ☐ UNCLASSIFIED/UNLIMITED ☐ SAME AS RPT. ☐ DTIC USERS	21. ABSTRACT SECURITY CLASSIFICATION Unclassified
22a. NAME OF RESPONSIBLE INDIVIDUAL	22b. TELEPHONE (Include Area Code) | 22c. OFFICE SYMBOL

TOPICAL MEETING ON

LASER AND OPTICAL REMOTE SENSING:

INSTRUMENTATION AND TECHNIQUES

TECHNICAL DIGEST

Summaries of papers presented at the
Laser and Optical Remote Sensing:
Instrumentation and Techniques
Topical Meeting

September 28–October 1, 1987

North Falmoth, Massachusetts

Cosponsored by

Optical Society of America
Army Research Office
National Aeronautics and Space Administration

TABLE OF CONTENTS

SUNDAY, SEPTEMBER 27, 1987

CONFERENCE FOYER

6:00 PM-9:00 PM   REGISTRATION/RECEPTION

MONDAY, SEPTEMBER 28, 1987

CONFERENCE FOYER

7:30 AM-5:00 PM   REGISTRATION/SPEAKER CHECKIN

CONFERENCE ROOM 5

8:30 AM-8:45 AM   OPENING REMARKS

8:45 AM-10:15 AM
MA, LIDARS IN SPACE
Dennis K. Killinger, *University of South Florida, Presider*

8:45 AM-9:15 AM   (Invited paper)
MA1   Progress in Solid-State Lasers for Spaceborne Lidars,
Frank Allario, *NASA Langley Research Center.* NASA's
science and applications program for the Space Sation is
planning a lidar facility to conduct science experiments. To
accommodate the facility, solid-state laser technology is be-
ing developed. An overview of NASA's systems and technol-
ogy program is presented. (p. 2)

9:15 AM-9:45 AM   (Invited paper)
MA2   Lidar In-Space Technology Experiment, Richard R.
Nelms, Richard H. Couch, John W. Cox, Carroll W. Rowland,
M. Patrick McCormick, *NASA Langley Research Center.* The
lidar in-space technology experiment (LITE) is a multimission
Space Transportation System (STS) program to evaluate the
capability of a lidar experiment to make measurements of
aerosols and other atmospheric paramters from a space-
borne platform. (p. 5)

9:45 AM-10:00 AM
MA3   Lidar Experiment on Spacelab LEOS, M. Endemann,
V. Klein, *Battelle Institut e.V., F. R. Germany;* W. Renger, *In-
stitut for Atmospheric Physics, F. R. Germany;* H. Quenzel,
U. Munich, F. R. Germany. A small backscatter lidar for
measurements from the Spacelab facility is proposed to ex-
plore the measurement capabilities of a spaceborne lidar. A
first flight opportunity may arise with the German D2 mission
in the early 1990s. (p. 9)

MONDAY, SEPTEMBER 28, 1987 — *Continued*

CONFERENCE ROOM 5

10:00 AM-10:15 AM
MA4   Performance Testing of the Shuttle Laser Altimeter,
Jack L. Bufton, James B. Garvin, *NASA Goddard Space
Flight Center.* A laser altimeter instrument capable of opera-
tion from orbital altitude on the Space Shuttle has been de-
veloped. Instrument design and performance testing are
summarized. Sample terrain profile data acquired in airborne
simulations of the Shuttle mission are presented. (p. 13)

10:15 AM-10:45 PM   COFFEE BREAK

CONFERENCE ROOM 5

10:45 AM-12:30 PM
MB, DIAL MEASUREMENTS OF ATMOSPHERIC GASES
Robert T. Menzies, *Jet Propulsion Laboratory, Presider*

10:45 AM-11:15 AM   (Invited paper)
**MB1   Development of Lasers and Spectral Equipment for
Measurement of Atmospheric Molecular Gases,** V. E. Zuev,
U.S.S.R. Academy of Sciences, Siberian Branch. We con-
sider the problems of laser use and laser equipment devel-
oped to study the absorption spectra of atmospheric molec-
ular gases as well as the measurements of their concentra-
tion in field conditions carried out at the Institute of Atmos-
pheric Optics. (p. 18)

11:15 AM-11:45 AM   (Invited paper)
**MB2   DIAL System for High Resolution Water Vapor Meas-
urements in the Troposphere,** Jens Bosenberg. *Max-Planck-
Institute for Meteorology, F. R. Germany.* The system is de-
scribed, sources of error and test methods are discussed,
and results of field experiments are presented. (p. 22)

11:45 AM-12:00 M
**MB3   Differential Absorption Lidar System for Measure-
ments of Tropospheric NO, NO_2, SO_2 and O_3,** Barrie W. Jollif-
fee, Elizabeth Michelson, Nigel R. Swann, Peter T. Woods.
National Physical Laboratory, U.K. A new mobile DIAL facil-
ity is described and results of simultaneous measurements
of two atmospheric gases in urban and industrial areas are
presented. (p. 26)

12:00 M-12:15 PM
**MB4   Range-Resolved Heterodyne-Detection Dual CO_2
DIAL Measurements,** William B. Grant, Alan M. Brothers.
David M. Tratt *Jet Propulsion Laboratory.* Measurement
results are presented on atmospheric parameters and sys-
tem performance for the mobile atmospheric pollutant map-
ping system (MAPM). (p. 31)

12:15 PM-12:30 PM
MB5 DIAL Measurements of Atmospheric Water Vapor, HCl, and CH₄ Using a Continuously Tunable 1.7-μm Co:MgF₂ Laser, Dennis K. Killinger, Norman Menyuk, *MIT Lincoln Laboratory.* A 1.7-μm Co:MgF₂ DIAL system has been used to measure water vapor, HCl, and CH₄ in the atmosphere, including both path-averaged and range-resolved measurements at ranges up to 6 and 3 km, respectively. (p. 35)

12:30 PM-2:00 PM   LUNCH BREAK

CONFERENCE ROOM 4

2:00 PM-5:00 PM
POSTER SESSION
MC, LIDAR MEASUREMENTS AND ANALYSES
Jack Bufton, *NASA Goddard Space Flight Center,*
   Copresider
Tadeshi Aruga, *Ministry of Posts and Telecommunications,*
   Japan, Copresider

MC1 Analysis of Information Content of Multifrequency Laser Sounding of Aerosol and Molecular Atmosphere, V. E. Zuev, S. I. Kavkyanov, G. M. Krekov, *U.S.S.R. Academy of Sciences, Siberian Branch.* The processing methods are considered and comparative analysis of information content of single-frequency and multifrequency laser sounding of aerosol and molecular profiles is made. (p. 40)

MC2 Remote Determination of Meteorological and Optical Parameters of the Atmosphere Using a Raman Lidar, Yu. F Arshinov, S. M. Bobrovnikov, S. N. Volkov, V. E. Zuev, V. K Shumskii, *U.S.S.R. Academy of Sciences, Siberian Branch* The results of the experiments on measuring meteorological and optical parameters of the atmosphere using a Raman lidar are discussed. (p. 44)

MC3 Instrumental and Atmospheric Considerations in the Development and Application of an Airborne/Spaceborne Water Vapor DIAL System, Edward V. Browell, *NASA Langley Research Center;* Syed Ismail, *ST Systems Corp.* The operational requirements for an airborne/spaceborne water vapor DIAL system are derived, and the data analysis techniques to optimize the retrieval of water vapor profiles are discussed. (p. 47)

MC4 Advanced Airborne DIAL System Capabilities for Ozone and Multiwavelength Aerosol Measurements, A. F. Carter, E. V. Browell, J. H. Siviter, N. S. Higdon, *NASA Langley Research Center;* C. F. Butler, *ODU Research Foundation;* N. Mayo, *PRC Kentron.* The NASA Langley airborne DIAL system has been modified for simultaneous nadir and zenith measurements using eight transmitted laser beams. Unique system characteristics developed for the 1987 Amazon Boundary Layer Experiment and Antarctic Ozone Hole Experiment are described. (p. 51)

MC5 Simulation of Lidar Pressure and Temperature Profile Measurements from the Earth Observing System (EOS) Satellite, C. Laurence Korb, *NASA Goddard Space Flight Center;* Chi Y. Weng, *Science Systems & Applications, Inc.* Simulation of lidar experiments from the EOS with a high resolution alexandrite laser transmitter and narrowband detection shows pressure and temperature accuracies better than 0.4% and 1 K, respectively. (p. 55)

MC6 Adaptive Kalman-Bucy Filter for Differential Absorption Lidar Time Series Data, Russell E. Warren, *SRI International.* An adaptive extension of the Kalman-Bucy algorithm for on-line estimation of path-integrated concentration from differential absorption lidar time series data is presented. (p. 59)

MC7 Optimization of Lidar Boundary Layer Height Retrieval, Stephen F. Palm, *Science Systems & Applications, Inc.;* James D. Spinhirne, *NASA Goddard Space Flight Center.* Boundary layer height is retrieved using data from a low sensitivity, high altitude lidar system and from simulated spaceborne lidar systems of varying sensitivities. (p. 63)

MC8 Improvement of Laser Doppler Anemometer Results by Simultaneous Backscatter Measurements, Friedrich Kopp, *German Aerospace Research Establishment, F. R. Germany.* Simultaneous measurement of Doppler lidar signals and aerosol profiles offer the possibility to improve the range allocation and to compare shortwave and IR backscatter profiles. (p. 67)

MC9 High Spectral Resolution Lidar Measurements of Cirrus Cloud Optical Properties, C. J. Grund, E. W. Eloranta, *U. Wisconsin.* The HSRL has achieved calibrated eye-safe day and night measurements of cirrus cloud backscatter cross section, extinction cross section, and backscatter phase function. (p. 71)

MC10 Optically Significant Cirrus Clouds may be Rendered Invisible to Spaceborne Simple Lidar Systems, C. J. Grund, E. W. Eloranta, *U. Wisconsin.* Observed cirrus cloud backscatter cross sections often diminish with height. From space, simple lidar systems will miss clouds where the backscatter increase cancels the extinction. (p. 75)

MC11 Dedicated System for Routine Cloud Measurements, Richard Dubinsky, *Science & Technology Corp.* We present cirrus cloud data using a lidar operating at 0.53 μm and the design of a dedicated system for routine cloud measurements. (p. 79)

MC12 Detection of Methane Leaks with a Correlation Lidar, E. Galletti, *CISE Tecnologie Innovative S.p.A., Italy.* An infrared optical parametric oscillator source has been developed for use in a correlation lidar system for remote sensing of methane gas leakages. The system operates on a small truck in urban environments. (p. 80)

CONFERENCE FOYER

7:30 AM-3:00 PM   REGISTRATION/SPEAKER CHECKIN

CONFERENCE ROOM 5

8:30 AM-10:15 AM
TuA, OPTICAL TECHNIQUES FOR EARTH SYSTEM SCIENCE
J. Fred Holmes, *Oregon Graduate Center, Presider*

8:30 AM-9:00 AM   (Invited paper)
TuA1   Satellite Remote Sensing for Earth System Science: NASA's Earth Observing System (Eos), Robert Curran, *National Aeronautics and Space Administration*. The presentation will describe the general approach taken in developing the Eos concept. This includes it's contribution to the NASA's proposed thrust entitled "Mission to Planet Earth." The remainder of the discussion will focus on more of the details of several of the active and passive instruments which use optical techniques. (p. 114)

9:00 AM-9:30 AM   (Invited paper)
TuA2   Remote Sensing of Earth and Planetary Atmospheres Using Gas Correlation Spectroradiometry, Daniel J. McCleese, *Jet Propulsion Laboratory*. Gas correlation spectroradiometry is one of the most frequently used techniques for remote sensing of atmospheric properties. The technique, instrumentation, and its applications are described. (p. 116)

9:30 AM-9:45 AM
TuA3   Remote Sensing of Structure Properties in the Middle Atmosphere Using Lidar, C. R. Philbrick, D. P. Sipler, U. S. *Air Force Geophysics Laboratory;* G. Davidson, W. P. Moskowitz, *Photometrics, Inc.* The results from a mobile lidar have been used to derive density and temperature profiles between 25 and 85 km over central Alaska during Feb.-Apr. 1986. (p. 120)

9:45 AM-10:00 AM
TuA4   Remote Sensing of N_2O_3 and $ClONO_2$ in the Lower Stratosphere, J. Brasunas, J. Herman, V. Kunde, W. Maguire, *NASA Goddard Space Flight Center;* L. Herath, W. Shaffer, *Science Systems & Applications, Inc.;* S. Massie, *National Center for Atmospheric Research;* A. Goldman, *U. Denver.* A cryogenic balloon-borne spectrometer has measured nighttime stratospheric chlorine nitrate and dinitrogen pentoxide. The observations are compared with previous measurements and with model simulations. (p. 124)

10:00 AM-10:15 AM
TuA5   Imaging Bistatic Lidar Technique for Upper Atmosphere Studies, Byron Welsh, Chet Gardner, *U. Illinois at Urbana-Champaign.* An imaging bistatic lidar technique for studying the structural characteristics of the sodium layer is analyzed and discussed. (p. 128)

10:15 AM-10:45 AM   COFFEE BREAK

CONFERENCE ROOM 5

10:45 AM-12:30 PM
TuB, UNIQUE APPLICATIONS OF OPTICAL REMOTE SENSING
Claude Cahen, *Electricite de France, France, Presider*

10:45 AM-11:15 AM   (Invited paper)
TuB1   Uses of Laser Remote Sensing Techniques in Cell Biology and Medicine, Humio Inaba, *Tohoku U., Japan.* Experimental studies are reported on laser sensing of cytotoxic T-cells, which play an essential role in the rejection episode in clinical organ transplantation, and of microscopic fluorescence-intensity distribution in various single cells. (p. 134)

11:15 AM-11:45 AM   (Invited paper)
TuB2   Distributed Temperature Sensing in Optical Fiber Waveguides, Arthur Hartog, *York VSOP, U.K.* We review the measurement of temperature distributions among optical fibers, including the principal sensing methods, implementations, and performance of current and future instruments. (p. 135)

11:45 AM-12:00 M
TuB3   Time Resolved Lidar Fluorosensor for Oil Pollution Detection, A. Ferrario, P. L. Pizzolati, E. Zanzottera, *CISE Tecnologie Innovative S.p.A., Italy.* A fluorosensor system able to perform time and spectral analysis of oil fluorescence is being developed for sea pollution detection. The system is based on a triple Nd:YAG laser and on a streak camera. (p. 139)

12:00 M-12:15 PM
TuB4   Simultaneous Measurements of Ocean Surface Roughness and Atmospheric Pressure with a Centimeter Resolution Two-Color Laser Altimeter, James B. Abshire, Jan F. McGarry, *NASA Goddard Space Flight Center.* A 50-ps pulse width laser altimeter operating at 355 and 532 nm has been used to measure ocean surface roughness and atmospheric pressure from an aircraft over the Chesapeake Bay and the Atlantic Ocean. (p. 143)

12:15 PM-12:30 PM
TuB5   Cloud Liquid Water Derived from Lidar Observations, James D. Spinhirne, *NASA Goddard Space Flight Center;* William D. Hart, *Science Systems Application, Inc.;* Reinout Boers, *U. Maryland.* NASA ER-2 lidar observations of marine stratus cloud tops have been applied to derive the structure of cloud top liquid water with comparison to *in situ* observations. (p. 147)

12:30 PM-2:00 PM   LUNCH BREAK

CONFERENCE ROOM 4

2:00 PM
POSTDEADLINE PAPERS POSTER SESSION

CONFERENCE ROOM 4

7:00 PM–10:00 PM
POSTER SESSION
TuC, OPTICAL REMOTE SENSING METHODS
AND DEVICES
Chester S. Gardner, *University of Illinois, Copresider*
Norman Barnes, *NASA Langley Research Center,*
Copresider

TuC1 Advances in Gas Analyzers Based on IR Molecular
Lasers, Yu. M. Andreev, P. P. Geiko, V. V. Zuev, V. E. Zuev, O.
A. Romanovskii, S. F. Shubin, *U.S.S.R. Academy of Sciences,*
Siberian Branch. Trace gase analyzers with CO_2 and CO
laser parametric frequency converters provide measure-
ments of atmospheric-gas component (CO, NO, OCS, etc.)
concentrations. (p. 152)

TuC2 Simple Optical Method of Simultaneous Measure-
ment of Characteristic Scales and Intensity of Atmospheric
Turbulence, A. F. Zhukov, V. V. Nosov, *U.S.S.R. Academy of*
Sciences, Siberian Branch. A simple optical device is sug-
gested for simultaneous measurement of scales and intens-
ity of atmospheric turbulence. A set of transparencies with
different transmission coefficients is used. (p. 156)

TuC3 Textural Edge Extraction with an Optical Heterodyne
Scanning System, Ting-Chung Poon, Jinwoo Park, *Virginia*
Polytechnic Institute & State U. A technique for textural edge
extraction using an optical heterodyne scanning system is
proposed. Experimental results are presented. (p. 160)

TuC4 Free Flying Experiment to Measure the Quantum
Linewidth Limit of a 300-THz laser Oscillator, C. E. Byvik, A. L.
Newcomb, Robert L. Byer, *Stanford U.* Linewidths of the
order of 10 kHz have been achieved in a diode laser pumped
Nd:YAG nonplanar laser ring oscillator recently developed at
Stanford University. Refinements in the thermal control,
laser pump source, nonplanar ring design and host material
for the neodymium ion are expected to significantly reduce
the linewidths presently achievable in a terrestrial-based lab-
oratory. The free flight experiment is described and uses of
stable, narrow linewidth oscillators to gravity wave measure-
ments and frequency standards are discussed. (p. 164)

TuC5 Development of a Laser Heterodyne Radiometer for
Monitoring Stratospheric Air Pollution, Mitsuo Ishizu, Toshi-
kazu Itabe, Tadashi Aruga. *Radio Research Laboratory.*
Japan. Heterodyne radiometers using a CO_2 laser and a Pb-
salt diode laser were developed and many absorption lines
were successfully measured in the solar spectrum by
ground-based observation. (p. 165)

TuC6 Experimental Measurement of the Susceptibility of
Spatial Filter Profiling Techniques to Saturation, G. R. Ochs.
Reginald J. Hill, *NOAA Wave Propagation Laboratory.* Meas-
urements made on an incoherent light optical profiling
system that employs transmitting and receiving spatial
filters reveal pronounced saturation effects at high inte-
grated turbulence levels. (p. 169)

TuC7 Simultaneous Measurements of Turbulence Level
and Inner Scale Using Laser Scintillation, R. G. Frehlich. *Co-*
operative Institute for Research in the Environmental
Sciences. Estimates of the level of turbulence C_n^2 and the in-
ner scale of turbulence are obtained from measurements of
the spatial covariance of laser scintillation in weak scatter-
ing conditions. (p. 173)

TuC8 Atmospheric Correction Algorithm of Real and Sim-
ulated Space Imagery Using a Radiative Transfer Code,
Hongsuk H. Kim, *NASA Goddard Space Flight Center.* An im-
age processing algorithm has been developed to perform
pixel by pixel calculation of atmospheric radiance for a varie-
ty of Mie and view angles up to 60°. Examples of real and
simulated images corrected by this method are shown.
(p. 177)

TuC9 GASCOSCAN and GASCOFIL: Remote Sensing
Gas Correlation Spectrometers for Tropospheric Trace Gas
Measurements, W. H. Morrow, R. W. Nicholls. *York U.,*
Canada. The design and testing of two gas filter spectrom-
eters for making measurements in the 0.2-11-μm spectral
region on trace atmospheric gases are discussed. (p. 181)

TuC10 Signal Requirements for Remote IR Limb Sounding
of Atomic Oxygen and Temperature in the Thermosphere, R.
D. Sharma, *Air Force Geophysics Laboratory;* A. S. Zachor.
Atmospheric Radiation Consultants, Inc. Described are sen-
sitivity and spectral resolution requirements for limb sound-
ing of upper-atmospheric oxygen atom density and transla-
tional temperature using the 147- and/or 63-μm (OI) lines.
(p. 184)

TuC11 Concepts for Future Meteorological Earth Observ-
ing Sensors, David L. Glackin. *Aerospace Corp.* Concepts for
future earth observing sensors are described, including lidar.
DIAL, and millimeter wave radar. Applications include
atmospheric, terrestrial, and sea surface parameters.
(p. 185)

TuC12 Large Aperture Measurements of Optical Turbu-
lence, D. M. Winker, *U.S. Air Force Weapons Laboratory.*
Measurements of the phase and intensity of starlight at the
pupil plane of an astronomical telescope have been made to
study the effects of atmospheric turbulence on optical prop-
agation. (p. 189)

TuC13 Compact Wide-Field Sensor for Remote Sensing of
Ocean Phenomena, Thomas S. Pagano, Loren M. Woody.
Hughes Aircraft Co. A low-cost high-performance sensor de-
sign for low-earth orbit ocean-color remote sensing is pre-
sented with system trade-offs and performance estimates.
(p. 191)

WEDNESDAY, SEPTEMBER 30, 1987

CONFERENCE FOYER

7:30 AM-5:00 PM   REGISTRATION/SPEAKER CHECKIN

CONFERENCE ROOM 5

8:30 AM-10:15 AM
WA, REMOTE SENSING TECHNOLOGY: 1
John Petheram, *RCA Astro Electronics, Presider*

8:30 AM-9:00 AM   (Invited paper)
WA1   Diode Pumped Solid State Lasers for Remote Sensing, Robert L. Byer, *Stanford U.;* Thomas J. Kane, *Lightwave Electronics Corp.* A diode laser pumped monolithic nonplanar ring oscillator, followed by a 62-dB gain optical amplifier has been used for successful demonstration of coherent laser radar at 282 THz (1064 nm). (p. 234)

9:00 AM-9:30 AM   (Invited paper)
WA2   Focal Plane Array Technology for Optical Remote Sensing, James A. cutts, Martin H. Leipold, *Jet Propulsion Laboratory.* Progress in the development of solid-state self-scanned imaging arrays for remote sensing in the infrared region highlighting recent developments is reviewed. (p. 236)

9:30 AM-10:00 AM   (Invited paper)
WA3   Sum Frequency Mixing of Two Tunable Nd:YAG Lasers for Sodium Fluorescence Lidar Measurements, T. H. Jeys, *MIT Lincoln Laboratory.* A new source of sodium resonance radiation is being developed for sodium fluorescence lidar measurements. This source has several advantages over conventional dye laser sources. (p. 237)

10:00 AM-10:15 AM
WA4   Dual Alexandrite Laser for Autonomous Lidar Applications, John J. Degnan, *NASA Goddard Space Flight Center.* Progress on a tunable dual alexandrite laser transmitter for an autonomous DIAL lidar mission in the NASA ER-2 high altitude research aircraft is described. (p. 240)

10:15 AM-10:45 AM   COFFEE BREAK

WEDNESDAY, SEPTEMBER 30, 1987—*Continued*

CONFERENCE ROOM 5

10:45 AM-12:30 PM
WB, REMOTE SENSING TECHNOLOGY: 2
Martin Endemann, *Battelle Institut, F. R. Germany, Presider*

10:45 AM-11:15 AM   (Invited paper)
WB1   Progress in Solid State Lasers for Remote Sensing, Aram Mooradian, *MIT Lincoln Laboratory.* (p. 246)

11:15 AM-11:45 AM   (Invited paper)
WB2   Sources and Technology for Coherent Lidar Wind Measurement, Michael Vaughan, *Royal Signals & Radar Establishment, U.K.* The required characteristics of laser sources, both pulsed and cw, are described and illustrated. Technology questions in attaining quantum-limted system performance are briefly outlined. (p. 247)

11:45 AM-12:15 PM   (Invited paper)
WB3   Development of Coupled-Cavity Laser Diodes for Remote Sensing, Richard K. DeFreez, Richard A. Elliott, Joseph Furetz, Jon Orloff, *Oregon Graduate Center.* We discuss the performance characteristics of electronically tunable coupled-cavity diode lasers and their use in short range remote detection of methane. The devices were fabricated by focused-ion-beam micromachining. (p. 248)

12:15 PM-12:30 PM
WB4   Laser-Excited Optical Filter: Experiments in Rb Vapor, T. M. Shay, J. D. Dobbins, *Los Alamos National Laboratory;* Y. C. Chung, *Utah State U.* We report the first experimental demonstration of a laser-excited optical filter in Rb vapor. Measurements of filter linewidth are presented. (p. 251)

12:30 PM-2:00 PM   LUNCH BREAK

CONFERENCE ROOM 4

2:00 PM-5:00 PM
POSTER SESSION
WC, OPTICAL SYSTEMS AND COMPONENTS
Harvey Melfi, *NASA Goddard Space Flight Center, Copresider*
Nobuo Takeuchi, *The National Institute for Environmental Studies, Japan, Copresider*

WC1   Airborne Polarization Lidar for Sounding Clouds and Underlying Surface, A. I. Abramochkin, V. V. Burkov, V. E. Zuev, I. V. Samokhvalov, V. I. Shamanaev, *U.S.S.R. Academy of Sciences, Siberian Branch.* An automatized lidar has been constructed based on different types of polarization and simultaneous return reception in several fields of view. (p. 254)

WC2 Raman-Shifted Dye Laser for DIAL Measurements of Atmospheric Temperature, Pressure, and Density, Upendra N. Singh, Rita Mahon, Thomas D. Wilkerson, *U. Maryland.* Generation of narrowband, Raman-shifted dye laser radiation in the oxygen A-band (760–770 nm) is characterized for atmospheric temperature, pressure, and density DIAL measurements. (p. 258)

WC3 CO₂ Laser Preamplifier for Lidar Application, Kinpui Chan, *U. Research Foundation;* Jack L. bufton, *NASA Goddard Space Flight Center.* A CO₂ laser preamplifier has been tested in the laboratory for use in a CO₂ lidar system. A pulsed optical gain of nearly 700 was verified for a CO₂ TEA laser input pulse at 10.59 μm. (p. 262)

WC4 Low-Pressure Gain-Cell Laser-Detector Operation with a CO₂ Transversely Excited Atmospheric (TEA) Laser, Jan E. van der Laan, *SRI International.* Operation of a low-pressure CO₂ gain cell is evaluated experimentally as an optical receiver preamplifier for CO₂ TEA laser lidar applications. (p. 266)

WC5 Laser Sources and Sensitivity Calculations for a Near-Infrared DIAL System, Martin J. T. Milton, Barrie W. Jolliffe, Roger H. Partridge, Peter T. Woods, *National Physical Laboratory, U.K.* The design of a DIAL system to operate at ~3300 nm is considered, including the spectroscopy of target gases and possible laser sources. (p. 270)

WC6 Simple System for Frequency Locking Two CO₂ Lasers, Douglas C. Fraper, J. Fred Holmes, John M. Hunt, John Peacock, *Oregon Graduate Center.* Two cw CO₂ lasers in a heterodyne remote sensing system are frequency locked using the signal from the target and a cavity length transducer. (p. 274)

WC7 Pulsed, Frequency Stable, Narrow Linewidth Lasers and Optical Remote Sensing, K. K. Lee. *Perkin-Elmer Corp.* A method of constructing a pulsed, frequency stable, narrow linewidth laser is described, and its applications to optical remote sensing are discussed. (p. 278)

WC8 Rapid Tuning Device for a CO₂ Lidar, V. Klein. M. Endemann, *Battelle Institut e.V., F. R. Germany.* A rapid tuning device for a pulsed CO₂ laser is presented that enables us to tune the laser within < 3 ms to line pairs and to emit up to ten discrete wavelength pairs within 1 s. (p. 282)

WC9 Airborne Wavemeter for an Atmospheric DIAL Experiment, Joseph H. Goad, Jr.. *NASA Langley Research Center.* A wavemeter for laser wavelength centroid and wavelength profile measurements is being developed and designed. This subsystem is part of a downlooking differential absorption lidar experiment that will measure vertical water vapor and aerosol profiles from a NASA ER-2 aircraft. (p. 286)

WC10 Detector Response Characterization for DIAL Application, H. S. Lee, *SM Systems & Research Corp.;* Geary K. Schwemmer, C. Laurence Korb, *NASA Goddard Space Flight Center.* The response of a photomultiplier tube is studied to characterize the gain stability, linearity, and the cause and effect of signal-induced noise. (p. 290)

WC11 Speckle Effects on Laser Wavelength Measurements with a Fizeau Wavemeter, Coorg R. Prasad, C. Laurence Korb, Geary K. Schwemmer, *NASA Goddard Space Flight Center.* The presence of speckle produces errors in the measurements of laser frequency and line shapes. Measurement accuracy is improved by the use of thin diffusers, wide detectors, and signal averaging. (p. 293)

WC12 Development of Spectral Equipment for Investigations of Atmospheric Gases, V. E. Zuev, V. P. Lopasov, Yu. N. Ponomarev, L. N. Siitsa, I. S. Tyryshkin, A. B. Antipov, *U.S.S.R. Academy of Sciences, Siberian Branch.* The results of development of a set of high-resolution laser spectrometers in the 0.2–10-μm spectral range and experimental investigations of gas absorption spectra are presented. (p. 297)

WC13 Effective Source of Coherent Radiation Based on CO₂ Lasers and ZnGeP₂ Frequency Converters, Yu. M. Andreev, V. G. Voevodin, P. P. Geiko, A. I. Gribenyukov, V. V. Zuev, V. E. Zuev, *U.S.S.R. Academy of Sciences, Siberian Branch.* Several ZnGeP₂-monocrystal frequency converters of CO and CO₂ lasers have been constructed. The external energy conversion efficiencies are tenths to 49%. (p. 300)

WC14 Enhanced Direct Detection of CO₂ Lidar Returns Using a Laser Preamplifier, Dennis K. Killinger, *MIT Lincoln Laboratory;* Jack L. Bufton, *NASA Goddard Space Flight Center;* E. J. McLellan, *Pulse systems, Inc.* A CO₂ laser preamplifier has been used in a direct-detection single-frequency CO₂ lidar system. An increase by a factor of up to 200 in the SNR of the lidar returns has been achieved. (p. 304)

WC15 Plans for an Airborne Multispectral Laser Imaging Polarimeter System, James E. Kalshoven, Jr., *NASA Goddard Space Flight Center.* Preliminary design of a system using a polarized laser and linear array detectors to measure the depolarization characteristics of the earth's surface is described. (p. 308)

WC16 Design Concepts for an Advanced Airborne Meteorological Lidar (LASE II), Geary Schwemmer, *NASA Goddard Space Flight Center.* Injection locked alexandrite laser and tandem etalon filter design concepts for a high altitude airborne differential absorption lidar to measure atmospheric temperature profiles are examined. (p. 311)

WC17 Advanced Lidar for an Atmospheric Temperature Profile Measurements Program: an Overview, Bertrand L. Johnson, C. Laurence Korb, John Degana, Harvey Melfi, Geary Schwemmer, Louis Uccellini, *NASA Goddard Space Flight Center;* Pierre Flamant, *CNRS Laboratoire de Meteorologie Dynamique, France;* Mireille Bourdet, *CNRS Institut National d'Astronomie et de Geophysique, France;* Gerard Megie, *CNRS Service d'Aeronomie, France.* The LASE II (laser atmospheric sensing experiment) is the development of a lidar instrument system, using a dual alexandrite laser transmitter, to remotely measure temperature profiles of the earth's atmosphere from an ER-2 aircraft. The proposed instrument development is discussed. (p. 313)

WC18 Implementing a New High-Spectral-Resolution Lidar Technique for Backscatter Ratio and Atmospheric Temperature Profiling, C. Y. She, R. J. Alvarez II, H. Moosmuller, D. A. Krueger, *Colorado State U.* Experimental implementation of a proposed new high-spectral-resolution lidar technique for backscatter ratio and atmospheric temperature measurements using a pulsed laser system is discussed. (p. 316)

WC19 0.53-μm Incoherent Doppler Lidar: Current Status, J. Sroga, A. Rosenberg, *RCA Astro-Space division.* We describe the current status of the 0.53-μm incoherent Doppler lidar. A description of the system along with preliminary atmospheric measurements is presented. (p. 320)

WC20 Portable UV-DIAL System for Ground-Based Measurements of Lower-Stratospheric Ozone Profiles: Design and Performance Simulation, M. O. Rodgers, J. D. Bradshaw, D. D. Davis, *Georgia Institute of Technology;* R. E. Stickel, *Atlanta U. Center;* K. Asai, *Tohoku Institute of Technology, Japan.* Comparison of alternative designs for a portable, lightweight UV-DIAL ozone system is discussed. Focus is on suitability of each for operation in remote areas. (p. 324)

WC21 Introduction to the 100-in. Lidar System, Richard Richmond, Jan Servaites, *Wright-Patterson Air Force Base.* The WPAFB 100-in. collimator is being utilized as the receiver optics for what will be the largest operating lidar in the world. (p. 328)

WC22 400-Hz Line Center Stability in a GaAlAs Diode Laser, T. M. Shay, J. D. Dobbins, *Los Alamos National Laboratory;* Y. C. Chung, *Utah State U.* A solitary GaAlAs laser system is presented which demonstrates a long-term center frequency stability of 0.4-kHz in closed loop operation and 4-kHz in open loop operation. (p. 332)

7:00 PM-10:00 PM
CONFERENCE BANQUET
(New England Lobster/Clambake)

CONFERENCE FOYER

7:30 AM-12:00 PM   REGISTRATION/SPEAKER CHECKIN

CONFERENCE ROOM 5

8:30 AM-10:15 AM
ThA, SCATTERING AND TURBULENCE
Eugenio Zanzottera, *CISE S.p.A., Italy, Presider*

8:30 AM-9:00 AM   (Invited paper)
ThA1 Nonlinear Optical Interaction of Laser Radiation with Water Droplets, Richard K. Chang, *Yale U.* Nonlinear optical scattering and emission from large transparent water droplets irradiated with a high-intensity laser above and below the dielectric breakdown threshold are reviewed. (p. 334)

9:00 AM-9:30 AM   (Invited paper)
ThA2 Remote Sensing of Refractive Turbulence with Optical Spatial Filters, James H. Churnside, *NOAA Wave Propagation Laboratory.* The strength of refractive turbulence in the atmosphere can be measured remotely using incoherent optical spatial filtering techniques. High spatial resolution can be achieved. (p. 338)

9:30 AM-9:45 AM
ThA3 Minilidar for Pollution Monitoring and Multiple Scattering Studies, Christian Werner, *German Aerospace Research Establishment, F. R. Germany.* A simple backscatter lidar was developed to measure aerosol and cloud backscatter in different polarization directions. Different modules for airborne and ground-based measurements are available. (p. 342)

9:45 AM-10:00 AM
ThA4 Improved Diode-Laser Random-Modulation cw Lidar, Hiroshi Baba, Katsumi Sakurai, *U. Tokyo, Japan;* Nobuo Takeuchi, *National Institute for Environmental Studies, Japan;* Toshiyuki Ueno, *Chiba U., Japan.* A portable diode-laser random-modulation cw lidar was developed, to measure the daytime aerosol profile as well as the nighttime using a narrowband optical filter. (p. 346)

10:00 AM-10:15 AM
ThA5 Turbulence Measurements in the Convective Boundary Layer with a Short-Pulse CO$_2$ Doppler Lidar, Wynn L. Eberhard, R. Michael Hardesty, *NOAA Wave Propagation Laboratory;* Tzvi Gal-Chen, *U. Oklahoma.* Turbulence and momentum flux in convective conditions are measured by an azimuthally scanning Doppler lidar, with the gas mix selected to optimize the pulse length. (p. 350)

10:15 AM-10:45 AM   COFFEE BREAK

CONFERENCE ROOM 5

10:45 AM-12:30 PM
ThB, TROPOSPHERIC REMOTE SENSING
James Hawley, *SAIC, Presider*

10:45 AM-11:15 AM   (Invited paper)
ThB1   The Leandre Project: a French Airborne Lidar System for Meteorological Studies, J. Pelon, *U. Pierre et Marie Curie, France.* In the Leandre project an airborne lidar system is developed for atmospheric studies. It includes three phases with complementary objectives and different laser sources which are presented. (p. 356)

11:15 AM-11:45 AM   (Invited paper)
ThB2   Lidar Measurement of Boundary Layer Parameters, Edwin W. Eloranta, *U. Wisconsin.* Lidar techniques for measurement of atmospheric boundary layer parameters will be presented along with data from a new lidar system optimized for the observation of three-dimensional atmospheric structures. (p. 360)

11:45 AM-12:00 M
ThB3   Lidar Measurements of the Troposphere, A. I. Carswell, S. R. Pal, A. G. Cunningham, *York U., Canada.* Multiwavelength lidar measurements of the troposphere have been made using elastic and inelastic scattering processes and the results have been compared with *in situ* measurements. (p. 363)

12:00 M-12:15 PM
ThB4   Lidar Moisture Measurements During COHMEX, S. H. Melfi, David Whiteman, Richard Ferrare, *NASA Goddard Space Flight Center.* Raman lidar is used to measure atmospheric moisture profiles from near the surface to 7 k with 150-m vertical and 2-min temporal resolution. (p. 367)

12:15 PM-12:30 PM
ThB5   Accuracy of Temperature Measurements Using High Spectral Resolution Lidar, David A. Krueger, C. Y. She, *Colorado State U.* The effects of uncertainties in parameters and of noise in limiting the accuracy of remote temperature and pressure measurements using HSRL are reported. (p. 371)

MONDAY, SEPTEMBER 28, 1987

CONFERENCE ROOM 5

8:30 AM–10:15 AM

MA1–4

LIDARS IN SPACE

Dennis K. Killinger, University of South Florida,
Presider

Frank Allario

Progress in Solid-State Lasers for Spaceborne Lidars

Summary

As part of the National Aeronautics and Space Administration's (NASA) Space
Station program, a lidar facility is being planned to conduct a series of
scientific experiments from a polar orbiting platform. The thrust of these
experiments is to improve our understanding of atmospheric chemistry and
dynamics, altimetry, and meteorology. A number of scientific experiments
were recently developed by a panel of scientists and lidar technologists
and included both atmospheric backscatter (Lidar) and Differential
Absorption and Lidar (DIAL) experiments. The major investigations to be
conducted include measurements of the vertical profiles of atmospheric
aerosols, the height of the Planetary Boundary Layer (PBL), the
distribution of cirrus clouds, vertical profiles of water vapor in the
lower and upper atmosphere, vertical profiles of ozone, and measurements of
the vertical profiles of pressure and temperature. These experiments were
developed by the Lidar Atmospheric Sounder and Altimetry (LASA) panel, and
have been summarized in a NASA document.

As part of this activity, NASA's Langley Research Center has been given the
responsibility to conduct conceptual definition studies of the LASA
facility, in order to scope the instrumentation for the facility to
maximize the scientific return from a series of experiments (to be defined)
from the Space Station, polar orbiting platform. These studies are being
conducted in order to conceptually define such parameters as weight, power

Frank Allario

Progress in Solid-State Lasers for Spaceborne Lidars

and volume, the size of the receiver telescope, electronic processing

systems and data systems. Results of these studies will be used as

"baseline" parameters for the Announcement of Opportunity (AO) to be

issued, soliciting detailed scientific experiments and the associated lidar

transmitter, aft-optics and detector systems. As part of the LASA

definition studies, including in-house and industry studies, tradeoff's

have been conducted on the telescope, several laser technologies and the

associated thermal systems. Results of these studies have shown that

significant reductions in weight, power and volume are achievable by

utilizing emerging technologies in light-weighted mirrors and tunable solid

state lasers, pumped by semiconductor laser arrays. These technological

improvements are essential, especially to meet the full spatial and

temporal measurements desired by the scientific community.

As part of NASA's Active Sensing Experiments program within the Office of

Aeronautics and Space Technology (OAST), research is being conducted to

provide an assessment of solid state laser and detector technology for the

space station program. This program is a combined government, industry,

and university thrust which includes materials growth, laboratory test and

characterization of new solid state materials, infrared detectors/detector

arrays, and development of prototype lidar systems for aircraft and space

platform experiments. During the past 2 years, this program has focussed

on titanium-doped sapphire. Significant achievements were realized in

improving the technology for space-based, remote sensing experiments for

lidar and DIAL experiments. In the future the program will focus on new

3

Frank Allario

Progress in Solid-State Lasers for Spaceborne Lidars

solid state laser materials to broaden the wavelength coverage into the middle infrared range of the electromagnetic spectrum in order to enable space and aircraft measuremments of tenuous molecules in the Earth's atmosphere.

In this paper, an overview of the scientific needs of the Space Station, science and applications program will be described including the status of the LASA conceptual definition studies. Additionally, the status of the OAST research program in solid state laser materials and infrared detectors will be highlighted and will include current knowledge of the tradeoff studies in the telescope, solid state laser technology, detectors and semiconductor laser arrays as they relate to the LASA facility.

LIDAR In-Space Technology Experiment

Richard R. Nelms
NASA Langley Research Center
Hampton, Virginia 23665-5225

SUMMARY

The LIDAR In-Space Technology Experiment (LITE) is a multimission Space Transportation System (STS) program to evaluate the capability of a lidar experiment to make measurements of aerosols and other atmospheric parameters from a space platform.

The objectives of the first flight of the LITE experiment are to verify certain lidar technologies. These technologies are the systems operation in space, such as lifetime thermal dissipation, alinement control, environmental levels, and autonomous operations. The second technology objective is the evaluation of lidar techniques in space, such as signal-to-noise verifications, resolutions of Δz and Δh, and atmospheric characteristics at different wavelengths and at different altitudes. The third technology objective is to provide a test bed for new lidar techniques such as a Doppler lidar system or a Differential Absorption Lidar (DIAL) system on following flights, or to evaluate new emerging laser technologies such as Ti:Sapphire. We would also at some future time like to fly some wavelength control systems such as the wavemeter being developed for LASE.

In order to verify these technology objectives have been met, we will make measurements of cloud-top heights, planetary boundary-layer heights, tropospheric aerosols, stratospheric aerosols, and temperature and density measurements from 10 to 40 km.

The first flight of the LITE experiment should be flown on the STS system in the early 90's. A conceptual design of the LITE experiment has been initiated at Langley Research Center using a solid-state laser having a minimum of 1-J output at the fundamental wavelength, 1.06 μm incorporating a second and third harmonic generating crystal to provide the green and blue light. In addition, a 1-m telescope will be necessary to provide the sensitivity required to make high signal-to-noise ratio measurements of the return signals. The laser is being developed under contract and at the present time we have a working laboratory version. The telescope will be a 1-m telescope that was acquired from Goddard Space Flight Center on loan and is a engineering model of an OAO telescope. It is being updated and retested at Langley Research Center.

The LITE experiment is of a modular configuration, as shown in the attached figure, that facilitates components or subsystem replacement during field servicing or upgrades from future missions. The modules which comprise the LITE are as follows: a laser transmitter (LTM), a telescope receiver, aft-optics assembly, systems electronics, boresight system, camera system, environmental measuring system, and the experiment plateform.

The laser transmitter module consists of a flashlamp-pumped, Q-switched, Nd:Yag laser with a fundamental output of 1.06 μm. The fundamental output energy is in excess of 1 J per pulse with the selectable pulse rates of

either 1 or 10 pulses per second. In addition, the module includes second and third harmonic generation which converts part of the fundamental energy into harmonic energy at .532 µm and 355 µm. The net energy at 1.06 µm is 200 mJ, 400 mJ at .532 mJ and 150 mJ at .355 µm. The laser is housed in a sealed container and cooled by way of a heat-transfer unit which is connected to the enhanced MDM pallet coolant system.

The telescope receiver as mentioned before is a 1-m, Ritchey-Cretien form of a Cassegrain telescope. The secondary mirror is fused quartz with an aluminum reflecting surface and the primary mirror features a beryllium substrate with a Kanigen overcoat and has an aluminum reflecting surface.

The aft-optics assembly contains the optical and detector components which receive and separate the backscattered laser signals. The optical assembly is mounted on an optical bench and suspended under the primary mirror of the telescope. The optics assembly design contains a variable field stop controlled either by command or autosequence operation. A moveable mirror just beyond the field stop will redirect the return signal into a separate optical train for automatic boresighting of the laser output signals to the telescope optical axis.

The boresight system consists of a two-axis mirror which maintains colinearity between the laser transmitter and the telescope receiver. This colinearity is accomplished through automatically redirecting the outgoing laser beams by a closed-loop feedback system that uses a four quadrant detector to determine the location of the backscattered laser signal.

The system electronics consists of a system computer unit and a high-speed digitizer. The computer provides the interface to the STS Orbiter for uplink and downlink command services as well as all the control functions in the instrument. The high-speed digitizer contains an analog-to-digital converter and a buffer memory which allows data from the detectors to be acquired and stored at a very high rate during the data taking mode and reproduced at a lower rate for downlinking.

A camera system is onboard and uses a false color infrared film to continuously photograph daytime cloud cover and ground tracks thereby furnishing correlative assistence for science data analysis.

There is an environmental measuring system called OEX Autonomous Supporting Instrumentation System (OASIS) onboard to monitor the environmental levels seen at various places on the optical bench during the launch orbit and descent modes of the experiment.

All of the subsystems are mounted on a platform that is an orthogrid structure utilizing an existing Marshall Space Flight Center design and one that has flown in the past on the STS missions.

The LITE program is currently manifested for the early 90's with a second flight planned 2 years after. The design phase of the program is presently underway and a Preliminary Design Review has been completed.

LITE PRELIMINARY DESIGN
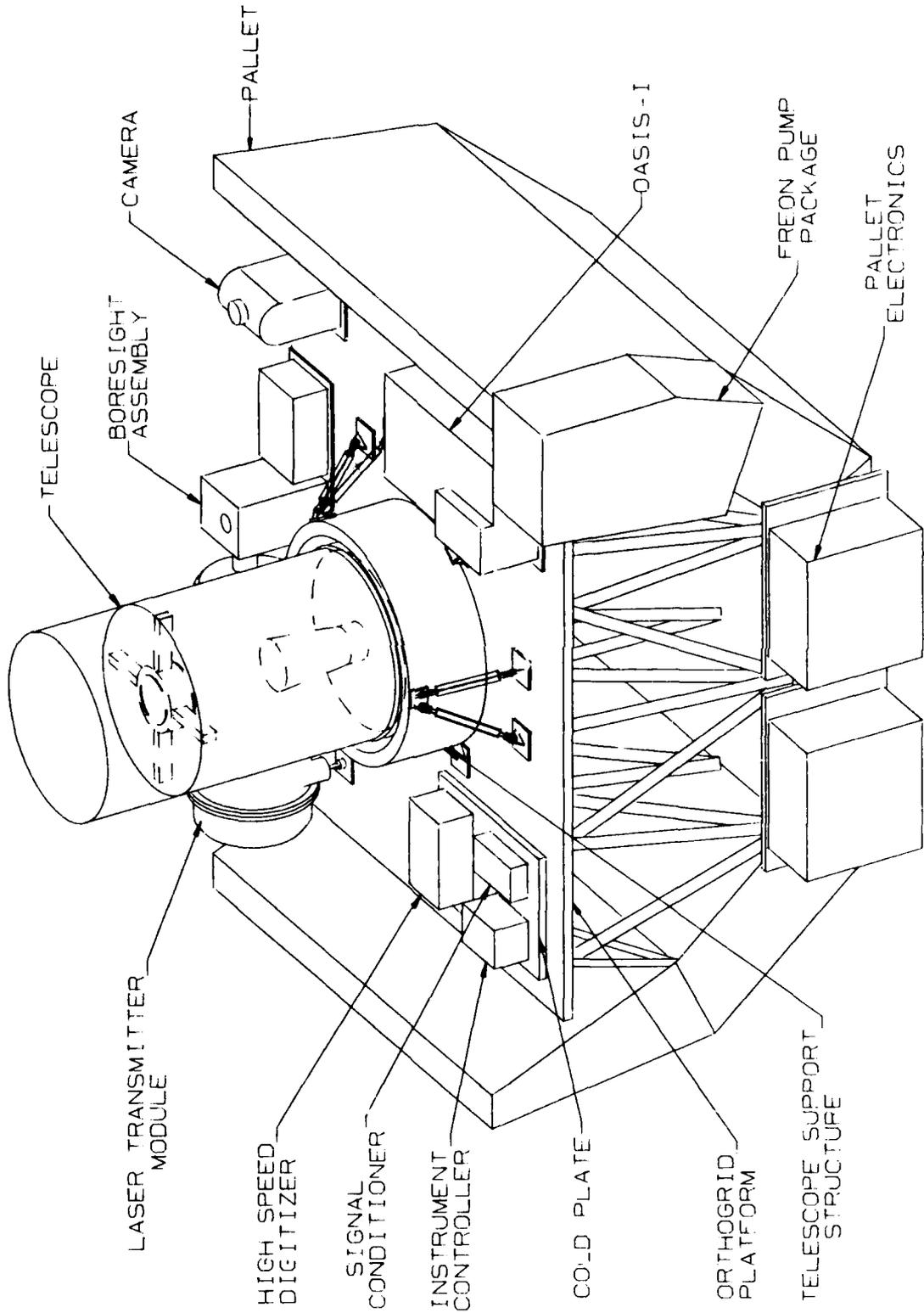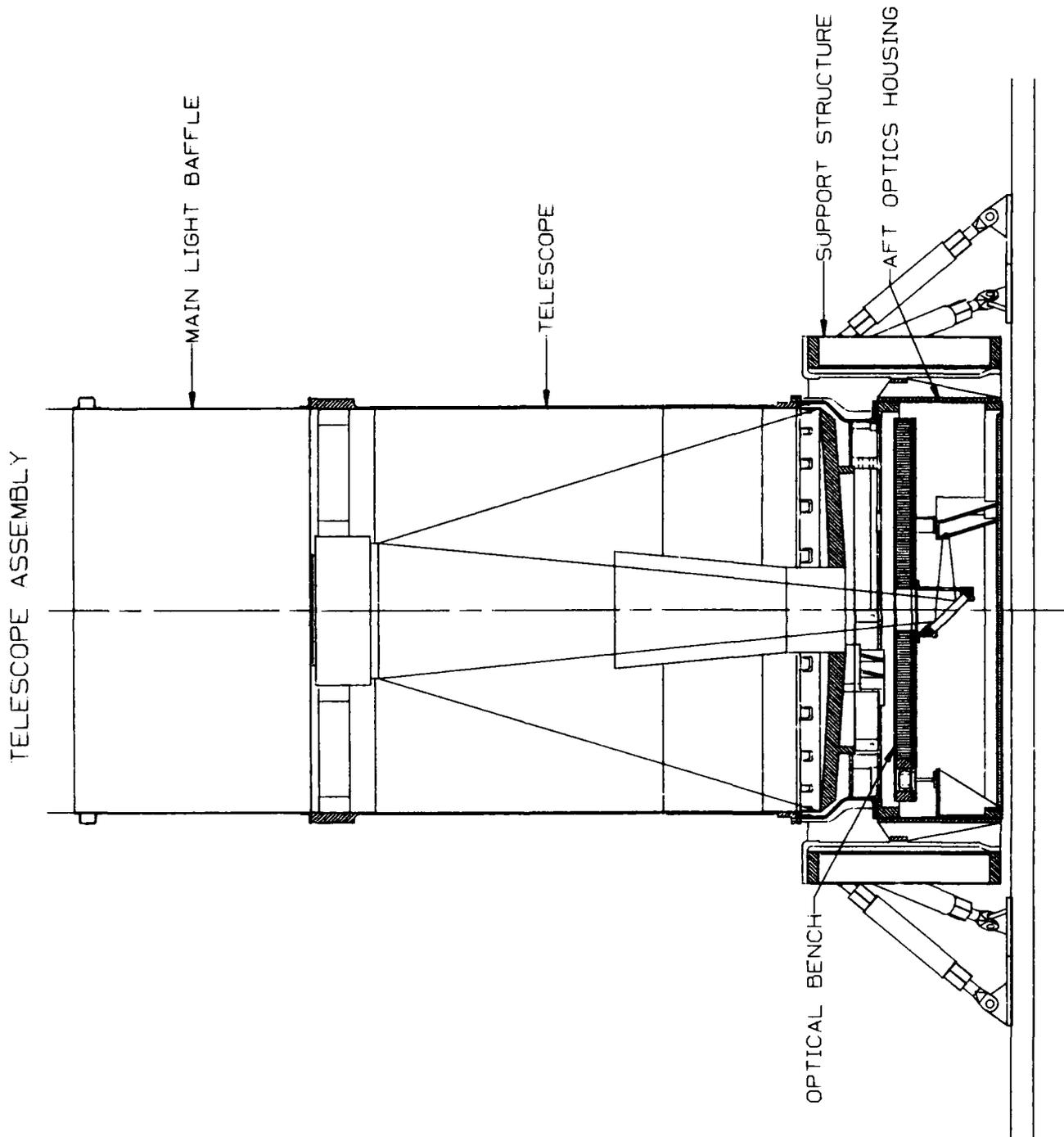
PALLET

CAMERA

TELESCOPE

BORESIGHT ASSEMBLY

OASIS-I

FREON PUMP PACKAGE

PALLET ELECTRONICS

LASER TRANSMITTER MODULE

HIGH SPEED DIGITIZER

SIGNAL CONDITIONER

INSTRUMENT CONTROLLER

COLD PLATE

ORTHOGRID PLATFORM

TELESCOPE SUPPORT STRUCTURE

TELESCOPE ASSEMBLY

MAIN LIGHT BAFFLE

TELESCOPE

SUPPORT STRUCTURE

AFT OPTICS HOUSING

OPTICAL BENCH

Lidar Experiment On Spacelab LEOS

M. Endemann, V. Klein
Battelle-Institut e.V.
Am Römerhof 35, D-6000 Frankfurt a.M. 90, FRG

W. Renger
Institute for Atmospheric Physics, DFVLR
Postfach, D-8031 Oberpfaffenhofen, FRG

H. Quenzel
Meteorologisches Institut der Universtät München
Theresienstr. 37, D-8000 München 2, FRG

Introduction

There are plans for a second German spacelab mission (D2-mission) (originally scheduled for late 1988) which will be basically a zero-g mission, but will also include earth observation experiments. Encouraged by our experience with airborne lidar systems and the results from theoretical studies, we have proposed a backscatter lidar for this or later spacelab missions.

Since the lidar is only an add-on experiment during the D2-mission, and since the available time to construct the experiment is short, we are driving the following guidelines:

- Use presently available techniques
- Use available space-qualified pressursized containers to contain the various critical subcomponents (e.g. laser, power-supplies) to minimize qualification testing
- Demonstrate the expected benefits of the active technique in combination with passive sensors
- Validate lidar data by independent measurements

We present an outline of the measurement goals, the instrument design and performance evaluations.

Measurement Goals

The Spacelab-lidar is designed to evaluate the measurement applications of spaceborne backscatter lidars for meteorology and climatology with a comparatively simple instrument. It forms an intermediate step between an airborne lidar and an operational spaceborne lidar on future earth observation satellites. This step is necessary to gain more insight into the technological points of the lidar design, but also to obtain first atmospheric backscatter data from a spaceborne platform.

The Spacelab-lidar will allow to perform a number of different measurements with the goal to obtain performance data for the design of future operational spaceborne lidar instruments:

- Cloud top heigths
- Height of the planetary boundary layer
- Optical thickness and cloud base height of thin clouds
- Tropospheric aerorsols
- Stratospheric aerosols
- Tropopause height

It is planned to perform measurements of these atmospheric parameters at different times over a selected location with good probability for adequate weather conditions. At the present status of planning, this site will be in the western sahara desert. Each measurement over this site will take only some 5 minutes and yield data from a strip of about 2000 km length. Simultaneous to the lidar measurements from Spacelab, a gound truth campaign will be carried out to validate the data gathered by the Spacelab-lidar with groundbased and airborne instrumentation.

Another set of measurements performed with the Spacelab-lidar will yield atmospheric backscatter data along a strip of some 8000 km length (20 min measurement duration) over central Europe. Data from this measurement will cover a wide variety of meteorological situations. These data can be validated with measurements from a passive radiometer that is part of the Spacelab-lidar, and with data from passive sounders on other meteorological satellites and from ground based observation stations.

Instrument Design

The figure shows the Spacelab-lidar as it is mounted in Space Shuttle. It is located in two Getaway-Special (GAS-) containers that are mounted to the Unique Support Structure (USS) of the Spacelab Facility. The GAS-containers have been selected as primary structure for the lidar since they provide an environment to house non-space qualified parts in orbit. Thus the time- and cost-consuming qualification procedures for each lidar component of the lidar can be strongly reduced to an overall qualification of the complete system.

One GAS-container holds the complete transmitter assembly with laser and beam expanding telescope, as well as the power supply. Also included is a passive IR-radiometer for validation measurements.

The transmitter laser is a flashlamp-pumped Nd:YAG laser with frequency doubler. The transmitted energy is 300 mJ at the fundamental frequency of 1.06 µm and 200 mJ at the harmonic at 0.532 µm. Both frequencies are emitted simultaneously with a pulse rate of 10 Hz. The beam divergence behind the beam expansion telescope can be as low as 0.2 mrad at 1.06 µm. Power consumption of this laser is 600 W (average).

One feature of the transmitter assembly is that the laser beam can be directed over an angle of 8 mrad in each direction. This

beam steering capability is required for an active alignment of transmitter and receiver containers of the lidar in space.

Since the laser is mounted in the GAS-container, it can operate in a nitrogen atmosphere at normal pressure. It is foreseen that the laser is cooled with a heat exchanger to the Freon-loop of the Spacelab. However, since it is not certain yet if the freon-loop is present in the spacelab mission, a radiation cooler on the GAS-container can be used as an alternative. In this case, the duty cycle of the transmitter laser must be reduced somewhat during the longer measurements.

The receiving telescope with signal and alignment detectors are mounted in a second GAS-container with a lid that is opened for the measurement. This container has an extension on the rear side that houses the detectors and receiver electronics, as well as a video camera for the navigation of the data. This extension is pressurized to atmospheric pressure, while the receiving teles-cope in the main structure of the GAS-container is open to the space environment.

A compact Cassegrain-telescope is used as photon collector. It has a diameter of 0.48 m and an overall length of only 0.65 m. Diameter and length are limited by the size of the GAS-container. The short length is achieved by using a primary mirror with small focal length (F = 2), and a relatively large secondary mirror. The obscuration by this secondary mirror is 19 %, and including the mounting structure, the effective area of the receiver is 0.15 m^2. This corresponds to an unobscured telescope with 0.41 m diameter.

The extra alignment channel is necessary since transmitter and receiver are mounted in separate containers. A quadrant-detector is used that 'sees' the strong return signal from the ground or optically dense clouds. The signal from this alignment detector is used to steer the transmitted laser beam into the center of the receiver FOV. This is usually done in an automated feedback loop, but also can be done manually from a control module in Spacelab.

The detection electronics is also housed in the extension of the receiver-GAS. The signals from the red and green channels are digitized with a 12 bit, 3 MHz ADC, while the alignment channel can operate with reduced accuracy and bandwidth (8 bit, 0.5 MHz). The digitized signals are transmitted by a serial bus to the recorder module in Spacelab.

The Spacelab-lidar will operate as an autonomous instrument, but can also be operated manually from Spacelab. The control unit is rack-mounted and comprises a signal-scope, an indicator for the alignment detector signal and a joystick for manual realignment. Measurement data are stored on a Winchester disk that is housed in this control unit. The interface to the transmitter/receiver modules is a serial 'MACS'-bus for measurement-, control- and

house keeping data. The data from the video camaera are stored by a Spacelab video-recorder rack.

Time Scale

The design of the Spacelab-lidar is sufficiently simple to allow its construction within a time frame of 19 months. However, for the integration of the instrument in Spacelab, another 12 months is required, and the Shuttle integration takes another year. Due to the uncertain launch date of the next Spacelab mission, it is not certain yet, when the Spacelab-lidar will actually be flown.
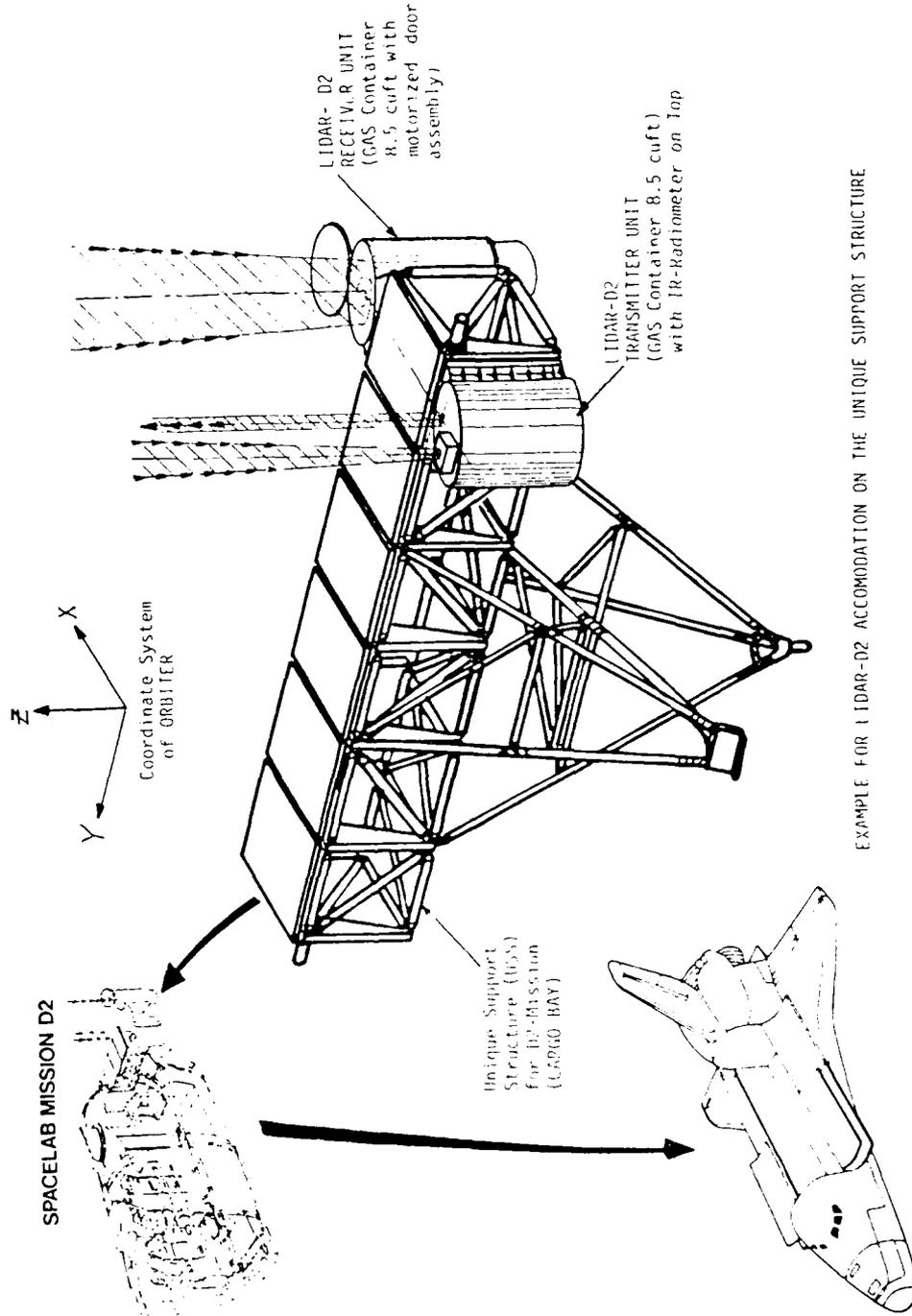
EXAMPLE FOR LIDAR-D2 ACCOMODATION ON THE UNIQUE SUPPORT STRUCTURE

LIDAR-D2 RECEIVER UNIT (GAS Container 8.5 cuft with motorized door assembly)

LIDAR-D2 TRANSMITTER UNIT (GAS Container 8.5 cuft) with IR-Radiometer on top

Coordinate System of ORBITER

Unique Support Structure (USS) for D2-Mission (CARGO BAY)

SPACELAB MISSION D2

PERFORMANCE TESTING OF THE SHUTTLE LASER ALTIMETER

Jack L. Bufton and James B. Garvin

Goddard Space Flight Center
Greenbelt, Maryland 20771

A laser ranging instrument has been developed for altimetry measurements of the Earth's surface along the nadir track of the Space Shuttle. The Shuttle Laser Altimeter is designed for transmission of a short laser pulse and reception of the backscattered laser radiation from the Earth's surface. The source laser is a Q-switched Nd:YAG operating at its fundamental wavelength of 1.064 μm. A reflector telescope and silicon avalanche photodiode are the basis of the altimeter receiver. Laser, telescope, detector, data processing and storage electronics, and dc power supplies are packaged for spaceflight into two adjacent Get-Away-Special canisters. This provides the basis for a very compact and low-cost interface to the Space Shuttle.

Primary data produced by this instrument are the laser pulse time-of-flight, pulse energy, and the spreading of the laser pulse by the target surface. Laser altimeter time-of-flight data provide meter-level resolution topography measurements. The pulse waveform measurements yield additional information on target backscatter cross-section and target structure within the laser footprint. Prime applications of this instrument are measurement of topographical profiles of volcanic, mountain-region, and desert landforms.

While awaiting spaceflight opportunities, the Shuttle Laser ALtimeter (SLA) has been tested from a high-altitude aircraft platform. The primary objectives in these tests were the verification of instrument performance and the simulation of laser ranging from a spacecraft platform. For these tests the SLA instrument was positioned for nadir observations from the NASA T-39 Sabreliner high-altitude jet aircraft. Data were acquired on a number of flights at altitudes as high as 12 km above sea level. Altimetry results are available from flights over mountain-region terrain in the Eastern U.S., Atlantic Ocean coastal waters, various cloud-layers, and a variety of volcanic, erosional, and impact-related landforms in the vicinity of Flagstaff, AZ. These datasets permit instrument performance to be assessed as a simulation of space-based laser altimeter measurements.

An assembly view of the SLA instrument appears in Fig. 1. One canister, equipped with a motorized door assembly, contains the laser transmitter, receiver telescope, and detectors of the laser altimeter instrument. It also has a large diameter glass window to maintain up to 1 atm of pressure inside the canister and still provide the maximum clear aperture of 0.38 m for laser altimeter operation. The motorized door is closed during launch and landing and then opens on-orbit for experiment operation. The second G.A.S. canister contains the battery power supply, altimeter data-acquisition electronics, flight computer, tape recorder, camera, and IR radiometer. This canister also is sealed to provide up to 1 atm of internal pressure. Its upper lid contains two 7 cm diameter (clear aperture) windows for observations with a camera and IR radiometer. Both of these instruments provide data products for post-mission identification of altimetry targets. The support module is joined with the laser altimeter module by a power and data cable. Battery power from the support module is routed to the major power user, the laser, in the altimeter canister. Altimetry data pulses from the detectors are transferred by this cable in the other direction to the support canister for processing and recording.

The overall block diagram of Fig 2. indicates the interconnection of the various sensor, data-processing, and data-storage electronics. Figure 3 illustrates the details of the ranging and waveform digitization electronics. The transmit pulse, from a Si PIN photodiode at the laser output, is split to provide signals to start the time-interval-unit and measure transmitted pulse energy. The receive pulse from the Si avalanche photodiode detector is also split in order to stop the time-interval-unit, provide input to the receiver pulse energy monitor, and provide input to 12 channels of waveform digitization. The table gives a summary of transmitter and receiver instrument parameters for the Shuttle Laser Altimeter.

Figure 1 Shuttle Laser Altimeter instrument.
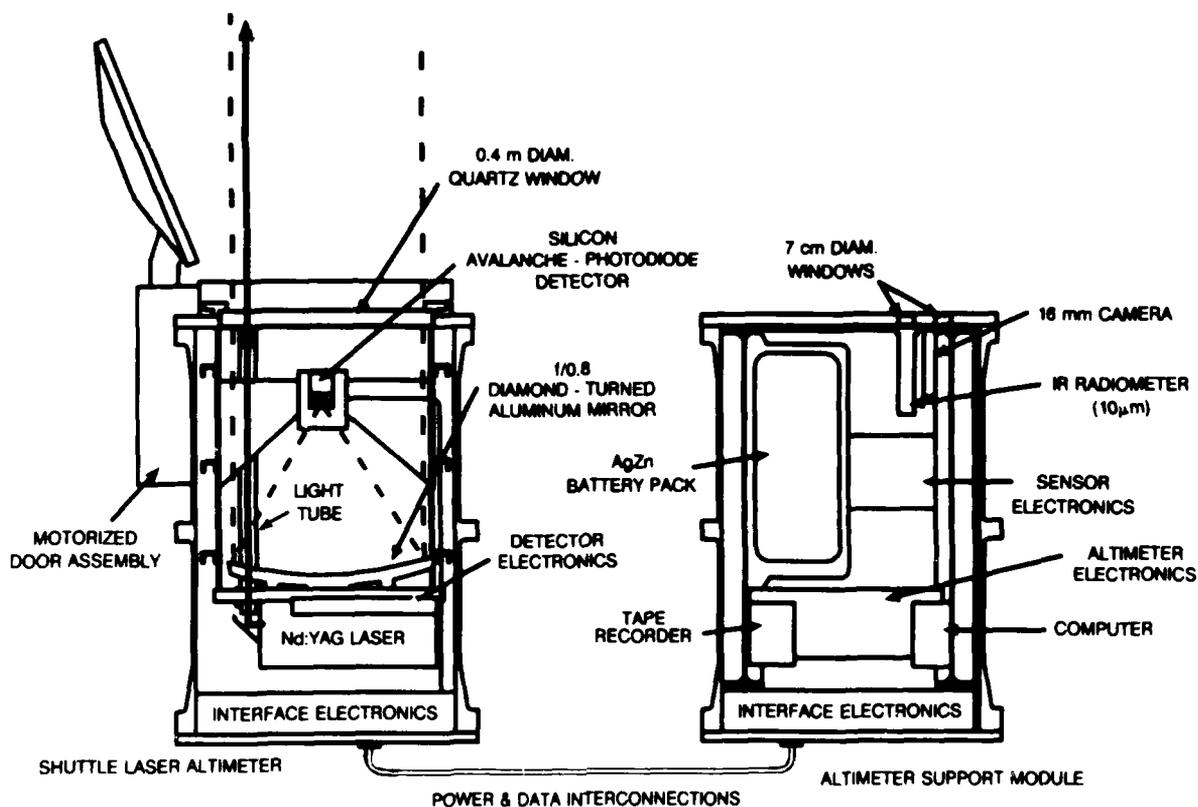
LASER TRANSMITTER

LASER TYPE:	flashlamp-pumped Nd:YAG, multi-mode output,
WAVELENGTH:	1.064 μm
Q-SWITCH:	LiNbO$_3$
PULSEWIDTH:	19 nsec FWHM
REPETITION-RATE:	1 - 20 Hz
DIVERGENCE:	0.9 mrad
COOLING:	closed-loop, liquid-to-air heat exchanger

ALTIMETER RECEIVER

TELESCOPE TYPE:	f/0.8 diamond-turned aluminum parabola
TELESCOPE DIAMETER:	0.4 m
OPTICAL FILTER:	5 nm bandpass
DETECTOR TYPE:	silicon avalanche photodiode, 0.8 mm diameter
FIELD-OF-VIEW:	2 mrad
QUANTUM EFFICIENCY:	36%
RESPONSIVITY:	36 amp/watt
SENSITIVITY:	1 nanowatt
BANDWIDTH:	11 - 40 MHz
TIME-INTERVAL COUNTER:	1 nsec resolution
WAVEFORM DIGITIZER	12 channels, 7 nsec resolution, 10 nsec channel width 10-bit amplitude resolution

Figure 2 Shuttle Laser Altimeter component diagram.

Figure 3 Shuttle Laser Altimeter ranging and waveform electronics.

15

The SLA instrument operation is based on a high signal-to-noise environment in which each laser pulse can be used for a unique range measurement. No pulse-to-pulse averaging is used for terrain profiles, since it is most important to maximize horizontal resolution from orbit while simultaneously minimizing laser pulse rates. Laser altimeter signal strength depends on laser pulse power backscattered from the target surface and collected by the receiver telescope. Competing processes are optical background noise and detector noise. Calculations of these quantities can be used for comparison with measurements of signal-to-noise ratio in altimeter field tests.

Figure 4 presents an example record from the SLA airborne science mission in Northern Arizona in October 1986. These data illustrate topographic profiling, pulse-spreading due to rough terrain, and surface-albedo variations. The Earth-surface target for this dataset was the SP Lava Flow north of Flagstaff, AZ. These data were acquired at an altitude of 3.4 km above ground level at a 15 pps laser repetition-rate with a T-39 ground speed of about 110 m/sec. The laser altimeter footprint on the surface was about 3 m in diameter with successive pulses separated by 7.3 m for a 45% duty-factor coverage of the surface. Data acquired over the flat desert adjacent to the flow exhibit rms range variations at the sub-meter level that are consistent with the nsec-level instrument resolution and the high signal-to-noise of these measurements. Over the rough, blocky lava flow the range record shows a distinct increase in pulse-to-pulse variation and the rms pulse width nearly doubles from a nominal 0.9 m to 1.7 m. There is also a factor-of-two decrease in peak pulse amplitude over the flow. All three effects are apparent in the data record of Fig. 4. The top trace is a series of pulse waveforms in which each plot is the average over ten adjacent waveforms. The lower amplitude and wider pulses over the Flow are apparent. The lower trace of the altimetry range record reveals the 10 m step function at the edge of the SP Lava Flow and the fine structure of the jagged volcanic material for the lava flow traverse.

Similar profiles and waveform measurements are available for a variety of other landforms in Northern Arizona. Notable among these are topographic profiles with 1-2 km of vertical relief and surface slopes up to 80° for the Grand Canyon and Humphrey's Peak and the first very-high resolution profiles of the young impact structure, Meteor Crater, near Winslow, AZ. These and other East-Coast data sets will be examined to determine the signifcance of the geoscience investigations and the engineering performance of the Shuttle Laser Altimeter from a space platform.

Figure 4 Laser altimetry of the SP Lava Flow, AZ; N-S traverse, 23 October 1986.

ACKNOWLEDGEMENTS

MONDAY, SEPTEMBER 28, 1987

CONFERENCE ROOM 5

10:45 AM–12:30 PM

MB1–5

DIAL MEASUREMENTS OF ATMOSPHERIC GASES

Robert T. Menzies, Jet Propulsion Laboratory, *Presider*

Development of Lasers and Spectral Equipment for Measurement of Atmospheric Molecular Gases

V.E. Zuev

Institute of Atmospheric Optics, Siberian Branch, USSR
Academy of Sciences, Tomsk, 634055, U.S.S.R.

The paper considers the problems of laser applications and laser equipment developed to investigate the vibration--rotation absorption spectra of atmospheric molecular gases as well as the measurements of their concentration in the field conditions based on researches carried out at the Institute of Atmospheric Optics SB USSR Academy of Sciences.

1. The set of spectrometers developed includes:
- wide-band intracavity spectrometers;
- laser spectrometers with multipass gas cells with a basis up to 110 m;
- optoacoustic spectrometers;
- a fluorescent laser spectrometer.

Intracavity spectrometers allow the wide-range detection to be made with the width up to 200 cm^{-1} and threshold sensitivity to absorption $10^{-7} - 10^{-8} cm^{-1}$.

Laser spectrometers with external multipass cells with bases 3.30 and 110 m, spectral resolution $< 10^{-3}$ cm^{-1}, the operating temperature range 40 ... 80°C were developed using the ruby-, Nd-glass, alexandrite- and dye-lasers.

Optoacoustic spectrometers were developed using the ruby-, Nd-glass- and CO_2-lasers. A spectrophone was used as a receiver. The absorption sensitivity is $10^{-8} - 10^{-9}$ cm^{-1} W^{-1} $(cm^{-1}J^{-1})$.

A multipurpose laser spectrometer operates in the six spectral ranges within 0.2 -1.2 μm. The fluorescent channel sensitivity is 10^{-11} cm^{-1}.

2. Using the spectrometers developed the following absorption lines were recorded: some thousands of new absorption lines, tens of previously unknown H_2O, CO_2, C_2H_2, N_2O, NH_3, CH_4, HBr molecular absorption bands and their isotopes, various molecular interactions were studied.

The quantitative spectroscopic data obtained were widely used for laser gas analysis of the atmosphere.

3. During the last decade a great deal of research has been undertaken together with the development and use of laser spectrometers at the Institute of Atmospheric Optics in the field of laser application for determining concentrations of different atmospheric gases and, especially, atmospheric pollutants. Special attention is paid to the CO_2-laser use as being the most perspective for the above purposes [1] . In this case we have widely used the differential technique in the trace gas analyzers.

Over the last several years much attention has been focused on solving the problems of increasing applications of CO_2-laser and the other IR molecular lasers in the systems of operative atmospheric gas analysis. This has become possible for us due to the technological advances in obtaining the high--quality ternary semiconductor $ZnGeP_2$ monocrystal and in creating the high-efficiency nonthreshold parametric frequency converters of CO_2- and CO-laser radiation. Due to the approach developed this made it possible to analyze any gas with the absorption lines within the 2-11 μm wavelength range corresponding to the maximum transmission region of this crystal.

As follows from the analysis of optical linear and nonlinear characteristics, the $ZnGeP_2$ monocrystals are the most applicable for the frequency conversion of the 2 - 8.5 μm radiation. In particular, they are the most effective frequency doublers of CO-laser radiation and CO_2-laser second harmonic radiation, for example, when the cascade higher order harmonics are generated.

When using the $ZnGeP_2$ monocrystal the 2-11 μm wavelength range can be overlapped by the frequency-converted radiation of one CO_2-laser with application of two-cascade frequency converters capable to mix the CO_2-laser self-radiation and that of its harmonics. Dense overlapping of radiation spectrum is obtained with the use of two CO_2-lasers or one double-frequency laser. Additional possibilities are presented by mixing the CO_2- and CO-laser radiation frequencies.

Finally, we are faced with the problem of overlapping of

the entire wavelength range by a fine "tooth-comb" of synthe-
sized narrow (10^{-3} cm^{-1}) laser lines and on this basis it is
possible to develop the laser sets for analyzing any atmosphe-
ric gas with absorption lines in this wavelength range.

The joint results obtained until now at the Institute of
Atmospheric Optics and at the Siberian Physico-Technical Ins-
titute at Tomsk State University have made possible the growth
of the ZnGeP$_2$ single crystals with the diameter up to 20-25 mm
and the length up to 150 mm. The best samples are characteri-
zed by the values of absorption coefficients in the region of
maximum transmission of$\leq$0.1 cm^{-1}.

Our investigations supported the possibility of creating
the efficient sources of coherent radiation in the middle
infrared on the basis of CO$_2$-lasers and frequency converters
with the ZnGeP$_2$ monocrystals.

High damage level of ZnGeP$_2$ operation characteristics al-
lows the CO$_2$-laser radiation frequency converters with ZnGeP$_2$
to be competitive with those based on CdGeAs$_2$ and another
nonlinear crystals.

Previously we reported on the measurement of CO concentra
tion using a mobile trace gas analyzer equipped with a frequ-
ency-doubled CO$_2$-laser [2]. As the measurements indicated,
the unit was capable to detect the CO concentration up to
4 ppb at the 2 km path. At present we have developed an im-
proved variant of a mobile fully automatized gas analyzer.

Figure 1 shows a block-diagram of the modernized gas analy-
zer including low-pressure two frequency-tuned CO$_2$ and one
CO-lasers and a set of the ZnGeP$_2$ monocrystal frequency conve-
rters.

The laser wavelength tuning, piezoelectric frequency ad-
justment and adjustment of ZnGeP$_2$ monocrystal to synchronism
direction as well as digitizing and processing of photorecei-
ver signals are made using a computer complex "CAMAC MERA-60"
The potentialities of this complex are expanded when using
a memory on hard magnetic disks.

The results of simulated estimation were supported by fi-
eld measurements of the multicomponent real atmosphere and
demonstrated high-operational characteristics both of the
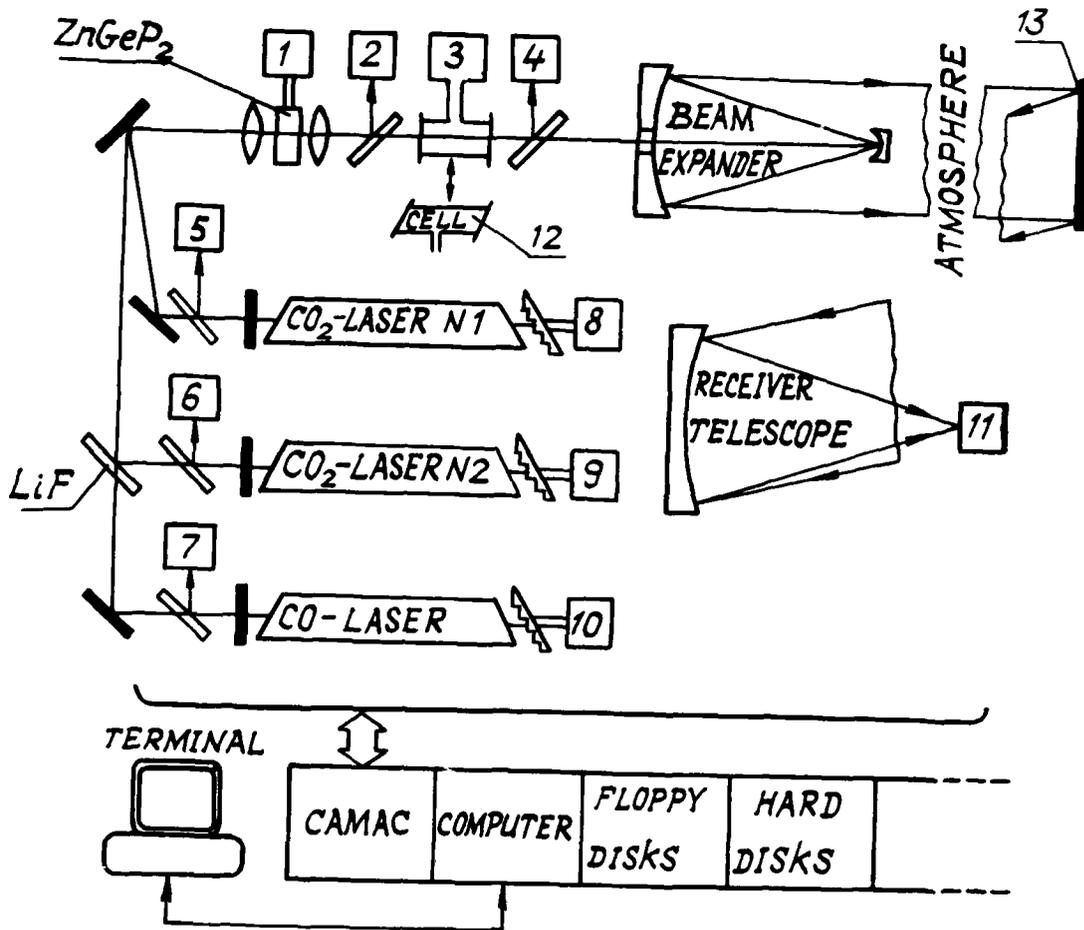
Fig.1. A block-diagram of trace gas analyzer with a set of
frequency converters. 1,8,9,10 - step motors ;
2,4,5,6,7,11 - receivers; 3 - an optoacoustic detec-
tor; 12 - a gas cell; 13 - a reflector.

frequency converters developed and the entire measurement
complex.

References

1. D.K.Killinger, N.Menyuk. Remote probing of the atmospnere
using a CO_2 DIAL system.- IEEE J. of Quant. Electron.,
v.QE -17, No.9, p.1917, 1981.

2. V.E.Zuev, Yu.M.Andreev, A.I.Gribenyukov, etc., Thirteenth
International Laser Radar Conference. Toronto, Ontario,
Canada. NASA Conference. Publication N 2413, 1986, p.108.

A DIAL System for High Resolution Water Vapor Measurements in the Troposphere

Jens Bösenberg
Max Planck Institut für Meteorologie
Bundesstr. 55, 2000 Hamburg 13, Bundesrepublik Deutschland

Water vapor is a minor constituent of the atmosphere which is of great importance for many atmospheric processes. Rather small changes in concentration can strongly affect other parameters, e.g. the radiation budget by formation of clouds. In our institute the request for experimental data on water vapor originated from studies of organized convection, where the transport of water vapor and the associated condensation obviously is one of the key processes. From this we derived our definition of the term "high resolution", it is meant to be a spatial and temporal resolution sufficient for studies of at least medium scale convective processes, or in approximate numbers, 30 sec in time, 100 m in height, 5% accuracy within the mixed layer (about 1.5 km). The same system can be used for measurements up to greater heights. Temporal and spatial resolution are of course decreasing with height, but compared to conventional radiosonde measurements this resolution can still be considered "high" throughout the troposphere.

The system we have built up to meet the requirements of convection studies is sketched in fig.1, in principle it is similar to systems which have been described by other groups before. One important feature is the use of 2 dye lasers . which are synchronously pumped with a time difference of 200 μsec. The reason for this is, that because of the small beam diameter (<1 m for heights < 2 km) the aerosol in the scattering volume may be exchanged faster than a single laser can be switched between 2 wavelengths. Then the basic assumption in the derivation of the DIAL equation may be violated, that backscatter coefficients do not differ for on and off line wavelengths. The use of 2 lasers avoids this problem, but introduces the problem of different beam shapes and pointing. Even slightly different beam shape for the 2 lasers prevents us from using the region of incomplete overlap with the field of view of the telescope for height resolved measurements, and signal dynamics cannot be reduced by geometric compression. For the region of complete overlap the pointing accuracy can be made sufficiently good by using ultra high precision beam steering components.

Another crucial point is the wavelength stability of the laser, as well as the tuning accuracy. The stability (without active stabilization) is very good, we have measured 0.01 cm^{-1} drift within 4 hours of operation. For tuning to the linecenter we are using a photoacoustic cell filled with H_2O at about 15 mbar. The tuning accuracy to the center of the low pressure line is estimated as 0.004 cm^{-1}. Bandwidth averaged over 100 shots

typically is 0.03 cm^{-1} (FWHM), measured by a Fizeau multibeam interferometer.
The most critical point in high gain lasers with oscillator-amplifier configuration is spectral impurity, defined as fraction of power out of assumed laser line shape (usually broadband amplified spontaneous emission with very low spectral power density). For errors in water vapor retrieval less than 10% up to an optical depth of 2 spectral impurity less than 1.5% is required. The specification of our laser is ASE < 1%, in practice this can be achieved only by a very tedious adjustment procedure, because at the present time the result of adjustments can be seen only by performing test measurements in the atmosphere.
A basic difficulty for a remote sensing system like this is the assessment of accuracy. The usual method of intercomparison with a radiosonde is not adequate, because of the different sampling properties, both in space and time, and because of the limited accuracy of radiosondes, too. Since the accuracy of a DIAL system is strongly dependent on its adjustment, self test capabilities are mandatory. Intercomparisons with other instruments for every new adjustment are almost impossible. So, since the density of water vapor in the measurement volume is unknown, one has to look for other quantities which can be used for testing. It should be remembered, that the DIAL equation gives the product $n*(\sigma_{on}-\sigma_{off})$. So a convenient test is to choose on and off line wavelengths such that $\sigma_{on}=\sigma_{off}$, the result then does not depend on the number density n. If both lasers are tuned to an off line wavelength, errors due to detector and electronics nonlinearities, beam geometry, incorrect timing, and signal noise (underestimated) can be detected. This is a very simple test which already covers a large number of error sources, it is routinely applied during our measurements. A more critical test results if both lasers are tuned to an on line wavelength. Then in addition errors due to incorrect tuning and differences in spectral purity are detected, errors due to signal noise are overestimated in this case. Unfortunately this test requires that both lasers are optimally adjusted for narrowband operation, which is not necessary for the DIAL experiment itself. So we did not perform this test for all measurements.
Yet another test, which shows the error due to spectral impurity, is to use 2 lines with different linestrengths. The ratio of optical depths for the 2 lines then should be constant with height (equal to the ratio of the line strengths), from the deviations spectral impurity can be calculated.
When our system had passed these tests successfully, we always got reasonable results, i.e. the distribution of water vapor concentration in space and time was in accordance with the meteorological situation, and the agreement with radiosonde ascents was within the limits given by the different sampling properties (we had to compare with ascents started about 100 km away). Figures 2 and 3 show examples, fig.2 for an unstable stratification during the afternoon with a patchy pattern typical for a convective situation. Fig.3 is a measurement on the same day in the late evening. Stratification was stable in this case,

and this is reflected by the smooth and somewhat wavy pattern. More results will be presented at the meeting, including measurements extending to heights of several kilometers.

We believe to have demonstrated, that high resolution DIAL measurements of water vapor are possible with good accuracy, and that the results are very useful for studies of atmospheric processes.
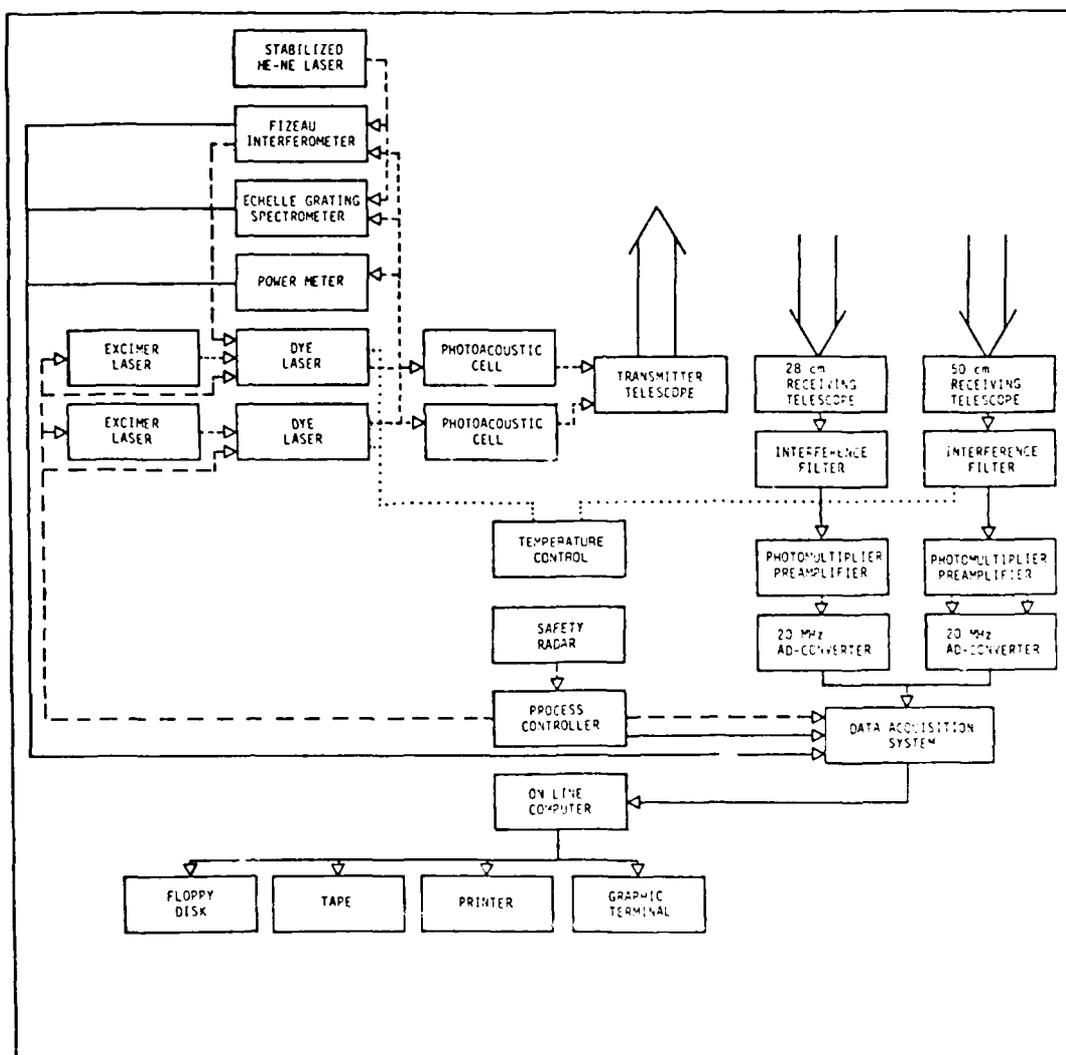
Fig. 1 : Differential absorption LIDAR system, schematic.
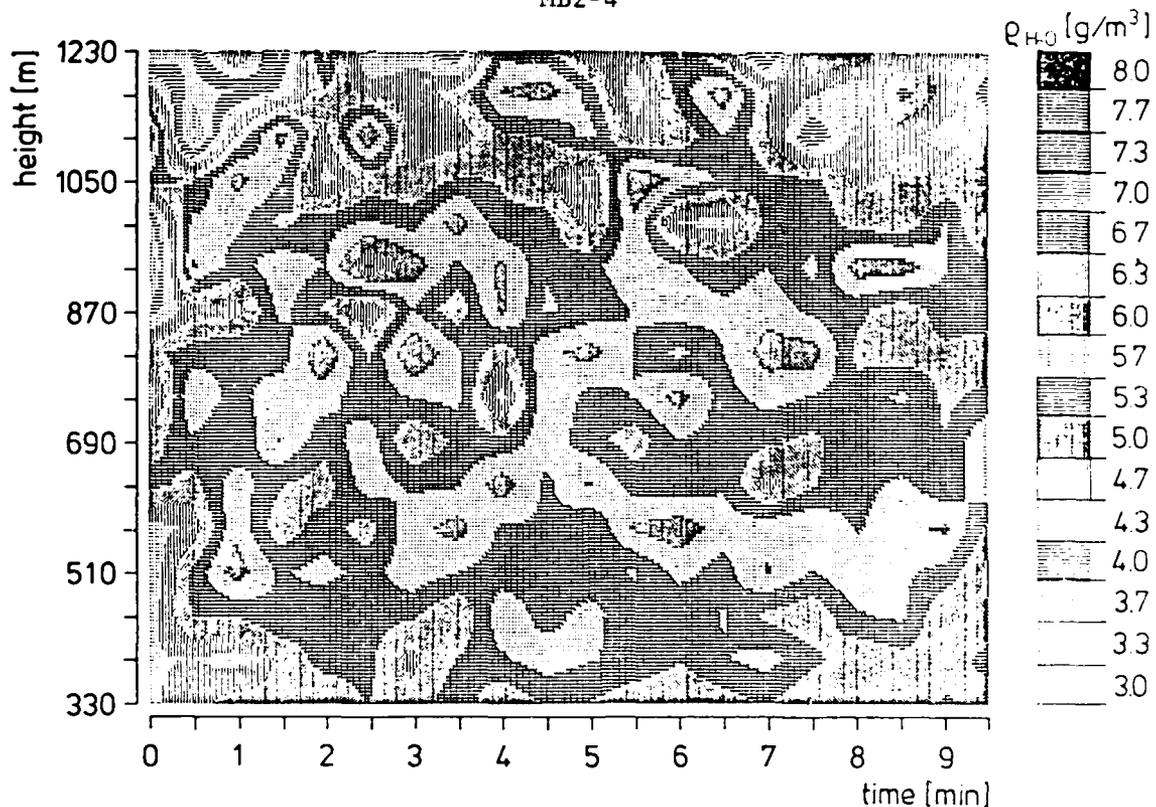
Fig. 2 : DIAL water vapor retrieval 06/12/1986 16ʰ30'. Time average over 300 shot (30 sec), range cell 60 m (smoothed by 120 m gliding average).
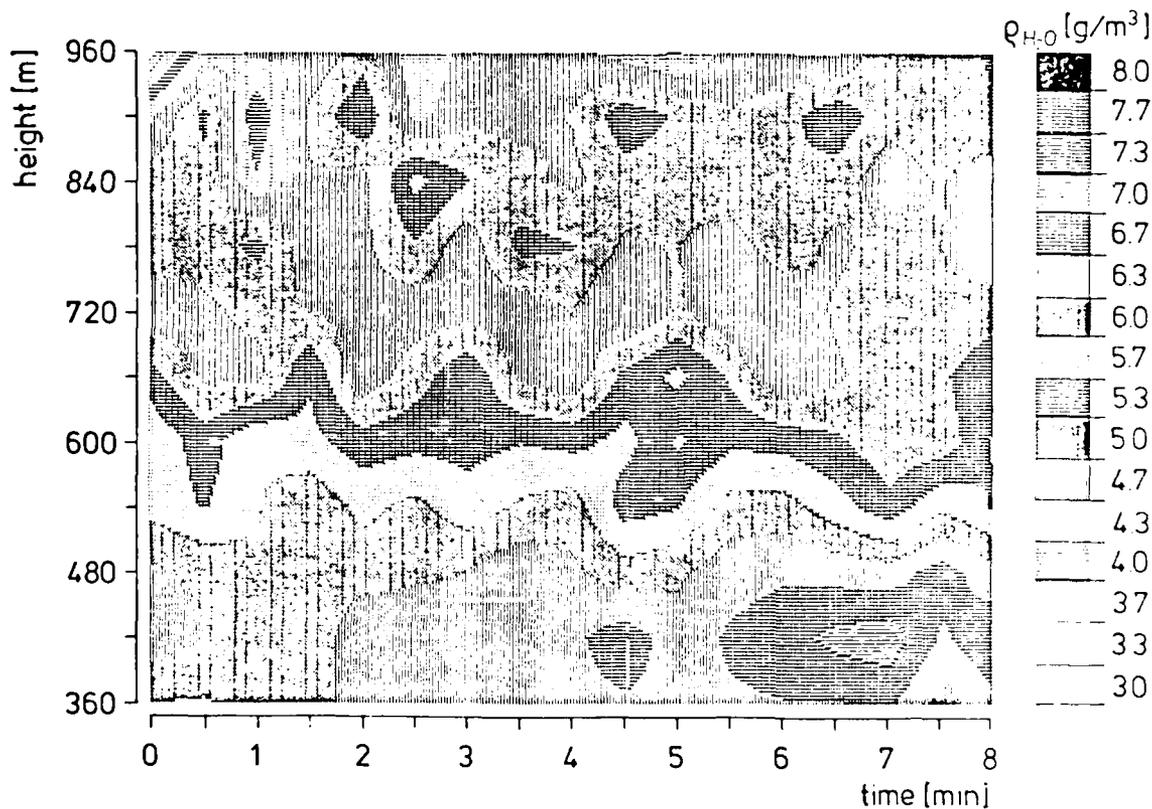
Fig. 3 : DIAL water vapor retrieval 06/12/1986 21ʰ40'. Time average over 300 shot (30 sec), range cell 60 m (smoothed by 120 m gliding average).

A Differential Absorption Lidar System for Measurements of Tropospheric NO, NO_2, SO_2 and O_3

Barrie W Jolliffe, Elizabeth Michelson, Nigel R Swann
and Peter T Woods
Division of Quantum Metrology, National Physical Laboratory
Teddington TW11 0LW, UK

1.   INTRODUCTION

A differential-absorption lidar facility has been developed by the National Physical Laboratory and mounted in a custom-built vehicle.   It is now being deployed in a range of field measurement exercises.   The facility operates in either a mobile or a stationary scanning mode.   It is presently capable of range-resolved measurements of the atmospheric concentrations of NO, NO_2, SO_2 and O_3 in the troposphere in the visible and ultraviolet regions of the spectrum.   The system can be configured to monito. up to three species near-simultaneously and is currently being extended so that it can be operated in the infrared.

The novel scientific features of the laser transmission system, the optical receiver, and the electronic data-collection and processing systems are presented below and their effects on system performance will be outlined.   Examples of measurements around industrial and urban areas are also presented.

2.   LASER TRANSMISSION SYSTEM

The DIAL facility uses frequency-doubled and -tripled YAG lasers to excite three tunable narrow-linewidth dye lasers.   Figure 1 shows a schematic of the laser transmission and receiving systems.   The oscillator cavities of the dye lasers have elements within them so that each laser generates alternate pulses with two independent wavelengths. NO_2 measurements are made at wavelengths around 448 nm; SO_2 and O_3 measurements are made by frequency-doubling dye laser radiation at wavelengths around 600 and 580 nm respectively; NO measurements are made using radiation at 226 nm which is generated by frequency mixing 1.06 μm YAG radiation with that of a frequency-doubled dye laser at 576 nm. Radiation at 1.06 μm is also transmitted to provide data on atmospheric particulate scattering. All of the beams are transmitted collinearly into the atmosphere via an off-axis reflective collimator and beam expander.

The laser wavelengths are monitored using both a calibrated monochromator with diode-array readout, and absorption gas cells.   The system is being upgraded to incorporate an on-line wavemeter.

3.   RECEIVING SYSTEM

The Dall-Kirkham receiving telescope is capable of being scanned to provide three-dimensional coverage of the atmosphere.   The transmitted beams are propagated coaxially with the telescope.   The backscatter-return signals are collimated, separated in wavelength by dichroic beam splitters and directed via narrow-bandwidth interference filters onto one of three photomultipliers or an infrared detector (Figure 1).   It has been demonstrated that the design of the receiving telescope and interference filters in combination affects the capabilities of the DIAL system, particularly in the near field.   Reliable measurements are now achieved at ranges of > 50 m.

4.   DATA COLLECTION AND PROCESSING SYSTEM

The mobile DIAL facility houses a dedicated LSI 11/73 minicomputer (with associated storage media) to control the data collection system.   A second LSI 11 is used for data processing. A CAMAC system (Figure 2) which serves as the interface for instrument control and data collection, houses four transient recorders (20 MHz at 10 bits or 10 MHz at 12 bits) to digitise the data from the four detection channels.   All the transient recorders used have demonstrated non-ideal performance and some effects of this will be presented.   Their resolution may effectively be improved under certain operating conditions by adding a variable voltage offset to the backscatter signals.   This has provided improvements in the signal-to-noise ratio of the measurements by at least a factor of two at certain ranges.

5.   MEASUREMENT RESULTS

DIAL measurements have been carried out around a number of industrial areas and examples are given below.   The results have also been compared with those obtained by calibrated in-stack monitors.

(i) SO_2 Measurements

Three-dimensional profiles of atmospheric SO_2 concentrations have been measured around oil refineries and power plant.   Figure 3 shows the concentration profiles of a plume emitted by a 2GW power plant at three distances downwind and illustrates the 'touch-down' of the plume onto the ground.   Alternatively the total SO_2 emissions of any source can be determined by scanning the laser beam across the emitted plume close to the stack exit. Measurements have been carried out which agree with those obtained by calibrated monitors within the stack to ± 10%.

(ii) NO_2 Measurements

DIAL measurements have been carried out around industrial and urban areas as part of a project to demonstrate UK compliance with the European Community Directive on NO_2 air quality.   Figure 4(a) shows a result obtained when monitoring the dispersal of NO_2 emissions downwind of a nitric-acid production plant.   Figure 4(b) shows the concentrations of traffic-related NO_2 in a street in central London, illustrating that maximum NO_2 concentrations do not always occur at road levels but can occur where the effects of atmospheric mixing produce conditions of maximum oxidation of NO to NO_2.

(iii) Simultaneous NO and NO_2 Measurements

Simultaneous range-resolved measurements of these two gases have been carried out to provide data on the dispersion and chemical reactions occurring in industrial plumes and urban atmospheres, and examples of the results will be presented.

(iv) O_3 Measurements

The vertical concentration profiles of tropospheric ozone have been measured for 24 hr periods during a European-Community project to evaluate the production and build-up of photochemical ozone around the London area.   The results have also provided data on the effects of differential backscatter of aerosols on DIAL measurements of ozone concentration.

FIGURE 1   OVERALL SCHEMATIC OF OPTICAL SYSTEM
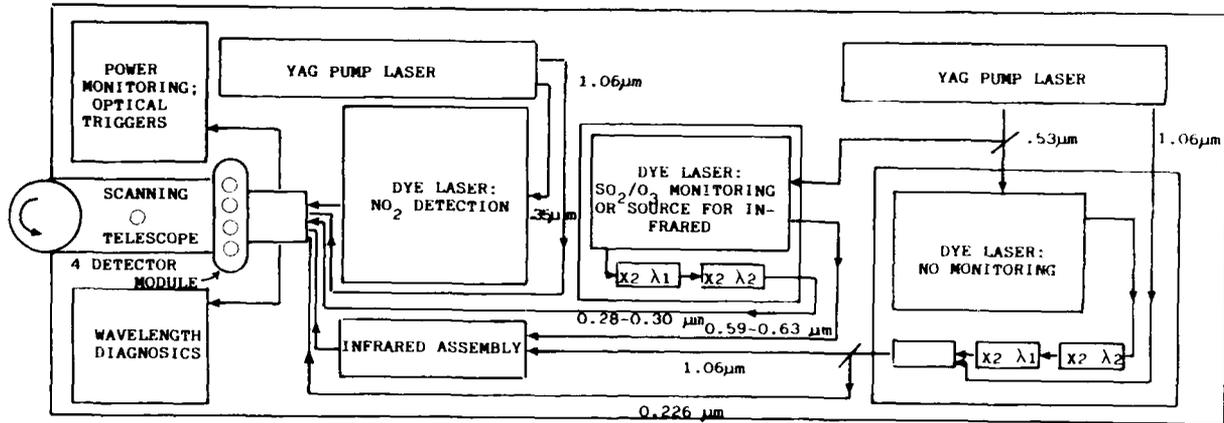
FIGURE 2:   SCHEMATIC OF DATA COLLECTION AND PROCESSING SYSTEM
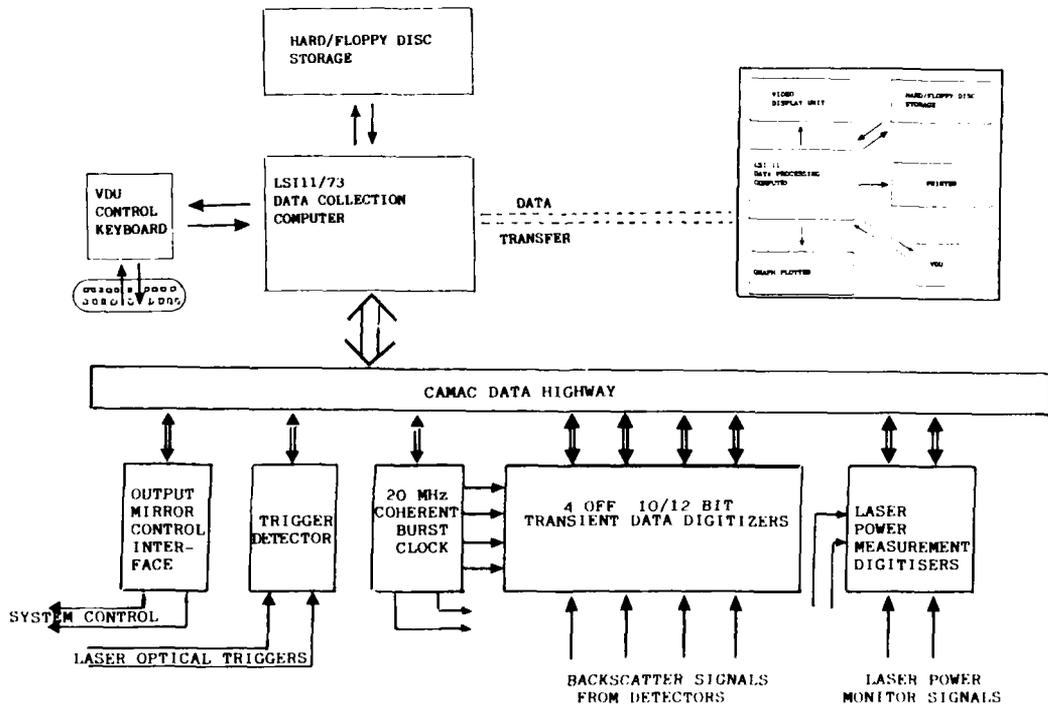
FIGURE 4A:

NO$_2$ CONCENTRATION PROFILE MEASURED 100 METRES DOWNWIND OF A NITRIC ACID PLANT
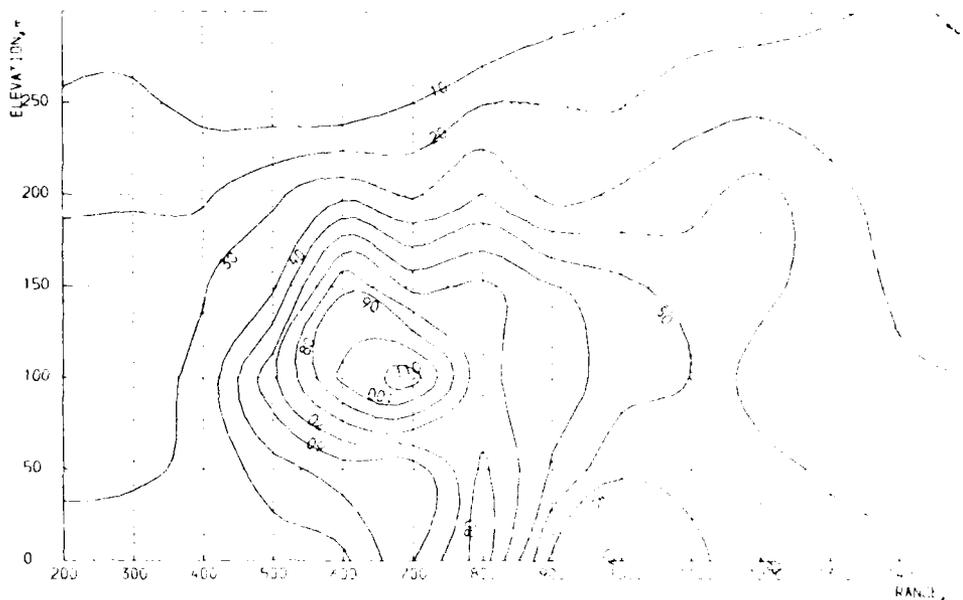
FIGURE 4B: CONCENTRATION PROFILES OF TRAFFIC RELATED NO$_2$ IN CENTRAL LONDON

BUILDING SHADOW
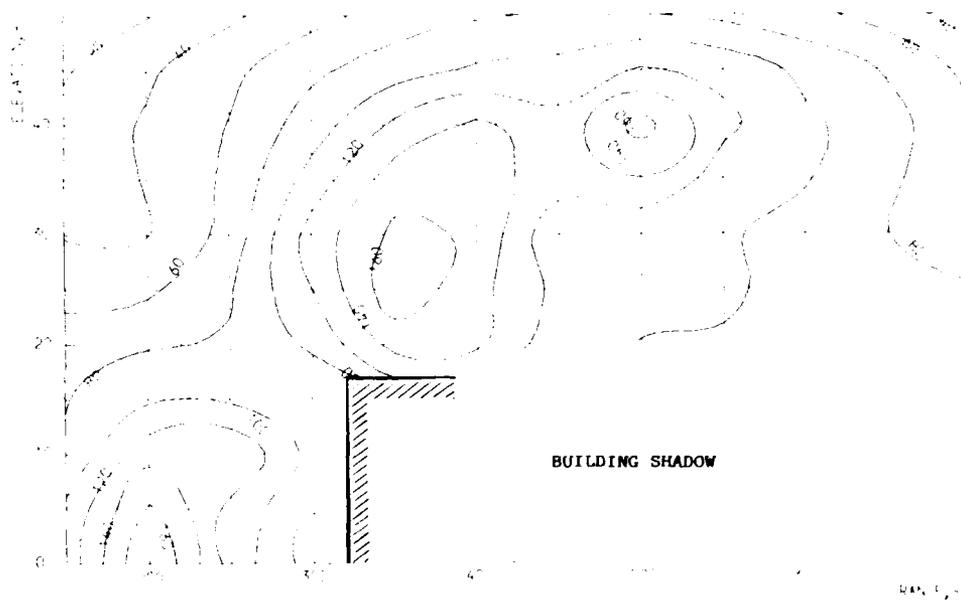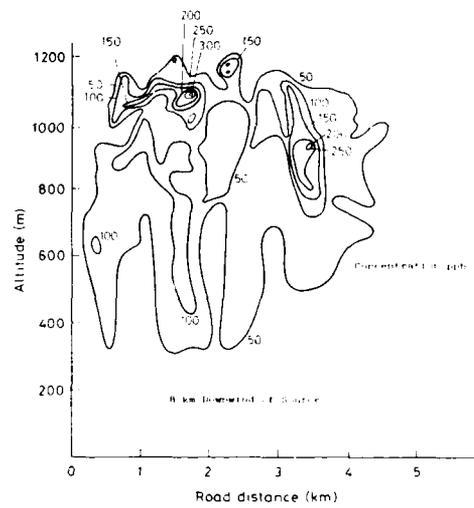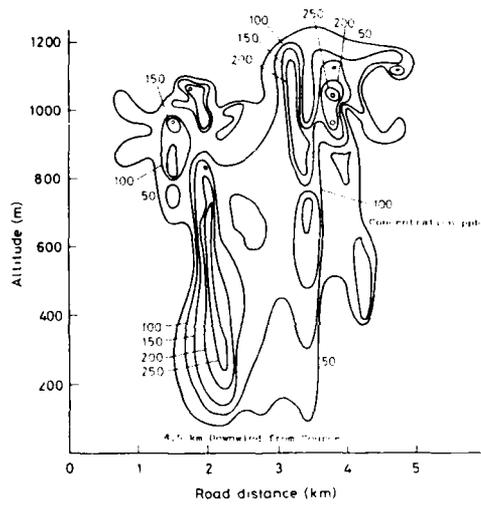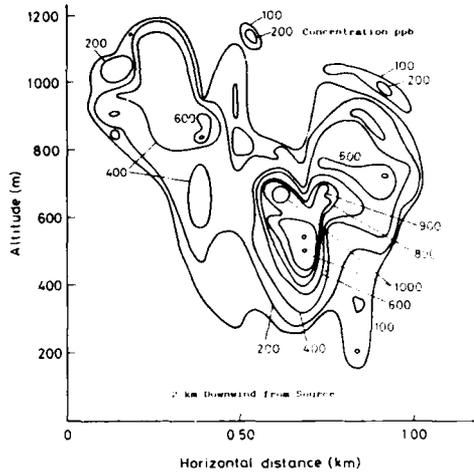
Fig. 3 So₂ distribution in a power station plume measured at 3 distances downwind of the source.

Range-Resolved Heterodyne Detection Dual CO_2 DIAL Measurements

William B. Grant, Alan M. Brothers, and David M. Tratt,
Jet Propulsion Laboratory, California Institute of Technology, 4800 Oak Grove
Drive, Pasadena, California 91109

Introduction

There are a number of measurements of atmospheric trace species and aerosols of potential interest in the 9 to 11 micron spectral region covered by CO_2 lasers. While direct detection CO_2 lidar systems have been used for such range-resolved measurements, the measurement range for such systems is limited to 2 to 4 km (Flanigan, 1986). Heterodyne detection CO_2 DIAL was proposed by Kobayasi and Inaba, 1975, and first realized by Fukuda et al., 1984 and Hardesty, 1984, using single laser lidar systems. Heterodyne detection offers increased range (to 10 km or more), but demands greater system and data analysis complexity. This paper will describe measurements made using the Mobile Atmospheric Pollutant Mapping System (MAPM).

MAPM Description

MAPM is a dual CO_2 laser DIAL system mounted in a semitrailer. The more important system components are listed in Table 1.

The 50-mJ pulse energy is sufficient in typical Pasadena atmospheres ($\beta = 10^{-7}$ m^{-1}) to give a single-pulse, speckle-limited signal-to-noise ratio (see Shapiro et al., 1981) of greater than 0.9 for ranges out to 2 - 3 km, after which it decreased per the lidar equation.

Signal Processing

Since a linear amplifier is used after the photomixer, and since there are large signal fluctuations from shot-to-shot due to speckle, the signal processing is much more complex than for direct detection. The algorithm developed for handling the data included the steps of smoothing the data over several 30-m range bins, finding the minimum noise level, subtracting it from the raw data, squaring the revised values, subtracting the pre-pulse noise level, then adding together the values of the individual pulse pairs to form an average value. Since speckle is so pronounced, several thousand pulse pairs must be averaged to obtain signals appropriate for DIAL measurements. While this procedure leads to a slight artificial enhancement of the low signal values from long ranges due to cross terms with the noise, it leads to reasonable aerosol and DIAL results.

Measurements

MAPM has been operational since September 1986. During that time it has been used to make measurements both of atmospheric parameters and system performance.

MAPM was used early in the program to address the question of DIAL signal averaging dependence with the number of lidar signals averaged, N, raised by Menyuk et al., 1985, with other references included therein. They analyzed data obtained using backscatter from a fixed hard target, and found significant departures from the expected $N^{-1/2}$ reduction in the measurement standard deviation. MAPM was used to demonstrate that for atmospheric backscatter, the $N^{-1/2}$ law was obeyed out to N = 1000 or more. This result arises because the aerosols decorrelate in times of a few microseconds, so that independent speckle patterns are measured for each lidar pulse, which is not the case for the fixed hard target. These results agree with those of Milton and Woods, 1987. In addition, it was shown that if the lidar pulse-pair ratio changes during the course of the measurement, significant departures from $N^{-1/2}$ dependence are to be expected. This would be the case if the gas concentration changed during the measurement, if the aerosol distribution changed when there is significant molecular Rayleigh scatter, or if the aerosol spectral properties changed during the measurement. (See Grant et al., 1987a.)

MAPM was next used to assess the ability of heterodyne-detection CO_2 lidar to measure water vapor concentrations at long ranges, and in the process, a thorough study of water vapor absorption coefficients at CO_2 laser frequencies was made. It was shown that the four or five sets of CO_2-laser measured water vapor coefficients can be brought into substantial agreement by using a value for the ethylene absorption coefficient at the 10P(14) CO_2 laser line (used for calibrating spectrophones) of 35.0 ± 2.0 atm^{-1} cm^{-1}, and that the values for the water vapor continuum so determined are about 30% higher than the currently accepted value quoted by the AFGL (Clough et al., 1986), based on the spectrometer measurements by Burch and Alt, 1984. MAPM was then used to measure water vapor concentrations using three different line pairs, each optimal for a different concentration-range product. (See Grant et al., 1987b.)

MAPM has also been operated on CO_2 laser line pairs appropriate for other trace species, such as ozone, methanol, and ethylene. These data were used to help determine how the measurement uncertainty changes with range. For the 50-mJ pulse energy typically used, and for an average of 6000 pulse pairs (5 minutes), with the concentration determined using the derivative approach over each 510-m range interval, the measurement uncertainty was found to be about 2% at 2 km, increasing thereafter per the lidar equation. This result is significantly better than the 8% demonstrated by Fukuda et al., 1984 and Hardesty, 1984, using single CO_2 laser heterodyne DIAL systems, as expected because both lasers can track the same atmosphere. These findings will be related to trace gas measurement sensitivities as well as to estimating how coherent-detection DIAL sensitivity scales with pulse energy.

Future Uses of MAPM

Among the possible uses for MAPM, several can be considered in the near future: measurement of SF_6 tracer releases (see, e.g., Uthe, 1986); studies of emissions from factories; studies of aerosol spatial, temporal, and spectral properties in the free troposphere (see, e.g., Menzies et al., 1984); and studies of the aerosol spectral properties as they affect DIAL measurements (see Petheram, 1981).

Acknowledgements

References

D. E. Burch and R. L. Alt, 1984. "Continuum Absorption by H_2O in 700-1200 cm^{-1} and 2400-2800 cm^{-1} Windows, Report No. AFGL-TR-84-0128 to the Air Force Geophysics Laboratory.

S. A. Clough, F. X. Kneizys, E. P. Shettle, and G. P. Anderson, 1986. "Atmospheric Radiance and Transmittance: FASCOD2," Proc. of Sixth Conference on Atmospheric Radiation, sponsored by the Am. Meteorol. Soc., Williamsburg, VA.

D. F. Flanigan, 1986. "Detection of Organic Vapors with Active and Passive Sensors: A Comparison," Appl. Opt. 25, 4253.

T. Fukuda, Y. Matsuura, and T. Mori, 1984. "Sensitivity of Coherent Range-Resolved Differential Absorption Lidar," Appl. Opt. 23, 2026.

W. B. Grant, J. R. Bogan, and A. M. Brothers, 1987a. "DIAL Signal Averaging," submitted to Applied Optics.

W. B. Grant, J. S. Margolis, A. M. Brothers, and D. M. Tratt, 1987b. "CO_2 DIAL Measurements of Water Vapor," Appl. Opt. 26, 000.

R. M. Hardesty, 1984. "Coherent DIAL Measurment of Range-Resolved Water Vapor Concentration," Appl. Opt. 23, 2545.

T. Kobayasi and H. Inaba, 1975. "Infrared Heterodyne Laser Radar for Remote Sensing of Air Pollutants by Range-Resolved Differential Absorption," Optical and Quantum Electonics 7, 319.

N. Menyuk, D. K. Killinger and C. R. Menyuk, 1985. "Error Reduction in Laser Remote Sensing: Combined Effects of Cross Correlation and Signal Averaging," Appl. Opt. 24, 118.

R. T. Menzies, M. J. Kavaya, P. H. Flamant, and D. A. Haner, 1984. "Atmospheric Aerosol Backscatter Measurements Using a Tunable Coherent CO_2 Lidar," Appl. Opt. 23, 2510.

M. J. T. Milton and P. T. Woods, 1987. "Pulse Averaging Methods for a Laser Remote Monitoring System Using Atmospheric Backscatter," Appl. Opt. 26, 000.

J. C. Petheram, 1981. "Differential Backscatter from the Atmospheric Aerosol: The Implications for IR Differential Absorption Lidar," Appl. Opt. 20, 3941.

J. H. Shapiro, B. A. Capron, and R. C. Harney, 1981. "Imaging and Target Detection with a Heterodyne-Reception Optical Radar," Appl. Opt. 20, 3292.

E. E. Uthe, 1986. "Airborne CO_2 DIAL Measurement of Atmospheric Tracer Gas Concentration Distributions," Appl. Opt. 25, 2492.

Table 1. Major MAPM Components

Item	Supplier*	Model No.	Specifications
Semitrailer	Diamond B Co.		35' long
Pulsed CO_2 Lasers	Laser Science, Inc.	PRF 150S	50 Hz
cw CO_2 Lasers	Ultra Lasertech	3822	1-2 W
Laser Coolers	Neslab	RTE-4, HX-75	
HgCdTe Detector-Signal	New England Research Center		0.25 mm x 0.25 mm 77K
HgCdTe Detector Mon.	Boston Electronics	R005A	1 mm x 1 mm 300K
Transient Digitizer	Hewlett-Packard	5182A	20 MHz 7.7 eff. bits
Data Computer	Hewlett-Packard	1000,Micro 29	
Scan Mirror Mount, Controller	Aerotech	AOM 130-24M UNIDEX III	24" aperture
Optical Table	Modern Optics		4' x 10' x 1' & lower shelf
Beam-expanding Teles.	S.O.R.L.	COAR 10X15	10X, 15 cm diam.
Optical Chopper	Rofin-Sinar	7505	10-200 Hz
Linear Phase Filter	Cir-Q-Tel		0.2 to 2.5 MHz
Off-Axis Parabolic Receiver Mirror	J. L. Wood Optical		4" off axis, 12" diam.
Flat Mirrors	Prisms Unlimited		24" dia, 1 5/8" thick
Window	Hardware store		0.4 mil polyethylene
Dome	B. E. Meyers & Co.		2-m diam. fiberglass
Linear IF amplifier	RHG Electronics	EST 3010LD	$f=$ 30 MHz, $\Delta f=$ 10 MHz
Digital Delay Generator	California Avionics	103 CR	100ns resolution to 10 s

* Mention of the supplier's name does not constitute an endorsement of the supplier by the Air Force, NASA, or JPL.

DIAL Measurements of Atmospheric Water Vapor, HCl, and CH$_4$ Using a Continuously Tunable 1.7 µm Co:MgF$_2$ Laser*

Dennis K. Killinger and Norman Menyuk
Lincoln Laboratory, Massachusetts Institute of Technology
Lexington, Massachusetts 02173-0073
(617)863-5500, Ext. 4740

There is a need for the development of new, tunable high-power lasers in the near-to-middle IR to serve as sources in lidar systems for remote sensing of the atmosphere. We report on the development and use of a new solid-state, cobalt-doped magnesium fluoride laser (Co:MgF$_2$), which is continuously tunable from 1.5 to 2.3 µm, and describe the use of this laser in a DIAL system to measure water vapor, HCl, and CH$_4$ in the atmosphere. Both path-averaged and range-resolved DIAL measurements have been made at ranges up to 6 km and 3 km, respectively.

Early investigations of the Co:MgF$_2$ laser by Moulton[1] established that the laser was continuously tunable from 1.5 to 2.3 µm, could operate either cw or pulsed, and could radiate at a single frequency. Lovold et al.[2] modified the original design to permit simultaneous Q-switching and accurate wavelength control of the laser. These modifications were necessary to make the Co:MgF$_2$ laser a practical radiation source for remote sensing measurements.

The schematic of the Co:MgF$_2$ DIAL system used in our experiments is shown in Fig. 1.[3] The Co:MgF$_2$ laser was cooled to 77°K and was longitudinally pumped by a 1.32 µm Nd:YAG laser which emitted 400 mJ, 800 µs duration, linearly polarized, TEM$_{00}$ pulses at a 3 Hz pulse repetition frequency; the output power of the Co:MgF$_2$ laser was approximately 10 mJ per pulse with a Q-switched pulse-length of 300 ns.

Coarse tuning and linewidth control of the laser was obtained using a three-element birefringent tuning filter which reduced the linewidth to approximately 1 cm^{-1} and permitted laser tuning over the spectral range from 1.6 to 1.9 µm, the maximum range obtainable with a single set of laser cavity mirrors. A quartz intracavity etalon, 0.25 mm thick and coated for 20% reflectivity, reduced the linewidth to 0.15 cm^{-1} and was angle tuned for precision scanning of the laser wavelength over a limited range of the order of 5 cm^{-1}.

As seen in Fig. 1, the bulk of the Co:MgF$_2$ laser output is used for remote sensing, but portions of the output are sampled using beamsplitters to provide diagnostics of the laser wavelength and power. The remote sensing portion of the output beam was expanded to a 3 cm diameter and directed to the target with a 50 cm beam steering mirror. The return lidar beam was sent through a 30 cm Cassegrain telescope and detected by a cooled InSb detector. The output signal was then measured by an A/D converter or a waveform digitizer and analyzed by the computer. The computer also controls and scans the wavelength of the laser by use of a Burleigh "Inchworm" which changes the slant angle of the thin etalon in the laser cavity.

The system can run the wavelength control of the laser either in a continuous scanning mode, or in a differential-absorption (DIAL) mode. In this latter case only two wavelengths, on and off an absorption line, are employed and the position of the etalon is toggled between these two positions. In the continuous scanning mode, the output of the Fabry-Perot is used to calibrate the relative wavelength of the laser and to correctly scale the wavelength scan of the laser and lidar returns.

The system has been operated in the continuous scanning mode to obtain path-averaged (column-content) measurements using backscattered returns from topographic targets. Figure 2 shows a plot of the normalized lidar return obtained from foliage on hillsides located 3 km and 6.7 km from the Laboratory as a function of the laser wavelength. The wavelength scan covers approximately 5 cm^{-1}. All the major absorption regions can be identified with known water vapor absorption lines.

The $Co:MgF_2$ DIAL system has sufficient transmitted laser energy and optical detection sensitivity to measure the lidar backscatter from natural occurring aerosols in the atmosphere, and thereby provides the capability of detecting the range-resolved concentration of various species in the atmosphere. As an example, Fig. 3 shows the lidar signal, averaged over 50 pulses, as a function of range for atmospheric backscatter. As seen, the $Co:MgF_2$ DIAL system is capable of detecting aerosol backscatter at ranges out to 3.8 km, with significant signal levels at ranges of 0.2 to   km.

We have also investigated the utility of the $Co:MgF_2$ DIAL system for the detection of HCl and CH_4 in the atmosphere. By scanning across the prominent lines of HCl and CH_4 near 1.7525 µm and 1.6713 µm, respectively, the sensitivity of the DIAL system was established; within these sensitivity limits there was little indication of detectable HCl (< 0.2 ppm) or of CH_4 (< 2 ppm) in the atmosphere. Further studies using an artificial plume of HCl injected into the atmosphere were conducted which demonstrated range resolved DIAL measurements of an HCl plume with a sensitivity of a few ppm and range resolution of 200 m.

References

1.   P. F. Moulton, IEEE J. Quantum Electron. QE-18, 1185 (1982).
2.   S. Lovold, P. F. Moulton, D. K. Killinger, and N. Menyuk, IEEE J. Quantum Electron. QE-21, 202 (1985).
3.   N. Menyuk and D. K. Killinger, Appl. Opt. (1 August 1987).
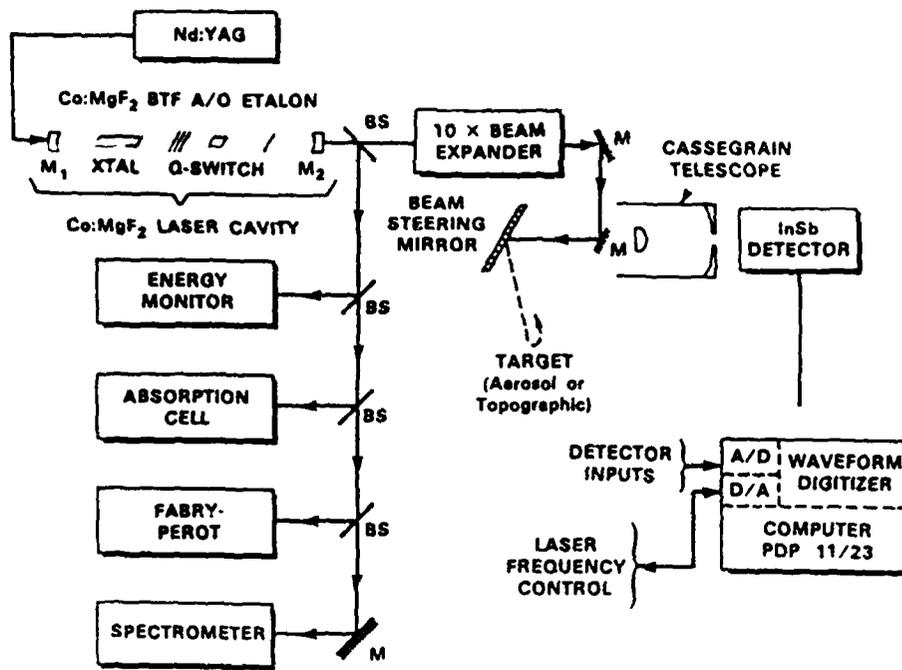
Fig.1 Schematic of Co:MgF$_2$ DIAL System

(a) HILLSIDE AT RANGE = 3 km

├─ 0.2 cm^{-1}

(b) HILLSIDE AT RANGE = 6.7 km

WAVELENGTH (μm)
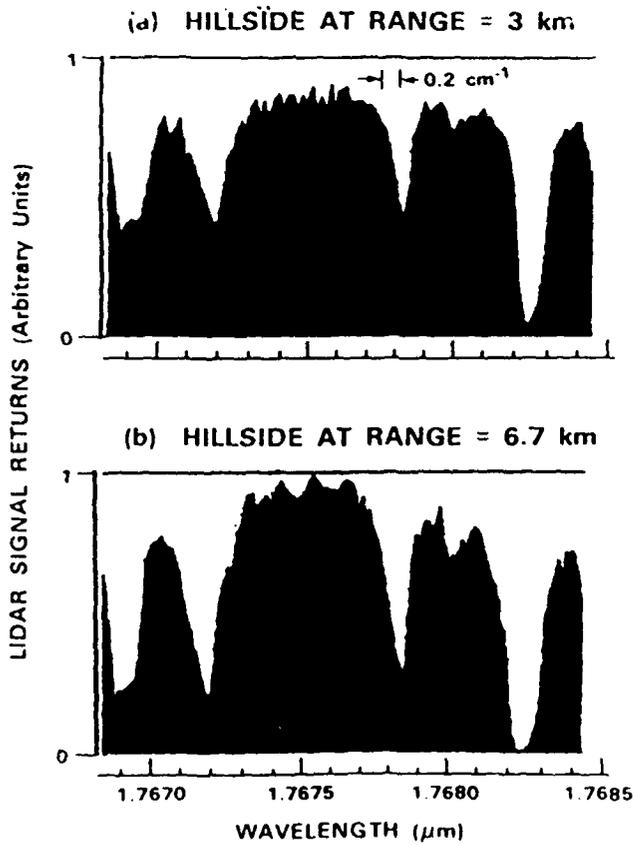
Fig.2 LIDAR Returns backscattered from Hillside; absorption features are due to water vapor in the atmosphere.
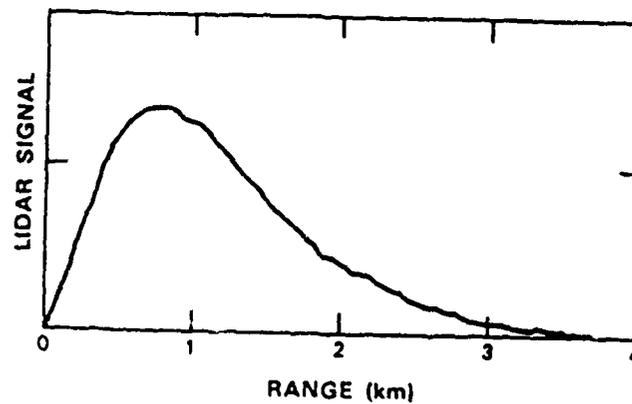
Fig. 3. Range-resolved Co:MgF$_2$ lidar returns

MONDAY, SEPTEMBER 28, 1987

CONFERENCE ROOM 4

2:00 PM–5:00 PM

MC1-21

POSTER SESSION
LIDAR MEASUREMENTS AND ANALYSES

Jack Bufton, NASA Goddard Space Flight Center, *Copresider*

Jadeshi Aruga, Ministry of Posts and Telecommunications, Japan, *Copresider*

Analysis of Information Content of Multifrequency Laser
Sounding of Aerosol and Molecular Atmosphere

V.E. Zuev, S.I. Kavkyanov, G.M. Krekov
Institute of Atmospheric Optics, Siberian Branch, U.S.S.R.
Academy of Sciences, Tomsk, 634055, U.S.S.R.

The use of a single-frequency lidar for investigating
the space-time structure of atmospheric aerosol has a limi-
ted field of application due to a possible ambiguity of in-
terpreting the experimental data [1-3]. This paper considers
the potentialities of spectral measurements for obtaining
more complete data on the aerosol profiles.

Neglecting by the effects of incoherent scattering,
the dependence of the lidar signal intensity received at
the frequency of emitted signal on spatial distribution of
two-component aerosol and molecular mixture in the atmosphe-
re is determined by the known equation

$$S(z,\lambda) = \left[\beta_a(z,\lambda) + \beta_m(z,\lambda)\right] exp\left\{-2\int_{z_c}^{z}\left[\sigma_a(z',\lambda) + \sigma_m(z',\lambda)\right]dz'\right\} \quad (1)$$

where $S(z,\lambda)$ is the signal normalized in the point z_o; σ_a
and β_a are the aerosol coefficients, and σ_m and β_m are
the molecular coefficients of total scattering and backscat-
tering.

The number of unknown functions in (1) exceeds that of
the measured ones by a factor of three (taking into acco-
unt the known relation $\beta_m(z,\lambda)/\sigma_m(z,\lambda) = g_m = 3/8\pi$)
for any number of sounding wavelengths λ_i. At single-frequ-
ency sounding the introduction of the profile $g_z(z) =$
$= \left[\beta_a(z) + \beta_m(z)\right]/\left[\sigma_a(z) + \sigma_m(z)\right]$ and the use of any a priori
information on its characteristics was the only possible
method for making supplementary definition [1-3] (it was
impossible to separate aerosol and molecular components).
In the case of multifrequency sounding one can limit oneself
to some functional peculiarities of spectral behavior of the
functions being restituted to separate them on the basis of
(1). A more general method for making supplementary defini-
tion is the substitution of the spectral behavior $\beta_a(\lambda)$, $\sigma_a(\lambda)$

by the expansion over a certain set of known functions, with the estimate of the parameters of expansion by the laser sounding data. When using the series on powers of increments $(\lambda - \lambda_i)/\lambda_i$ (in logarithmic scale)

$$\ln \beta_a(z,\lambda) = \ln \beta_a(z,\lambda_i) + \frac{\partial \ln \beta_a}{\partial \ln \lambda}\left(\frac{\lambda - \lambda_i}{\lambda_i}\right) + \frac{1}{2}\frac{\partial^2 \ln \beta_a}{\partial \ln \lambda^2}\left(\frac{\lambda - \lambda_i}{\lambda_i}\right)^2 + \ldots \quad (2)$$

$$\ln \sigma_a(z,\lambda) = \ln \sigma_a(z,\lambda_i) + \frac{\partial \ln \sigma_a}{\partial \ln \lambda}\left(\frac{\lambda - \lambda_i}{\lambda_i}\right) + \frac{1}{2}\frac{\partial^2 \ln \sigma_a}{\partial \ln \lambda^2}\left(\frac{\lambda - \lambda_i}{\lambda_i}\right)^2 + \ldots \quad (3)$$

One can often limit oneself in (2,3) only by the first increments correct to the two parametric functions
$\eta_\beta(z,\lambda) = -\partial \ln \beta_a/\partial \ln \lambda$, $\eta_\sigma(z,\lambda) = -\partial \ln \sigma_a/\partial \ln \lambda$, characterizing the relative decrease of β_a , σ_a with the λ increase, and varying within the limits to be estimated (as a rule, $0 \lesssim \eta_\beta, \eta_\sigma \lesssim 2$ [4]). In the analogous (2,3) expansion for β_m , σ_m the parameter $\eta_m = 4$, and the terms being of more than the first order of magnitude are equal to zero. The number of parametric functions in the expansion (2,3) in the sum with a series of restituted profiles should not exceed the number of operating wavelengths in Eq.(1). For simultaneous restitution of three profiles β_a , σ_a , σ_m even in the case of the use of only linear parts of expansions (2,3) without taking into account the a priori information on η_σ , η_β the number of operating frequencies must not be less than five. In practice, with less number of operating frequencies one should use any simplifying assumptions or the accompanying measurements (model estimates).

Figures 1 and 2 present the results of the numerical experiment on single-frequency (Fig.1) and double-frequency (Fig.2) sounding of aerosol profiles (the aerosol model [4] was used).

A comparison of Figs.(1) and (2) indicates that the double-frequency sounding even with rough simplifying assumptions allows the lidar measurement information content to be increased versus single-frequency information content. Further increase of the number of sounding wavelengths allows the decrease of arbitrariness in selecting the spectral dependences η_β , η_σ and their estimate from the lidar data.
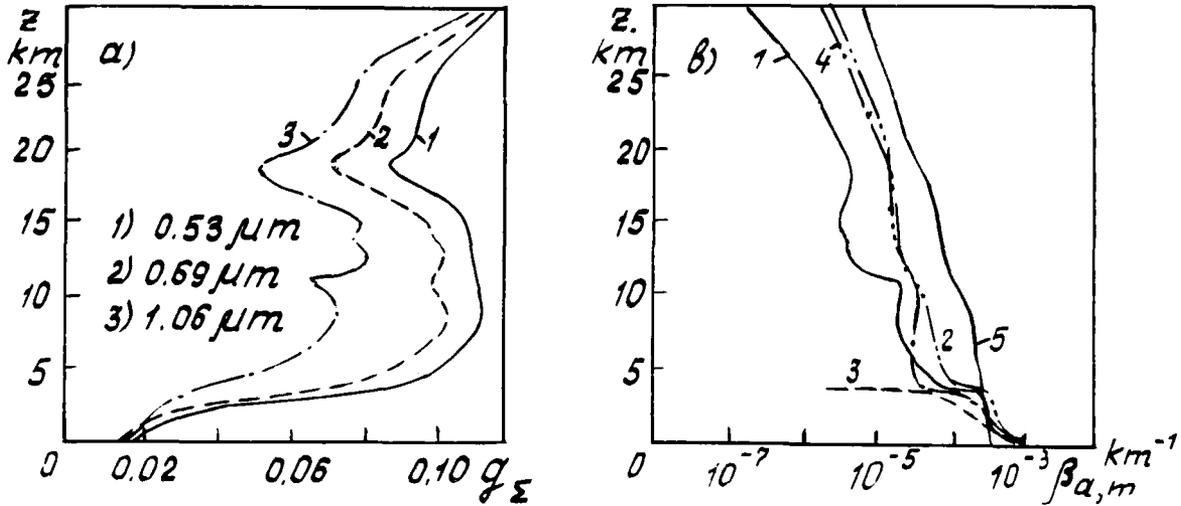
Fig.1. a) Altitude behavior of the lidar ratio g_Σ for $\lambda = 0.53$, 0.69, $1.06\,\mu m$. b) The results of restituting the model profile $\beta_a(z)$ (curve 1) when using the simplifying assumptions on the altitude behavior $g_\Sigma(z)$: curve 2-

$-g_\Sigma(z) = g_\Sigma(0)$; curve 3 $- g_\Sigma(z) = g_\Sigma(30)$; curve 4 $- g_\Sigma(z) =$

$= g_\Sigma(0) + z[g_\Sigma(30) - g_\Sigma(0)]/30$ ($\lambda = 0.69\,\mu m$). The profile $\beta_m(z)$

(curve 5) when restituting $\beta_a(z)$ is assumed to be given.
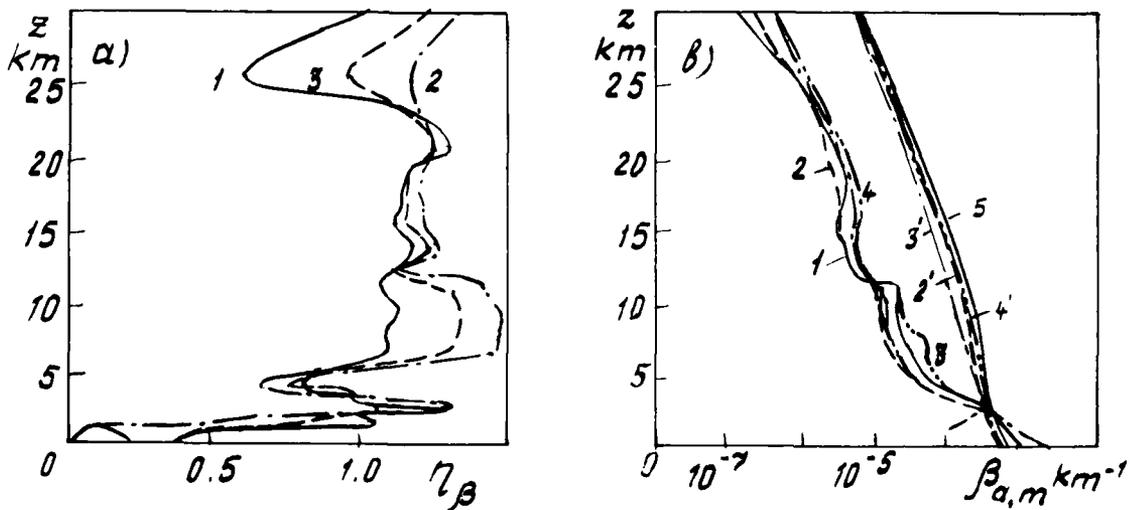
Fig.2. a) Altitude behavior of the index $\eta_\beta(z)$ for three pairs of wavelengths: 1 - 0.53 and $0.69\,\mu m$; 2 - 0.69 and $1.06\mu m$; 3 - 0.53 and $1.06\,\mu m$. b)The results of restituting the model profiles β_a and β_m (curves 1 and 5) using the simplifying assumptions on the altitude behavior η_β : curves 2.2'- $\eta_\beta(z) = \eta_\beta(0)$;

$3,3'$ $-\eta_\beta(z) = \eta_\beta(30)$; $4,4'$ $-\eta_\beta(z) = \eta_\beta(0) + z[\eta_\beta(30) - \eta_\beta(0)]/30$ ($\lambda_1 = 0.69$, $\lambda_2 = 1.06$).

At restitution the attenuation was assumed to be absent ($\sigma_a = 0$).

Leaving for simplicity of computations only the linear parts of increments $\ln\beta_a$ and $\ln\sigma_a$ in (2,3) we obtain after logarithmic operations and differentiation (1) over $\ln\lambda$ for the relative spectral behavior of the lidar signal $\eta_s = -\partial\ln S/\partial\ln\lambda$:

$$\eta_s(z,\lambda) = \eta_\beta(z,\lambda)\frac{\beta_a(z,\lambda)}{\beta_\Sigma(z,\lambda)} + \eta_m\frac{\beta_m(z,\lambda)}{\beta_\Sigma(z,\lambda)} - 2\int_{z_0}^{z}\left[\sigma_a(z',\lambda)\eta_\sigma(z',\lambda) + \eta_m\sigma_m(z',\lambda)\right]dz' \quad (4)$$

Let us substitute in the set (1) all the equations, except the first, by the equations of (4) type. Now we obtain an equivalent set of equations which is completed with equations following from (2,3)

$$\frac{\lambda_i}{\lambda_i-\lambda_1}\ln\frac{\sigma_a(z,\lambda_i)}{\sigma_a(z,\lambda_1)} = -\eta_\sigma(z); \quad \frac{\lambda_1}{\lambda_i-\lambda_1}\ln\frac{g_a(z,\lambda_i)}{g_a(z,\lambda_1)} = -\eta_g(z); \quad \frac{\lambda_1}{\lambda_i-\lambda_1}\ln\frac{\sigma_m(z,\lambda_i)}{\sigma_m(z,\lambda_1)} = -\eta_m \quad (5)$$

The set of equations (1),(4) and (5) can be solved using the iteration methods that makes it possible to use the a priori information available for making supplementary definition and stabilization of analytical solutions of Eq.(1), (4) over the variable z [1-3]. For example, when assigning the initial approximation $\sigma_m(z,\lambda_1)$, $g_a(z,\lambda_1)$ in Eq.(1), one can obtain

$$\sigma_a(z,\lambda_1) = \frac{S}{g_a}\exp\left\{-2\int_{z_0}^{z}\left(\frac{g_m}{g_a}-1\right)\sigma_m\right\}\left\{\frac{1}{\beta_\Sigma(z_0)} - 2\int_{z_0}^{z}\frac{S}{g_a}\exp\left[-2\int_{z_0}^{z'}\left(\frac{g_m}{g_a}-1\right)\sigma_m\right]\right\}^{-1} - \frac{g_m}{g_a}\sigma_m.$$

When recalculating successively the profiles σ_m, σ_a, g_a for η_σ, η_g from λ_i to λ_{i+1}, taking into account Eq.(5) and initial approximation, one can refine the values η_σ, g_a using the analytical solutions of Eqs.(4)

$$\eta_\sigma(z) = \frac{\beta_a(z_0)}{\beta_\Sigma(z_0)}e^{-2\int_{z_0}^{z}\beta_\Sigma/g_a}\left\{\eta_\sigma(z_0) + \frac{\beta_\Sigma(z_0)}{\beta_a(z_0)}\int_{z_0}^{z}\left[2\eta_m\sigma_m + \eta_s' - \left(\frac{\beta_a\eta_a+\beta_m\eta_m}{\beta_\Sigma}\right)'\right]e^{-2\int_{z_0}^{z'}\beta_\Sigma/g_a}\right\},$$

$$g_a(z,\lambda_1) = g_m\frac{\sigma_m}{\sigma_a}\left[(\eta_m-\eta_s) - 2\int_{z_0}^{z}(\eta_m\sigma_m + \eta_\sigma\sigma_a)dz'\right]/\left[\eta_s-\eta_g-\eta_\sigma\cdot 2\int_{z_0}^{z}(\eta_m\sigma_m+\eta_\sigma\sigma_a)dz'\right].$$

The analytical estimates can be also obtained for σ_m, η_g.

Model calculations with the use of three wavelengths and given processing scheme have made it possible to estimate simultaneously the aerosol altitude behavior $\beta_a(z)$ and molecular $\beta_m(z)$ profiles as well as $\eta_\beta(z)$ used when restituting $\beta_a(z)$, $\beta_m(z)$.

References

1. V.E.Zuev, S.I.Kavkyanov, G.M.Krekov. Izv.Akad.Nauk SSSR Fiz.Atmos.Okeana, 1983,N3.
2. V.E.Zuev, S.I.Kavkyanov, G.M.Krekov. Adv.Space Res.,1985,N6.
3. G.M.Krekov, S.I.Kavkyanov, M.M.Krekova. Interpretation of signals of atmospheric optical sounding, Novosibirsk, Nauka,1987.
4. V.E.Zuev, G.M.Krekov. Optical Atmospheric Models. L., Gidrometeoizdat, 1986.

Remote Determination of Meteorological and Optical Parameters
of the Atmosphere Using a Raman Lidar

Yu.F.Arshinov, S.M.Bobrovnikov, S.N.Volkov, V.E.Zuev,
V.K.Shumskii
Institute of Atmospheric Optics, Siberian Branch,USSR Academy
of Sciences, Tomsk, 634055, U.S.S.R.

As known, the boundary atmospheric layer is just the re-
gion between the Earth's surface and the free atmosphere
where most dynamic processes take place. The investigation
of these processes is very important for obtaining the in-
formation on the conditions of temperature inversions forma-
tion as well as on the diffusion of various atmospheric com-
ponents including pollutions. It is also important for stu-
dying the heat transfer from the ground to the atmosphere.

The determination of characteristics of the boundary at-
mospheric layer, normally, requires the information about
the profiles of meteorological parameters and about the ver-
tical stratification of aerosol.

In this connection the lidar methods for obtaining the
above atmospheric characteristics are, of course, the most
promising, taking into account higher spatial and temporal
resolutions they can provide in comparison with the conven-
tional radio-sonde techniques.

This paper presents some results of lidar measurements of
the atmospheric temperature profiles and the profiles of so-
me optical parameters of the atmosphere obtained with the
Raman lidar.

The combined Raman lidar used in the study allowed the de-
termination of temperature profiles and the profiles of op-
tical parameters to be made simultaneously using pure rota-
tional Raman spectra of N_2 and O_2 and the lidar return due
to Mie light scattering.

Basic parameters of the lidar facility as well as key
ideas of the technique for measuring temperature profiles
one can find in [1] , while some details of the method for
remote determination of optical parameters of the atmosphere
are described in [2] and [3] .

The temperature profile is retrieved from the profile of the intensity ratio of two portions from the pure rotational Raman spectrum of N_2 and O_2 molecules. The attenuation of summed signal from both portions of pure rotational Raman spectra of N_2 and O_2 corrected for squared range dependence provides for information on the atmospheric transmission profile. Thus obtained data allows one to assess simultaneously the profiles of atmospheric temperature, extinction coefficient, backscattering coefficient and the profile of the so-called lidar ratio, which is the parameter relating the latter two optical parameters.

Figures 1a, b and c present the results of measurements carried out in the outskirts of Tomsk. The data obtained with the Raman lidar are presented by solid lines, while the dashed curve in Fig.1a shows the temperature profile obtained with the aircraft facility. In Fig. 1b the dashed curve presents the profile of aerosol backscattering coefficient obtained using a single frequency Mie scattering lidar [2]. Figure 1c shows the lidar ratio profile measured with the Raman lidar solely, because, unfortunately, there were no other instrumentation providing for such information at the time the experiments were carried out.

The atmospheric situation occurring during this experiment can be characterized by the presence of a deep temperature inversion layer in which the optically thick aerosol layer is trapped, as it is clearly seen from the altitude behavior of the extinction coefficient (see Fig. 1b).

Good agreement between the Raman lidar data and those data obtained independently convincingly illustrate the capabilities of the combined Raman lidar in its application to study the boundary atmospheric layer.

References

1. Yu.F.Arshinov, S.M.Bobrovnikov, V.E.Zuev and V.M.Mitev, Appl. Opt., v.22, p.2984, 1983.

2. Yu.F.Arshinov, Yu.S.Balin, S.M.Bobrovnikov, I.A.Rasenkov, Sov.Journ. of Quant.Electr., v.10, N2, pp.390-397, 1983.

3. S.M.Bobrovnikov, In book: The 7-th All-Union Symposium on Laser and Acoustic Sensing of the Atmosphere, Tomsk, 1982, pp.16-18.

November 13, 1986, 20^{00} ЛТ
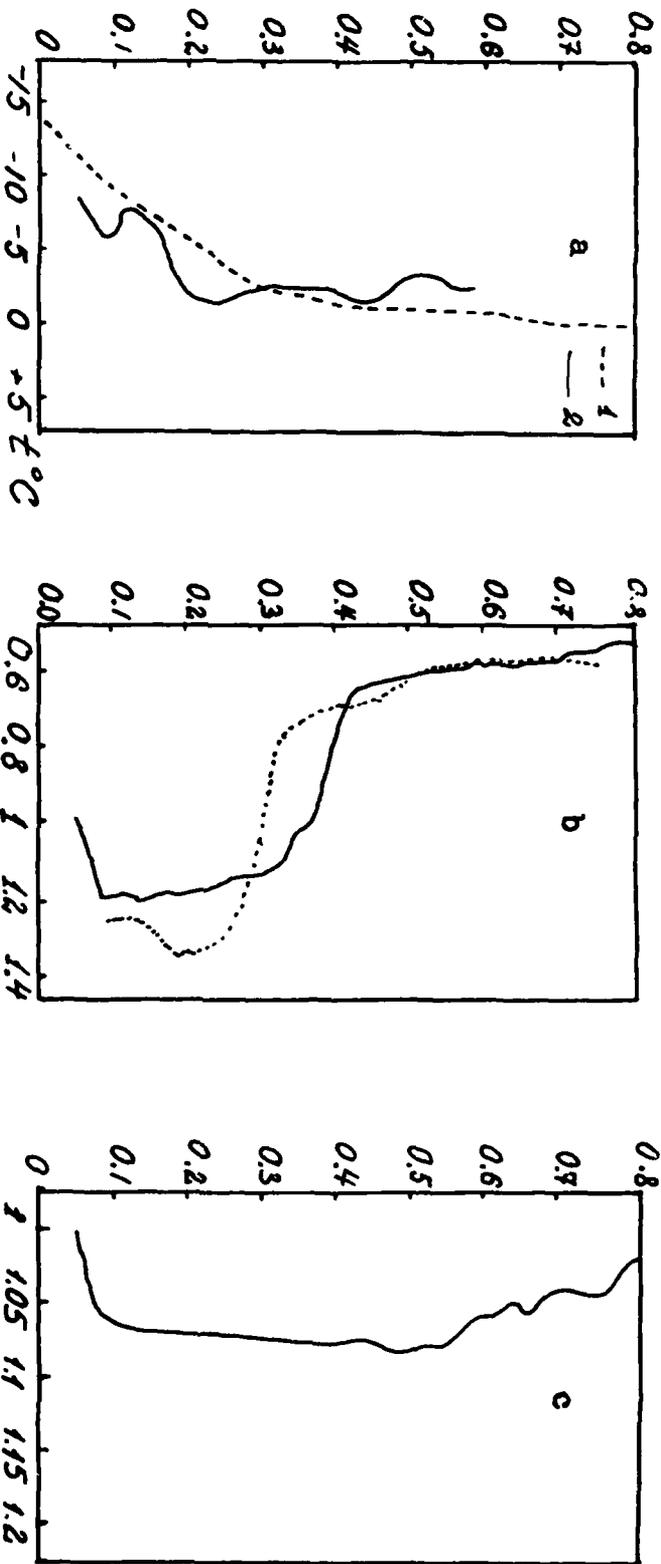
temperature

Extinction coefficient
(relative units)

lidar ratio
(relative units)

Fig.1

Vertical distribution of atmospheric parameters:

a) temperature profiles measured with the Raman lidar (solid line) and aircraft (dashed curve);
b) vertical distribution of extinction coefficient measured with the Raman lidar (solid line) and with single frequency Mie scattering lidar (dashed curve).
c) the profile of lidar ratio restored from the Raman lidar data.

Instrumental and Atmospheric Considerations in the Development and Application of an Airborne/Spaceborne Water Vapor DIAL System

Edward V. Browell
Atmospheric Sciences Division
NASA LaRC, Mail Stop 401A
Hampton, VA 23665-5225

and

Syed Ismail
ST Systems Corporation
28 Research Drive
Hampton, VA 23666

Introduction

The Differential Absorption Lidar (DIAL) technique can be used to measure concentration profiles of many atmospheric gases[1]. Atmospheric water vapor (H_2O) has been measured with the DIAL technique from ground-based[2-4] and airborne systems[5]. In the DIAL technique, two laser wavelengths are transmitted near simultaneously, one "on" the peak of the H_2O absorption line and another away from, or "off" the peak. In the range resolved DIAL measurement, H_2O concentration between two ranges is calculated using the well known DIAL equation[1], which is a function of the on and off signals at the two ranges and the effective H_2O differential absorption cross section. Random errors due to noise in the detected signal and systematic errors due to uncertainties in the knowledge of the effective cross section, $\Delta\sigma$, contribute to inaccuracy in the DIAL measurements. The development of a DIAL system must give full consideration to these two sources of error and any known systematic offsets can be at least partially compensated for in the DIAL data analysis phase. A brief discussion of these effects is given in this paper, and a more detailed description of these effects is given in Ismail and Browell[6].

The strength of the lidar signal depends upon the lidar range, laser pulse energy, area and optical efficiency of the receiver, and detector quantum efficiency. The signal also depends upon atmospheric backscattering at the measurement range and atmospheric extinction (including absorption by H_2O) to that range. Using Poisson statistics, the signal-to-noise ratio is given by $\sqrt{S}$, where S is the total number of photoelectrons during the signal observation interval Δt. This implies that the lidar parameters should be chosen, where possible, to maximize S. However, consideration must also be given to other noise sources like the background light, detector dark current, signal amplifier and digitizer errors, noise spikes in the detector that do not follow the Poisson statistical model, and signal induced noise effects.

We have carried out signal measurement error simulations for the Lidar Atmospheric Sensing Experiment (LASE)[7] for day/night background conditions using several H_2O lines and summer midlatitude atmospheric profiles.

The LASE parameters are given in Table 1. A silicon avalanche photodiode detector (APD) was selected for this system because of its high quantum efficiency and reasonable noise characteristics over the expected signal range of the LASE measurements. The resulting signal-to-noise characteristics of the APD system were found to be superior to those of the best available photomultiplier tubes (Kenimer, private communication, 1985). The signal measurement simulations for LASE showed that using two H_2O lines, the H_2O profiles in the 0-10 km region can be measured with an accuracy of <5% due to the combined signal random errors. The horizontal and vertical resolution of these measurements would be 10 km and 200 m, respectively, during nighttime and 20 km and 300 m, respectively, during daytime.

Simulations of a spaceborne H_2O DIAL system[8] in the 727-nm region showed that, because of the lower lidar signals, photomultiplier tubes will be superior to photodiodes which have limiting high dark current noise. The DIAL measurement errors in the lower troposphere (0-5 km altitude) would be $\leq$5% using a horizontal resolution of 250 km and a vertical resolution of 500 m during nighttime. Daytime measurements would require Fabry-Perot interferometers for solar background rejection.

Absorption Cross Section Influence

Large systematic errors in DIAL measurements can arise due to uncertainties in the knowledge of the differential absorption cross section. Because of the non-monochromatic nature of the laser spectral profile and the atmospheric influences on the H_2O absorption profile, uncertainties arise in the calculated effective absorption cross section. This leads to additional inaccuracy in the DIAL H_2O measurement. The instrumental and atmospheric effects that contribute to uncertainties in the knowledge of the absorption cross section are: (a) Influence of H_2O absorption on laser spectral profile, (b) Doppler broadening of Rayleigh backscattered signal and other atmospheric spectral broadening effects, (c) Pressure shift of absorption lines, (d) Temperature sensitivity of absorption lines, (e) Laser spectral purity, and (f) Laser position uncertainty and tuning error. Many of these effects have been fully discussed in the literature (Ref. 6 and references therein). These effects are applicable to both airborne and spaceborne DIAL systems and are not laser energy dependent.

The H_2O absorption in the atmosphere distorts the laser spectral profile. Ideally, monochromatic laser radiation will eliminate this influence. However, other effects in the atmosphere may reduce the sensitivity of this effect. Clearly, laser spectral profiles with widths $\geq$ 3 pm could severely limit DIAL measurements, and narrower spectral widths ~1 pm appear to be acceptable. Any small systematic effect (<0.5%) left by the 1 pm linewidths could be reduced by a first order estimate of the H_2O profile. The spectral distribution of laser energy is modified in the backscattering process due to motion of molecules and aerosols. Because of their mass, aerosols are relatively less effective in the Doppler broadening than air molecules. Under standard atmospheric conditions, Doppler broadening (DB) halfwidth $\Delta\lambda \approx 1.7$ pm in the 727-nm region. It is estimated that under normal atmospheric conditions this will cause a systematic underestimate in the DIAL measurement by <1% in the boundary layer to about 12-15% at 15 km altitude. However, this systematic effect can be estimated and, therefore, removed to a first order. Assuming a 10% error in the knowledge of the atmospheric temperature

profile and a 50% error in the knowledge of the aerosol scattering ratio (with a minimum of 20% error in the knowledge of the total scattering ratio), the Doppler broadening effect can be reduced to <2% over regions free of large aerosol gradients. Pressure shift of H_2O absorption lines causes a relative detuning of the laser line from the H_2O line. This effect can cause significant (>10%) errors at high altitudes (>10 km). Knowing the pressure shift and tuning the laser line to coincide with H_2O line at the appropriate pressure level can eliminate this error. It can be easily seen that tuning the laser to coincide with the H_2O line at lower pressures would be less sensitive to pressure shift effects than one tuned to higher pressure H_2O lines. To make DIAL measurements insensitive to variations in atmospheric temperature changes, H_2O lines should be selected that are relatively insensitive to this effect. For H_2O number density measurements, ground-state energy values in the range 100-300 cm^{-1} should be used for <1% error when assumed temperature differs by <10°K from actual. For mixing ratio measurements, ground-state energy levels in the range 300-450 cm^{-1} should be used. Laser spectral purity control is necessary to avoid an unabsorbed component of energy in the on-line laser output that will lead to an underestimation of DIAL H_2O concentrations. In general, a laser spectral purity of >99% is needed for a DIAL system. A spectral purity of >99.95%, which is more desirable, can be achieved by recently developed Alexandrite laser systems. Tuning of the lasers to near the peak of the H_2O absorption lines is necessary to avoid large measurement errors due to any uncertainty in the knowledge of the position of the laser.

Total LASE System Accuracy

It is useful to study the sensitivity of the DIAL measurement error to one parameter at a time as has been demonstrated in several studies; however, the presence of one parameter can influence the sensitivity of another. It is, therefore, important to study the coupled influence of several important parameters. A good example is the Doppler broadening effect, which reduces the sensitivity of DIAL H_2O measurement errors due to the finite laser linewidth, laser position uncertainty, and laser spectral resolution measured by a wavemeter. This effect also reduces errors due to an uncorrected pressure shift of the H_2O absorption line with altitude.

The combined estimated accuracy of the DIAL H_2O measurement by the LASE system is illustrated in Figure 1. The total error is a combination of errors due to both signal and system uncertainties. It is assumed that the Doppler broadening effect can be removed to first order. This can be done during data analysis using off-line signal to obtain aerosol scattering information and by using a climatological temperature profile. Laser line distortion effects can be corrected by using an approximate H_2O profile (20%) derived from an uncorrected H_2O DIAL measurement. Additional improvement in the DIAL measurement accuracy can be achieved by increasing the laser spectral purity to >99.95%. Figure 1 illustrates that using a single H_2O line, a H_2O DIAL measurement with <10% error over an altitude range 0-6 km can be made with a horizontal resolution of 10 km and a vertical resolution of 200 m during nighttime and 20 km by 300 m, respectively, during daytime. Spaceborne lidar could yield global H_2O profiles with similar accuracies with a horizontal resolution of 250 km and a vertical resolution of 500 m.

References

1. Schotland, R. M., _J. Appl. Meteorol._, _13_, 71, 1974.
2. Schotland, R. M., in Proceedings, _Fourth Symposium on Remote Sensing of Environment_, U. Michigan, Ann Arbor, April 12-14, 1966, pp. 273-283.
3. Browell, E. V., et al., _Appl. Opt._, _18_, 3474, 1979.
4. Cahen, C., et al., _J. Appl. Meteor._, _21_, 1506-1515, 1982.
5. Browell, E. V., et al., Conference Digest, _12th Int. Laser Radar Conf._, Aug. 13-17, 1984, Aix-en-Provence, France, pp. 151-155.
6. Ismail, S., and E. V. Browell, Submitted to _Appl. Optics_, July 1987.
7. Browell, E. V., et al., _13th Int. Laser Radar Conf. Abstracts_, Toronto, Canada, Aug. 11-15, 1986, pp. 6-9.
8. Browell, E. V., et al., _AIAA/NASA EOS Conference_, Oct. 8-10, 1985, Virginia Beach, VA, Paper No. 85-2091.

Table 1. LASE H_2O DIAL Parameters

RECEIVER

Area (Effective)	0.11 m²
Field of View	1.23 mrad
Filter Bandwidth (FWHM)	0.3 nm (Day) 1.0 nm (Night)
Optical Efficiency (Total)	23% (Day) 50% (Night)
Detector Efficiency	80% APD (Si)
Noise Eq. Power (APD & Amplifier)	2.1×10^{-14} W/Hz$^{1/2}$

TRANSMITTER

Energy	150 mJ (On & Off)
Linewidth	1.1 pm
Rep. Rate	5 Hz
Wavelength	726.5 - 732.0 nm
Beam Divergence	0.73 mrad
Pulse Width	300 ns
Aircraft Altitude	16-21 km
Aircraft Velocity	200 m/s
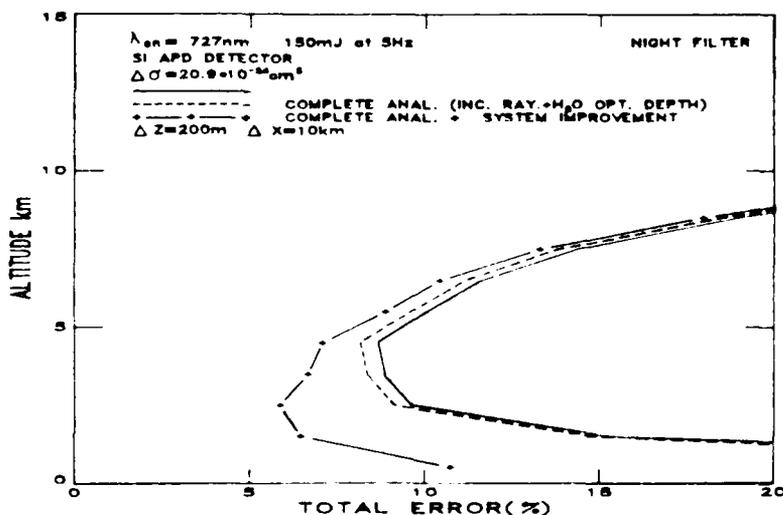
Figure 1. LASE H_2O DIAL combined errors from all sources.

Advanced Airborne DIAL System Capabilities for Ozone and Multiwavelength Aerosol Measurements

A. F. Carter, E. V. Browell, J. H. Siviter, N. S. Higdon
Atmospheric Sciences Division
NASA LaRC, Mail Stop 401A
Hampton, VA   23665-5225

C. F. Butler
ODU Research Foundation
Norfolk, VA   23508

N. Mayo
PRC Kentron
Hampton, VA   23666

The NASA Langley airborne DIAL system has been modified to give significantly increased measurement capability for conducting atmospheric science investigations. The major modification to the DIAL system was incorporating the capability to make ozone and aerosol measurements above and below the aircraft simultaneously. This was accomplished by a total redesign of the transmitting and receiving sections of the DIAL system to accommodate eight lidar returns simultaneously. Additional modifications were also made to remotely control transmitted laser beam properties and direction; to incorporate a new filtering system for high UV throughput and complete cutoff; and to increase real-time data availability for real-time mission decisions.

Two recent experimental programs have been conducted using the modified DIAL system. They include the Amazon Boundary Layer Experiment conducted from Manuas, Brazil, in April-May 1987 and the Antarctic Ozone Hole Experiment conducted from Punta Arenas, Chile, in August-September 1987. Unique DIAL system characteristics developed for each of the missions will be discussed.

Modifications for the Atmospheric Boundary Layer Experiment (ABLE-2B)

The NASA DIAL system has been extensively used since 1984 in numerous Global Tropospheric Experiments sponsored by NASA Headquarters. The instrument has been used not only to measure tropospheric ozone and aerosols, but also to direct the aircraft in real time for optimizing the in situ measurement strategy. Prior to 1987, the lidar system could make ozone measurements primarily in either the nadir or zenith, but not both simultaneously. Because of the need for data throughout the troposphere, the DIAL system was modified to provide simultaneous measurement capability for both ozone and aerosols in both nadir and zenith directions for the ABLE-2B mission over the Amazon. A total redesign of the transmitting and receiving optical systems was

required. A second optical platform for laser beam transmission was required, and new optics were added to provide beam attenuation and divergence changes (see Figs. 1 and 2). A remotely controlled optical system was designed and built for beam alignment with the receiver and for optimizing the transmitted laser energies. Two new receiver optical systems were designed and built, including two custom-built celestron telescopes. Each receiver has optics and detectors capable of receiving the four transmitted wavelengths, 285 nm, 300 nm, 599 nm, and 1.06 μm, at a maximum rate of 10 Hz. The capability to produce color plots of both ozone and aerosol data simultaneously in real time was also incorporated into the system.

Modifications for the Antarctic Ozone Hole Experiment

The NASA DIAL system was selected as the prime instrument on the NASA Ames DC-8 aircraft for remote measurements of ozone profiles in the stratosphere over the South Pole during August and September 1987. Ozone measurements were required over the vertical region from 12 to 20 km, and, therefore, only zenith operation is needed from the DC-8, which will fly at 12 km altitude. Due to the higher ozone concentrations in the stratosphere compared to the troposphere, the on-line and off-line UV wavelengths were increased to 302 and 312 nm to give improved accuracy over the 12- to 20-km altitude range. New UV doublers were necessary, as well as new filters, for the UV and visible receiver channels. A redesign of the transmission optical platform was necessary because the receiving package (and, therefore, the transmitting path) had to be moved to the front of the laser support structure. The final design incorporated both visible channels and both 1.06 μm channels as well as the on- and off-line UV. The rationale for this approach was to improve signal-to-noise ratio in the visible and infrared channels as well as provide redundancy for the aerosol measurements. Since only one receiver system was used for this mission, the telescope is lowered until the transmitted beams coming off the optical platform are turned coaxial with the telescope axis by the optics on the end of the telescope. This reduces transmitting optics and improves reliability and ease of alignment. The receiver system was modified to use two UV photomultiplier tubes for optimum detection and digitization of the UV DIAL returns over different altitude intervals.

Details of the airborne DIAL system characteristics for the Amazon Boundary Layer Experiment and the Antarctic Ozone Hole Experiment are discussed in this paper.

AIRBORNE DIAL SYSTEM SCHEMATIC

FORWARD

LASER BEAMS 286, 300 nm
599 nm
1.06 μm

ZENITH TELESCOPE

LASER TABLE

NADIR TELESCOPE

POWER RACK

NASA WALLOPS ELECTRA
NASA 429

LASER BEAMS 286, 300 nm
572 nm
1.06 μm
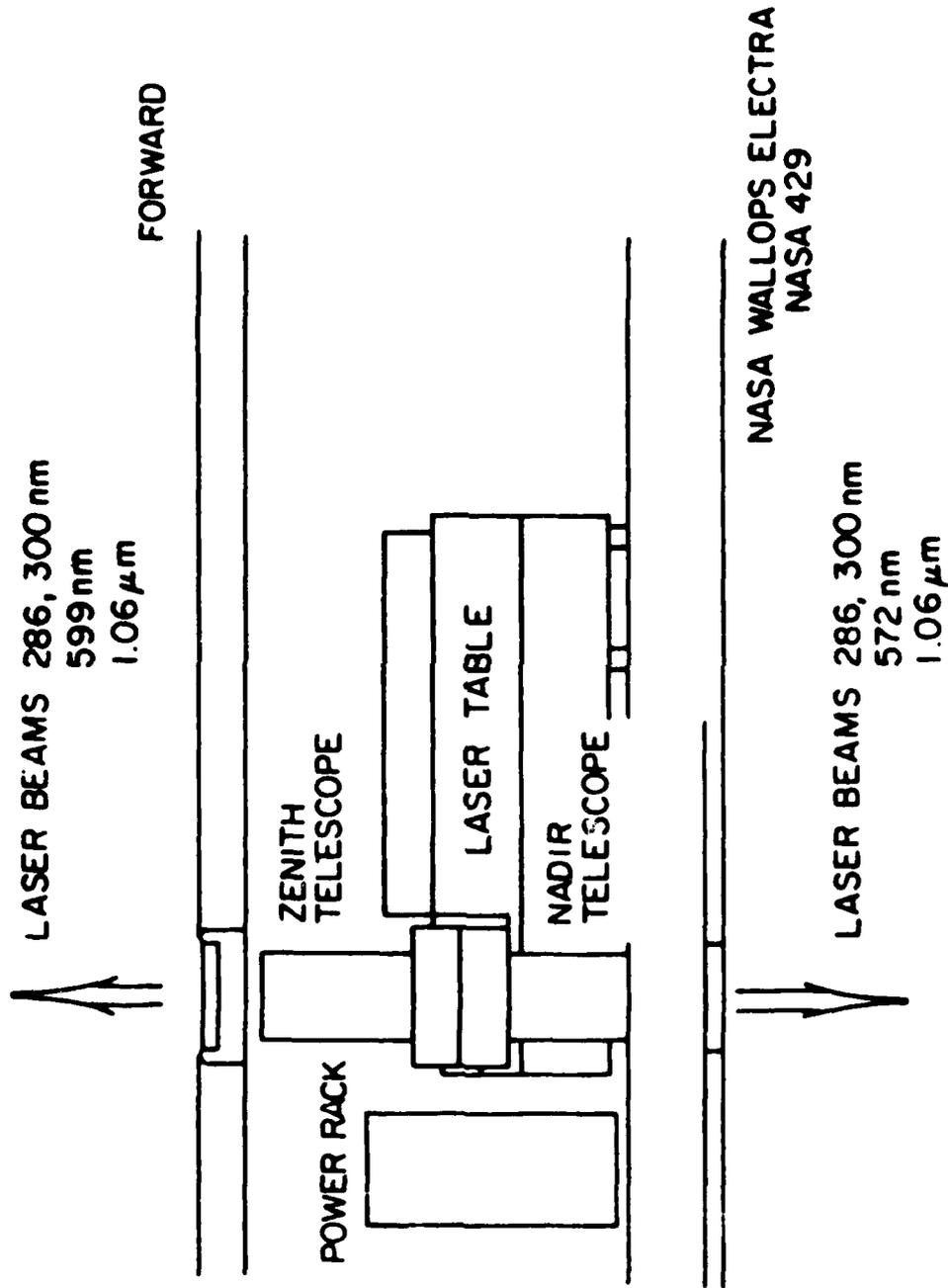
FIGURE 1

O₃ DIAL TRANSMISSION OPTICS
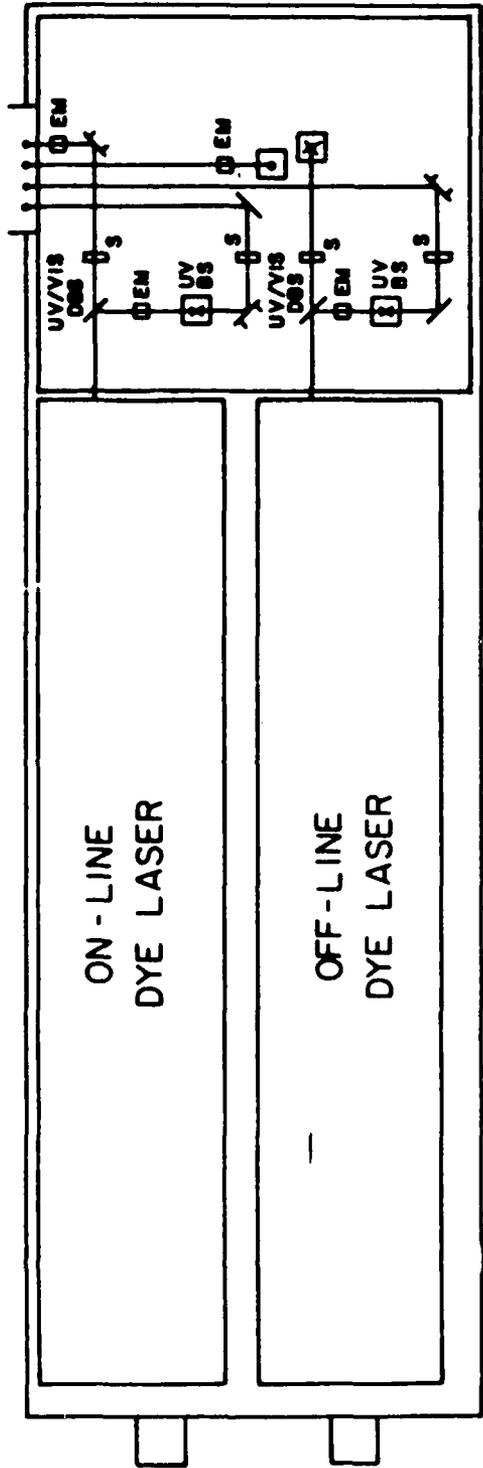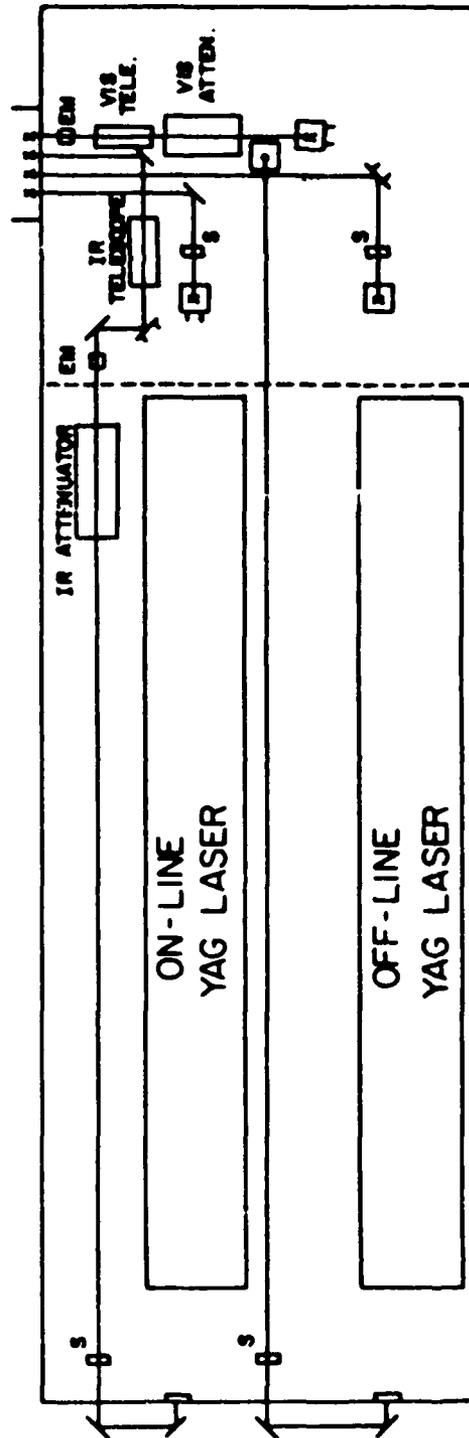
FIGURE 2

Simulation of Lidar Pressure and Temperature Profile Measurements from the Earth Observing System (EOS) Satellite

C. Laurence Korb
NASA/Goddard Space Flight Center
Code 617
Greenbelt, MD   20771

and

Chi Y. Weng
Science Systems and Applications, Inc.
Seabrook, MD   20801

The atmospheric pressure and temperature fields are two of the basic variables of fundamental importance in meteorology, climate studies, and for all scales of weather forecasting. The pressure field is used to describe the state of the atmosphere, frontal characteristics and to determine mass movement. The temperature field is needed for determining tropopause height, the depth and structure of the planetary boundary layer, and frontal and air mass characteristics. This paper presents an analysis of the sensitivity and instrumental parameters needed for lidar differential absorption (DIAL) measurements of pressure and temperature from the Earth Observing System (EOS) satellite. The proposed Lidar Atmospheric Sounder and Altimeter (LASA) facility on the EOS platform will allow global measurements of pressure and temperature profiles from a 700 km polar orbit.

The pressure[1] and temperature[2] experiments are two-wavelength DIAL techniques utilizing the backscattered energy from the clear atmosphere in the case of profile measurements or from the Earth's surface in the case of surface pressure. An integrated path absorption method is used for pressure. A measurement highly sensitive to pressure is obtained by locating one wavelength in a trough region, the region of minimum absorption between two strongly absorbing lines in the oxygen A-band near 760 nm (13150 cm^{-1}). The absorption in the trough is proportional to the square of the pressure. The reference wavelength is located in a nearby weakly absorbing region. The temperature measurement is made in a differential ranging mode. A measurement highly sensitive to temperature is obtained by locating one wavelength on a high J line in the oxygen A-band near 770 nm ($13,000$ cm^{-1}) where the variation of absorption coefficient with temperature is as high as the sixth power of temperature. A second wavelength located in a weakly absorbing region with a shift of 0.02 to 0.5 nm is used as a reference.

A two-wavelength solid-state alexandrite laser tunable in the 760 nm region is used for the pressure and temperature experiments. It has a spectral resolution of 0.005 cm^{-1} or better, a pulse length of less than 100 ns, and an energy of 0.5 J/pulse. The two wavelengths are separated in time by a nominal 300 µs which allows temporal separation and single-channel detection of both the on-line and reference wavelengths. An energy monitor measures the transmitted laser energy at each wavelength and a wavemeter is used to

precisely measure and control the laser frequency, each to an accuracy of 0.001 cm^{-1}.

The atmospheric model used for the simulations is a one-dimensional model with up to 50 homogeneous vertical layers. The temperature and pressure data are taken from the mid-latitude January U.S. Standard Atmosphere Model and the aerosol composition data are taken from the Elterman model. The simulations were performed using a high spectral resolution atmospheric transmission code. The transmission at a given frequency is calculated using the Voigt line profile and integrated vertically over the layers from space to altitude z. The simulations include detailed calculations of laser finite bandwidth and Rayleigh broadening in the scattering process.[3] The effects of background radiation including surface reflectance, aerosol scattering, and Rayleigh scattering have been considered.

The simulations used the following parameters for measurements from a 700 km EOS platform: a 0.5 J alexandrite laser transmitter, a repetition rate of 10 Hz, a narrowband transmitter with a bandwidth of 0.005 cm^{-1} or less, a telescope diameter of 1.25 m, a receiver FOV of 0.15 mrad for daytime and 0.5 mrad for nighttime experiments, and a PMT quantum efficiency of 0.2. An optical efficiency of 0.59 was used for nighttime simulations, which includes a wideband 1 nm spectral detection filter, and an optical efficiency of 0.38 was used for daytime simulations, which includes a narrowband 0.12 cm^{-1} filter.

Figure 1 shows the results of simulations of pressure profiling for a nadir-viewing daytime experiment. As shown, for 1 km vertical and 250 km horizontal resolution, good accuracy (<0.4 percent) can be obtained over a large portion of the troposphere using the pressure-sensitive absorption troughs located at either 13150.86 or 13153.79 cm^{-1}. We note that the use of a 0.15 mrad FOV and a 0.12 cm^{-1} spectral detection filter minimizes the effects of background radiation and allows high accuracy daytime measurements.

Figure 2 shows the results of simulations of temperature profiling for a nadir-viewing daytime experiment. As shown for the line at 12999.95 cm^{-1}, 2.5 km vertical resolution allows high accuracy measurements with less than 1 K error for altitudes up to 10 km. In addition, the use of the stronger absorption line at 13010.81 cm^{-1} with 3 km resolution allows high accuracy measurements to be extended to 15 km altitude. The effects of background are small for the 12999.95 cm^{-1} measurement but become significant for the 13010.81 cm^{-1} measurement.

Additional results will be discussed for the case of cross-track scanning, nighttime measurements, varying daytime albedo, and high vertical resolution (1.25 km) tropospheric temperature measurements.

References

1. Korb, C. Laurence and Chi Y. Weng, "Differential Absorption Lidar Techniques for Measurement of the Atmospheric Pressure Profile," Applied Optics, 22, 3759-3770, 1983.

2. Korb, C. Laurence and Chi Y. Weng, "A Theoretical Study of a Two-Wavelength Lidar Technique for the Measurement of Atmospheric Temperature Profiles," Journal of Applied Meteorology, 21, 1346-1355, 1982.

3. Korb, C. Laurence and Chi Y. Weng, "The Theory and Correction of Finite Laser Bandwidth Effects in DIAL Experiments," 11th International Laser Radar Conference, 78-81, 1982.
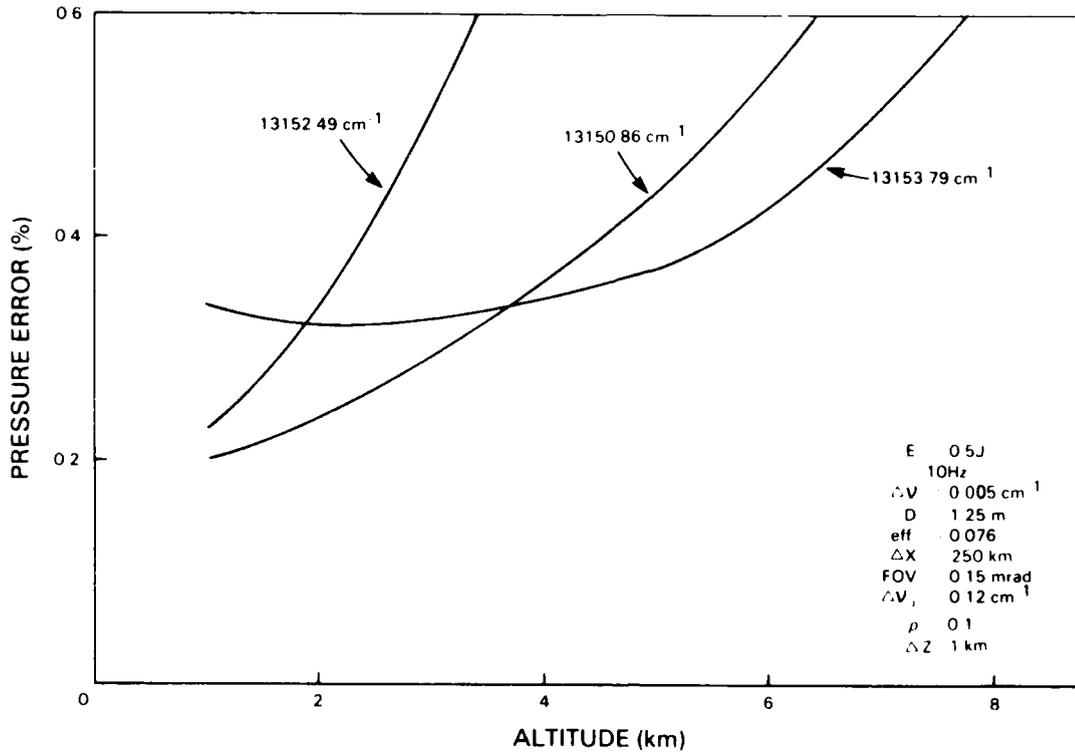
FIGURE 1 PRESSURE PROFILING ACCURACY FOR SIMULATED EOS EXPERIMENT AT 700 Km – DAY
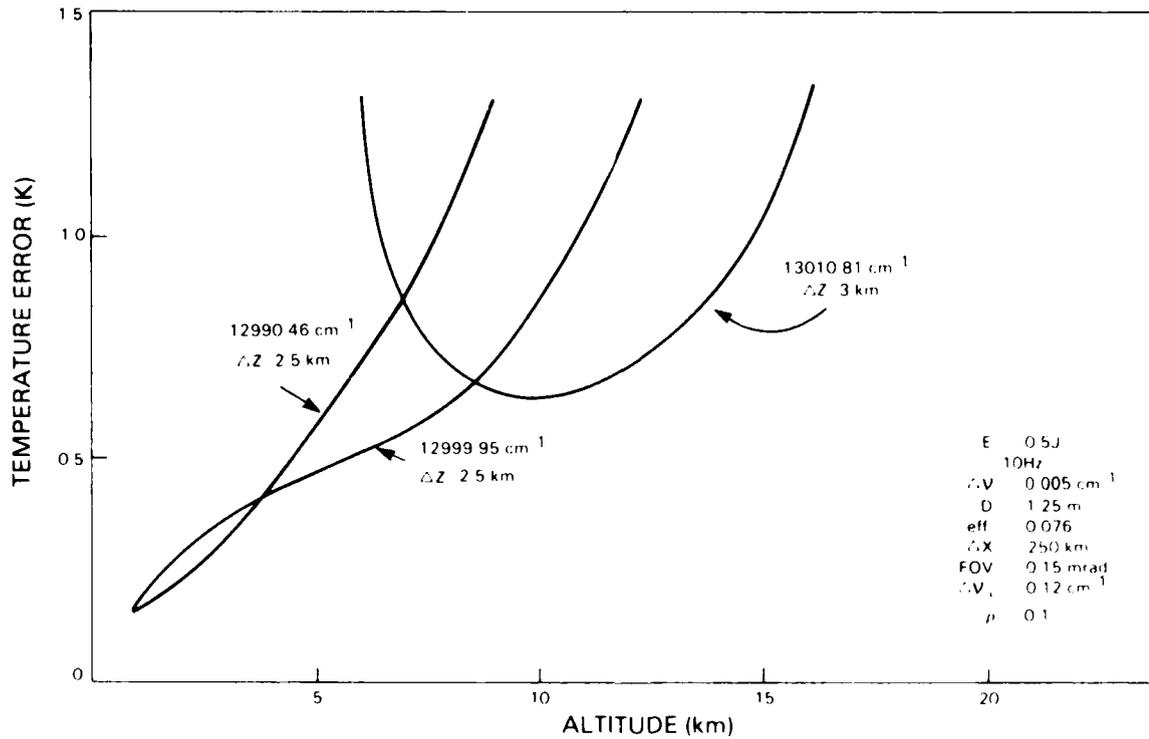
FIGURE 2 TEMPERATURE ACCURACY FOR SIMULATED EOS EXPERIMENT AT 700 Km – DAY

AN ADAPTIVE KALMAN-BUCY FILTER FOR DIFFERENTIAL
ABSORPTION LIDAR TIME SERIES DATA

Russell E. Warren
Electro-Optics Systems Laboratory
SRI International
Menlo Park, CA 94025

An earlier work[1] described a generalization of two-wavelength differential absorption lidar to the case of multiple wavelength channel returns for estimating the path-integrated concentration (CL) for multiple materials. A maximum likelihood (ML) estimator was constructed for the N-dimensional vector $\underline{CL} = [CL_1,\ldots,CL_N]^T$ of path-integrated concentration values in terms of lidar returns $p_i(k)$ collected simultaneously at $i = 1,\ldots 1$, $M \geq N+1$ wavelengths at time step k. Those returns were used to define an observation vector $\underline{s}(k)$, Eq. (1), which could be expressed approximately as Eq. (2) in terms of the M-1 × N-dimensional matrix of absorptivity differences $R_{i\ell} = \rho_i^\ell - \rho_{i+1}^\ell$ of material ℓ at wavelength i. The measurement noise $\underline{n}_s(k)$ was taken to be additive, uncorrelated, and zero-mean with covariance $\Lambda_s(k,k') = <\underline{n}_s \underline{n}_s^T>\delta_{kk'}$. The ML estimator for CL was shown to be given by Eq. (3) in terms of the ML estimate for the CL covariance Λ_{CL}^{ML}, Eq. (4).

Because the ML estimate of CL makes no use of the time series nature of practical data collection, a generalization was made to an on-line recursive filter based on the Kalman-Bucy[2,3] algorithm. Use of recursive filtering can greatly improve estimation performance with little or no additional processing delay. The classical Kalman-Bucy filter is based on a priori system and measurement models. Eq. (2) provides the measurement model in this case. In the absence of a detailed fluid mechanics model for the evolution of the clouds of interest, a first order Taylor series, Eq. (5), was adopted as the system model in which the random CL time derivative, $\dot{CL}(k)$ at time k plays the role of a "process noise" with statistics given by Eqs. (6)-(7).

The Kalman-Bucy algorithm for CL estimation is summarized by Eqs. (8)-(12) in which Eqs. (8)-(9) provide the extrapolation of the estimate and its covariance to the next time step. Eq. (10) represents the Kalman gain, and Eqs. (11)-(12) provide the update to the extrapolated value of CL and its covariance at time k. Eq. (11) shows that the recursive estimate of CL is a linear superposition of the ML estimate at time k and the extrapolated estimate $\underline{CL}_-(k) = \underline{CL}_+(k-1)$ based on the last time step. For the Kalman gain, G_k, small, the new estimate is dominated by the past value, whereas for $G_k \simeq I$, the estimator discards the old data in favor of the new ML estimate. Because G_k increases with increasing Q_k, the state model determines the relative importance placed on the new data at each time step.

For application to environments with rapidly changing concentration typical of toxic chemical detection, no fixed choice of state model covariance Q_k is suitable. The need to accurately estimate large concentrations while preserving high sensitivity for low concentrations has motivated the adaptive estimation of Q_k using a moving average estimate of the CL time derivative, Eq. (13), with the weighting coefficients[4] chosen to provide the first derivative of a local least squares fit to a low order polynomial through the current and previous ML estimates of <u>CL</u>. The system model covariance is estimated by Eq. (14).

Figure 1-a shows the maximum likelihood estimates of CL from low concentration data taken with a four-wavelength lidar for which the cloud of interest was generated by evaporation of a volatile liquid beneath the lidar line-of-sight. The adaptive (with a 15 point first order derivative estimate) and non-adaptive [$Q = 2$ $(mg/m^2)^2$] Kalman-Bucy filters produce the CL estimates shown in Figures 1-b,c. The non-adaptive filter provides somewhat less than optimal filtering, particularly for longer times for which the cloud has disappeared. Figures 1-d,e,f provide a comparison of the same filters using high concentration data produced at 3 minutes after the start of data collection. The non-adaptive filter produces a delay in responding to the vapor injection by overfiltering the ML estimates. In both cases the adaptive filter was able to maintain excellent noise reduction and response time in the presence of widely differing concentrations.

References

1. R. E. Warren, "Detection and Discrimination Using Multiple-Wavelength Differential Absorption Lidar," Appl. Opt. <u>24</u>, 3541 (1985).

2. R. E. Kalman, "A New Approach to Linear Filtering and Prediction Problems," Trans. ASME, J. Basic Eng., Series 82D, 35 (1960).

3. R. E. Kalman and R. S. Bucy, "New Results in Linear Filtering and Prediction Theory," Trans. ASME, J. Basic Eng., Series 83D, 95 (1961).

4. A. Ralston, <u>A First Course in Numerical Analysis</u>, McGraw-Hill, Inc., New York (1965).
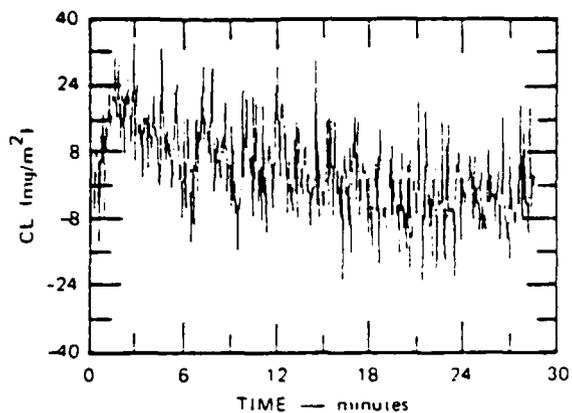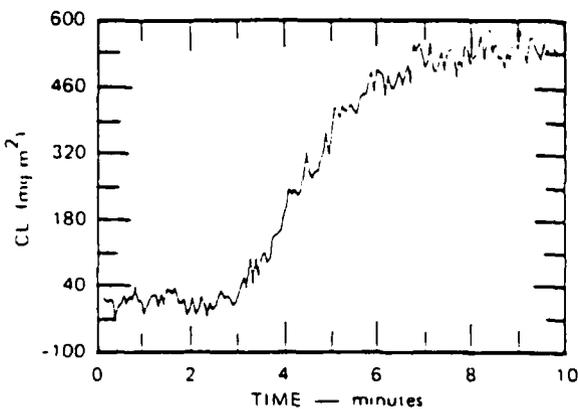
FIGURE 1   APPLICATION OF ADAPTIVE AND NONADAPTIVE KALMAN-BUCY FILTERS TO
CL TIME SERIES DATA

Table 1. Algorithm Summary

ML Estimate

$$s_i(k) = \frac{1}{2} \ln \frac{P_{i+1}(k)}{P_i(k)} \qquad , \qquad i = 1,\ldots, M - 1 \geq N \tag{1}$$

$$\underline{s}(k) = R \underline{CL}(k) + \underline{n}_s(k) \tag{2}$$

$$\hat{\underline{CL}}_{ML}(k) = \Lambda_{CL}^{ML} R^T \Lambda_s^{-1} \underline{s}(k) \tag{3}$$

$$\Lambda_{CL}^{ML} = \left(R^T \Lambda_s^{-1} R \right)^{-1} \tag{4}$$

State Model

$$\underline{CL}(k+1) = \underline{CL}(k) + \underline{\dot{CL}}(k) \tag{5}$$

$$\langle \underline{\dot{CL}}(k) \rangle = \underline{0} \tag{6}$$

$$\langle \underline{\dot{CL}}(k) \underline{\dot{CL}}^T(k') \rangle = Q_k \delta_{kk'} \tag{7}$$

Kalman-Bucy Filter

$$\hat{\underline{CL}}_-(k) = \hat{\underline{CL}}_+(k-1) \tag{8}$$

$$\Lambda_{CL_-}(k) = \Lambda_{CL_+}(k-1) + \hat{Q}_{k-1} \tag{9}$$

$$G_k = \Lambda_{CL_-}(k) \left[\Lambda_{CL_-}(k) + \Lambda_{CL}^{ML} \right]^{-1} \tag{10}$$

$$\hat{\underline{CL}}_+(k) = G_k \hat{\underline{CL}}_{ML}(k) + \left[I - G_k \right] \hat{\underline{CL}}_-(k) \tag{11}$$

$$\Lambda_{CL_+}(k) = \Lambda_{CL_-}(k) \left[\Lambda_{CL_-}(k) + \Lambda_{CL}^{ML} \right]^{-1} \Lambda_{CL}^{ML} \tag{12}$$

Adaptive State Model Estimate

$$\hat{\underline{\dot{CL}}}_J(k) = \sum_{i=1}^{J} \beta_i \hat{\underline{CL}}_{ML}(k + i - J) \tag{13}$$

$$\hat{Q}_k = \hat{\underline{\dot{CL}}}_J(k) \hat{\underline{\dot{CL}}}_J^T(k) \tag{14}$$

Optimization of Lidar Boundary Layer
Height Retrieval

Stephen P. Palm
Science Systems and Applications Inc.
Seabrook, MD 20706

James D. Spinhirne
Laboratory for Atmospheres/617
Goddard Space Flight Center
Greenbelt, MD. 20771

1. Introduction

A highly significant application for lidar sounding of the atmosphere is the retrieval of the height of the planetary boundary layer (PBL). The PBL height is an important factor in the transport of energy from the surface to the free troposphere and is directly related to the initiation and development of mesoscale events. Thus PBL height is a very useful input and validation parameter for Global Circulation Models. Currently there is no effective passive retrieval technique for PBL height. However the detection of PBL height from lidar aerosol scattering has been widely demonstrated. A primary consideration for lidar PBL height retrieval is the minimal detectability in terms of either atmospheric scattering structure or lidar system signal to noise sensitivity. Global measurements of PBL height from space borne lidar systems are envisioned. A primary consideration is how reliably PBL height may be detected for given lidar system parameters. The cost of a space borne system may be significantly reduced by minimizing telescope size and transmitted laser power.

The detection of PBL height has been studied through aircraft lidar experiments. A compact Nd:YAG Cloud and Aerosol Lidar System (CALS) has been operated from a NASA ER-2 (U-2) aircraft (Spinhirne et al., 1983). A routine to optimally determine PBL height from the relatively low sensitivity signals from the ER-2 lidar has been developed and tested. The methodology has been applied to model PBL height detection for space borne lidar systems. In addition the optimized scheme has been used to enhance results from airborne boundary layer experiments.

2. Experimental

Over the past few years the CALS has participated in a number of coordinated aircraft experiments . In the Fall of 1983 an experiment was organized to study the frequent and persistent occurrence of marine stratus clouds over the eastern Pacific. Analysis of lidar data obtained during that experiment has demonstrated that cloud top height of even very low (less than 1000 meters) stratus clouds can accurately and reliably be determined (Boers et al.,1987). Though the lidar system is normally operated over cloudy regions, there were some flight segments that had been conducted over clear areas. In these regions it is possible to use the lidar data to detect the top of

the PBL. We will present lidar data from one such clear air case
and describe an objective, computerized technique which was
developed to obtain reliable PBL height measurements from the
relatively noisy lidar data.

3. Retrieval Technique

The optical depth of a typical PBL is much less than that of
low lying stratus clouds and it is thus much more difficult to
detect the top of the PBL using lidar data. Because the CALS is a
compact system employing only a modest size telescope (15 cm) and
relatively low laser energy (30 mJ/pulse), the signal to noise
ratio at ranges of 18-20 km is so small that detection of the PBL
top from a single lidar shot is almost impossible. However by
averaging shots together and applying a vertical smoother, it is
possible to reduce the noise sufficiently so that reliable PBL
height detection is feasible. The computer algorithm that was
developed works with groups of 50 lidar shots (3.0 km of data).
For each shot the ground return is detected and a vertical
smoother is applied to the data. An average backscatter profile
is then generated from the 50 lidar shots. From this profile the
average PBL height is computed by looking for the distinctive
drop in aerosol scattering associated with the top of the PBL.
This is accomplished by computing a running average 6 data points
wide (45 meters) in the vertical and then searching for the point
where the smoothed signal drops to 25 percent of its maximum
value. Next, each individual shot from the group of 50 shots is
inspected using the average PBL height as the baseline. Each
individual shot is examined in only a 'window' region 300 meters
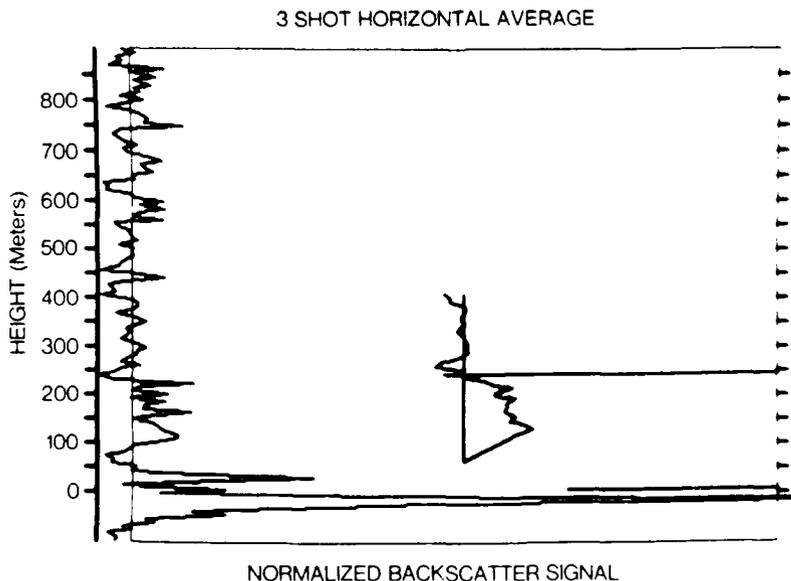
Fig. 1.   A typical lidar profile (left) and 60 meter
          running mean through the PBL (right).

wide and centered on the average PBL height. The PBL height for
the individual shot is then determined in a way.similar to the
procedure used for finding the average PBL height. Figure 1

shows typical lidar data acquired on 10/3/83 from the CALS system. Along the left vertical axis is plotted a 3 shot average of lidar return data and at center right is the running vertical average used to locate the PBL top. The increase in backscattered signal associated with the PBL top can be seen in both the unsmoothed (left) and smoothed (right) signals occurring at about 250 meters. In the smoothed signal, however, the noise fluctuations are much smaller and false determination of PBL top is less likely to occur.

3. Results

The algorithm to detect PBL height was applied to data taken by the CALS on 10/3/83. Figure 2 shows a 52 km data segment taken over the western San Joaquin valley. The solid line at the bottom of the figure represents the ground and the dots are the retrieved PBL height. A portion of the Diablo mountain range can be seen between 0 - 16 km on the figure. The PBL height over the valley appears fairly constant at about 900 meters but does contain a noticeable fluctuation at a scale of 2 - 4 km. This is consistent with convective scales of motion which tend to be between 2 - 4 times the average PBL height (Melfi et al.,1984).
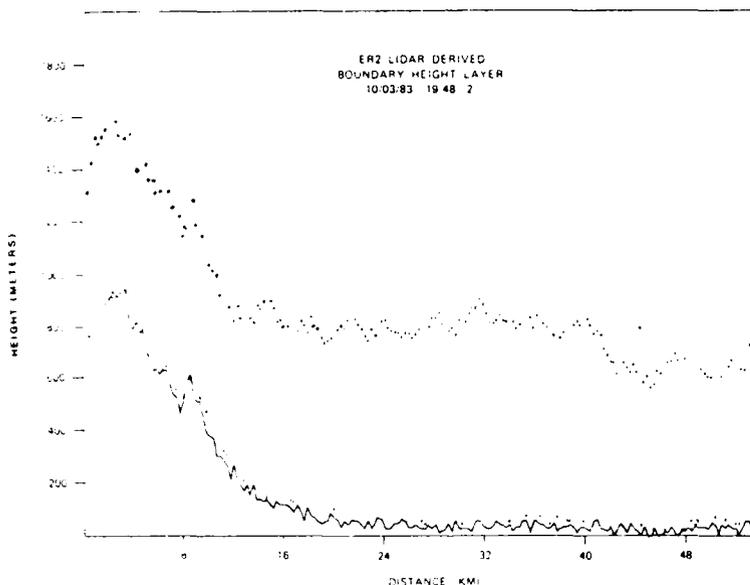
Fig. 2. PBL height as determined from CALS data.

Our results from the analysis of ER-2 lidar data indicate that it may be possible to detect the PBL top from space using a relatively small lidar system. To test this hypothesis, simulated lidar signals were generated for 4 different lidar system configurations. The same PBL height detection algorithm was used and the standard deviation of the retrieved height as a function of horizontal resolution was computed. The results are presented in figure 3 and indicate that reasonable PBL retrieval accuracy can be obtained for the two low power laser cases (curves C and D) if enough shots are averaged together. This, however, reduces

the horizontal resolution that can be obtained. Curves A and B show that if the laser power is increased by an order of magnitude, extremely good results can be obtained with less averaging.

RMS DEVIATION OF PBL HEIGHT FOR SATELLITE SIMULATED DATA
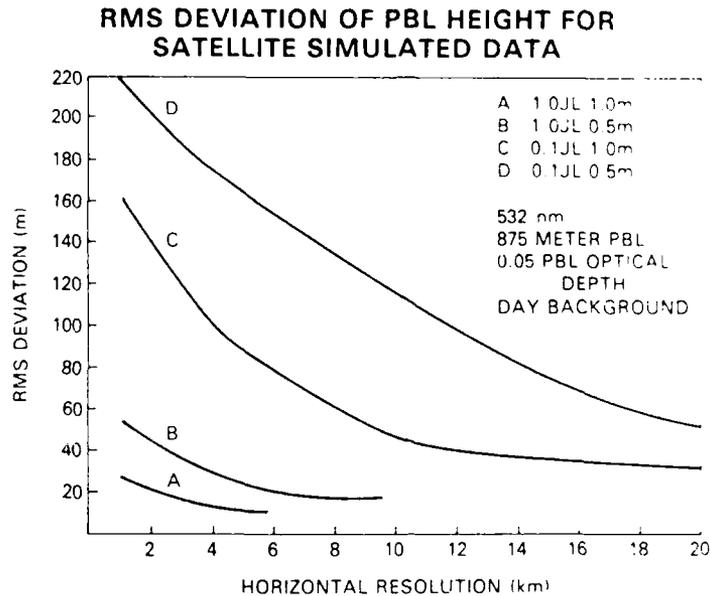
Fig. 3. Standard deviation of PBL height retrievals as a function of horizontal resolution.

4. Conclusion

It is possible to detect the PBL height from a high altitude, low sensitivity lidar system such as the Cloud and Aerosol Lidar System that has been flown aboard the NASA ER-2 aircraft. Noise inherent in such signals can be reduced by horizontal averaging of successive lidar shots and by applying vertical filters to the data. Simulations of lidar data indicate that PBL height retrievals can be made from a space borne lidar system at an altitude of 700 km. However to achieve useful horizontal resolution and to provide sufficient vertical accuracy would require a lidar system with at least a 1 Joule laser operating at 10 Hz and a 0.5 - 1.0 meter telescope under daytime background conditions.

References
    Boers, R., J.D. Spinhirne and W.D. Hart, 1987, "High Altitude Lidar Observations of Marine Stratocumulus Clouds", Submitted to J. Atmos. Sci.
    Melfi, S.H., J.D. Spinhirne, S-H Chou and S.P. Palm, 1985, "Lidar Observations of Vertically Organized Convection in the Planetary Boundary Layer Over the Ocean" J. Climate Appl. Meteor., 24, 806.
    Spinhirne, J.D., M.Z. Hansen and J. Simpson, 1983, "The Structure and Phase of Cloud Tops as Observed by Polarization Lidar", J. Appl. Meteor., 22, 1319.

Improvement of laser Doppler anemometer results by simultaneous backscatter measurements

Friedrich Köpp

Institute for Optoelectronics

German Aerospace Research Establishment (DFVLR)

D-8031 Wessling, Fed. Rep. of Germany

Introduction

Infrared Doppler lidar systems have proven very efficient for remote measurements of atmospheric wind and turbulence. During the last five years the cw CO_2 laser Doppler anemometer (LDA) from DFVLR has been successfully used for different routine applications, for example, the measurement of vertical wind profiles up to 750 m altitude or wind profiles close to the sea surface. Another type of applications covers the investigation of turbulence structures, especially the detection and tracking of aircraft wake vortices. Despite all the accurate results gained during these and additional field experiments, some difficulties became evident which can influence the LDA measurements in unfavourable cases. One of those cases is the presence of strongly scattering layers like fog or low clouds within or nearby the sensing volume. This paper describes the possibilities which arise by simultaneous measurements of aerosol profiles and cloud heights using a backscatter lidar and a ceilometer.

Improved range determination

For wind measurements with a cw Doppler lidar it is necessary to focus the cw laser radiation at a certain range R. The

length of the sensing volume ΔL is

$$\Delta L = \frac{8}{\pi} \left(\frac{R}{D}\right)^2 \lambda \ , \tag{1}$$

where D is the diameter of the focusing optics and λ is the
wavelength (10.6 μm). In case that the backscattering aerosol
particles are homogeneously distributed, more than 80 % of
the signal is due to backscattering in the sensing volume.
But often, the atmospheric boundary layer shows inhomogeneous
aerosol structures sometimes with extreme conditions like fog
or low altitude clouds. In a former paper (1) we have
presented some examples of fog and cloud influence on LDA
measurements. Since different atmospheric layers are normally
connected with different wind quantities, the frequency
spectra show more than one wind peak. In the meantime, our LDA
has been equipped with a multiple peak finder and the corres-
ponding evalution algorithm which allows to separate the velocity
peaks of a fog layer or low altitude cloud from the wind peaks
above or below (2). Difficulties still arise at ranges where
the effects of fog and clouds overlap the effects of the un-
disturbed atmosphere.

Another approach to improve the range allocation of wind
signals makes use of the presence of different aerosol layers.
If, for example, a layer of increased aerosol concentration
(inversion layer)is present within the wind profiling height
the LDA signal may consist of three components: one from above,
one from inside, and one from below that layer. The signal-to-
noise ratio (SNR) of each component can be calculated. The
relation between all three SNR values depends on the back-
scatter values and on the position of the focussed volume re-
lative to the inversion layer. The backscatter values can be
estimated using the simultaneously measured aerosol distri-

bution. In that way, the peak in the velocity spectrum which corresponds best to the range setting can be identified by means of the calculated signal strength. In case of large sensing volumes at long ranges this method allows a finer range resolution if there is a inversion layer identified within the sensing volume.

The measurement of the aerosol profiles is performed by the DFVLR Minilidar which is based on a Nd:YAG laser (3). Moreover, an Impulsphysik Laser Ceilograph (4) is available for monitoring of cloud base heights.

Aerosol backscatter measurements

With respect to the Global Backscatter Experiment (GLOBE) it is desirable to achieve aerosol backscatter data at 9.1 and 10.6 μm. Therefore, the LDA Doppler signals will be treated in a similar way as the LATAS alggorithm which was developed to derive aerosol backscatter data from airborne cw CO_2 Doppler lidar measurements (5).

The simultaneously measured aerosol profiles at a wavelength of 1.06 μm offers the possibility to check the LDA derived backscatter profiles. Moreover, the relation between backscatter coefficients at 1.06 and 10.6 μm can be investigated.

References

1   Werner, Ch., F. Köpp, and R.L. Schwiesow:
    Influence of clouds and fog on LDA wind measurements.
    Appl. Opt. 23, 2482 (1984).

2   Werner, Ch.:
    Fast sector scan and pattern recognition for a cw laser
    Doppler anemometer.
    Appl. Opt. 24, 3557 (1985).

3   Herrmann, H., F. Köpp, and Ch. Werner:
    Remote measurement of plume dispersion over sea surface
    using the DFVLR minilidar.
    Opt. Eng. 20, 759 (1981).

4   Instruction manual Laser Ceilograph LD-WHX-03.
    Impulsphysik GmbH, Postfach 57 13 49, 2000 Hamburg.

5   Rothermel, J., J.M. Vaughan, and D.A. Bowdle:
    Algorithm to calculate aerosol backscatter from airborne
    cw focused CO_2 Doppler lidar measurements.
    Private communication (1987).

High Spectral Resolution Lidar Measurements of Cirrus Cloud Optical Properties

C. J. Grund and E.W. Eloranta

University of Wisconsin

Department of Meteorology

1225 W. Dayton

Madison, WI. 53706

(608) 263 - 9363

Lidar backscatter signals are generated by scattering from both molecules and particles. The spectral distribution of light scattered by molecules is Doppler-broadened by rapid, thermally induced, molecular motions. Light scattered by aerosols and cirrus particles is essentially unshifted because of the relatively slow Brownian motion of particles. Using this difference, the High Spectral Resolution Lidar (HSRL)[1,2] interferometrically separates particulate from molecular backscatter. By using the distribution of molecular scattering as a known target, the HSRL achieves unambiguous, calibrated measurements of atmospheric extinction, backscatter cross section, and backscatter phase function.

The HSRL was used during the FIRE IFO experiment (Oct.-Nov. 1986) to observe the optical properties and occurrence of cirrus clouds at Madison, Wisconsin. Significant improvements in instrument and calibration technique were accomplished which enabled the HSRL to perform optical property measurements at cirrus cloud altitudes. Successful eye-safe measurements were achieved during both day and night conditions using only 50 mW of average power. A schematic of the current system configuration is presented in fig. 1. A summary of system specifications is presented in table 1.

Range-time indicator displays of the lidar backscatter signal were generated which depict the height, occurrence and layer thickness of the clouds. Part of the data were analysed and calibrated backscatter cross section profiles (fig.'s 2 - 6) were produced as well as time and range averaged values of extinction and backscatter phase function. Backscatter phase functions ranged from .027 - .045 sr-1, with no apparent dependence on in-situ temperature (fig. 7). A summary of the optical property measurements is presented in table 2.

1) Shipley, S.T., D.H. Tracey, E.W. Eloranta, J.T. Trauger, J.T. Sroga, F.L. Roesler, and J.A. Weinman (1983) High spectral resolution lidar to measure optical scattering properties of atmospheric aerosols. 1: Theory and instrumentation. App.Opt., 22, pp 3716-3724.

2) Sroga, J.T., E.W. Eloranta, S.T. Shipley, F.L. Roesler, and P.J. Tryon (1983) High spectral resolution lidar to measure optical properties of atmospheric aerosols. 2: Calibration and analysis. Appl.Opt., 22, pp 3725-3732.

3) Platt, C.M.R. and A.C. Dilley (1981) Remote sounding of high clouds. IV: Observed temperature variations in cirrus optical properties. J.Atmos.Sci., 38, pp1069-1081.

Table 1: HSRL System Parameters

HSRL Receiver:

Telescope:

Primary diameter	.35 m
Secondary diameter	.114 m
Focal length	3.85 m
F.O.V. (full width)	320 μR

Pre-filter: 50 mm diameter plates

Fiber optic Scrambler	100 mm X 1.23 mm dia
	.66 N.A., F-2 glass
Interference filter (FWHM)	1 nm at 510.6 nm
Etalon spacers (E_1, E_2)	1.003, .726 mm
Combined bandwidth (FWHM)	2.5 pm

High resolution etalon: 150 mm diameter plates

Etalon spacer	12.786 mm
Bandwidth (FWHM)	.6 pm

Photomultiplier tubes: EMI Gencom 9863B/100

HSRL Transmitter:

Laser: $CuCl_2$ (lasing on Cu lines at 510.6 nm and 578.2 nm)

Beam expansion factor	3
Transmitted beam diameter	30 mm
Transmitted power	50 mW at 510.6 nm
Bandwidth (stripped FWHM)	.4 pm
Pulse repetition rate	8 kHz
Pulse length	15 ns
Input power	4 kv , .5 A at 8 kHz

Table 2: Data Summary

Date	Time	Altitude	β_a	$\mathbb{P}_a/4\pi$	T	RH
	GMT	km	10^{-5} m^{-1}	sr^{-1}	C^0	%
10/27/86	23:00	8.0	4.2±.85	.028	-32.6	70
10/31/86	14:25	10.5	2.4±.80	.030	-59.0	59
10/31/86	15:05	10.2	1.9±.72	.032	-51.5	62
10/31/86	15:45	9.1	2.7±1.1	.024	-41.5	68
10/31/86	16:25	8.6	1.8±.83	.039	-38.0	69
10/31/86	16:25	12.1	1.2±.71	.023	-66.5	43
10/31/86	17:05	8.8	1.2±.45	.034	-39.3	69
10/31/86	17:05	12.1	.68±.52	.045	-66.5	43
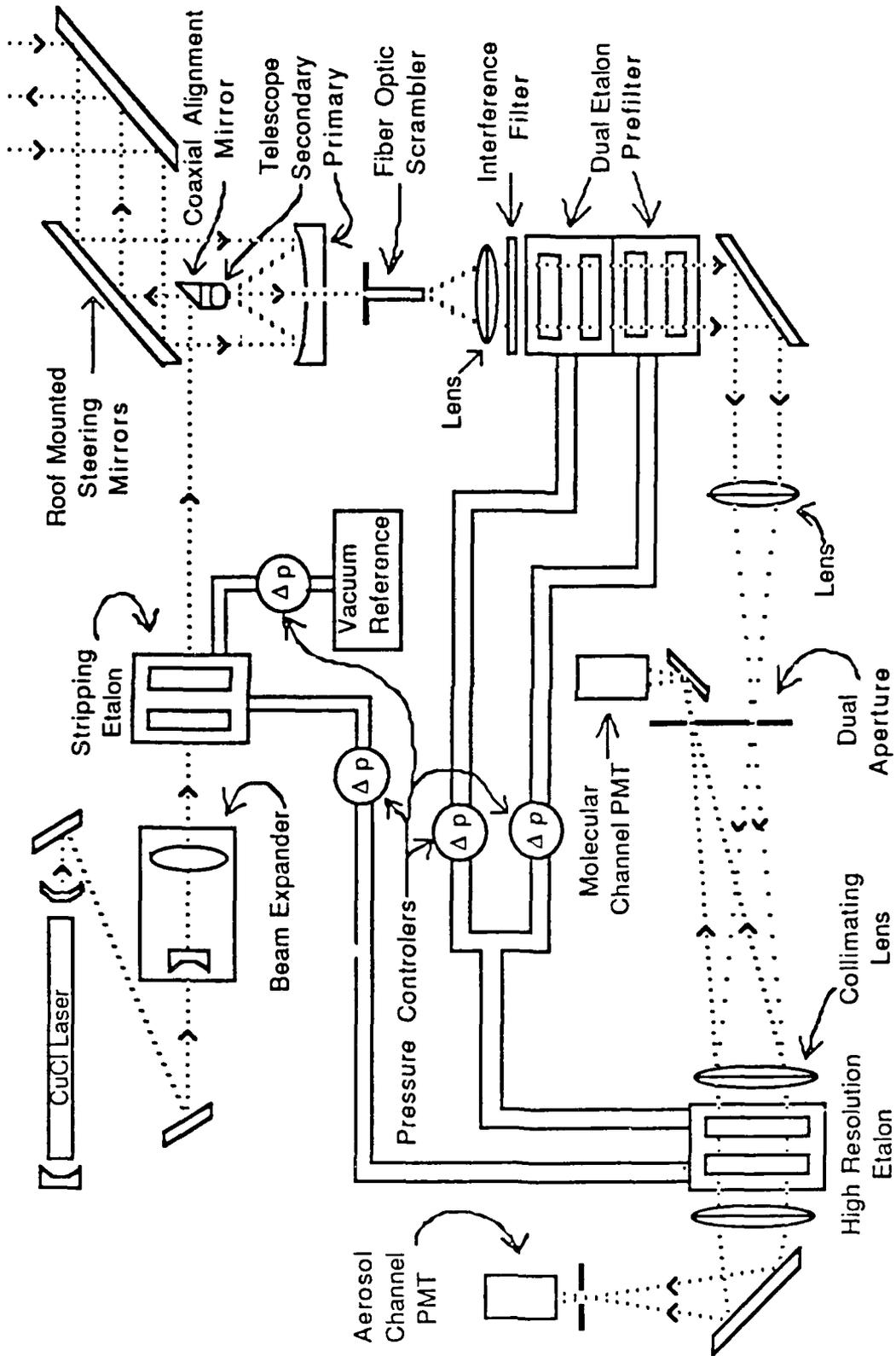
Fig. 1 HSRL Receiver/Transmitter

Fig. 2 Backscatter X-Section (M^{-1} SR^{-1}) 23:00 GMT 10/27/86

Fig. 5 Backscatter X-Section (M^{-1} SR^{-1}) 16:25 GMT 10/31/86

Fig. 3 Backscatter X-Section (M^{-1} SR^{-1}) 14:25 GMT 10/31/86

Fig. 6 Backscatter X-Section (M^{-1} SR^{-1}) 17:05 GMT 10/31/86

Fig. 4 Backscatter X-Section (M^{-1} SR^{-1}) 15:05 GMT 10/31/86

Backscatter Phase Function vs. Temperature
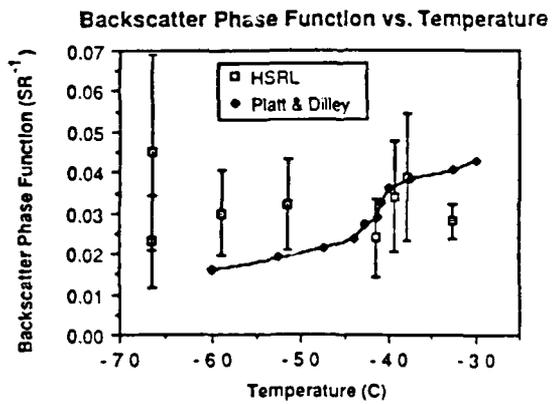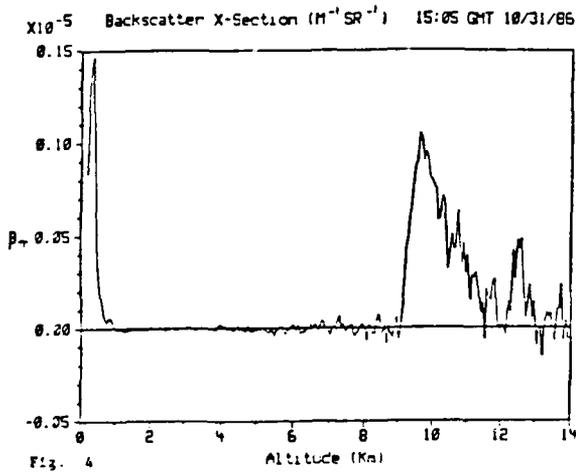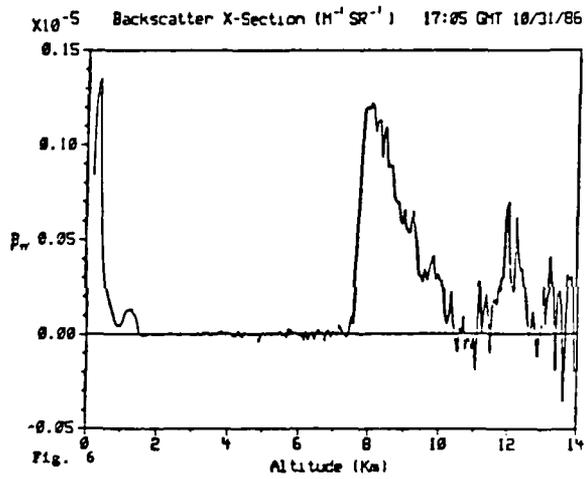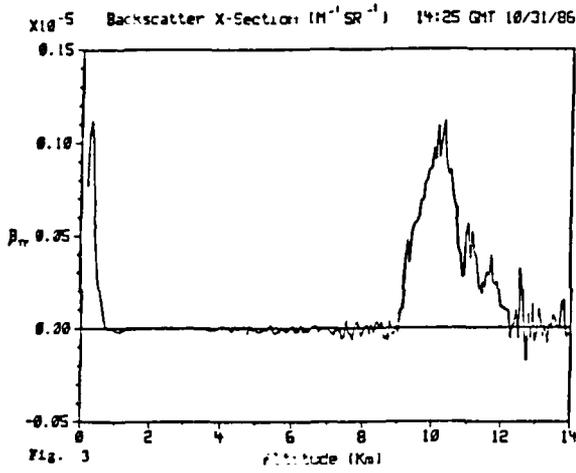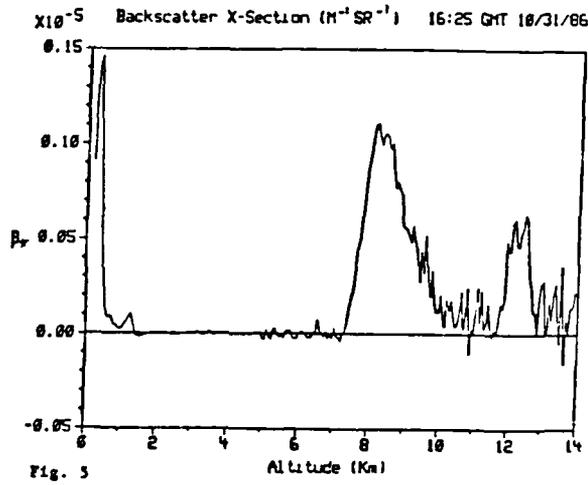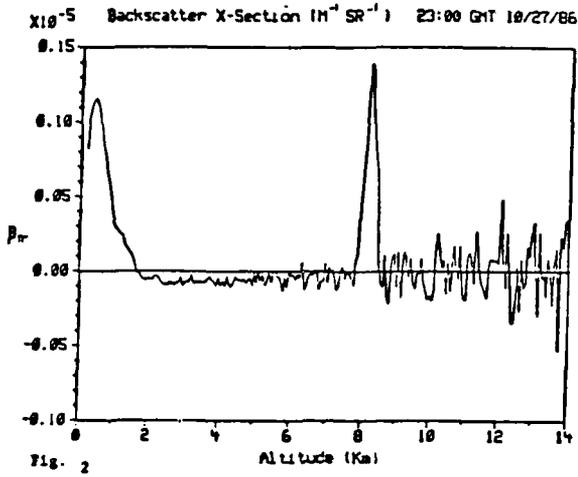
Fig. 7 The relationship of $\mathbb{P}_a(\pi)/4\pi$ to temperature as reported by Platt & Dilley[3] is compared with the independent HSRL measurements acquired during FIRE. A clear cut relationship between backscatter phase function and temperature is not apparent in the latter data set.

Optically Significant Cirrus Clouds may be Rendered "Invisible" to Space-borne Simple Lidar
Systems

C. J. Grund and E. W. Eloranta

University of Wisconsin

Department of Meteorology

1225 W. Dayton

Madison, WI. 53705

(608) 263 - 9363

Recently, there has been much discussion among lidar researchers concerning the infinite solution set of extinction profiles which can be produced from a given simple-lidar backscatter profile[1]. This ambiguity is caused by the measured backscatter signal dependence on both the backscatter cross section and on the profile of extinction. Simple lidar systems produce only one measurement from which to deduce these two range-dependent parameters. Thus, simple lidar measurements must be augmented by additional measurements or knowledge of the physical relationship between backscatter and extinction before meaningful profiles of extinction can be produced. One simple lidar retrieval method assumes independent knowledge of extinction at at least one range and an assumed relationship between the backscatter cross section and extinction[2]. A second method seeks a common solution to several simple lidar profiles produced by observations at different viewing angles[3,4,5].

Due to the rigorous weight, power and reliability requirements imposed by the space environment, the first generation of space-borne instruments will be of the non scanning, simple lidar type, and will have modest signal detection capabilities. These systems will be co-located with passive radiometers. They are expected to provide detailed cloud existence, height and thickness information to improve the accuracy of radiometer soundings.

The University of Wisconsin High Spectral Resolution Lidar (HSRL)[6,7,8] makes unambiguous, measurements of backscatter cross section, extinction, and backscatter phase function by spectrally separating the Doppler-broadened backscatter from molecules from the unbroadend return from particles. The distribution of air molecules is then used as a known calibration target available at every range. HSRL measurements indicated that cirrus clouds often exhibit backscatter cross section which decrease with height (e.g. lower altitude cloud layer shown in fig. 1). It is possible that such cloud-top profiles might potentially render these cirrus

"invisible" to space-borne simple lidar systems if the increase in backscatter cross section with range is just sufficient to offset the loss of signal due to extinction with increasing cloud penetration.

In order to demonstrate this effect, it is possible to solve the lidar equation for a family of extinction profiles which would yield straight log-linear R^2 corrected return signals with a slope S. Assuming a constant ratio between the extinction and backscatter cross section, one may write the range derivative of the logarithm of the lidar equation as:

$$S = \frac{d \ln\left[\beta_\varepsilon(R) \right]}{dR} - 2\beta_\varepsilon(R)$$

(1)

Where S is the log slope of the R^2 corrected expected return signal, R is the range and β_ε is the extinction. A Bernoulli solution may be employed to reduce this representation to a first order linear equation with the solution:

$$\beta_\varepsilon(R) = \frac{1}{\left[\dfrac{1}{\beta_0} + \dfrac{2}{S} \right] e^{\left[(R_0 - R)\, S \right]} - \dfrac{2}{S}}$$

(2)

Where R_0 is the range at which the cloud begins, and β_0 is the extinction at that range.

Fig. 2 presents the extinction profiles of three hypothetical clouds which would be "invisible" to nadir viewing lidars with the signal detection limits of 6, 4 and 1 (denoted A, B, and C) times the expected molecular backscatter signal from 8 km calculated at a wavelength of 510 nm (hereafter referred to as the scattering ratio). The clouds depicted in profiles A, B and C have respective optical depths of 1.1, .46, and .08 through the 3 km cloud thickness, and are thus both realistic and radiatively significant. Curves A, B, and C were calculated from eq. 2 to yield a log slope near 0 for a nadir lidar profile constructed according to the lidar equation. β_0 was then chosen so that the resultant down-looking profile would produce a scattering ratio of 6, 4, or 1 for curves A, B, and C, respectively. Thus, for example, a nadir viewing lidar with a minimum scattering ratio detection limit of 6 would not be capable of distinguishing from noise the backscatter signals produced clouds A, B, or C.

Fig.'s 3, 4, and 5 depict the expected scattering ratio observations from lidar systems viewing clouds described by the β_ε profiles A, B, and C, respectively. The simulations assumed a fixed backscatter cross section to extinction ratio of .03 sr^{-1} for the cloud particles. Lidar profiles are

plotted for each cloud profile for both zenith viewing and nadir lidar observations. Note that for a cloud with this soft top/distinct bottom structure, it is possible to see the cloud bottom from below, but it may be possible to miss the cloud entirely from above. Also note that in all cases the up-looking lidar would not see the cloud tops because the backscatter cross section at this range must decrease to a level insufficient to produce a signal which exceeds the noise floor.

1) Kunz, G.J. (1987) Lidar and missing clouds. In Letters to the editor, Appl.Opt. 26, p 1161
2) Klett, J.D. (1981) Stable analytical inversion solution for processing lidar returns. Appl.Opt, 20, pp 211-220.
3) Spinhirne, J.D., J.A. Reagan, B.M. Herman (1980) Vertical distribution of aerosol extinction cross section and inference of aerosol imaginary index in the troposphere by lidar technique. J.Appl.Meteor., 19, pp 426-438.
4) Eloranta, E.W., and D.K. Forrest (1986) Generation of attenuation corrected images from lidar data: in Thirteenth International Laser Radar Conference, NASA conference publication 2431, pp. 291-294.
5) Weinman, J.A. (1984) Tomographic lidar to measure the extinction coefficients of atmospheric aerosols. App.Opt., 23, pp 3882-3888.
6) Shipley, S.T., D.H. Tracey, E.W. Eloranta, J.T. Trauger, J.T. Sroga, F.L. Roesler, and J.A. Weinman (1983) High spectral resolution lidar to measure optical scattering properties of atmospheric aerosols. 1: Theory and instrumentation. App.Opt., 22, pp 3716-3724.
7) Sroga, J.T., E.W. Eloranta, S,T. Shipley, F.L. Roesler, and P.J. Tryon (1983) High spectral resolution lidar to measure optical properties of atmospheric aerosols. 2: Calibration and analysis. Appl.Opt., 22, pp 3725-3732.
8) Grund, C.J., and E.W. Eloranta (1985) Measurements of aerosol Backscatter phase function and extinction by high spectral resolution lidar. In the digest from: Topical Meeting on Optical Remote Sensing of the Atmosphere, Op. Soc. of Amer., pp WC11-1 - WC11-4.

Extinction Profiles of "Invisible" Clouds
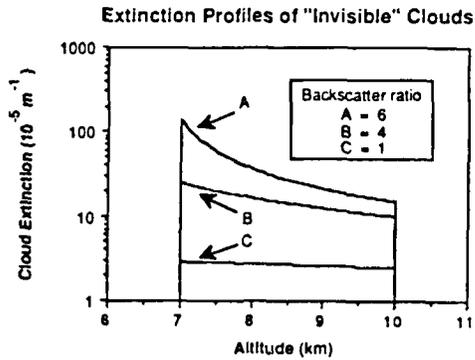
Fig. 2 From space, simple lidar systems with the detection limits A, B or C (see text) would not be capable of recognizing a cloud with the indicated extinction profile.

Lidar Profiles Calculated from Extinction Curve A
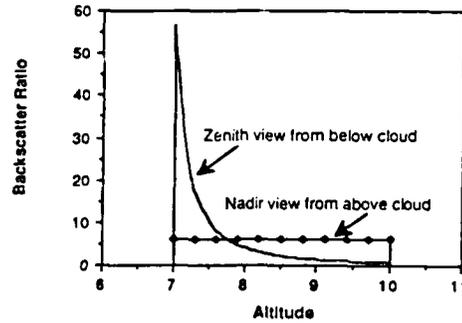
Fig. 3 Simulated lidar profile calculated from extinction profile A.

Lidar Profiles Calculated from Extinction Curve B
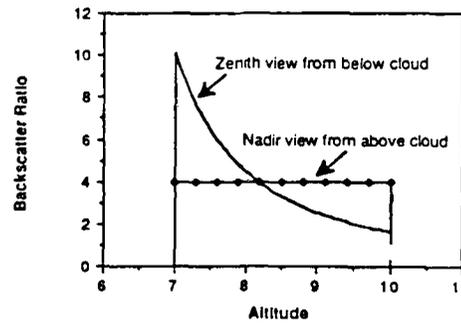
Fig. 4 Simulated lidar profile calculated from extinction profile B

Lidar Profiles Calculated from Extinction Curve C

Fig. 5 Simulated lidar profile calculated from extinction profile C

Backscatter X-Section (M⁻¹SR⁻¹)   16:25 GMT 10/31/86
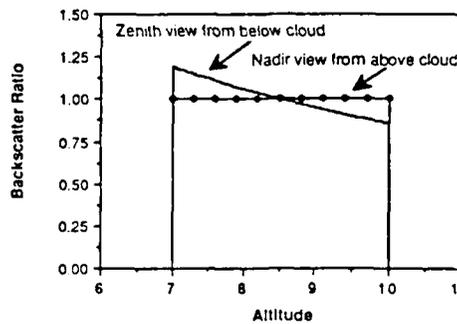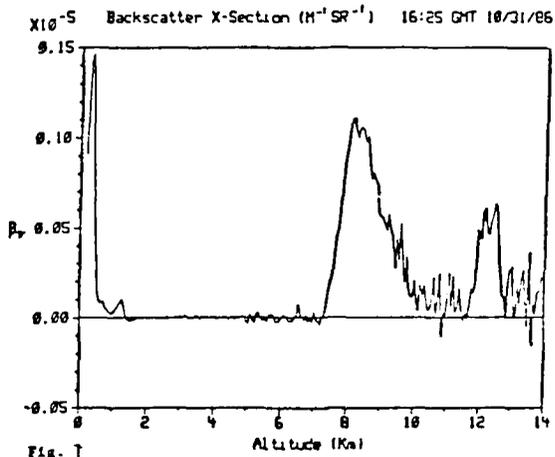
Fig. 1

LIDAR DETECTION OF SUB-VISIBLE CIRRUS CLOUDS

R.Dubinsky, W.Hunt, J.Moore, M.Osborn

Science and Technology Corp., Hampton, VA

Cloud measurements using a ground based NdYAG Lidar operating at a wavelength of 0.53 um showed important backscatter returns from an altitude of approximately 12 km. during visually clear atmospheric conditions. The Lidar return signal is attributed to sub-visible cirrus clouds having backscatter ratios of 6.1 to 7.6 and a backscatter coefficient of 2.64 to 3.43 x 10(E-03) /km/sr. The measurements were taken during the FIRE (First International Satellite Cloud Climatology Project Regional Experiment),IFO (Intensive Field Observations) in Wisconsin during October and November 1986. The results are compared with collaborative measurements (eg. satellite, air sampling, radiometric etc. during the FIRE trials), Lidar data from Langley Research Center (LaRC) and literature results.

The requirements for a dedicated Lidar system to monitor cirrus clouds for ETO (Extended Time Observations) developed as a result of the above measurements. The design is based on a NdYAG laser and is discussed in terms of optimizing components with respect to S/N ratio (signal/noise) simulations. A range of specifications are considered in terms of transmitter, receiver, detectors, electronics, computerized data processing/display, automation, platform and logistics.

Detection of Methane Leaks with a Correlation Lidar

E.Galletti

CISE Tecnologie Innovative S.p.A.

P.O.Box 12081, 20134 Milano, Italy

SUMMARY

An IR light source based on a Lithium Niobate Optical Parametric Oscillator (OPO) has been developed to measure small average concentrations of atmospheric pollutants by LIDAR technique.

The OPO source is pumped by a Q-switched Nd:YAG laser with a Self Filtering Unstable Resonator (SFUR) cavity[1] and polarization output coupling to obtain with a high efficiency a smooth, near diffraction limited beam. As it is known, a good pump beam quality is very important to achieve reliable OPO operation. Our SFUR laser meets this requirement with pulses of about 150 mJ energy, 20 ns duration and 10 pps of repetition rate. Reflection of pump beam light back in the laser cavity by $LiNbO_3$ facets is prevented by slightly tilting the crystal, thus avoiding the use of a Faraday insulator.

OPO cavity is about 20 cm long; the resonator consists of a plane mirror with 70% reflectivity for signal wavelengtht and of a gold coated, 2.8 micron blazed diffraction gratings. The bandwidth is about 1 cm^{-1}. The source is actually optimized to operate in the 3 micron region. Output energy is about 1 mJ at signal wavelength with 130 mJ of pump energy. OPO threshold has been measured using a plane, gold coated mirror instead of the grating and it is about 70 mJ with a signal + idler conversion efficiency of 10% at twice the threshold.

The OPO source is actually part of a correlation LIDAR system[3] designed to measure small average concentrations of methane gas in atmosphere. The system has a sensitivity in the ppm range on integration paths of some hundred metres. It uses topographic targets as reflectors and it is operated on a small truck.

The gas correlation technique used for this system makes it possible to self normalize the return signal obtained from a single laser pulse, while conventional DIAL method requires two laser shots to obtain the reference and the absorption signals. This fact may lead to important errors when the system is used to make measurement on moving platforms, while the gas correlation method leaves any time dependent effect such as target reflectivity, at the expense of a lower sensitivity and a greater effect on the measurement of interfering molecules.

The gas correlation approach requires a fixed wavelength rather broadband source which spectrum wholly overlaps an absorption line of the target molecule. The back-scattered signal from a topographic target is half-splitted and focused on two detectors. Light passing in the "direct" branch straight overtakes the photodiode, whereas in the "correlation" path there is a gas filter correlation cell in front of it. This is filled with a large amount of the target molecule and in this way the detected energy of the pulse in the "correlation" arm is nearly uneffected by the presence or

absence of the target gas in the atmosphere. After a
calibration, the ratio between the two branches is thus
related to the average concentration of the target molecule on
the operating path. The rather wide bandwidth of the source
also brings about some disadvantages. First, a lower
sensitivity since the measured transmission has a rather slow
dependence on the gas concentration. Second, the system is
more sensitive to interfering molecules which modify the ratio
between the two arms thus leading to calibration errors.

Because reliable operation requires good stability of
source bandwidth, two internal "direct" and "correlation"
paths which see a signal tapped from the transmitted one are
used to monitor the OPO working.

Preliminary data on the methane concentration
measurements in an urban area will be presented and
discussed.
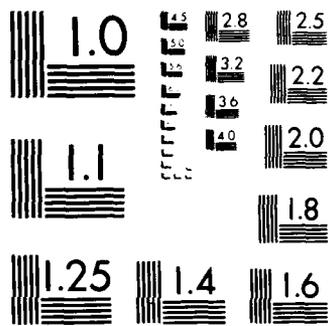
REFERENCES

1. Gobbi P.G., Moroni S.,Reali G.C.,Zarkasi S, "Novel unstable resonator configuration with self-filtering aperture: experimental characterization of the Nd:YAG loaded cavity", Appl.Opt.,Vol.24, pp.26-33,1985.

2. Brosnan S.J.,Byer R.L., "Optical Parametric Oscillator Threshold and Linewidth Studies", IEEE J.Quant.Electron.,Vol.QE-15, pp.415-431, 1979.

3. Edner H.,Svanberg S., Uneus L., Wendt W:. "Gas Correlation Lidar", Private Communication.

High Altitude Lidar Observations of Marine Stratocumulus Clouds

Reinout Boers[+*] and James D. Spinhirne[+]

[+]Laboratory for Atmospheres, code 617
Goddard Space Flight Center
Greenbelt, MD 20771

[*]University of Maryland
College Park, MD 20742

William D. Hart

Science Systems Application Inc.
Lanham, MD 20706

The present study describes the cloud top structure of an East Pacific marine stratocumulus cloud layer as observed from a downward-pointing lidar system aboard the NASA ER-2 aircraft. The lidar observations were coordinated with in situ observations of cloud parameters. These data are applied to study important statistical properties of the stratus clouds. The study of cloud top structures is highly relevant for detailed radiation budget calculations. Because large gradients in temperature and humidity exist near the cloud top, cloud top emmitted radiation varies significantly in the vertical. Precise knowledge of cloud top location allows for a precise determination of cloud top cooling and thus determines an important loss/gain in the atmospheric thermodynamic energy budget. Cloud top topography and periodic structures influence the solar reflectance and therefore the albedo of the clouds.

The cloud lidar system aboard the NASA ER-2 consists of a Nd/YAG laser transmitting at 532 nm with firing repetition rate of 3.5 Hz. Along the line of flight, lidar shots are collected every 70 m. The digitization rate of individual lidar profiles is 20 MHz and corresponds to a vertical spatial resolution of 7.5 m. In situ data of cloud characteristics were collected by a Beechcraft Super King Air aircraft. Lidar and in situ data were supplemented by detailed pictures of the clouds taken by cameras aboard the ER-2 aircraft and by radiometer data obtained with the Multispectral Cloud Radiometer (MCR). This instrument recorded upwelling radiation in visible and near infrared wavelength bands.

The data descibed here was taken on September 28, 1983, during an experiment of 2.5 hours duration carried out in a region of 120 by 60 km over the Pacific Ocean near San Fransisco. The ER-2 flew at an altitude of 18 km in a racetrack pattern with east-west flight legs along $30°30'$ and $36°40'$ north near $124°30'$ west. The in situ aircraft flew racetrack patterns in the upper part of the cloud deck (700 - 1000 m) with occasional ascents and descents through the cloud-topped boundary layer (CBL).

The mean weather pattern on this day was typical summer-like with a northerly flow over the East Pacific. Therefore the cloud tops were sampled in a direction perpendicular to the mean CBL-wind. CBL potential temperature was

$14^{\circ}C$ with a mean specific humidity of 8 g/kg. At the cloud top, the mean potential temperature increased to $21^{\circ}C$ with rapidly decreasing specific humidity. Sea surface temperature was $17^{\circ}C$, so that the sensible heat flux into the atmosphere was positive. We have therefore reason to believe that the CBL was not in stationary balance with the ocean surface. Mean CBL wind speed was 12 m/s out of the north-northwest. At the CBL-top, winds dropped sharply and turned to the northeast.

During data analysis each signal was searched for its maximum backscatter value. This value does not necessary correspond to the cloud top since the backscatter increases rapidly upon encountering cloud water droplets. Cloud top height was computed as the first data level with a backscatter value above the ambient noise level just above the height of maximum backscatter. Cloud height measurements were corrected for aircraft roll, pitch and yaw, and for pressure altitude offsets.
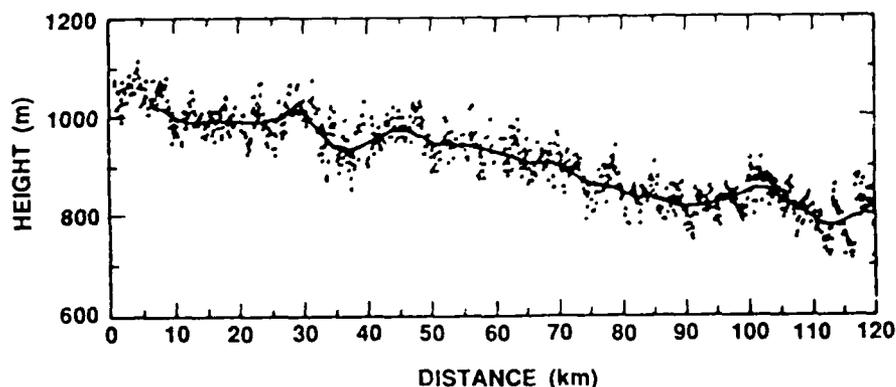
Figure 1. Cloud top heights as measured by the lidar. Individual data points and local mean (solid line) are shown.

Figure 1 shows the lidar measurements of cloud top height as a function of horizontal distance in west-east direction. Cloud top heights varied between 1050 m in the west to 800 m in the east. A remarkable fine-scale vertical variation in cloud top of the order of 80 m was present. Repeated flight legs along the same position showed no change in mean cloud height. However large variations were present on the smaller 1-5 km scale. Local mean cloud top height was removed from the data and cloud top height distributions were computed relative to the mean height. The average distribution function was normalized by the variance and by the integral of the distribution function.

Figure 2 shows the normalized distribution function fitted by a Gaussian and by a Gramm-Charlier expansion (GCE). This measured distribution function is based on 10338 individual lidar observations. The GCE is accepted as the proper fit to the measured distribution function based on a x^2-analysis.
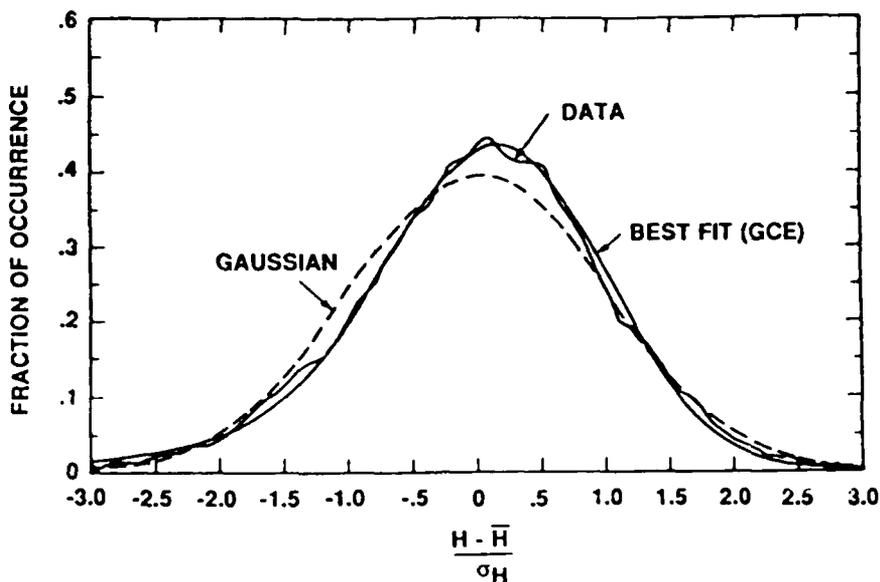
Figure 2. Measured and fitted cloud top distribution functions.
The distribution is measured relative to the mean and normalized
by the standard deviation.

It is evident that the average distribution function is negatively skewed.
This means that on the average clouds have flat tops and deep cusps at their
side. This is in accordance with close-up pictures of local cloud top
variations. The reason for the negative skewness is that upward-moving
convective motions in the cloud are damped by the existence of the strong
temperature inversion at the CBL-top, causing the local cloud tops to
spread out sideways. Downward moving parcels of radiatively cooled air do
not encounter such a natural boundary.
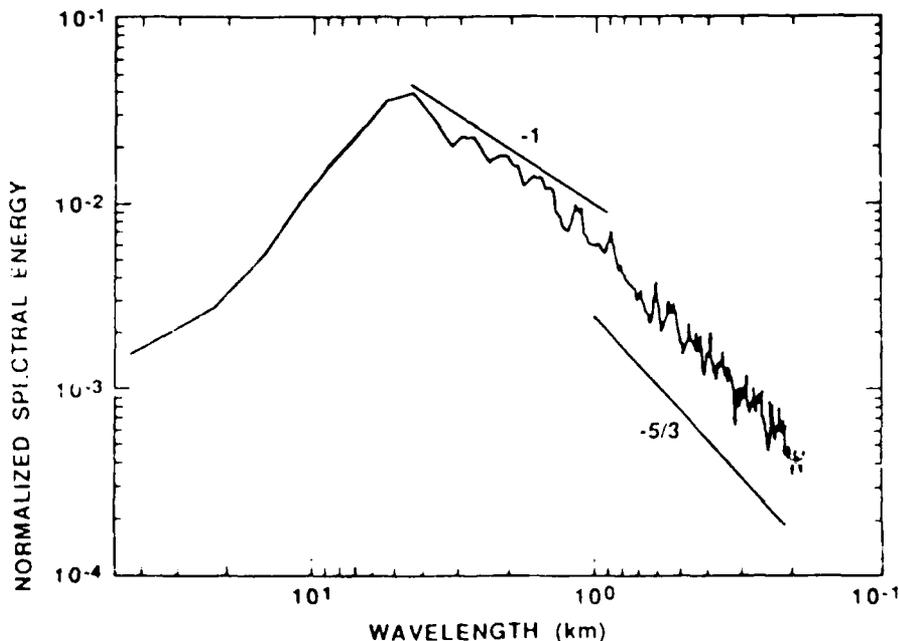
Figure 3. Average spectrum of cloud top variations with respect
to the mean cloud height.

Spectra of cloud top variations with respect to the local mean were computed and averaged. The average is shown in Figure 3. Plotted on a log-log scale are the normalized spectral variances as functions of wavelength. A wave lenght corresponds here to the size of a horizontal periodic structure. The spectral peak is found at 4.5 km or 6 times the depth of the CBL. A similar peak was also found in spectra derived from the visible channel (753nm) of the MCR and from in situ data of in-cloud parameters. It can therefore be established beyond reasonable doubt that the dominant cloud size in the direction perpendicular to the mean CBL-wind speed was 4.5 km. In the spectrum shown in Figure 3, two linear segments can be identified. One is following a k^{-1} law, the other a $k^{-5/3}$ law. The change in spectral slope at 900 m is significant as it corresponds to the mean CBL depth. The $k^{-5/3}$ law for cloud top fluctuations suggests a direct proportionality with an in-cloud turbulence parameter of which the most likely candidate is the vertical velocity w.

In conclusion, this study shows that detailed cloud top measurements can be made using a lidar system flying at high altitudes. Over a distance of 120 km cloud top heights varied as much as 300-350 m, while local variations were found of the order of 80 m. Therefore, cloud top cooling is present over at least those distances. This impacts CBL-modeling that uses a realistic cloud top inversion structure.

Airborne Sodium Lidar Measurements of Mesospheric Gravity Wave

Horizontal Structure over the Rocky Mountains and Great Plains

Kevin Kwon, Dan Senft and Chet Gardner

Department of Electrical and Computer Engineering
University of Illinois at Urbana-Champaign
1406 West Green St.
Urbana, IL 61801

In November 1986 an airborne lidar campaign was conducted to study the horizontal structure of the sodium layer. The campaign was based in Denver, CO, and 14 hours of data were collected during three flights over a total baseline of 7,500 km. The aircraft was a Lockheed-Electra operated by the NCAR RAF.

The flight plans are summarized in Table 1, and the flight paths are shown in Figure 1. The sodium layer appears to change significantly with latitude and longitude as shown in Figure 2 where some of the density profiles taken on the westbound leg of the eastward flight are plotted. The longitudinal variations of the centroid height measured on the eastward flights are shown in Figure 3. The centroid heights over the Rocky Mountains were higher than those over the Great Plains. These centroid height differences may be related to the orographic forcing over the Rocky Mountains.

The intrinsic gravity wave parameters can be estimated from the airborne sodium lidar data. The vertical wavelengths, amplitude and growth lengths are estimated from the spatial power spectra of vertical Na density profiles. The wave propagation directions and the ratio of vertical to horizontal wavelengths are estimated from the altitude variations of the Na density peaks or valleys. The background wind velocity in the direction of wave propagation can also be estimated

from the altitude variations of the density peaks or valleys. The
intrinsic periods are estimated using the dispersion relation, $T = T_g \lambda_h / \lambda_z$
where T_g is the Brunt-Vaisala period ($\simeq$ 5 min at the mesopause). These
parameters, which were calculated from the data taken on the westward
flight, are listed in Table 2.

Table 1. Summary of Flight Plans

Flight #	1	2	3
Date	Nov. 13	Nov. 15-16	Nov. 17-18
Time (MST)	2119-2358	2210-0306	2141-0503
Measurement Duration (hours)	2.65	4.93	7.37
Flight Pattern	Triangular	Eastward	Westward
	(Denver-NM-AZ-WY-Denver)	(Denver-Springfield IL-Denver)	(Denver-Pacific Coast-Denver)

Table 2. Intrinsic Wave Parameters (Westward Flight, Nov. 17-18, 1986)

Time	0020-0218 MST	Vert Phase Vel	0.64 m/sec
Vert Wavelength	6.40 km	Hori Phase Vel	21.56 m/sec
Hori Wavelength	716 km	Amplitude	5.2 %
Period	167 min	Growth Length	12.16 km
Wave Propag Angle (w.r.t. north)	177.8°	Meridional Background Wind	9.67 m/sec
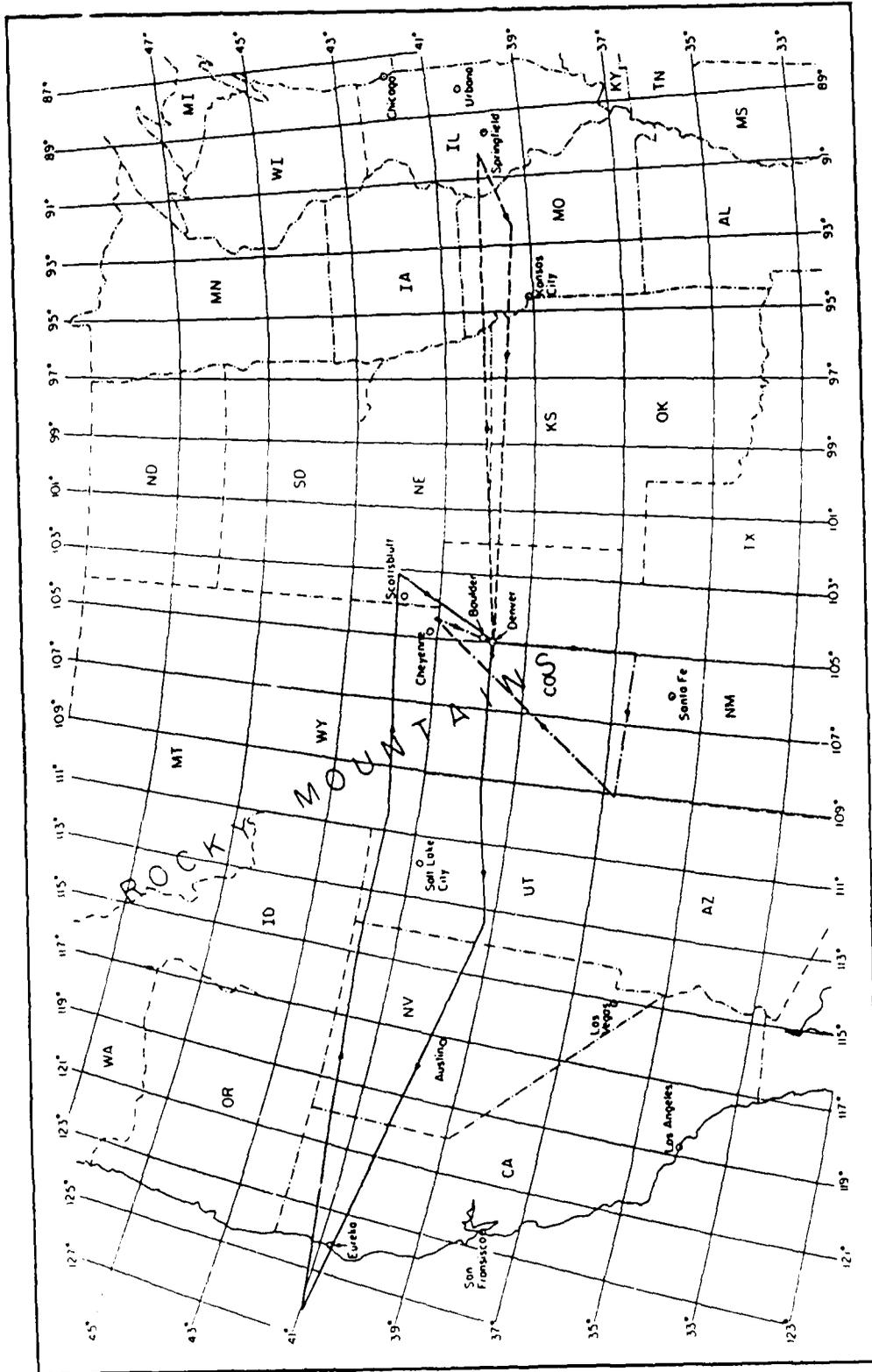
Figure 1. Flight patterns.
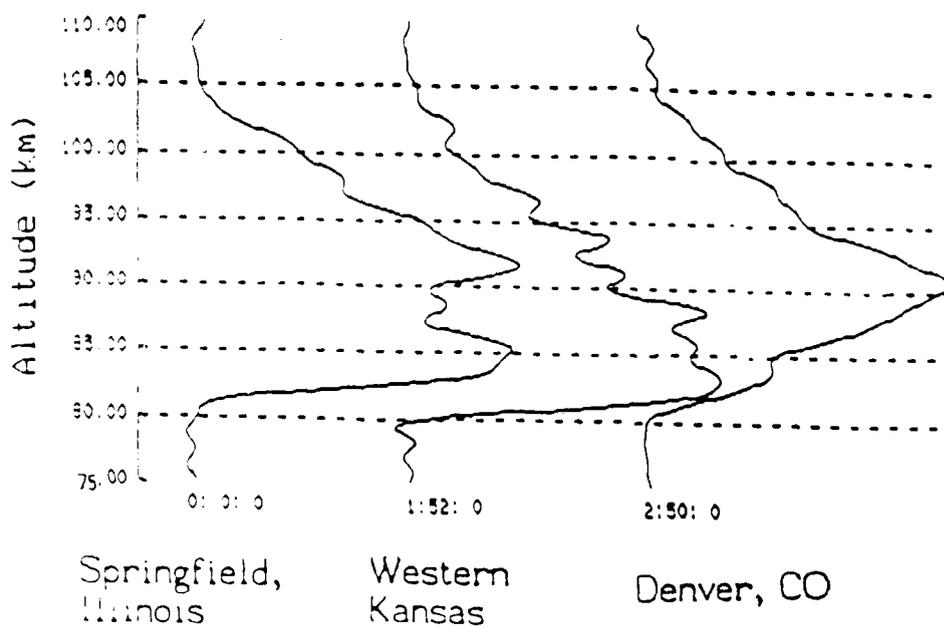
Figure 2. Density profiles taken on the westbound leg of the eastward flight.
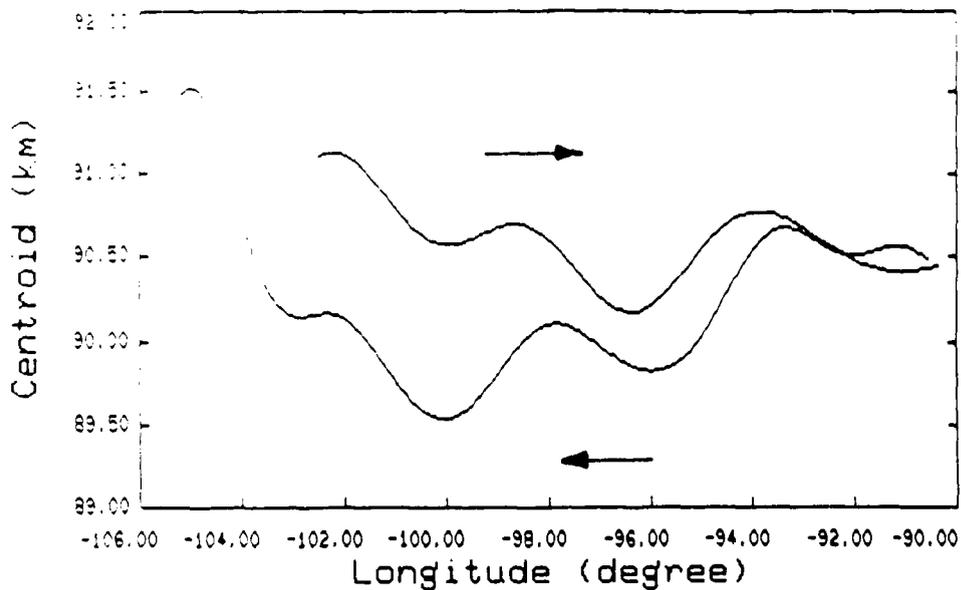
Figure 3. Centroid height variations observed on the eastward flight.

Sodium Lidar Measurements of the Seasonal and Nocturnal Variations of the Gravity Wave Vertical Wavenumber Spectrum

Daniel C. Senft, Chester S. Gardner, and Chao H. Liu

Department of Electrical and Computer Engineering
University of Illinois at Urbana-Champaign
1406 West Green Street
Urbana, IL 61801

Introduction

A method for computing the gravity wave vertical wavenumber spectrum and rms wind velocity from the data obtained by a sodium lidar system is described. The spectral slope and rms wind velocity temporal and altitude variations are determined.

Theory

The sodium layer response to gravity waves in the absence of chemical effects and diffusion is [Gardner and Voelz, 1987]

$$n_s(z,t) \simeq \exp[-\int_{-\infty}^{t} \nabla \cdot \underline{V} \, d\tau] \, n_0[z - \int_{-\infty}^{t} V_z d\tau]$$

where

n_s = sodium density

n_0 = sodium density in the absence of winds

$\underline{V}$ = wind field

V_z = vertical wind

z = distance from layer centroid.

The divergence term distorts the sodium layer by compression and rarefaction, while the vertical wind displaces the steady-state layer. The steady-state layer is modelled as a gaussian

$$n_0(z) = C \exp(-\frac{z^2}{2\sigma_0^2}) = C \exp[-g(z)].$$

To first order in $\underline{V}$,

$$\ln n_s(z,t) = -\int_{-\infty}^{t} \nabla \cdot \underline{V} \, d\tau + \ln C - g(z) + g'(z) \int_{-\infty}^{t} V_z \, d\tau.$$

The steady-state layer effects are removed, resulting in

$$f(z,t) = \ln n_s(z,t) - \ln C + g(z)$$

$$= \int_{-\infty}^{t} \nabla \cdot \underline{V} \, d\tau + \frac{z}{\sigma_o^2} \int_{-\infty}^{t} V_z \, d\tau .$$

The gravity wave polarization and dispersion relations can be used to relate $f(z,t)$ and its spectrum to horizontal wind velocity V_x and the vertical wavenumber spectrum. The variance of the horizontal wind velocity is

$$\langle V_x^2 \rangle \simeq \frac{\gamma(\gamma-1) \, Hg}{1 + \frac{1}{12} \left(\frac{\gamma HL}{\sigma_o^2} \right)^2} \; \frac{1}{L} \int_{-L/2}^{L/2} f^2(z) \, dz$$

where

L = altitude range of measurement ($\sim$ 20 km).

The vertical wavenumber spectrum is given by

$$E(k_z) \simeq \frac{1}{2} \; \frac{\gamma(\gamma-1) \, Hg}{1 + \frac{1}{12} \left(\frac{\gamma HL}{\sigma_o^2} \right)^2} \; \Phi_F(k_z)$$

$$\Phi_F(k_z) = \frac{1}{L} \left| \int_{-L/2}^{L/2} f(z) \, e^{ik_z z} \, dz \right|^2 .$$

Results

The vertical wavenumber spectrum for March 8-9, 1984, is shown in Figure 1. The spectral slope is -2.96, which is the expected result for saturating waves. The modelling results of Dewan and Good [1986] and Weinstock [1985] are shown for comparison.

Figure 2 shows the nocturnal variation in rms wind velocity. The increase in wave activity in the early morning is typical of the results from other dates. The variation with altitude of the rms wind velocity is shown in Figure 3. The amplitude growth length is less than the unsaturated value of 1/2H, supporting the conclusion that the waves are saturating. Around the layer peak it is not possible to calculate the rms wind velocity using the linear layer resp..nse since nonlinear effects are dominant. Seasonal variations in rms wind velocity are shown in Figure 4. The average, maximum, and minimum values for each night are shown. There appears to be a strong semiannual component with minima at the equinox.

Acknowledgement

References

Dewan,E.M. and R.E. Good, Saturation and the "Universal" Spectrum for Vertical Profiles of Horizontal Scalar Winds in the Atmosphere, J. Geophys. Res., 91, 2742-2748, 1986.

Gardner, C. S. and D. G. Voelz, Lidar studies of the nighttime sodium layer over Urbana, Illinois: 2. Gravity Waves, J. Geophys. Res., 92, 4673-4694, 1987.

Weinstock, J., Theoretical gravity wave spectrum in the atmosphere: Strong and weak wave interactions, Radio Sci., 1295-1300, 1985.
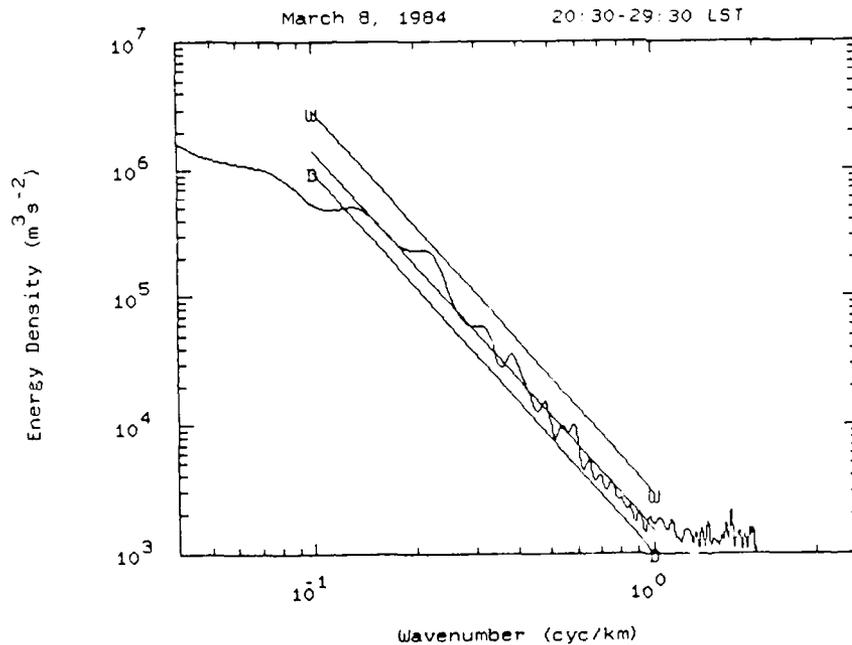
Figure 1.
Vertical wavenumber spectrum for March 8-9, 1984. Dewan and Good [1986] and Weinstock [1985] models are designated by D and W, respectively.
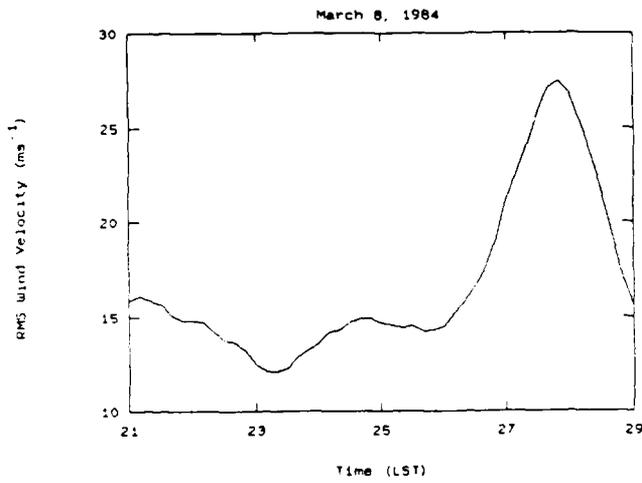
Figure 2.
Nocturnal variation
in rms wind velocity.
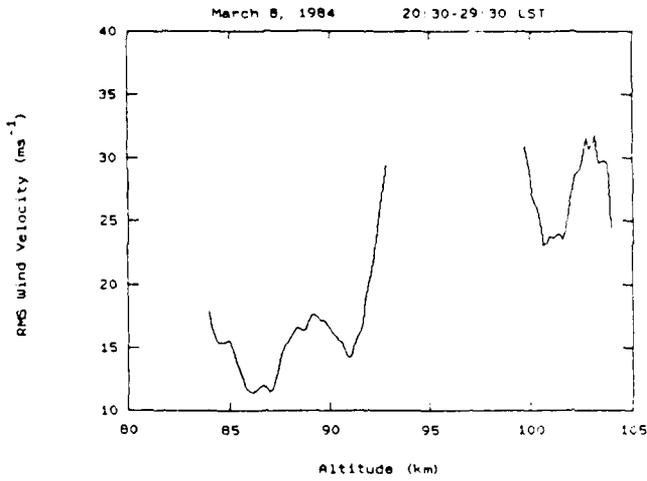
Figure 3.
Altitude variation
in rms wind velocity.
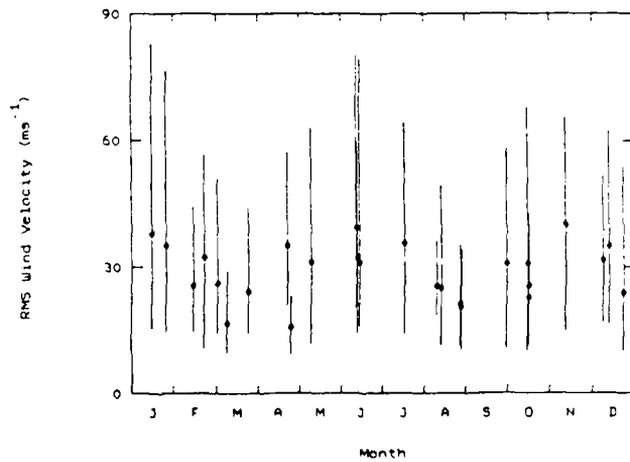
Figure 4.
Seasonal variation
in rms wind velocity.

Target Analysis by Differential Reflectance Lidars

L.Pantani, I.Pippi
Istituto di Ricerca sulle Onde Elettromagnetiche del CNR
Via Panciatichi 64, I 50127 Firenze, Italy

P.Vujkovic Cvijin, D.Ignjatijevic
Institut of Physics, P.O.B. 57, 11001 Beograd, Yugoslavia

The spectral reflectance, namely the fraction of the incident radiation flux reflected at a given wavelength, is an intrinsic characteristic of each natural or artificial surface. It seemed therefore interesting to investigate the potential of multiwavelength lidars in target identification by means of a spectral reflectance analysis; because of its wavelength agility the CO_2 laser is a very attractive one for this kind of analysis. The aim of this paper is to present the results of spectral reflectance measurements of relevant target surface materials at the CO_2 laser wavelengths in order to forecast the performances of a differential reflectance lidar.

Laboratory Measurements

The experimental setup is based on a grating tunable pulsed TEA CO_2 laser, the transmitted beam is sent on the sample, and the reflected radiation is detected by a suitable optics and a pyroelectric detector. A second detector which receives a small part of the outgoing radiation i used for energy normalization. The sample is placed on a rotating turntable in order to average the surface irregularities.

the samples were divided in four classes:
- Calibration targets and reflectance standards (6 samples)
- Geological materials (15 samples)
- Construction materials (4 samples)
- Vegetation (13 samples)

For what concern the calibration targets it is known that suitable materials should be: durable, reproducible, easy to fabricate, Lambertian, and with a known and uniform spectral reflectance in the wavelength range of CO_2 lasers. As a result of the experiment diffusely reflecting aluminum targets represent the right choice even if they are not always strictly Lambertian.

The geological and construction materials are generally of complicated chemical structure with variable mineral composition giving reflectance spectra that could notably vary from sample to sample. Neverthless the important reflectance maxima produced in this wavelength region by silicate minerals show a good potential in differential reflectance remote sensing.

The vegetation samples were composed by foliage, grass, and some plants of agricultural interest. The spectra of grass were remarkably different from the spectra of foliage, and here is a difference in the 10 micron region between deciduous and coniferous trees. Changes were also observed in spectra of wheat at different vegetation times and in other crops of agricultural interest.

Data Processing

The spectra were processed in order to identify the wavelength

couples which allow the target identification. As a result of
this processing the possibility of detecting different geolo-
gical species and vegetation samples with a maximum of four
wavelengths was shown.

References

1) L.Pantani, I.Pippi: Optica Acta, 30, 1473 (1983)

2) L.Pantani, I.Pippi: "The differential reflectance lidar
   and its potential in remote sensing of natural and human
   made targets." II Col.Int. Signatures spectrales d'objets
   en teledetection, Le Colloques de l'INRA n.23, 823, INRA,
   Paris 1983

3) P.Vujkovic Cvijin et alii:"Spectral reflectance of topogra-
   phic target surface materials: implications on wavelength
   scanning CO_2 laser based lidars." 12 th ILRC, Aix en Provence
   August 1984

Investigation of the Photosynthetic Process by Lidar Fluorosensors

F.Castagnoli, G.Cecchi, L.Pantani, B.Radicati, M.Romoli
Istituto di Ricerca sulle Onde Elettromagnetiche del CNR
Via Panciatichi 64, I 50127 Firenze, Italy

P.Mazzinghi
Istituto di Elettronica Quantistica del CNR
Via Panciatichi 56, I 50127 Firenze, Italy

Chlorophyll plays a fundamental role in the photosynthetic process of living plants, it is therefore obvious that each phenomenon related to chlorophyll may also be related to the photosynthetic process. Since chlorophyll a shows a strong fluorescence emission in the wavelength region between 670 nm and 740 nm it is attractive to analyze the potential of laser fluorosensors in the remote sensing of living plants. While a quite large number of papers were devoted to the lidar remote sensing of chlorophyll fluorescence in phytoplancton only few papers has been devoted to the remote sensing of chlorophyll fluorescence in living plants. A research program in this field was started as a part of a national program on agriculture improvement (IPRA Project), the analysis was carried out in the laboratory by means of a lidar simulator and in fields by means of the lidar fluorosensor FLIDAR-2.

High resolution spectra were detected and processed in order to investigate their behavior, and particularly the two components at 685 nm and 730 nm, and the relationships with the photosynthetic process with the aim of investigating the potential of lidar fluorosensors in the detection of plant health.

Laboratory Experiments

The laser excited fluorescence in living plants was analyzed by means of a "lidar simulator" composed by different laser heads, both pulsed and CW, a suitable focusing and receiving optics, a grating spectrometer, and a PAR OMA-2 multichannel analyzer. Different phenomena were investigated like the change of the intensity and behavior of the fluorescence spectrum with the excitation wavelength, the exposure time to the laser radiation, the background radiation, etc.

As a result of this analysis a physical model of chlorophyll a fluorescence in living plants and of its relationships with the photosynthetic process was developed; this model fits quite well the experimental results.

A second part of the laboratory experiments was devoted to the detection of laser excited fluorescence spectra of living plants submitted to water stress or to cold stress. These experiments showed the influence of the stresses on the ratio between the two peaks of the fluorescence spectrum at 685 nm and 730 nm.

Field Experiments

Field experiments were carried out whith the high spectral re-solution fluorosensor FLIDAR-2; these experiments started in October 1986.

The FLIDAR-2 operates at the same time as a fluorosensor and as a passive spectrometer. The reflectance spectra detected in the spectrometer operation are used both for the subtraction of background from the fluorescence spectra and for the evaluation

of the leaf area index (LAI).

In the first experiment the change of the fluorescence spectrum with the solar radiation intensity was investigated on some Douglass firs. A good agreement was found between the intensity of the photosynthetic active radiation (PAR) and the ratio between the fluorescence emission at 685 nm and 730 nm. This result confirmed the detectability in operational conditions of the photosynthetic process behavior by means of laser fluorosensors.

Other field experiments are planned in Summer 1987.

References

1) G.Cecchi et alii:"Vegetation remote sensing: a new field for lidar applications" ECOOSA 1984, SPIE Vol.:492, 180, SPIE, Bellingham 1985

2) G.Cecchi et alii:"Fluorescence lidar remote sensing of the environment: laboratory experiments for the characterization of oil spills and vegetation." in LASER, Optoelectronics in Engineering, 660, Springer, Berlin 1986

3) G.Cecchi, L.Pantani, I.Pippi:"Lidar remote sensing of vegetation" in Physics in Environmental and Byomedical Research, 375, World Scientific Pub. Co., Singapore 1986

4) F.Castagnoli et alii:"A fluorescence lidar for land and sea remote sensing" in Laser Radar Technology and Applications, SPIE Vol.: 663, 212, SPIE, Bellingham 1986

FLIDAR-2 a Compact Lidar Fluorosensor and Spectrometer

F.Castagnoli, G.Cecchi, L.Pantani, B.Radicati

Istituto di Ricerca sulle Onde Elettromagnetiche del C.N.R.,
Via Panciatichi 64, I 50127 Firenze, Italy

The FLIDAR-2 is the result of the researches carried out at IROE-CNR on the remote sensing of the environment by lidar fluorosensors and passive optical sensors.

The FLIDAR-2 is the first lidar fluorosensor having high spectral resolution, and it is based on a new idea in remote sensing of the environment because it operates at the same time as a lidar fluorosensor and a passive spectrometer. The use of the same device for active and passive remote sensing allows a perfect comparison between the data and reduces weights and costs.

The System

The FLIDAR-2 is divided in three modules:
- Sensor
- Control Electronics
- Gas Handling

Sensor - This module contains the excitation laser, the receiving system, and a standard TV camera.

The laser was expressly designed for this application and is composed of an excimer laser operating at 308 nm, a dye laser and/or a Raman shifter; the last two units are pumped by the excimer laser. This solution gives an excitation wavelength which can be shifted from UV to the near IR. The receiving system is composed by a newtonian telescope having in its focus the

entrance slit of a grating spectrometer; the output spectrum is detected by an intensified and gatable photodiode array.

Control Electronics - This module contains the minicomputer which controls the acquisition, presentation, and recording of data. It contains also the battery power supply and the TV recorder.

Gas Handling - This module contains the gas cilinders and the whole gas handling system for the excimer laser; the module is connected to the lidar only during the refilling of the excimer laser. This solution allows an important reduction of weights and sizes during the field experiments because the system operates only with the first two modules.

```
SENSOR MODULE
Excimer Laser (Xe-Cl, 308 nm)
Pulse Energy: 80 mJ                    Max p.r.f.: 10 Hz
Pulse Length: 15 ns
Dye Laser and Raman Shifter
- Data depending from the particular system used
Receiving System
- f:4, 250 mm Ø, Newtonian telescope
- f:4 grating spectrometer with three gratings interchangeable during the
  measurement:
  Dispersion (nm/mm)  3.0 - 6.0 - 24.0
  Spect. Range (nm)   37.5 - 75.0-300.0
- Detector: 512 elements, intensified, gatable, diode array
- Over all size: 1x1.2x0.6 m          Weight: 84 kg (without batteries)
CONTROL ELECTRONICS MODULE
- Console PAR OMA-3, with 20Mb hard disk and floppy disk
- Batteries, inverter, video recorder
- Over all size: 0.77x 0.5x0.5 m      Weight: 63 kg (without batteries)
GAS HANDLING MODULE
- Over all size 1.5x0.5x0.7 m         Weight: depending from the cilinders
POWER SUPPLY
- 24 V dc 20 A/h (laser) and 63 A/h (electronics),   220 V 50 Hz optional
```

Table I - Technical characteristics of FLIDAR-2

Applications

The FLIDAR-2 allows the remote sensing of high resolution spectra of laser stimulated emissions like fluorescence and Raman (lidar function) and of target reflectance (spectrometer function). The system was expressly designed for operations from fixed and moving platforms; its size and weight are particularly suitable for airborne use also with small aircrafts.

On the basis of the laboratory and field experiments carried out in the past a set of software packages was developed and stored in the control electronics module. By means of this software it is possible to process the detected spectra in order to:
- Measure the thickness of oil film over the water
- Identify the oil in spills
- Analize the photosyntetic process in living plants

Other software packages are under development at present.

The FLIDAR-2 is also an important help in the design of remote sensing systems, fluorescence lidars and spectrometers, for specific applications. The high resolution spectra can be in fact processed via software in order to forecast the performances of lower resolution systems.

The field tests, which started in October 1986, have confirmed the forecasted performances of the FLIDAR-2.

Future Improvements

Also if the FLIDAR-2 is a very powerful remote sensor for environmental applications its performances can be improved with a time resolved channel, for sea bathymetry and vegetation thickness measurements.

References

1) P.Burlamacchi et alii: Appl. Opt., 22, 48 (1983)

2) G.Cecchi et alii:"Lidar investigation of oil films on
   natural waters" in OPTOELECTRONICS IN ENGINEERING, 517,
   Springer, Berlin 1983

3) G.Cecchi et alii:"Vegetation remote sensing: a new field
   for lidar applications", ECOOSA 1984, SPIE Vol.:492, 180,
   SPIE, Bellingham 1985

4) G.Cecchi et alii:"Fluorescence lidar remote sensing of the
   environment: laboratory experiments for the characterization
   of oil spills and vegetation" in LASER, OPTOELECTRNICS IN
   ENGINEERING, 660, Springer, Berlin 1986

5) F.Castagnoli et alii:"A fluorescence lidar for land and sea
   remote sensing" in LASER RADAR TECHNOLOGY AND APPLICATIONS,
   SPIE Vol.:663, 212, SPIE, Bellingham 1986

Oil Film Detection and Characterization by Lidar Fluorosensors

G.Cecchi, L.Pantani, B.Radicati, A.Barbaro
Istituto di Ricerca sulle Onde Elettromagnetiche del CNR
Via Panciatichi 64, I 50127 Firenze, Italy

P.Mazzinghi
Istituto di Elettronica Quantistica del CNR
Via Panciatichi 56, I 50127 Firenze, Italy

The use of lidar fluorosensors in the detection of oil films
over the water surface is well known and laboratory and field
experiments were done by different authors in the past years.
A systematic analysis of fluorosensor performances in dete-
ction and characterization of oil films was carried out as a
part of the IROE program of environmental remote sensing. The
investigation concerned the definition of the best laser wave-
lengths, the measurement of film thickness, the identification
of the minimum detectable film thickness, the identification of
the oil which composes the film. The results of this analysis
were the base of the development of IROE FLIDAR-2 hardware and
software.

The analysis was mainly done using a "lidar simulator" built
with an excimer laser, an excimer pumped dye laser, a suitable
transmitting and receiving optics, a grating spectrometer, and
a PAR OMA-2 optical multichannel analyzer. The fluorescence
spectra were detected and processed and the appropriate software
was developed for each one of the abovementioned problems in
view of the use on operational systems.

Source selection and minimum detectable thickness

The first experiments were devoted to the identification of the
most suitable laser source for oil detection. The parameters

taken into account were:

- The oil fluorescence efficency
- The atmospheric absorption at both the excitation and fluorescence wavelengths
- The laser efficency

The XeCl excimer laser gave the best compromise for thin oil layers, while an excimer pumped dye laser operating in the range of 420 nm gave the best compromise for thick layers.

The minimum film thickness detectable with XeCl excitation was identified in around 10 nm.

Film thickness measurements

If the film thickness is lower than the optical penetration depth in the oil at the involved wavelengths it can be measured or by intensity of the fluorescence signal, which increases with the thickness, or by the intensity of the water Raman signal, which decreases with thickness. The experiments showed that the use of Raman signal depression is more suitable for thicknesses below 100 nm.

In the measurement of film thickness the oil absorption at the involved wavelengths is an important parameter which is practically impossible to obtain by standard techniques. An original and easy technique for the measurement of the extinction coefficient in high absorbing fluids was identified during these experiments.

Oil identification

The potential of the lidar fluorosensor in the identification of the oil which composes the film was investigated with the

aid of a library of fluorescence spectra of more than 60 differen mineral oils; a particular attention was devoted to techniques which may allow an automatic processing and presentation of data.

Crosscorrelation techniques showed a good potential in the identification of the oil class (crude, light, heavy) while the use of the ratio between the fluorescence intensities at two properly selected wavelengths showed the same potential and the possibility of an identification inside the class.

References

1) P.Burlamacchi et alii: Alta Frequenza, 52, 233 (1983)

2) P.Burlamacchi et alii: Appl. Opt., 22, 48 (1983)

3) G.Cecchi et alii:"Lidar investigation of oil films on natural waters" in Optoelectronic in Engineering, 517, Springer Berlin 1983

4) F.Castagnoli et alii:"Remote sensing of oil on the sea: Lidar and passive IR experiments" Proc.EARSeL/ESA Symp.: "European Remote Sensing Opportunities, ESA SP233, 121, ESA Paris 1985

5) D.Diebel-Langhor et alii:"Measuring oil at sea by means of an airborne laser fluorosensor" in "The ARCHIMEDES 1 Experiment, EUR10216 EN, 123, CEC, Luxemburg 1985

6) G.Cecchi et alii:"Fluorescence lidar remote sensing of the environment: laboratory experiments for the characterization of oil spills and vegetation" in Laser, Optoelectronics in Engineering, 660, Springer, Berlin 1986

7) F.Castagnoli et alii:"A fluorescence lidar for land and sea remote sensig" in "Laser Radar Technology and Applications, SPIE 663, 212, SPIE, Bellinghem 1986

Dr Claude CAHEN
Direction des Etudes et Recherches
Electricité de France
25, Allée Privée - Carrefour Pleyel
93206 Saint-Denis - CEDEX 1
FRANCE

AEROSOLS AND HUMIDITY PROFILES
RECORDED USING THE ALEXANDRITE LASER :
PRELIMINARY RESULTS AND SYSTEM TESTS

Since 1983 we were developing fully mobile new DIAL system to monitor the major meteorological parameters (humidity, temperature, aerosols) using the alexandrite laser as the transmitter.

During july 1987, a field campaign was started to evaluate the actual performances of the system after a one year testing in our laboratory. The aim of this campaign was twofold :

- First, the evaluation of the entire system performances in terms of range detectivity, ultimate accuracies and limitations,

- Second, the records of first water vapour profiles using the alexandrite laser.

EVALUATION OF THE SYSTEM PERFORMANCES

To check for the system performances we used an emitted wavelength in the range 750-755 nm, a region free of absorption and corresponding to the maximum available energy of the laser source.

Comparisons of daytime and nighttime ranging have been performed ; a precise quantification of the transmitter/receiver optics efficiency has been computed. Systematic comparisons of the different accuracies corresponding to different gains of the switchable gain micro-processor controled ADC converter have been made.

The analysis of the obtained results will be reported at the meeting.

FIRST WATER VAPOUR MEASUREMENTS WITH THE ALEXANDRITE LASER

Different measurements using couples of wavelengths attainable within a reasonable operation of the alexandrite laser will be slow. Using the numerous realtime laser controls which are performed during an acquisition sequence, we will try to estimate the relative importances of the different tests. A detailed discussion of the actual accuracy of the measured profiles will be adressed. The influence of the sequential acquisition scheme will be partly discussed.

Spatial Sampling of the Measuring Volume by the
Introduction of Dedicated Apertures in Lidar Systems

Steen Hanson
Risoe National Laboratory, Denmark

In ordinary Laser Doppler Anemometry (LDA) light scattered from single particles from two different beams of laser light is mixed coherently on a photodetector surface. The detector current contains information on the velocity of single particles, and various temporal moments of the velocity distribution can be deducted from the readings. LIDAR systems for velocity determination based on infrared sources are usually depending on parametric amplification and will therefore solely probe the longitudinal flow velocity, whereas systems based on lasers emitting visible light are independent of a local oscillator facilitating the probing of all three velocity components in a small measuring volume.

It will be shown how the introduction of dedicated apertures in the Fourier plane of the scattered field from the particles will bring about a method for conditional sampling of the measuring volume. This implies that only fields scattered from particles with a fixed relative - but not absolute - position will mix coherently on the detector. A system based on dedicated apertures will therefore give the velocity difference between particles having a well-defined and known spatial separation.

The effect of the dedicated aperture can be analyzed by writing up the field in the Fourier plane of a single emitted beam LIDAR system which is either monostatic or bistatic. This field is the Fourier transform of the scattered field from the particles which is essentially a sum of delta functions. The dedicated aperture function is multiplied to give the field incident on the detector. The intensity is the field absolutely squared which is integrated over the detector surface to give the detector current. Parseval's theorem can be used to transfer this integral from the Fourier plane to the measuring volume. The integral is now changed into an integral of the absolute square of the sum of delta functions from the scattering particles convoluted with the Fourier transform of the dedicated aperture. If, for instance, the dedicated aperture is a grating-like function, the Fourier transform will be a double delta function with a separation given by the grating constant, the wavelength of the light, and the focal length of the lens. The convolution in the measuring volume picks out particle pairs with the right mutual separation. The detector current will therefore have a frequency content which with this aperture is given by the velocity difference between particles with the known relative separation.

It will be shown how the introduced aperture can be employed simultaneously in the transmitter and receiver part of the system to enhance the signal quality.

The use of matched dedicated filters in separated transmitter and receiver aperature will be shown to alleviate the demands for temporal and spatial coherence of the source.

Schemes for measurement of vorticity in the atmosphere will be presented. A cloud of particles rotating as a rigid body can be probed. The rotational speed around, e.g., the y-axis is completely determined if the velocity difference in the z-direction is measured provided that the separation in the x-direction is known. The same concept can be employed in a monostatic CO_2-system relying on parametric amplification of the scattered radiation.

References:

1) S.G. Hanson: "The Laser Gradient Anemometer", Photon Correlation Techniques in Fluid Mechanics, Springer Verlag Berlin, Heidelberg, New York (1981) pp. 212-220.

2) S.G. Hanson: "Laser-based Method for Analyzing Rotational Speed and Vorticity", International Symposium on Laser Anemometry-FED-Vol. 33 published by the American Society of Mechanical Engineers.

TUESDAY, SEPTEMBER 29, 1987

CONFERENCE ROOM 5

8:30 AM–10:15 PM

TuA1-5

OPTICAL TECHNIQUES FOR EARTH SYSTEM SCIENCE

J. Fred Holmes, Oregon Graduate Center, *Presider*

Satellite Remote Sensing for Earth System Science:
NASA's Earth Observing System (Eos)

Robert J. Curran
Office of Space Science and Applications
National Aeronautics and Space Administration
Washington, DC 20546 U.S.A.

Environmental concerns of a global nature are influencing the development of a multidisciplinary approach to understanding the Earth as a system. In recent years these concerns have become more prominent due to a series of problems involving large geographic regions such as; understanding the effects of the increases in carbon dioxide, understanding the causes and consequences of changes in the ozone layer, and resolving the anthropogenic influence on the acidity of precipitation. Clearly the global scope of these and other problem areas requires both a multidisciplinary, as well as a multinational approach for their solution. In order to address these problems, observational capabilities must be employed ranging from in situ and laboratory measurements to satellite based global remote sensing. An Earth Observing System (Eos) is planned to meet many of these requirements for remote sensing from low Earth orbiting satellites. A number of instruments are under consideration as the payload for the sun-synchronous satellite platforms. The payload is conceptually grouped into three packages to illustrate the synergistic relationships that exist among the instruments.

The first package of Eos instruments is termed the Surface Imaging and Sounding Package (SISP). It includes four capabilities: Moderate-Resolution Imaging Spectrometer (MODIS), High-Resolution Imaging Spectrometer (HIRIS), High-Resolution Multifrequency Microwave Radiometer (HMMR), and Lidar Atmospheric Sounder and Altimeter (LASA). If flown together, this package of instruments will probe the same atmospheric conditions, which will enable their data to be compared and combined in detail to produce more information

The second package consists of three radar techniques -- and is called Sensing with Active Microwaves (SAM). This package consists of three instruments: Synthetic Aperature Radar (SAR), Radar Altimeter, and Scatterometer. In general, the variables observed with these three instruments are sufficiently persistent (land, ocean, and ice features) to permit them to be flown in different orbits from one another without significant sacrifice of scientific return.

The third package is the Atmospheric Physics and Chemistry Monitors (APACAM). The Eos strategy relies upon the operational payloads for soundings of atmospheric temperature, coarse vertical profiles of moisture, and general characterization of clouds. The remote sensing of the atmosphere can be broken down into measurements of the troposphere or lower atmosphere and of the stratosphere and mesosphere or upper atmosphere. It can also be divided into measurements of the temperatures, chemical species, and aerosols, which comprise the atmospheric composition and structure, and measurements of the winds. This pair of dichotomies in atmospheric variables to be measured results in four general instrument types being included in the Eos payload --
Laser Atmospheric Wind Sounder (LAWS) measurements of the lower atmosphere, tropospheric composition measurements, upper atmosphere temperature and composition measurements, and Fabry-Perot Interferometry measurements of upper atmospheric

winds. Within the APACM package there is a need to fly the upper atmospheric instruments together. These all use limb scanning to achieve sufficient vertical resolution. The tropospheric devices could be flown separately from the upper atmospheric devices.

The presentation will describe the general approach taken in developing the Eos concept. This includes it's contribution to the NASA's proposed thrust entitled "Mission to Planet Earth." The remander of the discussion will focus on more of the details of several of the active and passive instruments which use optical techniques.

REMOTE SENSING OF EARTH AND PLANETARY ATMOSPHERES USING GAS CORRELATION SPECTRORADIOMETRY

Daniel J. McCleese
Jet Propulsion Laboratory
Pasadena, California

INTRODUCTION

Gas correlation spectroradiometry is one of the most frequently used techniques for remote measurements of atmospheric properties. It is a relatively simple and robust technique which is most useful in applications where very high spectral discrimination (up to the line Doppler width) is required and yet signal levels are low. Such is the case for Earth upper atmospheric temperature and species abundance measurements and for numerous planetary measurement objectives. The first spaceborne gas correlation experiment (Abel et al 1970) was flown on Nimbus 4 by Oxford University to obtain global measurements of stratospheric temperature. Since the launch of that instrument in 1970, eight Earth orbital instruments and one planetary experiment have used this technique for a variety of atmospheric investigations. Gas correlation spectroradiometry continues to offer significant advantages over other instrumental approaches for investigations in which instrument capability and complexity are equally important considerations. For example, the atmospheric sounder now being developed at JPL for the Mars Observer planetary mission (McCleese et al 1986) uses gas correlation spectral channels to achieve a resolution of 0.01 cm^{-1} in the mid-infrared using hardware of minimum complexity and having substantial flight heritage.

GAS CORRELATION SPECTRORADIOMETERS

In each of the various approaches to implementing gas correlation spectroradiometry a path of gas is contained within the instrument. There is, therefore, a requirement inherent in the technique that the atmospheric gas of interest be selected in advance. It is also essential that the spectroscopic characteristics of that gas be well understood. Consequently, correlation techniques are most effective when applied to focused measurement objectives. Global mapping of atmospheric fields over extended periods represent a particularly appropriate use of correlation spectroradiometry. The selective chopper and pressure modulator radiometers on the Nimbus and TIROS Earth orbiting spacecraft are examples for which the routine, global mapping of atmospheric temperature was conducted almost continously for 12 years. However, the technique is not suited to surveys of atmospheric composi-

tion as is required in the early phases of the exploration of a planet. Instrument complexity increases almost linearly with the number of molecular species to be observed, so that correlation spectroradiometry becomes inappropriate when more than a few atmospheric components are to be measured.

The most significant advantages of these instruments, high spectral discrimination and species selectivity coupled with a large energy grasp, can be realized only when the observed spectral line widths are small compared with the interline spacing. For this reason correlation spectroradiometry is only infrequently applied to studies of the Earth's troposphere in which pressure boardening tends to blend the spectral lines of the gas of interest. Simple filter radiometry is often more appropriate in these situations.

Selective Chopper Radiometers

The Nimbus 4 Selective Chopper Radiometer (SCR) was the first spaceborne implementation of correlation spectroradiometry. This instrument made nadir viewing emission radiometry measurements of stratospheric temperature using the 15 micron band of CO_2. In a selective chopper two optical paths having different amounts of gas are sampled alternately by a detector. The radiometric difference between these two paths is a measure of the radiation originating from the atmosphere within the spectral line profiles of the reference gas. Although simple in concept, the selective chopper suffers from considerable difficulties in achieving a radiometric balance between the two optical paths; an imbalance introduces a large offset in the signal. This radiometric imbalance is frequently very much larger than the atmospheric signal. Long-term calibration of these instruments is, as a consequence, difficult. Nevertheless, the Nimbus 4 and succeeding Nimbus 5 SCR investigations were very successful and provided our first global maps and long-term record of temperature in the Earth's upper atmosphere (Barnett et al 1972; Ellis et al 1973).

Pressure Modulator Radiometers

An elegant solution to the radiometric calibration problems associated with selective chopping has resulted in the highly successful pressure modulator radiometer (Taylor 1983). In this approach a single path of gas is used in the correlation measurement. A piston driven at resonance modulates the line of sight amount of gas in a cell. The correlation signal is derived from the phase sensitive detection of the resulting modulation of radiation transmitted by the cell. First used on the Nimbus 6 spacecraft launched in 1975, these devices have since been flown on Nimbus 7 for limb measurements of stratospheric and mesospheric temperature and species abundances (Drummond et al 1980; Barnett et al 1985) including CO, CH_4, NO, N_2O and H_2O, and on the TIROS series of operational spacecraft. The Pioneer Venus mission carried a pressure modulator to study the thermal structure of the upper atmosphere of Venus (Taylor et al 1979). Two new infrared limb viewing instruments employing pressure modulation are under development at the present

time. The Improved Stratospheric and Mesospheric Sounder uses eight pressure modulation units, and will be flown on the Upper Atmospheric Research Satellite for temperature and species measurements. The Pressure Modulator Infrared Radiometer (McCleese *et al* 1986) is to fly on the Mars Observer spacecraft and will obtain vertical profiles of water vapor abundance and temperature throughout the lower and middle atmosphere of Mars using two modulators, one containing water vapor and other containing carbon dioxide.

The evolution of pressure modulation radiometry has brought significant sophistication to the technique. By means of careful selection of path length, gas mean pressure and compression ratio the spectral selectivity of the modulator can be tuned to sample the centers, or the near or far wings of the atmospheric lines. For Mars, the species specificity and high spectral discrimination capabilities of correlation techniques are crucial to successful atmospheric measurements. The ubiquitous atmospheric dust virtually rules out techniques which are unable to distinguish between continuum spectral features and those arising from gaseous line emission. Because of the large amount of CO_2 in the Martian atmosphere, high spectral resolution is required to achieve measurements with adequate vertical resolution (one-half scale height). A spectral resolution of 0.01 cm^{-1} is needed to sense the near wings of the lines, while avoiding the inverted line centers which are dominated by emission from the upper atmosphere.

Electrooptic Phase Modulation Gas Correlation Spectroradiometers

The direct measurement of upper atmospheric winds has become the focus of a new application of gas correlation techniques (McCleese and Margolis 1983). The very high spectral discrimination and large energy grasp of correlation spectroradiometry are particularly attractive attributes for the task of remotely sensing winds. The wind induced Doppler shift in the emission spectrum of a stratospheric gas is a small fraction of the width of a spectral line, yet the measurement of that Doppler shift is a direct determination of the wind speed. However, from a spacecraft platform and for the viewing geometry required to determine wind vectors, the relative motion between the instrument and atmosphere introduces a Doppler shift approximately 200 times greater than that due to the wind. To accomodate the large spectral offset and measure winds, a group at JPL has devised a technique which optically modulates the observed spectrum to produce a correlation signal. An electrooptically active crystal whose refractive index is changed by an applied electric field replaces the mechanically induced modulation of the pressure modulator (Rider *et al* 1986). In addition, the frequency distribution of the observed spectrum is under the control of the instrument, making frequency correlation measurements, and thus wind sensing, possible. Numerical simulations of the performance of an Earth orbiting electrooptic phase modulation gas correlation spectroradiometer show that winds in the 20 to 120 km altitude range can be measured with one-half scale height vertical resolution and an accuracy of better than 5 m/s.

REFERENCES

P. G. Abel *et al*, "Remote Sounding of Atmospheric Temperature from Satellites II. The Selective Chopper Radiometer for Nimbus D", *Proc. R. Soc. Lond. A320*, pp.35-55 (1970).

D. J. McCleese, J. T. Schofield, R. W. Zurek, J. V. Martonchik, R. D. Haskins, D. A. Paige, R. A. West, D. J. Diner, J. R. Locke, M. P. Chrisp, W. Willis, C. B. Leovy, and F. W. Taylor, "Remote Sensing of the Atmosphere of Mars Using Infrared Pressure Modulation and Filter Radiometry", *Applied Optics 25*, pp. 4232-4245 (1986).

J. J. Barnett *et al*, "The First Year of the Selective Chopper Radiometer on Nimbus 4", *Quart. J. R. Met. Soc. 98*, pp. 17-37 (1972).

P. J. Ellis *et al*, "Remote Sounding of Atmospheric Temperature from Satellites, IV. The Selective Chopper Radiometer for Nimbus 5", *Proc. R. Soc. Lond. A334*, pp. 149-170 (1973).

F. W. Taylor, "Pressure Modulator Radiometry", *Spectrometric Techniques*, Vol. III, pp. 137-197 (1983).

J. R. Drummond, H. T. Houghton, G. D. Peskett, C. D. Rodgers, M. J. Wale, J. Whitney, and E. J. Williamson, "The Stratospheric and Mesospheric Sounder on Nimbus 7", *Phil. Trans. R. Soc. London, Ser. A296*, pp. 219-241 (1980).

J. J. Barnett, M. Corney, A. K. Murphy, R. L. Jones, C. D. Rodgers, F. W. Taylor, E. J. Williamson, and N. M. Vyas, "Global and Seasonal Variability of the Temperature and Composition of the Middle Atmosphere", *Nature 313*, pp. 439-443 (1985).

D. J. McCleese and J. S. Margolis, "Remote Sensing of Stratospheric and Mesospheric Winds by Gas Correlation Electrooptic Phase-Modulation Spectroscopy", *Applied Optics 22*, pp. 2528-2534 (1983).

D. M. Rider, J. T. Schofield, J. S. Margolis and D. J. McCleese, "Electrooptic Phase Modulation Gas Correlation Spectroscopy: A Laboratory Demonstration", *Applied Optics, 25*, pp. 2860-2862 (1986).

Remote Sensing of Structure Properties in the Middle Atmosphere Using Lidar

C.R. Philbrick, AFGL, Hanscom AFB, MA 01731
D.P. Sipler, AFGL, Hanscom AFB, MA 01731
G. Davidson, Photometrics, Inc. Woburn, MA 01801
W.P. Moskowitz, Photometrics, Inc. Woburn, MA 01801

ABSTRACT
The results from a mobile lidar have been used to derive density and temperature profiles between 25 and 85 km over central Alaska during February-April 1986.

INTRODUCTION
During the period between February and April 1986 a new mobile lidar, GLINT (Ground-based Lidar INvestigation-Transportable), was used to obtain data on the variations which occur in the high latitude region of the atmosphere between 20 and 85 km. The lidar measurements were undertaken to provide an improved data base on which the reentry flight characteristics of the Space Shuttle descent from a polar orbit could be based. The lidar can measure profiles with improved altitude and time resolution compared to standard rocket techniques. This is important for better understanding of the dynamical processes of the middle atmosphere. Data was obtained on 26 nights during the program. Standard meteorological balloon and rocket payloads were used to make measurements and provide a comparison study with the lidar data. More than a thousand profiles of atmospheric density were obtained with the lidar and twenty meteorological rockets were launched.

The measurement campaign has resulted in several conclusions: (1) the lidar data has provided the opportunity to observe small-scale variations and the background granularity of the atmosphere, (2) planetary waves may be associated with more than half of the total density variation in the middle atmosphere, (3) density and temperature variations can be used to study the source, intensity, and propagation characteristics of gravity waves in the high latitude winter atmosphere, (4) these measurements provide a major step in demonstration of the capabilities of lidar as a tool for routine meteorological and atmospheric measurements.

The properties of the mobile sounder are shown in Table I. The mobile sounder is housed in a 32 foot trailer which is air transportable. The trailer uses an undercarriage which can transport the trailer over the road. Adjustable jacks have been included to allow the trailer to be lowered onto a solid base and leveled at an operating site. Figure 1 shows a drawing of the trailer configuration and a layout of the hardware within the facility. Figure 2 shows the arrangement of the laser, small detector and the beam steering mirror. A 30 cm telescope is co-aligned with the laser beam and a mirror is used to steer over a range of elevation and azimuth. A larger receiver of 62 cm dia. is used for zenith measurements.
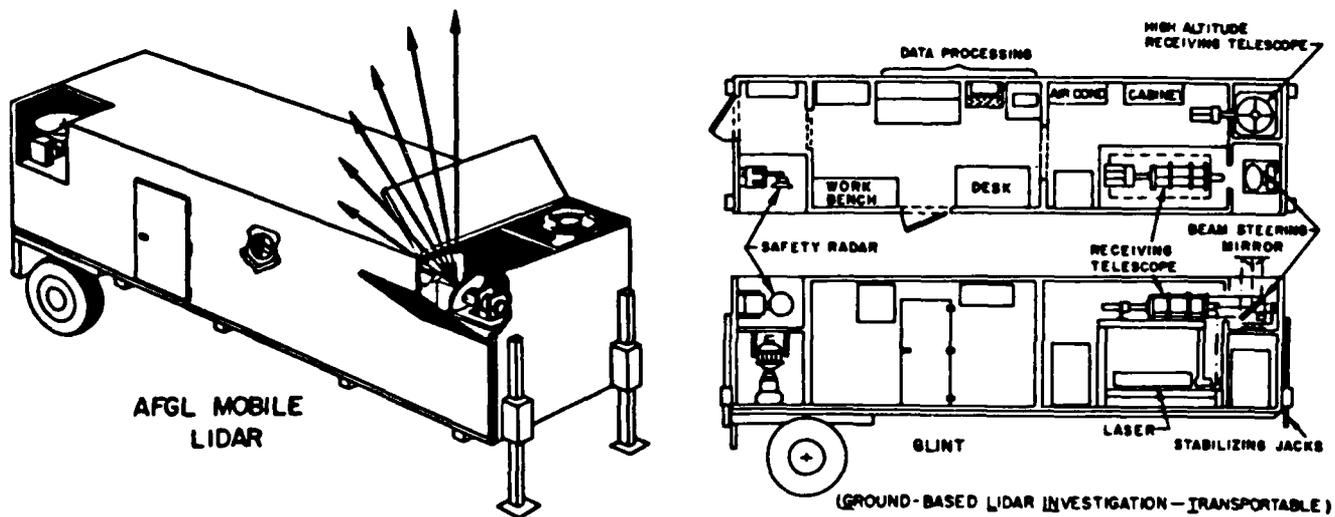
Figure 1. An artist sketch of the GLINT trailer and the primary components of the lidar. Top and side views of the lay-out of the equipment in the trailer are shown.
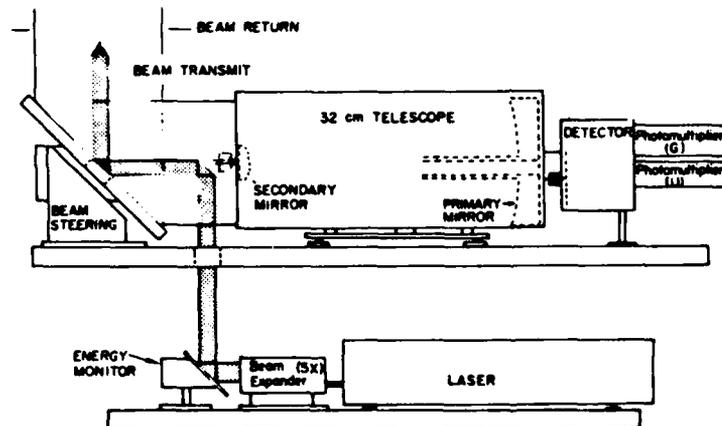
Figure 2. A side view of the optical layout of the lidar shows the principle components and the relationship of the transmit beam path and the collected signal.

Table I. The principle components of the mobile lidar.
 Transmitter - Nd:YAG laser, 10 Hz, Q-switch, 15 watt
       600 mj @ 532 nm, 250 mj @ 355 nm
       5X beam expander with final divergence 0.16 mrad
 Receiver - 32 cm telescope (steerable) photon counting
       with shutter closed below 15 km and variable
       aperture up to 40 km - nominal fov 1.0 mrad
          - 62 cm telescope (vertical pointed) photon
       counting with mechanical shutter below 40 km
 Data System - Lecroy 3500 multichannel scaler with 2
       microsecond range bins (300 meter resolution) for
       each detector - data stored on magnetic disk
 Safety System - Electrical interlocks and radar used to
       automatically disable the laser

SUMMARY OF RESULTS

On each evening of lidar operation, a series of 3-5 profiles
were obtained using the ultraviolet wave length at 355 nm and
the visible wavelength at 532 nm, simultaneously. Figure 3
shows an example of the profiles measured by the green and
ultraviolet detectors on the 32 cm telescope. Above 30 km, the
profiles are in complete agreement and below 30 km, the signal
from the green detector is significantly higher than that for
the ultraviolet detector. The ultraviolet return is relatively
larger for the molecular scattering and thus less sensitive to
the particulate scattering. This fact is due to the $1/\lambda^4$
dependence of the molecular scattering cross section. By using
the two colors, green and ultraviolet, it is possible to
resolve the question of what altitude regions can be properly
analyzed as pure Rayleigh scatter from which density and
temperature can be directly determined.
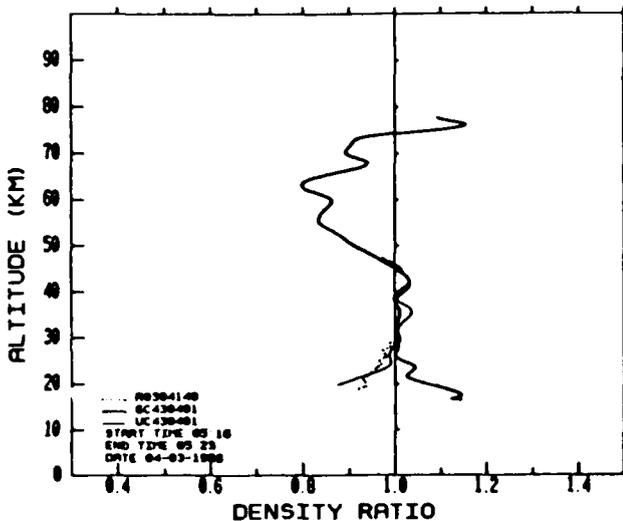
Figure 3. Comparison of the
visible and ultraviolet lidar
profiles.
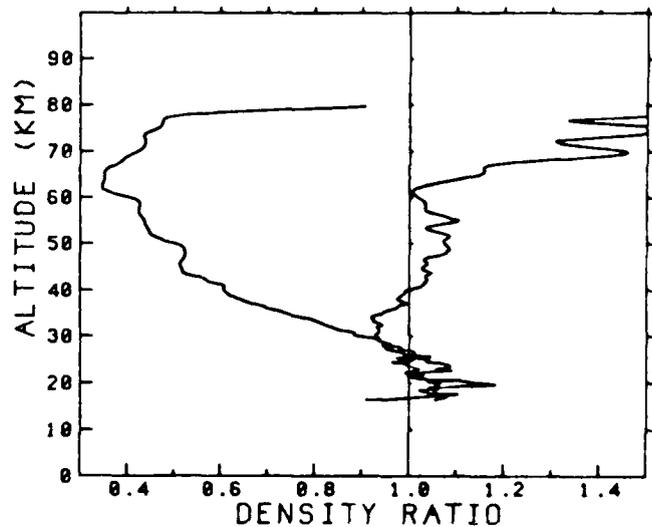
Figure 4. Comparison of the
seasonal extremes measured
on 14 February and 27 April.

Figure 4 shows an example of the extremes of the measured
conditions. The profiles are shown as a density ratio to the
USSA76 model. The profile of 14 February is typical of the
lower winter density in the mesosphere and the higher density
of the summer is represented by the 27 April profile. The high
latitude atmosphere exhibits these large seasonal changes due
to the change from complete darkness in winter to continuous
sun in the summer. The solar control drives large changes in
the circulation of the atmosphere in the polar region. Note
that the region between 18 and 25 km exhibits intense narrow
layers. This signal is due to the aerosols, polar
stratospheric clouds, and volcanic dust.

The measurements conducted during this campaign represent the
first serious attempt to compare lidar data and profiles from
meteorological rockets. An example of the lidar profile
obtained during the flight of a datasonde is shown in Figure 5.

The size of the ± 1σ error bar is shown on the lidar data with
a spacing which indicates the length of the smoothing interval.
The example exhibits rather strong wave activity, which was
observed frequently in March. Cases of both excellent
agreement and significant difference between the rocket and
lidar results were obtained. Figure 6 shows an example of the
planetary wave variations measured with the lidar during a
major stratospheric warming which peaked on 20 February. The
mean night profiles provide a graphic picture of the
development of the stratospheric warming.
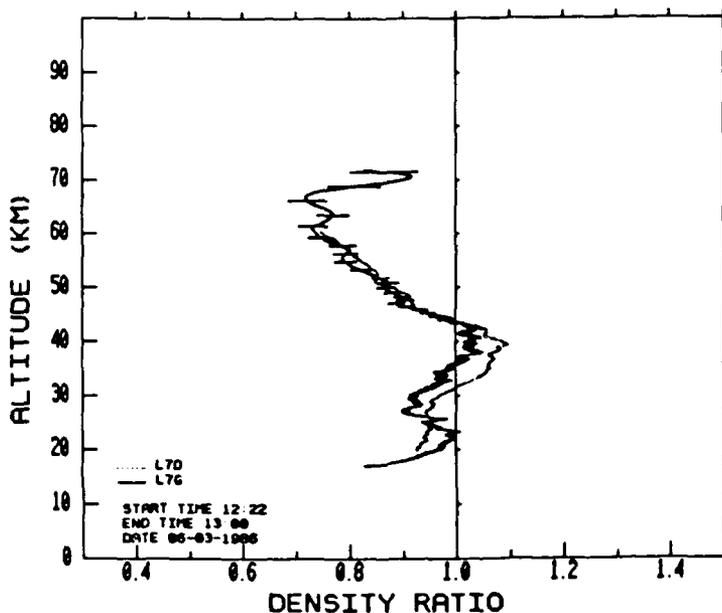
Figure 5. Comparison of the lidar profile from the 32 cm
telescope detector(G) with a standard datasonde profile(D).
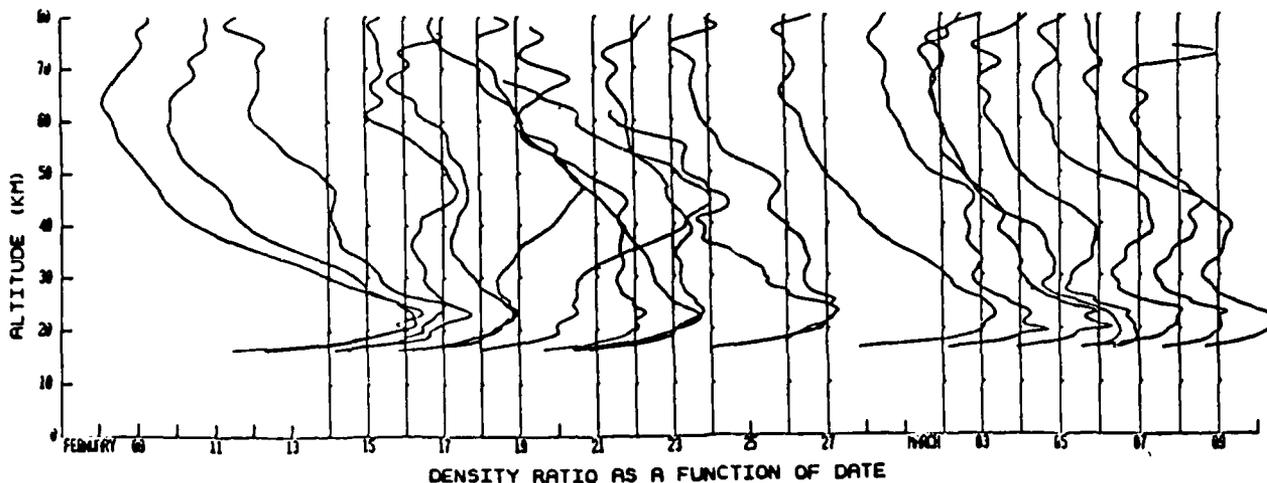
Figure 6. Sequence of mean night profiles of the density
ratio to the USSA model which show the change in response
to a major stratospheric warming.

123

REMOTE SENSING OF N_2O_5 AND $ClONO_2$ IN THE LOWER STRATOSPHERE

J. Brasunas, J. Herman, V. Kunde, W. Maguire
NASA/Goddard Space Flight Center
Laboratory for Extraterrestrial Physics
Greenbelt, Maryland 20771

L. Herath, W. Shaffer
Science Systems and Applications, Inc.
Seabrook, Maryland 20706

S. Massie
National Center for Atmospheric Research
Boulder, Colorado 80307

A. Goldman
University of Denver
Denver, Colorado 80208

INTRODUCTION

The stratospheric ozone concentration depends on a combination of radiation, chemistry and dynamics. Central to the chemistry are the nitrogen, chlorine, and hydrogen cycles of catalytic ozone destruction. Verification of the photochemical models that attempt to predict ozone trends requires the simultaneous measurement of ozone, temperature, and the trace species which participate in the ozone destruction.[1]

Limb-emission spectroscopy provides the ability to measure simultaneously many trace species over a range of altitudes with 3 km vertical resolution and over a continuous diurnal cycle. SIRIS (stratospheric infrared interferometer-spectrometer) has so far measured 15 molecular species, two of which are the temporary reservoir species $ClONO_2$ and N_2O_5. These reservoir species, which temporarily remove ClO and NO/NO_2 from active ozone destruction, are particularly sensitive to remaining uncertainties in atmospheric chemical reaction rates.[2] Figures 1) and 5) show one-dimensional photochemical model simulations of their diurnal variations.

OBSERVATIONS AND DISCUSSION

SIRIS is a liquid-nitrogen-cooled Fourier transform spectrometer of resolution 0.02 cm^{-1} (unapodized) that records a spectrum every 1-3 minutes. The five liquid-helium-cooled photoconductor detectors cover segments of the spectrum between 700 and 2000 cm^{-1} (5-15 um).[3,4] SIRIS has thus far collected good data during two balloon flights. The first, with a ~40 km float altitude on the afternoon of November 6, 1984, recorded spectra with tangent heights of 14-40 km. The second, with a ~40 km float height during the evening of September 15-16, 1986, recorded spectra with tangent heights of 8-40 km.

Figure 2) shows 1986 nighttime measurements of N_2O_5 in the 1220-1280 cm^{-1} region, at a 24 km tangent height; figure 3) shows a corresponding synthetically generated spectrum for the same tangent height, using measured temperature profiles and

representative trace-gas profiles. The synthetic spectrum was generated with a multi-layer radiative transfer code that uses spectroscopic line parameters from the AFGL tape[5]; the synthetic spectrum does not include N_2O_5. Figure 4) is a synthetic spectrum with N_2O_5, using the 4:00 profile from figure 1), together with the absorption coefficients measured by Massie and Goldman.[6] It is seen that the observed spectrum agrees reasonably well with the synthetic spectrum only if N_2O_5 is included. The upper curves of figure 6) show 1984 daytime measurements of $ClONO_2$ in the 779-781 cm^{-1} region at a 23 km tangent height (dashed line), together with a synthetic spectrum not including $ClONO_2$ (solid line); the lower curves gives the same comparison, but this time the synthetic spectrum includes $ClONO_2$. It is seen that the inclusion of $ClONO_2$ (also modeled via Massie-Goldman coefficients), markedly improves[2] the agreement between observed and synthetic.

At the current, preliminary, stage of analysis for N_2O_5 agreement is reasonable between the nighttime SIRIS data and one-dimensional model results. 1984 data during the day do not show an N_2O_5 feature, which is consistent with a model prediction of more than a five-fold decrease from night to day. As for previous observations, ATMOS data[7] indicate a concentration of 1.6 ppbv at 35 km at sunrise. For $ClONO_2$ the SIRIS data indicate afternoon mixing ratios of about 1.3 ppbv at 29 km and 1.0 ppbv at 22 km; figure 7) shows this is consistent with the model at 30 km, but in excess of the model at 22 km. The apparent disagreement between theory and observation suggests that a re-evaluation of the $ClONO_2$ photolysis rate is warranted.[8] ATMOS data[9] show concentrations of about 1.3 and 0.7 ppbv at 29 and 22.3 km, respectively.

REFERENCES

1) World Meteorological Organization, "Atmospheric Ozone 1985: Assessment of our Understanding of the Processes Controlling its Present Distribution and Change", Report 16 (Global Ozone Research and Monitoring Project, Geneva, 1986).

2) D.J. Wuebbles, "Reservoir species discovered in the stratosphere", Nature 319, 538 (1986).

3) J.C. Brasunas et al., "Balloon-borne cryogenic spectrometer for measurement of lower stratospheric trace constituents", SPIE 619, 80 (1986).

4) V.G. Kunde et al., "Infrared spectroscopy of the lower stratosphere with a balloon-borne cryogenic Fourier spectrometer", Applied Optics 26, 545 (1987).

5) L.S. Rothman et al., "AFGL atmospheric absorption line parameters compilation: 1982 edition", Applied Optics 22, 2247 (1983).

6) S.T. Massie et al., "Approximate absorption cross sections of F12, F11, $ClONO_2$, N_2O_5, HNO_3, CCl_4, CF_4, F21, F113, F114 and HNO_4", Applied Optics 24, 3426 (1985).

7) G.C. Toon et al., "Detection of stratospheric N_2O_5 by infrared remote sounding", Nature 319, 570 (1986).

8) S.T. Massie et al., "Atmospheric Infrared Emission of $ClONO_2$ Observed by a Balloon-Borne Fourier Spectrometer", subm. to J.G.R.

9) R. Zander et al., "Observations of several chlorine nitrate ($ClONO_2$) bands in stratospheric infrared spectra", G.R.L. 13, 757 (1986).
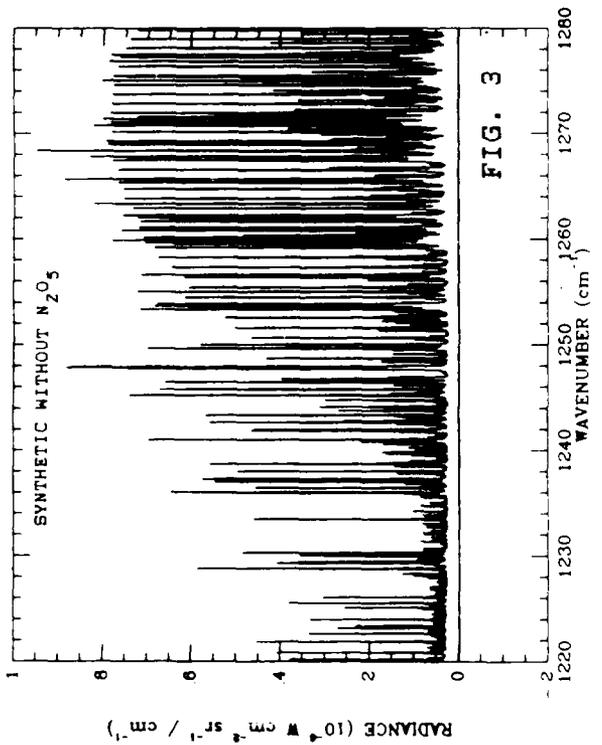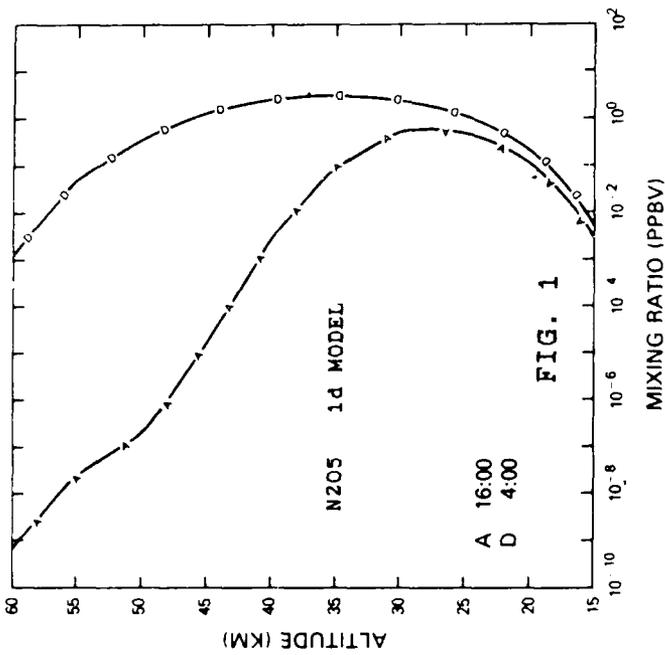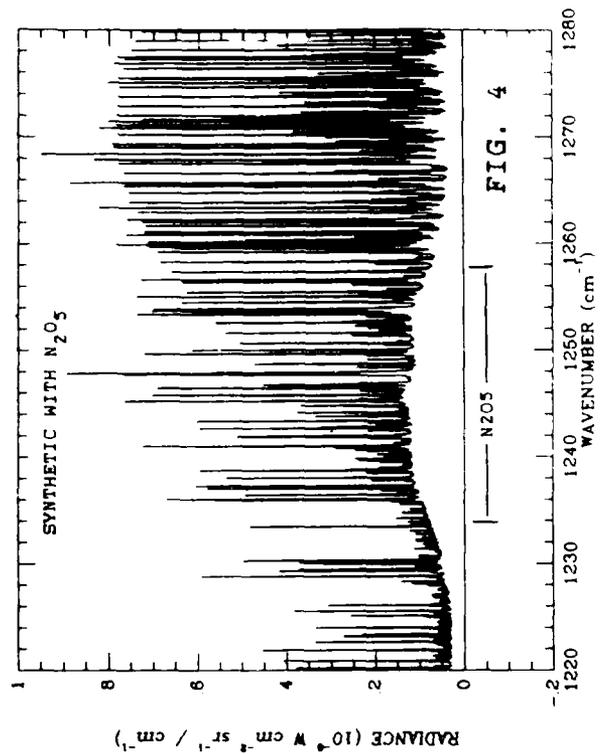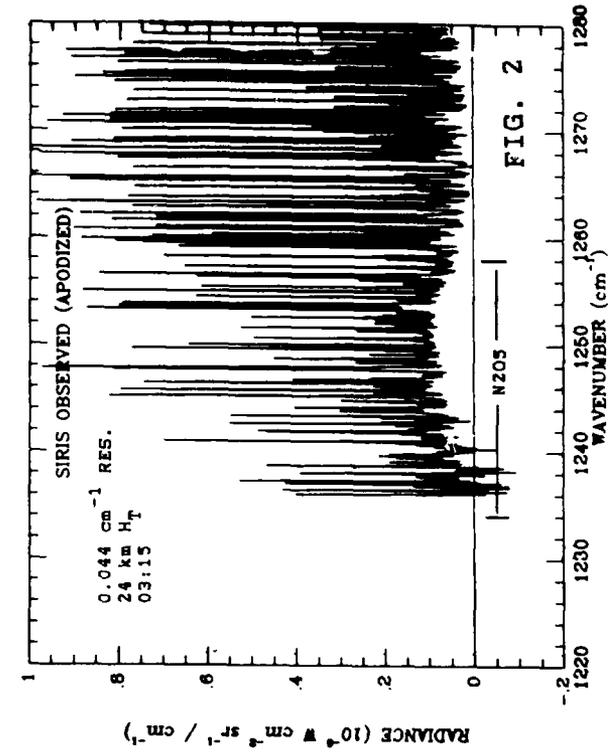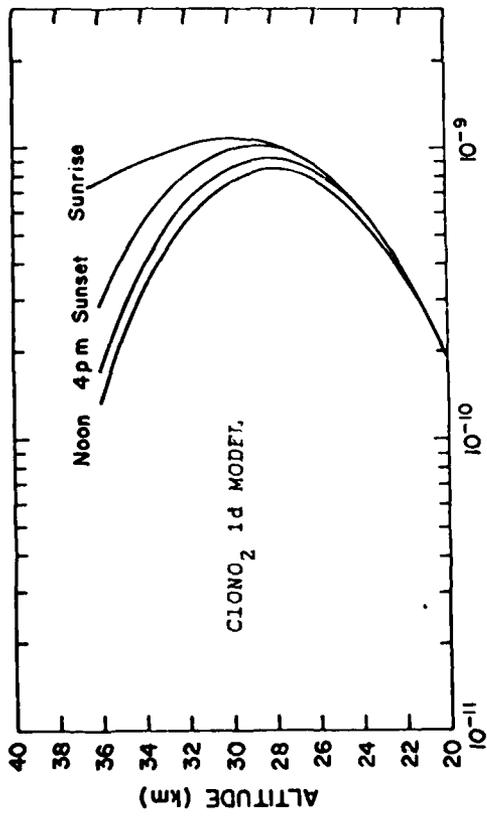
FIG. 1
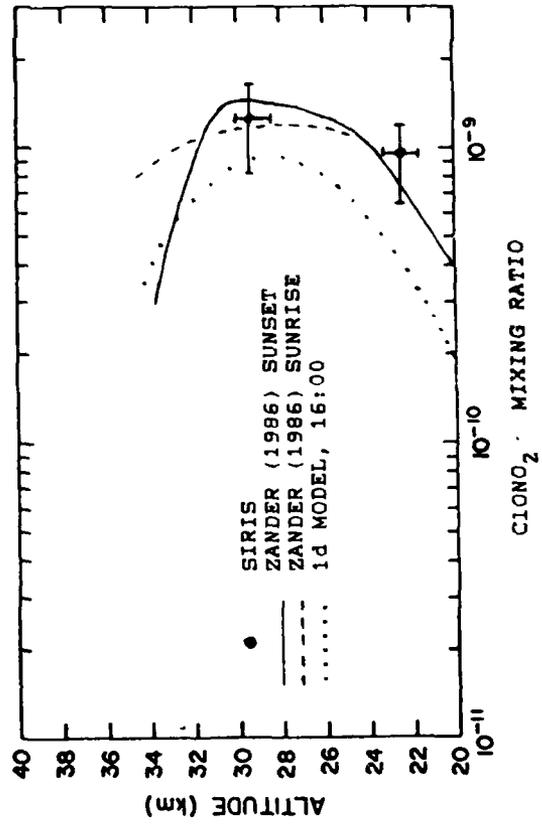
FIG. 2

FIG. 3

FIG. 4

FIG. 6

FIG. 5

FIG. 7
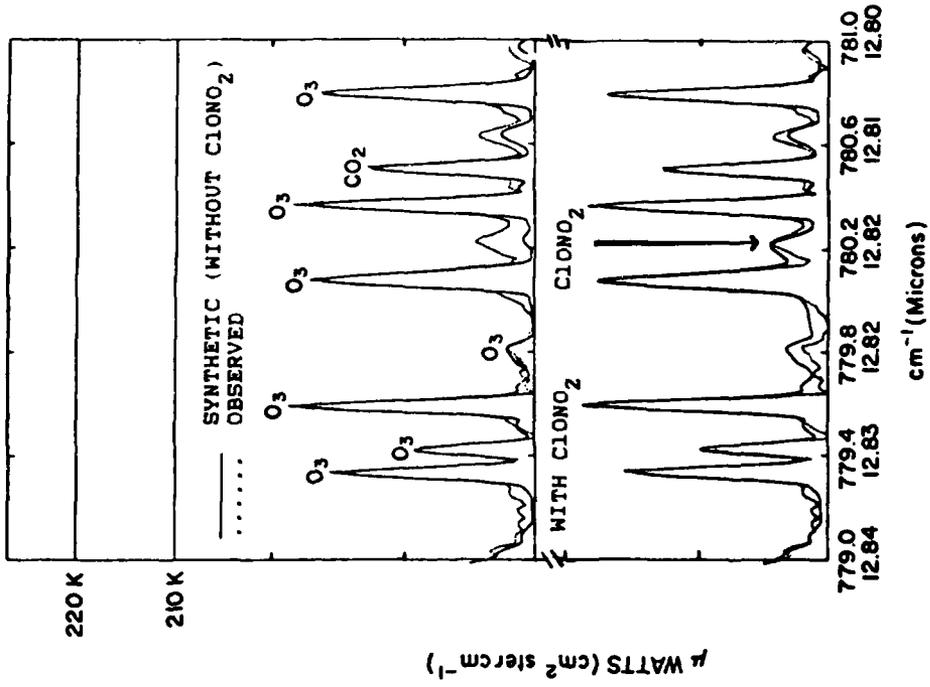
IMAGING BISTATIC LIDAR TECHNIQUE
FOR UPPER ATMOSPHERE STUDIES

Byron Welsh and Chester S. Gardner
Department of Electrical and Computer Engineering
University of Illinois at Urbana-Champaign
Urbana, IL 61801

The structural characteristics of the sodium layer are of considerable interest in the study of mesosphere dynamics. Much of the past and current research of the sodium layer have made use of monostatic lidar measurements to study these characteristics. An alternate approach is to use a bistatic lidar configuration, consisting of a cw laser to illuminate the sodium layer, and an imaging system to record the laser spot created by the resonant sodium scattering. The basic idea is to infer the structural characteristics of the layer from selected profiles of the imaged laser spot.

Figure 1 illustrates a possible physical setup for the imaging measurement system. The imaged laser spot will be elliptical in shape due to the finite thickness of the sodium layer and the offset of the imaging system from the laser. A vertically oriented profile through the recorded image (a profile along the laser beam direction) contains information about the sodium layer's vertical structure, while a horizontally oriented profile (a profile perpendicular to the laser beam direction) only contains information about the laser beam's divergence. Figure 2 illustrates a contour plot of an imaged laser spot. The laser spot was generated by the University of Illinois lidar system installed at the Mauna Kea Observatory. The laser spot was imaged by the University of Hawaii 2.2 meter telescope, located 117 m southeast of the laser. The spot dimensions were approximately .41 mrad x 70 mrad FW @ e^{-2}. The layer centroid height was 95.1 km and the measurement system was at an altitude of 4.2 km.

ANALYSIS

If we consider the proposed measurement system in Figure 1, we can write the expected photon count arriving at the imaging system for a particular observation angle as [1]

$$N_s(\theta,\psi) = \eta \frac{T_A^2 \lambda A_r \sigma_{eff}}{hc (4\pi)} \int_0^\infty \frac{J(z'\sin\theta\cos\psi, z'\sin\theta\sin\psi)}{z'^2} n_s(z'\cos\theta)dz' + N_B \quad (1)$$

where

$n_s(z)$	sodium density at altitude z, m^{-3};
$J(x,y)$	laser energy cross section in the horizontal plane at the nominal sodium layer height, J;
N_B	expected photocount due to background, and dark counts;
σ_{eff}	effective sodium backscatter cross section, m^2;
h	Planck's constant, 6.63×10^{-34} J s;
c	velocity of light, $3. \times 10^8$ m/s;
λ	optical wavelength, m;
A_r	receiver aperture area, m^2;
η	overall imaging system efficiency
T_A	atmospheric transmittance

Equation (1) is an expression for the intensity of the image at a particular point in the image plane. As mentioned above, the horizontal profiles of the image only contain information about the laser beam shape. Since we are not interested in this information, equation (1) can be simplified by integrating over the horizontal profiles of the image (equivalent to integrating over ψ). If we assume we can write $J(x,y)$ as $J_x(x)J_y(y)$ and also assume $x = z'\sin\theta\cos\psi$ is approximately equal to $z'\sin\theta$ for small variations of ψ about zero (i.e. for the values of ψ contributing to the integral in equation (1)), the integration over ψ results in

$$N_s(\theta) = \eta \, \frac{T_A^2 \, \lambda A_r \, \sigma_{eff} K}{hc \, (4\pi)} \int_0^\infty \frac{J_x(z'\sin\theta)}{z'^2} \, n_s(z'\cos\theta)dz' + N_B \qquad (2)$$

where K is the factor, resulting from the integration. If we also assume the variation of z' over the nonzero values of the integrand is small relative to the magnitude of z', we can replace z' with z_s' -- the nominal distance from the imaging system to the sodium layer. Using this last approximation and making the change of variable, $z = z'\cos\theta$, equation (2) reduces to

$$N_s(\theta) = \eta \, \frac{T_A^2 \, \lambda A_r \sigma_{eff} K}{hc \, (4\pi z_s'^2)} \, \frac{1}{\cos\theta} \int_0^\infty J_x(z\tan\theta)n_s(z)dz + N_B \qquad (3)$$

Equation (3) describes a vertical profile of the image and as evident from the form, the profile is a result of the convolution of $J_x(z\tan\theta)$ with $n_s(z)$. The profile $N_s(\theta)$ obviously contains information about the structure of the sodium layer $n_s(z)$, but the question is: How can we obtain an accurate estimate of $n_s(z)$ from the measured data $N_s(\theta)$?

DISCUSSION

Since equation (3) is a convolution we can interpret it using the concepts of linear system theory. In the following discussion, for simplicity, we ignore the multiplicative and additive constants in equation (3). Applying linear system concepts to equation (3) gives the equivalent operation illustrated in Figure 3: $N_s(\theta)$ is the output of a filter having impulse response $J_x(z\tan\theta)$ and input $n_s(z)$. The filtering action distorts the shape of $n_s(z)$. The degree of this distortion is dependent on the spatial bandwidth of $J_x(z\tan\theta)$. Using this interpretation the desirable characteristics of $J_x(z\tan\theta)$ are obvious. To extract $n_s(z)$ from $N_s(\theta)$ we want $J_x(z\tan\theta)$ to have the characteristics of a sifting function -- a function having a very narrow main lobe relative to the width of $n_s(z)$ and low sidelobes. From these characteristics we see that the width of $J_x(z\tan\theta)$ is a suitable measure of the resolution of the measurement system. Ideally we'd like $J_x(z\tan\theta)$ to approximate a dirac-delta function, resulting in virtually no distortion in the filtering operation of $n_s(z)$.

To get an accurate estimate of $n_s(z)$ from $N_s(\theta)$ we obviously need high resolution. From the above discussion two approaches to increase the measurement resolution are evident. The first is by simply decreasing the

laser beam width, thus decreasing the width of $J_x(z\tan\theta)$. The second approach is increasing the offset distance, D, between the imaging system and laser. Intuitively this approach will give us more resolution since we observe the layer from a less oblique angle. Mathematically the advantage of increasing D is clear if we write $J_x(z\tan\theta)$ as $\cdot J_x(z\tan(\theta_0+\theta'))$ where θ' is the observation angle relative to θ_0, and $\theta_0 = \tan^{-1}(D/z_s)$ -- the nominal angle corresponding to the center of the sodium layer. This representation illustrates that an increase in D compresses the width of $J_x(z\tan\theta)$ with respect to z. Of course, the disadvantage of a larger offset D is the increased atmospheric transmission and propagation losses incurred.

EXAMPLE

If we assume the laser beam has a Gaussian beam shape we can write

$$J_x(z\tan(\theta_0+\theta')) = \frac{J_0}{\sqrt{2\pi}\sigma} \exp\left[\frac{-(z\tan(\theta_0+\theta') - D)^2}{2\sigma^2}\right]$$

$$= \frac{J_0}{\sqrt{2\pi}\sigma} \exp\left[\frac{-(z - D/\tan(\theta_0+\theta'))^2}{2(\sigma/\tan(\theta_0+\theta'))^2}\right] \qquad (4)$$

where σ is the rms width of the laser beam. For a fixed $\theta_0+\theta'$, J_x has a Guassian shape with mean $D/\tan(\theta_0+\theta')$ and rms width $\sigma/\tan(\theta_0+\theta')$. Using this rms width as a measure of the resolution of our system we see that the resolution improves for a decrease in σ (laser beam width) and also for an increase in θ_0 (increase in D).

For the imaged spot shown in Figure 2, $\sigma = 8.08$m, D = 177m and $\theta_0 = \tan^{-1}$ (.117km/(95.1-4.2)km). Using these parameters along with an assumed Guassian laser beam shape, gives a rms width for J_x equal to 6.2 km. The actual rms width of the sodium layer for this particular measurement was 5.1 km. Since the rms width of J_x is comparable to the rms width of the layer we expect considerable smearing of $n_s(z)$ in the convolution operation of equation (3). Figure 4 shows a plot of the sodium profile $n_s(z)$, and the image profile $N_s(\theta)$ (note: in the plot of $N_s(\theta)$ the horizontal axis has been converted to altitude for comparison purposes). These plots illustrate the smearing and loss of detail in going from $n_s(z)$ to $N_s(\theta)$. If, for example, D is increased to 1000 meters the rms width of J_x is 727 meters. This value of D would result in a much higher resolution measurement and would not have the large degree of smearing and distortion characteristic of the profile shown in Figure 4.

REFERENCES

1. Gardner, C. S., D. G. Voelz, C. F. Sechrist, Jr. and A. C. Segal, J. Geophys. Res., 91, 13659-13673 (1986).
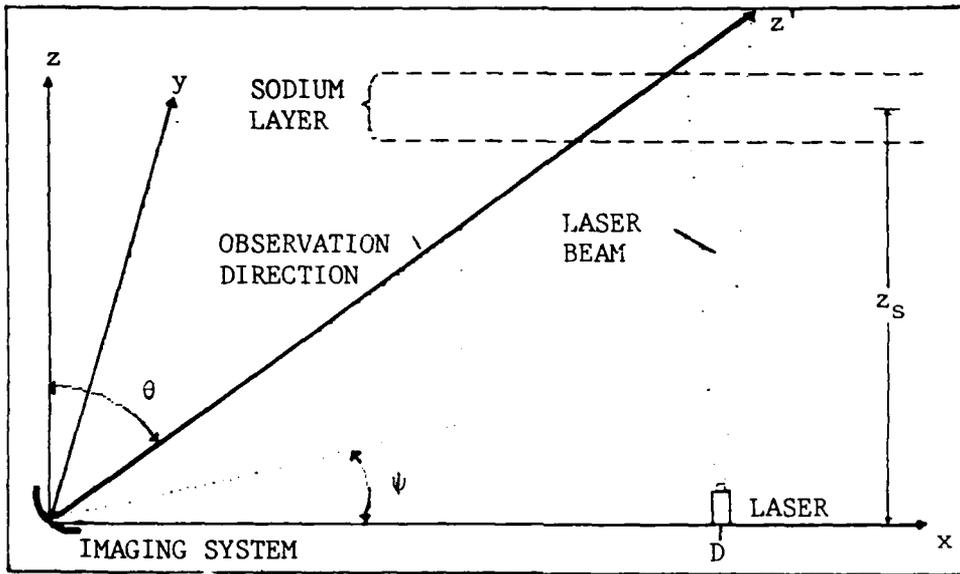
FIGURE 1.   Imaging measurement system setup.
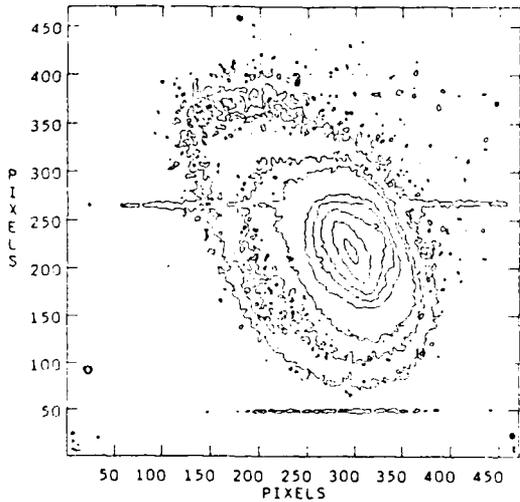
FIGURE 2.   Photon count contour plot of the laser spot image. The pixel size is 3.4 μrad. The countours are 300, 350, 400, 600, 700, 800, 1000, 1300 counts/pixel.
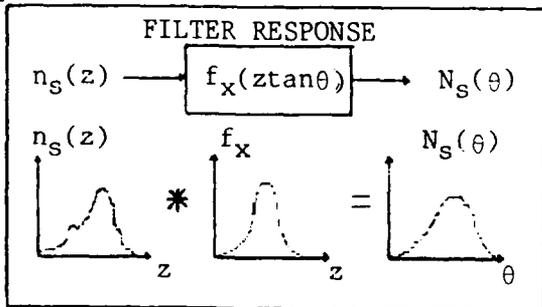
FIGURE 3.   Convolution operation of equation (3).
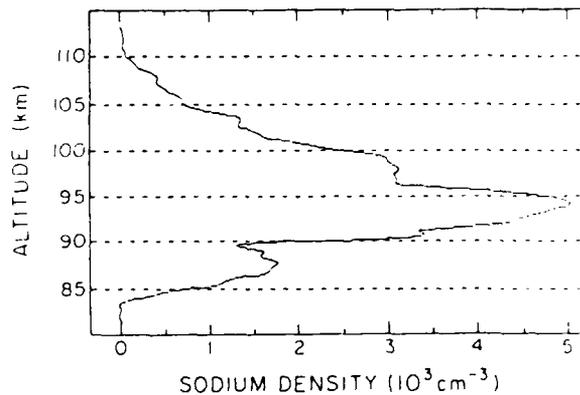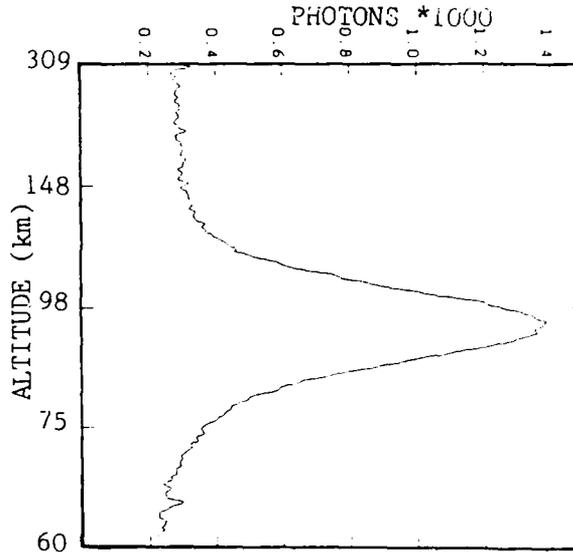
FIGURE 4.   Upper plot is vertical profile through image. Lower plot is sodium density profile, $n_s(z)$.

TUESDAY, SEPTEMBER 29, 1987

CONFERENCE ROOM 5

10:15 AM–12:30 PM

TuB1-5

UNIQUE APPLICATIONS OF OPTICAL REMOTE SENSING

Claude Cahen, Electricite de France, France, *Presider*

Applications of Laser Remote Sensing to Cell Biology and Medicine

Humio Inaba
Research Institute of Electrical Communication
Tohoku University, Japan

Experimental studies are reported on laser sensing of cytotoxic T-cells, which play an essential role in rejection episode in clinical organ transplantation, and of microscopic fluorescence-intensity distribution in various single cells.

Remote Temperature Distribution Sensing Along Optical Fibers.

A.H. Hartog,
York VSOP Ltd
School Lane
Chandlers Ford, Hants
UK

1. Introduction.

The use of optical fibres as transducers is currently the subject of active research justified by the promise of sensors able to offer high accuracy and measurement bandwidth, small size and immunity from interference even over long transmission paths. However, single point sensors only seldom utilise the very high intrinsic bandwidth of the optical fibre transmission medium. The need has therefore emerged to multiplex a number of sensing elements onto a single fibre or fibre pair and thus to form a sensor network distributed in space. This paper reviews recent progress in a particular class of distributed fibre optic sensors, based on the principle of optical reflectometry, which has considerable similarity to some of the LIDAR measurements reported in the literature.

Perhaps in contrast with LIDAR, the driving force behind the development of distributed fibre sensors has been the need for cheap, compact equipment used in industrial environments and with sufficient projected reliability to allow regular monitoring for long periods without intervention.

This contribution first summarises the basic method for distributed optical fibre sensing and discusses some of the implementations with particular emphasis on temperature sensing including the performance of near commercial systems and finally examines the future prospects for the technique.

2. Principles of reflectometric distributed sensing in optical fibres.

Optical time-domain reflectometry is a method now in everyday use in the optical communications industry for the evaluation of fibres, cables and installed links. A short, high intensity pulse is launched into the fibre and a measurement is made of its backscatter as a function of time. The signal consists of light scattered during the progress of the pulse down the fibre and re-captured by the waveguide in the return direction; it takes the following well known form as a function of the position z of the scattering element dx:

$$P_u(z) = \tfrac{1}{2} \, P_o \, W. \, v_g \, . \, \alpha_s \, . \, S \, \exp\left[\int_0^z -2 \, \alpha \, dx \right] \tag{1}$$

where P_o is the power launched, W, the pulse width, v_g the group velocity. Here α_s and α are the scattering and total losses, respectively, and can both be functions of position along the fibre. S is the capture fraction

i.e that proportion of the scattered light collected by the optical system. Equ. (1) is very similar to the classic LIDAR signal power expression, except that that the group velocity is substantially lower than in air and that here S is does not contain a z·² term and is simply related to the numerical aperture of the fibre. The range of a fibre reflectometer is thus largely dominated by fibre loss, rather than by the z·² term.

In order to use optical reflectometry in a distributed sensor, it is clear from Equ.I1) that the scattering loss α_s, the local capture fraction S (which affect the signal directly) or the local fibre attenuation α must be functions of the quantity to be measured (and of nothing else!). Most of the results reported to date have involved the measurement of temperature although in principle other measurands can also be addressed and the detection of magnetic fields has been reported.

3. Performance criteria.

The performance of distributed sensors is judged not only on their accuracy, measurement range and measurement time but on the length of fibre they can cover and their spatial resolution, i.e. their ability to distinguish adjacent points in the fibre. Clearly in a system where the measurement accuracy is limited by the signal-to-noise ratio, the measurement time (or integration time) will vary as the square of the accuracy required.

However, the criteria specific to distributed sensors also impact the measurement time since, as the required fibre length increases, so too does the system loss and the signal to noise ratio is thus degraded. Similarly as the spatial resolution is made finer, the pulse width must be reduced (which, in peak-power limited systems, reduces the signal proportionately) and the receiver bandwidth must be increased, which degrades the system noise.

There is therefore a trade off between the various performance criteria and, for a fixed accuracy in the measurement, the integration time increases rapidly with the spatial resolution and the total loss of the the sensing fibre.

4. Implementations.

(a) modulation of the fibre loss. According to (1), if the loss of the fibre varies with the measurand of interest, this should be detectable by reflectometry. This has been demonstrated by inserting thin colour glass filters at selected positions in the fibre and more recently [1] in fibres doped with rare-earth ions, providing a sensitivity of loss to temperature via the shift of absorption bands with temperature. In either case, the effect of the temperature on loss may be separated from other causes by referencing the measurement to another wavelength at which the loss insensitive to temperature.

The main drawback of these approaches is that the number of sensing points is limited by attenuation induced directly by the measurand: if the fibre is sensitive, its loss will sometimes be high, which will then leave little power to probe the following point. In practice approximately 10

hot-spots can be measured simultaneously, which could be sufficient in a number of applications.

In other cases it is desirable to use approaches which do not require the fibre loss to be high; this is case when the scattering loss, the capture fraction or the polarisation of the light is modulated.

(b) polarisation effects. In single-mode fibres, the backscatter signal carries information on the evolution of the state of polarisation to the scattering point and back[2]. This approach has been used[3] to detect magnetic fields via the Faraday effect but never taken much beyond demonstration owing to considerable difficulties in separating the information of interest from a number of spurious effects which mask the desired signal.

(c) modulation of the scattering loss. The first distributed fibre temperature sensor[4] to be demonstrated used a special fibre having a liquid core. In the core, increasing temperature results in greater molecular agitation and thus in a larger scattering coefficient, the sensitivity of the scattered signal being of order 0.5%/ K. This resulted in a distributed temperature sensor able to resolve around 0.1 K over 100m with a spatial resolution of 2.5m after averaging 1000 pulses; similarly a resolution of 1 K, with 1m spatial resolution over 100m of fibre were achievable with 1000 pulses, a measurement time well below 1s.

This performance is still the best that has been reported but the approach is out of favour since liquid-filled fibres are inconvenient to work with, have limited temperature range and unproved lifetimes. The sensitivity of the scattered signal to temperature in glasses is orders of magnitude lower and different means are thus required for solid fibres.

(d) Inelastic scattering. The scattering coefficient in optical fibres is caused principally by Rayleigh scattering and is attributable to density and composition fluctuations frozen-in to the material in the drawing process. This type of scattering is largely independent of ambient temperature provided that the thermo-optic coefficients of the fibre constituents are are similar. There is however a small contribution to the scattered power from Raman and Brillouin spectral lines which originate in thermally driven molecular and bulk vibrations, respectively. The intensity of these spectral lines is temperature sensitive and the finite sensitivity of the total scattered signal in solid fibres is largely attributable to the contribution of Brillouin scattering. By selecting only one of these parts of the scattered light spectrum the sensitivity of the measured signal to temperature can be greatly enhanced.

In practice, the Brillouin lines are shifted by only a few tens of GHz from the incident radiation frequency. This puts demands on the linewidth and frequency stability source and filter which are presently incompatible with the use of semiconductor lasers which are prefered for their small size, cost and reliability. In contrast, the Raman spectrum is well separated from the incident wavelength and can be readily separated by means of standard optical filters. Unlike that of free atoms and molecules, the Raman spectrum of high-silica glasses consists of very broad bands with a 200cm^{-1} wide band centered around 440cm^{-1}. Some of the details which can

be used in Raman LIDAR are thus lost to us in glasses. However the information is sufficient to obtain the temperature distribution along the fibre[5,6] and to eliminate spurious effects caused, for example, by fibre attenuation[6].

This approach provides a practical solution to a number of measurement problems and instruments are becoming commercially available which are able to measure more than 1 km of fibre with a spatial resolution between 5 and 10m, temperature noise of 1 K rms all in a measurement time of a few seconds. This device uses standard telecommunication fibre, which is readily available and relatively inexpensive.

5. Future prospects.

The performance of existing distributed fibre optic temperature sensors, sufficient for a number of applications, falls short of the requirements for many others. In particular, the spatial resolution will need to be improved for many industrial applications and work is progressing in this area. Eventually, this will involve the development or adaptation of more suitable sources, refinements of the electronics and possibly of the fibre itself. It is expected that a spatial resolution of 1m, over 1km of fibre, with 1K accuracy and measurement times of a few seconds will appear in the near future. Conversely, other applications, such as pipeline monitoring will demand extreme range and it is projected that systems spanning about 20km of fibre should be achievable without unduly sacrificing performance in other respects. Progress is also expected in the methods used for processing the signals; for example beyond a spatial resolution of 1m or so, measurement in the frequency domain may offer useful performance advantages.

In the longer term, attention will turn to the measurement of other physical parameters and this will almost certainly involve the development of special fibres with tailored sensitivity.

6. References.

[1] M.C. Farries et al, Electron. Lett. 1986, vol 22, pp418-9.
[2] A.H. Hartog et al, Proc 6th European Conf. Optical Communication (post deadline session) York, UK 1980.
[3] J.N. Ross, Electron. Lett, 1981, vol 17, pp596-597.
[4] A.H. Hartog, J. Lightwave Technol. 1983, vol LT-1, pp498-509.
[5] J.P. Dakin et al, Electron. Lett 1985, vol 21, pp569-570.
[6] A.H. Hartog et al, Electron. Lett 1985, vol 21, pp 1061-3.

Time Resolved Lidar Fluorosensor for Oil Pollution Detection

A.Ferrario, P.L.Pizzolati, E.Zanzottera

CISE Tecnologie Innovative S.p.A.

P.O.Box 12081, 20134 Milano, Italy

SUMMARY

Introduction.-

This work is based on a preliminary experimental research made by researchers of JRC-Ispra[1] according to which an airborne fluorosensor system, able to jointly perform a time and spectral analysis of oil fluorescence, is useful for the detection and the characterisation of oil spills on the sea surface. They have demonstrated that while spectral analysis alone can hardly enable to distinguish between two oils of the same class (for example two crude oils), the time-spectral analysis can easily discriminate between two oils with nearly the same spectral pattern.

On these premises CISE labs have been asked by JCR-Ispra to design[2] and construct a fluorosensor system fulfilling the following specifications:

- time range : 30 - 75 ns
- time resolution : 1 ns
- spectral range : 350 - 760 nm
- spectral resolution : 10 nm.

The above specifications have required a great engineering effort in designing a short pulse reliable laser source and a streak camera based detector.

Laser System.-

The laser source consists of a Nd-YAG laser, able to produce about 120 mJ energy pulses at 1060 nm with a 10 Hz repetition rate. The emission at the third harmonic at 355 nm is 30 mJ, with pulse duration less than 1 ns. The laser utilizes a single oscillator configuration, with a new type of resonator named SFUR (Self Filtering Unstable Resonator)[3]. The SFUR is a Negative Branch Unstable Resonator (NBUR) with a suitable small aperture placed in the intracavity focal plane, acting as a low-pass spatial filter. Short pulse laser emission is achieved by means of active mode locking with an acousto-optic modulator. This device is able to give a single transverse, diffraction limited mode, providing good beam divergence and good pointing stability. SFUR is also more insensitive to misalignment, in comparison with other types of unstable resonator, and this property is very important for an airborne system.

In addition to the emission at 355 nm, useful for oil detection, the Nd-YAG laser can provide an auxiliary emission at 532 nm useful for chlorophylls excitation.

Detection System.-

Streak cameras are currently used for the analysis of fast optical phenomena, with resolution up to 1 ps: however, their two-dimensional patterns have been fully utilized in a few spectroscopic applications. In these cases the streak cathode is coupled to the output of a polychromator, so that one streak axis becomes the spectral axis, orthogonal to the time axis.

The return signal consists of the backscattering at laser wavelength from the water surface and the bulk water, of the water Raman signal (at 400 nm) and of the fluorescence signal of oil and of suspended organic materials.

The signal is collected by the receiver optics consisting of a 30 cm newtonian telescope and is sent, through a 0.4 mm diameter fiber optic, into a polychromator. The fiber provides an optical delay for the optical signal, this delay is required because the streak camera must be triggered a few nanosecond prior to event. The streak camera signal is then intensified by an image intensifier directly coupled to the streak camera phosphor and is digitized by using a CCD read-out system. The digitized signal is transmitted to a Microvax II computer as a matrix of about 40 spectral channels by 90 time channels, and stored on a 70 Mbytes disk for subsequent analysis.

System specifications.-

The performances of the system are below summarized. The total power consumption is expected to be about 2 Kwatt, the total weight about 300 Kg. The system will be operational at the end of 1987.

The specifications of the optical subsystem are:

Laser type: Nd-YAG

Emission Wavelength: 355 and 532 nm

Energy: 70 mJ

Pulse duration: 1 ns

Repetition rate : 10 Hz

Telescope type: 30 cm diameter, newtonian

Telescope focal length: 85 cm

Telescope field of view: 0.45 mr

Receiver spectral range: 350-760 nm

Number of spectral channels: 40

Polychromator resolution: 10 nm

Receiver optical efficiency: 20%

The specifications of the detection subsystem are:

Temporal ranges: 30-75 ns
Temporal resolution: 1 ns
Dynamic range: 1000
Computer system: Microvax II

REFERENCES

1. Camagni P, Colombo G.,Koechler C., Omenetto N., Pedrini P.,
    Rossi G., and Tassone G., Remote Fingerprinting of Oil
    Pollution by Means of Time Resolved Fluorosensing,
    Procs.1984 World Conference on Remote Sensing, Bayreuth 8-
    11 October 1984, K.M.Morgan Ed.: University of Bayreuth and
    Texas Christian University.

2. Ferrario A., Pizzolati P.L., Zanzottera E., Feasibility
    Study for an Airborne Lidar Fluorosensor, Final Report CISE
    2563, March 1985.

3. Gobbi P.G., Morosi S., Reali G.C., Zarkasi S., "Novel
    Unstable Resonator Configuration with Self-filtering
    Aperture", Applied Optics, Vol.24, pp.26-31, 1985.

Simultaneous Measurements of Ocean Surface Roughness and Atmospheric Pressure with a cm Resolution Two-Color Laser Altimeter

James B. Abshire

Jan F. McGarry

NASA - Goddard Space Flight Center

Instrument Electro-Optics Branch

Greenbelt MD 20771

May 1987

Summary:

Gardner has proposed a technique for measuring both atmospheric pressure [1] and ocean surface roughness [2] by using a short pulse two-color laser altimeter. Two sets of airborne altimeter measurements have been performed using this technique, both of which utilized < 100 psec wide modelocked laser pulses. The impulse response of the initial PMT-based altimeter receiver was 800 psec [3], while that of the later streak camera-based receiver was 85 psec [4]. In the first airborne tests, the atmospheric pressure accuracies of the high resolution altimeter were 3-7 mbar [4].

The transmitter of the high resolution altimeter is a passively dye modelocked ND:YAG laser, which simultaneously emits 50 psec wide pulses at 532 nm and 30 psec wide pulses at 355 nm at a 4 pps rate. The time-resolved laser backscatter from the ocean surface at both 532 and 355 nm is collected by a 36 cm diameter f/12 telescope mounted in a bistatic nadir-viewing configuration and is recorded by a dual-channel streak camera detector. When integrated into the altimeter receiver, the streak camera has a 85 psec impulse response and a 5 psec sampling time. Waveform and 100 psec accuracy range data are stored onto the system's LSI 11/23 computer's floppy disk at a 1 pps

rate. The details of the system configuration are listed in Table 1. Some data from the ground-based altimeter calibration tests have been recently published [5].

During the April 1985 test flight of the altimeter, data was collected at 324, 464 and 658 m altitudes. The Lockheed-Electra aircraft traversed a dog-leg flight path at 100 m/sec from near Pocomoke Sound, well within the Chesapeake Bay, to Cape Henry VA on a SSW heading and out over the open Atlantic Ocean on a SE heading. This flight line was selected to pass near four in-situ National Weather Service sensors, which recorded both wind direction and speed near the flight line, as well as average ocean wave height at the Chesapeake Light off Cape Henry. The data from these are listed in Table 2.

The 1800 dual wavelength altimeter waveforms have now been analyzed to examine their dependence on ocean surface conditions. The waveforms at all altitudes and locations retained sharp-high bandwidth features consistent with specular reflection from capillary wavelets on the ocean surface. The data analysis shows consistently high (0.9) correlations between the 532 and 355 nm waveforms, although the correlation decreased for the roughest ocean water. The altimeter received pulse energies decreased by a factor of 3 in a nearly monotonic fashion as the flightline traversed the upper to lower Chesapeake Bay and out over the open Atlantic Ocean. The rms bandwidth as well as the -10 dB and -20 dB bandwidths all decreased by ~ 50% from 3, 7.5, and 11 GHz respectively over the same flight line. Such variations are all consistent with the ocean surface scattering theory, which predicts less backscattered pulse energy and more pulse broadening from the rougher ocean surfaces.

References:

1. C.S. Gardner, "Technique for remotely measuring atmospheric pressure from a satellite using a multicolor laser ranging system," Appl. Opt., Vol. 18, 3184 (1979).

2. B.M. Tsai and C.S. Gardner, "Remote sensing of sea state by laser altimeters," Univ. Illinois Radio Research Lab. Publ. No. 514, Urbana IL, December 1981.

3. J.B. Abshire, J.F. McGarry, and R.S. Chabot, "Airborne measurements of atmospheric pressure with a two-color streak camera-based laser altimeter," Proc. 1985 Conf. Lasers and Electro-Optics (CLEO'85), paper PD-6, Baltimore MD, May 1985.

4. J.B. Abshire and J.F. McGarry, "Two color short-pulse laser altimeter measurements of ocean surface backscatter," Appl. Opt., Vol. 26, 1304 (1987).

5. K.E. Im, C.S. Gardner, J.B. Abshire and J.F. McGarry, "Experimental evaluation of the performance of pulsed two-color laser ranging systems," Jour. Opt. Soc. Amer.- A, Vol. 4, 820 (1987).

Table 1 - System Parameters - 4/03/85 Flight

Laser: Quantel YG40 - Passively modelocked ND:YAG
    Pulse widths: 50 psec @ 532 nm, 30 psec @ 355 nm
    Pulse energies: 0.3 mJ @ 532 nm, 0.5 mJ @ 355 nm

Laser Divergence: Elliptical, 2.8 mrad by 1.3 mrad @ 10% points
    532 and 355 nm beams coaligned within 10%

Telescope: Celestron 14 - 36 cm diameter Schmidt Cassegrain
    Area = 0.091 sq. meters

Mirrors: CVI Laser Double Stack Dielectric, Max R @ 355 and 532 nm

Trigger PMT: Hamamatsu R1294U, Dual MCP
    QE= 4% @ 532 nm, Gain = 1.3×10^6

Optical Delay: 8 pass White Cell, 40 nsec total

Streak Camera: Hamamatsu C1370, 5 psec/channel at sweep=2 setting
    Impulse response = 85 psec in system

Streak Camera Readout: Hamamatsu C1098, Dual Channel, DMA Interface

Discriminator: Ortec 934

TIU: HP 5370A, 100 psec accuracy

Computer: DEC LSI 11/23 with Dual Floppy Disks

Table 2 - National Weather Service Coastal Reports
for 4/03/85

Wind Direction and Speed (mph)

Location	4:00 pm	6:55 pm	10:35 pm
Tangier Island	S23	S15	NNE23
Cape Henry	SW14	SW15	SW15
South Island, BB Tunnel	WSW12	SW12	SW12
Chesapeake Light (CL)	SSW22	SSW15	SW25
CL Ave Wave Height (ft)	1.5	1.5	3.0
CL Air Temp (deg. F)	54	57	55

Cloud Liquid Water Derived from Lidar Observations

James D Spinhirne
Laboratory for Atmospheres/617
Goddard Space Flight Center
Greenbelt, MD 20771

William D. Hart
Science Systems Application Inc.
Lanham, MD 20706

Reinout Boers
University of Maryland
College Park, MD   20742

1. Introduction

The distribution of liquid water at the top of clouds has an important relation to the radiative and dynamical interactions within clouds. As a significant example, the formation and structure of marine stratus clouds are maintained primarily by radiative cooling at the cloud top. Understanding the formation of marine stratus is important climatalogically since the cloud type has a significant global influence on the balance between reflected visible and emitted thermal radiation. Models have shown that the interaction between radiative cooling and the cloud development are largley a function of the distribution of the liquid water at the cloud top.   Although liquid water may be obtained from in situ measurements, only one dimensional observations are possible. Lidar liquid water observatios can provide a more complete two dimentional representation of the liquid water structure of cloud tops. In this contribution we will describe the lidar retrieval of cloud top liquid water during an experiment in which marine stratus clouds were studied by combined remote sensing and in situ observations.

2. Experimental

In September 1983 marine stratus clouds off the California coast were overflown by the NASA ER-2 aircraft. On board instrumentation included the cloud and aerosol lidar system (Spinhirne et al, 1983) and several passive sensors. The basic parameters of the lidar system are a 30 mJ doubled Nd:YAG laser, a 15 cm receiver, logarithmic signal compression and 20 mHz signal digitization. The ER-2 overflights were directly coordinated by in situ cloud physics measurements obtained by the University of Wyoming King Air aircraft. The in situ observations included PMS probe droplet size ditributions and liquid water from a Johnson Williams instrument. During the flight missions the two aircraft maintained a single racetrack flight pattern of 120 l.m length and 20 km separation for a period of several hours in order to develop a statistical comparison between in situ and remote observations. An example of the lidar return data along a short segment of one flight line is shown in the first figure.

3. Liquid Water Retrieval

There are two main steps to the procedure by which cloud top liquid water is computed from the lidar return data. First the lidar return signal must be corrected for attenuation in order to derive the backscatter cross section for the cloud top within the effective range of the signal return. Second the backscatter must be related to the liquid water content. The scattering cross section is obtained from a solution of the lidar return equation. The liquid water is derived from the scattering cross section through application of a model based on the available in situ particle measurements. The lidar signal solution involves the standard solution equation based on a constant value of ratio of the extinction to backscatter cross section. The constant ratio assumption may be applied in the case of water clouds since as shown by Pinnick et al (1983) the value is insensitive to the droplet size distribution although consideration must be given to muliple scattering. The value of the effective extinction to backscatter cross section to be used for the solution is derived from analysis of the integrated pulse reflection from the cloud as a function of increasing optical thickness. The effective backscatter to extinction ratio is twice the limiting value of the integrated backsatter as optical thickness tends toward infinity (Platt, 1979).
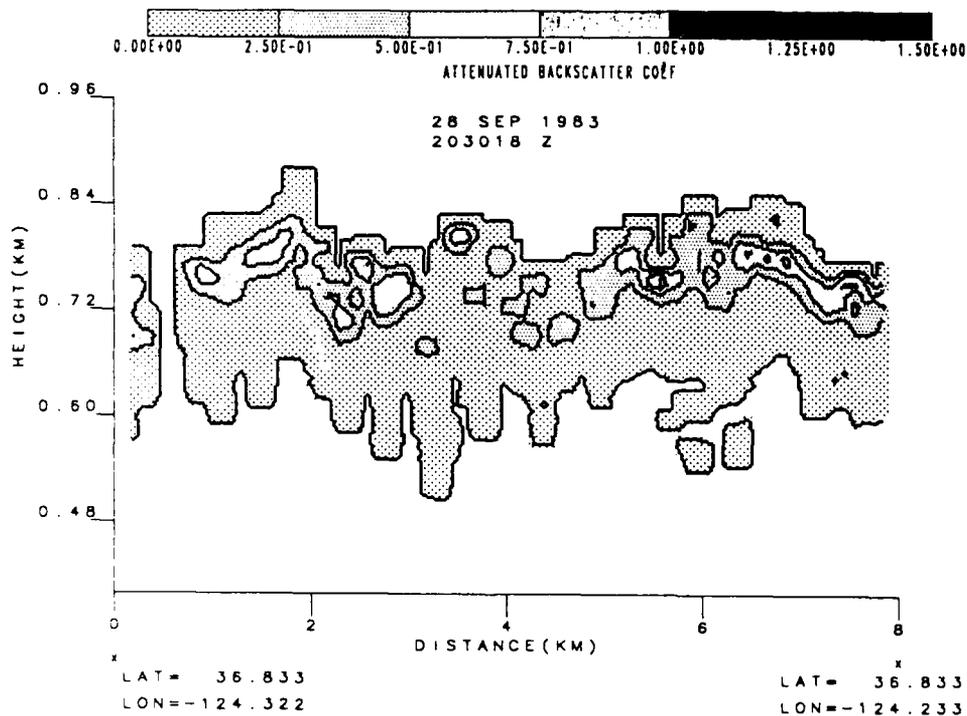
Fig. 1. Lidar signal from the top of a marine stratus cloud

To a first approximation the ratio between the liquid water content and the cloud scattering coefficient is proportional to the droplet mode radius. A more accurate relation given by Pinnick which involves the second and third moment of the size distribution was applied to relate the liquid water to the lidar backscatter cross section. A parameterization of the vertical profile of the size distribution parameters was developed from in situ measurements and applied for the cloud top liquid water calculation. The parameterization is represented by the linear fit as shown in the second figure.

4. Results

An example of the derived liquid water is given in the third figure for a segment of one flight line. The data case was characterized by broken cloud cells which were associated with greater than normal wind shear across the cloud top inversion. In addition to the two dimensional liquid water retrieval from the lidar data, the third figure also shows the flight track and measurements of the in situ aircraft at the observation time. Althougth a direct comparison is influenced by the approximately one kilometer uncertainty in the aircraft navigation, a general correlation between the in situ and remote observation is seen. In order to judge the validity of the lidar liquid water retrieval, the average values from the lidar and the JW probe along a series of flight lines for the in situ aircraft were compared. The results indicated that the two different liquid water observations agreed well within the measurement variance.

An important aspect ofthe lidar liquid water retrievals is the depth of cloud for which a result may be obtained. The depth
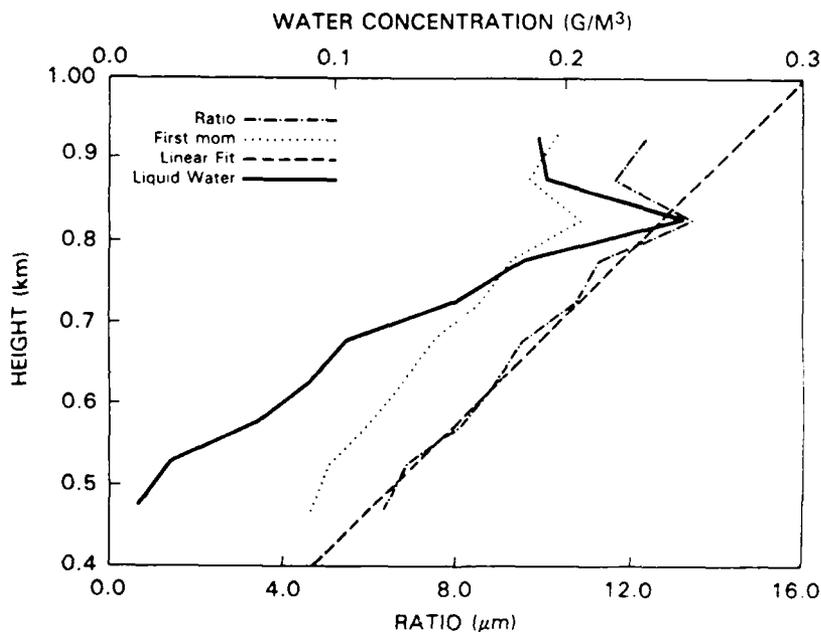
Fig. 2. Average result from in situ measurements for the marine stratus observations.

is limited in practice by the increase of signal noise due to attenuation and the error of the attenuation correction with increasing optical thickness. As a result, the lidar retrieval was limited to a cloud top optical thickness of 1.5. In the third figure the 1.5 optical depth limit is indicated by the deletion of the lower contour boundary. As may be seen, in most instances the effective optical thickness of the marine stratus clouds are less than the limit value.

5. Conclusion

Cloud top lidar observations may be combined with in situ cloud particle measurement to provide a more complete two dimensional structure of the cloud top liquid water distribution. Independent visible wavelength lidar observation of cloud top liquid water is possible if a model of the droplet size distribution parameters may be applied. The primary uncertainty of the lidar liquid water retrievals results from inaccuracy of the droplet distribution parameters.
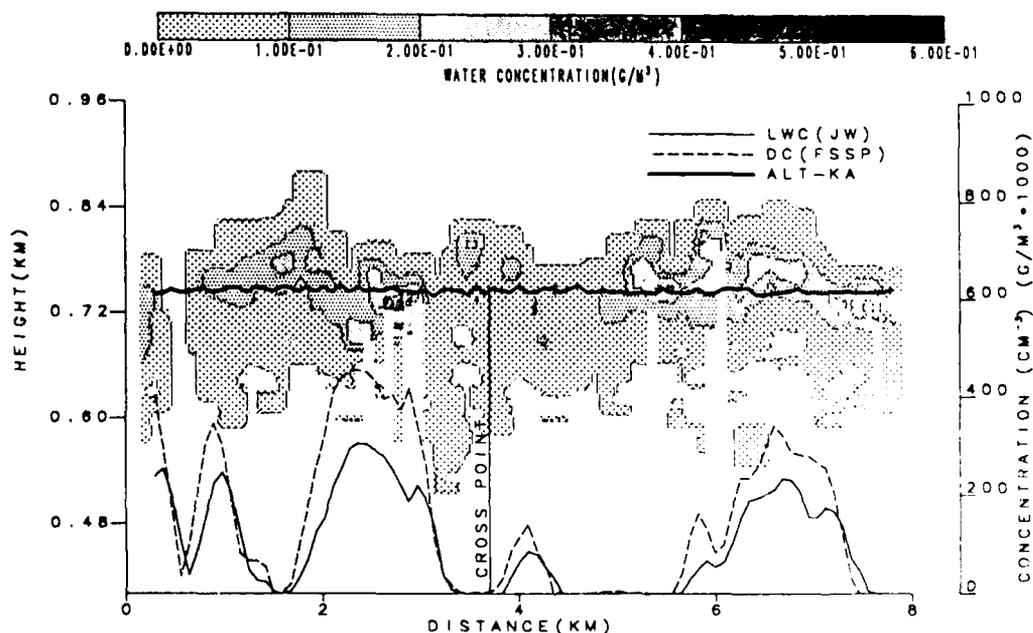
Fig. 3. Calculated liquid water distribution from lidar data and corresponding in situ measurements.

References

R.G. Pinnick, S.G. Jennings, P. Chylek, C. Ham and W. T. Grandy, "Backscatter and Extinction in Water Clouds," J. Geo. Res. 88, 6787(1983).

C.M.R. Platt,"Remote Sounding of High Clouds: I. Calculation of Visible and Infrared Optical Properties of Lidar and Radiometer Measurements," J. Appl. Meteor. 18,1130(1979).

J.D. Spinhirne, M.Z. Hansen and J. Simpson,"The Structure and Phase of Cloud Tops as Observed by Polarization Lidar," J. Appl. Meteor.22,1319(1983).

TUESDAY, SEPTEMBER 29, 1987

CONFERENCE ROOM 4

7:00 PM–10:00 PM

TuC1–24

POSTER SESSION
OPTICAL REMOTE SENSING METHODS
AND DEVICES

Chester S. Gardner, University of Illinois, *Copresider*

Norman Barnes, NASA Langley Research Center, *Copresider*

Advances in Gas-Analyzers Based on IR Molecular Lasers

Yu.M. Andreev, P.P. Geiko, V.V. Zuev, V.E. Zuev,
O.A. Romanovskii, S.F. Shubin

The Institute of Atmospheric Optics, Siberian Branch
USSR Academy of Sciences, Tomsk, 634055, U S S R

High operation and power characteristics of CO_2 lasers sti-
pulate their wide application in absorption gas-analyzers
and lidars [1]. On the other hand, the gas-analyzer possibili-
ties are limited by their narrow spectral emission range. The
molecular CO, NH_3, HF, HBr lasers generating in different IR
regions do not compensate for this disadvantage by different
reasons.

We think the effective nonthreshold parametric CO_2 and
CO lasers frequency converters (FC) with the $ZnGeP_2$ and
$CdGeAs_2$ monocrystals developed can improve this situation [2].

The main IR atmospheric transmission windows can be over-
lapped, and the concentrations of many atmospheric gas compo-
nents, including different pollutants, can be measured (Fig.
1 a) using these FC. The spectral transmission regions of
$ZnGeP_2$ and $CdGeAs_2$ supplement each other, Fig. 1 b. In fact,
all the main atmospheric transmission windows can be over-
lapped by frequency transformed radiation of a single CO_2 la-
ser using two-cascade FC of its self-radiation and second
harmonic (SH). A fine "tooth-comb" spectrum overlapping is
observed when using two CO_2 lasers or one two-frequency laser.
The mixing of CO_2 and CO lasers radiations is of interest
here.

Table 1 presents some coincidences of CO_2 laser SH fre-
quencies with the atmospheric gas absorption lines. We re-
ported [3] CO concentration measurements with a mobile trace
gas analyzer equipped with a frequency-doubled CO_2 laser. The
CO concentration sensitivity was 4 ppb at a 2 km path. Table
2 shows possible frequency combinations of two CO_2 lasers
for obtaining sum frequency $\nu_1 + \nu_2$ coinciding with the
CO R(18) absorption line center. The number of reference fre-
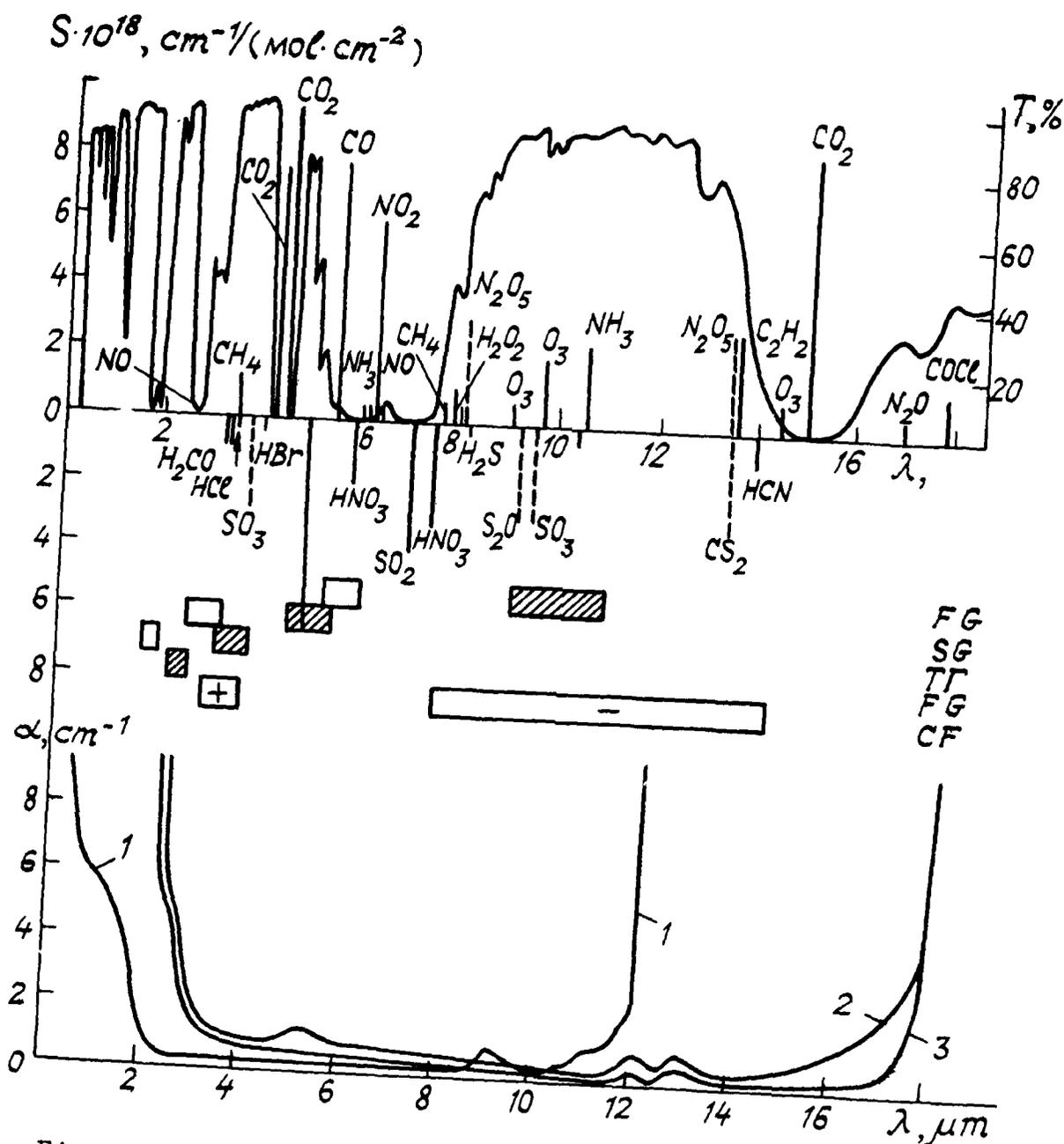
Fig. 1. The transmission spectrum T of the simulated atmosphere for a 1 km ground path, the centers location and intensities of the gas absorption bands. The regions of generation (FH) of CO and CO_2 (shaded) lasers and their second (SH), third (TH) and fourth(FH) harmonics, sum (+) and difference (-) frequencies of CO_2 laser radiation and its SH. Below are the transmission spectra of $ZnGeP_2$(1) and $CdGeAs_2$ at 300K(2) and 80 K (3).

Table 1. Coincidence of CO_2 laser SH frequencies with absorption lines

Gas	S_o, cm/mol	ν of line cm^{-1}	νSH, cm^{-1}	line number	isotope	$\Delta\nu$,cm^{-1}
H_2O	1.10×10^{-20}	1847.784	1847.794	10P39	626	0.0099
CO	2.60×10^{-19}	2154.596	2154.605	9P18	626	0.0091
N_2O	4.99×10^{-19}	2196.669	2196.635	9P22	828	0.0342
NO	$(2)2.29 \times 10^{-20}$	1929.031	1929.041	10P7	626	0.0098
OCS	5.79×10^{-19}	2058.888	2058.885	9P38	626	0.0029

quency combinations resulting in overlaping with the absorption line can reach 100. Thus the radiation sources developed are not worse than those of continuously tuning lasers when studying the atmospheric ground layer.

Table 2. The SF radiations coincidence with the R(18) CO absorption line at $\nu_o = 2154.596$ cm^{-1}

Iso-tope	Line number	ν_1, cm^{-1}	ν_2, cm^{-1}	Line number	Iso-tope	$\nu_1 + \nu_2$, cm^{-1}	$\Delta\nu$, cm^{-1}
626	P62	1099.6961	1054.9155	P7	626	2154.6117	0.0157
626	P52	1095,6664	1058.9488	P6	626	2154.6151	0.0191
626	P18	1077.3026	1077.3026	P18	626	2154.6051	0.0091
626	P18	1048.6609	1105.9425	P36	828	2154.6034	0.0074
828	P44	1109.8780	1044.7078	P28	838	2154.5858	0.0102
828	P26	1100.5926	1054.0143	P38	828	2154.6069	0.0109

A block-diagram of the modernized gas analyzer includes low-pressure two frequency-tuned CO_2 and one CO lasers and a set of $ZnGeP_2$ FC. The gas analyzer is fully automatized. The gas analyzer is provided for with the possibility of measurements at $10°1-10°0$ and $00°2-10°1$ bands of CO_2 laser radiation. The set of FC includes SHG of these radiation bands and SFG which operate according to the block-diagram of Fig.2.

The results of simulated estimation were supported by
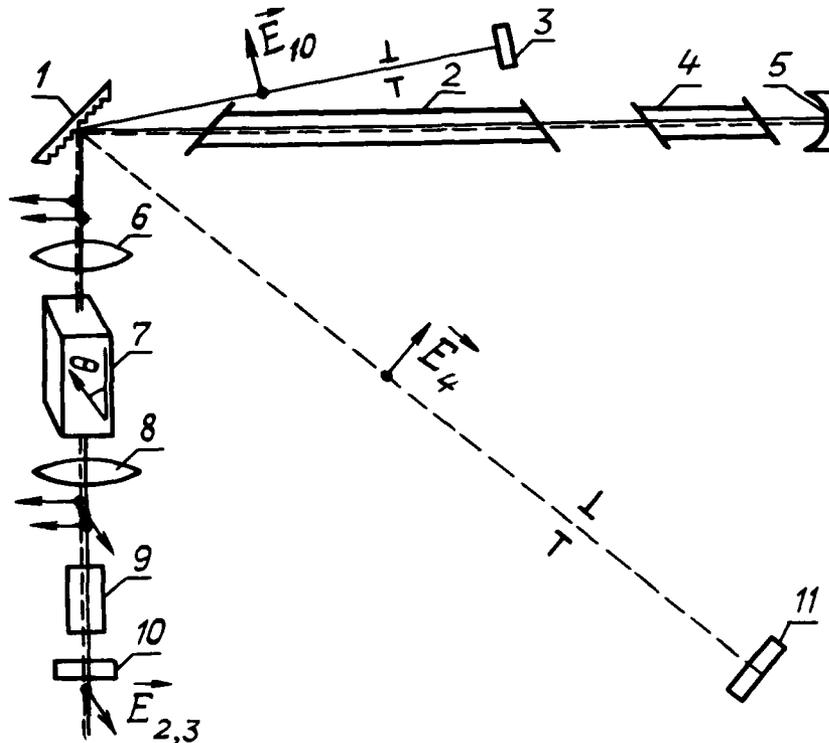
Fig. 2. A block-diagram of frequency converter
of the CO_2-laser radiation bands $10°1$-
$-10°0$ and $00°2-10°1$: 1 is a diffraction
grating, 2 is a discharge tube; 3,4 and
11 are the 100% mirrors, 5 and 7 are the
focused and collimated lenses, 6 is $ZnGeP_2$,
8 and 9 is a two-element filter, $\vec{E}_4, \vec{E}_{10}$,
$\vec{E}_{2,3}$ are the electric-field intensity vec-
tors of the 4.3 um, 10.4 um radiations,
their SH and SF radiation.

field measurements of the multicomponent real atmosphere and
demonstrated high-operational characteristics both of FC de-
veloped and the entire measurement complex.

References

1. D.K.Killinger, N.Menyuk. IEEE J.Quant.Electron.,v.QE-17,
   N9, p.1917 (1981).

2. Yu.M.Andreev, T.V.Vedernikova, V.G.Voevodin et al. Kvant.
   Elektron., v.12, N7, p.1535 (1985).

3. V.E.Zuev, Yu.M.Andreev, A.I.Gribenyukov et al. 13 Intern.
   Laser Radar Conf., Toronto, Ontario, Canada, NASA Conf.
   Publ. N2413, p.108 (1986).

A Simple Optical Method of Simultaneous Measurement of Characteristic Scales and Intensity of Atmospheric Turbulence

A.F. Zhukov and V.V.Nosov

Institute of Atmospheric Optics SB USSR Academy of Sciences, Tomsk, 634055, U.S.S.R.

For solving a large number of problems on optical radiation propagation in the atmosphere the atmospheric turbulent characteristics should be determined. There are the inner ℓ_0 and outer L_0 scales of turbulence, structural characteristics of fluctuations of the refractive index C_n^2. The value of C_n^2 determines the turbulence intensity. All these characteristics are the parameters in the spatial spectral density $\varphi_n(\mathscr{x})$. The function is given as [1,2]

$$\varphi_n(\mathscr{x}) = A_0 C_n^2 \mathscr{x}^{-11/3} \ell^{-\mathscr{x}^2/\mathscr{x}_m^2}(1 - \ell^{-\mathscr{x}^2/\mathscr{x}_0^2}), \quad A = 0,033 \tag{1}$$

where $\mathscr{x}_m = 5,92/\ell_0$, $\mathscr{x}_0 = 2\pi/L_0$. In the inertial subrange ($\mathscr{x}_0 \leqslant \mathscr{x} \leqslant \mathscr{x}_m$) the model (1) coincides with the Kolmogorov spectrum of turbulence.

At present a great number of optical methods of measuring the parameters C_n^2, ℓ_0 , $\mathscr{L}_0$ is known [2]. In this case a separate optical unit for determining a single parameter was used. A laser serves as a radiation source in this unit. For simultaneous measurements of the parameters C_n^2, ℓ_0 , $\mathscr{L}_0$ the corresponding number of separate units must be used. However, it is more comfortable, economical and reliable to use one unit based on application of simple technology of reception and processing of an optical signal. An inexpensive and reliable in operation thermal (incoherent) source is preferable for the use as a light source in such a unit.

The paper presents a simple optical method for simultaneous measurement of the parameters C_n^2, ℓ_0 , L_0. The thermal light source with the wavelength λ and the effective radius a is used. The optical radiation propagated through the tubulent atmospheric path X is received with

a conventional optical receiver. The radius of the receiving telescope lens is a_t, the focal distance is F. A device for separating the received light flux into four identical beams (for example, a combination of semitransparent prisms) is located on the optical axis of the receiver. In every beam (in a focal plane) a common quadratic photoreceiver (photoreceivers are identical) is placed. Before the photoreceivers the matrices (transparencies) are located. The matrices have the given transmission coefficients of radiation intensity τ_n (n is the number of the beam, n = 0, 1, 2, 3):

$$\tau_0 = 1, \quad \tau_1 = \tau_1(y) = \beta y + \eta, \quad \tau_2 = \tau_2(y) = 2y^2 + h$$

$$\tau_3 = \tau_3(z) = \begin{cases} 1, & |z| < a_s \\ 0, & |z| \geqslant a_s \end{cases} \tag{2}$$

Here y, z are the lateral coordinates in focal plane (y is the vertical, z is the horizontal axis), β, η, α, h are the given constants, a_s is the halfwidth of slit diaphragm τ_3.

The current at the photoreceiver output in the channel (n = 0, 1, 2, 3) is denoted by i_n. At the photoreceiver output the mean (in time) values $\langle i_0 \rangle$, $\langle i_2 \rangle$, $\langle i_3 \rangle$, $\langle (i_1/i_0)^2 \rangle$ are measured using an averaging device.

When using the results of the wave propagation theory in the turbulent atmosphere [1,2] one can theoretically estimate the relation between the signals measured and the parameters C_n^2, ℓ_0, $\mathcal{L}_0$. In this case, we should take into account that the values $\langle (i_2/i_0)^2 \rangle$, $\langle i_2 \rangle$ and $\langle i_3 \rangle$ [2-4] strongly depend on $\mathcal{L}_0$, ℓ_0 and C_n^2, respectively. For a horizontal homogeneous path whose mean altitude above the underlying surface H satisfies the condition $H \geqslant 20$ we obtain

$$C_n^2 = \frac{0.57}{k^{1/3} X F^{5/3}} \left(\left[\frac{\langle i_0 \rangle^2}{\langle i_3 \rangle^2} - 1 \right] a_s^2 - v \right)^{5/6}$$

$$\ell_0 = \left(\frac{1.1 \alpha\, C_n^2\, X\, F^2}{\frac{\langle i_2 \rangle}{\langle i_0 \rangle} - h - \frac{\alpha v}{2}} \right)^3$$

$$L_0 = 3.1 \alpha_t \left(1 + \frac{\eta^2 \langle (i_1/i_0)^2 \rangle}{0.73 \beta^2 C_n^2 F^2 \alpha_t^{1/3} X}\right)^{-3}$$

where $\nu = \frac{F^2}{k^2 \alpha_t^2} + \frac{F^2 \alpha_t^2}{X^2} + \frac{F^2 \alpha^2}{X^2}$, $k = \frac{2\pi}{\lambda}$. The slit width of the receiving aperture $2\alpha_s$ should be essentially less than the characteristic size of a source image in the focal plane ($\alpha_s \lesssim \sqrt{\nu}$). Besides, the condition $k\sqrt{\nu}/F \lesssim 1200$ m^{-1} must be fulfilled. It imposes restrictions on the receiver size α_t.

To eliminate the errors, due to the transverse shift of the source relative to the receiver optical axis and regular radiation refraction in the atmosphere, adjustment of the unit is used. Adjustment involves the preliminary minimizing of the value $\langle i_2 \rangle$. The angle between the axes y and z equals 90°.

It should be noted that in the suggested unit the presence of the four beams is not obligatory. The lesser number of the beams or even one channel may be used when the value i_0 is slightly different from $\langle i_0 \rangle$, and, hence, $\langle (i_1/i_0)^2 \rangle \approx \langle i_1^2 \rangle / \langle i_0 \rangle^2$. For this purpose, before the photoreceiver a device with removable matrices is located (2). The values $\langle i_n \rangle$, n = 0, 1, 2, 3, $\langle (i_1/i_0)^2 \rangle$ (or $\langle i_1^2 \rangle$) are measured alternately. The time for averaging is 5-7 minutes.

References

1. S.M.Rytov, Yu.A.Kravtsov, V.I.Tatarskii. Introduction to Statistical Radiophysics. P.I. Random Fields. -Moscow: Nauka, 1978, 463 p.
2. Laser Radiation in the Turbulent Atmosphere / A.S.Gurvich, A.I.Kon, V.L.Mironov et al. - Moscow: Nauka, 1976, 277 p.
3. Z.I.Feizulin, Yu.A.Kravtsov. On Laser Beam Broadening in the Turbulent Medium.-Izv.Vyssh.Uchebn. Zaved. Radiofiz., 1967, v.10, No.1, p.68-73.

4. V.L.Mironov, V.V.Nosov, B.N.Chen. Laser Source Optical
   Image Scintillation in the Turbulent Atmosphere.- Izv.
   Vyssh. Uchebn. Zaved. Radiofiz., 1980, v.23, No.4,
   p. 461-469.

Textural edge extraction with
an optical heterodyne scanning system

Ting-Chung Poon and Jinwoo Park
Department of Electrical Engineering
Virginia Polytechnic Institute and State University
Blacksburg, Virginia 24061

I. Introduction

In many classes of images, some of the important features can be recognized by repetitive structures over a large region. Such a spatial feature provides useful information in image segmentation and classification. Various digital image processing schemes to extract textural information have been reported based on local operators manipulating image pixels, often to extract local statistics from images [1]. Other schemes exploiting the textural information in the frequency domain have also been investigated along with some successful demonstrations [2, 3]. In this paper, textural edge detection by bandpass filtering is considered. A simple technique for realizing the bandpass filter in a heterodyne optical scanning system is described and illustrated experimentally. Section II discusses textural edge detection by bandpass filtering in the context of textural image modeling and frequency domain filter function construction. Section III describes the optical scanning system capable of extracting the edge in the texture and presents some experimental results.

II. Textural edge extraction by bandpass filtering

We consider the textural images as spatially repetitive structures. A 1-D textural image with two textural may be defined as [4, 5]

$$\Gamma(x) = U(-x) \cos(\omega_1 x) + U(x) \cos(\omega_2 x), \tag{1}$$

where $U(x)$ is a unit step function, and ω_1 and ω_2 are the so-called textural frequencies in radians per unit length which characterize the spatially repetitive structures in the textural regions. The textural edge is located at $x = 0$, and Fig.1 (a) illustrates the situation. A Gaussian bandpass filter, $H(\omega)$, shown in Fig. 1 (b), is used to process the input. The filter has the following transfer function

$$H(\omega) = C \exp[-(\frac{\omega - \omega_2 - \Delta\omega}{W})^2], \tag{2}$$

where C is an arbitrary amplitude constant, W is a passband parameter to control the bandwidth, and $\Delta\omega$ determines the amount of shift of the center of the Gaussian function from the textural frequency ω_2. The processed output is shown in Figs. 1 (c) and (d). We see that the filter of Fig. 1 (b) will extract the boundary of the domain of textural frequency ω_2. In fact, it will extract the boundary between ω_2 and any neighboring textures. Note that the Gaussian filter is offset by an amount $\Delta\omega$ from ω_2. This is necessary in order to suppress the textural frequency as best as possible. Decreasing $\Delta\omega$ results in some leakage of the textural frequency ω_2. The effect of leakages is illustrated in Fig. 1 (c).

III. Optical heterodyne scanning system

In this section we propose an optical scanning system to synthesize the filter of the form shown in Fig. 1 (b). The set-up is shown in Fig. 2. Two Gaussian laser beams, u and v, having different temporal carrier frequencies generated acousto-optically are sent toward the input $\Gamma(x)$. The receiving photodetector spatially integrates the transmitted light (or backscattered light if $\Gamma(x)$ is an intensity reflectant object) and delivers a heterodyne current at the beat frequency of the two receiving beams. As the input is scanned, the heterodyne output current

carries the processed version of the input, which can be displayed with an oscilloscope. The optical transfer function (OTF) of the heterodyne scanning system is the cross-correlation of two pupil functions u and v [6, 7]:

$$OTF(f_x) = \int_{-\infty}^{\infty} u(x)\, v^*(x - \lambda f_i f_x)\, dx, \tag{3}$$

where f_x is the spatial frequency. Since u and v used in the experiment are Gaussian laser beams, they may be described in general by

$$u(x) = e^{-(\frac{x}{W_0})^2} \quad \text{and} \quad v(x) = e^{-(\frac{x - \Delta x}{W_0})^2}, \tag{4}$$

where Δx is the spatial offset between the two Gaussian beams, which can be introduced by translating the beamsplitter used to combine the two beams. Substituting the expressions for u and v into (3), we obtain

$$OTF(f_x) = e^{-\frac{1}{2}(\frac{\lambda f_i}{W_0})^2 (f_x - \frac{\Delta x}{\lambda f_i})^2}. \tag{5}$$

Note that this OTF is a Gaussian, one-sided bandpass filtering function as shown in Fig. 1 (b).

The laser in use operates at $\lambda = 632.8$ nm, and the laser beam width W_0 is about 0.8 mm. The Fourier transform lens L_2 in the experimental setup has a focal length f_i of 610 mm. To simulate the textural image of the input object in the experiment, a Ronchi ruling with 80 lines/inch is used, corresponding to a fundamental frequency of about 3.15 cycles/mm. The left half of the Ronchi ruling is blocked, yielding a boundary between a textural frequency of 3.15 cycles/mm and a uniform region ($\omega_i = 0$). The textural image achieved by lowpass filtering with $\Delta x = 0$ is shown in Fig. 3 (a). Increasing Δx in the pupil function v, the textural edge detection by bandpass filtering can be realized as it is evident from Fig. 3 (b).

It should be pointed out that by using this optical heterodyne scanning technique, the textural edge information is obtained optically prior to electronic detection, thereby allowing high speed, multiplexing and interactive adaptation. In addition to imaging and real-time pre-processing, the optical heterodyne system is capable of ranging by phase tracking or by holographic means [7], as well as of target velocity determination via Doppler shift measurements simultaneously.

References

1. R. M. Haralick, "Statistical and Structural Approaches to Texture," Proc. IEEE, vol. 67, pp. 786-804, 1979

2. H. Maurer, "Textural Analysis with Fourier Series," in Proc's. Ninth International Symposium on Remote Sensing of the Environment, pp. 1411-1420, 1974

3. W. K. Stromberg and T. G. Farr, "A Fourier-Based Textural Feature Extraction Procedure," IEEE. Trans. Geosci. Remote Sensing, vol. GE-20, pp. 722-731, 1986

4. J. K. Townsend, K. S. Shanmugan, and V. S. Frost, "Optimal frequency domain textural edge detection filter," Appl. Opt. vol. 24, pp. 2067-2071, 1985

5. J. Park, T. -C. Poon, and G. Indebetouw, "Two-dimensional textural edge detection using ω − Gaussian filter," Appl. Opt. vol. 25, pp. 2357-2364, 1986

6. T. -C. Poon and A. Korpel, "Optical transfer function of an acousto-optic heterodyning image processor," Opt. Lett., vol. 4, pp. 317-319, 1979

7. T. -C. Poon, "Scanning holography and two-dimensional image processing by acousto-optic two-pupil synthesis," J. Opt. Soc. Am. A, vol. 2, pp. 521-527, 1985
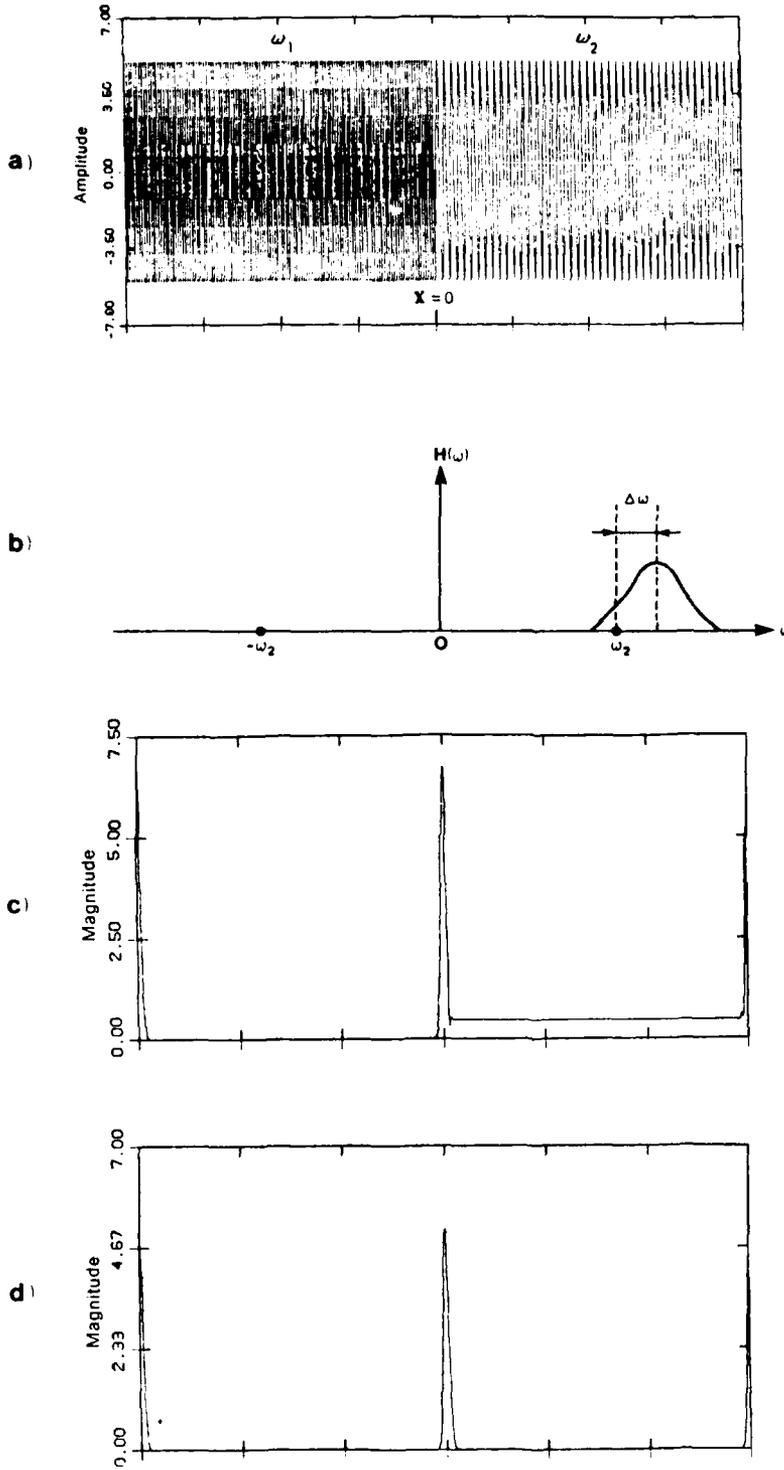
Figure 1. (a) 1-D input image with two textural regions where $\omega_1 = \pi/2$ and $\omega_2 = \pi/6$; (b) Gaussian bandpass filter; (c) output magnitude response with the Gaussian bandpass filter when $W = 0.1\ \pi$ and $\Delta\omega = 0.2\pi$; (d) output magnitude response with the same W as in Fig. 1 (c) but for $\Delta\omega = 0.3\ \pi$.
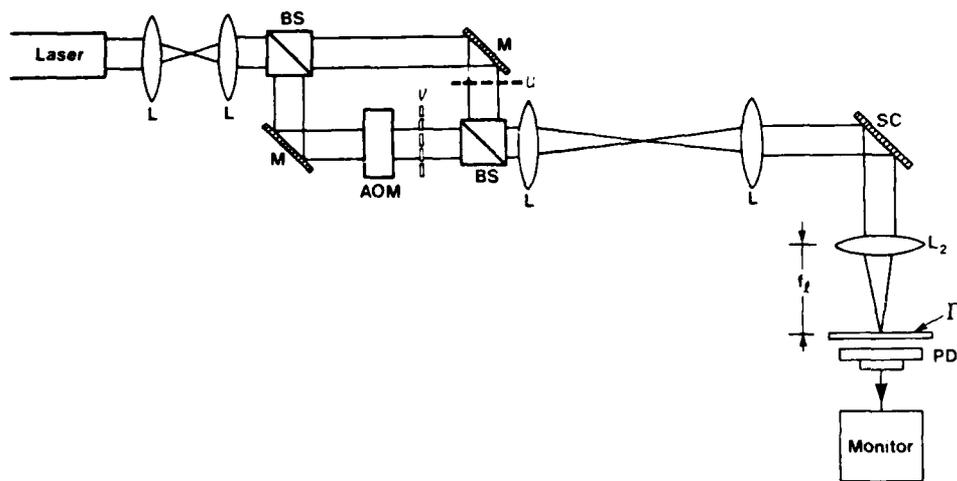
Figure 2. An optical heterodyne scanning system: BS denotes the beamsplitter, L the lens, M the mirror, AOM the acousto-optic modulator, SC the optical scanner, u and v the pupils, L_2 the Fourier transform lens, and PD the photo-detector.

a)

b)
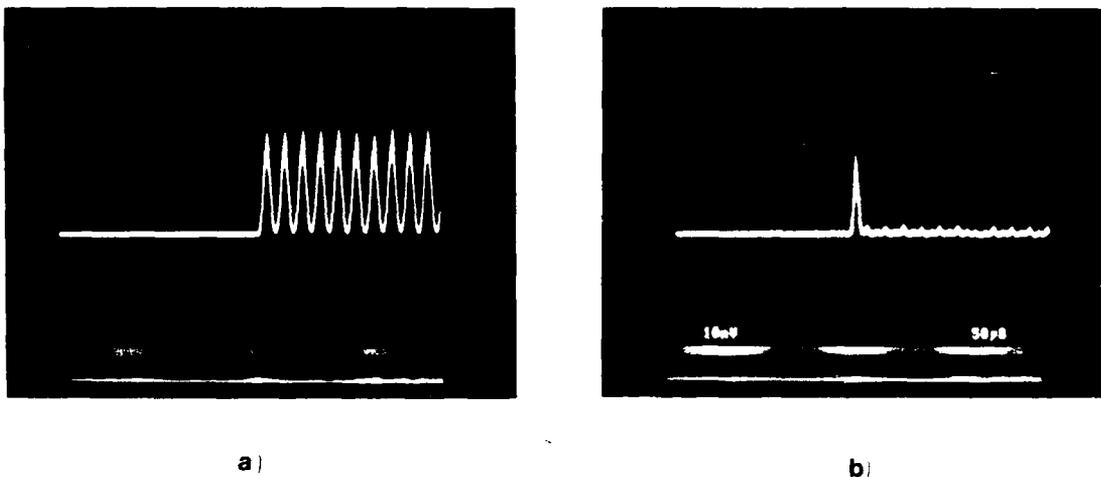
Figure 3. (a) Lowpass filtered input image ($\Delta x = 0$); (b) Optical textural edge extraction with two offset Gaussian beams ($\Delta x = 2.69 mm$)

A Free Flying Experiment to Measure the Schawlow-Townes Linewidth Limit of a 300 THz Laser Oscillator

by

C. E. Byvik. A. L. Newcomb and R. L. Byer

SUMMARY

Progress at Stanford University in the development of a LIDAR operating at one micron in a master oscillator power amplifier configuration required a reasonably stable, narrow linewidth laser oscillator. The required stability was achieved by the development of a non-planar Nd:YAG ring oscillator pumped by a ten-stripe diode laser array. Ten kilohertz linewidths are typical for this 300 THz oscillator. The Schawlow-Townes linewidth limit for this laser oscillator is predicted to be 1Hz per milliwatt output. A first time measurement of this linewidth limit for a laser oscillator operating at 300 THz is the objective of a proposed free-flying space experiment.

Sources for line broadening include mode fluctuations in the multi-striped laser diode array used as a pump source for the non-planar ring oscillator (NPRO) and the acoustical and thermal fluctuations in the terrestrial-based laboratory. The research leading to the space-based experiment has been aimed at optimizing the NPRO design, exploring low loss host materials for the Neodymium ion, host materials with optimum thermo-optical properties, and low noise coherent diode lasers for the pump source.

The battery powered space experiment consists of three NPRO's with linewidths determined by a simple beat note heterodyne technique. The third oscillator is included for redundancy. Detector redundancy will also be achieved by including two detector systems. Data acquisition and system controls will be accomplished through the use of a microcomputer.

The demonstration of a stable, narrow linewidth laser oscillator will enable space-based experiments such as proposed for a gravity wave interferometer detector, geopotential measurements, and frequency standards.

Development of Laser Heterodyne Radiometer
for Monitoring Stratospheric Air Pollution

Mitsuo Ishizu, Toshikazu Itabe and Tadashi Aruga

Radio Research Laboratory, Ministry of Posts and
Telecommunications
4-2-1 Nukuikita-Machi, Koganei, Tokyo 184, Japan

Laser heterodyne radiometers using a CO_2 laser and a
Pb-salt diode laser as local oscillators have been developed
for the detection of the stratospheric minor constituents.
Among them, sulfer bearing compounds such as OCS and SO_2 are
related to the formation of the stratospheric aerosols, and
they are the main concern of our study. According to a direct
sampling method, the mixing ratio of OCS molecules in the
atmosphere has been estimated to be 0.5 ppbv at the altitude
of lower than about 20km and to decrease monotonically in the
upper atmosphere. Due to the small amount of the stratospheric
OCS molecules, a solar occultation measurement using a
balloon-borne laser heterodyne radiometer will be required
for the detection. The radiometers which are described below
have been constructed for a laboratory measurement and resulted
in successful detection of many absorption lines in the solar
spectrum around a wavelength region of 10 um.

Fig.1 shows the experimental setup of CO_2 laser heterodyne
system which mainly consists of a grating-tuned CO_2 laser,
a high-speed HgCdTe photomixer, a low-noise preamplifier, a
beam combining optics and a Dicke chopper. The IF signal
generated in the photomixer was frequency-analyzed using a
microwave spectrum analyzer as a tunable filter, which
determined the resolution bandwidth of 15 MHz and swept the
IF signal in the range of 5-1200 MHz by a sweep rate of 10
MHz/sec. The sensitivity of this system was estimated to be
1.7×10^{-19} W/Hz by means of a S/N measurement using a calibrated

infrared light source.

Figs.2-3 show examples of the ozone absorption lines observed in the solar spectra. The data were obtained by one IF spectral sweep with a time-constant of 1 sec at the laser lines of 9P(30) and 9P(32), respectively. In these figures the dot represents spectral radiance calculated from the data at each IF interval of 11.3 MHz, and the bar-graph indicates the ozone line strength at the IF frequency of to be appeared in the spectrum derived from the AFGL atmospheric absorption line compilation. The coincidence between the measured and the compiled data are very good except for the line at 940 MHz in Fig.2. This line was always absent in the solar spectrum in the subseqent observations.

The diode laser heterodyne system used in this work is depicted in Fig.4. The diode laser was mounted in a closed-cycle helium refrigerator and operated in a single longitudinal mode with an output power of 100-200 μW. The small available power of the laser was compensated by minimizing aberrations of the focusing lenses and by utilizing a grating filter for both of the signal and the local light beams. As well as this optical design, a low-noise pre-amplifier of NF = 0.55 dB was also specially constructed. The IF signal was frequency-analized by the same circuit as in Fig.1, but the spectral feature was obtained by the sweep of the injection current of the laser. The sensitivity of this diode laser heterodyne system was estimated to be 5.9×10^{-19} W/Hz, which was only the factor of 3.5 degradation than that of the CO_2 laser heterodyne system. We are understanding this sensitivity is one of the best results that ever reported.

An example of the solar spectrum is shown in Fig.5 as well as a Fabry-Perot fringe pattern of the laser light for monitoring the wavelength. The sweep rate was 0.5 mA/sec and the integration time-constant was 1 sec. It could be seen that the laser covered the spectral range of 18GHz without any mode-hop and a number of absorption lines were clearly observed. Unfortunately the identifications of the lines have

not been made because absolute wavelength has not been decided so precisely in our present system.

From these results of the construction and testing of the laser heterodyne radiometers, an airborne system has been under development and will be operated soon.
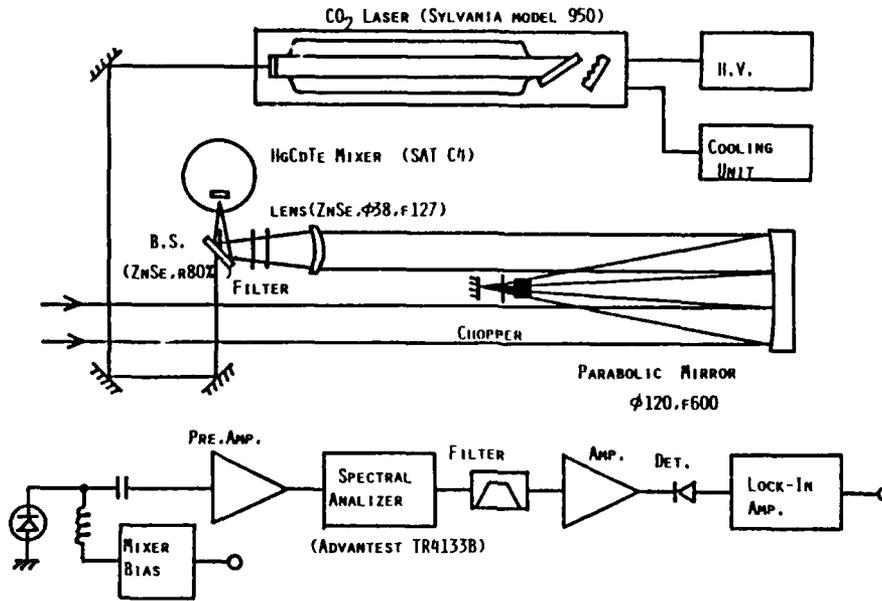
Figure 1. CO_2 laser heterodyne radiometer
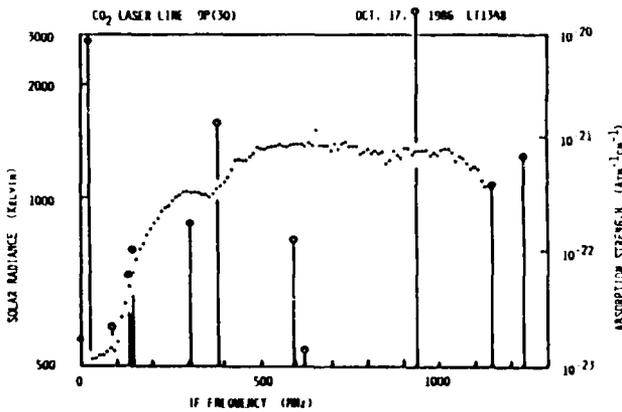
Figure 2.   Solar spectrum   Figure 3.   Solar spectrum
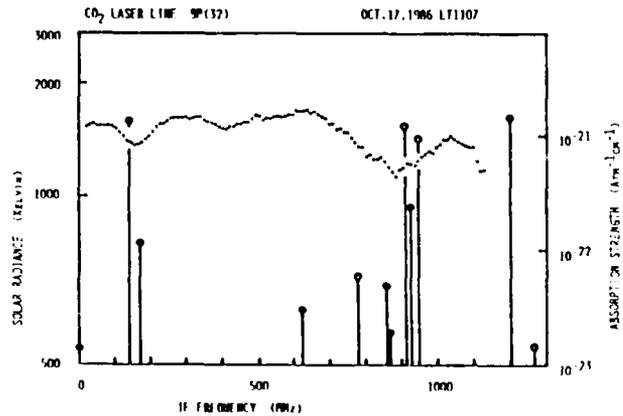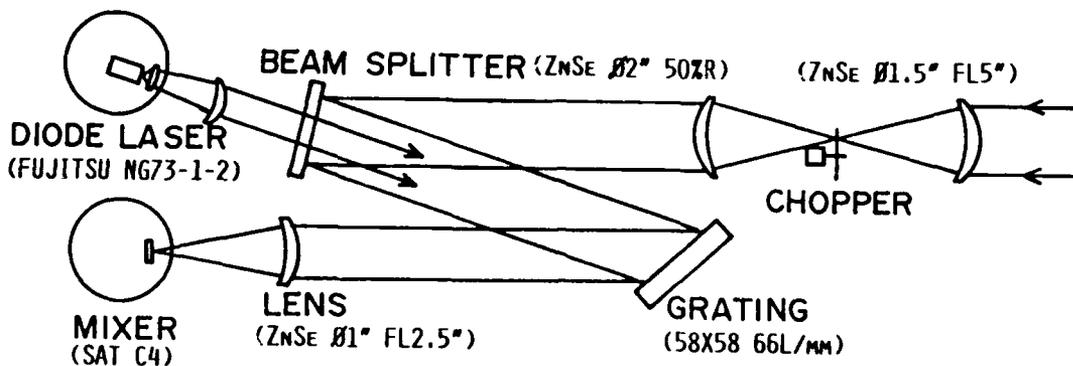
Figure 4.   Diode laser heterodyne radiometer
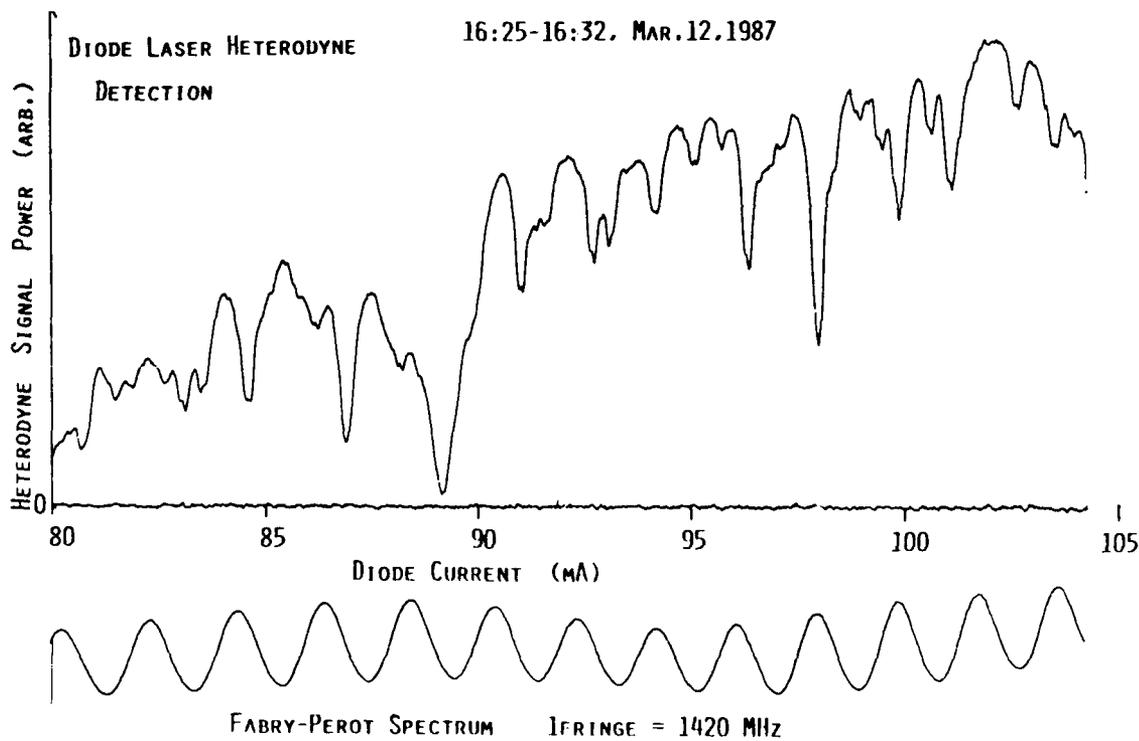
Figure 5.   Solar heterodyne spectrum

AN EXPERIMENTAL MEASUREMENT OF THE SUSCEPTIBILITY OF SPATIAL FILTER PROFILING TECHNIQUES TO SATURATION

G. R. Ochs and R. J. Hill
NOAA/ERL Wave Propagation Laboratory
Boulder, Colorado 80303

The current interest in the use of spatial filtering techniques to profile wind and refractive-index turbulence raises the question of how saturation of scintillation may affect these systems. Some experimental observations of saturation effects have now been made with a wind profiling system that is under development at the Wave Propagation Laboratory. The wind profiling technique, which is a modification of a method originally proposed by Lee,[1] employes zero-mean spatial filters at both the transmitter and receiver to restrict the observation of refractive-index irregularities moving across a light path to those of a particular spatial wavelength and at a particular location along the path. The wind profiling system employs a number of sets of spatial filters of different spatial wavelengths to measure winds simultaneously at various path positions.

To observe saturation effects, the system was altered to measure intensity variances from one pair of transmitter and receiver filters having 20 cm spatial wavelength, and another pair having 5 cm spatial wavelength. The transmitter and receiver filter geometry is shown in Fig. 1. Two separate Fresnel lenses are used to form the transmitting filters. A single Fresnel lens and 32-element photodiode array, connected simultaneously for both spatial wavelengths, are used to form the receiver filters. Note that although the elements of the transmitting array fill the aperture, the receiver elements are half the width of the transmitting elements and have gaps between adjacent elements. This arrangement results from the design of the wind Profiler, which uses an interleaved receiving array to obtain wind direction information. This configuration formed spatial filters at the center of the path of 10 and 2.5 cm wavelength. The optical path length between transmitter and receiver was 1 km. A separate optical system was employed to measure the refractive-index structure parameter C_n^2.

The mean square signal fluctuations for the 2.5 cm ($x^2_{2.5}$) and for the 10 cm spatial wavelength (x^2_{10}) were measured and compared with C_n^2 and with each other. The data points in Figs. 2-4 represent 15-min averages; a 5-point running average was applied to the data points to show the trends. The relationship is nearly linear in Fig. 2, where we plot x^2_{10} vs. C_n^2; however, the situation is quite different in Fig. 3, where we plot $x^2_{2.5}$ against C_n^2. The value of C_n^2 at which $x^2_{2.5}$ begins to saturate is about the same as the value at which the onset of saturation would be observed for single, circular, incoherent, uniformly-illuminated transmitter and receiver apertures having 2.5 cm diameter. At higher turbulence levels, however, the variance of the signal drops off severely. This is shown clearly in Fig. 4, a linear plot of $x^2_{2.5}$ vs. x^2_{10}. At the highest turbulence levels, the variance is about one third that of the peak.

There is at present no theoretical description of the saturation effects on spatial-filter measurements. On the basis of the heuristic theory of

saturation, and its success in predicting the onset of saturation for large-aperture $C_n{}^2$ scintillometers,[2] one would roughly estimate that the onset of saturation would occur as the parameter $\lambda L/2.4\,\rho_0$ becomes larger than the spatial wavelength being observed; here λ is optical wavelength, L is path length, and the field coherence length $\rho_0 = 1.44\ (k^2 L C_n{}^2)^{-3/5}$, where $k = 2\pi/\lambda$. The data do not violate this notion, although it was hoped that they would. Sensitivity to a narrow range of path positions requires many cycles on the transmitter and receiver. If these cycles must be wide, say 10 cm or greater, to resist saturation effects routinely for long propagation paths, then the transmitter and receiver spatial filters will be very large and difficult to construct.

Reference

1. Lee, R. W. 1974, Remote probing using spatially filtered apertures, J. Opt. Soc. Am. 64(10), 1295-1303.

2. Ochs, G. R. and R. J. Hill, 1982, A study of factors influencing the calibration of optical $C_n{}^2$ meters, NOAA Tech. Memo. ERL WPL-106.
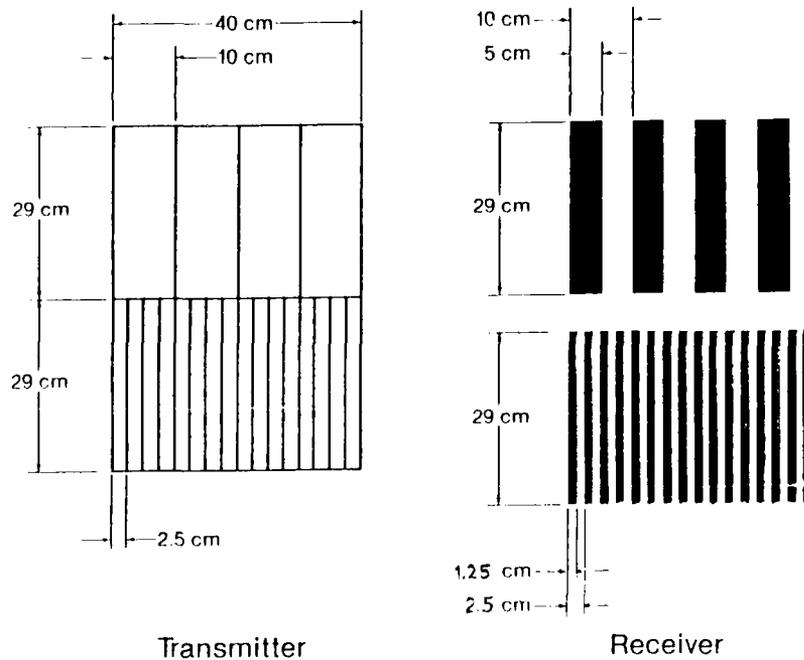
Fig. 1. Transmitting and receiving apertures.
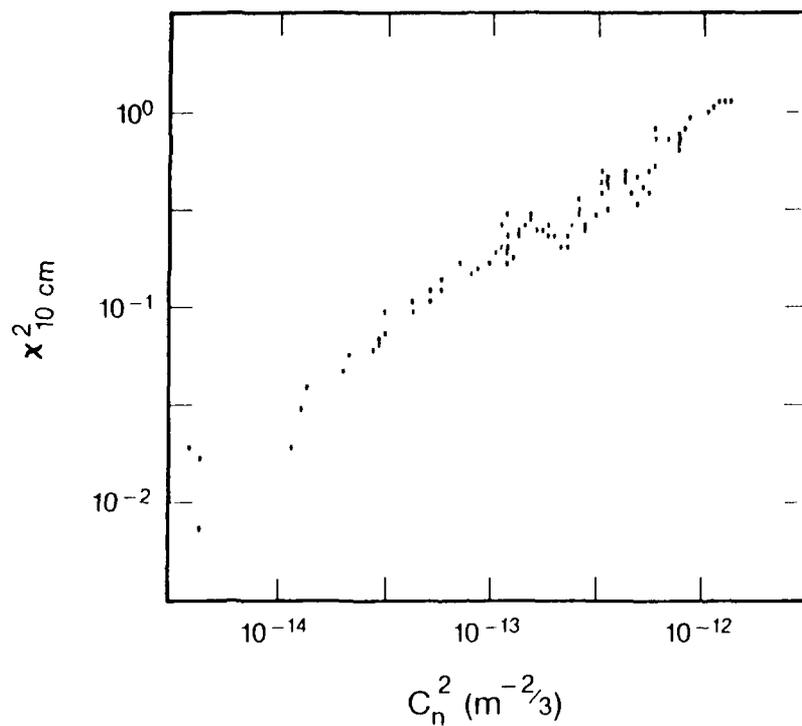
Fig. 2.   Variance at 10 cm spatial wavelength vs. C_n^2.
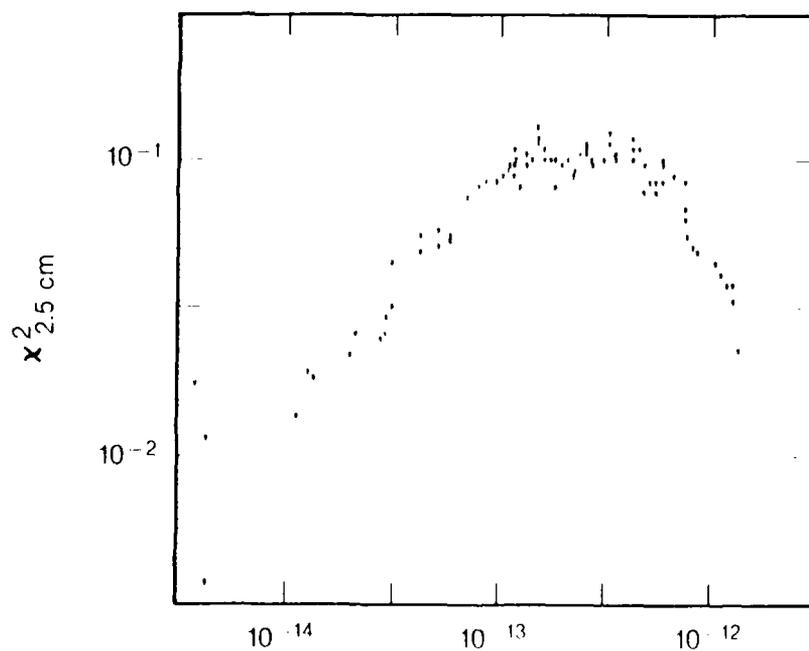
Fig. 3.   Variance at 2.5 cm spatial wavelength vs. C_n^2.
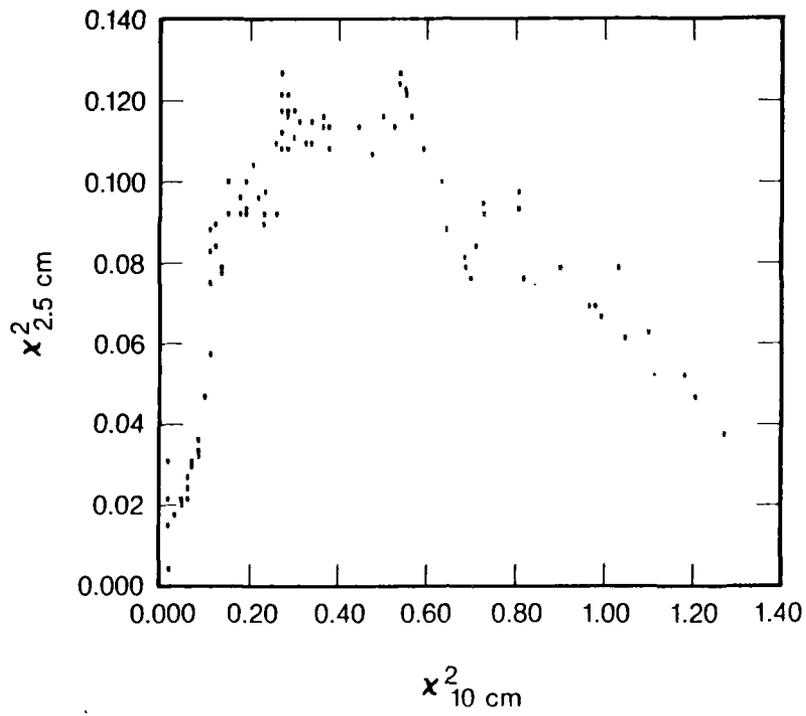
Fig. 4. Variance at 2.5 vs. 10 cm spatial wavelength.

Simultaneous Measurements of Turbulence Level and
Inner Scale Using Laser Scintillation

R.G. Frehlich

Cooperative Institute for Research in the Environmental Sciences (CIRES)

University of Colorado/NOAA

Boulder, CO 80309

INTRODUCTION

Laser propagation through the atmosphere produces random scintillation patterns. The statistics of these intensity fluctuations is determined by the refractive index spectrum of the atmosphere $\Phi_n(\vec{q})$ where $\vec{q}$ denotes spatial wavenumber. Tatarskii proposed the following model for the turbulence spectrum[1]

$$\Phi_n(\vec{q}) = .033 C_n^2 q^{-11/3} \exp[-l_0^2 q^2/4] \tag{1}$$

where C_n^2 is a measure of the level of turbulence and l_0 is proportional to the inner scale λ_0 ($\lambda_0 = 2.95 l_0$). The inner scale is defined as the intercept of the two power law regions of the three dimensional structure function of refractive index fluctuations.

The level of turbulence has been estimated[2] from the normalized variance of a large incoherent source. This statistic is dominated by the inertial range of the turbulence. The inner scale has been measured[3] by comparing this statistic to the normalized variance of a diverged laser. The accuracy of these two methods is determined by the number of independent samples observed with the incoherent source. The inner scale has also be estimated[4,5] by a measurement of the spatial covariance function

$$C(\vec{p}) = \frac{<I(0,R)I(\vec{p},R)>}{<I(0,R)><I(\vec{p},R)>} - 1, \tag{2}$$

in weak scattering. Here, $\vec{p}$ is the transverse separation, I is intensity, R is the propagation distance, and $< >$ denotes ensemble average. For a point source, the covariance in weak scattering is related to the turbulence spectrum by

$$C(\vec{p}) = 4\pi k^2 \int_0^R \int_{-\infty}^\infty \Phi_n(\vec{q})\{1 - \cos[\frac{q^2}{k}z_1(1 - \frac{z_1}{R})]\}\exp\left(i\,\vec{q}\cdot\vec{p}\frac{z_1}{R}\right) d\vec{q}\,dz_1 \tag{3}$$

The measurements of Ref. 5 were performed with two moving detectors and the observation time was too long to obtain stable estimates. This limitation will be removed by using an array of photodetectors to measure the covariance.

EXPERIMENT

Typical values of the inner scale of turbulence near the ground ranges from 3mm to 10mm. In order to sample the covariance function adequately, spacings from 1mm to 20 mm are required. The photodiode array shown in Figure 1 samples the covariance from .75mm to 36mm. The photodiodes are United Detector HS008 chips mounted on a circuit board. The active area of each photodiode is .2X.2mm square. Therefore there was no aperture averaging of the signals. The electronic design is described in Refs. 6,7. The bandwidth was 10KHz, the mean signal level was 10 volts and the rms system noise was 50 millivolts. The 8 channels were sampled simultaneously and digitized with 12 bit accuracy using a PC digital acquisition system. The system noise was calibrated by shuttering the laser for 1.6 seconds. A 5 milli watt Uniphase laser was focussed through a pinhole and diverged to approximate a point source. The laser fluctuations were less than .1% during a measurement sequence.
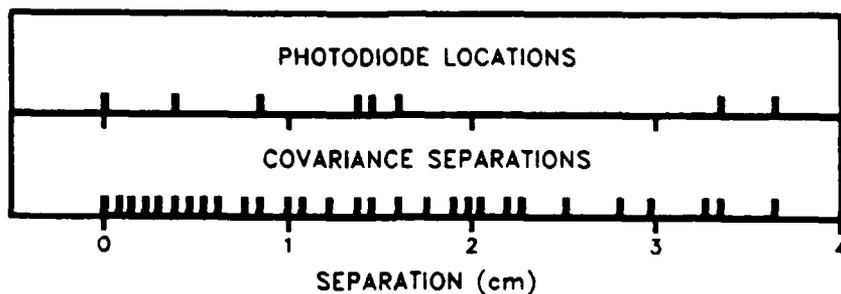
Figure 1 Photodiode array geometry.

RESULTS

Figure 2 displays 4 covariances obtained from 1.6 seconds of data each. This data was collected on a sunny day with moderate windspeed. The propagation path was 30m long and 1.5m above the ground. During the 8 seconds of observation, the covariances appear stable. However, the covariances obtained 3 seconds later (Figure 3) indicate a noticeable increase (note the change of scale). The same behavior was observed on a 20m propagation distance.
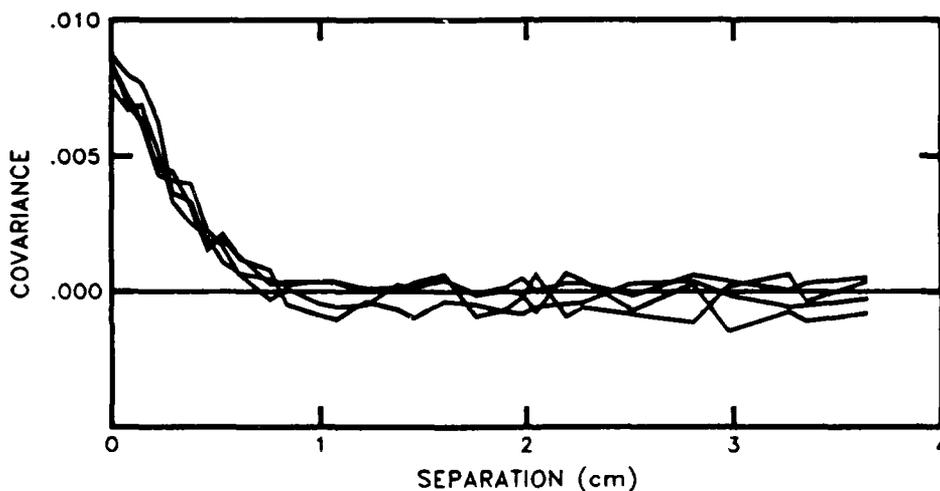
Figure 2 Covariance measurements for locally stationary conditions.
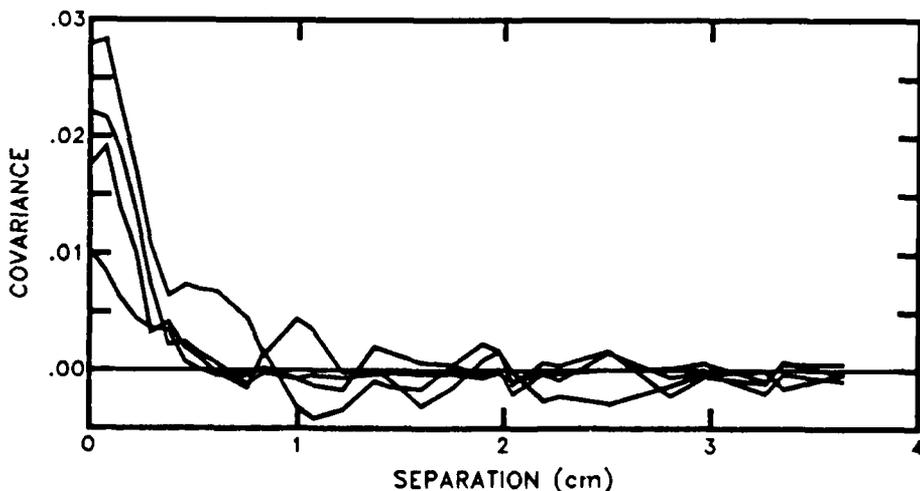
Figure 3 Covariance measurements for locally nonstationary conditions.

Figures 4 and 5 display the covariances for data collected on an overcast summer day with a light wind. The propagation distance was 50m. Again, note the rapid change in the covariances. These regions of enhanced turbulence are most likely due to the passage of thermal plumes[8].
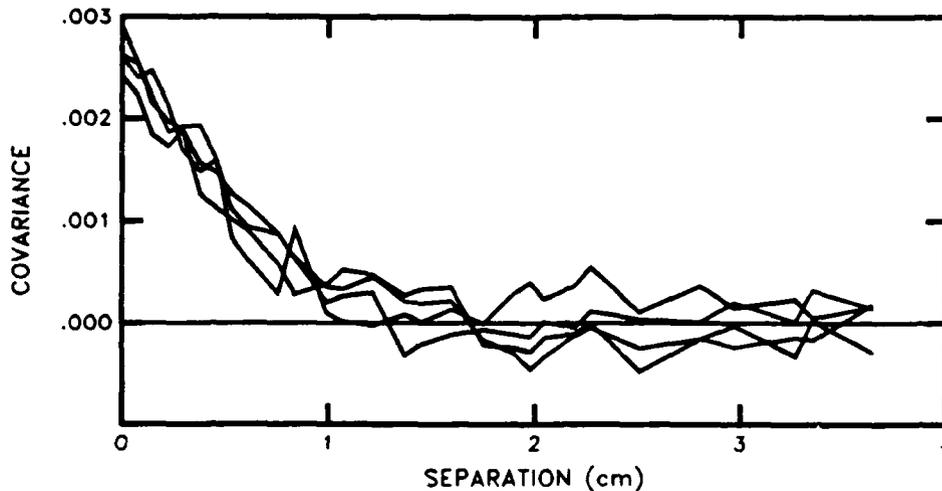
Figure 4 Covariance measurements for locally stationary conditions.
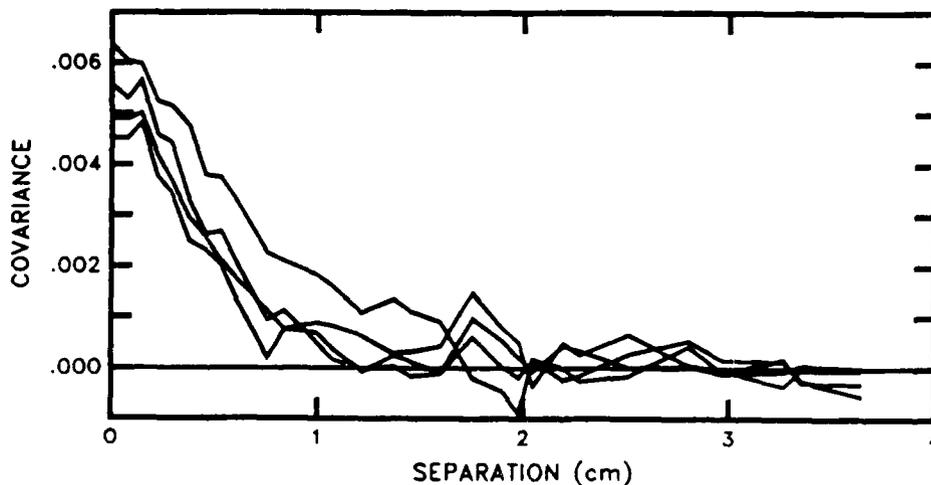
Figure 5 Covariance measurements for locally nonstationary conditions.

The average of 72 seconds of data during a more stable period is shown in Figure 6 along with the best fit theoretical covariance assuming the Tatarskii turbulence spectrum. The two curves are very similar but more data is required in order to determine the exact shape of the turbulence spectrum. It is believed that when the Reynold's number is high and the air is dry, then the turbulence spectrum is described[9] by a universal fu. ction. Given this universal spectrum, the covariance measurements will provide accurate estimation of the spectral parameters C_n^2 and l_0. These two parameters provide essential information about the boundary layer energy processes.

The atmospheric surface layer is a complicated random fluid. These measurements indicate that the turbulence spectrum changes quickly and substantially. The atmosphere is not

homogeneous and stationary. A complete description of this random field is required in order to predict the statistics of wave propagation in the atmosphere.
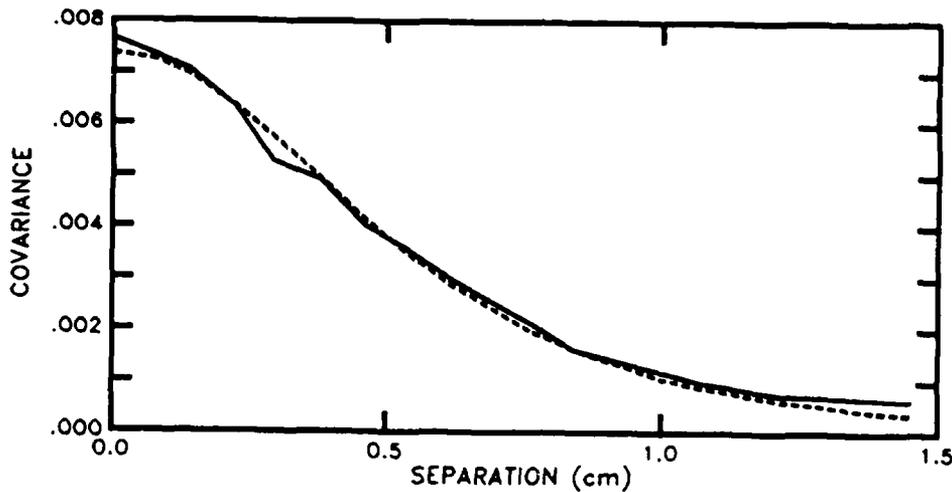
Figure 6 Measured covariance function (——) compared with theoretical covariance function (- - -) using Tatarskii's spectrum with $C_n^2 = 9.4 \times 10^{-13} m^{-2/3}$ and $\lambda_0 = 9.59 mm$.

REFERENCES

1   V.I. Tatarskii, *The Effects of the turbulent Atmosphere on Wave Propagation* (Keter, Jerusalem, 1971), p. 65-66.

2   Ochs, G.R., and Ting-i Wang, "Finite aperture optical scintillometer for profiling wind and C_n^2, Appl. Opt., 17, 3774-3778, (1978).

3   Ochs, Gerard R. and Reginald J. Hill "Optical-scintillation method of measuring turbulence inner scale," Appl. Opt., 24, 2430-2432, (1985).

4   Strohbehn, J.W. "The feasibility of laser experiments for measuring the permittivity spectrum of the turbulent atmosphere," J. Geophys. Res., 75, 1067-10766, (1970).

5   Gray, D.A., and A.T. Waterman, Jr. "Measurement of fine-scale atmospheric structure using an optical propagation technique," J. Geophys. Res., 75, 1077-1083, (1970).

6   W.A. Coles, and R.G. Frehlich, "Simultaneous measurements of angular scattering and intensity scintillations in the atmosphere," J. Opt. Soc. Am. 72, 1041-1048 (1982).

7   Frehlich, R.G. "Laser Propagation in Random Media," PhD Thesis, University of California, San Diego, (1982).

8   Wilczak, J.M., and J.E. Tillman "The three-dimensional structure of convection in the atmospheric surface layer," J. Atmos. Sci., 37, 2424-2443, (1980).

9   Hill, R.J. "Models of the scalar spectrum for turbulent advection," J. Fluid Mech. 88, 541-562, (1978).

"Atmospheric Correction Algorithm of Real and Simulated Space

Imagery Using Radiative Transfer Code"

By

Hongsuk H. Kim

NASA-Goddard Space Flight Center

Greenbelt, MD. 20771

An image processing algorithm which can be used not only to
simulate satellite mulitispectral imagery but also to derive
surface reflectance from satellite imagery is being developed. In
essence, the algorithm is a pixel by pixel modelling of the
atmospheric radiance which can be either added to a simulated
ground scene or subtracted from space data.

An established atmospheric radiative transfer model, known as Dave
Code, has been adapted for this pixel by pixel correction process.
1) The output of the code was modified by interpolation so that the
model's look angle matches the geometry of each pixel of a scan
line. The computed up and downwelling solar radiance of each pixel
was then arranged to give the upwelling radiance for ten surface
reflectances. This N by 10 dimensional matrix (N = the number of
pixel elements in a scan line) is reduced to N by 3 dimensions
using three quadratic coefficients which best fit intensity vs
ground reflectance slope. In table 1, a sample of the printout is
shown.

TABLE 1   UPWELLING RADIANCE IN THE FORM OF QUADRATIC
          COEFFICIENTS

Wavelength=472 nm
        Tmie=0.262   Size Parameter v=3.0
        SZA=48   AZI=90
Look

Angle	A1	A2	A3
0	0.063806	0.453468	0.105617
1	0.063816	0.453428	0.105599
2	0.063838	0.453381	0.105510
3	0.063875	0.453268	0.105480
4	0.063923	0.453187	0.105389
4	0.063986	0.453036	0.105359
5	0.064063	0.452918	0.105262
6	0.064155	0.452730	0.105226
7	0.064255	0.452585	0.105109
8	0.064372	0.452367	0.105056
9	0.064503	0.452161	0.104938
10	0.064651	0.451883	0.104884
11	0.064807	0.451654	0.104731
12	0.064982	0.451346	0.104648

For demonstration, a simulated ground reflectance scene for 472nm
that includes a variety of terrestrial targets such as highly
reflective snow, sandy soil, and dark ocean surfaces along with
land vegetation with built-in bidirectional reflectance behavior
was synthesized. 2) Since aerosol scattering and absorption are the
most important variables of the atmospheric effect on remote
sensing imagery, the simulated scene was processed using four
different aerosol optical thickness atmospheres. A wide field of
view of +/-60 deg simulates the data acquisition conditions of
NASA's future Eos/MODIS.1 At a glance, the resultant simulated
satellite images for four different (Mie) conditions shown in
figure 1 do not display visible differences that might be
associated with increasing aerosols. However, the changes induced
by the aerosols become more obvious in line profile plotting.
Analyses showed aerosol scattering is an important reason for the
brightening effect for dark surfaces such as ocean and vegetations
in the blue spectral region, while significant absorption is taking
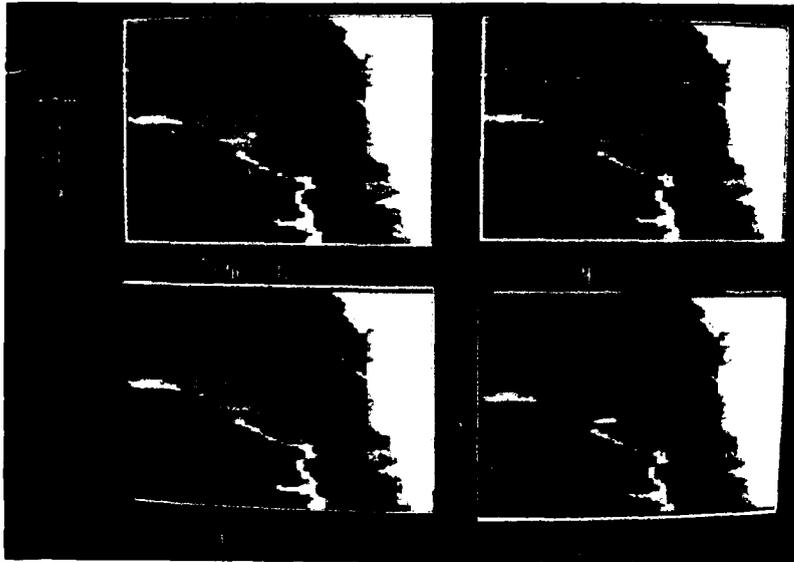
Figure 1 Simulated satellite images for four different optical
thickness atmospheres.

---

1   Moderate Resolution Imaging Spectrometer.

place for bright surfaces such as snow or sandy soil. Consequently
there exists a reflectance point at which the upward intensity is
insensitive to changes in aerosol optical thickness. Also the plot
showed, if an imager has a wide off-nadir view angle (i.e. MODIS,
AVHRR or CZCS), non-linear curlings in total radiance will occur
for both dark and bright surfaces at extreme angles.

These are quantitatively observable phenomena and become important
clues in searching for optimum atmospheric parameters to be used
for the removal of the atmospheric effects from space imagery. In
order to perform atmospheric correction, the earlier three
quadradic coefficents, A1, A2 and A3, are used in solving for the
reflectance, ρ_λ , from the following equation.

$$A3 \times (\rho_\lambda)^2 + A2 \times (\rho_\lambda) + A1 - L_\lambda = 0$$

where L_λ denotes the intensity of upwelling radiance at the
satellite. Using the line profiling method of the derived surface
reflectance, several different optical thickness atmospheres were
tested until a "correct" atmosphere was found. Incorrect optical
thickness parameters result in significantly exaggerated
reflectances, including negatives or values in excess of 1.0. It
would appear correct reflectance from a homogeneous targ?t yields a
single value and this can be only inferred from correct atmospheric
parameters.

This iterative approach was used in removing the atmospheric effect
from a TM scene which was taken over the nuclear power plant at
Chernobyl, USSR on April 29, 1986. An optimum aerosol optical
thickness was determined using line profile plots of the Chernobyl
cooling pond with several sets of $\mathcal{T}$(Mie) correction factors. A
water reflectance of 5% was assumed, hence an effective $\mathcal{T}$(Mie) of
0.39 was inferred. The left image of figure 2 is a ground
reflectance scene of the Chernobyl power station area processed by
this method. The validity of such processing cannot be confirmed at
this stage. However our earlier application of the Dave Code for
ocean atmospheric system modelling leaves us to believe the outcome
of the model has been reasonably accurate.3) This study
demonstrates use of the model can be expanded to pixel by pixel
correction of atmospheric effects from remote sensing imagery of
land and ocean. (Approximately 15 minutes presentation)

Figure 2. TM Chernobyl power plant scene with and without having
applied the atmospheric effects correction.

References:

1) Dave,J.V. "Development of Programs for Computing Characteristics
of Ultraviolet Radiation, Tech Report Scaler
Case (SPA-D)" IBM Palo Alto,CA.,NAS-Contract 5-2168, 1972

2) Walthal,C.L. J.M.Norman,J.M.Welles,G.Campbell and B.L.Blad,
"Simple Eqn to Approximate the Bidirectional Reflectance from
Vegetation and Canopies and Bare Soil Surfaces",Applied Optics, Vol
24,pp 382-7,1985

3) Kim,H.H. and G.Linebaugh "Early Evaluation of TM Data from
Coastal Process Studies" Adv. Space Res. Vol 5,pp 21-9,1984
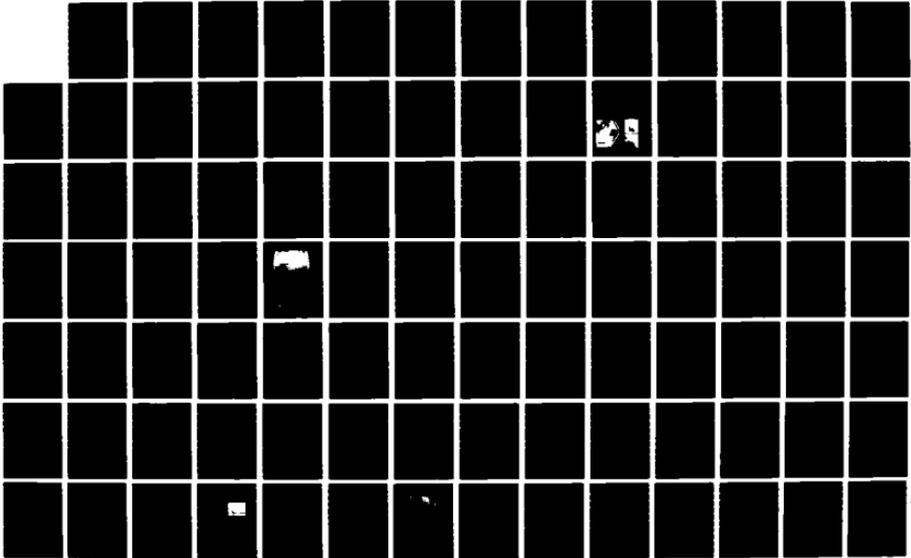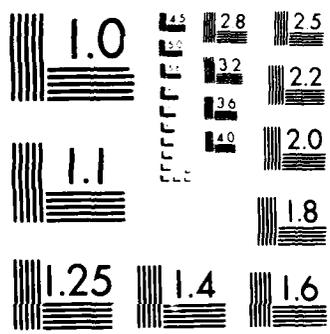
GASCOSCAN and GASCOFIL- Remote Sensing Gas Correlation Spectrometers for Tropospheric Trace Gas Measurements

W. H. Morrow and R. W. Nicholls

Centre for Research in Experimental Space Science (CRESS)
York University
4700 Keele St.
North York, Ont., M3J 1P3

Correlation spectroscopy, which is a powerful diagnostic tool for the determination and monitoring of trace atmospheric contaminants, involves a correlative comparison between the features of a "field spectrum" of a specific region of the atmosphere, and the features of a "mask function" which is representative of the spectral absorption features of the molecular species of interest. The degree of correlation between these can be interpreted quantitatively as a direct measure of the column density of the species of interest in the instrumental field of view.

Both of the spectrometers described here use the gas filter non-dispersive correlation method. They incorporate gas cells containing a sample of the gas to be detected in the tropospheric target. A block diagram of the system used in each is shown in fig. 1. Light from the target is collected by a telescope and passed through a gas cell chopper. The light transmitted by the chopper is sent through a spectrum analyzer (filters or spectrometer) and focused onto a detector (or array of detectors). The resulting time dependent signal is amplified by a preamplifier and sampled by an A to D converter attached to a microcomputer data buss. Synchronization with the chopper is obtained triggering interrupts in the microcomputer with signals derived from optical pickoffs on the gas filter wheel.

The simpler, smaller and most portable of the two instruments, GASCOFIL uses four gas cells on a 10 cm. filter wheel to make correlation measurements, (see fig 2.) This system has been field tested at the Ontario Hydro Lakeview Thermal Generating plant, as a plume tracker, SO_2 monitor, and quantitative SO_2 remote sensor. Fig 3. shows some of the results of this survey (Reported earlier in Morrow, Nicholls).

The larger instrument, GASCOSCAN, uses an echelle polychromator to isolate the spectral regions of interest. This allows up to 16 detectors to view separate spectral regions in the UV and IR in the range of .2 to 11 microns. In addition, the GASCOSCAN polychromator has a motorized micrometer drive. This allows scanning through the spectral features of interest which can be used to establish an zero level for the correlation signals.

The GASCOSCAN optical system is shown in fig. 4. GASCOSCAN has been operated as a passive remote sensor or as an active folded path sensor. In the passive mode IR and UV flux in the field of view is collected by a Newtonian telescope, passed through a high speed chopper and a gas cell chopper and spectrally analyzed and detected with the polychrometer/ detector system. In the active mode UV and IR flux from a lamp source is passed through the gas cell chopper and a high speed chopper. The high speed chopper is arranged to modulate the light between a reference path and the 300 meter atmospheric path.

The GASCOSCAN system is currently undergoing field trials for the detection of NO_2, SO_2, CO, CO_2, N_2O, NH_3 and other trace species of tropospheric interest.

REFERENCES

Morrow W. H. and Nicholls R. W.," GASCOFIL A GAS CORRELATION SPECTROMETER FOR REMOTE SENSING OF TRACE ATMOSPHERIC CONSTITUENTS" Proceedings of the Optical Society of America Topical Meeting on Atmospheric Remote Sensing pp8 (Incline Village, Nevada, Feb. 1985

Fig. 2 - GASCOFIL OPTICS

Fig 1.-Gas Filter Correlation Spectrometer Block Diagram
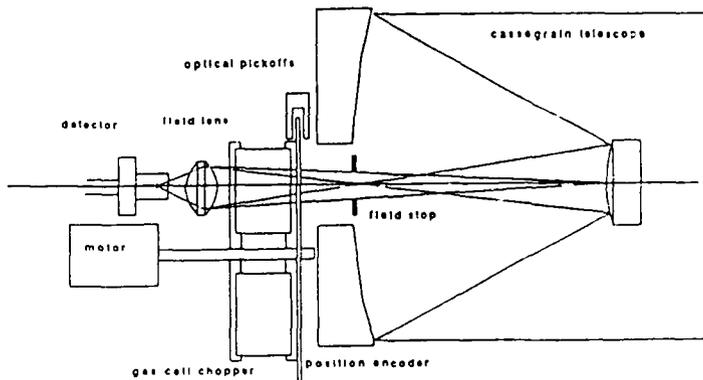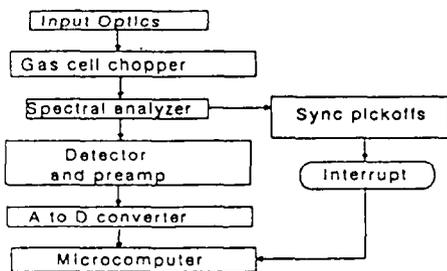
Fig 3.- Signal In SO2 Channel VS. Time
For Lakeview G. S. Survey
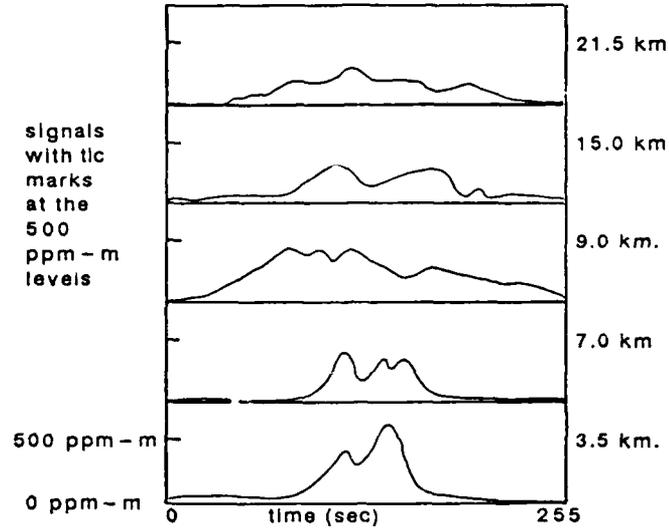
DIFFUSION OF THE LAKEVIEW PLUME
AS A FUNCTION OF DISTANCE FROM
THE SOURCE

(note the abscissa time is a measure
of distance travelled by GASCOFIL
at a constant speed perpendicular to
the plume)

Fig 4. GASCOSCAN OPTICS
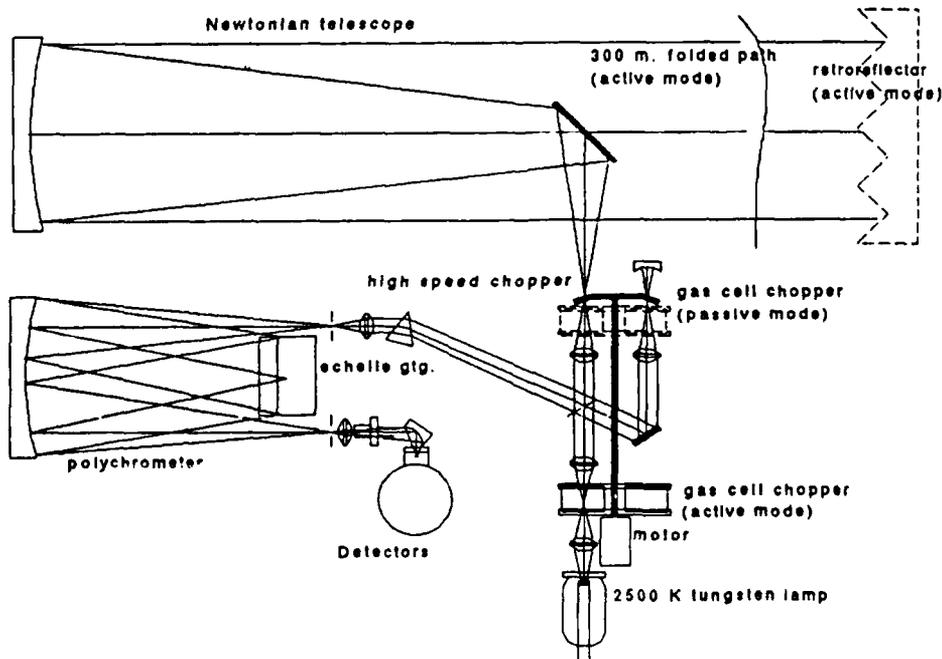
Signal Requirements for Remote IR Limb Sounding of Atomic Oxygen and Temperature in the Thermosphere

R. D. Sharma
Air Force Geophysics Laboratory
Hanscom AFB
Massachusetts 01731

A. S. Zachor
Atmospheric Radiation Consultants, Inc.
ა9 High Street
Acton, Massachusetts 01720

SUMMARY

Atomic oxygen plays an important role in chemical and collisional processes in the earth's mesosphere and thermosphere. Current techniques, both in situ and remote, for measuring oxygen atom densities in this altitude regime have produced results with unexplained large disparities. We are investigating the feasibility of an approach wherein vertical profiles of translational temperature and oxygen atom density are recovered from measurements of the earth's limb radiance profile near 147 micrometers and/or 63 micrometers wavelength, corresponding to the OI ($^3P_0 - ^3P_1$ and $^3P_1 - ^3P_2$) transitions of the ground electronic state of atomic oxygen. The assumption that the ^3P fine structure levels are in thermodynamic equilibrium (LTE) with the local translational temperature is crucial to the proposed technique, but seems a reasonable one based on the very long radiative lifetimes of the level transitions.

The two sought-after vertical profiles can, in principle, be recovered from a) a pair of limb radiance profiles representing the total (spectrally integrated) apparent intensities of the two OI lines, or b) a spectrally resolved limb radiance profile for just one of the lines. The use of spectrally resolved data, which makes the LTE assumption less critical, implies an instrument with resolving power somewhat greater than 10^5, which could be achieved using a Fabry-Perot system with metal mesh etalons. An IR heterodyne system, if one could be designed to operate near 147 micrometers wavelength, would be more complex but would easily provide the required high resolving power.

Reported in this paper are the results of one-dimensional inversions, by an onion-peel technique, of synthetic data representing both the spectrally resolved and unresolved cases for various resolving powers and signal-to-noise levels. The results define the basic sensor performance requirements for remote IR limb sounding of atomic oxygen and temperature.

Concepts for Future Meteorological Earth Observing Sensors

David L. Glackin

The Aerospace Corporation
P. O. Box 92957
Los Angeles, California 90009

Introduction

The Aerospace Corporation is currently surveying advanced sensor concepts for environmental monitoring from space in the late 1990's and beyond. The parameters to be measured include a wide variety of atmospheric, terrestrial, and oceanographic items. The specific sensor concepts to be described apply to the measurement of clouds, winds, temperature, and humidity. Special emphasis in this presentation will be placed on the subject of clouds. The sensor concepts include:

1) a scanning radiometer for low Earth orbit cloud observation,

2) a meter-class telescope for geosynchronous altitude cloud observation,

3) a millimeter wave radar for cloud top, layer, and base sensing,

4) a stereo imager with a lidar sounder for cloud top sensing,

5) a lidar wind sensor, and

6) a differential absorption lidar (DIAL) for temperature and humidity profiling.

Clouds

Sensors that are capable of measuring cloud cover, cloud type, and cloud top, layer, and base height have been studied. The height of cloud layers and bases is a particularly difficult measurement. Sensors in orbits that range from low Earth orbit to geosynchronous orbit have been considered. The goal is to arrive at a system that can cover the troposphere and stratosphere over the globe with a horizontal pixel size of 0.5 km, a vertical resolution of 30 to 300 m, depending on altitude, and a refresh rate of 15 minutes. The refresh rate might be attained by striking a balance between the number of satellites in orbit and the predictive capability of numerical models.

The multispectral imaging sensor concept is for a scanning radiometer that operates in the visible and the near, mid, and long wave IR. Day/ night sensing of cloud cover and type is provided by the visible and mid to long wave IR channels. A channel in the 3.7 micron window band is used to reveal low clouds and fog, which are often not evident in the long wave IR. Discrimination of snow from clouds is done with a channel at 1.6 microns, in the daytime. The reflectance of snow is low at this wavelength, while that of clouds remains high. The synergy of this sensor with other environmental parameters of interest is high. It can be used to map regions of snow cover and ice, to discriminate liquid water from ice clouds, and to measure cloud-tracked winds, albedo, and sea surface temperature.

High-resolution imaging at geosynchronous altitude calls for a different concept. A meter-class diffraction-limited three-mirror visible/IR telescope has been studied for such applications. The goals of this Large Meteorological Telescope (LMT) are the same as those of the scanning radiometer for low Earth orbit, but the available coverage and timeliness are better for a large fraction of the globe. This sensor concept is similar to that described by Maxwell (1986).

The measurement of cloud layer and base height from space poses a much greater problem than that of cloud cover and type. Lidar cannot fully penetrate any clouds but cirrus. Owing to the very high scattering found in non-cirrus clouds, a lidar sensor could not be used to probe their vertical structure over depths of more than a few hundred meters. There is no "magic wavelength" at which more extensive profiling is possible with lidar. Cloud top height, on the other hand, can be measured quite accurately with a lidar sounder (see below).

Owing to the limitations of lidar outlined above, another sensor concept has been studied. Dense clouds are essentially opaque to radiation at infrared wavelengths and shorter, and are usually transparent to radiation at centimeter wavelengths and longer. In the intermediate millimeter wavelengths (1 mm to 1 cm) clouds are semitransparent. A radar operating at wavelengths having sufficient measureable backscatter but also sufficient transparency has the potential for measuring cloud top, layer, and base height from orbit. A range-gated dual-frequency millimeter-wave radar (MIWAR) operating in the window bands at 35 and 94 GHz should be able to profile clouds having a wide range of liquid water content. Drier clouds such as stratus and cumulus should be more easily profiled at 94 GHz, while wetter clouds such as cumulonimbus should be more easily profiled at 35 GHz. Multiple frequencies will also help to separate the effects of attenuation from backscatter. The exact performance of the instrument is difficult to predict, partly because the physics is complicated and partly because the requisite data base of cloud observations does not yet exist. Meteorological radar operating at 94 GHz is now being used on the ground for preliminary cloud studies (Lhermitte, 1986). Owing to power and aperture considerations, the MIWAR does not appear to be appropriate for high orbits.

The space-based radar concept outlined above is an expensive and risky proposition. As a partial alternative, an infrared sounder can be used to measure cloud top height, but with unacceptably large error, and to make a crude estimate of cloud thickness (Yeh and Liou, 1983). There appears to be no potential for accurate inference of layer and base height from such an instrument. Hence, an IR sounder is not a viable alternative to the MIWAR.

Another partial alternative is a stereo imaging sensor with a lidar for precise range calibration. This Stereo Imager/Lidar Atmospheric Sounder (SILAS) would consist of a device that acquires images while looking forward and backward along the satellite track, for the purpose of measuring cloud height from the offsets in stereo image pairs. An associated lidar sounder would measure precise reference points at selected intervals, for accurate calibration cf the height scale. The lidar could also be used to detect high-altitude subvisual cirrus (Carswell, 1983). The concept is similar to that proposed by Lorenz (1983). Stereo pairs of images have been acquired from many geostationary satellites (e.g., Hasler, 1981), but the use of overlapping geostationary fields of view is unsuitable in an operational environment. Although it is a powerful technique, the SILAS concept only solves part of the cloud height problem. Thus, implementation of the MIWAR concept is indicated.

Winds

Sensors that are capable of measuring the wind vector to +/-2 m/s throughout the troposphere and stratosphere have been surveyed. The concept is for a coherent doppler lidar similar to one of those reviewed by Menzies (1986). Further details will be provided in the presentation.

Temperature and Humidity Profiling

Sensors that are capable of measuring the vertical temperature profile to +/-1K and the vertical humidity profile to +/-1 g/m^3 have been surveyed. The concept is for a DIAL (differential absorption lidar) instrument. Further details will be provided in the presentation.

References

Carswell, A. I., 1983, Lidar Measurements of Clouds. In Optical and Laser Remote Sensing, ed. D. K. Killinger and A. Mooradian, Springer-Verlag.

Hasler, A. F., 1981, Stereographic Observations from Geosynchronous Satellites: An Important New Tool for the Atmospheric Sciences. Bull. Amer. Meteorol. Soc., 62, 194.

Lhermitte, R. M., 1986, Cloud and Precipitation Observations with a 94 GHz Doppler Radar. _Proceedings, Cloud Physics and Radar Conference_, Snowmass, Sept. 21 - 27.

Lorenz, D., 1983, Stereoscopic Imaging from Polar Orbit and Synthetic Stereo Imaging. _Adv. Space Res._, _2_, 133.

Maxwell, M. S., 1986, High-Resolution Observations of Low Contrast Phenomena From an Advanced Geosynchronous Platform. _J. Geophys. Res._, _91_ (C2), 2517.

Menzies, R. T., 1986, Doppler Lidar Atmospheric Wind Sensors: A Comparative Performance Evaluation for Global Measurement Applications from Earth Orbit. _Appl. Opt._, _25_, 2546.

Yeh, H. Y. and K. N. Liou, 1983, Remote Sounding of Cloud Properties from a Combination of Infrared and Microwave Channels. _J. Clim. Appl. Met._, _22_, 201.

Large Aperture Measurements of Optical Turbulence

D. M. Winker

AFWL/ARBA, Kirtland AFB
Albuquerque, NM 87117

There exists a significant body of literature, developed over the last
10 years or so, concerned with the theoretical analysis of atmospherically
induced wavefront aberrations in terms of Zernike polynomial decompositions
and power spectra of the Zernike modes (1-4). To date there has not been
a satisfactory experimental verification of these analyses.

An experiment to collect data concerning the effects of atmospheric
turbulence on the propagation of starlight through the atmosphere has been
conducted since spring 1986 on the 107" telescope located at McDonald
Observatory in west Texas. The experiment measures phase and intensity of
atmospherically aberrated starlight with high spatial and temporal resolu-
tion. The data being gathered will provide data relevant to the develop-
ment of atmospheric turbulence theory. Observations are scheduled to
continue through the first half of 1987.

The experimental setup is relatively simple. A lenslet array con-
sisting of a 50 mm diameter region filled with 1 x 1 mm^2 square lenslets is
used to perform a Hartmann test (5) on the wavefront at the telescope
entrance pupil. About 900 lenslets are located in the unobscured portion
of the aperture. The focal spots formed by this lenslet array are recorded
on photographic film for later analysis. A gated image intensifier
controls the exposure time. Signal levels are adequate to allow one milli-
second exposures, sufficient to "freeze" the atmosphere. A fast scanning

mirror gives the ability to record two wavefronts separated by a time delay which may be as short as one millisecond, allowing the measurement of phase decorrelation times. Simultaneous measurements of Fried's coherence parameter, r_0, using a separate instrument, and measurements of temperature differences along the optical path within the telescope are used to gauge the importance of turbulence within the dome versus the turbulence in the free atmosphere.

The intensities of the recorded spots give scintillation information and the spot positions are used to reconstruct the phasefront. This information is analysed in various ways. Of primary interest is the decomposition of the phasefronts into Zernike polynomials, from which the variance of the coefficients of the various Zernike modes can be derived and compared with theoretical predictions. Recent work (6) predicts significant attenuation of low spatial frequency Zernike modes on large aperture telescopes due to finite outer scale. Measurement of the degree of attenuation can be used to characterize the outer scale. A comparison of results with the relevant theory will be presented.

1. Noll, R. J., 1976: Zernike Polynomials and Atmospheric Turbulence, JOSA, 66, p207-211.

2. Greenwood, D. P., 1977: Bandwidth Specification for Adaptive Optics Systems, JOSA, 67, p390-392.

3. Greenwood, D. P. and D. L. Fried, 1976: Power Sectra Requirements for Wavefront-Compensative Systems. JOSA, 66, p193-206.

4. Tyler, G. A., 1984: Turbulence-induced Adaptive optics. Performance Degradation: Evaluaton in the time domain. JOSA A, 1, p251-262.

5. Malacara, D., 1978: Optical Shop Testing, Wiley and Sons, NY, NY.

6. Winker D. M., 1986: Digest of the International Conference on the Optical and Millimeter Wave Propagation and Scattering in the Atmosphere, May 27-30, 1986, Florence, Italy.

A Compact Wide-Field Sensor for
Remote Sensing of Ocean Phenomena

by

Thomas S. Pagano and Loren M. Woody
Santa Barbara Research Center
Hughes Aircraft Company
75 Coromar Dr.
Goleta, Ca. 93117

Abstract

A low-cost, high-performance sensor design for low-earth-orbit ocean-color remote sensing is presented with system tradeoffs and performance estimates.

Introduction

Global and mesoscale oceanographic applications and coastal zone studies require remotely sensed ocean color and sea surface temperature measurements for diverse applications including mapping of sediments and phytoplankton and estimating sea-surface temperatures. Phytoplankton concentrations can be used to determine the locations of fish and other sea life and are essential to gaining an understanding of the carbon dioxide cycle, a link to global climate changes. This paper describes a compact wide-field sensor for measuring ocean color and sea-surface temperature from low earth orbit, designed to meet the requirements specified by the NASA/NOAA/EOSAT Sea-viewing Wide-Field Sensor (SeaWiFS) Working Group [Ref. 1].

System Requirements and Constraints

Several key user requirements and orbital constraints influenced the design of the SeaWiFS. The required spectral bands and their purpose are shown in Table 1.

Table 1: Spectral Bands for the SeaWiFS Sensor

Band	Wavelength (μm) Center	Width	Purpose
1	0.443	0.020	Chlorophyll Absorption
2	0.500	0.020	Pigment Absorption
3	0.565	0.020	Sediments/Hinge Point
4	0.665	0.020	Atmospheric Correction
5	0.765	0.040*	Atmospheric Correction
6	0.865	0.045	Atmospheric Correction
7	11.00	1.000	Sea-Surface Temperature
8	12.00	1.000	Sea-Surface Temperature

* Blocked from 0.759 - 0.770 μm to avoid oxygen absorption.

User requirements, program schedules, spacecraft accommodations, and ground-station compatibility all constrain the sensor design. The Landsat-6 spacecraft is the proposed platform, and its scheduled launch date limits the design to an instrument that can be implemented in 18 to 20 months. Also, since the primary mission of Landsat-6 is the Thematic Mapper, only a small, lightweight instrument with low power consumption can be considered. In order to maximize the utility of the data, the data output format was constrained to be compatible with the High-Resolution Picture Transmission (HRPT) format used by existing ground stations to receive Advanced Very High Resolution Radiometer (AVHRR) data [Ref. 2].

To avoid sun glint, the field of view must be pointable ±20° along-track, and to provide daily coverage, it must scan ±58.5°. Instrument polarization sensitivity must be less than 2% to enable existing atmospheric correction algorithms to be used. Because the "water-leaving" radiance is small, all six of the visible and near infrared (VNIR) bands must be extremely sensitive. Finally, the cost of the sensor and the risk associated with it must be low; therefore, only those features that appeared most promising and affordable were considered.

System Design

An isometric view of the resulting SeaWiFS sensor concept is shown in Figure 1. The telescope rotates a full 360° cross-track and can be tilted along-track to one of three positions; +20°, 0°, and -20°. A fold mirror in the telescope reflects the scene energy to a mirror that rotates with the telescope. The scene energy is then intercepted by a half-angle mirror that rotates at half the rate of the telescope, relaying the scene energy to the dichroic beamsplitters and aft assembly objective lenses. The SeaWiFS scanning technique results in less than 1.7% polarization sensitivity with no image rotation.

A single detector width along-track is used for each band, resulting in a raster scan system. To be compatible with the HRPT format, the sensor must trace 6 scans per second; therefore, for the Landsat's polar orbit at an altitude of 705 km, the along-track sample spacing must be 1.13 km. This results in an instantaneous field of view (IFOV) of 1.6 mrad and an dwell time of 42.32 µs.

A 4.8 mil (122 µm) detector pitch was selected for ease of manufacturing of the long-wavelength infrared (LWIR) detectors. To make the footprint projection of these detectors equal the along-track sample spacing (1.13 km), the optical focal length of the system was chosen to be 7.64 cm.

The SeaWiFS telescope is a 3x magnification, three-mirror, f/1.3 afocal system with a 5.9 cm aperture and a 25% area obscuration by the secondary mirror. The eight spectral bands are arranged in four groups of two; each group has its own refractive focusing objectives, tailored to the spectral bands of the group. On-focal-plane spectral filters are used to separate the individual bands within the groups.
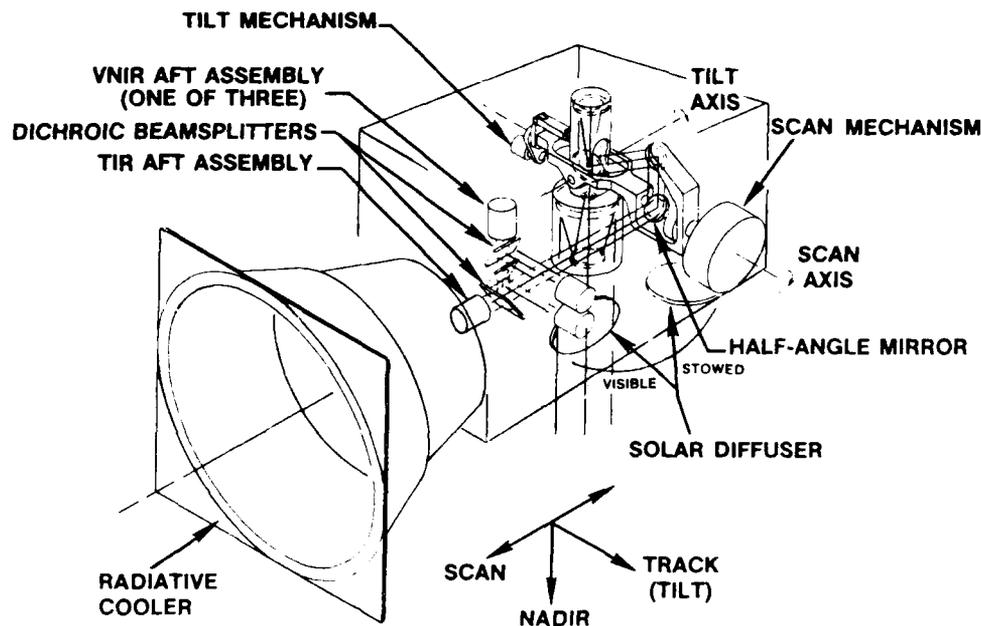
Figure 1: SeaWiFS Ocean-Color Sensor

The 360° scan, in addition to providing the required 117° scene scan, allows viewing of an internal blackbody for DC-restore of the LWIR channels. A space view for zero reference and a solar diffuser that folds into the view of the scanning telescope are provided for calibration. DC-restore is performed once per scan and solar calibration can be performed once per orbit.

Six of the eight spectral bands lie in the VNIR region of the spectrum. Time delay and integration (TDI) of five discrete photodiodes per spectral band is required to meet the desired signal-to-noise ratio for these channels. Since each focal plane contains two spectral bands, each VNIR focal plane contains 10 photodiodes arranged in a line array with a one-IFOV filter-coupling space between the groups of five elements. This results in a total optical field of view of 1°. The imaging elements are space-qualified discrete

silicon photodiode-preamplifier hybrids operating in the photovoltaic mode. TDI is performed off-focal-plane after digitization using a custom TDI electronic processor. Two discrete photoconductive mercury cadmium telluride (PC: HgCdTe) detectors are used for the LWIR bands. Cooling is achieved using an A.D. Little radiative cooler, and the operating temperature provided by the radiative cooler is 110K.

The SeaWiFS design resulted in a sensor envelope of 12.6" x 12.0" x 12.0" weighing 18 lbs with an additional electronics module weighing 7 lbs. The average system power dissipation, including the electronics module, is 60 Watts. The SeaWiFS data rate is 665 kbps (HRPT format).

Sensor Performance

The expected performance of the SeaWiFS sensor was estimated for the VNIR and LWIR bands using the sensor parameters described above. For the VNIR channels, ocean radiance conditions corresponding to the reflectances of the MODIS specification [Ref. 3] were used to evaluate the sensor, and the distribution function of a blackbody of 300K was used to compute the infrared radiances. Table 2 lists the resulting performance parameters. These performance values meet the requirements identified by the joint NASA/NOAA/EOSAT SeaWiFS Working Group [Ref. 1].

Table 2: Signal-to-Noise Ratio (SNR) and Noise Equivalent Temperature Difference (NEΔT) for the SeaWiFS sensor.

Band	Wavelength (μm) Center	Width	Spectral Radiance (mW/cm^2-ster-μm)	SNR
1	0.443	0.020	5.8	474
2	0.500	0.020	4.5	507
3	0.565	0.020	2.8	401
4	0.665	0.020	1.7	350
5	0.765	0.040	1.0	343
6	0.865	0.045	0.4	243
			NEΔT (300K)	
7	11.00	1.000	0.20	
8	12.00	1.000	0.23	

Conclusions

A sensor concept was developed to satisfy the primary requirements of an ocean color sensor. This concept uses a raster scan with a rotating telescope and results in a small, lightweight, low-power, high-performance instrument.

References

1. Putnam, E.S., ed. 1987 (in press). *System Concept Definition for Wide-Field-of-View Landsat-6 Observations of Ocean Phenomena.* Lanham, MD: EOSAT.

2. Foote, R., and L.T. Draper. 1980. TIROS-N Advanced Very High Resolution Radiometer (AVHRR). In *Proc. Sixth Annual Conf. Remote Sensing Soc., 18-19 Dec. 1979.* Reading, England: Remote Sensing Soc.

3. Goddard Space Flight Center. 1986. *Moderate Resolution Imaging Spectrometer-Nadir (MODIS-N).* Draft Phase B Specification. Greenbelt, MD: NASA/GSFC.

Optimum Local Oscillator Levels for Coherent Detection Using Photoconductors

John M. Hunt, J. Fred Holmes, and Farzin Amzajerdian
Oregon Graduate Center
Department of Applied Physics and Electrical Engineering
19600 N.W. Von Neumann Drive
Beaverton, Oregon 97006-1999

SUMMARY

Photoconductors can be used as optical heterodyne detectors and they have the advantage of lower cost and larger size. Much literature is available for the perfect case where the circuit connected to the detector has no effect on the response of the detector. For direct detection when the signal is very small these results may be satisfactory. However, application of an optical local oscillator in the milliwatt range to the photoconductor modifies its conductance sufficiently to have a considerable effect on both the responsivity of the detector and its interaction with the signal processing circuitry. Penin et al. [1] recognized that there was a local oscillator induced interaction with the circuit and derived a formulation for the noise factor of a photoconductive detector as a function of local oscillator power. Unfortunately, they did not recognize that the equivalent source term is also modified by the local oscillator; and consequently, their result is not correct. In this paper, the signal to noise ratio (S/N) is derived for a photoconductive detector as a function of local oscillator power and includes both effects. It will be found that there is a finite level of local oscillator power for which the S/N is a maximum.

In the linear region, the conductance of the photoconductive detector can be modeled as

$$G_{detector} = G + G'P_{in} \tag{1}$$

where G is the dark conductance, G' is a constant (at a given frequency) and P_{in} is the optical power applied to the detector. In order to obtain a signal from the detector, a bias must be applied. A circuit to accomplish that is shown in Figure 1 where V_B is the applied direct current bias voltage which, because of the inductor, is applied only across the detector. The current that flows through the detector is given by

$$i = V_B \, G_{TOT}\,(\omega, P_{in}) = I_{DC} + i_{Het} + \text{higher order terms} \tag{2}$$

where

$$P_{in} = P_{LO} + P_{Het} = P_{LO} + 2\sqrt{P_{LO}P_S} \tag{3}$$

$$G_{TOT} = G + G'P_{LO} \quad \text{for } \omega = 0 \tag{4}$$

$$G_{TOT} = \frac{G_L\,(G + G'P_{in})}{(G + G'P_{in} + G_L)} \quad \text{for } \omega = \omega_{Het} \tag{5}$$

and P_{LO} is the applied local oscillator power that establishes an operating point about which there will be small fluctuations due to the signal power P_s. Now by expanding in a series as indicated in Eq.(2), i_{Het} can be found and is given (neglecting higher order terms) by

$$I_{DC} + i_{Het} = V_B(G + G'P_{LO}) + 2V_BG'\sqrt{P_{LO}P_s} \frac{G_L^2}{(G + G_L + G'P_{LO})^2} \qquad (6)$$

where use was made of

$$i_{Het} = V_B \left[\frac{\partial G_{TOT}(w, P_{in})}{\partial P_{in}} \right]_{P_{in} = P_{LO}} \frac{\partial P_{in}}{\partial P_{Het}} P_{Het} \qquad (7)$$

The second term in Eq.(6) is the signal current that flows through the AC coupled conductance. This corresponds to the small signal circuit shown in Figure 2 where

$$i_s = 2V_BG'\sqrt{P_{LO}P_s} \frac{G_L}{(G + G_L + G'P_{LO})} \qquad (8)$$

It can be seen from Eq.(6) that the signal current is a function of P_{LO} and a simple calculation shows that it peaks for

$$P_{LO} = \frac{G + G_L}{3G'} \qquad (9)$$

The noise sources are generation-recombination (g-r) noise due to the bias and Johnson noise from the conductances with the same equivalent circuit as for the signal. This corresponds to a total noise current variance (neglecting noise on the local oscillator) of

$$<i_n^2> = 4I_{DC}eBg + 4kT_D(G + G' P_{LO})B + 4kT_eG_LB \qquad (10)$$

where e is the electronic charge, g is the photoconductive gain, I_{DC} is the bias current, B is the bandwidth, k is Boltzmann's constant, T_D is the temperature of the detector, and T_e is the equivalent noise temperature of the terminating conductance and any amplifier that follows.

Using Eq.(6) and Eq.(10) the signal to noise ratio is given by

$$\frac{S}{N} = \frac{V_B^2 (G')^2 P_{LO} P_s}{B \left((G + G'P_{LO}) (V_B^2 h\nu G'/\eta + kT_D) + kT_eG_L \right)} \frac{G_L^2}{(G + G_L + G'P_{LO})^2} \qquad (11)$$

where use has been made of $g = \dfrac{h\nu V_B G'}{\eta e}$ and h is Planck's constant, ν is the optical frequency, and η is the quantum efficiency of the detector. For the usual case where the g-r noise is dominant, this can be rewritten in a form more suitable to

graphing as

$$(S/N)_{Normalised} = \frac{S}{N}\frac{B\,h\nu}{P_s\,\eta} = \frac{y^2 x}{(1+x)(1+y+x)^2} \qquad (12)$$

where

$$x = \frac{G'P_{LO}}{G} \qquad \text{and} \qquad y = \frac{G_L}{G} \ .$$

Equation (12) is shown in Figure 3. A simple calculation shows that S/N peaks at a finite P_{LO} for which

$$\text{Optimum } P_{LO} = \frac{G}{4G'}\left[\sqrt{9 + 8G_L/G} - 1\right] \qquad (13)$$

Reference

1. N. A. Penin, N. Sh. Khaykin and B. V. Yurist, "Investigation of the Noise Factor of an Optical Heterodyne Receiver with an Extrinsic Photoresistor," RADIOTEKHN. I ELEKTRON. (USSR), translated in RADIO ENG. and ELECTRON. PHYS (USA), 792-796, May 1972.
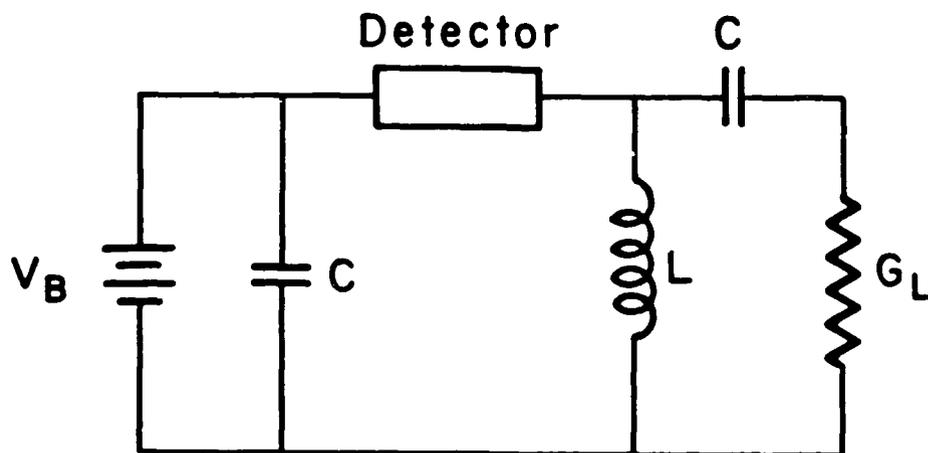
Fig. 1 - Bias Circuit
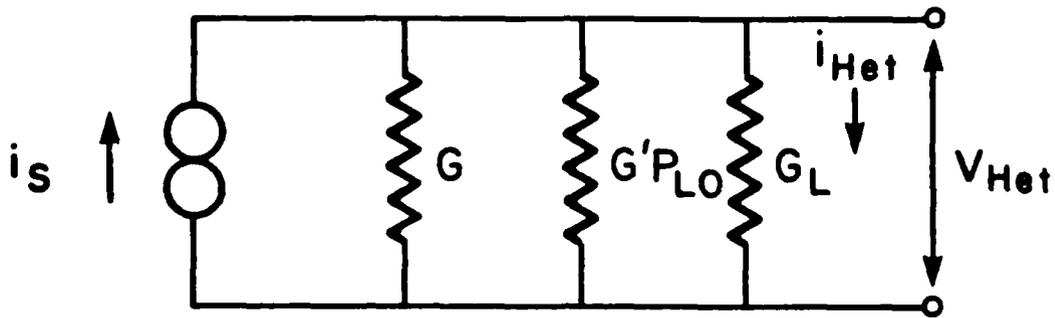
Fig. 2 - Small Signal Equivalent Circuit
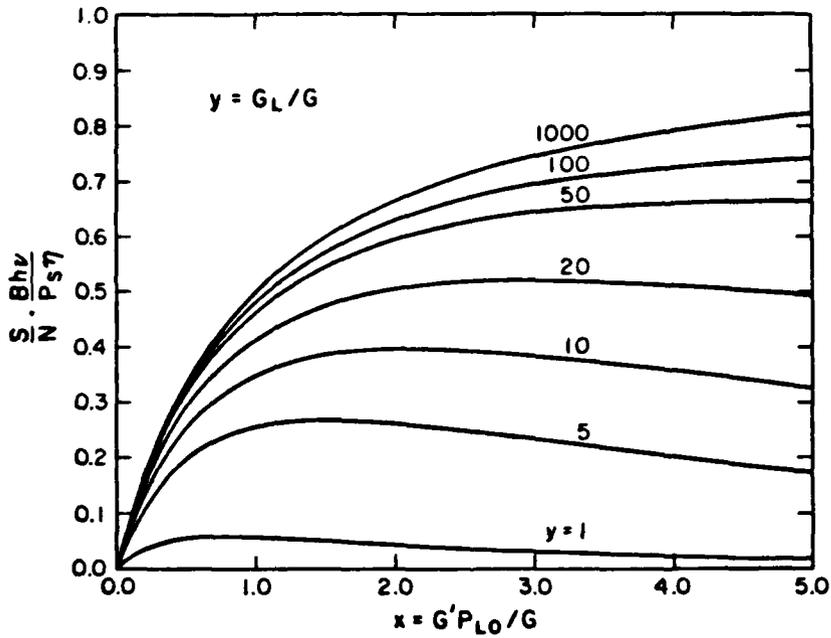
Fig. 3 - Normalized Signal to Noise Ratio

RADIANCE RATIO CLASSIFICATION OF EARTH SURFACE FEATURES-- A SPACEBORNE SHUTTLE EXPERIMENT

W. E. Sivertson, Jr.
NASA Langley Research Center
Hampton, VA 23665

Abstract

New spaceborne technology is being developed for autonomously detecting and classifying four primary Earth features--water, vegetation, and bare land, and a cloud-snow-ice class. Using this technology, a space-based remote imaging system could provide automatic pretransmission screening and selection of remotely sensed information. Classification is based on camera output radiance ratio values. The hardware is relatively small and could be operated in concert with other spaceborne sensors to remotely monitor Earth resources. This paper discusses the technology concept and spaceborne Shuttle test flight results.

Introduction

Land, vegetation, water, clouds, snow, and ice are unique classes of Earth features (Ref. 1). New technology has been tested onboard the Space Shuttle that will allow an instrument to automatically classify these features (Ref. 2). An image generated by the instrument is subdivided into pixels. Each pixel is identified relative to its Earth feature class and its location within the image. The experiment is identified as the Feature Identification and Location Experiment (FILE).

Overview

The FILE instrument (Figs. 1 & 2), flown on the October 1984 Space Shuttle 41-G mission, includes a sensor electronics unit containing two charged couple device (CCD) silicon detector cameras with their associated classification electronics, a buffer solid-state memory data storage unit, two magnetic tape recorders, two 70-mm film cameras, and a telemetry and tape select control interface unit. Image data are generated by the CCD sensors, are stored in the buffer memory, and are transferred to a tape recorder. The tape recorder is selected via telemetry control. Each image includes VR and IR digital images, Earth feature classification counts, and Greenwich Mean Time (GMT). The two Hasselblad 70-mm film cameras record images simultaneously with the CCD cameras.

Each CCD camera is configured as a two-dimensional array of 100 by 100 detector diodes providing 10,000 pixels for each CCD image. The two cameras are equipped with an optical assembly including a 10.6-mm focal length, 4-element, 30° field angle lens; an F/5.7 aperture stop; and an interference filter having a half-power bandwidth of approximately 11.2 nm. One camera operates with a filter having a spectral band centered at 0.65 μm. The second camera operates with a filter having a spectral band centered at 0.85 μm. The field-of-view for the FILE instrument is approximately 21.4° by 16.2°.

Each 70-mm film camera uses a 100-mm focal length lens with a square field-of-view of 29.2° by 29.2°. All CCD and film cameras are boresight aligned to allow the film camera images to correlate with the CCD images for use in postflight analysis of FILE classification accuracy.

Calibration for Clouds

The FILE instrument uses a simple ratio technique for making a classification decision (Ref. 3). Each CCD camera voltage ouput is a function of input radiance level. The voltage ratio is compared to a simple linear algorithm, derived from spectural signature information (Ref. 4), to determine the Earth feature class for each pixel location within the detector array.

The FILE instrument is calibrated to provide a full-scale output voltage signal in response to a maximum expected radiance input. Clouds provide the highest expected reflected radiance values. Estimates of cloud radiance values sensed in orbit should be 75 percent of the solar spectral radiance measurement values viewed on the surface of the Earth (Ref. 5). For the 41-G mission, solar zenith angle was estimated as 24° and the solar spectral radiance values are reduced by a factor equal to the cosine of 24°. The product of measured solar spectral radiance times the zenith angle factor of 0.9 and the factor of 0.75 for cloud reflectance at orbital altitude, results in the expected maximum radiance values (FILE full-scale signal) for clouds equal to 29.8 mw/cm^2-sr-μm for the 0.65 μm camera and equal to 21.8 mw/cm^2-sr-μm for the 0.85 μm camera. Based on these values and full-scale response, an f stop value of 5.6 was selected for each camera.

Mission and Data Collection

The FILE instrument was integrated on a Pallet payload and flown onboard the Shuttle Challenger on the 9-day STS 41-G mission. The vehicle was launched from the Kennedy Space Center (KSC) in Florida, on October 5, 1984. Orbital altitude ranged from approximately 372 km to 225 km during FILE data collection. A total of 242 images was recorded. Sun angle over the image set ranged from approximately 23° to 63°. Each Earth-view image data set includes: a VR image, an IR image, real-time-decision classification counts, and GMT. Electronic CCD camera data are recorded on the tape recorders and are retrieved postflight via electronic readout. Each postflight processed classification image is compared with the FILE 70-mm correlative photographs to aid in evaluating the system performance.

Processing and Analysis

All FILE/41-G images were processed and resulted in rendering good agreement between postflight processed classification images and their companion correlative 70-mm film images. The pixel ratio is initially processed using an algorithm analytically defined from spectral signature data and an image is generated in which each pixel is properly located within its ratio image and the pixel is color coded as to the Earth feature class. An 8- by 10-inch color classification image is generated and is compared with its companion FILE 70-mm Earth views of the scene via an optical transfer scope. Co-registration of the images in the transfer scope along with photo interpretation allows the evaluation of the accuracy of FILE classification. A FILE image from the 41-G mission is shown in Fig. 3. The outlined area in the 70-mm image in Fig. 3 is a map of the embedded area covered by the CCD cameras. An experimentally defined algorithm is shown in Fig. 4 and was used to process all FILE/41-G images. Resulted classification images were in good agreement with their companion correlative film images.

A subset of 37 FILE cloud images was selected and studied. These cloud data subsets were analyzed to statistically define VR values and ratio values. The mean and standard deviation values for clouds are as follows: VR = (1.083 ± 0.074) IR. The VR cloud level is VR ≥ 199.23 ± 38.52 out of a full-scale value of 255.

Concluding Remarks

Two-channel (0.65 μm and 0.85 μm) ratio detection technology can be used to autonomously classify Earth features from low Earth orbital altitudes. A simple straight line algorithm can be implemented to function in real time with Earth surface targets illuminated with Sun angles ranging from 23° to 63°. An experimentally successful algorithm has been defined with a water decision slope of 0.8 (VR = 0.8 IR) and a vegetation decision slope of 0.695 (VR = 0.695 IR) and a cloud decision VR threshold of 44 percent of the VR full scale response value. The experimentally defined algorithm effected classification decisions that were in good agreement with 70-mm correlative images.

Solar-elevation angle varied over a range from 23° to 63° during the data takes, and this resulted in a calculated mean cloud radiance signal of approximately 70.3 percent of the expected full-scale value. The mean of the measured cloud signal level values for a set of 37 cloud images is 199.23 out of 255 or 78 percent of the full-scale signal level and is in good agreement with the expected value.

The FILE Shuttle spaceflight results obtained from the 41-G flight demonstrate the suitability of radiance ratio technology using a simple y = mx algorithm to autonomously classify the four Earth surface features water, bare land, vegetation, and clouds/snow/ice. The technology is potentially useful for developing advanced decision-making automatons for use with space-based real-time sensor systems. The FILE technology is especially attractive as a cloud sensor where, in advance of or during a mission, a threshold value for percentage of cloud cover can be programmed and/or adaptively modified for use in the control of other remote sensors.

REFERENCES

1. W. Eugene Sivertson, Jr., et. al., "Spectral Feature Classification and Spatial Pattern Recognition," Society of Photo-Optical Instrumentation Engineers, 23rd Annual International Technical Symposium and Instrument Display, San Diego, California, August 27-30, 1979.
2. W. Eugene Sivertson, Jr., et. al., "Autonomous Earth Feature Classification-Shuttle and Aircraft Flight Test Results," AIAA-83-04-17, AIAA 21st Aerospace Sciences Meeting, Reno, Nevada, January 10-13, 1983.
3. Vincent, R. K., "Spectral Ratio Imaging Methods for Geological Remote Sensing from Aircraft and Satellites," Proc. Amer. Soc. Photogram., Management and Utilization of Remote Sensing Data Conference, Sioux Falls, South Dakota, 1973.
4. R. T. Schappell, et. al., "Landmark Identification,"NASA CR-145-122, December 1976.
5. Turner, R. E., "Atmosphere Effects In Multispectral Remote Sensor Data," NASA-CR-ERIM 109600-15-F, May 1975.

Fig. 2. FILE System

Fig. 4. FILE Experimental Algorithm
(41-G Mission Data)
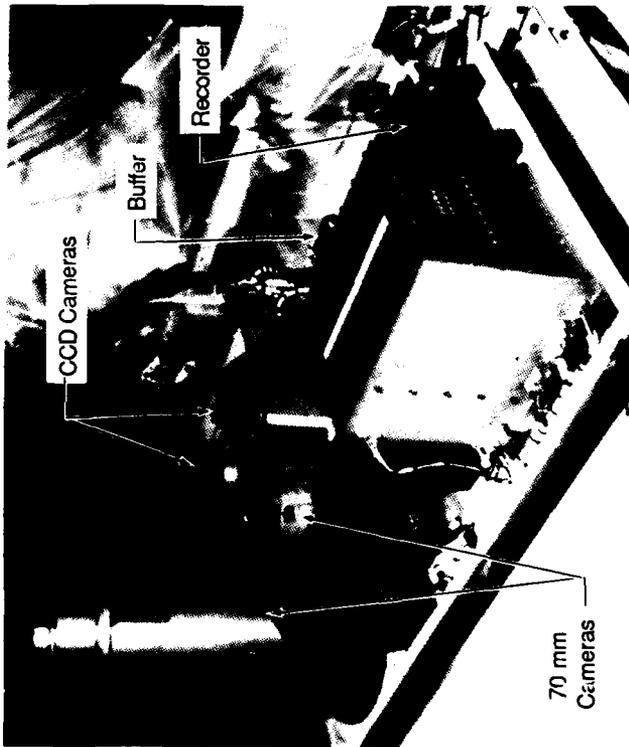
Fig. 1. FILE Shuttle Flight Instrument
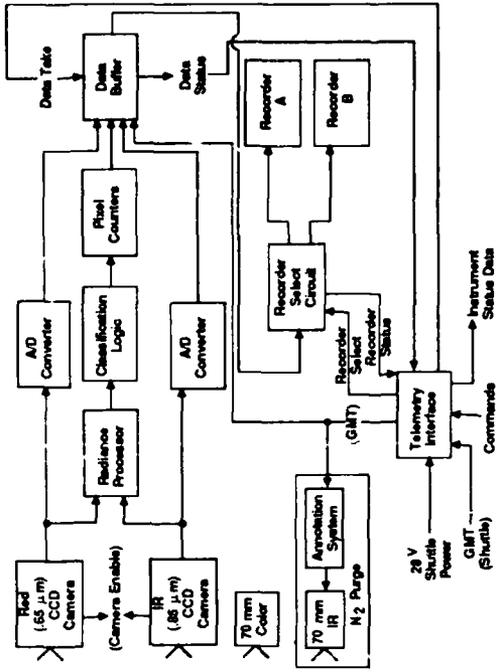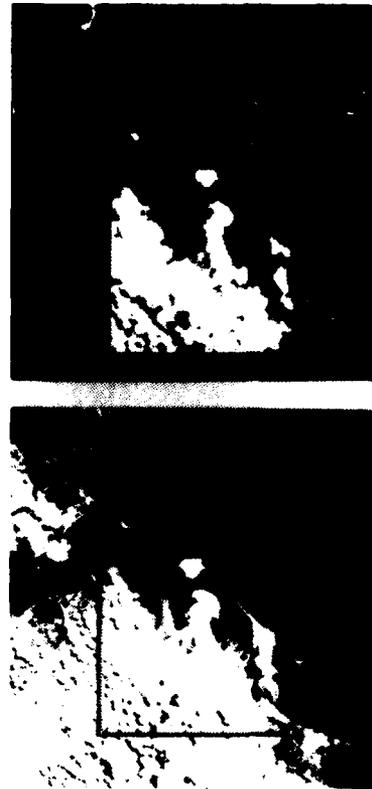
Fig. 3. FILE Flight Data (41-G, October 1984)

TWO SCINTILLATION METHODS OF MEASURING THE INNER SCALE

Reginald J. Hill
NOAA/ERL/Wave Propagation Laboratory
325 Broadway, Boulder, Colorado 80303

THE TWO METHODS OF INNER-SCALE MEASUREMENT

Let $\sigma^2(L, k, C_n^2, \ell_o)$ be the irradiance variance of a monochromatic spherical wave of wavelength λ and wavenumber $k = 2\pi/\lambda$ after propagating along a path of length L. The turbulence is assumed isotropic with refractive-index structure constant C_n^2 and inner scale ℓ_o. Similarly let $\sigma_{12}^2(L, k_1, k_2, C_n^2, \ell_o)$ be the irradiance correlation, $<(I_1-<I_1>)(I_2-<I_2>)>/<I_1><I_2>$ for irradiances I_1 and I_2 from spherical waves of wavelengths λ_1, and λ_2. Let $\sigma_{LA}^2(L, D, C_n^2, \ell_o)$ be the irradiance variance of radiation propagating along the same path and transmitted through a circular, uniformly-illuminated, phase-incoherent aperture of diameter D and measured using a receiving aperture of diameter D. It is assumed that D exceeds two Fresnel-zone sizes so σ_{LA}^2 is approximately independent of the optical wavenumber. Define scaled variances by dividing by the asymptotic expressions for $\ell_o = 0$,

$$\tilde{\sigma}^2(\ell_o/\sqrt{L/k}) = \sigma^2(L,k,C_n^2,\ell_o)/0.5 \, k^{7/6}L^{11/6}C_n^2 \tag{1}$$

$$\tilde{\sigma}_{LA}^2(\ell_o/D) = \sigma_{LA}^2(L,D,C_n^2,\ell_o)/0.9 \, L^3 D^{-7/3}C_n^2 . \tag{2}$$

The important point in (1) and (2) is that the normalized variances depend only on one parameter.[1,2]

For the method of Ochs and Hill[2,3] the inner scale is obtained from the quantity

$$q(x,d) = \frac{\tilde{\sigma}^2(\ell_o/\sqrt{L/k})}{\tilde{\sigma}_{LA}^2(\ell_o/D)} = \frac{0.9}{0.5} \left(\frac{D}{\sqrt{L/k}}\right)^{-7/3} \frac{\sigma^2(L,k,C_n^2,\ell_o)}{\sigma_{LA}^2(L,D,C_n^2,\ell_o)} \tag{3}$$

$$x = \ell_o/\sqrt{L/k} \qquad , \qquad d = \sqrt{L/k}/D .$$

The importance of the normalized variances in (1) and (2) is that they clearly show that q is a function of only two dimensionless parameters; one is the desired result, $\ell_o/\sqrt{L/k}$, and the other, $\sqrt{L/k}/D$, is known. For the bichromatic method[4] the inner scale is obtained from the quantity

$$Q(L,k_1,k_2,\ell_o) = \frac{\sigma_{12}^2(L,k_1,k_2,C_n^2,\ell_o)}{\sqrt{\sigma^2(L,k_1,C_n^2,\ell_o) \, \sigma^2(L,k_2,C_n^2,\ell_o)}} \tag{4a}$$

$$Q(L,k_1,k_2,\ell_o) = \frac{1}{(1-\delta^2)} \frac{[\sigma^2(L,k_\star,C_n^2,\ell_o) - \delta^{-1}\sigma^2(L\delta,k_\star,C_n^2,\ell_o)]}{\sqrt{\sigma^2(L,k_1,C_n^2,\ell_o)\,\sigma^2(L,k_2,C_n^2,\ell_o)}}$$ (4b)

$$Q(x,r) = \frac{R^{7/6}}{(1-\delta^2)} \frac{\tilde{\sigma}^2(ax) - \delta^{5/6}\tilde{\sigma}^2(bx)}{\sqrt{\tilde{\sigma}^2(\sqrt{r}x)\,\tilde{\sigma}^2(x)}}$$ (4c)

where

$$r = k_1/k_2 \quad , \quad k_\star = R\sqrt{k_1 k_2} \quad , \quad x = \ell_o/\sqrt{L/k_2}$$

$$\delta = |k_1 - k_2|/(k_1 + k_2) = |r-1|/(r+1)$$

$$R = \sqrt{k_1 k_2}/[(k_1 + k_2)/2] = 2\sqrt{r}/(r + 1)$$

$$a = \sqrt{k_\star/k_2} = \sqrt{2r/(r + 1)} \quad , \quad b = \sqrt{k_\star/k_2}\,\delta = \sqrt{2r/|r - 1|} \quad .$$

Equation (4b) follows from (4a) using a trignometric identity in the Rytov integrand;[5] (4b) expresses the bichromatic intensity covariance in terms of monochromatic variances for hypothetical radiation of wavenumber $k_\star$ propagating on paths of length L and Lδ. The advantage of introducing the scaled variances in (4c) is that Q is then obviously a function of only two dimensionless parameters x and r, not of the four parameters L, k_1, k_2, and ℓ_o separately.

GRAPHICAL COMPARISON OF THE TWO METHODS

Figure 1 shows the quantities q(x,d) and Q(x,r) as functions of $x = \ell_o/\sqrt{L/k}$ for q and $x = \ell_o/\sqrt{L/k_2}$ for Q. The accurate refractive-index spectrum of Hill[1] is used to produce this figure. Three cases are shown for Q corresponding to r = 0.05970, 0.5947, and 1.440. These values of r can be obtained from the wavelength pairs (λ_1, λ_2) = (10.6 μm, 0.6328 μm), (1.064 μm, 0.6328 μm), and (0.4400 μm, 0.6328 μm), respectively; although any wavelength pair resulting in one of these three values of r is also shown since Q depends only on x and r. Assuming k in (3) and k_2 in 4(a,b,c) corresponds to the wavelength 0.6328 μm, then the range of the abcissa in Fig. 1 is sufficient to include all cases L from 40 m to 1000 m and ℓ_o from 1 mm to 20 mm. Two cases are shown for q corresponding to d = 0.116 and 0.0667. The value d = 0.116 applies to the experiment by Ochs and Hill,[3] namely L = 260 m, k = 2π/0.6328 μm, and D = 4.4 cm. The value d = 0.0667 could be obtained from the case L = 1000 m, k = 2π/0.6328 μm, and D = 15 cm. Of course, any other combination of L, k, and D resulting in one of the two given values of d is also presented in Fig. 1. The bump in the refractive-index spectrum[1] produces a maximum in the curves for q(x,d) and a minimum in the curves for Q(x,r), the x-position of which depends on d and r.

Consider the sensitivity to errors S_q and S_Q given by

$$\frac{\Delta q}{q} = S_q \frac{\Delta \ell_o}{\ell_o} \quad , \qquad \text{so} \qquad S_q \approx \frac{\partial \log_{10} q}{\partial \log_{10} x}$$

$$\frac{\Delta Q}{Q} = S_Q \frac{\Delta \ell_o}{\ell_o} \quad , \qquad \text{so} \qquad S_Q \approx \frac{\partial \log_{10} Q}{\partial \log_{10} x} \quad .$$

where Δq, ΔQ, and $\Delta \ell_o$ are the errors in the respective quantities. The logarithmic derivatives give S_q and S_Q in the limit of small errors. These sensitivities, S_q and S_Q, relate the fractional error in the inner scale to the fractional error in the measured quantities q and Q. The values of S_q and S_Q are therefore the slopes of the curves in Fig. 1. Large absolute values of S_q and S_Q are desired, so steep slopes are desired. Systematic errors, which are difficult to assess, are more likely to limit the accuracy of the inner scale measurement than are the errors due to noise. Saturation of scintillation is a systematic error in both systems. Errors due to noise will be significant under conditions of very small C_n^2 in both methods.

On Fig. 1, the steepest slope at x > 0.6 for q(x,0.0667) is about twice, in magnitude, the steepest slope of the curve for Q(x,0.05970). The slope of the q-curves remains steep for yet greater x whereas the Q-curves become flat. Hence for x > 0.6 the method of Ochs and Hill[2,3] has an advantage. The experiment performed by Ochs[3] obtained ℓ_o from 3 mm to 10 mm, which corresponds to 0.6 < x < 2. The curve for q(x,0.0667) has twice the magnitude of slope at x = 0.6 as does the curve for Q(x,0.5947). However, for yet smaller x, the q(x,0.0667) curve reaches a maximum where S_q vanishes and thereafter decreases, thereby introducing a possible ambiguity in the measured value of ℓ_o. The curve for Q(x,0.5947) reaches its minimum at x ≈ 0.1 and increases to its asymptote as x decreases further. Therefore there is an advantage to the bichromatic method[4] for x < 0.6, but x must be greater than some value, which depends on r, to maintain unambiguous sensitivity to ℓ_o.

References

1. R.J. Hill and S.F. Clifford, Modified spectrum of atmospheric temperature fluctuations and its application to optical propagation, J. Opt. Soc. Am. 68, 892-899, 1978.

2. R.J. Hill and G.R. Ochs, Fine calibration of large-aperture optical scintillometers and an optical estimate of inner scale of turbulence, Appl. Opt. 17, 3608-3612, 1978.

3. G.R. Ochs and R.J. Hill, Optical-scintillation method of measuring turbulence inner scale, Appl. Opt. 24, 2430-2432, 1985.

4. Z. Azar, E. Azoulay and M. Tur, Optical bichromatic correlation method for the remote sensing of inner scale, (preprint).

5. M. Tamir, E. Azoulay, S. Tsur and U. Halavee, Aperture-averaged spectral correlations of beams in a turbulent atmosphere, Appl. Opt. 23, 2359-2362, 1984.
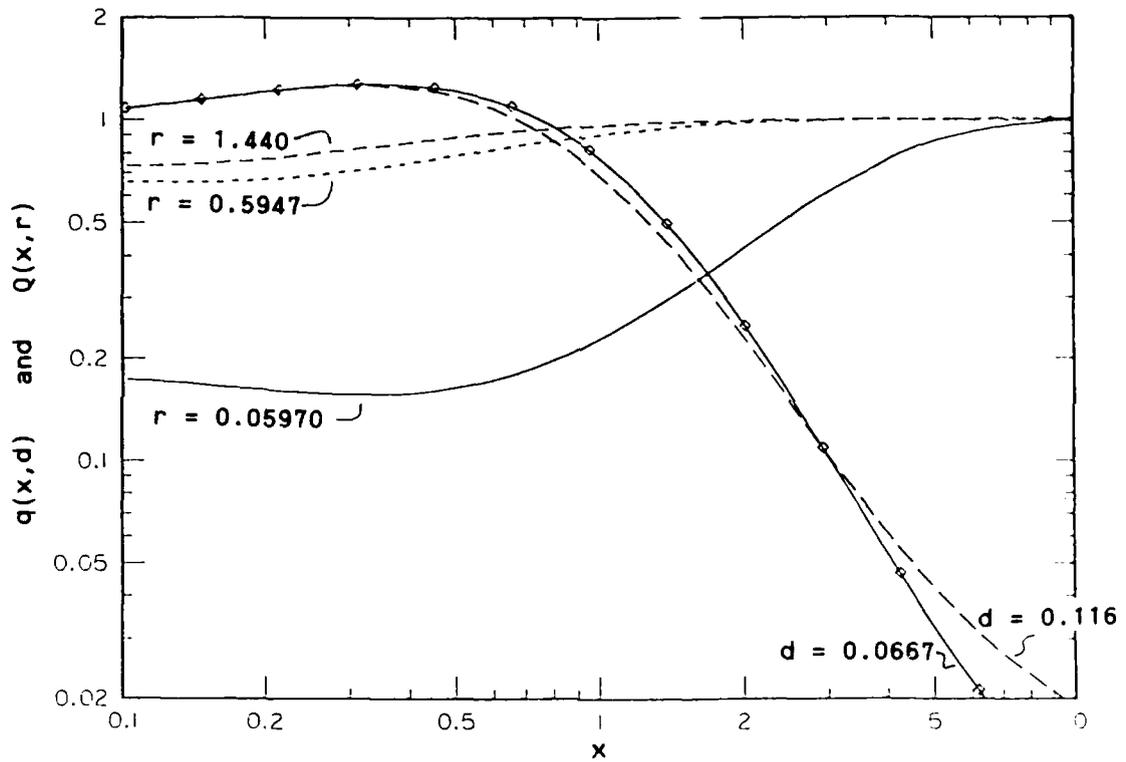
Fig. 1. The curves for $Q(x,r)$ are labeled by their values of r, and those for $q(x,d)$ are labeled by their values of d.

LASER-EXCITED OPTICAL FILTERS: LASER POWER REQUIREMENTS

by T. M. Shay

Los Alamos National Laboratory, P.O. Box 1663, CLS-5 MS/E535
Los Alamos, New Mexico 87545

SUMMARY

Narrow bandwidth optical sources are readily available. However, tunable narrow bandwidth, wide field-of-view optical filters are not available. The laser-excited optical filters (LEOF) presented here are in principle tunable narrow bandwidth, wide field-of-view optical filters. These filters can simultaneously provide high resolution (0.001 nm), wide field-of-view (2π), high quantum efficiency, and electrically tunable optical filtering. Narrow bandwidth operation of laser-pumped atomic vapor filters were first demonstrated by Gelbwachs et al.[1] ,by Marling et al.[2], and recently by Chung et al.[3] The first electrical tuning of these devices was demonstrated by Gelbwachs et. al.[4] In addition, alkali vapor based LEOFs can operate on 130 transitions between 921 and 474 nm. LEOFs are ideally suited for extracting weak narrow bandwidth signals buried in strong nonresonant optical background radiation. Potential applications of these filters include laser radar, laser communications, detection of Raman radiation, atomic spectroscopy, etc.

LEOFs represent a significant advance in optical filter technology. They provide for the first time a narrow linewidth, high sensitivity, wide field-of-view, and wide spectral coverage simultaneously. These filters should also be relatively simple, compact and reliable. As a result of these characteristics , we expect LEOF receivers to be utilized in in many practical applications in remote sensing, optical communications, and any other application where a narrow bandwidth optical signal needs to be extracted from strong non-resonant background noise.

LEOFs are atomic resonance filters which utilize photon absorption from the first excited state of an atom up to a higher lying level. A narrow bandwidth laser is used to pump the necessary population into the atom's first excited state. The filtering process is initiated by photon absorption from the first excited state of the atom to a higher lying level. Subsequent radiative cascade from the upper level of the absorbing transition results in the emission of blue-shifted photons proportional to the number of absorbed photons. Because only photons which are within the doppler width of a particular atomic transition are frequency shifted these filters are inherently narrow bandwidth. Thus LEOFs are very narrow bandwidth frequency shifters. The wavelength shift is typically between 100 nm and 500 nm. With such large wavelength shifts, colored glass can be used to isolate the unshifted background radiation from the photodetector while transmitting the blue-shifted (signal) photons to the photodetector. Since the atomic absorption of photons is an isotropic process these filters

are also intrinsically wide field of view . Furthermore, since the key step in this filter is a simple resonant absorption process single photons can be filtered. Hence, this optically pumped filter concept may realize a very sensitive quantum counter.

The basic LEOF receiver concept consists of three parts. The first part is a prefilter which provides coarse filtering and transmits only radiation centered around the signal wavelength through to a laser pumped atomic resonance cell. The main function of the prefilter is to eliminate any violet noise photons from the entering the atomic vapor cell. The second part is a laser pumped atomic vapor cell which acts as a narrow bandwidth frequency shifter, this element shifts incident photons within a narrow signal bandwidth into the violet spectrum. Finally, a spectral filter which passes the shifted radiation and blocks the unshifted radiation is utilized to ensure that only the shifted violet photons reach the photo-detector and the background noise photons are effectively rejected.

The net result of sandwiching the atomic vapor cell between the prefilter and the spectral filter is that no incident light can be detected by the photo-multiplier unless it has been shifted in frequency through the quantum absorption process in the atomic vapor.

A simplified theoretical model which is used to calculate the laser pump power required to achieve a given realizable filter quantum efficiency is presented. This is the first LEOF filter model which includes the effect of resonance trapping. The effects of resonance trapping on both the laser pump power and the filter realizable quantum efficiency is included in this model. The required laser pump power will be a dominant factor in determining the practicality of LEOF. The results of these calculations will be presented for several wavelengths of a Rb LEOF. The model calculations show a highly nonlinear dependence of laser pump power on the realizable filter quantum efficiency. In addition, these results demonstrate that a quantum efficiency of >10% should be possible with laser pump powers of as low as 4 mW per square centimeter of aperture. This low pump power is significant since it eliminates the major practical problem in implementing these filters, i.e., the complexity of the pump laser. As a result of this lower pump power requirement, simple, efficient, continuous semiconductor lasers are now suitable sources for pumping atomic vapor filters. Single semiconductor laser arrays have demonstrated output powers of several watts. Thus single semiconductor arrays at this power level can be used to pump filter apertures as large as a thousand square centimeters. The use of semiconductor lasers as the excitation source for laser-pumped atomic vapor filters makes these filters highly practical, because semiconductor arrays are reliable, efficient, and long lived devices. The results of laser power versus realizable quantum efficiency calculations for the 532.4 nm and the

523.5 nm Rb transitions will be presented. The 532.4 and
523.5 nm transitions correspond to the wavelengths of the
doubled Nd:YAG and doubled Nd:YLF lasers respectively and
hence are of interest for practical laser systems. However,
many other wavelengths are also available from alkali LEOFs.

1.   J. A. Gelbwachs, C. F. Klein, and J. E. Wessel, IEEE
Journal of Quantum Electronics, QE-14, 77 1970.

2.   J. B. Marling, J. Nilsen, L. C. West, and L. L. Wood,
Journal of Applied Physics 50, 610, 1980.

3.   Y. C. Chung, J. D. Dobbins, and T. M. Shay,
International Conference on Lasers'86, Nov. 3-7,1986, paper
MK12.

4.   J. A. Gelbwachs and J. E. Wessel, IEEE Trans. on
Electron Devices ED-27, 99, 1978; J. A. Gelbwachs, C. F.
Klein, and J. E. Wessel, IEEE Journal of Quantum
Electronics, QE-16, 137, 1980.

LASER REQUIREMENTS FOR
WIND SHEAR DETECTION FROM AIRCRAFT

Stephen E. Moody, Stanley R. Byron, and T. Rhidian Lawrence

Spectra Technology Inc.
2755 Northup Way
Bellevue, Washington 98004

and

Russell Targ
Lockheed Missiles and Space Co.
3251 Hanover Street
Palo Alto, California 94304

Summary

Wind shear events that are threatening to aircraft safety can potentially be detected directly from the aircraft by Doppler lidar techniques. The main requirements for such a system are sufficient range and reliability under realistic conditions to provide advance warning of shear conditions. With remote wind sensing from the aircraft, it should be possible to significantly improve aircraft safety by allowing pilots to better respond to, or even avoid, wind shear events.

As a starting point, we have evaluated the feasibility of wind shear detection from an aircraft using existing CO_2 Doppler lidar technology. Coherent CO_2 lidars have well proven capability for remote wind speed measurement. Experimental systems have operated from both the ground and from aircraft. Solid-state laser technology may offer a more attractive solution in the long term. However, at present, there is no proven solid-state technology that is both coherent and eye safe. Therefore, we have chosen to investigate the feasibility of a nearer term CO_2 solution to the wind shear detection problem.

Based on an estimate of the performance needed to support pilot avoidance of wind shear, we have arrived at the lidar performance objectives summarized in Table 1. While the specific values are certainly debatable, the general features embodied in this specification are important if the lidar approach is to see actual deployment. The cost, power, and volume constraints of this specification were established by demanding that the lidar not substantially degrade the economics or the logistics of aircraft operation.

Table 1. Wind Shear Lidar Objectives

Direction:	Forward Looking
Range:	>3 km
Range Resolution:	<0.3 km
Wind Velocity Resolution:	<2 m/sec Along Flight Direction
	<8 m/sec Transverse to Flight
Wind Field Update Interval:	<1.0 sec
Weather:	Clear Air to Heavy Rain
Size of Optical Head:	<0.1 m^3
Power Input:	<300 W
Cost:	<$100,000

To establish laser requirements for such a lidar, we have exercised a model that incorporates the effects of atmospheric backscatter, atmospheric transmission, and the heterodyne detection process. This model includes the effects of precipitation, based on relatively crude estimates taken from a compilation of literature values. Based on this model, one can derive a map of required CO_2 transmitter performance, which is summarized in Figure 1. The bolded curve of this figure indicates a region of pulse energy and PRF performance that can meet the desired performance goals. Limits on PRF are set at the low end by the data update requirements and at the high end by signal processing throughput capability. The high-end PRF limit will tend to move to the right with time, as computing technology improves, and therefore, the indicated limit should be treated as only an indication of the problem. However, there is also an absolute upper limit established by the propagation time to the range of interest.
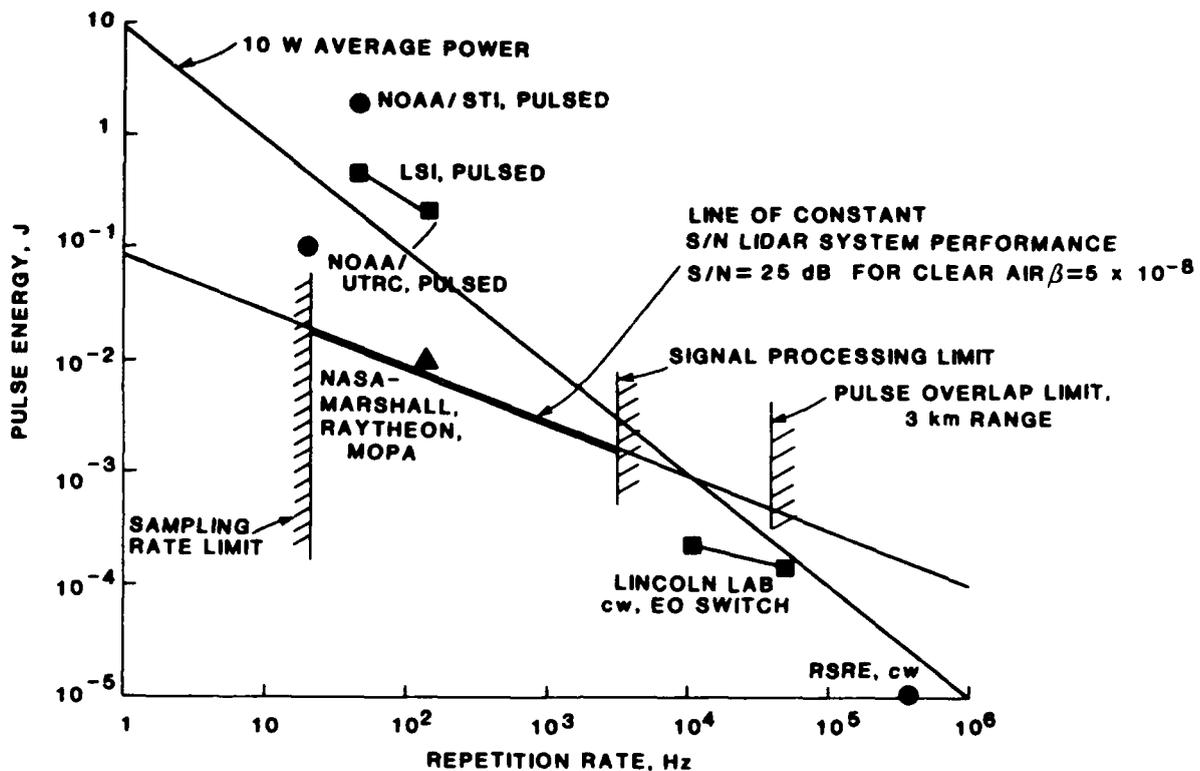
Figure 1. Performance Map of CO_2 Coherent Lasers for
Wind Shear Detection

Figure 1 also shows the performance of a wide variety of actual existing
coherent CO_2 transmitters. It should be clear that the needed performance
envelope is surrounded by existing capability for a wide variety of design
conditions. Consequently, the selection of a design point becomes a matter of
practical considerations.

Pulsed excited CO_2 lasers generally scale in size and weight with pulse
energy rather than average power. In addition, size and weight are more
important considerations than input power. As a result, the low PRF region of
Figure 1 proves to be quite disadvantageous. While the detailed derivation
lies beyond the scope of this paper, the optimum transmitter PRF tends to fall
in the range of 1000 Hz, as a compromise between the average power scaling
which dominates at very high PRF, and the per pulse energy scaling which
dominates at very low PRF.

An example of a CO_2 laser approach, which matches this 1000 Hz optimum, is a Q-switched, cw-excited, low pressure discharge technology. We have adopted a laser performance baseline of 2 mJ/pulse, at 2 kHz PRF. Other pulsed CO_2 laser technologies can potentially also fulfill the requirements.

Figure 2 shows the predicted performance of the proposed system during rainfall, along with a tabular summary of the system parameters.

2 mJ/PULSE
100 PULSE INCOHERENT AVERAGE
1 MHz BANDWIDTH
20% RECEIVER EFFICIENCY
70% OPTICS EFFICIENCY
15 cm APERTURE
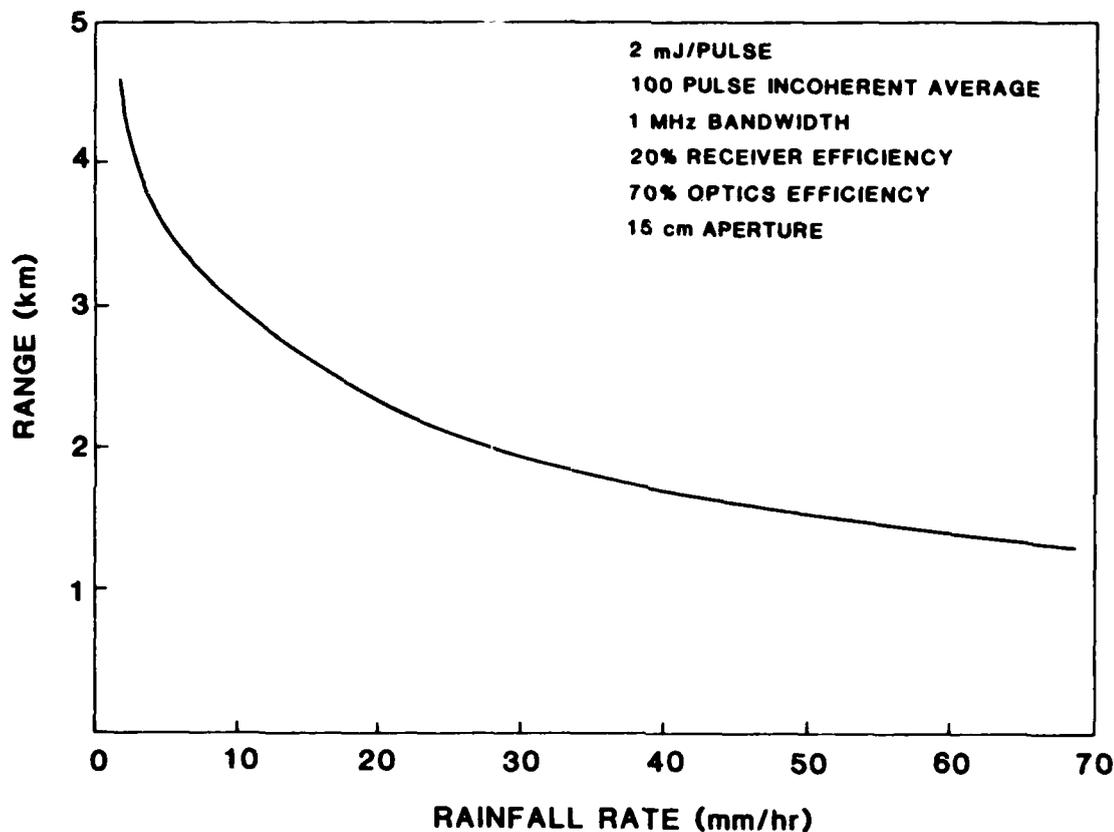
Figure 2. Predicted Lidar Range in Rain

In the past, focused cw type systems have been demonstrated, including actual operational in-flight testing by the RSRE (Great Britain). Unfortunately, it can be shown that for constant average power, the system signal/noise scales as $(\tau_s/\tau_p)^{0.5}$, where τ_p is the laser pulse length, and τ_s is the interpulse spacing. For the proposed approach, this factor provides an advantage of ≈ 30 over cw systems, which corresponds to a range advantage of more than 5. This factor is sufficient to make true cw approaches impractical in conditions of precipitation.

Experimental Observations of Line-Mixing In A Infrared CO_2 Q-Branch

Bruce Gentry
NASA Goddard Space Flight Center
Code 617
Greenbelt, MD 20771

and

L. Larrabee Strow
Dept of Physics
University of Maryland, Baltimore County
Catonsville, MD 21228

I. Introduction

The successful remote sensing of atmospheric temperature, humidity, pressure, and trace gas profiles depends upon a detailed knowledge of the radiative characteristics of atmospheric gases. For example, existing passive remote temperature and humidity sounders utilize infrared spectral channels that sense atmospheric CO_2, N_2O, O_3, and H_2O.

The retrieval of a temperature or humidity profile from the observed atmospheric radiances using iterative inversion techniques requires the ability to accurately calculate the average atmospheric transmittance across each sounding channel.[1] While reasonably accurate line parameters (strength, pressure-broadening coefficients, frequency, and lower-state energy level) are available for these calculations, an accurate model for the line shape must also be used to accurately interpret the soundings.

Line-by-line atmospheric radiance calculations generally assume that the observed spectra are due to the superposition of contributions from isolated lines having Lorentz or Voigt lineshapes. This isolated line approximation can break down when rotationally inelastic collisions produce interference effects among overlapping lines during the absorption process. This effect, which we call line-mixing appears as a redistribution of the intensity within a band and has its most dramatic effect in Q-branch spectra when the Q-branch profile tends to narrow as the pressure is increased. This is seen most often at pressures much greater than one atmosphere in Q-branches with very small rotational spacings. A number of papers treat the theory of this effect.[2,3]

Present sounders such as HIRS on the NOAA-9 satellite and the Upper Atmosphere Research Satellite(UARS) instruments CLAES and ISAMS utilize CO_2 Q-branch emission to determine atmospheric temperature profiles. Proposed Earth Observing System (EOS) passive sounders may also use CO_2 Q-branches for atmospheric sounding.

We present here the first observations of the effects of collision induced line-mixing in self-, N_2-, and O_2-broadened infrared CO_2 Q-branch for total gas pressures up to 1 atmosphere using a tunable diode laser spectrometer. The experimental absorption coefficients differ by as much as 65% in the Q-

branch wing from those calculated assuming an isolated Lorentzian line model. We have also developed an approach which uses the known pressure broadening coefficients and a simple energy gap scaling law to model the effects of line-mixing. Calculations incorporating this model require no additional fitting of the data to reproduce the experimental observations to within the accuracy of the data (standard deviations of 2-3% for self- and N_2-broadened spectra and approximately 5% for the O_2-broadened data).

II. Theory

The absorption coefficient may be written in the framework of the impact approximation as[3]

$$K(\nu) = \frac{N}{\pi} \, \text{IM} \left\{ \sum_{j,k} d_j \langle j | [(\nu - \nu_0) - iPW]^{-1} | k \rangle d_k \rho_k \right\}$$

where $|j\rangle$ and $|k\rangle$ denote doubled state vectors or, in other words, radiative transitions, d_j and d_k are dipole moment matrix elements, ρ_k are density matrix elements that give population differences between levels involved in the doubled state $|k\rangle$, ν is a diagonal matrix with $\langle j|\nu|k = \nu\delta_{jk}$ and ν is the frequency, ν_0 is the diagonal matrix $\langle j|\nu_0|k\rangle = \nu_j\delta_{jk}$ and ν_j is the transition frequency associated with the doubled state $|j\rangle$, P is the total pressure, N is the absorber number density, and W is the relaxation matrix in doubled state space or what is sometimes called line space. The diagonal elements of W are the pressure-broadened halfwidths. The off-diagonal W-matrix elements represent -1 times the rate at which collisions transfer intensity from one line to another. A spectrum corresponding to non-interacting Lorentzian lines results when the off-diagonal elements of W are zero. When the off-diagonal elements of W become large enough collisional narrowing of the Q-branch profile takes place. All of the parameters required for the calculation of the spectrum, except for the off-diagonal elements of W, can be obtained from experimental measurements.

Our approach for estimating the off-diagonal W-matrix elements is to first model the rotationally inelastic state-to-state rates in each vibrational state using a simple rotational energy gap law.[4] The off-diagonal W-matrix elements are then equated with the corresponding inelastic transition rate matrix elements. The procedures used to calculate and evaluate W have been discussed in some detail in our recent papers.[5,6]

III Experimental Results

Figure 1 is a plot of the self-broadened Q-branch of the $(110,030)_I$-000 CO_2 band centered at 2076 cm-1. The experimental data were obtained using a diode laser spectrometer and 10 cm cell. Figure 2 is a plot of the same CO_2 Q-branch broadened by N_2 taken with the same diode laser mode and a 40 m pathlength obtained with a White cell. The total pressure in both cases was 720 torr and the CO_2 partial pressure was 7.2 torr for the N_2 broadened spectrum. Both the observed Q-branch transmission as well as the absorption coefficients are shown. The percent deviations of the experimental absorption coefficients from those calculated assuming the both an isolated Lorentzian line model (no mixing) and our model including line-mixing are plotted in the

bottom graph. Clearly the theoretical spectrum that includes line-mixing reproduces the data much better than the spectrum calculated without line-mixing. We note again that the parameters used in this calculation to estimate the line mixing were not obtained from fits to the data but were calculated directly from the CO_2 line widths and strengths. Similar results were obtained for the self- and O_2- broadened spectra at total pressures of both 720 and 360 torr.

IV Conclusions

Line-mixing has been observed for the first time in the infrared absorption spectrum of a foreign gas broadened CO_2 Q-branch at pressures of up to one atmosphere. The experimentally determined absorption coefficients are up to 65% lower in the Q-branch wing and 20% larger inside the Q-branch than those calculated assuming an isolated Lorentzian line model. A procedure based on the use of a simple energy gap scaling law has been shown reproduce the effects of line-mixing to the level of the uncertainty in the data. The excellent agreement of the calculations with the observed spectra should provide confidence in similar calculations for other infrared Q-branches particularly those Q-branches in the thermal infrared which are candidates for use in remote sensing applications.

References

1. Susskind, J., and J. Rosenfield, 1980, in Proceedings of VAS Demonstration Sounding Workshop, NASA Conf. Pub. 2157, 41-55.

2. Ben-Rueven, A., Phys Rev.,145,7 (1966).

3. Smith, E. W., J. Chem. Phys., 74, 6658 (1981).

4. Rosasco, G. J., W. Lempert, and W. S. Hurst, J. Chem. Phys., 81,4241 (1984).

5. Strow, L. and B. Gentry, J. Chem. Phys., 84, 1149 (1986).

6. Gentry, B. and L. Strow, J. Chem. Phys., 86, 5722 (1987).

Figure 2. Same as Fig. 1 for 1% CO_2 in N_2, a total pressure of 720 torr, and a 4017 cm pathlength. A stick spectrum showing the locations of the Q-branch transitions is plotted for reference.

Figure 1. (a) Experimental and calculated transmission of the self-broadened Q branch. The pressure is 720 torr and the pathlength is 38.3 cm. △ = Lorentz calculation, + = line-mixing theory, solid line = experimental spectrum. (b) Experimental and calculated absorption coefficients. A stick spectrum showing the locations of the Q-branch transitions is plotted for reference. Below these plots is the percent deviation of the Lorentz and line-mixing calculations from the observed absorption coefficient.

THE EFFECT OF LINE MIXING ON ATMOSPHERIC BRIGHTNESS TEMPERATURES NEAR 15 μm

L. Larrabee Strow
Physics Department
University of Maryland Baltimore County
Catonsville, Maryland 21228

Dennis Reuter
Code 611, Laboratory for Atmospheres
NASA Goddard Space Flight Center
Greenbelt, Maryland 20771

1 Introduction

Rotational collisional narrowing, or line mixing, has recently been detected in the Q-branch spectra of two $\pi - \Sigma$ bands of CO_2 near 2000 cm^{-1} for both self- and N_2-broadening [1,2]. The observed line mixing, which is caused by rotationally inelastic collisions that produce interference effects among overlapping lines during the absorption process [3,4] was found to alter absorption coefficients by as much as 65% in the wings of these Q-branches. This paper considers the influence of Q-branch mixing on atmospheric radiative transfer near the strong ν_2 Q branch of CO_2 at 15 μm.

Advanced satellite borne infrared atmospheric temperature sounders have been proposed that will detect atmospheric emission in the region of the ν_2 Q branch at 15 μm with much higher resolution than existing instruments such as the HIRS sounder on the NOAA-9 satellite. Increases in resolution to 0.5 cm^{-1} or better will dramatically increase the sensitivity of the soundings to the CO_2 line shape. A candidate platform for a new high resolution infrared sounder is the proposed EOS (Earth Observing System) to be placed on the Space Platform [5]. We present here calculations of line mixing in the ν_2 Q branch using the same theoretical formulation that successfully predicted line mixing to an accuracy of better than 10% in the 2000 cm^{-1} CO_2 Q-branch spectra. Our results are presented as brightness temperatures at the top of the earth's atmosphere. These brightness temperatures correspond to radiances averaged over a 0.5 cm^{-1} wide channel.

2 Theory of Line Mixing

The absorption coefficient for overlapping lines may be written in the framework of the impact approximation as [3,4]

$$k\left(\nu\right) = \frac{N}{\pi}\mathbf{IM}\left\{\sum_{j,k} d_j \langle j | \left[(\nu - \nu_{,,}) - \imath P\mathbf{W}\right]^{-1} |k\rangle d_k \rho_k \right\},\tag{1}$$

where $|j\rangle$ and $|k\rangle$ denote doubled state vectors or, in other words, radiative transitions, d_j and d_k are dipole moment matrix elements, ρ_k are density matrix elements that give population differences between levels involved in the doubled state $|k\rangle$, ν is a diagonal matrix with $\langle j|\nu|k\rangle = \nu\delta_{jk}$ and ν is the frequency, $\nu_{,,}$ is the diagonal matrix $\langle j|\nu_{,,}|k\rangle = \nu_j\delta_{jk}$ and ν_j is the transition frequency associated with the doubled state $|j\rangle$, P is the total pressure, N is the absorber number density, and $\mathbf{W}$ is the relaxation matrix in doubled state space or what is sometimes called line space. If mixing is only allowed between the Q branch lines the diagonal elements of $\mathbf{W}$ are the Q-branch pressure broadening coefficients and $|j\rangle$, $|k\rangle$ represent the Q-branch transitions. The off-diagonal matrix elements of $\mathbf{W}$ are the negative of the rate at which collisions transfer intensity from one line to another. If these matrix elements are sufficiently small the spectrum becomes the sum of non-interacting Lorentzian lines.

The $\mathbf{W}$ matrix elements are calculated by way of a scaling law that parametrizes rotational energy transfer as a function of the energy gap between the rotational energy levels. The procedures followed here to generate the $\mathbf{W}$ matrix elements are similar to those described in Refs. 1 and 2. The pressure broadened

halfwidth for a single line can be written as

$$W_{JJ} = -\frac{1}{2}\left(\sum_{j'_{lower}\neq j} 2K_{j'j} + \sum_{j'_{upper}\neq j} K_{j'j}\right),\tag{2}$$

where W_{JJ} is the pressure broadening coefficient of $Q(j)$, and $K_{j'j}$ is the collision rate for transitions from j to j' within a single vibrational state. The odd rotational levels are missing in the ground state of CO_2 due to nuclear symmetry requirements so the sum over j'_{lower} in the lower vibrational level includes only states of even j. The sum over j'_{upper} in the upper level includes all j values except for the missing $j'_{upper} = 0$ level. The factor of two in the sum over the ground state relaxation rates reflects the fact that in the ground vibrational level the density of rotational states is one half that of the upper vibrational level.

For an energetically upward transition the state-to-state rates are modeled with the following scaling law,

$$K_{j'j} = a_1(T_o/T)^{0.5}\left(\frac{|\Delta E|}{B_o}\right)^{-a_2}\exp\left(\frac{-a_3|\Delta E|}{T}\right),\tag{3}$$

where a_1, a_2, and a_3 are the parameters to be determined. Detailed balance gives the rates for energetically downward transitions. The CO_2 rotation constant, $B_o = 0.4$ cm^{-1}, is included in the power law portion of Eq. 3 to give a_1 the unit of a rate. The $(T_o/T)^{0.5}$ term provides the hard sphere part of the collision rate while the exponential term provides a parameter to describe the temperature or velocity dependence of the collision cross-sections. There is no assurance that the resulting scaling law is physically reasonable beyond the required increase in the cross-sections with temperature. The least-squares determination of a_1, a_2 and a_3 was performed using widths for $j = 2$ to 50 at six temperatures between 200 and 250K on the left hand side of Eq. 2. These widths were assumed to vary with temperature as $(T_o/T)^{0.75}$ in accordance with numerous experimental observations [6]. The absorption coefficients are then calculated by letting $W_{j'j} = -K_{j'j}$, $j \neq j'$, which follows from the assumption that the collision rate is independent of vibrational state.

Once the relaxation matrix elements are determined the spectrum can be calculated in a straightforward manner using Eq. 1. For frequencies near the 15 μm CO_2 Q branch most of the radiance at the top of the atmosphere comes from pressures less than 200 torr. In this case the first-order approximation for Eq. 1 derived by Rosenkranz [7], which is exact in the low pressure limit, is sufficiently accurate and was used in this work.

3 Radiative Transfer and Atmospheric Model

Assuming a plane parallel atmosphere in local thermodynamic equilibrium and negligible scattering, one can write the monochromatic radiance at nadir at the top of the atmosphere as

$$R_\nu = \epsilon_\nu B_\nu(T_s)\tau_\nu(P_s) + \int_{\ln P_s}^{\ln P} B_\nu[T(P)]\frac{d\tau_\nu(P_s)}{d\ln P}d\ln P + R'_\nu,\tag{4}$$

where ϵ_ν is the emissivity of the surface, s, and $B_\nu(T)$ is the Planck function for emitted radiance of a blackbody at frequency ν and temperature T, $\tau_\nu(P)$ is the atmospheric transmittance from pressure P to the top of the atmosphere and R'_ν represents the contribution of reflected radiation, which is negligible in our case. Due to the strength of ν_2 of CO_2, most of the radiance originates from pressures less than 200 torr so the surface term is also negligable.

Radiances were calculated between 664 and 670 cm^{-1}, a spectral region that is of interest for sounding the upper troposphere and the stratosphere. Three temperature profiles corresponding to monthly mean zonally averaged climatological temperature profiles for April at 40° N and January at 20° N and 70° N were chosen for these calculations. These three profiles are quite different in the region of the tropopause. The January 20° N profile has a high, sharp tropopause while the January 70° N profile has a low tropopause and an almost isothermal region through much of the stratosphere. The April profile is intermediate between these two.

Two radiance calculations were performed for each of the three climatologies, one with line mixing and the second without line mixing. The radiances, calculated at a resolution of 0.01 cm^{-1}, were then averaged over a 0.5 cm^{-1} square bandpass to simulate the resolution of a satellite radiometer before being converted to effective brightness temperatures. A 66 layer atmosphere and line parameters from the AFGL Line Compilation [8] (except the ν_2 Q-branch parameters) were used. Only the Q-branch lines of the ν_2 fundamental were allowed to mix. The H_2O continuum is included in the calculations but contributes very little to the radiance near the strong ν_2 Q branch.

4 Results

The differences between the brightness temperatures calculated with and without mixing for each of the climatological temperature profiles are shown in Fig 1. As seen in this figure line mixing effects may alter the brightness temperatures by more than 3 K at 667 cm^{-1} directly below the Q-branch head. These deviations are dependent upon the profile, and for some profiles line mixing changes the calculated temperatures by much less. A weak dependence of the brightness temperature on line mixing is due in part to the fact that for some profiles the regions being sensed by the channels are in a relatively isothermal part of the atmosphere. However, 3 K effects are significantly larger than projected requirements of 1 K/km for temperature profiles obtained from future infrared sounders. Several other weaker CO_2 Q branches are currently being investigated for use in temperature sounding [5]. These weaker Q branches emit radiation from lower parts of the atmosphere that are not as isothermal and thus their brightness temperatures may be more sensitive to line mixing.

Clearly, line mixing can play a significant role in atmospheric radiative transfer for CO_2 and may affect the retrieval of atmospheric temperature profiles from future satellite radiometers operating in the 15 μm spectral region. Several of the proposed channels for future infrared temperature sounders which sense in the mid to upper stratosphere are centered in the spectral region shown in Fig 1 where mixing affects the spectrum most severely. The effects of mixing, if ignored, will introduce calibration errors in radiometer channels that are spectrally very close to each other. This defeats one advantage of using CO_2 Q branches for sounding, the ability to use sounding channels that are very close, and which are therefore affected similarly by calibration errors and atmospheric effects that vary slowly in frequency.

5 Conclusions

Calculated equivalent brightness temperatures at the top of the earth's atmosphere may be lowered by more than 3 K when the effects of line mixing are included. Thus atmospheric temperature retrieval methods which are dependent upon a model of atmospheric transmittance should include these effects if the retrieval products are to be accurate. Laboratory studies of room temperature line mixing in higher frequency CO_2 Q-branches broadened by N_2 and by O_2 have shown that line mixing can be accurately calculated if the standard line parameters are known. This line-mixing model should be sufficiently accurate for atmospheric radiance calculations in the 15 μm CO_2 Q-branch, if temperature dependencies are ignored. The temperature dependence of line mixing has not yet been measured in the laboratory, thus our methods for including temperature effects await experimental confirmation.

References

[1] L. L. Strow and B. M. Gentry. *J. Chem. Physics*, 84:1149–1156, 1986.

[2] B. Gentry and L. L. Strow. *J. Chem. Physics*, 86:5722–5731, 1987.

[3] A. Ben-Reuven. *Phys. Rev*, 145:7–22, 1966.

[4] E. W. Smith. *J. Chem. Physics*, 74:6658–6673, 1981.

[5] Joel Susskind and Dennis Reuter. private communication, 1987.

[6] C. Cousin, R. Le Doucen, C. Boulet, A. Henry, and D. Robert. *J. Quant. Spectrosc. Radiat. Transfer*, 36:521-538, 1986.

[7] P. W. Rosenkranz. *IEEE Trans Antennas Propag.*, AP-23:498-506, 1975.

[8] L. S. Rothman, R. R. Gamache, A. Barb, A. Goldman, J. R. Gillis, L. R. Brown, R. A. Toth, J. M. Flaud, and C. Camy-Peyret. *Appl. Opt.*, 22:2247-2254, 1983.
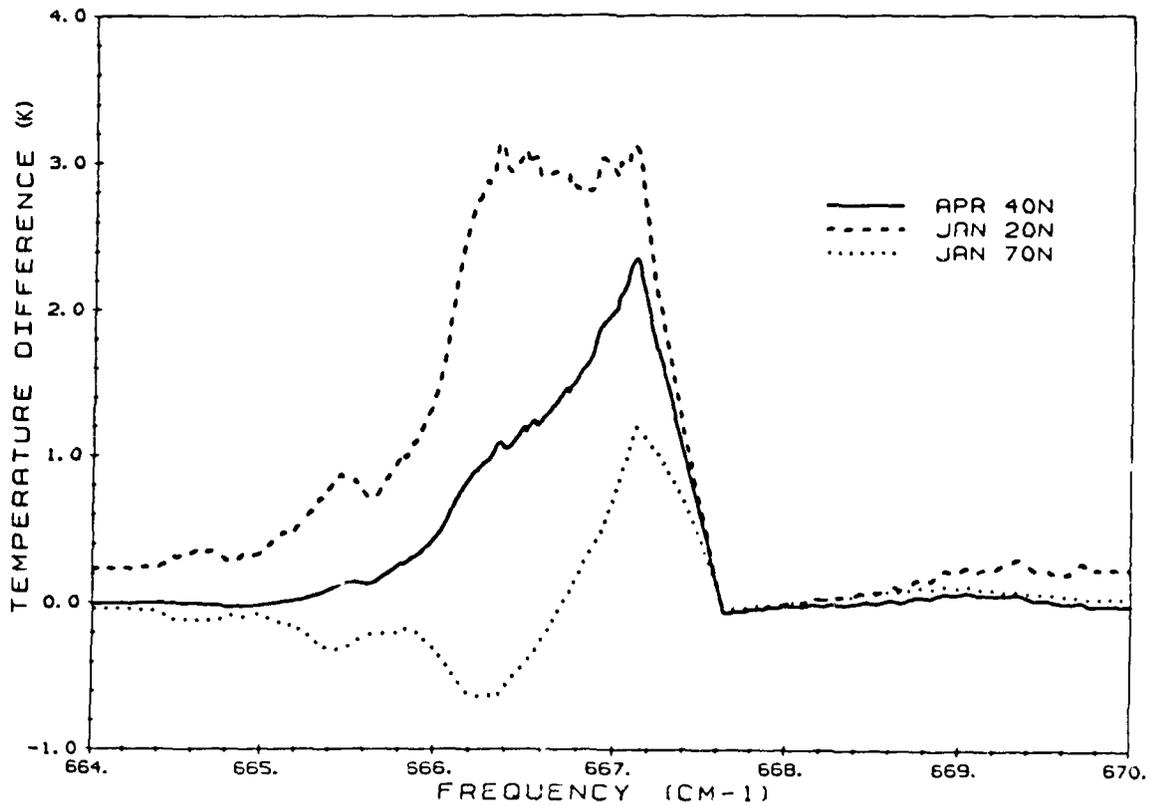
Figure 1: Brightness temperature calculated without mixing minus brightness temperature calculated with mixing, averaged over a 0.5 cm^{-1} square bandpass for three different climatologies.

TUNABLE WAVEGUIDE CO2 LASER LOCAL OSCILLATORS FOR SPACEBORNE INFRARED HETERODYNE SPECTROMETERS

J. J. Degnan, C. E. Rossey, H. E. Rowe, and J. F. McGarry
Instrument Electro-optics Branch, Code 723
NASA Goddard Space Flight Center
Greenbelt, MD 20771

and

U. E. Hochuli and P. R. Haldemann
Dept. of Electrical Engineering
University of Maryland
College Park, MD 20742

INTRODUCTION

For over a decade, the technique of infrared heterodyne spectroscopy has provided sub-Doppler resolution spectra of planetary atmospheres from Earth-based telescope facilities. The goals of our current local oscillator development program are twofold: (1) to design, build, and demonstrate a totally automated, compact, space-qualifiable engineering model of an RF-excited CO_2 laser local oscillator; and (2) to extend the lifetimes of such lasers to a degree where they can be seriously proposed for longterm near earth or planetary flight missions. The current status of these two research areas is discussed.

AUTOMATED LASER LOCAL OSCILLATOR

A photograph of the brassboard automated LO is shown in Figure 1. The unit is approximately 51 cm long by 33 cm wide by 10 cm high and is powered by a 28 volt source through a single connector. The system is built onto an aluminum baseplate which contains five cooling channels for carrying away heat. A block diagram of the automated laser local oscillator is shown in Figure 2. With the exception of an IBM Personal Computer interface board, all of the components of the block diagram are contained in the laser head pictured in Figure 1.

The CO_2 laser LO is powered by an RF drive unit consisting of a 144 MHz oscillator and an all solid state amplifier. The excitation RF power is computer-controlled up to the amplifier maximum of 30 Watts via a programmable variable attenuator at the input to the RF amplifier. A monitor circuit measures the RF output of the attenuator and relays it to the control computer. An impedance matching circuit, attached directly to the laser body, matches the 50 ohm output of the amplifier to the 1800 ohm laser plasma resistance following gas breakdown.

The waveguide CO_2 laser body is constructed from stainless steel and contains a 50 cubic centimeter gas reservoir which allows gas in the small active laser region to be replenished thereby

extending the life of the laser. The active waveguide is 9 cm long and has a 1.5 mm square bore formed by a thin flat beryllium oxide (BeO) plate on top of a BeO U-channel. The RF power is input, via a spring-loaded plunger, to a gold electrode stripe implanted in the outer surface of the thin plate. A second gold electrode implanted in the outer surface of the ceramic U-channel serves as the ground electrode and is mechanically pressed against a thin stainless steel plate which is conductively coupled, in a thermal as well as electronic sense, to the rest of the stainless steel housing. The ends of the waveguide are terminated by a 98% reflecting output mirror and a zinc selenide Brewster window. The laser is intentionally undercoupled (at the expense of output power) to permit operation on several low gain lines and to increase intraline tunability.

A 150 line per mm , first order Littrow grating in close proximity to the zinc selenide Brewster window forces the laser to operate on one of the available vibration-rotation transitions in the 9 to 11 micron region. The grating is rotated about the intersection point of its reflecting surface with the waveguide axis by a stepper motor driven optical mount. This permits the selection of the operating transition by the system microprocessor in either a preprogrammed or interactive mode. Figure 3 indicates the approximately 60 transitions in the 9 and 10 micron bands which have been observed to date from the 9 cm long discharge. Power observed in the zero order grating reflection is comparable to the power out of the 98% coupler suggesting that the grating loss is on the order of 2 or 3%.

The Littrow grating is mounted on a multistack piezoelectric translator (PZT). Application of 1 Kilovolt DC to the stack results in an approximate 6 micron change in the stack length which runs nearly parallel to the resonator axis of the laser. This permits tuning over a full free spectral range of the resonator. The precise operating wavelength within a given transition can be selected by applying a DC bias voltage to the PZT. The computer accomplishes this via a D/A converter output to a remotely programmable, high voltage power supply. A high voltage stack PZT was chosen over a low voltage bender bimorph type translator , which resembles a vibrating drum head, because of the former's greater alignment stability and relative lack of low frequency mechanical resonances.

Most of the laser power is directed out of the plane of Figure 1 by a beam splitter to a second level which, in the final full heterodyne spectrometer, is envisioned to contain the photomixer, low-noise preamplifier, and an acousto-optic spectrum analyzer. The remainder is directed by a series of beamsplitters into auxiliary circuits which provide absolute wavelength verification or wavelength stabilization and control.

We have attempted to provide good passive stability in the operating laser wavelength. Low ripple, low drift rate HV supplies have been selected for the PZT control. The structure supporting and maintaining the distance between the laser end

reflectors has been constructed entirely from low expansion, Super Invar which has a thermal expansion coefficient of about 3x10-7. This support structure is kinematically attached to the aluminum baseplate so that the aluminum baseplate and stainless steel laser housing are free to expand without stressing the Super-invar resonator structure or changing the laser beam alignment. Nevertheless, normal changes in the ambient environment would be expected to result in wavelength instabilities which exceed the one MHz target for high resolution heterodyne spectroscopy of planetary atmospheres. Thus, a portion of the laser output is passed through a 10 cm long confocal etalon controlled in temperature to about 0.01oC. Operation of the laser can be stabilized to any point on the CO2 transition gain curve by applying a DC bias voltage to the etalon PZT, applying a second DC bias voltage to peak the etalon transmission, and then dithering the etalon resonator length by applying a low voltage, 400 Hz sinusoid to the etalon PZT terminals. Phase sensitive detection of the modulated AC output is then used to detect a drift of the laser frequency from the etalon set point. This generates an error voltage which is added to the laser PZT bias to lock the laser to the etalon set point. Since the etalon fringe width is on the order of 7 to 10 MHz and the laser is expected to have reasonably good short-term passive stability, stabilization at the sub-Megaherz level should be possible.

Since mechanical wavelength references, such as the etalon, are not immune to long term shifts in their calibrated parameters, a miniature differential absorption spectrometer was included in the package. As the CO2 laser frequency is scanned by the laser PZT, the spectrometer observes the radiation through two gas cells – an empty reference cell and one containing an absorbing gas such as NH3. This permits an unequivocable identification of the CO2 transition and provides, if necessary, an absolute wavelength reference for inflight recalibration of the grating drive and/or frequency stabilization etalon.

LASER LIFETIME

With respect to laser lifetime, six of eight sealed-off RF-excited lasers built under the program survived beyond 10,000 hours (1.14 years) of continuous operation, four exceeded 20,000 hours (2.28 years), and two functioned for over 30,000 hours (3.42 years). The average life of the lasers was 18,000 hours or slightly more than two years which is more than adequate to support an interplanetary mission such as the Mars Observer. In many cases, lifetimes were shortened by failures in cooling systems which were not immediately detected and allowed the laser housing temperature to rise as high as 80 C. Some lasers recovered in a few days when cooling was restored while others suffered permanent reductions in power. In most cases, a gas refill brought the power back to its original level which suggests that outgassing at elevated temperatures may have been responsible for premature failure of these tubes.

BLOCK DIAGRAM: WAVEGUIDE CO₂ LASER LOCAL OSCILLATOR
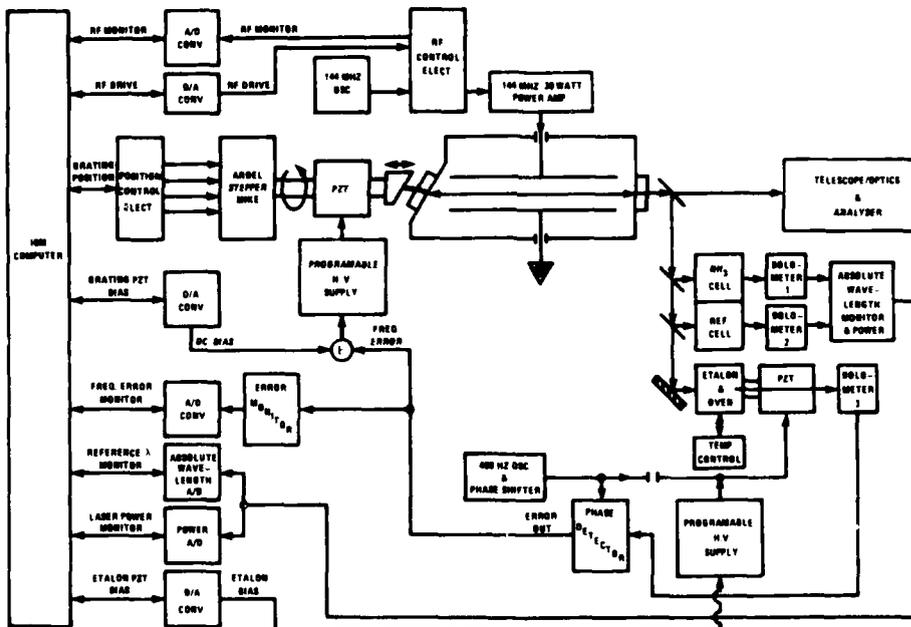
ON EACH BRANCH 2 TO 4 ADDITIONAL LINES CAN BE MEASURED,
BUT THEIR ACTUAL # COULD NOT BE VERIFIED ON THE SPECTROGRAPH.
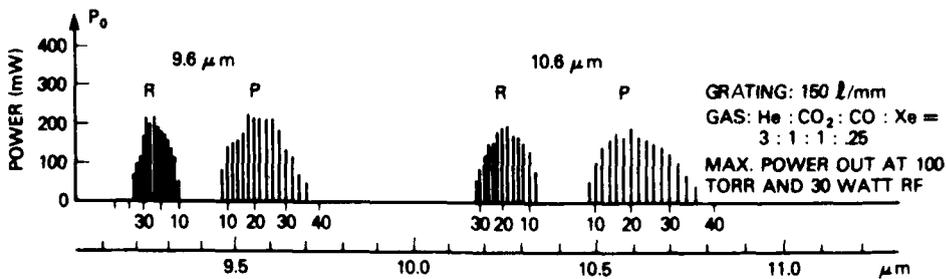
Electrooptic Phase Modulation Gas Correlation Spectroradiometry

David M. Rider, John T. Schofield, and Daniel J. McCleese

Jet Propulsion Laboratory
California Institute of Technology
4800 Oak Grove Drive
Pasadena, CA 91109

Recent work[1] has demonstrated a new type of gas correlation spectroscopy where electrooptic phase modulation of a molecular spectrum together with selective absorption by a reference gas is used to quantify the abundance of a gas phase species selectively. The use of electrooptic phase modulation for gas correlation measurements is a significant enhancement of the gas correlation technique because it provides a means for remotely measuring winds as well as atmospheric species abundances and temperature in the stratosphere and mesosphere[2,3].

Wind speeds are measured with this technique by determining the wind induced Doppler shift in the naturally occuring infrared atmospheric emission. Doppler shifts measured with a gas correlation wind sensor viewing the earth limb have contributions from spacecraft velocity, earth rotational motion and atmospheric winds. These contributions amount to an observed Doppler shift of ~ 600 MHz[3]. Doppler shifts are measured by determining the minimum in the gas correlation signal as a function of the phase modulation frequency. The wind speed measurement capability requires efficient phase modulators (EOPMs) that operate at frequencies near 600 MHz and tune over an 80 MHz range. Previous work[1] demonstrated the technique with 100 MHz phase modulation. In this paper we present laboratory gas correlations measurements made with high efficiency EOPMs working at frequencies near 600 MHz and performance measurements of a tunable ($\pm$ 55 MHz) 600 MHz EOPM.

Electrooptic phase modulators operate by the linear electrooptic effect where a change in the index of refraction of a material is induced by an electric field. This work has focused on cadmium telluride ($CdTe$) modulators which are suitable for applications in the midinfrared. Phase modulation is accomplished by applying a sinusoidally varying voltage across a properly oriented crystal of $CdTe$. This induces a sinusoidal variation in the index of refraction of the crystal so that light passed through it undergoes a periodic retardation of phase velocity—phase modulation. The effect of phase modulation on a spectral line is to redistribute the radiation into a series of upper and lower sidebands that are separated from the input line by multiplies of the frequency of the sinusoidal voltage applied to the $CdTe$ crystal. The relative intensity of a given order sideband is described by the square of the Bessel function of the same order.

The argument of the Bessel functions, a quantity called the modulation index, is determined

by the electrooptic coefficient of the crystal, the orientation and dimensions of the crystal, the amplitude of the applied voltage and the wavelength of the light.

Our approach to building tunable 600 MHz modulators has been to incorporate $1.5 \times 1.5 \times 50$ mm^3 $CdTe$ crystals into a high-Q series LC resonant circuit. In these circuits the crystal and in the tunable versions a tunable air spaced capacitor serve as the series capacitance. The inductor is constructed from a copper plate with a length chosen to provide the resonant inductance (~ 7.5 cm) and a width equal to the length of the $CdTe$ crystal (5.0 cm). A mica or air spaced capacitor in parallel with the series LC is used to impedence match the circuit to a broadband amplifier that supplies the RF drive power. Using this approach it has been possible to construct EOPMs that operate between 300 and 700 MHz, depending on the length of the inductor, with tuning ranges in excess of 100 MHz. Modulation indices greater than 0.7 have been achieved with less than 4 W of average drive power.
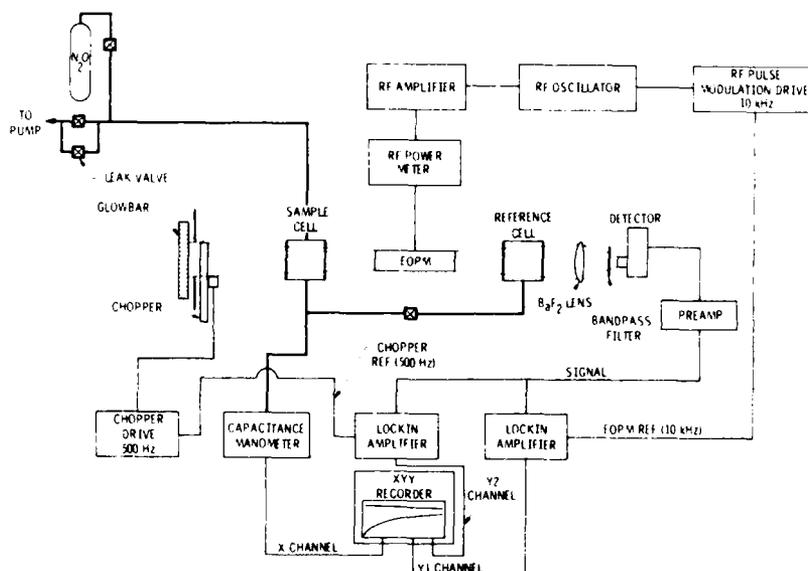
Fig. 1. Schematic of Laboratory setup for electrooptic phase modulation gas correlation measurements.

Electrooptic phase modulation gas correlation measurements are made with the modulators using the setup shown in Fig. 1. A 100 cm^{-1} portion of the ν_1 band of N_2O near 8 μm is used for the lab measurements. Nitrous oxide is the tracer species of choice for wind measurements in the 20 to 40 km altitude range. Measurements are made in absorption in analogy to solar occultation atmospheric measurements using a simple glow bar as the light source and a 1 cm path length sample gas cell to simulate the atmosphere. In the experimental setup the broad band light from the glow bar with the N_2O absorption spectrum imposed is directed through the EOPM and then through a 1 cm path length reference gas cell, also containing N_2O, and is imaged onto a cooled

mercury cadmium telluride detector. The spectral region of interest is isolated with a band pass filter.

The gas correlation signal is generated by squarewave modulating the RF power to the EOPM. This gives rise to the gas correlation signal due to changes in the spectral line overlap of sample gas and the reference gas spectra induced by phase modulation. This gas correlation signal produced with a 600 MHz EOPM for N_2O is shown in Fig. 2 as a function of sample cell pressure for a fixed reference cell pressure. The N_2O opacities between 0 and 10 torr span the range that would be
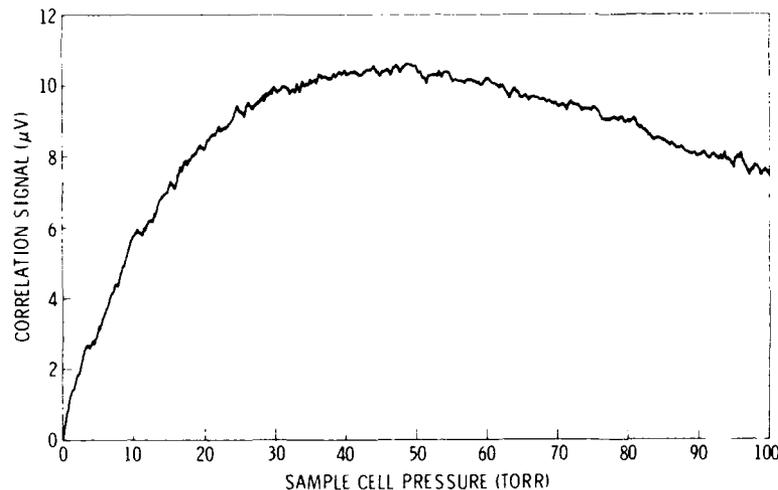
Fig. 2. N_2O Gas Correlation signal with 600 MHz phase modulation for
a reference cell pressure of 60 torr and 0–100 torr sample cell pressures.

observed from an orbiting platform in a 20 to 40 km altitude limb view of earth. The characteristic shape of the curve is determined by the amount of N_2O in the sample cell and the linewidths of the N_2O absorption. At low pressures where the absorption linewidths are small compared to the phase modulation frequency the signal increases with the amount of N_2O in the sample cell. At higher pressures where the absorption lines become saturated and pressure broadened the signal decreases with increasing sample amount. This effect results when the absorption linewidths become comparable to the modulation frequency and the phase modulation induced side bands lie within the linewidth of the unmodulated spectral line. This high pressure region is not sampled in the remote sensing application but the behavior of the curves at high pressures has been useful for accessing our models of the effects of phase modulation on molecular spectra. These results demonstrate that EOPMs can be used to generate a gas correlation signal at the modulation frequencies required for remote sensing of winds, species and temperature. They have validated our numerical models of the interaction of atmospheric spectra with EOPMs and the atmospheric wind sounder concept.

References

[1] D.M. Rider, J.T. Schofield, J.S. Margolis and D.J. McCleese, "Electrooptic phase modulation gas correlation spectroscopy: A laboratory demonstration," *Appl. Opt. 25*, 2860 (1986).

[2] D.J. McCleese, "Remote sensing of Earth and planetary atmospheres using gas correlation spectroradiometry," this meeting.

[3] D.J. McCleese and J.S. Margolis, "Remote sensing of stratospheric winds by gas correlation electrooptic phase-modulation spectroscopy," *Appl. Opt. 22*, 2528 (1983).

INVERSION TECHNIQUES FOR BACKSCATTER DATA FROM REMOTE SENSING SYSTEMS

John. R. Hummel
Kurt A. Kebchull
OptiMetrics, Inc.
121 Middlesex Turnpike
Burlington, MA 01803

Donald E. Bedo
Robert A. Swirbalus
Optical Physics Division
Air Force Geophysics Laboratory
Hanscom AFB, MA 01731

An examination of inversion techniques applicable to bakscatter data from remote sensing systems has been made. The purpose of the study was to develop an inversion technique that could be used with remote sensing systems under development at the Air Force Geophysics Laboratory (AFGL).

An inversion approach has been developed based on fundamental radiative transfer characteristics of the atmosphere. The approach is rooted in fundamental physics but, still, does not eliminate the problem of more unknowns than equations. For the approach to be used, one must still make an assumption about the type of aerosol responsible for the backscattered signal. Preliminary results from test flights of the balloonborne AFGL remote sensing system will be presented.

Polychromatic Holographic Correlation Techniques for Enhancing Resolution in Remote Sensing Applications

R. SAMBASIVAN
Publications & Information Direcorate
(Council of Scientific & Industrial Research)
Hillside Road
New Delhi 110012, INDIA.

In optical remote sensing by photo-reconnaissance satellites or in ground-observation by orbiting space telescopes, the diffraction-limited theoretical resolution possible, is degraded by accidental & vibratory motion of the imaging camera, defocussing, atmospheric turbulence effects on satellite-pictures transmitted, etc. For instance, an orbiting space telescope (height, h = 275km above earth) with an effective focal length, f = 57.6m and equipped with a CCD camera with pixel, d = 15 microns, has a theoretical resolution:

$$R = (hd/f) \longrightarrow = 7.16cm(!)$$

on ground; however, in practice due to image-degradation, the feasible resolution is of 10-15m only (which can be improved with rigid satellite attitude-control, to 1-2m) Increasing the pixels from 800 x 800 to 1600 x 1600 matrix, though could improve resolution 4 times, but makes the satellite data-transmitting antenna unwieldy. Again CCD-coupled multispectral scanner of the LANDSAT camera, has a spectral bandwidth of 150-250 nm as against the desired 10-25 nm bandwidth needed for high resolution true color imagery in remote sensing. High resolutions are needed in identifying rapidly moving missile targets. Thus, without reducing pixel size, it is shown possible using Fourier deconvolution methods, to achieve any desired resolution.

The basic principle of retrieving resolution in defective remote-sensing imagery is through the well-known 'spatial frequency filtering' proposed by Marchal and Croce in 1953 and developed by George Stroke, et al. [Stroke, "Introduction to Coherent Optics à Holography"(Academic Press Inc., USA), 169 edn; _Phys. Lett._, _51A_ (1975), 383]. But this procedure for image-deblurring using the point-spread function $h(x,y)$., which is the blurred image of a reference point source by the satellite camera (h is synthesized as Fourier Transform Holographic Filter devised by Stroke), applies to a single chosen wavelength; it is thus imperative to extend this work for deblurring _colour_ images, involving spectral components ($\lambda_1, \lambda_2, \dots \lambda_n$). However, devising holographic filter at each of the

...each of the....

three tristimulus wavelengths(λ_B, λ_G and λ_R) also introduces "cross-talk" in the deconvolved(corrected) image, due to $\lambda_i \neq \lambda_j$, for example, as in Leith-Upatnieks colour holography scheme.

In the new convolution method proposed for correcting defective image distribution $g_{\lambda_i}(x,y)$ ($i = 1,2,3...n$) to get the true(diffraction limited) image $f_{\lambda_i}(x,y)$, we have the imaging field($k_{ij}, i,j = 1,2,...n$)

$$k_{ij}(x,y) = g_i(x,y) \otimes h_{ij}(x,y) = f_i \otimes h_i \times h_{ij}^* \quad ....(1), \quad \text{---} \quad h_{ii} \equiv h_i$$

here $\otimes$ denotes 'convolution', $\times$ spatial autocorrelation and $*$ conjugate complex; $h_{ij}(x,y)$ is the multi-spectral spread function for the component wavelengths λ_i and λ_j. For the "cross-talk" imaging fields $k_{ij}(i \neq j)$ will vanish one must have:

$$h_i \times h_{ij}^*(x,y) = \delta(\overline{\lambda_i - \lambda_j} x, \overline{\lambda_i - \lambda_j} y) . \delta(x,y) \quad ..... (2),$$

here δ is Kronecker's delta, being 0, if either $i \neq j$, or $x \neq y \neq 0$
However, in synthesing the filter, as in monochromatic case, spread-functions for each of the spectral components (λ_i) must be laboriously recorded; instead it is possible to use/an extended white-light source, with all the spectral components co-existing, and the delta function can be replaced to a *sufficient degree of approximation by the sinc function*:

$$\delta_{ij} \approx \left(\frac{\sin[(\lambda_i - \lambda_j)\nu x]}{(\lambda_i - \lambda_j)\nu x} \right) \left(\frac{\sin[(\lambda_i - \lambda_j)\nu y]}{(\lambda_i - \lambda_j)\nu y} \right) \quad .... (3),$$

where ν is an adjustible parameter. Then the requsite polychromatic holographic filter can be synthesised as $H_{ij}(u,v)$ being the inverse Fourier Transform of h_{ij}^*, $= const. P(u_i)Q(v_i)$, for e.g. $P, Q \approx \frac{1}{2}$ in $(-\alpha \leqslant u_i \leqslant \alpha)$ and 0 in $|u_i| > \alpha$. Here $\alpha = (\lambda_i - \lambda_j)\nu / 2\pi$ (ν depends on temporal pass band of the filter, can be designed to nm-lengths).

Specific applications of the filter, and computation of the filter parameters for remote sensing applications, for example photography through fog in snow-clad mountains, detection of glacier movements are discussed.

————————

WEDNESDAY, SEPTEMBER 30, 1987

CONFERENCE ROOM 5

8:30 AM–10:15 AM

WA1–4

REMOTE SENSING TECHNOLOGY: 1

John Petheram, RCA Astro Electronics, *Presider*

Diode Pumped Solid State Lasers For Remote Sensing

Robert L. Byer and Thomas J. Kane
Edward L. Ginzton Laboratory
Stanford University
Stanford, CA 94305
(415) 723-0226

The potential for global wind sensing from a satellite platform using laser sources and coherent Doppler radar was first proposed by R. M. Huffaker[1]. The prospect for global remote wind sensing motivated our work at Stanford University toward the development of a solid state laser transmitter coherent radar system. The potential for coherent doppler wind velocity measurements using Nd:YAG was evaluated by Kane, Zhou and Byer in 1984[2]. That analysis showed the advantages of higher frequency coherent radar for improved backscattering and for improved depth resolution at a fixed velocity resolution.

In an important step in 1985, Zhou, Kane, Dixon and Byer[3] demonstrated a diode laser pumped monolithic Nd:YAG oscillator with a threshold of 2mW, a slope efficiency of 25% and a linewidth of 10kHz. Almost simultaneously, Kane and Byer[4] invented the nonplanar ring oscillator with the capability of single frequency output and the advantage of immunity to feedback.

When combined with previous progress in slab geometry lasers[5], the diode laser pumped solid state laser oscillator, coupled with single mode fiber to mixers and detectors led to the demonstration of coherent laser radar at 282THz. The Stanford Coherent laser radar coherently detected backscatter from clouds and from clear air[6]. It combined all of the elements of classical FM radar but in a compact, all solid state laser system.

With the rapid development of diode laser and diode laser arrays, it has become possible to conceive of an all solid state laser radar system with a transmitter efficiency of greater than 10% with operating lifetimes of greater than 20,000 hours and with a size and overall power requirements that is consistent with satellite platforms. Progress in the development of diode laser array pumped solid state lasers will be reviewed.

The diode laser pumped Nd:YAG could potentially have met all of the laser transmitter requirements for global remote wind sensing save one; eye safety. For coherent tranmission and detection, the beam must remain within a diffraction limited spot at the surface of the earth. The power density required for successful wind measurements placed the intensity at the surface of the earth near the eyesafety limit for 1064nm operation. To alleviate this problem, we have recently developed[7] a cw, room temperature, diode laser pumped 2010nm laser source in Tm:Ho:YAG. The properties of this laser source will be described and the potential for its application to global wind sensing revewed.

References

1. R. M. Huffaker, Ed., "Feasibility Study of Satellite-Borne Lidar Global Wind Monitoring System," NOAA Tech Mem. ERL WPL-37(1978)

2. T. J. Kane, Bingkun Zhou and R. L. Byer,"Potential for coherent Doppler wind velocity lidar using neodymium lasers," Applied Optics Vol 23, page 2477, August 1984

3. Binkun Zhou, T. J. Kane, G. J. Dixon, and R. L. Byer, "Efficienct, frequency-stable laser-diode-pumped Nd:YAG laser," Optics Letters, vol 10, page 62, 1985

4. T. J. Kane and R. L. Byer, "Monolithic, unidirectional single-mode Nd:YAG ring laser," Optics Letters, vol 10, page 65, 1985; T. J. Kane, Alan C. Nilsson and R. L. Byer, "Frequency Stable and offset locking of a laser-diode-pumped Nd:YAG monolithic nonplanar ring oscillator," Optics Letters, vol 12, page 175, 1987

5. T. J. Kane, W. J. Kozlovsky, and R. L. Byer, "62-dB-gain multiple-pass slab geometry Nd:YAG amplifier," Optics Letters, vol 11, page 216, 1987

6. T. J. Kane, W. J. Kozlovsky, and R. L. Byer, "Coherent laser radar at 1.06um using Nd:YAG lasers," Optics Letters, vol 12, page 239, 1987

7. T. Y. Fan, G. Huber, R. L. Byer, and P. Mitzsherlich, "Continuous Wave operation at 2.1um of a diode laser pumped, Tm-sensitized Ho:YAG laser at 300K," submitted for publication

Focal Plane Array Technology
for
Optical Remote Sensing

by

James A. Cutts and Martin H. Leipold
Jet Propulsion Laboratory
4800 Oak Grove Drive
Pasadena, CA 91109

Progress in the development of solid-state self-scanned imaging arrays for remote sensing in the infrared region highlighting recent developments is reviewed.

Sum Frequency Mixing of two Tunable Nd:YAG Lasers for Sodium Fluorescence Lidar Measurements*

T.H. Jeys

Lincoln Laboratory, Massachusetts Institute of Technology

Lexington, Massachusetts 02173 U.S.A.

An interesting coincidence of nature is that by sum frequency mixing the output of two appropriately tuned Nd:YAG lasers, the sum radiation may be made resonant with the sodium D_2 transition wavelength. By exploiting this coincidence we have generated high power pulsed sodium resonance radiation. We plan to use this new source of sodium resonance radiation for characterizing the sodium layer in the earth's atmosphere. Figure 1 shows the cw wavelength tuning curves of the two Nd:YAG laser transitions. The 1.064 μm laser has a tuning range of about 6 Å while the 1.319 μm laser has a tuning range of about 4 Å. By operating the lasers at the wavelengths indicated by the arrows in Fig. 1 it is possible to generate sodium resonance radiation. In addition, it is possible to easily tune the sum radiation over the complete sodium Doppler absorption profile.

A schematic of the apparatus for sum frequency generation of sodium resonance radiation is shown in Fig. 2. The output of two simultaneously Q-switched etalon tuned Nd:YAG lasers (one operating at 1.064608 μm and the other operating at 1.319224 μm) are superimposed and made to propagate coaxially by a dichroic mirror. The combined radiation is then focused into a lithium niobate crystal held at a temperature of 224 ˚C. As a result of the nonlinear response of the crystal to an electric

---

field, radiation is generated with a frequency corresponding to the sum of the two Nd:YAG frequencies. The sum radiation is then directed into a sodium vapor cell where resonance fluorescence is observed whenever the sum radiation is tuned to the sodium absorption transition.

Both Nd:YAG lasers operate with a pulse repetition rate of 2 kHz, pulse lengths of about 200 nsec., and within spectral envelopes of 1 GHz. The 1.064 μm laser operates with an average power of 2.45 Watts while the 1.319 μm laser operates with an average power of 1.2 Watts. Under these conditions, 600 mWatts of average sum power is generated. This corresponds to an average 16% conversion efficiency of Nd:YAG radiation into sum radiation. The sum radiation has a peak power of about 1.5 kW and is contained within a spectral envelope of 2 GHz.

Of course, laser radiation coincident with the sodium transition is usually obtained from dye lasers. However, the generation of pulsed resonance radiation by sum frequency mixing has some advantages over dye lasers. For example, this source of radiation should be more easily scaled to high powers and should prove to be more reliable at high power. In addition, tuning of the sum frequency may be easily controlled by a diode laser.

By injection seeding a 1.319 μm Q-switched Nd:YAG laser with the output radiation of a GaInAsP/InP diode laser, the Nd:YAG laser could be frequency tuned by current tuning the diode laser. In the absence of any intracavity frequency selective elements, 10^{-8} W of diode laser seed radiation narrowed the spectral envelope of the Nd:YAG laser from > 8 GHz to ≈340 MHz. By quickly current tuning the diode laser we have switched the frequency of a 5kHz Q-switched Nd:YAG laser by as much as 10 GHz on a shot to shot basis.

We are presently configuring our laboratory in order to transmit the sum radiation into the atmosphere and to receive the fluorescence from the mesospheric sodium layer.
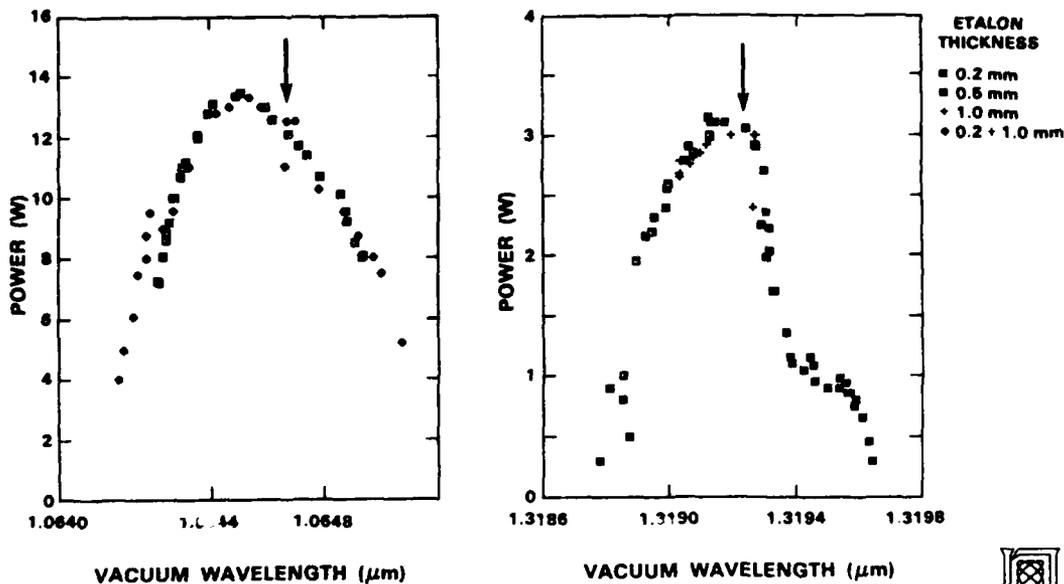
Figure1. CW tuning curves of the two Nd:YAG lasers. By operating each laser at the wavelength indicated by the arrows, it was possible to generate sodium resonance radiation.
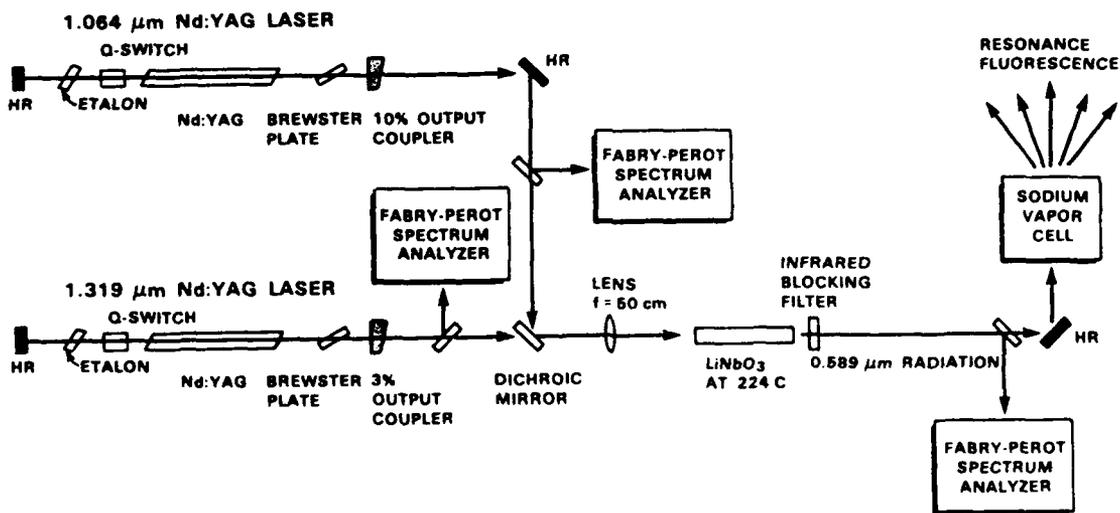
Figure 2. Schematic of the apparatus for sum frequency generation of sodium resonance radiation.

DUAL ALEXANDRITE LASER FOR AUTONOMOUS LIDAR APPLICATIONS

John J. Degnan
Instrument Electro-optics Branch, Code 723
NASA Goddard Space Flight Center
Greenbelt, MD 20771

INTRODUCTION

NASA's Lidar Atmospheric Sensing Experiment (LASE), a joint effort of the Langley Research Center and the Goddard Space Flight Center, is a first step toward the realization of the agency's goal of developing autonomous Differential Absorption Lidar (DIAL) instruments for future airborne and spaceborne remote sensing applications. The scientific goal of the first phase of the LASE program is to measure water vapor, aerosol, and cloud profiles from a high altitude ER-2 (extended range U-2) aircraft. The science motivation and overall system concept has been presented previously [1]. The present paper will discuss the design and performance characteristics of the Tunable Laser Subsystem (TLS) being developed at the Goddard Space Flight Center.

A simplified block diagram of the overall LASE facility is shown in Figure 1. The TLS consists of five subsystems – a dual wavelength Alexandrite laser head, a Laser Control Unit (LCU), a Laser Thermal Unit (LTU), and two Lamp Driver Units (LDU's). Each of these is described in the following sections.

LASER CONTROL UNIT

A modular 8-bit National Semiconductor MA2802 CPU is the microprocessor "brain" of the TLS. A fiberoptic RS232 port provides two way communications between the Langley Command and Data System (CDS) and the Goddard LCU while isolating them electrically. Through the LCU, the CDS can command the TLS to fire one or both lasers, move to new operating wavelengths, or perform wavelength scans. In a DIAL experiment, the TLS generates dual on -line and off-line pulses at a repetition rate of 5pps. The rate is determined primarily by prime power and thermal considerations in the aircraft.

The outgoing pulses are sampled by a high precision wavemeter which relays wavelength information to the CDS. The latter transfers the information back to the LCU and, if a wavelength correction is required, the LCU makes appropriate adjustments to the tuners in the laser head to hold the laser within 0.5 pm of the desired wavelength. Besides monitoring and controlling the other subsystems which make up the TLS (as outlined below), the LCU also controls and synchronizes the timing of the overall DIAL experiment by transmitting a TTL precursor pulse to the CDS near the start of each 200 millisecond fire interval. The LCU is 13.5 inches long by 10 inches wide by 7 inches high and weighs 17.5 pounds.

DUAL LASER HEAD

The laser head contains two identical Alexandrite lasers to generate the on and off line radiation in the DIAL water vapor experiment. The lasers are electro-optically Q-switched to provide approximately 170 mJ of energy in a 160 nanosecond pulsewidth. The on and off line pulses are separated spectrally by 70 picometers (pm) and temporally by about 400 microseconds although both parameters are adjustable. The temporal separation is long enough so that a common optical receiver can record the backscattered waveform and ground reflection of the first pulse before the second pulse is emitted but short enough so that the on and off line pulses see the same "atmosphere".

Coarse tuning of each laser over a 720 to 780 nm range is accomplished by a stepper-motor controlled 5-plate birefringent tuner. The spectral linewidth of each laser is further narrowed to about 1 pm by two angularly tuned intracavity etalons which are also controlled by stepper motors. The angular positions of the six tuning elements are controlled by the LCU which references software tables generated during preflight laboratory calibration experiments. Position sensors in the birefringent tuner and etalon mount assemblies permit accurate determination (to about one step) of a reference or "AT HOME" position for each tuner during flight.

The temperature within the ER-2 Q-bay compartment is expected to vary between 15 C and 40 C. In order to provide good wavelength stability and accurate calibrations during flight, the six tuners are housed inside a proportionally controlled oven. The oven controller, located in the LCU, maintains the temperature within + 0.1 C of a set temperature slightly above maximum ambient.

During flight, the Q-bay pressure can also vary from a nominal sea level value of 14.7 psia to 3.5 psia at cruise altitude. To minimize the complications of a changing pressure, the lasers are housed inside a pressure vessel formed by a lightweight but rigid machined aluminum isogrid optical baseplate and an aluminum half-cylinder covering most of its length. The all-metallic vessel also helps to shield nearby subsystems from radiated noise originating from high voltage flashlamp and Q-switch firings within the head. As an additional precaution, no data communication between subsystems occurs during the one millisecond interval per 5pps cycle when the two lasers fire.

The laser light passes through two windows in the pressurized case to an unpressurized forward optics compartment on the laser deck. Approximately 88% of the energy in each beam (or 150 mJ) is directed through a five power beam expander and deflected by a 45 mirror through the laser baseplate to windows in the aircraft fuselage to support the DIAL experiment. A series of beamsplitters directs the remaining 12% into a pyroelectric joulemeter for inflight measurement of the laser energy, a wavemeter for active feedback control of the laser wavelength, and a series of fiber optic cables which provide synchronization

and timing (T0A, T0B) signals to other LASE subsystems. The dual laser head is 46.8 inches long by 12 inches wide by 9.675 inches high and weighs about 95 lbs.

LAMP DRIVER UNIT

Each Lamp Driver Unit contains a 1500 Watt high voltage power supply, Pulse Forming Network (PFN), simmer supply, high voltage lamp trigger, and computer interface/control circuitry for one laser. Following ionization of two series lamps by the trigger circuit, a DC "keep alive" current of 0.5 amperes is maintained by the simmer supply. The high voltage power supply charges the 60 microfarad energy storage capacitors in the PFN to a value remotely set by the LCU up to a maximum value of 2.95 KV or 260 Joules. At the end of the charge cycle, the LTU verifies the voltage on the LDU capacitors and the presence of simmer current prior to issuing a flashlamp fire command. The capacitor is then discharged through the lamps in a 220 microsecond pulse (between 10% points).

Since the Alexandrite laser gain varies strongly with wavelength at a given pump level, the LCU selects an initial PFN charging voltage based on internal software tables generated during laboratory calibrations. This maintains the circulating optical power at a safe level over the full tuning range of Alexandrite. If the output energy of either laser exceeds or falls short of the desired value as determined by the joulemeter in the laser head, the LCU adjusts the respective PFN voltage accordingly within a range of the tabulated value to allow for reasonable variations in lamp output, field alignment, etc.

Each LDU weighs 65 lbs and is 19.5 inches long by 14.5 inches wide by 7 inches high. The major heat generating elements are mounted on a watercooled stainless steel baseplate. For additional cooling, a low noise brushless fan draws air from the Q-bay through an EMI screen, circulates air through the unit, and exhausts it into the Q-bay through a second EMI screen. To further reduce radiated EMI, a triaxial cable is used between the LDU and the laser head and RFI gaskets and filters are used throughout. Furthermore, since the LDU's are not pressurized, all high voltage components are encapsulated or conformal-coated to prevent arcing or corona at altitude.

LASER THERMAL UNIT

The LTU contains a 3 gpm low temperature loop (LTL) for cooling the laser flashlamps and power supplies and a 1 gpm high temperature loop (HTL) for independently controlling the temperature of the two Alexandrite rods. The HTL control temperature is set remotely between 43 and 80 C by the LCU based on internal tables of optimum temperature versus wavelength. To reduce weight, the LTL and HTL loops share a common coolant and an air-pressurized bellows reservoir. To maintain system purity over extended periods, the LTU uses a deionized water coolant, an all stainless steel design, and contains particulate and

deionizing filters. A 1KW heater in the HTL loop can raise the rod temperature at a rate of 3.2 degrees per minute. During laser operations, microprocessor-controlled solenoid valves permit leakage of lower temperature coolant from the LTL into the HTL to compensate for heat deposited by the flashlamps into the rod and maintain the HTL temperature within a 1 C control bandwidth. The LTU box is 10.375 inches long by 28 inches wide by 9.625 inches high and weighs 51.25 pounds when filled with coolant.

During flight, approximately 2.8 Kilowatts of heat deposited into the LTL is transferred, via a liquid-to-liquid heat exchanger in the LTU, to a 60/40 ethylene glycol/ water mixture in the Langley Thermal Control Unit (TCU). The TCU in turn exchanges the heat with air flowing through a liquid-to-air RAM exchanger on the belly of the aircraft.

ACKNOWLEDGEMENTS

REFERENCE

1. W. R. Vaughan, E. V. Browell, W. M. Hall, J. J. Degnan, R. D. Averill, J. G. Wells, D. E. Hinton, and J. H. Goad, "A Lidar Instrument to Measure H2O and Aerosol Profiles from the NASA ER-2 Aircraft", SPIE Proceedings Vol. 663, Paper [663-29], SPIE's 1986 Quebec International Symposium on Optical and Optoelectronic Applied Sciences and Engineering, June 2-6, 1986, Quebec City, Canada.

SYSTEM BLOCK DIAGRAM
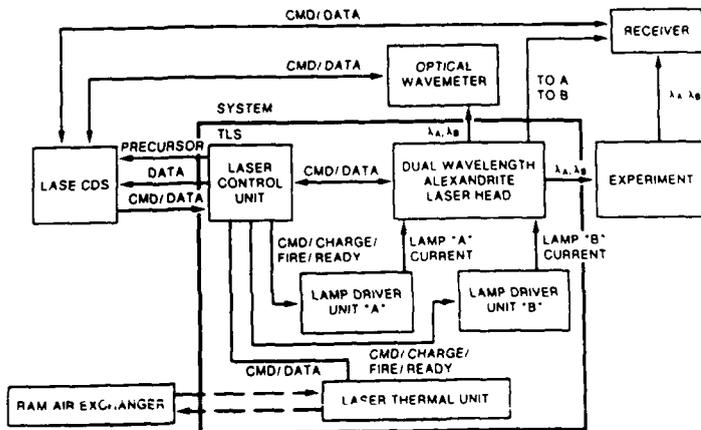
WEDNESDAY, SEPTEMBER 30, 1987

CONFERENCE ROOM 5

10:45 AM–12:30 PM

WB1–4

REMOTE SENSING TECHNOLOGY: 2

Martin Endemann, Battelle Institut, Federal Republic of Germany, *Presider*

Progress in Solid State Lasers for Remote Sensing

Aram Mooradian
MIT Lincoln Laboratory

Sources and Technology for Coherent Lidar Wind Measurement

Michael Vaughan
Royal Signals and Radar Establishments, U.K.

The required characteristics of laser sources, both pulsed and cw, are described and illustrated. Technology questions in attaining quantum limited system performance are briefly outlined.

Development of Coupled-Cavity
Laser Diodes for Remote Sensing

Richard K. DeFreez, Richard A. Elliott,
Joseph Puretz, and Jon Orloff
Oregon Graduate Center
19600 N. W. Von Neumann Drive
Beaverton, OR 97006-1999

Summary

Several recent developments in diode laser technology such as multiple emitter phase-locked arrays and epitaxial growth of materials that can be used to make lasers which emit at wavelengths ranging from the visible through the near infrared make these devices attractive candidates as sources for spectroscopic applications and remote sensing systems. The perceived advantages of diode lasers include efficiency, small size and weight, and direct modulation capability. But in fact mode hopping under current modulation, wavelength drift with temperature, and their relatively broad linewidths make conventional diode lasers less than ideal sources for laser spectroscopy. Elaborate stabilization schemes and external cavities are often used to overcome these shortcomings.

The invention of the cleaved-coupled-cavity (C^3) diode laser a few years ago introduced a new level of sophistication to diode lasers. Two section coupled-cavity diode lasers, of which the C^3 laser is an

example, are three terminal devices which allow the two sections of the laser cavity to be driven with different currents. In effect one section can be considered to be an electronically tunable Fabry-Perot etalon which controls the wavelength of the laser. Line narrowing and improved secondary mode suppression are also observed with these devices.

The major problem with C^3 lasers is their fabrication which involves cleaving a laser die and repositioning and precisely aligning the two cleaved sections. Ideally the width of the air gap between the two cavities should be a small integral number of half-wavelengths to maximize the coupling efficiency and it is also desirable to be able to choose the length of the two cavities. However the cleaving process is not capable of the precision required for reliably producing devices with the desired properties.

At OGC we have recently developed a micromachining facility utilizing a focused beam of ions from a liquid metal source. This system produces a 0.25 nA, 20 keV beam of Ga^+ ions focused to a 250 nm diameter spot which may be scanned with 50 nm precision over a working area of a few square millimeters. The focused ion beam (FIB) sputter-etches semiconductor materials at a rate of approximately 0.25 $\mu m^3 sec^{-1}$ and can be used to micromachine grooves and other features in wafer surfaces. The process is so precise and gentle that optically smooth surfaces can be formed wherever needed on a diode laser die to produce output mirrors, coupling etalons, and turning mirrors[1-3].

Micromachined-coupled-cavity (MC^2) diode lasers have been fabricated with the FIB system. These include modification of commercial devices, ten emitter phase-locked arrays, and broad area long wavelength devices. The commercial devices are Mitsubishi ML-4102 AlGaAs diode lasers with nominal emission wavelength of 786 nm. When modified to form MC^2 lasers they can be tuned to two discrete modes separated by 30 Å and each mode can be continuously tuned over 3 Å. Secondary mode suppression of more than 25 dB is

observed. The phase-locked arrays are Xerox PARC AlGaAs lasers which when micromachined to form coupled-cavity lasers produce 50 mW in a single tunable longitudinal mode.

The long wavelength devices are fabricated from $InP/In_{0.53}Ga_{0.47}As/InP$ double heterostructure material grown by MOCVD which produces lasers emitting at 1.65 µm. This wavelength lies in the $2\nu_3$ overtone band of methane hence these lasers are a potential source for methane DIAL systems. The performance characteristics of MC^2 lasers fabricated from this material are being determined and their suitability for use in methane detection systems evaluated.

References

1. J. Puretz, R. K. DeFreez, R. A. Elliott, and J. Orloff, "Focused-ion-beam micromachined AlGaAs semiconductor laser mirrors," *Electron. Lett.*, vol. 22, pp. 700-702, 19 June 1986.

2. R. K. DeFreez, J. Puretz, R. A. Elliott, J. Orloff, and L. W. Swanson, "CW operation of widely and continuously tunable micromachined-coupled-cavity diode lasers," *Electron. Lett.*, vol. 22, pp. 919-921, 14 August 1986.

3. J. Puretz, R. K. DeFreez, R. A. Elliott, J. Orloff, and T. L. Paoli, "300 mW operation of a surface-emitting phase-locked array of diode lasers," *Electron. Lett.*, vol. 23, pp. 130-131, 29 January, 1987.

LASER-EXCITED OPTICAL FILTER:
EXPERIMENTS IN Rb VAPOR

by

T. M. Shay and J. D. Dobbins

Los Alamos National Laboratory
P.O. Box 1663
CLS-5 MS/E535
Los Alamos, N.M. 87545
(505)-667-8390

and

Y. C. Chung

Utah State University
Department of Electrical Engineering
Logan, Utah 84322
(505)-667-8390

Narrow bandwidth optical sources are readily available; however, tunable narrow-bandwidth, wide field-of-view optical filters are not available. Laser-excited optical filters (LEOFs) are in principle, tunable narrow-bandwidth, wide field-of-view optical filters. LEOFs can simultaneously provide high resolution (0.001 nm), wide field of-view (2π), and high quantum efficiency. These devices are ideally suited for extracting weak narrow bandwidth signals buried in strong nonresonant optical background radiation. Potential applications of these filters include remote sensing, laser communications, laser radar, detection of Raman radiation, atomic spectroscopy, etc.

We report the first demonstration of a LEOF in Rb vapor and in addition the first pumping of a LEOF with semiconductor lasers. In our experiments, the $Rb(5p^2P_{3/2})$ level is populated by the absorption of 8.7 mW of laser power from a frequency-stable semiconductor laser tuned to the $Rb(5s^2S_{1/2} - 5p^2P_{3/2})$ transition. A cw tunable dye laser is used as a optical test oscillator. The dye laser frequency is scanned through the 572 nm Rb(5p to 7d) transition. When the dye laser photons are absorbed by the Rb(5p) atoms, violet sidelight fluorescence, from excited Rb atoms is observed at wavelengths of 421, 359, and 335 nm and is detected by a photomultiplier. Thus we are performing a laser induced fluorescence experiment, where 572 nm photons are absorbed and violet photons are emitted from excited Rb atoms. There is no detectable signal on our photomultiplier tube when the dye laser is tuned off the 572 nm Rb transition and a strong signal is detected when the dye laser is tuned to the 572 nm transition. Furthermore, the full-width-at-half-maximum of the sidelight fluorescence is measured to be 1.18 GHz , in good agreement with a calculated doppler width of 1.02 GHz. The results of these experiments will be presented.

WEDNESDAY, SEPTEMBER 30, 1987

CONFERENCE ROOM 4

2:00 PM–5:00 PM

WC1–22

POSTER SESSION:
OPTICAL SYSTEMS AND COMPONENTS

Harvey Melfi, NASA Goddard Space Flight Center, *Copresider*

Nobuo Takeuchi, The National Institute for Environmental Studies, Japan, *Copresider*

An Airborne Polarization Lidar for Sounding Clouds and Underlying Surface

A.I.Abramochkin, V.V.Burkov, V.E.Zuev, I.V.Samokhvalov,
V.I.Shamanaev

The Institute of Atmospheric Optics, Siberian Branch
USSR Academy of Sciences, Tomsk, 634055, U S S R

The information on the scattering coefficient of clouds and their phase state, as well as on the presence of oriented particles can be obtained, and the classification of an underlying surface can be made based on the analysis of lidar-return polarization.

An optical schematic of the lidar "Svetozar-3" is shown in Fig.1. Here 1 is a laser with a radiation wavelength 532 nm; 2,12 are phase plates $\lambda/4$; 3 is a Glan prism; 4 is a light-scattering cavity; 5,6 are phototubes; 7,8,9,11 are lenses; 10 is a diaphragm; 13 are interference filters; 14 is a Wollaston prism; 15,16 are photomultipliers. The lidar has three similar receiving telescopes with lenses 9 of 0.1 m diameter which are symmetric about a transmitting lens 8.

The lidar operates in several modes. 1 - At each laser flash the prism 3 turns at a given angle thus making the transmitter's polarization plate to rotate about a reference plane. A block consisting of a prism 14 and photomultipliers 15,16 also rotates in synchronism with prism 3. Polarization planes of the receiving channel of the transmitter remain coplanar. 2 - Prism 3 is removed, diaphragm 10 is the same in all three channels. The laser transmitter has circular polarization, and the Stokes vector of the received lidar return can be determined based on the signals from all the photomultipliers. 3 - Plate 2 is also removed, diaphragms 10 are different. The transmitter has linear polarization, but the lidar return is received from three different fields of view. Thus multiple scattering can be taken into account.

The recording system consists of a multichannel digitizer with a 25 ns interval and 6 bit accuracy, a microcomputer, a
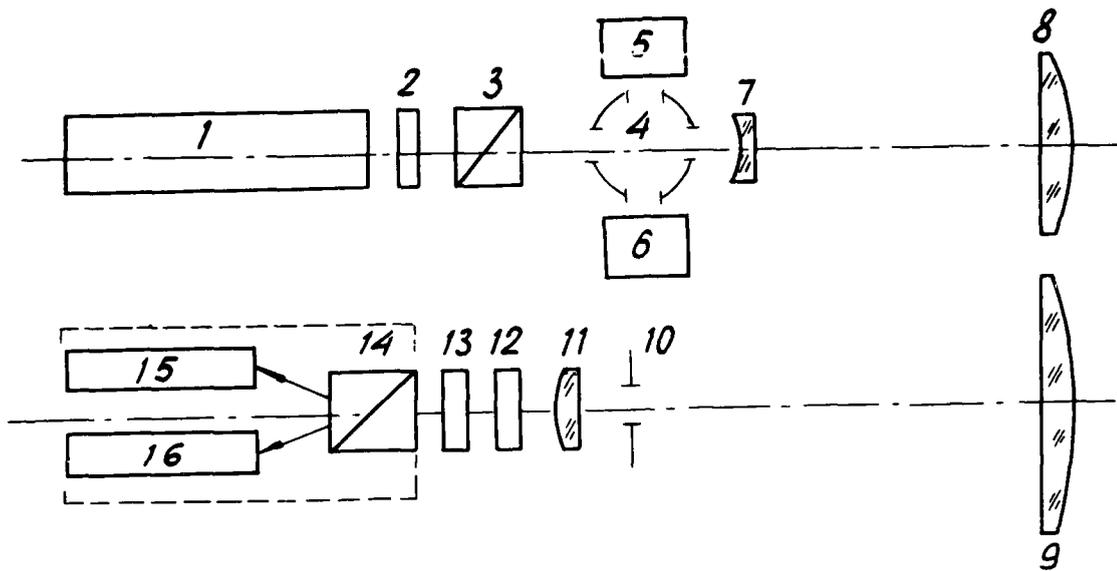
Fig. 1

video terminal, a disc recorder and corresponding interfaces.

The lidar power-supply system has been developed for an airborne electric circuit 115 V 400 Hz.

For sounding clouds, sea and Earth's surfaces from board of several types of aircrafts a slanted mirror, which changes the original state of light polarization, should be used. Such variation can be taken into account by utilizing a mirror reflection matrix. For a single radiation passage it has a form

$$
\begin{pmatrix}
1 & 0 & 0 & 0 \\
0 & \cos^2 2\theta - \sin^2 2\theta & 2\cos 2\theta \sin 2\theta & 0 \\
0 & -2\cos 2\theta \sin 2\theta \cos\Delta & (\cos^2 2\theta - \sin^2 2\theta)\cos\Delta & \sin\Delta \\
0 & 2\cos 2\theta \sin 2\theta \sin\Delta & -(\cos^2 2\theta - \sin^2 2\theta)\sin\Delta & \cos\Delta
\end{pmatrix}
\tag{1}
$$

Here θ is the angle between a mirror normal projection on the plane perpendicular to the lidar optical axis and a reference plane. An ellipsometrical angle Δ depends on an angle of radiation incidence to a metallized mirror surface φ . For the

$б, км^{-1}$

Fig.2

$P,\%$ a water $\delta^2=0,19\pm0,04$

$P,\%$ b wet ice $\delta=0,20\pm0,17$

$P,\%$ c ice + wet snow $\delta^2=0,75\pm0,14$

Fig. 3

$\delta(\varphi)$ 0°

90°
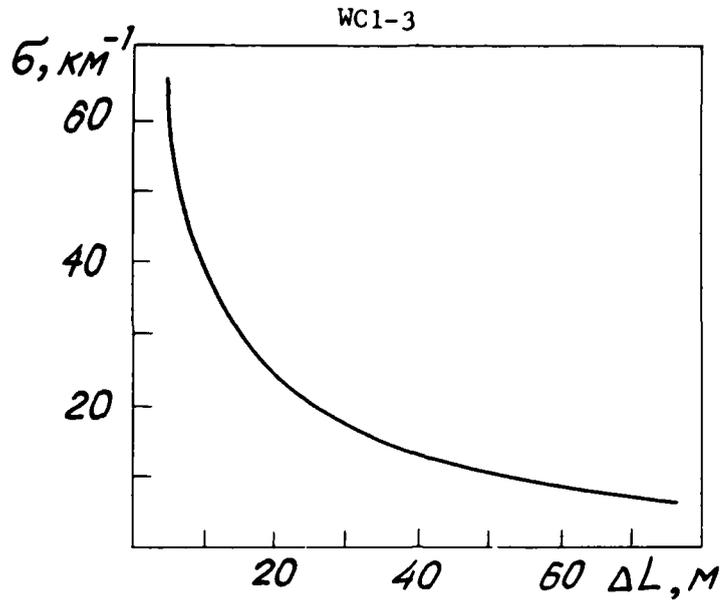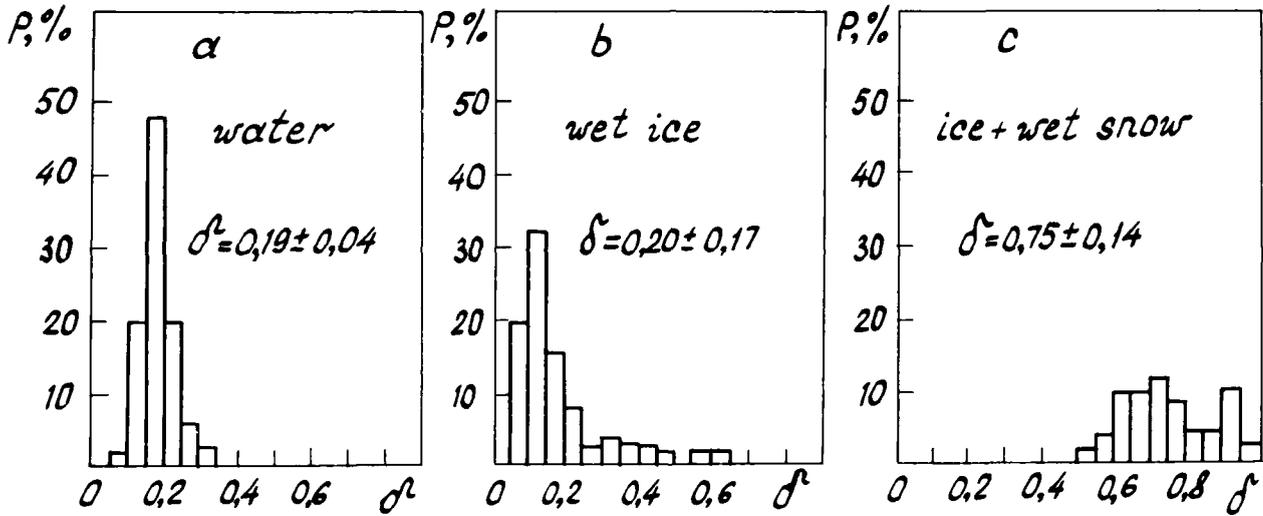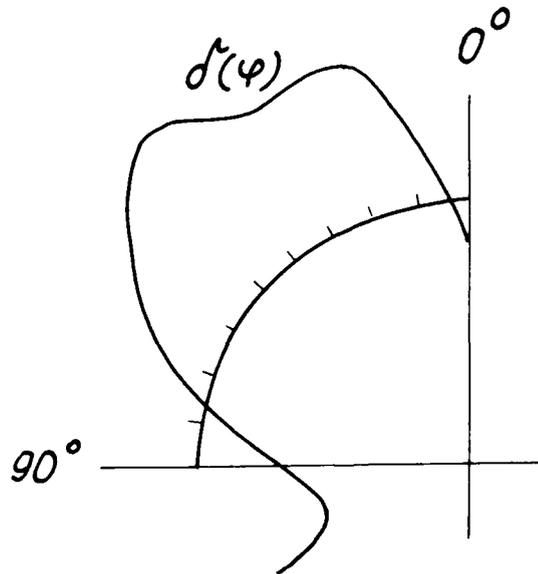
Fig. 4

angles $\varphi = 0°$; $20°$; $40°$ and $60°$ $\quad \Delta = 180°$, $170°$, $155°$ and $120°$, respectively. When $\theta = 45°$ the mirror reflection matrix is simplified to

$$
\begin{pmatrix}
1 & 0 & 0 & 0 \\
0 & -1 & 0 & 0 \\
0 & 0 & -\cos\Delta & \sin\Delta \\
0 & 0 & \sin\Delta & \cos\Delta
\end{pmatrix} \tag{2}
$$

To determine the Stokes-vector components at laser-beam circular polarization it is sufficient to use signals from four photomultipliers

$$S_1 = F(0°, 0) + F(90°, 0); \qquad S_2 = F(0°, 0) - F(90°, 0); \tag{3}$$

$$S_3 = F(45°, 0) - F(135°, 0); \quad S_4 = F(45°, \lambda/4) - F(135°, \lambda/4).$$

Figure 2 shows both calculated and experimental dependences of the distance ΔL between the maxima of polarized $F(t, 0°, 0)$ and cross-polarized $F(t, 90°, 0°)$ components of a lidar return on the cloud-scattering coefficient σ .

Figure 3 illustrates the probability density histograms P of the depolarization values δ obtained at sounding the upper layer of sea water (a), wet ice (b), and ice covered with wet snow (c). The possibility of detecting oriented particles in the atmosphere is shown in Fig. 4. This is a result of simulated experiment. The lidar in the circular polarization mode sounded the wire gauze of vertically oriented metallic filaments of thickness 0.1 mm. The curve $\delta(\varphi)$ illustrates the depolarization dependence on the rotation angle φ counted off from a reference plane. The problem of polarization sounding is considered in more detail in [2,3].

References

1. V.S.Shamanaev, A.I.Abramochkin, Izv.VUZov SSSR, Fizika, 1986, N2, p.125.

2. I.V.Samokhvalov, V.S.Shamanaev, Izv. VUZov SSSR, Fiz.Atmosf. Okeana, 1982, 18, N10, p.1050-1056.

3. V.E.Zuev, G.M.Krekov, M.M.Krekova, I.V.Samokhvalov, V.S.Shamanaev, Meteorol. Gidrol., 1984, N4, p.38-45.

**Raman Shifted Dye Laser for DIAL Measurements
of Atmospheric Temperature, Pressure and Density**

Upendra N. Singh, Rita Mahon, Thomas D. Wilkerson

Institute for Physical Science and Technology
University of Maryland
College Park, Maryland   20742

In recent years Differential Absorption Lidar (DIAL) measurements in the A-band of molecular oxygen have been suggested[1-5] as a means of profiling atmospheric variables such as temperature, pressure, and density. Laser sources of pulsed, tunable (760 - 770 nm) and narrow-bandwidth (0.02 - 0.03 cm^{-1}) radiation, having a high degree of spectral purity (>99%) in this region of the oxygen A-band, are thus highly desirable. This paper reports on the current state of progress in our laboratory efforts in this field.

Commercially available dye lasers can meet the tunability and linewidth requirements for the DIAL sources, but are usually found to have some amplified spontaneous emission (ASE). The ASE, being broadband in nature, results in a non-absorbed component when such a laser is tuned to the resonance frequency of absorption lines. Even 1% of ASE can make an absorption measurement inaccurate. Hence, great effort is needed in eliminating any source of ASE, namely by conservatively pumping the dye laser oscillator and by optically isolating the amplifiers by means of apertures and wedged dye cell windows.

Because the performance of dye lasers declines fairly rapidly with increasing wavelength above 700 nm, it is advantageous to utilize the Raman effect to generate radiation efficiently at the first Stokes frequency. The necessary tunability is retained in the dye laser pump. Because of their very small collision broadening coefficients[6], hydrogen and deuterium gases allow the preservation of the narrow linewidth output from the dye laser, at pressures in the Raman cell of up to about 14 atmospheres (~200 psi).

Experimental Setup: A diagram of the experimental arrangement is shown in Figure 1. This versatile setup allowed us to constantly monitor the performance parameters of the laser system. A frequency-doubled Nd:YAG-pumped Quanta-Ray PDL-2 dye laser (modified) was used in the experiments reported here. A high finesse etalon (F=30) was used to obtain a single mode, narrowband (0.02 cm^{-1}) output at 760 - 770 nm and 577 - 583 nm. The corresponding pulse energies were 20 mJ and 40 mJ. Radiation in the 760 - 770 nm spectral region was either generated directly in a dye laser or was produced by Raman shifting the visible dye laser radiation at 577 - 583 nm in H_2. The shift in H_2 is 4155 cm^{-1}, which corresponds to the frequency of the dominant vibrational phonon field. The Raman cell length was 1 m, and the beam waist was located in the center of the cell to keep the power density on the windows at a minimum. The beam confocal parameter was always much less than the length of the cell, being of the order of 10 cm for the 2 m focal length lens and less for the others.

The laser linewidth was measured with a Fabry-Perot interferometer (Tec-Optics FP-1). The wavelength of either laser was monitored both with a wavemeter (Lasertechnics 100 OCP) and by recording a high resolution absorption spectrum obtained with the White cell. The White cell consisted of two high reflectivity mirrors of 4.8 m radius of curvature and 30 cm diameter, separated by 2 m.

Result: The Raman conversion efficiency to the first Stokes line was measured as a function of the beam confocal parameter, the pressure of H_2, and the pump energy. While linewidth considerations restricted the usable pressure in the Raman cell to less than 14 atm, the conversion efficiency increased with increasing confocal parameter and with increasing pump energy. We measured 45% conversion efficiency to the first Stokes (58% quantum efficiency) at 14 atm of H_2 with a 2 m focal length lens and 29 mJ of pump energy at 580 nm. The linewidth of the Stokes output was measured to be 0.03 cm^{-1}. Figure 2a shows a plot of the conversion efficiency (first Stokes) as a function of pressure for two different confocal parameters. Figure 2b shows the first Stokes energy as a function of pump energy for various focussing parameters at 17 atm pressure of H_2.

With the experimental arrangement shown in Figure 1, we measured the differential transmission at the center of all 29 lines (FWHM 0.06 - 0.1 cm^{-1} at 1 atm) in the P-branch of the O_2 A-band {$b^1\Sigma(\nu=0)$-$X^3\Sigma(\nu=0)$} in air at NTP contained in a White cell of 60 m path length. Two sets of data are presented, corresponding in one case to the radiation being directly generated in a dye laser, and, in the second case, to the use of Raman shifted dye laser radiation. The results are shown in Figure 3a and b. Also shown for comparison, are the measurements of Ritter and Wilkerson[7] which assume a Voigt profile. The latter were obtained using a cw dye laser, having a 10^{-4} cm^{-1} bandwidth, and should inherently have a higher accuracy than the pulsed measurements. The discrepancies in our measurements can possibly be attributed to the finite linewidth of the pulsed laser or to the presence of some amount of ASE. For reliable LIDAR results these measurements must be reconciled, and further progress will be reported.

1. J.B. Mason, Appl. Opt., 14, 76-78 (1975).

2. H.I. Heaton, J. Quant. Spectrosc. Radiat. Transfer 16, 801 (1976); Astrophys. J. 212, 936 (1977).

3. G.K. Schwemmer and T.D. Wilkerson, Appl. Opt., 18, 3539-3541 (1979).

4. C.L. Korb and C.Y. Weng, J. Appl. Meteor. 21, 1346-1355 (1982); Appl. Opt., 22, 3759-3770 (1983); Proc. CLEO, 57, Phoenix, Ariz., (April 1982).

5. T.D. Wilkerson, G.K. Schwemmer, L.J. Cotnoir, and U.N. Singh, Proc. 13th Internat. Laser Radar Conf. 80-83, Canada (Aug 1986).

6. B.E. Grossmann, U.N. Singh, N.S. Higdon, L.J. Cotnoir, T.D. Wilkerson, and E.V. Browell, Appl. Opt., 26, 1617-1621 (1987).

7. K.J. Ritter and T.D. Wilkerson, J. of Molec. Spectrosc. 121, 1-19 (1987).

FIG. 1 : LIDAR EXPERIMENTAL SET-UP
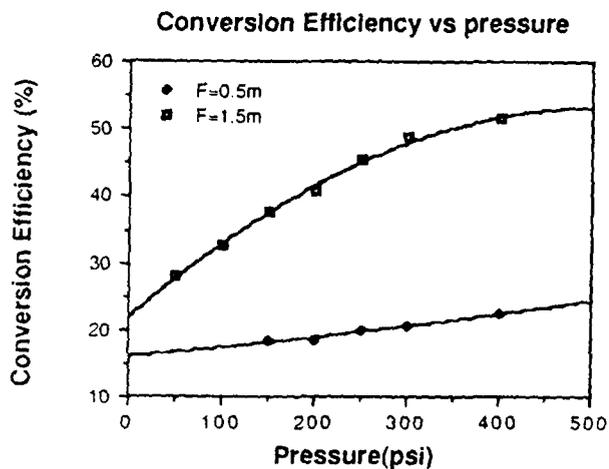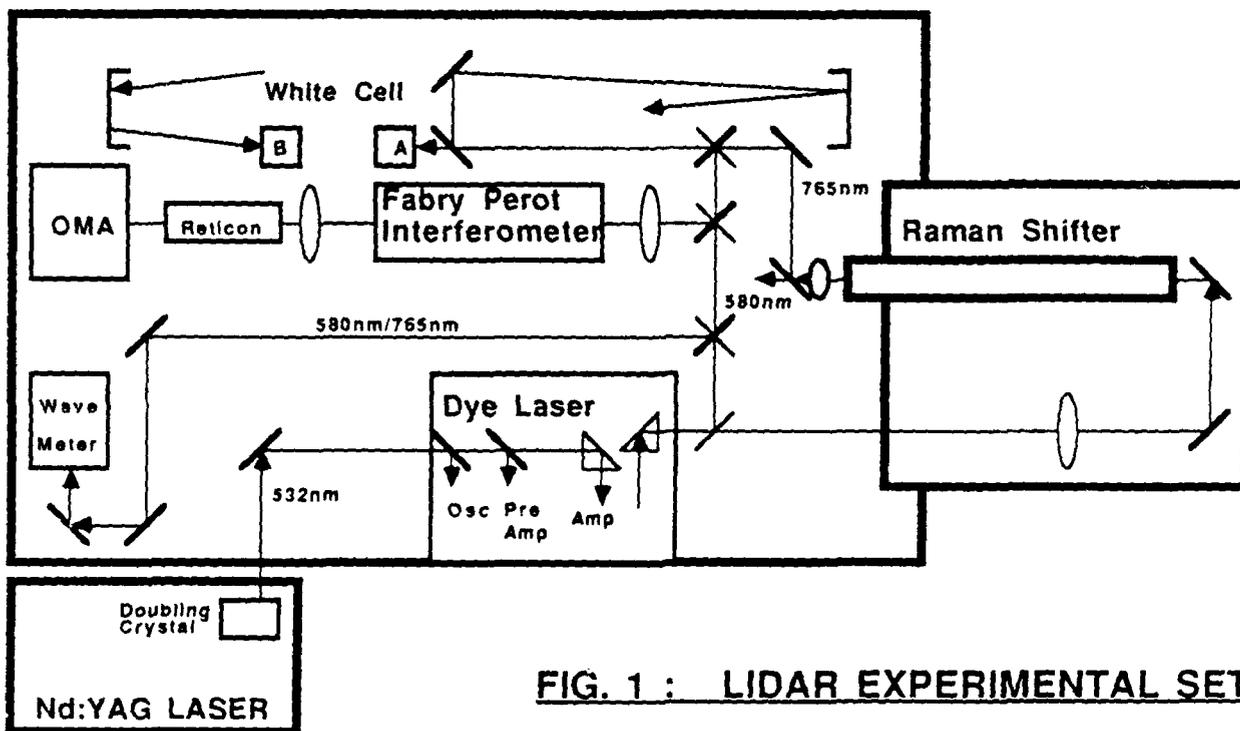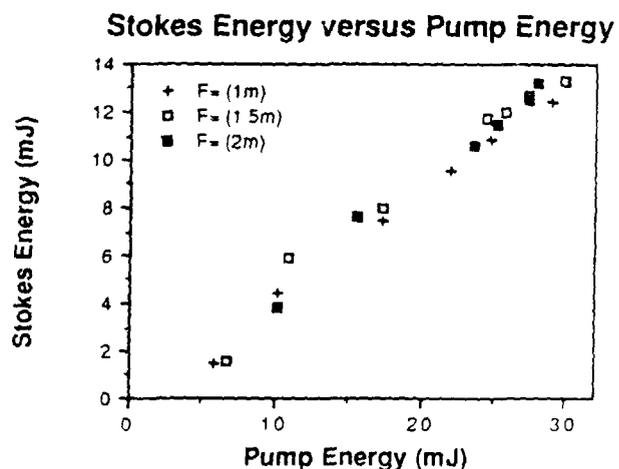
Figure 2(a)

Figure 2(b)

Oxygen Absorption Measurements

$S/\pi\,\gamma$ (10^{-24} cm^2 mol^{-1})
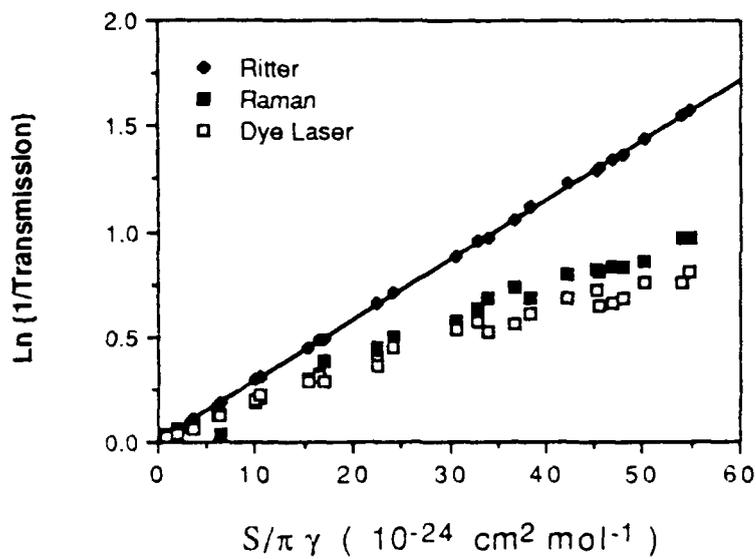
Figure 3(a)

Oxygen Absorption Measurements

Log_{10} [$S/\pi\,\gamma$] (10^{-24} cm^2 mol^{-1})
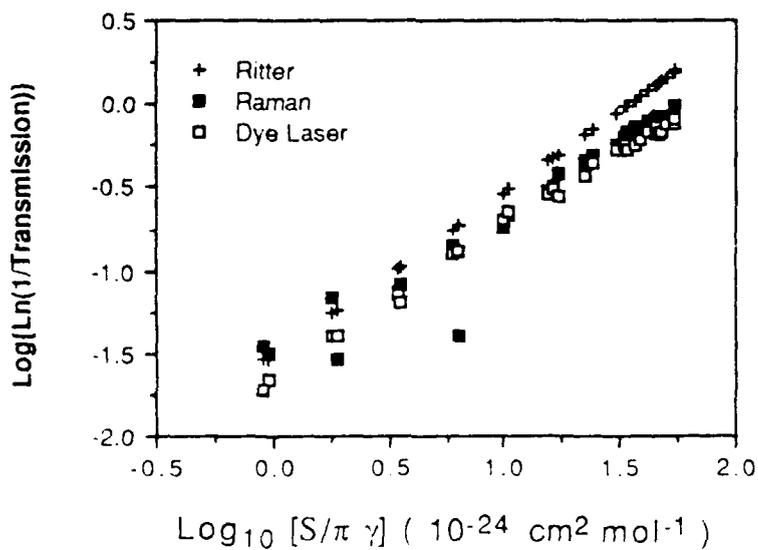
Figure 3(b)

CO$_2$ LASER PRE-AMPLIFIER FOR LIDAR APPLICATION

Kinpui Chan[*] and Jack L. Bufton

Goddard Space Flight Center
Greenbelt, MD 20771

A laser pre-amplifier based on the multiple-pass geometry inside a low-pressure, pulsed CO$_2$ laser discharge has been developed for lidar applications near 10 μm wavelength. The laser pre-amplifier produces a gain pulse on the order of 100 μsec duration with peak power gains as large as 1000 (30db). Design considerations, predicted preformance, and initial laboratory test results for this laser pre-amplifier have been previously presented (refs. 1 & 2). In this paper we report the results of a series of laboratory tests on the pulsed gain and gain stability when this laser pre-amplifier is used with a CO$_2$ TEA laser source. These measurements form the basis for application of the pre-amplfier to enhanced direct-detection in a CO$_2$ lidar.

Figure 1 is a schematic diagram of the CO$_2$ laser pre-amplifier test apparatus. The laser pre-amplifier developed at Pulse Systems Inc. consists of a 0.5 m long plastic tube with end-housings sealed for low pressure operation. Zinc selenide optical windows at each end of this tube provide input and output ports. The input port also has a 4X Galilean beam condenser telescope. Two optical flats, that are separated by an invar rod structure and are tilted toward each other at a 2° angle, provide a 7-pass optical cavity within the uniform, rectangular cross-section plasma of dimension 1.5 cm by 4 cm between electrodes. Total length of the optical gain region is 2.1 m. The triode discharge geometry uses a resistor array, a wire screen, and a pair of solid slabs as electrodes. The initial high-voltage discharge between the resistor array lead ends and the wire screen is followed by the main discharge of 1.4 to 2.8 kV between the wire screen and the slab electrodes.

Laser pre-amplifier operation can be achieved with a variety of operating pressures, gas mixes, and discharge voltages. Operating pressure in the range of 20 torr to over 100 torr is maintained with a vacuum pump and a flowing-gas mixture of helium, nitrogen, and carbon-dioxide. A typical TEA laser gas mixture of 70% He, 15% N$_2$, and 15% CO$_2$ works quite well. Pulse energy into the laser discharge in the range of 1 - 4 joule is varied by selecting discharge capacitors of 0.5 - 2 μf and using a variac to control input ac power for the high voltage transformer circuits. Variac voltage is typically set for the maximum value which still provides a uniform laser discharge. Continued increases in voltage above this value result in a free-running condition where discharges occur without a trigger input. At large voltage input into the discharge self-lasing can also occur if even small amounts of optical feedback are present.

The CO$_2$ TEA laser is modified to accept a low-pressure gain cell inside the laser cavity. The gain cell has an optical length of 15 cm and a measured gain of 2 at 15 - 20 torr operating pressure. It is based on the same low-pressure, low-voltage pulsed discharge used in the pre-amplifier. The hybrid CO$_2$ laser TEA laser is designed to confine TEA laser output to a narrow bandwidth of about a hundred MHz near CO$_2$ laser line center rather than the 3 - 4 GHz pressure-broadened gain envelope of TEA lasers. This is necessary since the laser pre-amplifier has a similar narrow bandwidth of amplification for its low operating pressure. The shape in frequency space of the optical gain function for both units is approximately Gaussian and is centered on the laser line. Typical full-width-at-half-maximum (FWHM) at 20 torr is 135 MHz. At 60 torr this optical bandpass increases to 330 MHz and to 650 MHz at 120 torr.

On the detector end of the pre-amplifier tube a positive lens is used to capture the amplified signal and

focus it onto a HgCdTe photoconductor detector element. Typical detector element size of 0.5 mm provides a normalized detectivity, $D^* = 10^{11}$ cm$^{1/2}$Hz$^{1/2}$/watt at a bandwidth of 5×10^6 Hz. The combination of detector size and lens focal length of 105 mm results in a field-of-view (f.o.v.) matched to $2a/L_{eff} = 4.8$ mrad, where 2a and L_{eff} are respectively the diameter of the pre-amplifier input port and the effective optical path length from the input port to the detector. A larger f.o.v. would collect no more amplified lidar signal but would collect more amplified spontaneous emission (ASE) power.

Laser gain pulses are observed at the output of the pre-amplifier on the various P and R branch lines in the 9.4 μm and 10.4 μm bands. Optical gain is primarily a function of pre-amplifier gas pressure and energy into the discharge. At low gas pressures (i.e. 30 - 40 torr) the gain is relatively high, achieving the largest peak gains for a given discharge energy. This results from a concentration of energy into the narrow optical bandwidth provided by the pressure-broadened CO_2 gain envelope. Optical gain decreases for CO_2 lines in the wings of each P & R branch in the same manner as it would for the output of a CO_2 laser source. The decrease in peak optical gain at the higher operating pressures can be compensated somewhat by increasing discharge energy input.

The temporal shape of the optical gain pulse is Lorentzian. Pulse duration is determined primarily by laser gas operating pressure. At the low pressure end near 20 torr, the pulse width is at a maximum near 250μsec FWHM. At higher pressures the pulsewidth falls inversely with pressure to less than 50 μsec FWHM at 120 torr. The pulse risetime is also much shorter at higher presssures achieving values near 5 μsec at 100 torr. Amplified spontaneous emission (ASE) power is readily observed on the detector at the pre-amplifier output, even in the absence of a TEA laser pulse input. Its time dependent waveform, identical to that of the optical gain pulse, has a peak power of about 1 nwatt. On the other hand, no increase is observed during the gain pulse in detetector noise level due to ASE noise.

Figures 2 and 3 report measured peak optical gain vs. time for CO_2 TEA laser pulses of about 200 nsec gain-spike duration. Operating wavelength was the 10P(20) line at 10.59 μm. Both the pre-amplifier and the gain cell were triggered together at a 1 Hz rate. The TEA laser trigger was delayed to coincide with the maximum of the pre-amplifier gain pulse. This maximum was evident from the peak of the ASE pulse. Measured peak gain of nearly 700 is noted in Fig. 2 for operating pressures of 40 torr and 15 torr respectively for the pre-amplfier and gain cell. The measured peak gain is consistent with a small-signal amplification of over 3%/cm for the 2.1 m optical gain length of the pre-amplifier. The decrease of gain with pre-amplifier pressure is illustrated in Fig. 3 where peak gain is about 200 for 80 torr pressure. The most dramatic difference in the time-history of optical gain in these two figures is the reduction in the periodic variation (approximately 100-second) in gain from a nearly 7:1 change at 40 torr in Fig.. 2 to only a 1.7:1 change at 80 torr in Fig. 3. This gain drift with time is likely a result of temperature-induced drifts in TEA laser output frequency. The reduction in peak-to-peak gain drift at the higher pressure is obviously a result of the wider pre-amplification bandwidth at that pressure.

Short-term gain stability is characterized by the standard deviation of gain with-respect-to the mean gain. Statisitics for thirty pulses near the peak gain in Fig. 2 gave a mean of 580 and a standard deviation of 56.3. For sixty pulses in Fig. 3 the mean and standard deviation are respectively 178 and 21.8. Both cases exhibit a short-term gain modulation of about 10%. Some of this variability may be due to limitations in our gain measurement procedure, which involved readings of peak gain from an oscilloscope display of each gain pulse. It is noteworthy that when the low pressure gain cell was disabled, amplification of the TEA laser pulses was highly variable. Measured short-term gain modulation was at least 35% and was superimposed on a 10:1 or greater periodic variation.

Despite the flexibility in achieving a variety of optical gains and bandwidths, the PSI laser pre-amplifier design is fixed at a given input aperture size, bore-diameter, and 7-pass folded optical

path. These physical size constraints result from practical choices and interactions among electrode spacing, gas pressures, and discharge voltages. The physical constraints have an important effect not only on the overall gain performance of the pre-amplifier, but also on its optical coupling to the collector telescope and the infrared detector. The pre-amplifier input aperture diameter (2a) is fixed at 12.7 mm. The collecting telescope in a LIDAR receiver must achieve beam reduction to this size while also providing a large diameter collector. The result is a trade-off in terms of collector telescope diameter and its field-of-view (f.o.v.). Calculations based on collimated beam propagation through the pre-amplifier predict a compromise is reached in the neighborhood of $A \cdot \Omega = 6$ cm $\cdot$ mrad, where A is the diameter of the collector telescope and Ω is the full angle ($1/e^2$) lidar divergence angle. At this operating point the optical insertion loss is about a factor of four.

In CO_2 lidar applications the net optical gain of 10 - 100 after insertion loss is expected to dramatically improve the performance of a direct-detection receiver. Pulse-to-pulse gain variability and gain drift can be minimized by operation at higher pre-amplifier pressures, but gain monitoring will be required on a pulse-to-pulse basis to achieve acceptable lidar system performance. Gain drift could also be reduced by frequency stabilization of the CO_2 TEA laser, but this would add undesirable instrument complexity. The increase of optical gain with time on the leading edge of the Lorentzian gain pulse could be used to achieve a time-dependent gain as partial compensation for the range-squared signal reduction in lidar returns. Further assessment of lidar application of the CO_2 laser pre-amplifier will require field trials.

Figure 1 CO_2 laser pre-amplifier test apparatus.
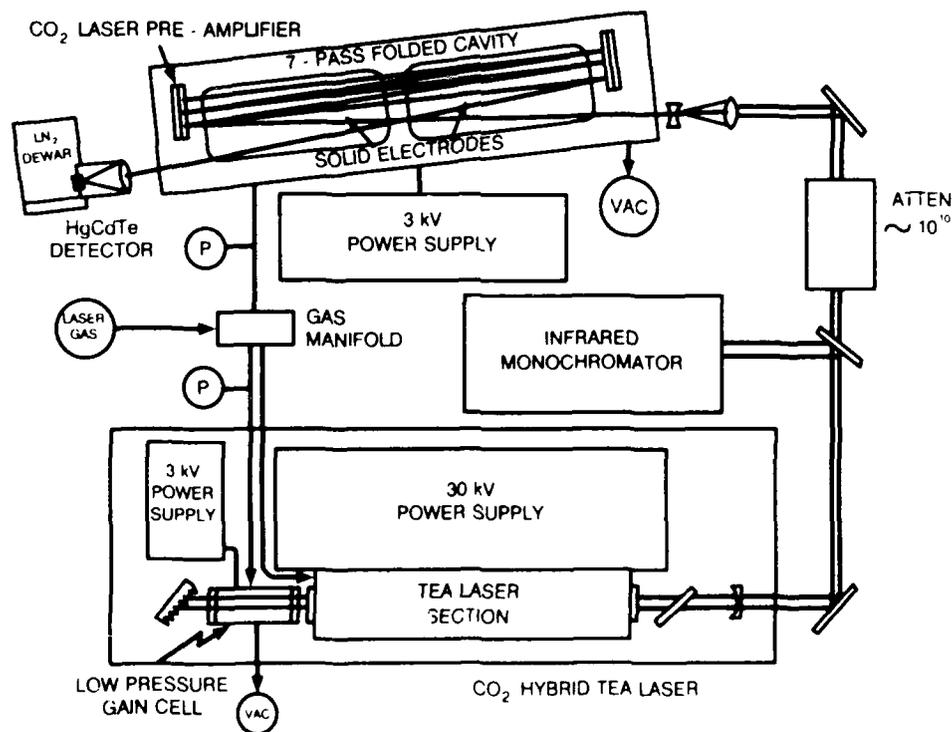
Measured CO_2 laser pre-amplifier optical gain for hybrid TEA laser pulses at 10.59 μm.
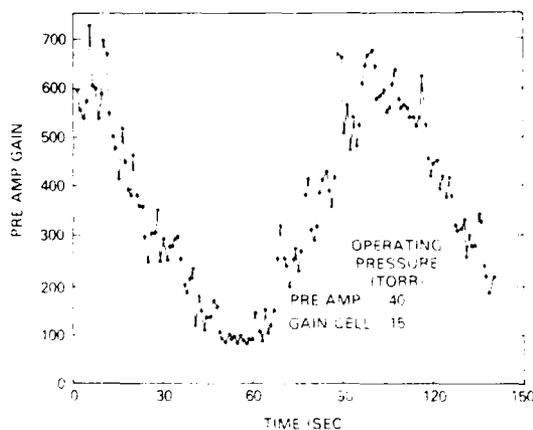
| Figure 2 | Figure 3 |
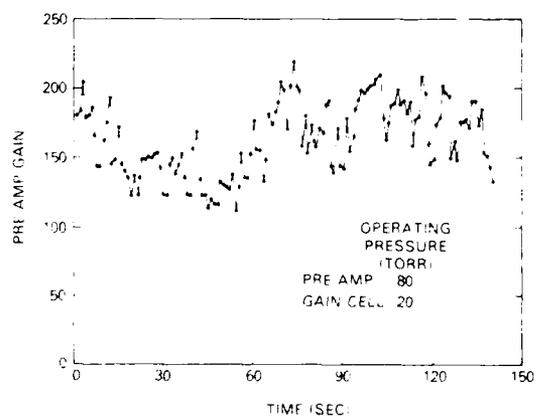
* University Research Foundation, Greenbelt, MD, 20770

ACKNOWLEDGEMENTS

REFERENCES:

1.   McLellan, E.J., Fisher, R., and Bufton, J.L., "Design of a CO_2 Laser Pre-Amplifier for Improved LIDAR and Rangefinder Sensitivity", Paper ThI3, Conference on Lasers and Electro-Optics, June 19-22, 1984, Anaheim, CA.

2.   McLellan, E.J., Fisher, B., Thomas, D.K., and Bufton, J.L., "Optical Pre-Amplifier Performance for CO_2 LIDAR Applications", Paper FB3, Conference on Lasers and Electro-Optics, June 9-13, 1986, San Francisco, CA.

LOW-PRESSURE GAIN-CELL LASER-DETECTOR OPERATION
WITH A CO_2 TRANSVERSELY EXCITED ATMOSPHERIC (TEA) LASER

Jan E. Van der Laan
Electro-Optics Systems Laboratory
SRI International
Menlo Park, CA   94025

The recent development of a low-pressure CO_2 gain-cell[1] preamplifier for optical receivers has stimulated renewed interest in the technique in the lidar community. Early work in this area[2] indicated that a gain factor of only 2.5 could be achieved using a 72-cm long gain cell. Because low gain did not appear to justify the added cost and complexity to a lidar system, interest in the technique decreased.

In 1985 Pulse Systems, Inc. (PSI) introduced the LDP-30 laser detector preamplifier and advertised it for use in laser range-finder receiver applications. Evaluations of PSI's LDP-30 operating at 30 torr show that it typically produces optical gains up to 1000 for pulse durations of 100 μs. This improvement in gain over previous work is achieved by using transverse discharge, low-pressure, and low-voltage CO_2 technology developed by PSI in a 7-pass 40-cm cell configuration (total gain-path length of 280 cm). The previous work was performed using conventional multimode longitudinal-discharge lasers.

To obtain the gains suggested, the laser signals being amplified must be generated by a laser with a line width less than or equal to the gain bandwidth of the amplifier gain cell. This requirement implies that a low-pressure CO_2 laser must be used as the source. Indeed, the LDP-30 characterization studies at PSI were conducted using a PSI low- pressure laser as the source.

Although the gain described by PSI is impressive, it should be understood that there are some fundamental problems using low pressure lasers in lidar and range-finder applications. First of all, most lidar applications and certainly range-finder use require reasonably high range resolution, which is ultimately determined by the laser

---

[1] Richard Cunningham, "Gain Cell Boosts Range of CO_2 Lidar", Laser and Applications, (September 1983). (Reports on work by Ed McLellan of Pulse Systems, Inc.)

[2] J. F. Lotspeich. "CO_2 Laser Preamplifier Capabilities for Low-Level 10.6-)m Direct-Detection Receivers", IEEE, J. Quant. Elect., Vol. QE-13, pp. 371 (1977).

pulse width. Currently used CO_2 TEA laser range-finders have pulse widths on the order of 100 ns. Low pressure lasers on the other hand tend to have very long pulse widths because of the long temporal gain of the plasma at low pressures (i.e., FWHM gains in excess of 200 μs at very low pressures, e.g., 20 torr). Clearly, low-pressure lasers are not appropriate for use in direct-detection range-finders unless some means is incorporated to reduce the pulse width. Several techniques are available to reduce the pulse width, but all involve a sacrifice in power. A trade-off study of the loss in power versus the gain achieved using the gain-cell preamplifier is required to resolve this issue.

A different approach for achieving the resolution required is to use currently available TEA laser range-finders and a low pressure gain cell in the receiver. Here, the problem is somewhat different in that the TEA laser has a very short pulse width because of the effects of atmospheric pressure (760 torr) on the temporal-gain characteristic and at the same time the effect of pressure on the gain bandwidth increases the laser line bandwidth to approximately 3 GHz (FWHM). The effect of this wide line width operated with a low-pressure gain cell is not difficult to see; because the TEA laser energy is distributed over 3 GHz and the preamplifier gain cell amplifies only a limited portion of this bandwidth, the net gain should be significantly lower than reported. Work being performed at SRI International using a TEA laser operating on the 10 μm R-22 transition, and low-pressure gain cell, however, indicates that gains in the order of 300 can be achieved. This gain appears to be higher than anticipated considering the narrow line width of the LDP-30 relative to the pressure-broadened TEA laser. Analysis of the laser configuration, however, explains this apparent anomally. Although the TEA laser operates in the TEM_{00} mode, the short gain length of the laser (23 cm) will support a number of axial modes. The effect of these axial modes have, in the frequency domain, is to redistribute the spectral power over the 3-GHz gain bandwidth into a comb of six lines having a FWHM gain of approximately 50 MHz as illustrated in Figure 1. In our test, the LDP-30 is operated at 80 torr, which provides a gain bandwidth of 440 MHz at the FWHM (linewidth derived from Voight line profiles). By adjusting the TEA laser grating to center the comb on the LDP-30 gain line as shown in Figure 1, maximum amplification can be achieved for that axial mode. Because our gain estimate of 300 is relative to the total unamplified energy, which inclues all axial modes, the single axial mode maximum gain is not fully realized, but it is much greater than would be achieved if the energy were evenly distributed over the full 3-GHz bandwidth. The high gain observed in our evaluations, however, cannot be fully employed using our current TEA laser system because of stability problems. Pulse-to-pulse frequency shifts of the aligned axial mode relative to the gain-cell center frequency results in fluctuation of the gain, which decreases the signal-to-noise ratio (SNR). The gain fluctuation in our setup is the noise-limiting mechanism rather than background or spontaneous emission noise. An example of the amplified TEA laser pulses is shown in Figure 2. In this example, ten amplified pulses and one unamplified pulse are observed by multiple exposure to illustrate the peak-to-peak fluctuation of the signal. Statistical evaluation indicates that the

unamplified SNR is 50:1, while the amplified SNR is 10:1. Calculations based on the line width of the axial modes and the LDP-30 at 80 torr suggest that a shift of 120 MHz of the axial mode frequency would account for the lower SNR. Although the stability is critical, once aligned on a single axial mode, the laser held that single axial mode for extended periods, which allowed other parameters to be measured. Among these measurements were temporal gain characteristics, which are shown in Figure 3, and a gain linearity evaluation shown in Figure 4.
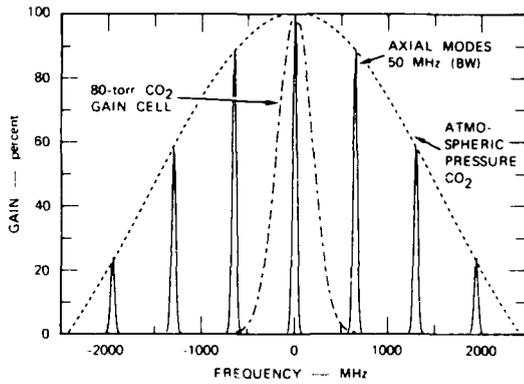
FIGURE 1 CO_2 PLASMA GAIN BANDWIDTH
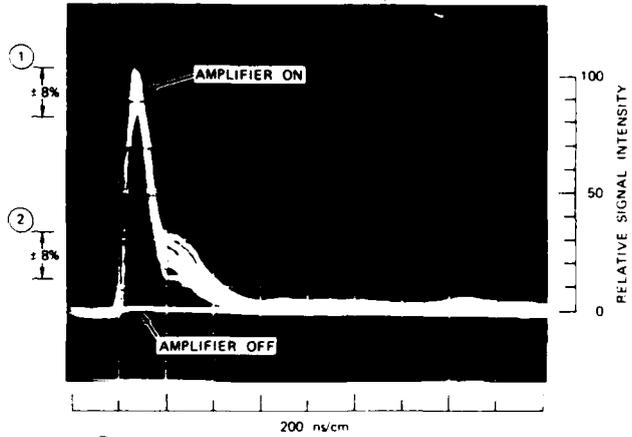
FIGURE 2   AMPLIFIER ON vs. AMPLIFIER OFF SIGNAL INTENSITY—10 SHOTS OVERLAY
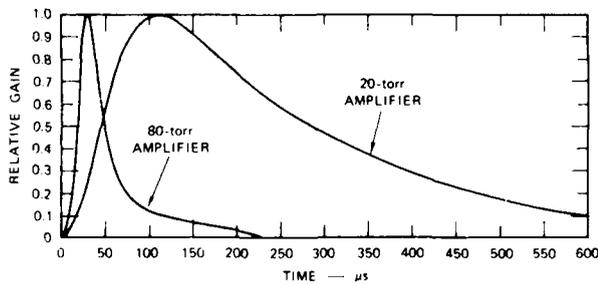
FIGURE 3   LOW PRESSURE AMPLIFIER TEMPORAL GAIN DISTRIBUTION
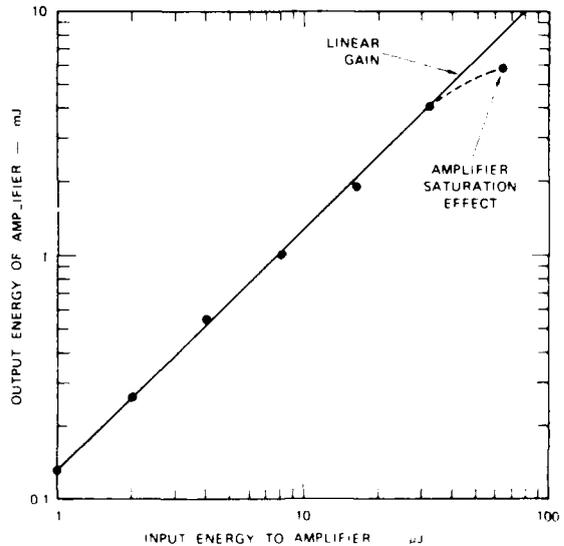
FIGURE 4   AMPLIFIER OUTPUT vs. INPUT ENERGY SHOWING SATURATION EFFECT

The temporal gain for the LDP-30 is shown for two presures, 80 and 20 torr. The 20 torr data was provided by PSI. This illustration clearly shows the pressure effects on the temporal-gain distribution. The FWHM gain is 30 μs at 80 torr and 240 μs at 20 torr.

The linearity data shown in Figure 4, indicates that the amplifier provides linear gain with inputs as high as 32-μJ. At 64-μJ input corresponding to an output of 5.8 mJ, saturation effects are observed. The exact mechanism for this saturation has not been determined because the purpose of the test was to evaluate the linearity at low levels of input. Not shown on this illustration, but obtained in subsequent test, two orders of magnitude more attenuation were added to the input signal, which extended the available data down to 0.03-μJ input. With the current instrumentation, we are unable to measure below this level with accuracy. It is recognized that during the linearity tests a gain factor of 130 was observed. This lower gain factor indicates that the laser was not aligned for the optimal axial mode during this measurement. This finding should not have any effect on the linearity of the data except that the saturation effects occur at a higher input level.

In summary, our evaluation to date using a low-pressure gain cell with a TEA laser indicates higher than anticipated amplifier gains can be achieved but at cost of SNR. The noise mechanism that limits our measurements was laser frequency instability. No attempt was made to stabilize our laser so it is not known how serious this problem is. The results suggest, however, that by reducing the TEA laser cavity length, thereby reducing the number of axial modes, the achievable gains may be even higher.

For range-finder applications in which a reasonably high SNR can be tolerated, the high gains obtainable using the TEA laser and low-pressure gain cell receiver preamplifier are very encouraging. For applications in DIAL measurements a better understanding of the system noise is needed. Additional work in this area is being conducted at SRI, which will include actual receiver measurements over a lidar range.

This work is being performed as a SRI IR&D effort with additional funding and support under Contract DAAK11-82-C-0158 with the U.S. Army Chemical Research, Development and Engienering Center, Aberdeen Proving Grounds, MD.

LASER SOURCES AND SENSITIVITY CALCULATIONS FOR A NEAR-INFRARED DIAL SYSTEM

Martin J T Milton, Barrie W Jolliffe, Roger H Partridge, and Peter T Woods
Division of Quantum Metrology
National Physical Laboratory
Teddington, Middlesex, TW11 OLW, UK

The applications of DIAL systems operating in the near ultraviolet and visible spectral regions are limited to the small number of species that absorb in those regions. However, the infrared spectral region offers the possibility of detecting a much larger number of gases, including most of the hydrocarbons. Although many DIAL systems have been constructed for use in the mid-infrared (at 10 μm in particular), relatively few attempts[1-4] have been made to use the near-infrared despite the large number of strong absorption lines, particularly around 3 μm. The design of a direct-detection DIAL system to operate in this region involves a considerable number of differences from DIAL systems operating in other spectral regions. We consider here: the spectroscopy of target gases, possible laser sources, and the sensitivity and accuracy that might be expected from such a system, with particular consideration to its use for measuring hydrocarbon concentrations at the ppm level in the atmosphere.

The Spectroscopy of Target Gases

Figure 1 is an atmospheric transmission spectrum of part of the near-infrared measured with a high resolution Fourier-transform spectrometer. It can be seen that the region 3.59 μm to 4.39 μm (2785-2280 cm^{-1}) is an atmospheric "window", with transmission in excess of 95% even for path lengths of several hundred metres. Figures 2 and 3 show the spectra of ethylene and butane, both measured atmospherically broadened by nitrogen. Both of these species, in common with most other hydrocarbons, exhibit absorption within the region 3.23 μm to 3.60 μm (2775-3100 cm^{-1}). The ethylene spectrum consists of a number of lines about 1 cm^{-1} wide and 5 cm^{-1} apart. This kind of structure is characteristic of other light hydrocarbons (for instance methane and ethane). The spectrum of butane shows no such structure (when measured with a resolution of 0.01 cm^{-1}), but only broad features with widths of the order 10 cm^{-1}. This is characteristic of other heavy ($>C_3$) hydrocarbons.

Three conclusions can be drawn from these properties of the spectra:

(i)   Speciation of light hydrocarbons should be possible with a source linewidth of < 0.5 cm^{-1}.
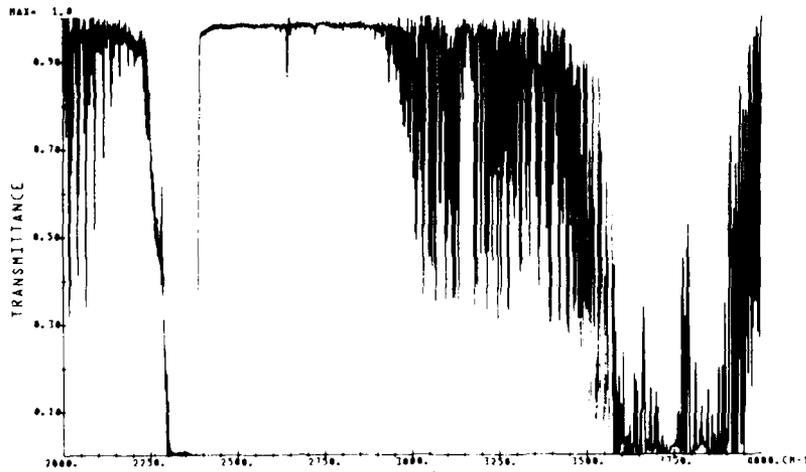
Fig.1. Atmospheric Transmittance 26 °C, 32 % RH, 60m path
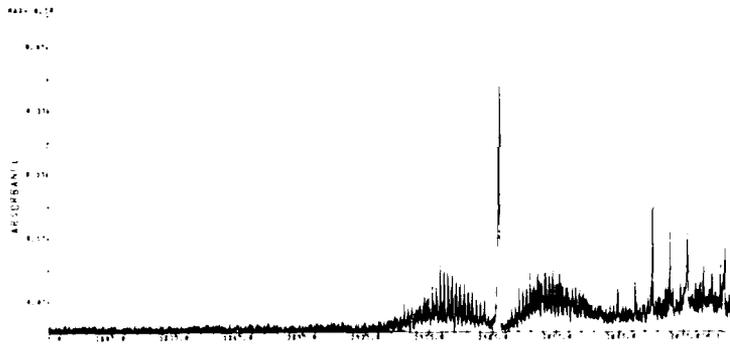
Fig.2. Ethylene (0.1 torr) atmospherically broadened
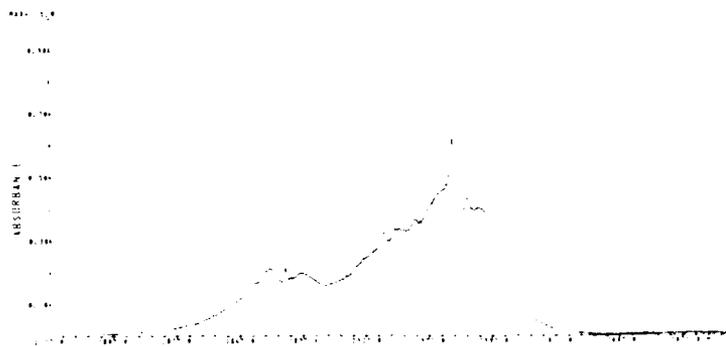
Fig.3. Butane (0.1 torr) atmospherically broadened

(ii) Speciation of heavy hydrocarbons is unlikely to be possible with any source linewidth.

(iii) Sources operating beyond the 3.59 ~ 4.39 μm window require a linewidth sufficiently small to avoid water-vapour lines, particularly for measurements over long path lengths.

Sources and Sensitivity

It is clear from these observations that two approaches can be taken towards the design of a mid-infrared source for DIAL measurements of hydrocarbons:

(i)   A broad linewidth source for measurements of heavy hydrocarbons, with a linewidth only limited by the need to avoid water vapour lines, but not capable of speciation.

(ii) A narrow linewidth source ($<$ 0.5 cm^{-1}) capable of speciating light hydrocarbons.

Clearly the linewidths and wavelengths required determine the type of laser system that can be used and the energy available for transmission. A pulse length of between 10 and 12 nsec is required, in order to give a range-resolution of approximately 3 metres.
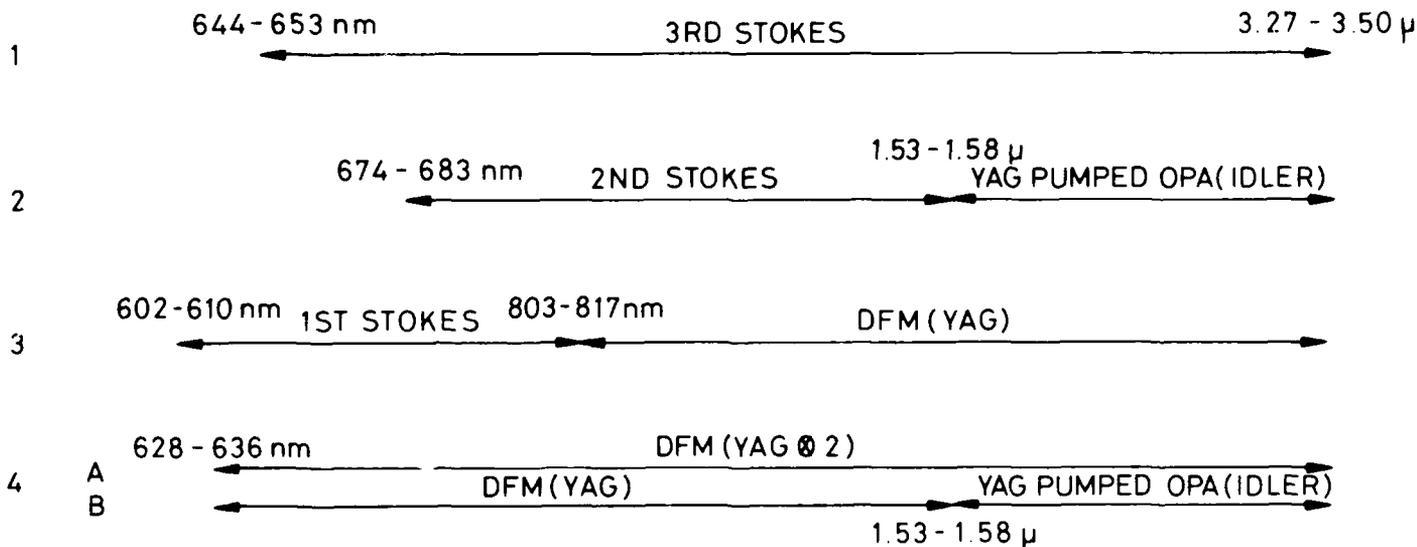
Fig. 4. Methods for generating near-infrared from a tunable dye laser using SRS and mixing.

The schemes considered here for generating pulsed tunable near-infrared laser radiation to meet these specifications all use Nd:YAG lasers as the primary laser energy source and visible dye lasers to introduce wavelength tunability. Figure 4 shows some possible methods for generating near-infrared using Stimulated Raman Scattering (SRS) and mixing. In this case we have only considered SRS in hydrogen, because of its high gain, large frequency shift and narrow linewidth. The possible mixing processes considered are Difference Frequency Mixing (DFM) and Optical Parametric Amplification (OPA). Although both of these processes rely upon the same nonlinear interaction within a crystalline medium, they differ in that for OPA, the highest frequency input beam is also the most intense, but for DFM the highest frequency input beam is the least intense. This distinction is only significant in the ideal case in which the process is saturated and all of the highest frequency input photons are downconverted. Hence, in the saturated case, OPA is only limited by the high intensity (fixed frequency) "pump", whereas DFM is limited by the "low" intensity (tunable) input.

Not only do the possible output energies of the various schemes vary, but their output linewidths also differ. For dye and YAG laser linewidths[5] of 0.1 cm^{-1} and 0.7 cm^{-1} respectively, the linewidth expected from scheme 1 is approximately 0.1 cm^{-1}, from schemes 2 and 3 is approximately 0.8 cm^{-1} and from scheme 4 is approximately 1.5 cm^{-1}.

Calculations of range and sensitivity of a DIAL system based on some of these infrared sources will be presented.

References

1. T. Henningsen, M. Garbuny and R.L. Byer, "Remote Detection of CO by Parametric Tunable Laser", Appl. Phys. Let. 24. 242 (1974).

2. D.J. Brassington, "Remote Pollution Detection using an Optical Parametric Oscillator Source", Central Electricity Research Laboratories, Laboratory Note RD/L/N 124/77 (Sept 1977).

3. R.A. Baumgartner and R.L.Byer, "Continuously Tunable IR Lidar with Applications to Remote Measurements of SO_2 and CH_4", Appl. Opt. 17, 3555 (1978).

4. E.Galletti, E.Zanzottera, S. Draghi, M. Garbi and R. Petroni, "Gas Correlation Lidar for Methane Detection" 13th International Laser Radar Conference, Toronto 1986, NASA CP 2431.

5. Measurements made on a Quantel YG 481C YAG laser and TDL IV pulsed dye laser.

A Simple System for Frequency Locking Two CO_2 Lasers

Douglas C. Draper, J. Fred Holmes, John Hunt, and John Peacock
Oregon Graduate Center
Department of Applied Physics and Electrical Engineering
19600 N.W. Von Neumann Drive
Beaverton, Oregon 97006-1999

SUMMARY

An optical heterodyne system requires a local oscillator which tracks the frequency of the transmitter. Otherwise the heterodyned signal, which has a frequency equal to the difference between the transmitted and local oscillator frequencies, would drift outside the bandwidth of the receiver.

In some remote sensing systems the same laser is used for both the transmitter and the local oscillator. One or both of the frequencies may be shifted to provide the desired difference frequency. Acousto-optic or electro-optic modulators can be used to shift the frequency. For systems where two different lasers are used a method is needed to keep the lasers locked at the desired frequency difference.

The system reported here accomplishes the locking without elaborate tracking systems using only the received signal to control a built in cavity length transducer. No modification of the normal optical paths are required. This system provides good isolation between the optical signals and requires only the addition of some simple electronic circuits.

The optical remote sensing system is shown in Fig. 1. The transmitter laser beam is expanded 30 times, and the local oscillator beam is expanded five times. The return signals are intercepted by one-inch mirrors and combined with the local oscillator using a beam splitter and then focused onto the HgCdTe optical detector. Quarter-wave plates are used to produce circularly polarized beams. The combination of the local oscillator and target signal fields will have a heterodyne component with a frequency equal to the difference between the two optical frequencies. This component which represents the heterodyned receiver signal can be used to control the optical frequency of either laser.

The lasers are standard three and five watt production models manufactured by Laakmann Electro-Optics, Inc. They are tunable by means of a diffraction grating which is manually adjusted with a micrometer dial. A canty length tuning mechanism is provided by a piezoelectric length transducer on which the rear laser mirror is mounted. An electrical signal applied to the transducer varies the laser frequency in response to the changing cavity length. After the two lasers are brought to the same spectral emission line by manually adjusting the diffraction grating, the system will maintain control by

detecting the frequency difference from the detector and applying a correcting voltage to one of the length transducers.

Figure 2 shows the control electronics. The received signal is amplified using existing signal processing circuitry and the frequency is detected by a phase locked loop (PLL). The PLL also removes amplitude variations on the signal before detection. The detected signal is amplified to provide large control loop gain for small frequency errors. Special filter circuits are needed to compensate for the response of the built in cavity length transducer which can cause instability.

The measured laser response to electrical control inputs as a function of the input frequency is shown in Fig. 3. The lasers respond at 20 MHz per volt at low frequencies. Of particular interest is the pronounced resonance at 3.4 kHz evidenced by the extreme increase in response and phase shift at this frequency. The response is that of a second order system with a damping ratio of 0.025 and is due to the piezoelectric length transducer in the laser. Because of this response the laser has a natural tendency for frequency modulation (FM) at the resonant frequency of 3.4 kHz, and any disturbances in the laser frequency at rates higher than the resonant frequency are virtually impossible to control. This limitation precludes the use of the transducer for phase locking.

To reduce the effects of the natural resonance, a notch filter at 3.4 kHz is added. An additional filter is also used to improve stability. The filter has a double pole at 4 Hz and a zero at 100 Hz. The double pole causes the control system gain to decrease rapidly with increasing frequency, and the zero reduces the phase shift at higher frequencies. A maximum control loop gain of 120 dB is obtained using this compensation. With these conditions the theoretical steady state error to a unit step input is 10^{-6} which for a frequency drift of 100 MHz translates to just 100 Hz error.

FM is observed from 5 kHz to 50 kHz on this system which represents 0.1% to 1% of the 5 MHz difference frequency. Any FM that occurs in either laser due to inherent laser instability or external disturbances such as vibrations cannot be removed by the system if the FM rate is above the 3.4 kHz maximum response of the length transducer. Any significant improvement in FM for these higher rates would require a frequency control element capable of responding to higher frequencies, such as a higher frequency transducer or electro-optic or acousto-optic modulators inserted in the laser beam. The long term steady state error in the difference frequency is of the order of 100 Hz or about 0.01 % of the 5 MHz control frequency. This drift is mostly due to the continual changes in the laser emission frequencies in response to temperature variations. The lasers drift 900 MHz per degree C and are controlled to within plus or minus 0.1 degree C by water cooling. Therefore a 0.1 degree change in temperature represents a 90 MHz change in laser frequency. The expected steady state error is 10^{-6} times 90 MHZ or 90 Hz which is consistent with the above measurement.

The performance reported has been demonstrated in the laboratory in a simulated field environment using a rotating diffuse target at 10 meters from the transmitter to

generate a fully developed speckle pattern at the receiver. The target rotation, which simulates the effect of turbulence, causes the speckle pattern from the target to have large fluctuations in received optical signal with random phase. Based on the detector sensitivity the received power level was measured at 10^{-12} watts. A similar system using a single laser and a stationary diffuse target at 1000 meters in an actual field environment produces a similar power level and variation at the receiver input with moderate wind and turbulence. Actual field tests of the two laser system are planned this summer.

This work was supported by the Army Research Office.
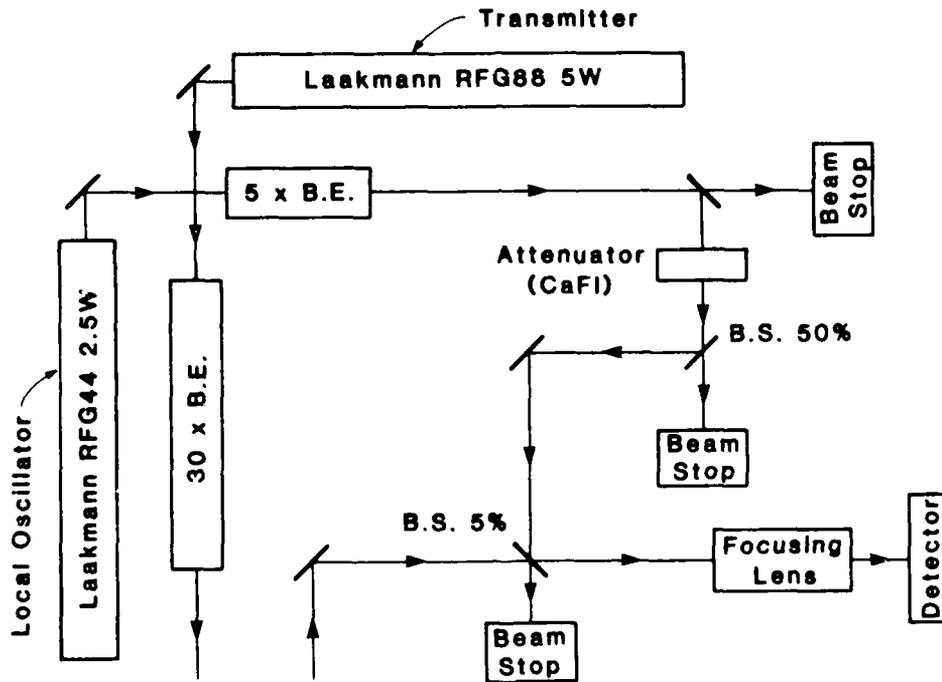
Figure 1 - Optical Remote Sensing System
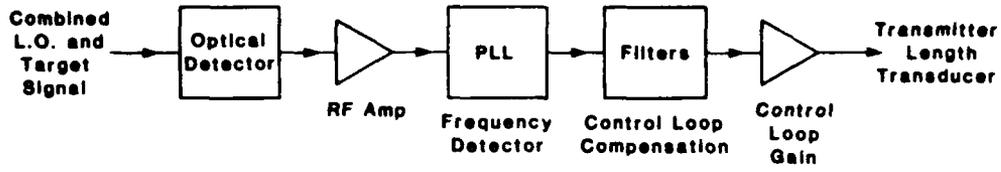
Figure 2 - Control Electronics
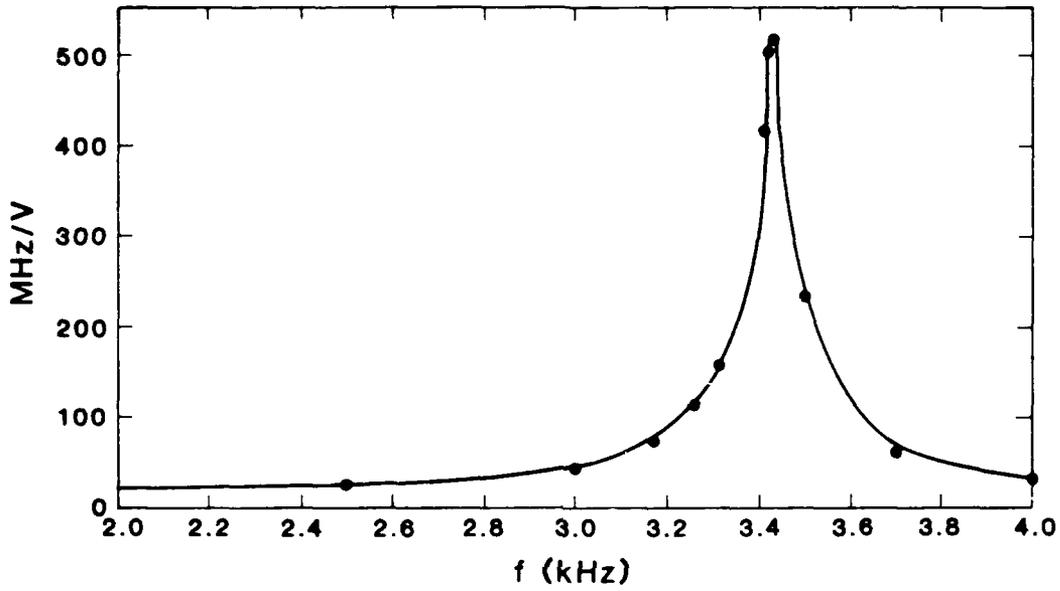
Figure 3a. - Frequency Response of Laser Due to Cavity Length Transducer
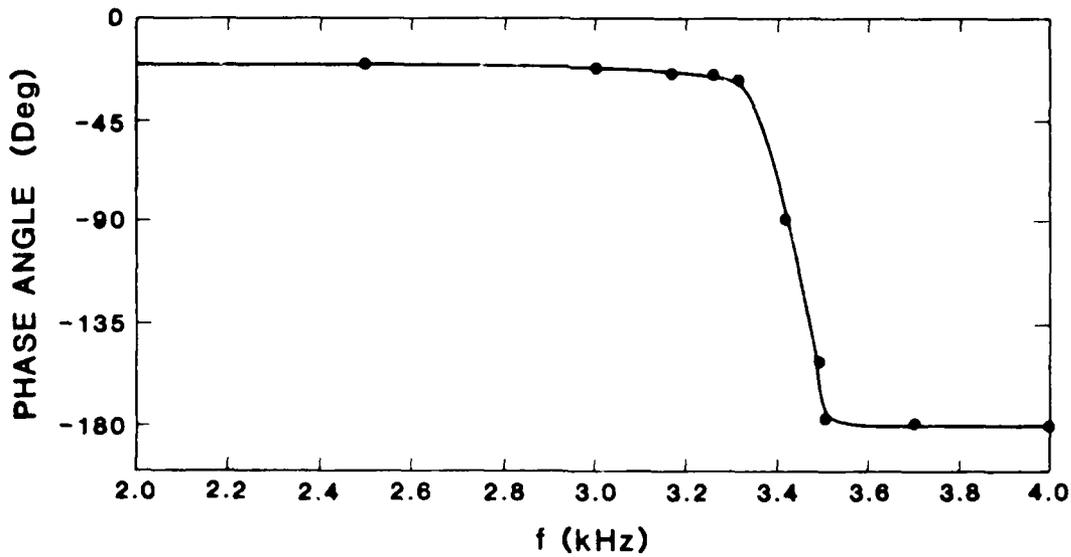
Figure 3b. - Phase Response of Cavity Length Transducer

PULSED FREQUENCY STABLE NARROW LINEWIDTH LASERS AND OPTICAL REMOTE SENSING

K.K. LEE

PERKIN-ELMER CORPORATION, 100 Wooster Heights Road, Danbury, Ct. 06810

Usually people consider single mode pulsed lasers to be frequency stablized. But in a pulsed laser, mode selection is not equivalent to frequency stablization. This is because with any type of mode selection method or device, a long term frequency drift may occur from pulse to pulse due to thermal or mechanical disturbances of the cavity length. Furthermore, short term frequency drift (chirping) may occur within one pulse due to rapid refractive index variations of the active gain medium.

Phase conjugation resonators (PCR) have been recognized mostly for the spatial or mode properties of their output beam.[1] Phase conjugation mirror (PCM) using nearly degenerate fourwave mixing (NDFWM) has also been recognized for its capability of providing narrow optical bandpass filter. Indeed, assuming adiabatic approximation, pump nondepletion, and weak nonlinear coupling, it is found that[2] as $|K|$ L increases, (here K is the complex coupling coefficient given by $K = 2\pi f \chi^{(3)}$ Ip/nc; Ip is the intensity of the pump, L is the nonlinear interaction length), the bandpass becomes more sharply peaked. When the oscillation condition is reached, (i.e., $|KL| \sim \pi/2$) the bandpass approaches zero.[2] The bandpass is only limited by the linewidth for the pump.

Frequency chirping is minimized if the pulse duration is longer than the cavity round trip time. We shall demonstrate that phase conjugation oscillator, with one phase conjugation "mirror" pumped by frequency very stable, cw, narrow linewidth laser, together with active amplitude modulation mode-locker, can provide a plused, frequency as stable and narrow linewidth as the cw pump laser.
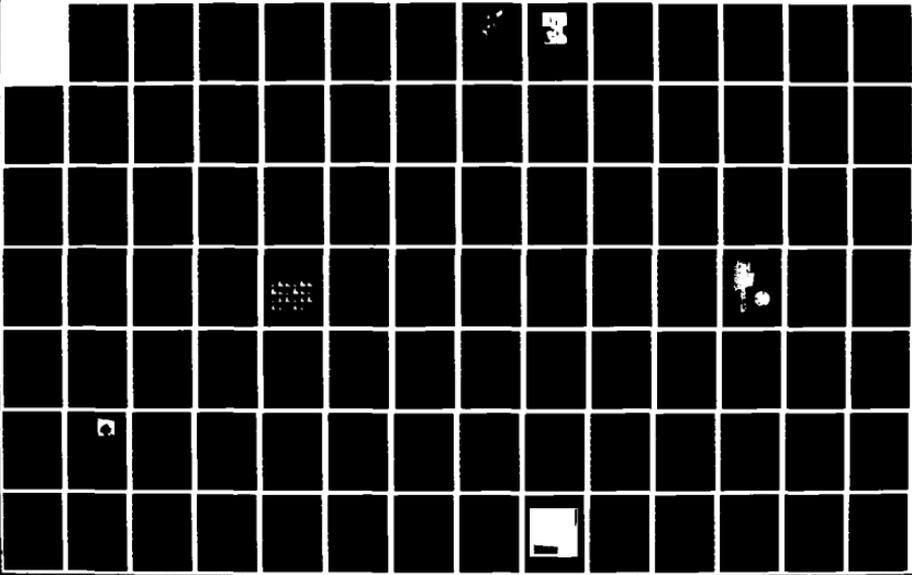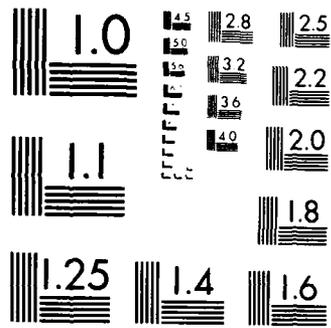
We begin by utilizing or constructing a frequency stable, narrow linewidth, cw laser a la Pound-Drever[3], as indicated in Figure 1. Then passing through some isolation elements, and frequency modulate the laser before pumping the four-wave mixer of the phase conjugation resonator, Figure 2. Let the frequency stable, narrow linedwidth, cw pump laser has central frequency of f_o and linewidth of Δf. Let the PCR has cavity length of L, then the cavity mode spacing is $\Delta f_c = c/4L$, half of the mode spaciang of usual oscillator[4]. Let the modulation frequency be fm and assume $\Delta f << f_m < \Delta f_c << f_o$. Then the pump beams of the PCM have three distinct lines, i.e., f_o, $f_o \pm f_m$, and each has linewidth of $\Delta f << fm$. When the oscillation condition is approached, the bandpass approaches zero and is only limited by the linewidth of the pump, which is Δf. Since $\Delta f << fm$, there will be no coupling between these f_o and $f_o \pm f_m$ lines. Thus if the PCM material is so chosen (such as resonance or resonance enhanced material) such that at f_o, the oscillation condition is met, then the two side bands are also very near the oscillation condition. Thus, the PCM also acts as a bandpass filter for both sidebands. Thus, the circulating optical frequencies in the PCR are the same as that of the pump waves which drive the PCM. These frequencies are the most likely to oscillate because the enhanced reflectivity of the PCM. Furthermore, one can show that [5] the standing waves with frequencies f_o and $f_o \pm f_m$ in the PCR cavity are not only frequency synchronized, but also phase synchronized in time to the phases of the pumping waves. A practical technique to enhance the bandpass selectivity, and synchronization of both frequency and phase in the PCR, one can inject a small amount of the cw pump via forward FWM at the PCM.

If we freqeuncy modulate the cw pump, due to the synchronization of both frequencies and phases in the PCR, and the negligible short term frequency chirping, the output of the pulsed oscillator preserves the frequency characteristics as well as the information content via FM in the pump.

Note that, the controlled frequency modulation of the pumps can not only encode information to be transmitted but also broadens the effective gain bandwidth of the PCR. Thus, for some laser media, subnanosecond frequency stable pulses can be obtained. Furthermore, since the resonance frequency of the PCR is independent of the cavity length, one can use a very short PCR cavity, such that the pulse width of the PCR can further be shortened.

We shall briefly describe the applications of such device to the study of optical remote sensing.

REFERENCES

1. There are numerous papers and review papers on phase conjugation. The most recent comprehensive review is the one by D. Pepper, in Laser Handbook, Vol. 4 ed. by M.L. Stitch and M. Bass (North-Holland, Amsterdam, 1985) Ch. 4.

2. D.M. Pepper and R.L. Abrams, Opt. Lett. 3, 212 (1978).

3. R.W. P. Drever, J.L. Hall, F.V. Kowalski, J. Hough, G.M. Ford, A.J. Munley, and H. Ward, Appl. Phys. B 31, 97 (1983).

4. A.E. Siegman, P.A. Belanger, and A. Hardy, in Optical Phase Conjugation, ed. by R.A. Fisher, (Academic Press, N.Y., 1983).

5. K.K. Lee, in preparation (to be published).
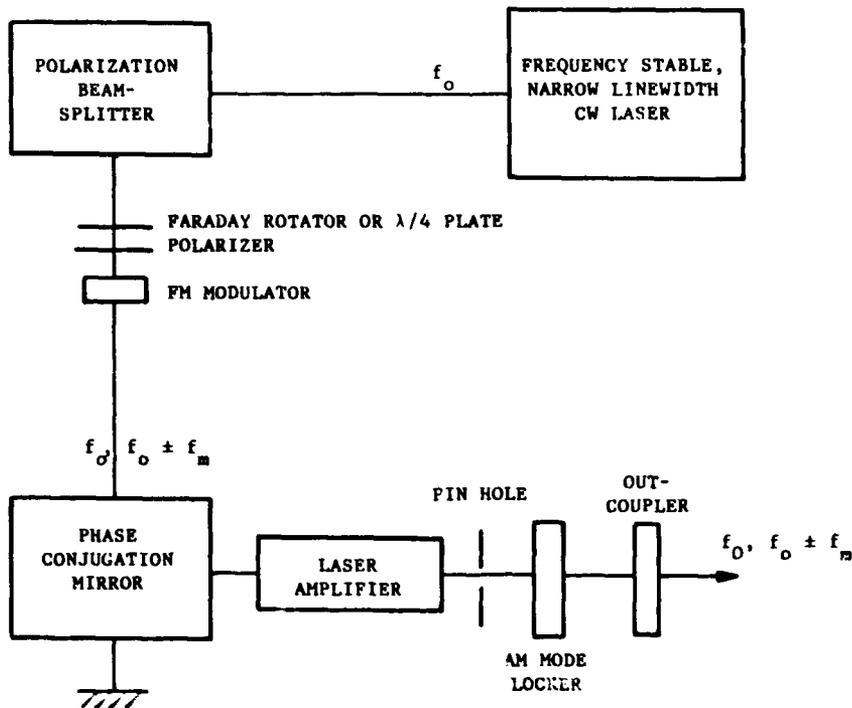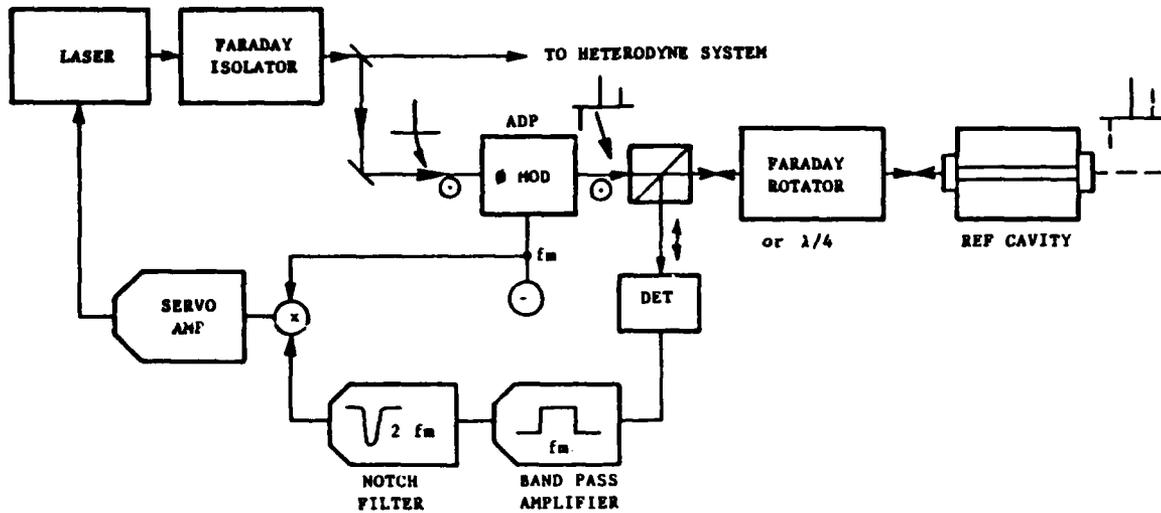
A Rapid Tuning Device for a CO_2 LIDAR

V. Klein   M. Endemann
Battelle Institut e.V
Am Römerhof 35
D-6900 Frankfurt/Main 90

1 Introduction

A rapid tuning device for a TEA CO_2 laser has been developed for multispectral DIAL measurements in the atmosphere. This equipment is part of a LIDAR experiment for the remote detection, identification and quantification of several atmospheric pollutants within a range of 2 km.

2 The Experimental Setup

For the accurate identification and quantification of numerous gaseous pollutants within a target volume in the atmosphere it is necessary to use the multispectral differential absorption technique (examination of this volume on several different wavelengths). The optical main components of this experiment are a 50mJ (P40) TEA CO_2 laser with a repetition rate of 300 Hz and the above mentioned rapid tuning device, forming the transmitter and a conventional 8"-Newtonian telescope with a LN-cooled HgCdTe-detector as the receiver, which is mounted directly besides the laser head. This LIDAR experiment is fully controlled by a 16 bit microprocessor system (68000 CPU). The laser is tuned on up to 10 discrete wavelengths in the fingerprint region of 9 µm through 11 µm by tilting reflective gratings at the rear side of the closed resonator.

For our application it is essential to perform this tuning in a very short time due to the high repetition rate of the laser to probe two wavelengths within the atmospheric correlation time ($\approx$10ms). This technique eliminates errors caused by temporal variations of the pollutant concentration within a given volume due to small scale atmospheric turbulence (eddies).

A single transmitter laser with high PRF (300 Hz) is used to simplify the alignment and to improve the overall reliability (compared to a two-laser-transmitter).

For our application it is desired to emit pairs of laser pulses, separated by 3 ms, at a repetition rate of typically 80 Hz. A rotating polygon mirror in combination with a fixed grating, constantly rotating grating or resonant galvanometer scanner would imply several technical difficulties. Therefore we selected an alternative approach.

We have developed a frequency switching device, that allows to change the emission wavelength within a timescale of 1 ms, and allows to probe up to 10 independent line pairs within 1 sec.

This device consists of an optical chopper as a light switch and two computer controlled reflective gratings (Fig.1). The chopper blade, equipped with two Si mirrors, is rotating at a constant speed (5.000 rpm) and is mounted in an angle of 45° with respect to the axis of the resonator. The laser pulses are emitted either when the beam is directed by the chopper mirror onto grating #1 or when the beam is passing through to grating #2.

The exact position for the mirror when the laser must fire is determined by two high resolution light sensors and a trigger mark on the outer surface of the rotating chopper mirror itself. The chopper is actually using only one of the two mirrors for switching the light, while the second one serves as a counterbalance and as a back up. The light is alternately pointed onto the two gratings which are directly mounted on the axis of two high resolution stepper motors (50.000 steps per rev.).

The deflecting angle of the gratings can be altered in smallest steps of 0.126 mrad. The maximum rotating speed is 10 rev. per sec.

The stepper motors are computer controlled via intelligent interfaces. Once these interfaces are programmed it is possible to perform even complex sequences of motion profiles by transmitting only a single start command from the host computer. This leads to a very flexible application of the tuning device. When several pairs of laser pulses have been emitted and averaged, both gratings are repositioned for the next set of wavelengths. The accurate position of the gratings is determined by high resolution optical encoders (100.000 steps per rev.). Fig. 2 shows the actual setup with the partly uncovered chopper housing.

Stepper motors are frequently showing a strong tendency for overshooting their final pointing position and are confined in a damped oscillating around this position once they have completed their operation. This oscillation may exceed the travel time itself and is heavily dependent on the torque of the motor and the dynamic load on its axis. For preventing this behaviour the present setup is equipped with an additional load in form of a small flywheel, which is significantly damping the disturbing oscillation.
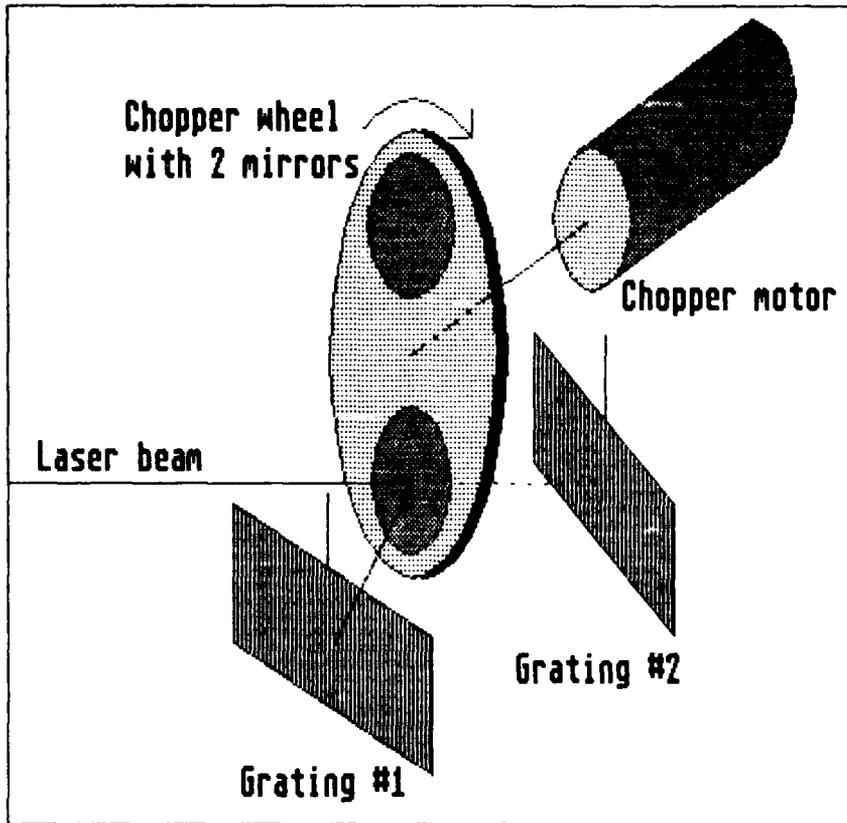
Fig.1   Three-dimensional view of the rapid tuning device

Design specifications of the rapid tuning device

Optical elements...1 Chopping Si mirror, 2 Reflective Gratings
(150 grooves per mm)

Chopper drive.................. DC motor (24 Volts, 5000 rpm)

Gratings drive........ Stepper motors (50.000 steps per rev.)

Pointing accuracy for the gratings............... 0.126 mrad

Maximum settling time for the gratings after
rotating into a new position........................... 20 ms

Shortest time between two pulses
on different wavelengths............................... 3 ms

Repetition rate for pulse pairs.................. typ. 80 Hz

Maximum acceleration of the grating drives.... 60 rev per sec^2

Maximum speed of the grating drives........... 10 rev per sec

Fig. 2 The complete tuning device, partly dismantled

3 Conclusion

A new rapid tuning device for a CO_2 laser has been developed
for an application within a LIDAR experiment. First laboratory
test results show the successful approach (3 ms pair separa-
tion). The minimum switching time between adjacent grating
positions can be as low as 20 ms. Thus the achievable
repetition rate for the pulse pairs can be nearly 50 Hz,
depending on the selected sequence of wavelengths. Further
laboratory test work and measurements in the open field will
lead to a nearly automated system, running under the
complete control of a micro computer.

An Airborne Wavemeter for an Atmospheric DIAL Experiment

Joseph H. Goad, Jr.
NASA Langley Research Center
Mail Stop 474
Hampton, Virginia 23665-5225

Summary

A wavemeter is being designed and developed as a subsystem to support the NASA LASE (Laser Atmospheric Sounding Experiment) ER-2 airborne project. The prime objective of this project is to use a DIAL remote sounding system with a pulsed tunable Alexandrite laser to measure vertical profiles of water vapor and aerosols. The technology to make the required wavelength centroid and wavelength profile measurements has been demonstrated by others in laboratory environments. The developmental effort in building this wavemeter is to operate within requirements inside the Q-bay environment of an ER-2 aircraft. In this environment, the temperature can vary from 15 to 40 degrees Celsius and the pressure can vary from 14.7 psi to 3.5 psi. The interferometers in the wavemeter must be isolated from this thermal and pressure variation. A thermally controlled housing and thermal vacuum chambers have been designed and brassboarded to demonstrate the required stability.

The wavelength centroid measurement to meet the atmospheric science requirement for the LASE experiment, is met by providing absolute spectral accuracy of ± 0.25 picometers at a nominal wavelength of 729 nanometers. The wavelength spectral profile accuracy is met by providing an instrumental resolution at full-width-half-maximum of less than 0.5 picometers with an amplitude uncertainty of 10 percent.

Fabry-Perot interferometers have been constructed of low thermal expansivity materials to form the three stage instrument. Two stages operating in a "bootstrap" mode provide the wavelength centroid position measurement; the third stage provides data to retrieve the wavelength profile. Two laser beam paths exist in the wavemeter: one for real-time control of the tunable Alexandrite laser, and the other to provide interferometer stability information for post-flight checking. The optical design is shown in figure 1. A graph of the long-term opto-mechanical stability is shown in figure 2. The data demonstrates that the instrument variations are well within ± 0.25 picometers. Figure 3 shows an example of a linearized fringe profile with an instrument resolution of 0.32 picometers. These preliminary experimental design data were measurements with a single mode, stabilized He-Ne laser.

PARTS LIST :

1A. BEAM BENDER
1B. BEAM BENDER
1C. 45 DEG MIRROR
2. SHUTTER
3. ATTEN/SPLITTER 105
4. BEAM SPLITTER
5. MIC OBJECTIVE
6. ETALON CHAMBER #3
7. LENS
8. 45 DEG MIRROR
9. 90 DEG MIRROR
10. ARRAY #3
11. ATTEN/SPLITTER
12. BEAM SPLITTER
13. MIC OBJECTIVE
14. ETALON CHAMBER #1
15. LENS
16. ARRAY #1
17. ATTENUATOR
18. BEAM SPLITTER
19. MIC OBJECTIVE
20. ETALON CHAMBER #2
21. LENS
22. 45 DEG MIRROR
23. ARRAY #2
24. HENE
25. SHUTTER
26. 45 DEG MIRROR
27. 45 DEG MIRROR
28. 45 DEG MIRROR

VAUGHN BEHUN
5/27/87
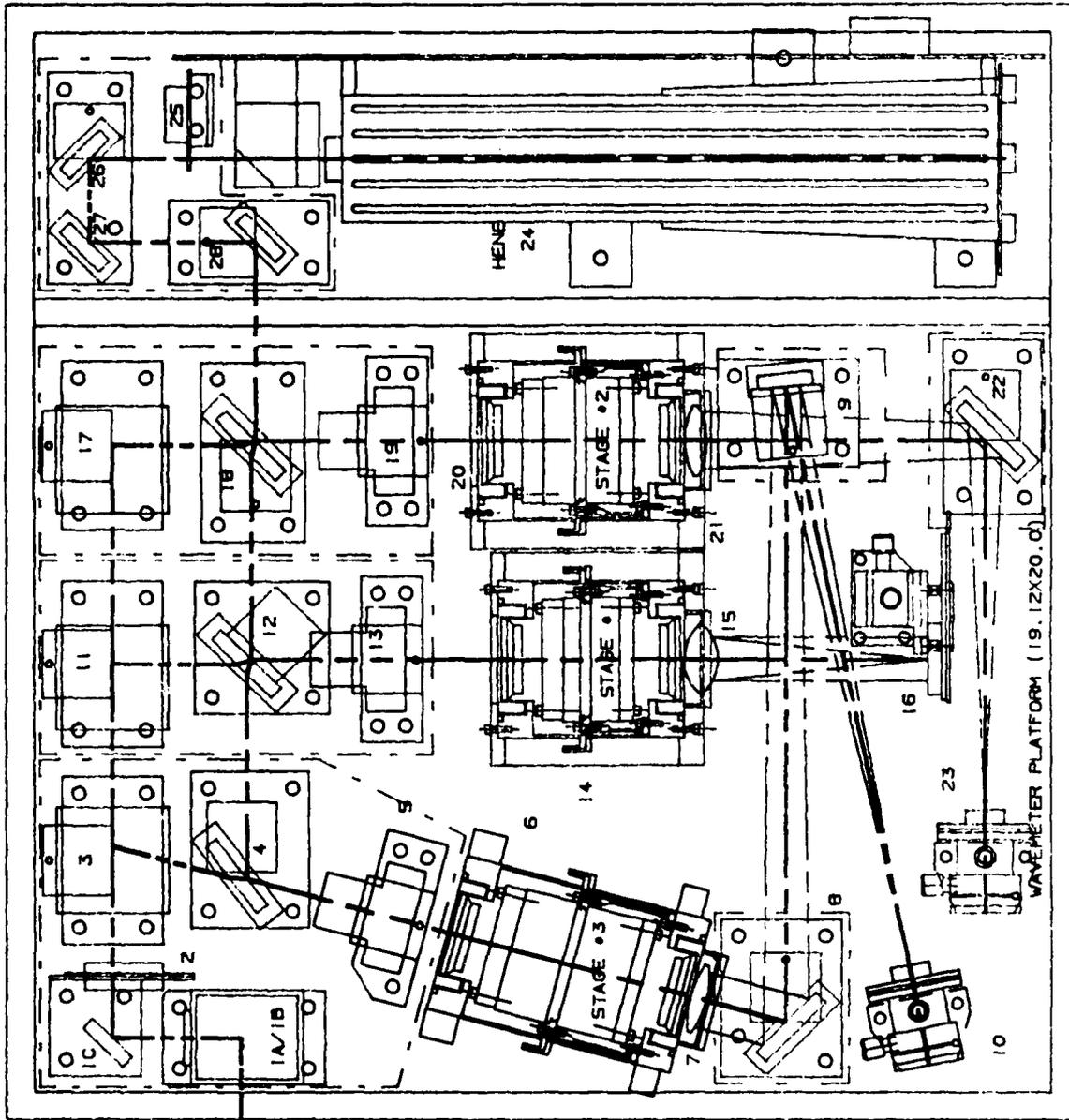
FIGURE 1. OPTICAL LAYOUT

287

DRIFT CHILDS 05-22-87 11:12:32

(REQUIREMENT ±0.25 PICOMETERS FOR 10 HOURS)
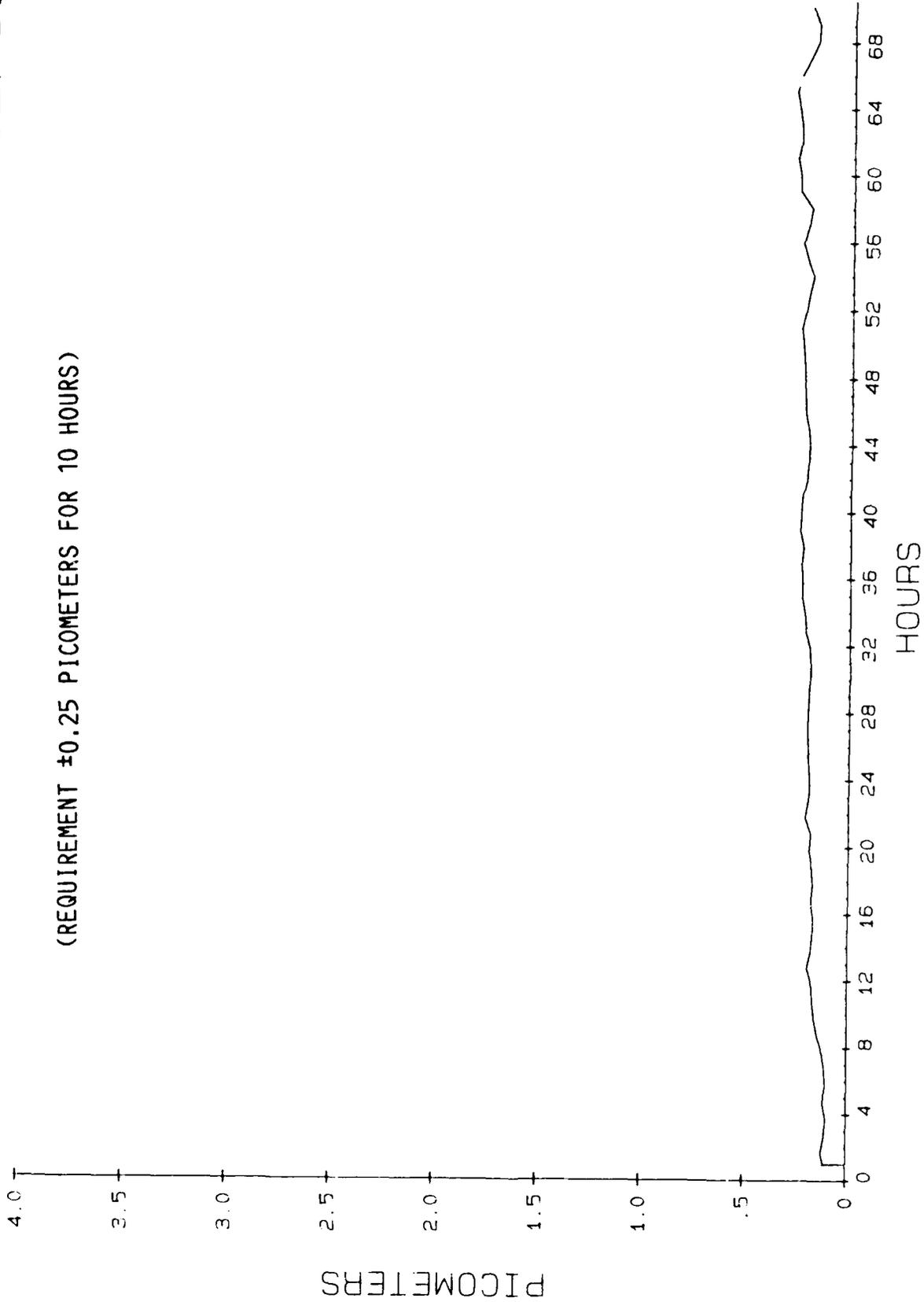
FIGURE 2. LONG-TERM STABILITY

10-16-86   12:51:47

.447   .684   .728   .998

(ABOVE NUMBERS FWHM IN PICOMETERS)
SPECTRAL PROFILE
SINGLE MODE He-Ne LASER
MEDIUM QUALITY PLATES
FSR = 9 PICOMETERS
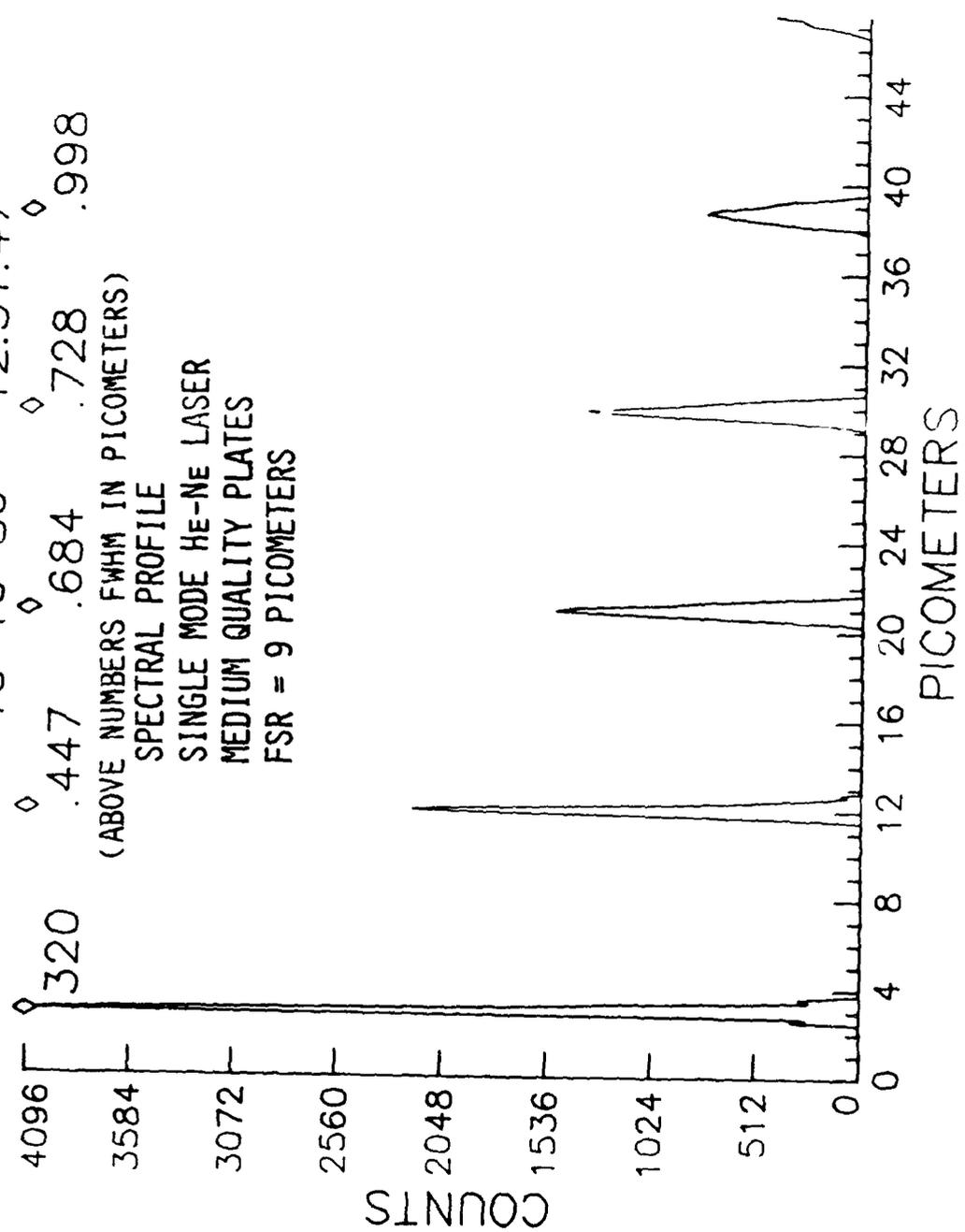
LINEARIZED LABORATORY FLAT FABRY-PEROT

FIGURE 3. WAVELENGTH PROFILE

Detector Response Characterization for DIAL Application

H. S. Lee
SM Systems and Research Corporation
8401 Corporate Dr., Suite 510
Landover, MD 20785

G. K. Schwemmer and C. L. Korb
NASA/Goddard Space Flight Center
Code 617
Greenbelt, MD 20771

For accurate DIAL measurements, the detector output should have a linear response to the input light signal. In addition to good linearity, the detector should also have good gain stability and negligible signal-induced noise.

The requirement for gain stability is less stringent compared to the other requirements as long as the gain stability pattern is preserved between the pair of on-line and off-line pulses. The linearity of the detector response is critical in the sense that the nonlinear behavior of the PMT responsivity is normally dependent upon the signal amplitude itself. Therefore, for off-line and on-line signals which are not identical, the effect of the non-linearity is not cancelled in the DIAL signal processing. The same argument applies for the signal-induced noise term. The cause and characteristics of the signal-induced noise which appears as a bias is not well understood.

To study the signal-induced noise characteristics, we have set up a laboratory experiment which simulates the effects of strong ground return signals from aircraft measurement. The setup consists of a stabilized single mode CW He-Ne laser, a spatial filter, a narrow slit (5 μm) mounted on a rotating chopper and a set of auxiliary optics as shown in Fig. 1. The simulated strong ground return lidar pulse is generated by chopping the CW laser beam focused on the slit. In this way, we generate a Gaussian pulse with a typical FWHM of 500 nsec. The spatial filter (SF) in the beam expander is used to create a near Gaussian profile of the laser beam which is directly transferred to a temporal pulse profile by the chopper. The PMT is operated in a gated mode. The PMT output signal is amplified, digitized, and recorded on a magnetic tape using the pressure-temperature lidar data acquisition system. For a given laser pulse shape, experiments are carried out by varying the intensity, PMT dynode voltage, and gating time. Preliminary results show a signal-induced bias (noise) effect with a duration >60 μs at the 0.1% level. Investigation to further chracterize the cause and effect is underway.

We have studied the gain stability of the detector system using a CW LED light source. The PMT is gated on for each signal in the on- and off-line pulse pair for a duration of a few tens of microseconds each. The temporal separation of the pulse pair is maintained at 300 μs to simulate field measurements. The PMT output signal is then amplified, digitized and recorded using the same data acquisition system. A set of data is acquired by varying

the light intensity, and PMT dynode voltage. Preliminary results show that the absolute gain stability is a strong function of the PMT dynode voltage as well as the light intensity. The relative gain is stable to 0.1% or better over a period of a few tens of μs. The error due to this effect is further reduced in a DIAL measurement.
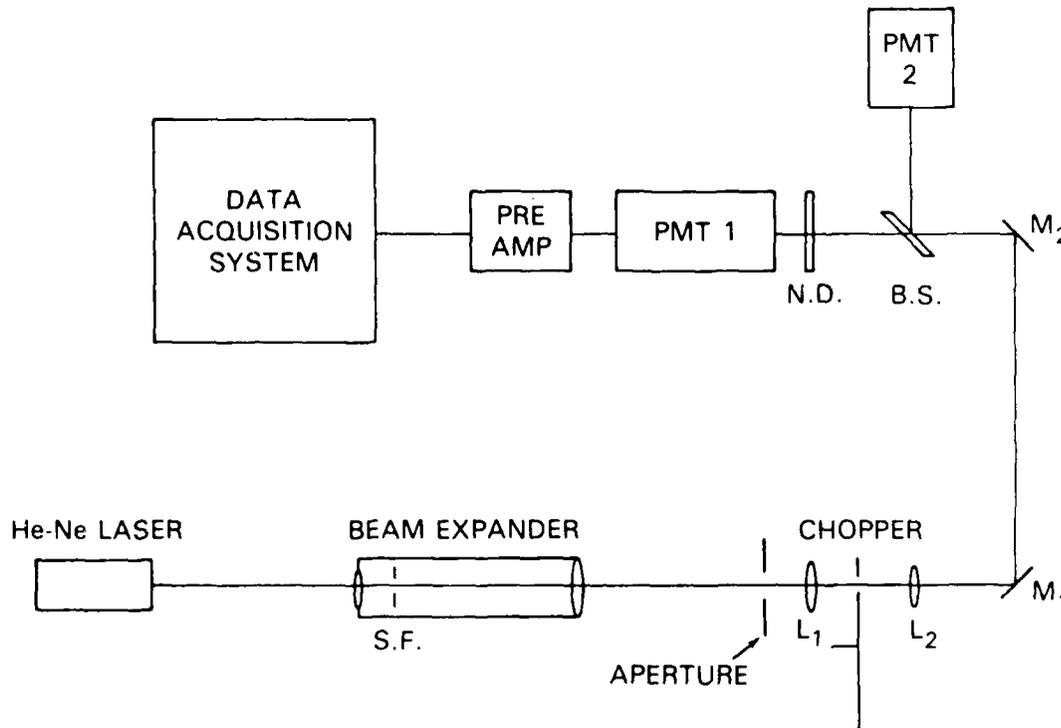
Figure 1. Schematic of Experimental Setup
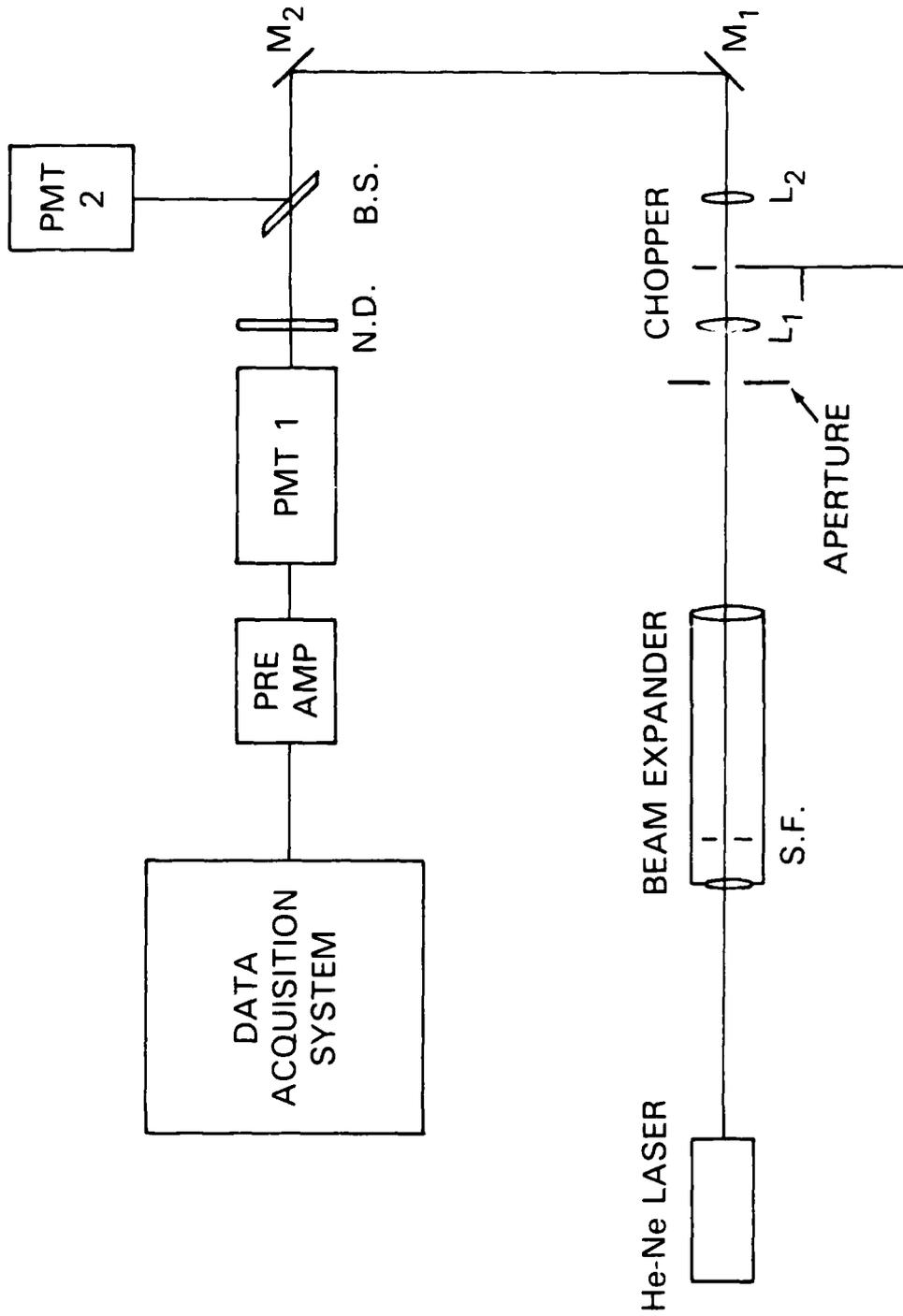
Speckle Effects on Laser Wavelength Measurements with a Fizeau Wavemeter
Coorg R. Prasad*, C. Laurence Korb, and Geary K. Schwemmer

NASA/Goddard Space Flight Center
Greenbelt, MD 20771
Code 617
*NRC Research Associate

In this paper, we present results of an investigation of laser wavelength measurement with a wavemeter incorporating a coated Fizeau high resolution wedge. The effect of speckle on the measurement has been studied and several approaches have been taken to reduce the effect of speckle.

Measurements of atmospheric pressure and temperature profiles by a differential absorption lidar operating in the 760 nm region and using absorption by oxygen in this region have been proposed by Korb et al.[1,2] Absorption troughs between pairs of strongly absorbing lines are used for the pressure measurements in order to desensitize the measurements to the effects of laser frequency instabilities. The results of measurements of the atmospheric pressure profile made remotely from an aircraft have shown an average deviation of less than 2 mb from radiosonde data.[3] Atmospheric temperature measurements call for the on-line laser to be centered on a narrow absorption line, whose widths range from 0.1 cm^{-1} (FWHM) at sea level to 0.03 cm^{-1} (FWHM) for the Doppler-broadened profile at high altitude. Hence, this calls for a laser transmitter with a bandwidth narrower than the line width (0.005 - 0.02 cm^{-1}) and a stability of the centroid frequency about a factor of ten better (0.001 - 0.002 cm^{-1}). Studies by Korb and Weng[4] have shown that for a three-mode laser the relative frequencies of each of these modes should be known to 0.0005 cm^{-1} and the mode energies to ten percent.

A wavemeter for measuring the mean wavelength and spectral shape of the pulsed narrow bandwith alexandrite lasers employed in the pressure-temperature lidar has been under development.[5] This instrument contains a high resolution (HR) multibeam Fizeau wedge[6] with a wedge angle of 8 arc/sec, a spacing of 5 cm and a reflectivity of 92% for the high resolution measurement of laser frequency and a low resolution wedge which was not used in this study. Laser light is input through a 50 μm core graded index optical fiber cable and collimated by an off-axis parabolic reflector. The fringe pattern from the wedge is incident on a Reticon photodiode array with 1024 elements (located on 25 μm centers). The laser light falling on the HR wedge displays a speckle pattern, with speckle sizes varying from 2 to 15 mm (spatial frequencies 0.067 to 0.5 mm^{-1}). This pattern is a random distribution of speckle that changes with any displacement or orientation of the fiber. Thus, the fringe pattern incident on the diode array exhibits an intensity variation due to speckle that severely distorts the fringe pattern produced by the wedge.

Earlier measurements[7] of the line shape of the narrow bandwidth alexandrite lasers using an interferometer have shown that both the lasers have a three-mode structure with a spacing of 0.027 cm^{-1} between the outermost modes for one laser and 0.016 cm^{-1} for a second laser. In addition, the three modes are not equally spaced. The laser output contains a mix of frequencies arising

from laser oscillation in many transverse modes as well as in three longitud-
inal modes. As a result of the spatially inhomogeneous multimode laser out-
put, mixing of the laser spatial modes is required to assure that the spectral
information measured by the wavemeter is the same as that which is used for
atmospheric measurement. However, the process of mixing the output generally
introduces speckle. One of the reasons for using the multimode optical fiber
is to scramble the laser modes while acting as a pinhole (50 μm) for the col-
limator. This approach however, produces large speckle elements with sizes
which are of the order of the fringe spacing of the HR wedge. Another example
of a mixer is a diffuser which can also take the form of an integrating sphere
and which also produces speckle.

Our approach has been to use a "thin" diffuser which mixes the different
spatial modes. We have performed a number of experiments to study the effects
of such diffusers on the speckle and also on the measured laser lineshapes.
For these experiments, the optical input system shown in Figure 1 was used.
The laser beam was taken either directly, or through the optical fiber, to a
spatial filter consisting of a 10x microscopic objective and a pinhole
assembly, and then collimated using the off-axis parabolic reflector before
going through the HR wedge. The output from the wedge falls on the Reticon
diode array. A cylindrical lens then may be introduced between the HR wedge
and the diode array. A continuous wave He-Ne laser oscillating on three modes
was used initially to characterize the system. The diffuser for mixing the
spatial modes was placed on the pinhole holder at the focus of the microscope
objective.

The diffuser can be considered as a random array of apertures or obstruc-
tions. In a "thin" diffuser, this array is essentially two-dimensional while
in a "thick" diffuser, a three-dimensional distribution of scatterers is
present. The pattern of light emerging from such a two-dimensional array is
better suited for our purpose since it does not degrade the finesse of the
system substantially by increasing the size of the source to be collimated. A
thick diffuser like opal perspex, while being a better diffuser, degrades the
finesse of the system.

Various diffusers were tried such as thin parchment, vellum paper, and opal
plastic films. The surface of the opal plastic film has microscopic grooves
which scatter light. Speckle is also produced by these diffusers. The size
of these speckles and their frequency can be changed by moving the diffuser
away from the focus of the microscopic objective. The spatial frequency was
as high as 4/mm when the diffuser is away from the focus, to as low as 0.04/mm
(i.e., a single speckle element covers the full aperture of the wavemeter)
when at the focus. The farthest displacement permissible is set by the
finesse desired (which is 40), and this corresponds to a speckle spatial
frequency of 4/mm. For this value of the finesse the laser spot size at the
diffuser can be fairly large ($\geq$100 μm), and the energy density in this spot,
that is necessary for obtaining an acceptable S/N ratio at the diode array, is
of the order of 0.1 J/cm^2. Hence, the chance of damage to the diffuser is
small.

Since these speckle patterns change randomly with any displacement of the
diffuser, the accuracy of measurement is improved by averaging over a number
of measurements wherein the diffuser is translated randomly in a plane

perpendicular to the optical axis. Further improvement in measurement
accuracy through reducing the speckle variance is possible by integrating
vertically along the fringes. This was accomplished by introducing a
cylindrical lens. But the cylindrical lens itself introduces errors if not
positioned precisely since the elements of the Reticon diode array are only
25 μm high. Instead of this, a larger array with 2.5 mm high array elements
was utilized.

For evaluating the effectiveness of these procedures, the diode array output
was acquired, digitized, and stored on magnetic tape. These data sets were
then analyzed to obtain the mean value and the variance of the frequency and
the relative intensities of the different modes that are contained in the
laser output.

The diffuser can also be used in conjunction with the optical fiber coupling
to increase the spatial frequency of the speckle and thus improve the accuracy
of the measurement. In the first series of experiments, the CW He-Ne laser
was the source, and comparison of the wavemeter data for different input
schemes was carried out. Following this, the pulsed alexandrite laser was
used as the source. The results of these experiments will be presented.

References

1. Korb, C. L. and C. Y. Weng, "Differential Absorption Lidar Techniques for
Measurement of the Atmospheric Pressure Profile," Applied Optics, 22, 3759
(1983).

2. Korb, C. L. and C. Y. Weng, "A Theoretical study of a Two-Wavelength Lidar
Technique for the Measurement of Atmospheric Temperature Profile," J. Appl.
Met., 21, 1346-1355 (1982).

3. Korb, C. L., G. K. Schwemmer, M. Dombrowski, J. Milrod, and H. Walden,
"Airborne Lidar Measurements of the Atmospheric Pressure Profile With Tunable
Alexandrite Lasers," Proc. 13th International Laser Radar Conference, NASA
Conf. Publ 2431, p52 (1986).

4. Korb, C. L. and C. Y. Weng, private communication.

5. Cotnoir, L. J., T. D. Wilkerson, M. Dombrowski, R. H. Kagann, C. L. Korb,
G. K. Schwemmer, and H. Walden, "A Wavemeter for Use with a Line Narrowed
Alexandrite Laser in Differential Absorption Lidar," Topical Meeting on
Tunable Solid-State Lasers, Arlington, VA, Technical Digest, FC5 (1985).

6. Morris, M. B., T. J. McIlrath, and J. J. Snyder, "Fizeau Wavemeter for
Pulsed Laser Wavelength Measurement," Applied Optics, 23, 3862 (1984).

7. Schwemmer, G. K., M. Dombrowski, C. L. Korb, J. Milrod, H. Walden, and R.
H. Kagann, "A Lidar System for Measuring Atmospheric Pressure and Temperature
Profiles," (submitted for publication to Rev. Sci. Inst.) (1987).
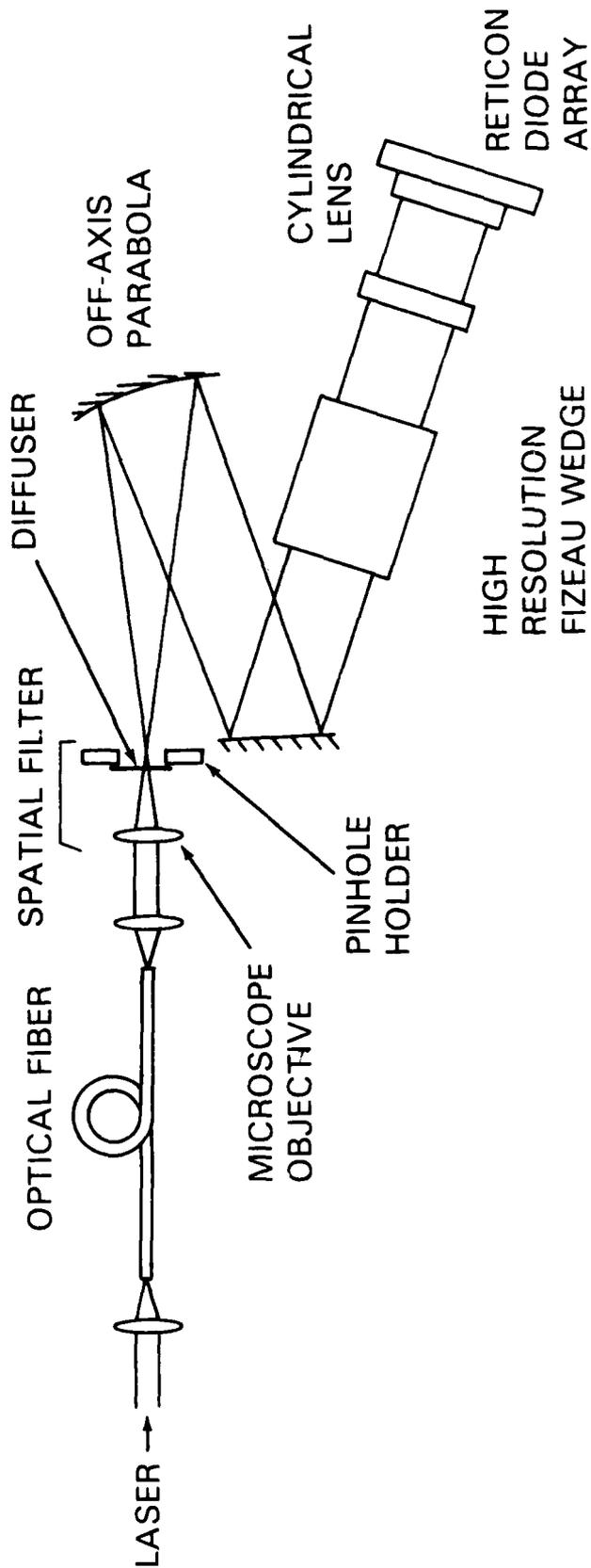
Figure 1. Schematic of Experimental Setup

Development of Spectral Equipment for Investigations of Atmospheric Gases

V.E.Zuev, V.P.Lopasov, Yu.N.Ponomarev, L.N.Sinitsa,
I.S.Tyryshkin, A.B.Antipov

The Institute of Atmospheric Optics, Siberian Branch
USSR Academy of Sciences, Tomsk, 634055, U S S R

High-resolution laser spectrometers developed at the Institute of Atmospheric Optics for investigating the absorption spectra of atmospheric and atmosphere contaminating gases at 0.2 to 10 μm are reported.

The complex of spectrometers consists of: wide-band intracavity laser spectrometers; laser spectrometers with multipass absorption cells with the base up to 110 m; opto-acoustic spectrometers; a fluorescence laser spectrometer.

The intracavity laser spectrometers allow the wide-range recording of 200 cm^{-1} width spectra to be made per pulse of generation ($\tau_{u} \sim 1$ ms) at spectral resolution 0.05 cm^{-1}. The threshold absorption sensitivity of spectrometers reaches 10^{-7} to 10^{-8} cm^{-1} that corresponds to use of 10000 m path length in classical spectroscopy.

Wide-band intracavity spectrometers based on Nd glass lasers, dye lasers, and thermostable, room-temperature F_2^+ and F_2^-:LiF color lasers have been developed. The total spectral range of spectrometers is 4000 cm^{-1} in the range 0.55 to 1.25 μm. The parameters of spectrometers are given in Table.

Laser spectrophotometers were constructed based on a classical scheme with external multipass absorption cells and lasers with a narrow (< 0.001 cm^{-1}) frequency-tuned line of generation. To determine the absolute values of weak spectral line parameters with high precision, the multipass absorption cells with bases of 3, 30 and 110 m have been designed. Multipass systems provide a pass length to 8000 m. A 30-m cell has two optical systems that allow simultaneous measurements in two spectral regions. The gases in the cells can be investigated in the temperature range −40 to +80°C. The spectrometers

based on ruby, Nd glass, alexandrite and dye solution lasers
have been constructed (see Table). They are equipped with the
wavelength measuring systems, systems for computer signal pro-
cessing and have spectral resolution to 10^{-4} cm^{-1} and the ab-
sorption sensitivity 10^{-8} cm^{-1}.

Opto-acoustic spectrometers provide high-precision measure-
ments of relative absorption coefficients of the gas under stu-
dy, and allow one to obtain information on the absorption satu-
ration parameters. At present the opto-acoustic spectrometers
based on ruby, Nd glass, CO_2 lasers have been constructed. The
spectral resolution of opto-acoustic laser spectrometers is de-
termined by laser radiation line width and reaches 10^{-1} -
- $5 \cdot 10^{-3}$ cm^{-1}. The use of high-power lasers with pulse dura-
tion 15-100 ms allows one to study nonlinear spectroscopic
effects in gases.

A multipurpose laser spectrometer. An automatized multi-
purpose laser spectrometer operating in the ultra-violet, vi-
sible and near IR has been constructed for obtaining absorpti-
on and fluorescence spectra. The spectrometer consists of:
1. a tunable frequency-doubled dye laser, 2. a fluorescence
cavity with a monochromator, 3. a spectrophone for recording
an opto-acoustic absorption spectrum, 4. a multipass gas cell
for recording the absorption spectra, 5. a system for proces-
sing the data and controlling a spectrometer based on a compu-
ter.

The parameters of the spectrometer are: spectral excitation
range - 265, 290-305, 350, 530, 580-610, 1060 nm; spectral
range of fluorescence recording - 0.2-1,2 µm; fluorescence
channel sensitivity - $10^{-11}cm^{-1}$; spectrophone threshold sen-
sitivity - $2 \cdot 10^{-8}$ cm^{-1}/J; optical path length of absorption
cell - 4.4-132 m; measurement error of signal ratio - 0.5%.

The results of spectroscopic investigations. High sensitivi-
ty of the spectrometers constructed allowed one to record se-
veral thousand of new absorption lines, many vibration-rota-
tion bands of H_2O, CO_2, C_2H_2, N_2O, NH_3, CH_4, HBr and their
isotopes. The recorded spectra have been assigned, the spect-
roscopic constants of molecules have been determined. The ab-

sorption spectra of atmospheric air in the range of laser radiation have been defined more accurately.

The spectral H_2O absorption line contour has been studied, the line shifts caused by buffer-gas pressure have been measured, that reveals the necessity of taking into account the line shifts in the atmospheric-optics problems to be solved.

Table. Parameters of the spectrometers

Spectrometer	Spectral range, μm	Spectral resolution, cm^{-1}	Absorption sensitivity, cm^{-1}	
Intracavity laser spectrometers				$\Delta\nu$ per pulse, cm^{-1}
Nd-glass	1.05-1.09	0.08	10^{-8}	20-100
F_2^+:LiF	0.89-0.96	0.08	10^{-7}	50-200
F_2^-:LiF	1.09-1.25	0.08	$3 \cdot 10^{-8}$	50-300
Dye	0.55-0.61	0.05	$5 \cdot 10^{-7}$	50-100
Laser spectrophotometers				Path length, m
Ruby	0.694	10^{-3}	10^{-8}	60-4000
Dye	0.56-0.64	$7 \cdot 10^{-4}$	$5 \cdot 10^{-9}$	60-8000
Alexandrite	0.71-0.8	$5 \cdot 10^{-3}$	10^{-8}	60-4000
Nd-glass	1.05-1.09	$7 \cdot 10^{-4}$	10^{-7}	12-288
Opto-acoustic spectrometers				Intensity, W/cm^{-2}
Ruby	0.69	10^{-2}	10^{-9}	10^8
Nd-glass	1.06	$5 \cdot 10^{-3}$	10^{-9}	10^8
Nd-glass (doubled frequency)	0.53	$5 \cdot 10^{-3}$	10^{-9}	$2 \cdot 10^7$
CO_2-laser	10.6	10^{-1}	10^{-8}	$2 \cdot 10^7$

Effective Source of Coherent Radiation Based on
CO_2 Lasers and $ZnGeP_2$ Frequency Converters

Yu.M. Andreev, V.G. Voevodin, P.P. Geiko, A.I. Gribenyukov,
V.V. Zuev, V.E. Zuev

The Institute of Atmospheric Optics, Siberian Branch
USSR Academy of Sciences, Tomsk, 634055, U S S R

The $ZnGeP_2$ monocrystals have high nonlinear figure of merit,
third after Te and $CdGeAs_2$. $ZnGeP_2$ is sufficiently birefringent
(B = + 0.04) for three-frequency matching mixing practically
all over the transmission range. However, mainly due to low op-
tical transmission of the monocrystals available, the experi-
mental studies of frequency converters (FC) have been limited
until recently to approbation of the CO_2 laser radiation up-
[1] and downconverters [2].

The technological advances allowed us to obtain the $ZnGeP_2$
monocrystal bulls of 20 to 25 mm diameter and 150 mm length.
The spectral behavior of the absorption coefficient α for
four crystals is presented in Fig. 1. The samples 3 and 4 are
unique [3]. The yield of samples with the maximum transmission
range $\alpha = 0.1...0.2$ cm^{-1} is several per cent. Significant ex-
ceeding of losses for the extraordinary waves has been obser-
ved in the region of so-called short-wave anomalous "shoulder"
of absorption. The difference is caused by the presence of
growth layers and oriented second-phase inclusions. The absorp-
tion peak at $9...9.1$ μm is assumed to be connected not with a
three-phonon absorption only [2], since crystal-to- crystal va-
riations of peak intensity are observed. As follows from the
analysis of optical properties, the $ZnGeP_2$ monocrystals are
most applicable for conversion of $2...8.5$ μm radiations. In
particular, they are the most efficient frequency doublers of
CO laser radiation. PM angle for SHG is presented in Fig. 2.

The characteristics of different CO_2-laser FC with $ZnGeP_2$
have been experimentally investigated. The work has been done
together with the laser designers [4-8]. The CO laser frequen-
cy doubler [9] enables one to study in detail the possibilities

Table. Parameters of Frequency Converters

Parametric FC	Lasers	Laser parameters		τ, s	External (internal) efficiency, %
		λ, μm	W/cm^2		
SHG with ZnGeP$_2$	Hybrid CO$_2$	9.23	10^9	$2\ 10^{-9}$	49 (83.5)
	Hybrid CO$_2$	10 μm band	10^9	$2\ 10^{-9}$	17
	Hybrid CO$_2$-laser SH	4.64	$0.3\ 10^9$	$2\ 10^{-9}$	14
	TEA CO$_2$	9.2...10.8	$6\ 10^7$	$1.7...2\ 10^{-7}$	9.3
	Q-switched CO$_2$	9.2...10.8	$0.5...1\ 10^6$	$10^{-4}...10^{-2}$	5
	Q-switched CO$_2$	4.3 μm band	—	$1.5...3.3\ 10^{-7}$	8.4 (10.1)
	CW CO$_2$	9.2...10.8	$2\ 10^5$	—	0.5
	Q-switched CO	5.3...6.1	—	$4.5\ 10^{-5}$	3.1 (5.6)
	CW CO	5.3...6.1	$2.5\ 10^5$	—	0.3
Cascade FHG with ZnGeP$_2$	Hybrid CO$_2$	9.23	$(1$ and $0.3)10^9$ in I and II cascades	$2\ 10^{-9}$	1.4
SFG with ZnGeP$_2$	TEA CO$_2$	9.2...10.6 and λ=4.3 and λ=10.4	$6\ 10^7$	$1.7...2\ 10^{-7}$	1
	Q-switched CO$_2$		—	$1.5...3\ 10^{-7}$ and $6\ 10^{-7}$	4W peak
	CW CO and CO$_2$	5.3...6.1 and 9.2...10.8	$2\ 10^5$		0.25 mW
	Combined CO : CO$_2$	5.3...6.1 and 9.2...10.8	10^6	$5\ 10^{-5}$	0.1 % CO laser power
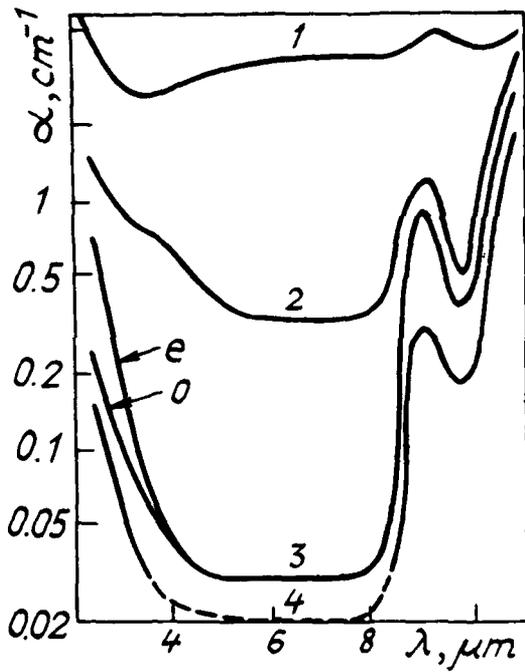
Fig.1. The transmission spectra of ZnGeP$_2$ monocrystals with different optical properties.
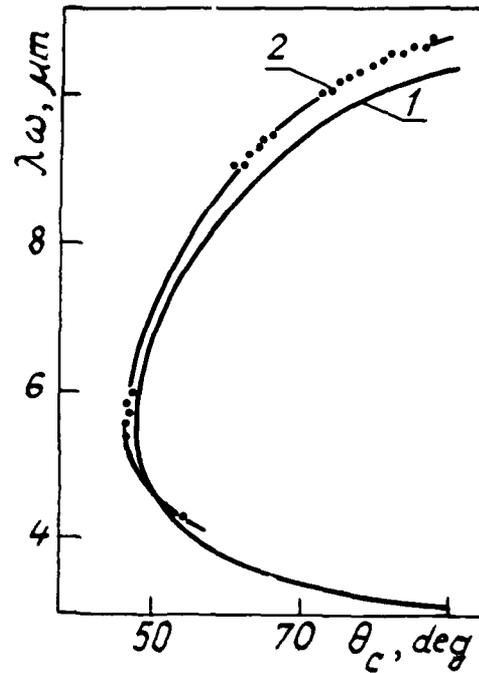
Fig.2. Phase matching angle for SHG versus the pumping radiation wavelength. 1 - theory, 2 - experiment.
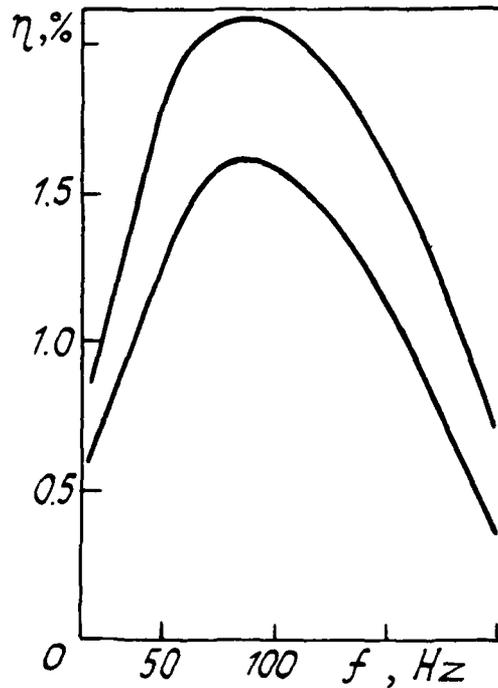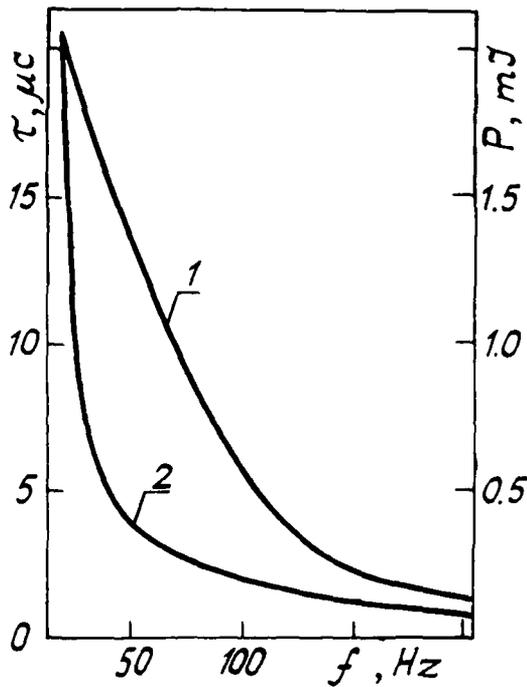
Fig. 3. CO laser generation pulses power (1) and duration (2) and the SHG external efficiency η versus modulation frequency f at different pumping-beam mode structures.

of cascade fourth-harmonic generation (FHG) of CO_2 lasers.

In all the cases the type I phase-matching conversions have been studied. Some crystals were partially anti-reflection coated, the others were oriented close to the Brewster angle. The crystal length was mainly 7...10.5 mm. A 3 mm crystal was used in the first cascade of FHG of a hybrid CO_2 laser, and a 7 mm crystal was used in the second one. The efficiency of the second cascade was limited by absorption of plasma formed on a LiF filter placed in front of it. The sum frequency generation of nonselective 5.7 W CO_2 laser radiation and 4.7 W CO laser radiation was obtained in a 3.1 mm crystal at a beam convergence angle 0.5°. A CO laser radiation parameters and SHG efficiency are presented in Fig. 3. The 3.1% maximum of average-power SHG efficiency of a Q-switched CO laser was obtained at 84.5 mW pumping at f = 75 Hz. The 4 mW maximum of the average SH radiation power was obtained at 194 mW at f = 89 Hz. The external angular acceptance width for SHG of CO_2 and CO lasers and sum-frequency harmonic were 4°, 2°06' and 2°50' (without radiation selection) respectively. The temperature synchronism widths were 45°C...50°C in the first case, and 80°C in the second case. The sources developed are applicable for solving many problems of applied spectroscopy.

References

1. G.D.Boyd et al., Appl.Phys.Lett.,v.18,N10,p.446 (1971).

2. J.L.Shay, J.H.Wernick, Ternary chalcopyrite semiconductors growth, electronic properties and applications. Pergamon Press, Oxford, 1975, Ch.6.

3. K.L.Vodopiyanov et al. Izv.Akad.Nauk SSSR Ser.Fiz., v.49, N3, p.569 (1985).

4. A.E.Akimov et al. Preprint Inst.Atom.Energy N3559, M.,1982.

5. Yu.M.Andreev et al. Kvant.Elektron.,v.11,N7,p.1511(1985).

6. Yu.M.Andreev et al. Kvant.Elektron.,v.12,p.1535 (1985).

7. A.S.Solodukhin et al. Kvant.Elektron.,v.13,N4,p.845(1986).

8. A.G.Basiev et al. Zh.Teor.Fiz.,v.50,N8,p.1740 (1980).

9. A.D.Belykh et al. Kvant.Elektron., v.12, N11, p.21 (1985).

Enhanced Direct-Detection of CO_2 Lidar Returns Using a Laser Pre-Amplifier*

by

D.K. Killinger
Lincoln Laboratory,Massachusetts Institute of Technology
Lexington, Massachusetts 02173-0073
(617) 863-5500, Ext. 4740,

J. L. Bufton
NASA/Goddard Space Flight Center
Greenbelt, MD 20771

and,

E.J. McLellan
Pulse Systems, Inc.
Los Alamos, NM

The relative merits and technical differences between direct-detection and heterodyne-detection for CO_2 lidar are well known. Direct-detection offers enhanced information concerning the average intensity of the lidar returns but at the expense of reduced signal-to-noise level. Heterodyne detection requires an increase in system complexity, provides an enhancement in the S/N ratio of 4 to 6 orders of magnitude, but is limited in its ability to scan rapidly through several CO_2 laser lines.

Recently a new detection technique has been studied which provides signal detection of the lidar returns and combines some of the advantages of both heterodyne and direct detection. In this technique, a CO_2 laser pre-amplifier is placed between the lidar telescope and optical detector and serves as an optical amplifier of the received lidar photons. The technique is not new. It was first used in the 1950's with the development of the ammonia maser, and was originally used to amplify optical emission from astronomical ammonia sources. Such optical amplifier techniques have been investigated in the past, but problems were often encountered with the gain, spontaneous emission noise, and entrance field-of-view , with the result that the device could not be used in a practical system. [1] Recently, the development of a low-pressure, pulsed discharge. multi-pass CO_2 laser amplifier has overcome most of these problems and has been shown to provide enhanced detection in laboratory experiments.[2]

In this paper we report the first experimental use of such a laser pre-amplifier in a tunable, single-frequency CO_2 lidar system. This technique has demonstrated an improvement in the S/N ratio of the lidar returns of up to 200. A schematic of the lidar

system is shown in Fig.1. A pulsed, hybrid-TEA CO_2 laser (Laser Science Inc., PRF-150) was used to generate 100 mJ, 300 ns duration, single-frequency, 3 Mhz linewidth, laser pulses which were tunable over approximately 40 lines . The output from the laser was monitored by spectrometers and power meters, and the majority of the laser output was directed out the laboratory window toward a topographic target(building) at a range of 300m. The backscattered lidar returns were detected by a 30-cm diameter telescope, recollimated into a 20 mm diameter beam with a length of 1.5 m, and focused onto a cooled HgCdTe detector. Measurements of the lidar signal level and background noise level were recorded.

The laser pre-amplifier placed infront of the detector was developed at Pulse Systems Inc. and consisted of a low-pressure (40 Torr), pulsed discharge CO_2 laser which was operated as a traveling-wave-amplifier within a seven-pass folded optical path.[2] The temporal profile of the optical gain of the pre-amplifier is shown in Fig. 2 and lasts for approximately 200 µs. The linearity of the laser pre-amplifier was tested in the laboratory by passing a CO_2 laser pulse through the pre-amplifier and measuring the change in the amplitude of the pulse. By varying the amplitude, the linearity of the optical gain was measured as a function of amplitude and the results are shown in Fig. 3. As can be seen, the pre-amplifier was linear in gain over a range of nearly 4 orders of magnitude in variation of the input pulse amplitude. Such results are important since they imply that the pre-amplifier can be used in a DIAL system without distorting the amplitude of the returned lidar pulse amplitudes. Further details of the design considerations of the laser pre-amplifier have been presented elsewhere[2] and in a companion paper at this meeting.

The lidar tests were conducted by first measuring the signal and noise values of the lidar detector signals as viewed on an oscilloscope without the pre-amplifier in the optical path. The pre-amplifier was then inserted into the optical path as shown in Fig.1. Measurement of the S/N values prior to turning on the discharge indicated that the optical insertion loss was a factor of 4. Finally, the pre-amplifier laser discharge was turned-on and the S/N values measured. The observed gain in the signal level of the lidar return after turning-on the pre-amplifier discharge was approximately 800, with no increase in the measured noise level observed. Taking into account the optical insertion loss, the appropriate gain in the lidar S/N ratio was , thus, 200. The gain was found to be sensitive to the relative optical alignment of the lidar telescope and entrance/exit optics of the pre-amplifier and detector. The amplitude stability of the returned lidar signals appeared to be the same as the laser pulse amplitude stability. While most of the optical gain tests were conducted using the 10.6 µm P(22) CO_2 line, similar results were obtained as the CO_2 laser was tuned through most of the prominent lines of the 9.6 µm and 10.6 µm bands.

In conclusion, these preliminary studies have indicated the advantages and technical difficulties in the use of the pre-amplifier. While, in general, the results are quite encouraging, several features and operating parameters have been quantified which appear to influence the utility of the pre-amplifier for use in a practical lidar system . These factors include, for brevity, (1) the advantage that only optical radiation falling within the linewidth of the CO_2 laser lines is amplified, (2) the use of a

pulsed, high-gain discharge results in significant signal gain without the usual increase in background optical noise, (3) amplified spontaneous emission (ASE) is the dominant noise source, (4) the optical design is a compromise of several factors which consider the interplay of total optical gain and ASE, and the field-of-view of the entrance and exit optics, (5) care must be used to make sure the pre-amplifier itself does not go into self-lasing, (6) while the optical gain varies during the 200µs pulse discharge, it is rather easy to measure the enhanced gain of the lidar pulse which appears on-top of the ASE pulse envelope (see Fig. 2), and (7) a hybrid-TEA CO_2 laser with frequency stability of only 10 to 20 MHz is quite adequate to ensure that the laser linewidth falls within the bandwidth of the pre-amplifier. Further studies are being conducted to investigate these factors and better quantify the gain parameters of the pre-amplifier.

References:

1. H. Hieslmair, C.J. Bickart, and J.N. Fulton, IEEE J. Quant. Elect. 86 (1970).

2. E.J. McLellan, B. Fisher, D.K. Thomas, and J.L. Bufton, "Optical Pre-Amplifier Performance for CO_2 Lidar Applications", Paper FB3, Conf. Lasers and Electro-Optics, June (1986).

Pulsed Hybrid TEA
CO2 Laser
(Single-Frequency)

HqCdTe
Detector

Pulsed CO2 Laser
Pre-amplifier
(7-Pass Folded Optical Path)

30-cm dia.
Telescope
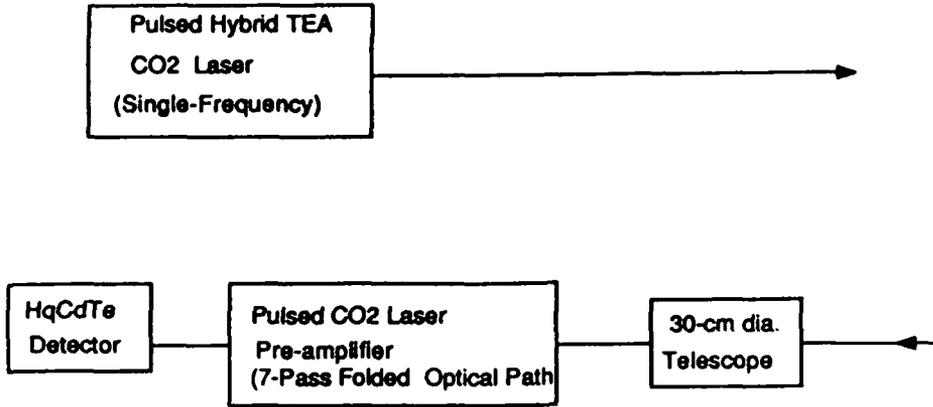
Fig.1 Schematic of CO_2 Lidar System

CO_2 LASER PRE-AMPLIFIER
Fig.2 SPONTANEOUS EMISSION POWER (P_s)

PEAK-TO-PEAK
14μsec — 7% VARIABILITY
RISETIME (32 pulses)

42 TORR OPERATING
PRESSURE

FWHM = 140μsec

P_s (watts) $\times 10^6$

TIME (μsec)
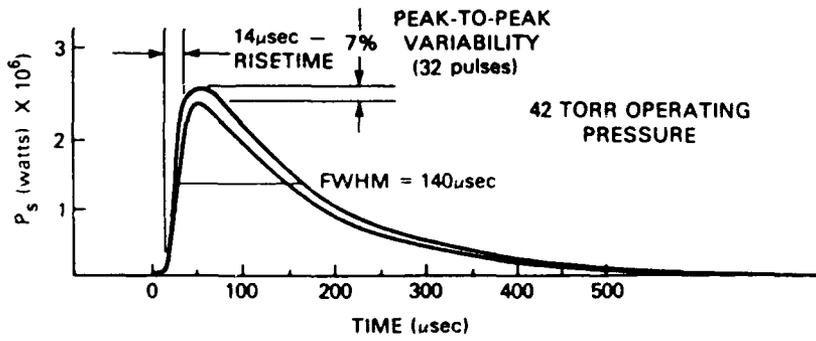
Fig.3 CO_2 LASER PRE-AMPLIFIER LINEARITY TEST
4/8/86
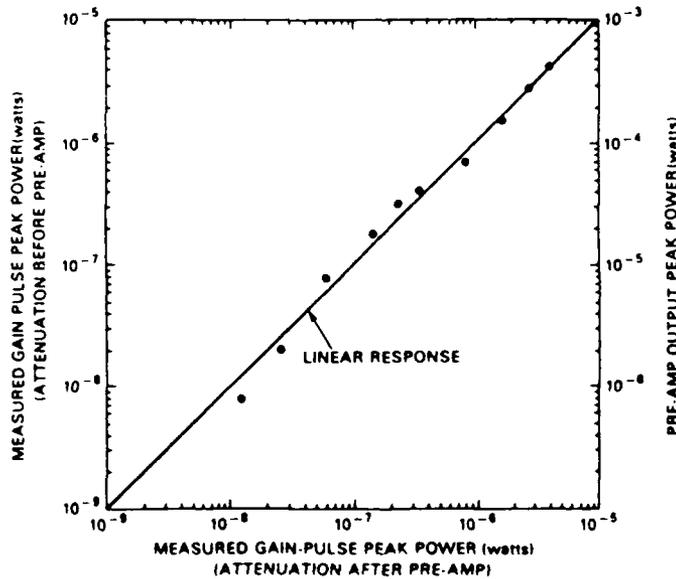
MEASURED GAIN PULSE PEAK POWER(watts)
(ATTENUATION BEFORE PRE-AMP)

PRE-AMP OUTPUT PEAK POWER(watts)

LINEAR RESPONSE

MEASURED GAIN-PULSE PEAK POWER (watts)
(ATTENUATION AFTER PRE-AMP)

Plans for an Airborne Multispectral Laser Imaging
Polarimeter System

James E. Kalshoven, Jr

NASA Goddard Space Flight Center
Sensor Concepts and Development Branch/625
Greenbelt, MD 20771

There has been difficulty in making effective use of the natural depolarization properties of the Earth's surface as a parameter in land remote sensing. This arises from the problem in building a theoretical foundation upon which to interpret the data from reflected polarized solar radiation which is complicated by atmospheric effects and a diversity of viewing and phase angles. By designing an experiment that substantially eliminates the atmospheric and phase angle effects, a data base could be developed upon which theoretical models could be verified, refined, and predictions made. This is the goal of an airborne imaging polarimeter system being planned at NASA Goddard Space Flight Center.

By illuminating the surface with 100% polarized light, the degree of depolarization can be measured by a remote sensor. This depolarization varies with surface characteristics, including soil type and moisture content, plant species and stress conditions, and ocean, lake, and river dissolved and suspended matter.[1],[2] By using different wavelengths, additional correlations can be made to extract information from the surface.[3]

The planned system would employ a frequency doubled, polarized Nd:YAG pulsed laser as the source to provide irradiance at 1060 and 530 nm. A cylindrical lens would diverge the laser beam along one axis while leaving it unaffected in the other axis. This line of light would then irradiate the surface of interest in a direction perpendicular to the line of flight. A dual telescopic receiving system would be used at each wavelength to detect the two orthogonal polarization states of the reflected radiation. Each wavelength would require two telescopes with the properly oriented polarization filter and narrow bandpass frequency filter. A third telescope could be added if the azimuth of polarization is desired as explained in the next paragraph. In the focal plane of each telescope would be mounted a linear array of detectors oriented parallel to the transmitted line of laser light. An image of the surface under investigation would then be generated as the system moves along in the aircraft perpendicular to the line of laser light. Each pulse of the

laser would contribute an additional narrow swath of crosstrack data to produce the continuous image.

Measurement of the orthogonal polarizations, A(0) and A(90), at the detector arrays allows the determination of the I and Q Stokes parameters for calculating the polarization factor, P, as follows:

$$I = A(0) + A(90)$$
$$Q = A(0) - A(90)$$

$$P = Q/I$$

By employing an additional receiving telescope and detector combination and measuring polarization at 0, 60 and 120 degrees, the additional U Stokes parameter can be determined to allow the calculation of the azimuth of polarization, θ, as follows:

$$I = 2/3[A(0) + A(60) + A(120)]$$
$$Q = 2/3[2A(0) - A(60) - A(120)]$$
$$U = -2/3[A(120) - A(60)]$$

$$\theta = 1/2 \arctan[U/Q]$$

Images can be generated as described by Prosch [4] in the triple telescope system, or through computer manipulation and enhancement in either the dual or triple telescope system.

There are many variations and tradeoffs possible on actual system specifications. Aircraft flight qualified Nd:Yag lasers with energy of at least 500 mj (@1060 nm) and 300 mj (@530 nm) per pulse are in use at NASA. Using a fast 50 mm lens for each polarization state and wavelength and a 512 element linear array with at least 5% Q.E. at 1060 nm, SNR's approaching 100 at 1060 nm and 50 at 530 nm can be obtained. This assumes a narrow spectral filter (less than 10 nm) for daytime observations. Each pulse would irradiate a surface area of about 2.5 by 400 meters from an altitude of 1000 meters. Depolarization measurements of 3 to 5% can be obtained.

Production of depolarization images of the Earth's surface, as opposed to "point measurements," will be significant to Earth resources analysis. It will provide a new field parameter for theoretical modeling programs and aid in the interpretation of passive spaceborne solar polarization measurements.

----

1. W. G. Egan, <u>Photometry and Polarization in Remote Sensing</u> (Elsevier, New York, 1985).

2. V. L. Granatstein <u>et</u>. <u>al</u>., "Depolarization of Laser Light Scattered from Turbid Water," Appl. Opt. <u>11</u>, 1870 (1972).

3. K. L. Coulson, "Effects of Reflection Properties of Natural Surfaces in Aerial Reconnaissance," Appl. Opt. <u>5</u>, 905 (1966).

4. T. Prosch <u>et</u>. <u>al</u>.. "Video Polarimetry: a New Imaging Technique in Atmospheric Science," Appl. Opt., <u>22</u>, 1360 (1983).

Design Concepts for An Advanced Airborne

Meteorological Lidar (LASE II)

Geary Schwemmer
Laboratory for Atmospheres
NASA/Goddard Space Flight Center
Greenbelt, MD 20771

The use of differential absorption lidar (DIAL) instruments in high altitude aircraft platforms for mesoscale meteorological applications dictates requirements on the instrument systems which approximate or approach spacecraft platform requirements. Unattended automated operation, power, mass, volume, and data rate may be constrained to some extent. The ability to utilize such a platform provides a good opportunity to demonstrate technology developments which will enhance the possibility of developing spaceborne lidar atmospheric sounders. This paper describes the investigation of techniques to increase alexandrite laser efficiency and frequency stability, and the use of Fabry-Perot etalons in a double narrow-passband receiver filter.

NASA/Goddard's Laboratory for Atmospheres is investigating the feasibility of a number of techniques to increase the capabilities of meteorological lidar as part of feasibility studies for LASE II. LASE II includes a DIAL instrument that will measure atmospheric temperature and pressure profiles for mesoscale meteorology. It is designed to modularly conform to the LASE facility developed by NASA/Langley Research Center. The LASE facility will be installed in NASA's ER-2 high altitude research aircraft. Considering the typical 0.1% efficiency of narrowband alexandrite lasers presently being used in ground- and aircraft-based lidar systems, an ER-2-based system would require between 3 and 4 kw of electrical power. A polar orbiting system would require about 8 kw.

The primary reasons for such a low efficiency are:

1) The xenon flashlamps used to pump alexandrite have a large portion of their energy in spectral regions which are not absorbed by the laser rod, and

2) The use of lossy intracavity etalons to spectrally narrow and tune the laser output increases laser threshold and decreases gain, therefore decreasing the laser efficiency. Alexandrite lasers that do not use high resolution tuning optics, and which are optimized for efficiency, routinely achieve 1% and greater efficiency.

To avoid the loss in efficiency due to tuning optics insertion losses, we are experimentally evaluating the use of tunable narrowband, single mode diode lasers as an injection source for high power pulsed alexandrite lasers. By forcing the pulsed laser radiation to build up from the narrowband injected radiation, most if not all of the frequency selective tuning optics may be removed from the cavity allowing large increases in efficiency. Injection locking a high power pulsed laser with low power narrowband laser radiation has long been used in CO_2 and dye lasers. Allied Corporation has successfully demonstrated the use of single mode diode lasers to injection lock a high

power pulsed alexandrite laser[1]. Under a contract from NASA,[2] Allied is developing a frequency-stabilized, diode injection locked narrowband alexandrite laser to characterize its output qualities and evaluate its potential as a LASE II transmitter. In addition, the Laboratory for Atmospheres is experimentally investigating techniques for active frequency stabilization of diode lasers to features in the oxygen absorption spectrum at 760 and 770 nm that we use to make lidar measurements of atmospheric pressure[3] and temperature.[4]

To address the problem of inefficient spectral match of flashlamp pumping and alexandrite absorption, we will be looking at the possibility of pumping alexandrite with the frequency doubled output of diode pumped Nd:YAG lasers, and, should they be developed, with visible red diode lasers. A small, continuous-wave alexandrite laser was operated with near 50% conversion efficiency when pumped with 647 nm radiation from a krypton laser.[5] Presently, our efforts are confined to modeling the characteristics of laser pumped alexandrite lasers.

The requirement to make daytime as well as nighttime temperature profile measurements with LASE II imposes design criteria on the receiver optics that are used to reduce the daytime background radiation by eight orders of magnitude. The receiver field of view should not be smaller than 1 mrad in order to completely encompass the transmitted laser beams which must have a divergence of 0.7 mrad or greater due to eye safety. Additional background rejection is accomplished by using optical filtering with a total bandpass of $0.48 \, cm^{-1}$ FWHM. Since the on-line and off-line laser wavelengths may be separated by more than this amount, a double bandpass filter is used, each with a bandpass of $0.24 \, cm^{-1}$ FWHM. To achieve the double narrow bandpass and high throughput, we are examining the use of tandem Fabry-Perot etalons with spacings chosen so that the resultant combined free spectral range is the product of the two individual free spectral ranges. Two of the resulting passbands are isolated and the others blocked using a suitable interference filter with a bandwidth of approximately 1 to 2 nm.

Design concept details for the diode laser injection locked alexandrite transmitter and the double narrow bandpass receiver filter will be presented and discussed.

References

1. Krasinski, J., P. Papenstor, J. Pete, and D. F. Heller, Tunable Solid State Laser Conf., Zig-Zag, Oregon, paper WB-4 (1986).

2. NASA Contract NAS5-30102.

3. Korb, C. L., G. K. Schwemmer, M. Dombrowski, and R. Kagann, in Tunable Solid State Lasers for Remote Sensing, R. L. Byer, E. K. Gustafson, and R. Trebino, Eds., Springer-Verlag, New York, 35, (1986).

4. Kalshoven, J. E., Jr., C. L. Korb, G. K. Schwemmer, and M. Dombrowski, Appl. Opt., 20 (11), 1967 (1981).

5. Lai, S. T. and M. L. Shand, J. Appl. Phys., 54 (10), 5642 (1983).

Overview of an Advanced Lidar for an Atmospheric Temperature Profile Measurements Program

Bertrand L. Johnson, Jr.[a], C. Laurence Korb[a], Pierre Flamant[b], Mireille Bourdet[c], John Degnan[a], Gerard Megie[d], S. Harvey Melfi[a], Geary Schwemmer[a], Louis Uccellini[a]

Introduction
The LASE (Laser Atmospheric Sensing Experiment) program is managed by the NASA Langley Research Center (LaRC) and is the development of a modular lidar facility which can be operated autonomously from the high altitude (60,000 feet) NASA ER-2 aircraft. Phase I of this program is the development of a lidar instrument system by LaRC to measure atmospheric water vapor profiles. Phase II (also refered to as LASE II) is the development by the NASA Goddard Space Flight Center (GSFC), in cooperation with the Centre National d'Etudes Spatiales of France, of an advanced lidar instrument system to measure temperature and pressure profiles of the earth's atmosphere. GSFC is developing the solid state (Alexandrite) laser transmitters for both phase I and phase II.

Science
The scientific objectives of the LASE II effort center on the study of mesoscale phenomena and take advantage of the high altitude capability of the ER-2 aircraft. The LASE II system will provide a unique data set to study the interaction between stratospheric extrusion and ocean-influenced planetary boundary layer prior to and during major oceanic cyclone events. The observational requirements are: for altitude range - 0 to 15 km; vertical resolution - 0.5 km; horizontal resolution - 10 km; and temperature accuracy - ≤ 1 degree K.

[a] National Aeronautics and Space Administration, Goddard Space Flight Center, Greenbelt, Maryland 20771, USA

[b] Ecole Polytechneque, Laboratoire de Meteorologie Dynamique du CNRS, 91128 Palaiseau Cedex, France

[c] CNRS Institut National d'Astronomie et de Geophysique, 77, avenue Denfert-Rochereau, 75014, Paris, France

[d] Centre National de al Recherche Scientifique (CNRS), Service d'Aeronomie, 91370 Verrieres-le-Buisson, France

Lidar Temperature Measurement

A differential absorption lidar (DIAL) technique forms the basis for the proposed high accuracy temperature and pressure measurement. It uses two tunable pulsed lasers, one located on a portion of a resonant absorption line of oxygen and a second at a nearby reference frequency. The energy backscattered at each frequency by aerosols and molecules in the atmosphere is measured as a function of time using a range gated receiver which allows the atmospheric oxygen absorption to be measured over a known path. Since oxygen is uniformly mixed in the atmosphere, and the mixing ratio is known a priori, then the measurements can be structured to determine either the temperature or pressure profile. A two-wavelength differential absorption lidar technique developed by Korb et al of GSFC is used for measuring the atmospheric temperature profile. The approach uses a measurement of the absorption at the center of a line in the oxygen A band which originates from a quantum state that depends strongly on temperature through the Boltzmann distribution and can be used to obtain a highly sensitive temperature determination . A small change in temperature produces a large change in absorption coefficient; roughtly 1.5% per degree K. The atmospheric absorption coefficient is found experimentally using the ratio of the on-line and reference backscattered signals.

Instrumentation

The laser transmitter to be developed for LASE II is a tunable dual wavelength Alexandrite; tunable over the range 759 to 770 nm. The Alexandrite laser transmitter for the LaRC LASE I program, presently undergoing integration and testing, is tunable over the range of 720 to 780 nm. The LASE II transmitter will be based on this development. The proposed baseline approach is for a long folded resonator design and injection-locking techniques are presently being studied to narrow the linewidth, and increase laser efficiency and frequency stability.

CNES/CNRS of France is developing the wavemeter which will measure the spectral characteristics of the laser beams for each emitted pulse. The values of the two centroid wavelengths are computed by the wavemeter in real time and are used in a servo-loop to provide active control of the laser frequency. The complete information on the measured spectral profiles is sent to the system computer for storage. True spectral energy distribution is computed during post analysis.

Daytime and nighttime measurements will be made and the receiving optics must reduce daytime background radiation greatly ($\approx 10^8$ times). To accomplish this, a dual bandpass filter system using Fabry-Perot etalons is being investigated. Laboratory studies to improve PMT detectors for this application are continuing.

To meet the scientific objectives of the experiment the laser linewidth must be narrower than 0.005 cm^{-1} and controlled to 0.001 cm^{-1}. The wavemeter must measure the absolute value of the frequency to 0.001 cm^{-1}. The required receiver bandwidth is 0.24 cm^{-1} for each laser wavelength.

Status

In-flight atmospheric pressure profiles have been made by Korb et al on the NASA Wallops Flight Facility Electra aircraft. Ground-based lidar atmospheric temperature measurements have also been made. This research program is continuing and an upgraded lidar system is scheduled to make further pressure measurements near the end of this year. With further system refinements flight lidar temperature profile measurements are planned late in 1988. We anticipate that the LASE II system will fly in 1993.

Implementing a New High-Spectral-Resolution Lidar Technique for

Backscatter Ratio and Atmospheric Temperature Profiling

C. Y. She, R. J. Alvarez II, H. Moosmüller, and D. A. Krueger
Physics Department
Colorado State University
Fort Collins, Colorado 80523

Lidar systems rely on backscattering from air molecules (Rayleigh scattering) and from suspended aerosol particles (Mie scattering) for their return signal. Due to the thermal motion of both molecules and particles the backscattered light is Doppler broadened in frequency. Molecular backscattering has a temperature dependent linewidth of 2 GHz. Aerosol particles, being many orders of magnitude heavier than molecules, show much slower thermal motion and the resulting Doppler broadening can be neglected in most circumstances. The spectrum of backscattered light, consisting of a wide Rayleigh and a narrow Mie scattering component, is shown in Fig. 1(a). Basic
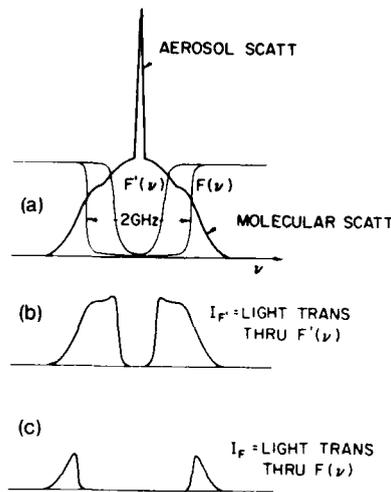
Fig. 1. **(a)** Rayleigh/Mie light scattering spectrum of air molecules consisting of a sharp aerosol peak and a broadened molecular Rayleigh spectrum. In the same figure, the transmission curves of two atomic filters, F'(ν) at low temperature and F(ν) at higher temperature, are shown. Residual scattering spectra after the transmission through the low temperature filter and high temperature filter are given in **(b)** and **(c)**, respectively.

lidar techniques do not separate these two signal components and a lot of interesting information inherent to the return signal is lost. What is left is the ability to localize spatial gradients in the density of backscatters, which are mostly due to clouds, haze, smoke plumes and inversion layers. Further information such as aerosol backscatter ratio and atmospheric temperature can be obtained from a basic lidar system only if assumptions on atmospheric extinction and air molecular density based on modeling or on other measurements are made. Techniques that can be used to measure these parameters directly are therefore of interest. While Raman scattering and differential absorption have been used to measure tropospheric temperature, the signal-to-noise of these lidar techniques is lower than that of the Rayleigh-Mie scattering technique. In order to extract atmospheric information from Rayleigh-Mie scattering, the aerosol- and molecular-scattering components, which are contained in a narrow bandwidth of 2 GHz, must be spectrally separated and analyzed. An obvious solution is to use a scanning Fabry-Perot interferometer to analyze the spectrum of the scattered light induced by a single-frequency laser. Indeed, the early and only atmospheric parameter measurement using Rayleigh-Mie scattering was performed in this manner.[1] In this 1971 experiment, Fiocco and co-workers made a remote temperature measurement at 4-km height; they achieved a measurement accuracy of a few degrees by averaging over a 2-km path and a 1-h time duration. Since much of the spectrum is undetected at any given instant, a scanning method is time consuming and therefore not suitable for lidar applications. A desirable high-spectral-resolution lidar (HSRL) technique should be one that uses a single-frequency laser as the light source and an adequate narrow-band blocking filter that permits separation of molecular scattering from aerosol scattering and analysis of the scattering spectrum without scanning. Such methods have been conceived. Using a Fabry-Perot interferometer at a fixed setting as the blocking filter, in 1983 Sroga et al.[2] made successful atmospheric backscatter ratio measurements despite alignment difficulties. In 1981 Schwiesow and Lading[3] proposed temperature profiling with a HSRI using an interferometer, although no experimental result has yet appeared in the literature. Realizing the problems in alignment difficulty and small dynamic range in aerosol rejection associated with interferometers, Shimizu et al. at Colorado State University proposed in 1983 the use of narrow-band atomic blocking (bandstop) filters in a HSRL for atmospheric parameter measurements.[4] These filters reject Mie scattering and transmit different portions of the spectrum of Rayleigh scattering as shown in Fig. 1. Theoretical calculations[4,5] indicate that when this HSRL technique is successfully implemented, many basic lidar systems can be modified to perform routine atmospheric temperature profiling with 1-K accuracy, 30-m depth resolution, and a 10-sec measurement time at a range of 5 km.

At Colorado State University, experimental efforts for implementing a prototype lidar system based on our 1983 proposal have begun. In this paper, we report the progress of this undertaking. Our experimental program has been divided into three stages of development. First, we develop a suitable atomic vapor filter (AVF) and test the proposed concept with a tunable cw dye laser system. Second, we setup a pulsed dye laser amplifier and repeat the laboratory experiment with a pulsed laser system. Third, upon the successful development of the first two stages of the program, we setup a prototype HSRL system for field measurement of tropospheric backscatter ratio and temperature profiling.

The laboratory measurements of atmospheric temperature and backscatter ratio using a cw laser system have been completed. For this experiment, a barium heat-pipe oven nas been constructed and is used as the AVF. By varying the oven temperature, the band width of this AVF may be varied from 1.4 GHz to 1.8 GHz with ease. The transmission profiles of the AVF at various settings, which are needed for the experimental determination of backscatter ratio and atmospheric temperature, are traced out with a single frequency tunable dye laser. Setting the frequency of a narrow-band dye laser (band width of 1 MHz) at the center of the barium absorption (5537 Å), the light scattered from a small volume in room air passes through the AVF and is monitored on and off the barium resonance at different oven temperature settings. Using the formulae in Ref. 4, the backscatter ratio and atmospheric temperature can be measured. In this manner, laboratory measurements of atmospheric temperature and backscatter ratio have been made, yielding an accuracy of 1 K and 3%, respectively. This result has been published recently.[6] We have achieved the same measurement accuracy under different atmospheric (temperature and pressure) conditions.

At present, we are in the process of conducting laboratory measurements with a pulsed tunable laser system. A pulsed dye laser amplifier has been constructed. When the cw dye laser is sent through the pulsed dye amplifier, a single frequency tunable pulsed output of 1 MW per pulse is obtained. The measured band width of this output is about 160 MHz, quite adequate for the proposed experiment. Unfortunately, in addition to the single frequency output, the beam contains a weak broad band flourescence whose spectral distribution has not been measured. Using this tunable source, the transmission profiles of the barium AVF at different settings have been taken. The functional shapes of these transmission profiles are, within experimental accuracy, identical to those taken with a cw tunable laser, indicating that the broader bandwidth (160 MHz) of the pulsed system causes no problem. However, unlike the transmission profiles obtained with the cw dye laser, the flat bottomed peak attenuation does not correspond to zero transmission. This residual transmission resulting from the weak broad band flourescence in the beam output ranges from 1.5% to 12% depending on the output power, and the condition of the dye as well as other parameters yet to be determined. We are investigating the factors affecting the amount of this residual transmission and are trying to minimize it. With the presence of the residual transmission, which is, of course measureable, the formulae for determining backscatter ratio, r, and the ratio of molecular factors, f_m/f'_m, can be given as:

$$r = \frac{1 - N_1 f_m/N_2 (1 + \epsilon)}{1 - \epsilon N_1/N_2 (1 + \epsilon)} \tag{1}$$

$$f_m/f'_m = \frac{1 - \epsilon' N_1/(1 + \epsilon') N_2}{1 - \epsilon N_1/(1 + \epsilon) N'_2} \cdot \frac{N_2}{N'_2} \tag{2}$$

where N_1 is the total (or off-resonance) scattered photon counts. N_2, f_m, and ϵ are respectively the on-resonance counts, molecular factor, and residual transmission of the AVF at one oven setting; the corresponding rimed parameters, N'_2, f'_m, and ϵ' are those at a second oven setting. As discussed previously,[4,6] atmospheric temperature may be determined by comparing the measured and calculated values of f_m/f'_m. We anticipate that the results of

laboratory measurements with the pulsed laser system along with the effects of residual transmission and signal strength on signal-to-noise of the measurement will be presented in the meeting.

We have ordered equipment and setup a remote sensing laboratory at the CSU Christman Field, an old University airport site. Among other items, a commerical pulsed dye laser amplifier has been ordered; its performance in broad band flourescence emission and residual transmission will be experimentally assessed. In addition, a transient digitizer has been acquired for range resolved measurements, and it is being interfaced with a computer. A schematic of our proto-type HSRL system is shown in Fig. 2.
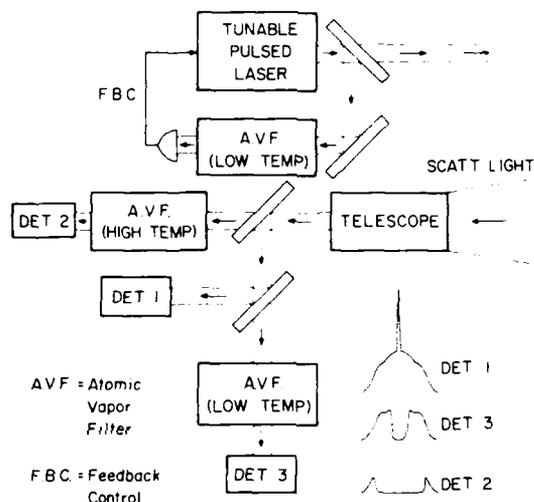
Fig. 2. Schematic of a HSRL system. The laser is tuned and locked to the absorption peak of an atomic barium filter. The lidar return is divided into three channels and detected after different filtrations.

REFERENCES

1. G. Fiocco, G. Benedetti-Michalangeli, K. Maischberger, and E. Madonna, Nature 229, 78 (1971).
2. J. T. Sroga, E. W. Eloranta, S. T. Shipley, F. L. Roesler, and P. T. Tryon, Appl. Opt. 22, 3725 (1983).
3. R. L. Schwiesow and L. Lading, Appl. Opt. 20, 1972 (1981).
4. H. Shimizu, S. A. Lee, and C. Y. She, Appl. Opt. 22, 1372 (1983).
5. H. Shimizu, K. Noguchi, and C. Y. She, Appl. Opt. 25, 1460 (1986).
6. F. J. Lehmann, S. A. Lee, and C. Y. She, Opt. Lett. 11, 563 (1986).

0.53 µm Incoherent Doppler Lidar: Current Status

J. Sroga and A. Rosenberg
RCA Astro-Space Division
PO Box 800
Princeton, NJ 08543-0800

INTRODUCTION

Measurements of the atmospheric wind field have been shown by simulations to improve global numerical weather prediction (Atlas, et al., 1985) and several spaceborne lidar systems have been proposed to meet the global wind measurement requirements.   Menzies (1986) has given a comparison of the relative performance of four potential spaceborne Doppler lidar systems utilizing either coherent (heterodyne) detection at 1.06 µm and 9-11 µm wavelengths or incoherent (direct) detection at 0.35 µm and 0.53 µm wavelengths.   This paper describes a ground based, 0.53 µm incoherent Doppler lidar and presents preliminary results of atmospheric testing to demonstrate this incoherent Doppler lidar technique.

System Description

Figure 1 shows a block diagram of the 0.53 µm Doppler lidar prototype.   The transmitter consists of an oscillator amplifier Nd:YAG laser constrained to yield transform limited, single frequency pulse with a KDP crystal converting the 1.06^4 µm radiation to the 0.53 µm Doppler lidar operating wavelength.   The transmitted beam is expanded by a 5X telescope and directed into the atmosphere via steering optics.   The operating characteristics of the transmitter are given in Table 1.   The backscattered signal is collected by a 31.75 cm diameter Cassegrain telescope and coupled into a high resolution Fabry-Perot Interferometer for analysis of the Doppler shift.   The FPI design utilizes a multichannel Image Plane Detector (IPD) and is similar to the one flown on the Dynamics Explorer Satellite (Hays et al., 1981).   Table 2 lists the characteristics of the receiver system.   The photoelectrons detected by the FPI-IPD system are converted in digital signals for storage and processing by a multichannel Data Acquisition System (DAS) consisting of several TRAQ1 multichannel ADC camac modules (12 bit, 500 kHz) interfaced to a Stride 460 microcomputer via a camac to IEEE 488 controller.   The Stride operates under a multiuser system with one megabyte of ram, 33 megabyte hard disk, one floppy disk drive, a quarter inch tape system and graphics capabilities.   The DAS sampling period is synchronized to within <50 ns of the laser transmitter pulse.

Preliminary Atmospheric Demonstration.

The 0.53 μm Doppler lidar is currently undergoing atmospheric testing to demonstrate the incoherent Doppler lidar technique. Figure 2a shows an example of the FPI-IPD spectra obtained with the system pointed vertically. The data are plotted as a histogram of the IPD signal intensity at various range gate samples with the sample label 1 being the transmitted laser spectrum which yields the system reference wavelength. The remaining samples are measurements of the atmospheric backscatter spectra sampled at the altitudes indicated. The IPD was operated at low gain to prevent the near field signal from saturating the IPD causing a nonlinear response. The data have not been corrected for the inverse range square attenuation but a scale change at $z-900m$ accentuates the spectral measurements at higher altitudes. The backscatter signal from the clear atmosphere ($z-300-1500m$) show the narrow band aerosol backscatter spectrum superimposed over the broader, molecular backscatter spectrum. A photomultiplier used to monitor the total backscatter signal showed multiple thin cloud layers between 5 and 6 km. The samples labeled 17-21 are the backscatter spectra from these clouds and show the same narrow spectral distribution as the transmitted laser.

This data has been analyzed according to the procedures described in Sroga and Rosenberg (1986) to estimate the total aerosol and molecular backscattered signals, relative Doppler shift and regression errors. Figure 3 shows the ratio of the total aerosol to total molecular backscatter deirved from the regression analysis of this data and shows the capability of this system to spectrally differentiate between aerosol, molecular and cloud backscatter. A coeleostat is currently being implemented in the system to allow slant path Doppler lidar measurements and improvements in the laser performance and detector dynamic range are planned. Results of these slant path measurements will be presented.

References

Atlas, R., E. Kalnay, W. E. Baker, J. Susskind, D. Reuter and M. Halem (1985) "Observing System Simulation Experiments at GFSC" in Global Wind Measurements, W. E. Baker and R. J. Curran Eds, A. Deepak Publishing. pp 65-71.

Hays, P. B., T. L. Killeen and B. C. Kennedy (1981) "The Fabry-Perot Interferometer on Dynamics Explorer," Space Sci. Instrum. V5, pp 395-416.

Menzies, R. T. (1986) "Doppler Lidar Atmospheric Winds Sensors: A comparative performance evaluation for Global Wind Measurement Applications from Earth Orbit," Appl. Opt. V25, pp 2546-2553.

Sroga, J. and A. Rosenberg (1986) "Calibration and Analysis for a 0.53 μm Incoherent Doppler Lidar" presented at thirteenth International Laser Radar Conference, Toronto, Ontario, Canada, Aug. 11-15, 1986.

TABLE 1. 0.53 μm Doppler Lidar Transmitter

Energy	50 mj/pulse (SLM)
Pulse Width	40 ns (FWHM)
Bandwidth (transform limit)	25 MHz (FWHM)
Beam Divergence	0.5 milliradians
Repetition rate	1 Hz

TABLE 2. 0.532 μm Doppler Lidar Receiver

Telescope	31.75 cm f/16 Cassegrain
Fiber Optic Coupling	f/6 final system
Fabry-Perot Interferometer	
Etalon Spacing	30.48 cm (Zerodur)
Etalon Reflectivity	73% @0.532 μm
Interference Filter	1.2 nm (fwhm)
Image Plane Detector	ITT model F4151
	Z-MCP
	S20 photocathode
Quantum Efficiency	5-10% @ 0.532 μm
Anode	12 Concentric, equal area rings

Wind Sensor Block Diagram

Figure 1.

Figure 3.

Aerosol : Molecular Backscatter Ratio

a.

b.
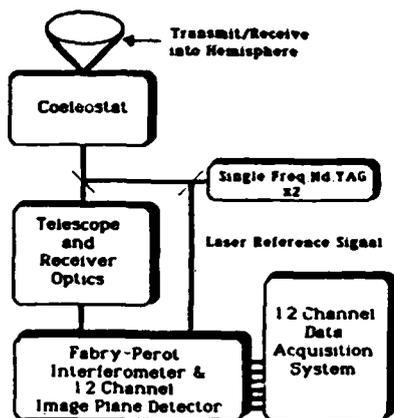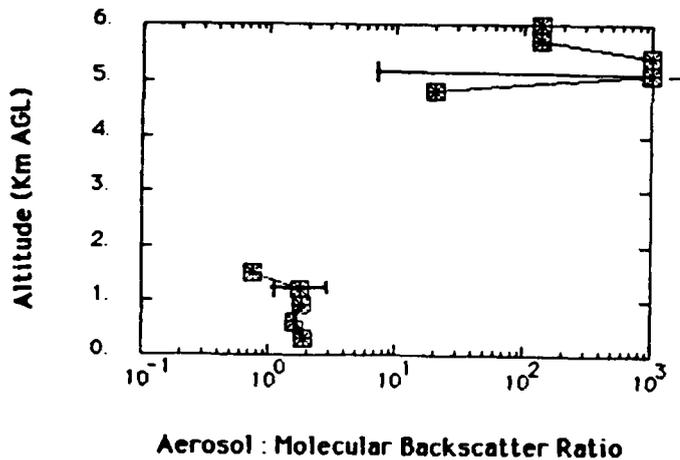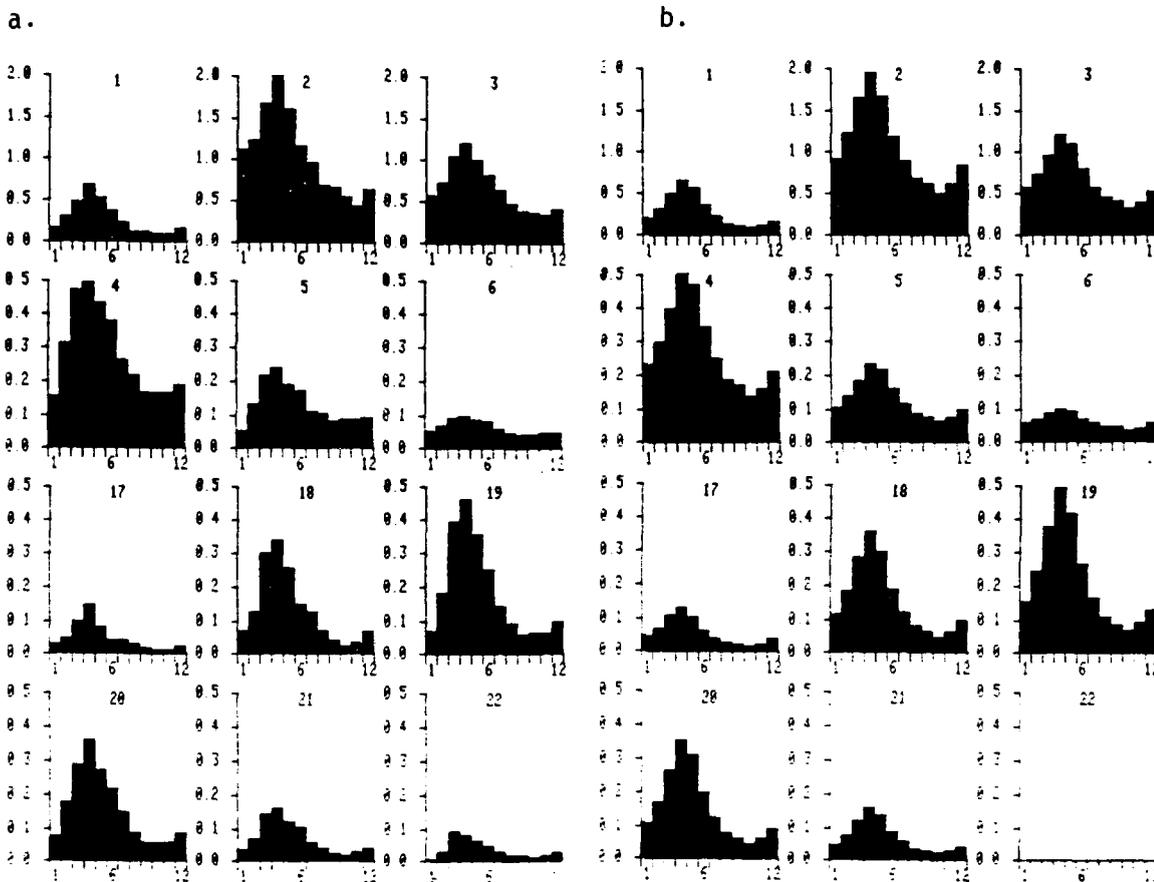
Figure 2. a) Atmospheric Data, b) Regression fit
1) Transmitted Laser Spectrum, 2) z=300 m, 3) z=600 m
4) z=900 m, 5) z=1200 m, 6) z=1500 m, 17) z=4800 m,
18) z=5100 m, 19) z=5700 m, 20) z=6000 m.

A Portable UV-DIAL System for Ground-Based Measurements
of Lower-Stratospheric Ozone Profiles:
Design and Performance Simulation

M.O. Rodgers[1], R.E. Stickel[2], K. Asai[3], J.D. Bradshaw[1], and D.D. Davis[1].

Recent developments in stratospheric chemistry such as the observation of a springtime "ozone hole" over the Antarctic[1], have illustrated the need for a rugged, lightweight instrument for the determination of lower stratospheric ozone profiles over remote areas. Variations of the widely-used UV-DIAL methodology[2] appear to provide the most promising approach to the development of such and instrument.

To date, the majority of ground-based UV DIAL ozone measurement systems[3] have been designed to produce ozone profiles over the entire stratospheric altitude range. In order to achieve usable signal returns from the middle and upper stratosphere, UV DIAL systems must typically employ very high energy laser transmitters and large receiving telescopes. In addition, they must operate at wavelengths of $\geq$ 305 nm to maintain atmospheric extinction within acceptable limits.

While these design features are essential to making high altitude stratospheric ozone measurements, they nevertheless present some difficulties if one is interested in lower stratospheric O_3 measurements especially when these measurements must be made at remote sites. As alluded to in the above text, the first, and perhaps most obvious of these difficulties, is that large telescopes (having apertures of up to about one-meter) and high energy lasers (often emitting $\geq$ 1J/pulse of energy) result in a system that is both large and heavy
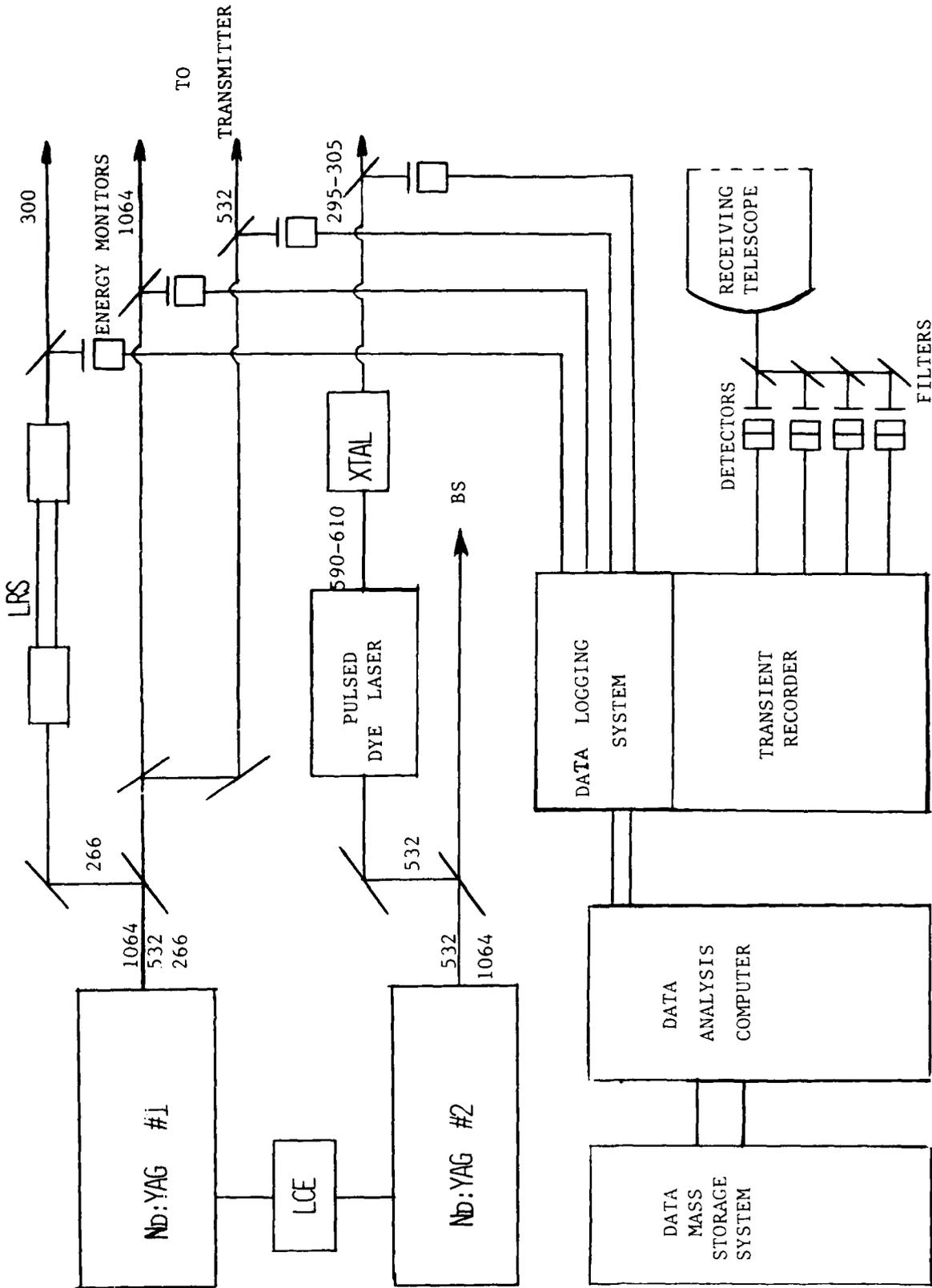
FIGURE 1: SCHEMATIC DIAGRAM OF ANTARCTIC UV-DIAL SYSTEM

LCE:Laser Coupling Electronics; LRS:Laser Raman Shifter; XTAL:Frequency Doubling Crystal.
BS:Beam Stop.

and one that consumes substantial amounts of electrical power. These systems therefore tend to be limited in their mobility, and thus, suitability for deployment at remotely located sampling sites. A second difficulty involves the large and sometimes variable background scattered UV solar flux collected by these systems. This scatter frequently overlaps the detection wavelengths of these systems. In many cases, this background can be sufficiently large as to restrict observations to nighttime conditions. However, if one is willing to sacrifice upper stratospheric O_3 measurements, both of the above problems can be significantly reduced in scope through the use of shorter ozone detection wavelengths. With the greater ozone absorption at these shorter wavelengths, smaller laser systems and receivers can be used while maintaining good system performance. Likewise, the solar backgound detected at ground level drops rapidly with detection wavelengths below about 305 nm and becomes undetectable at less than about 285 nm.

In this paper we present a comparative performance analysis of several alternative ozone detection schemes based on measurements in the 285-305 nm wavelength range. Each of these alternatives are critically compared in terms of size, weight and power consumption as well as projected system performance. Among the alternatives considered, perhaps the best compromise in terms of size/weight/power vs. performance is provided by the system illustrated in figure 1. In this system a fixed 299.5 nm generated by the first Stokes Hydrogen Raman Shift of a quadrupled Nd:YAG laser. This fixed frequency would be transmitted along with a second tunable wavelength ($\lambda = 305$ nm) generated by a frequency-doubled Nd:YAG driven dye laser to provide differential absorption measurements of the lower stratospheric ozone profiles. The estimated signal-to-noise ratio for this system for the determination both undepleted and depleted antarctic ozone profiles is given as table I.

Table I: Estimated Signal-to-Noise Ratios for Ozone Detection
Under Antarctic Conditions

Altitude	Standard Ozone Model		Reduced Ozone Model	
(km)	~ 6 min integration	~ 30 min integration	~ 6 min integration	~ 30 min integration
10	20	45	18	41
11	22	50	21	47
12	22	49	21	46
13	21	47	21	46
14	17	38	17	37
15	13	29	13	29
16	11	24	11	24
17	8.5	19	8.5	19
18	5.8	13	6.3	14
19	4.4	9.8	4.9	11
20	3.1	7.0	3.5	7.8
21	2.2	4.9	2.5	5.6
22	--	3.4	--	4.0
23	--	2.4	--	2.9
24	--	--	--	2.1

References

[1] Farman, J.C.; B.G. Gardiner, and J.D. Shanklin, Nature, 315, 207, (1985).

[2] See for example: Heaps, W.S.; T.J. McGee, R.D. Hudson and L.O. Candill, Appl. Opt., 21, 2265, (1982), and Browell, E.V.; A.F. Carter, s.T. Shipley, R.J. Allen, C.F. Butler, M.N. Mayo, J.H. Siviter and W.M. Hall, Appl. Opt., 22, 522, (1983).

[3] See for example: G. Megie; J.Y. Allain, M.L. Chanin and J. Blamont, Nature, 270, 329, (1977).

Introduction To The 100" Lidar System   (MEGALIDAR)

Richard Richmond
Electro-Optics Branch
Avionics Laboratory
Wright-Patterson AFB, Ohio 45433

Jan Servaites
Electro-Optics Branch
Avionics Laboratory
Wright-Patterson AFB, Ohio 45433

Introduction: The colossal 100" collimator facility is being developed into a lidar system. The collimator is a 12 story high chamber with a 100" diameter f/6 mirror at the bottom of the chamber. By opening the top of the facility, the collimator is converted into a vertically pointed telescope. By installing a suitable detector at the focal point of the telescope, the chamber becomes the receiver of a extraordinary lidar system. The purpose of this paper is to introduce the facility at Wright-Patterson and the efforts, both present and planned, being undertaken to make this one-of-a-kind LIDAR facility a reality.

Objective/Payoff: The objective of this effort is to develop the means to probe the middle and upper atmosphere (15-250 km) with a 100-inch aperture lidar which will provide the information necessary for investment, deployment and operational decisions concerning National systems which operate in or through the atmosphere. Current information has been obtained by expensive sounding rockets and satellites. Sounding rockets give only a single profile for a particular location and time. Satellites provide atmospheric density integrated along the orbit and over time. Such spotty data corrupts calculations about operation of systems such as Infrared Search and Track System (IRSTS), Strategic Defense Initiative (SDI), Trans-Atmospheric Vehicle (TAV) or Boost Glide Vehicle (BGV) or National Aerospace Plane (NASP), re-entry vehicle countermeasures, and low-altitude orbiting satellites.

Optical System: The 100 inch mirror is mounted at the bottom of the collimator and is six stories below ground level. A turning mirror is used to direct the focused return signal at the detector one story below ground. The entire interior of the tower is painted matte black, and the system is, in effect, a vertical fixed telescope. At ground level, there is a large cylindrical chamber connected to the collimator tower. This chamber was designed to house devices undergoing tests in the collimator. For LIDAR experiments, this area is large enough to easily hold laser sources and beam steering optics of the transmitter. This would allow the laser beam to be transmitted coaxially with the receiver. A diagram of the facility is shown in figure 1.

Because the return signal strength (or useful range) in a LIDAR system is directly proportional to the area of the receiver, the 55 ft^2 (5 m^2) area of the 100 inch collimator would make this system the most sensitive one in operation in the world at present. What this large aperture would mean in terms of extending the range of LIDAR measurements should be obvious.

Laser Source: During initial tests to study the feasibility of using the collimator as a Lidar system, a Q-switched Ruby laser was the source. The laser is capable of producing approximately 1 Joule with a pulse width of from 10 to 30 nanoseconds. Mechanical difficulties have prevented using the Q-switch during these initial tests. Without the switch, the pulse length is approximately 600 microseconds long, as seen in the top graph of Figure 2. This signal is the return obtained when the top of the collimator is opened and the laser is bounced off the roof of the building.

Data Acquisition System: The backscatter radiation collect by the telescope will be monitored by a photomultiplier tube that was mounted at the focal point of the telescope and connected to a transient digitizer for recording. A variable delay trigger will be used to trigger the recorder so that returns from a specific range or distance could be recorded.

First Results: Shown in the lower graph in Figure 2 is one of the first sky returns obtained with this system. This was using the laser without the Q-switch. Sky conditions were overcast with the base of the cloud less than 1000 ft above the ground. Because of the long length of the laser pulse, no attempt has yet been made to analyze this return. Useful data acquisition and analysis will be undertaken when a suitably short laser pulse is available.

Future Plans: The collimator facility can be considered as a wavelength non-specific lidar receiver. It is the size of the system that makes this device so attractive. Different wavelengths and detection schemes can easily be accommodated within the chamber. The quality of the mirror is such that it is usable from the visible through the infrared. It is possible that the mirror can also be used into the ultraviolet, but the mirror would have to be evaluated at those wavelengths before much work was done in the UV.

In any case, for each type of test to be conducted, a suitable detector would be installed at the focal plane of the telescope. The source would be a separate unit. It is not anticipated that the collimator mirror would be used as part of the transmitter optical path. If the transmitter is small enough, it can be installed within the collimator chamber and the beam steered up through the collimator tube. Larger sources can be installed immediately next to the chamber tube, either on the facility roof or at ground level.

REMOVABLE TOP

GROUND LEVEL TEST CHAMBER

TURNING MIRROR

FOCAL POINT

ROTATED 180° TO SHOW
AUXILIARY OPTICS

100 ' MIRROR
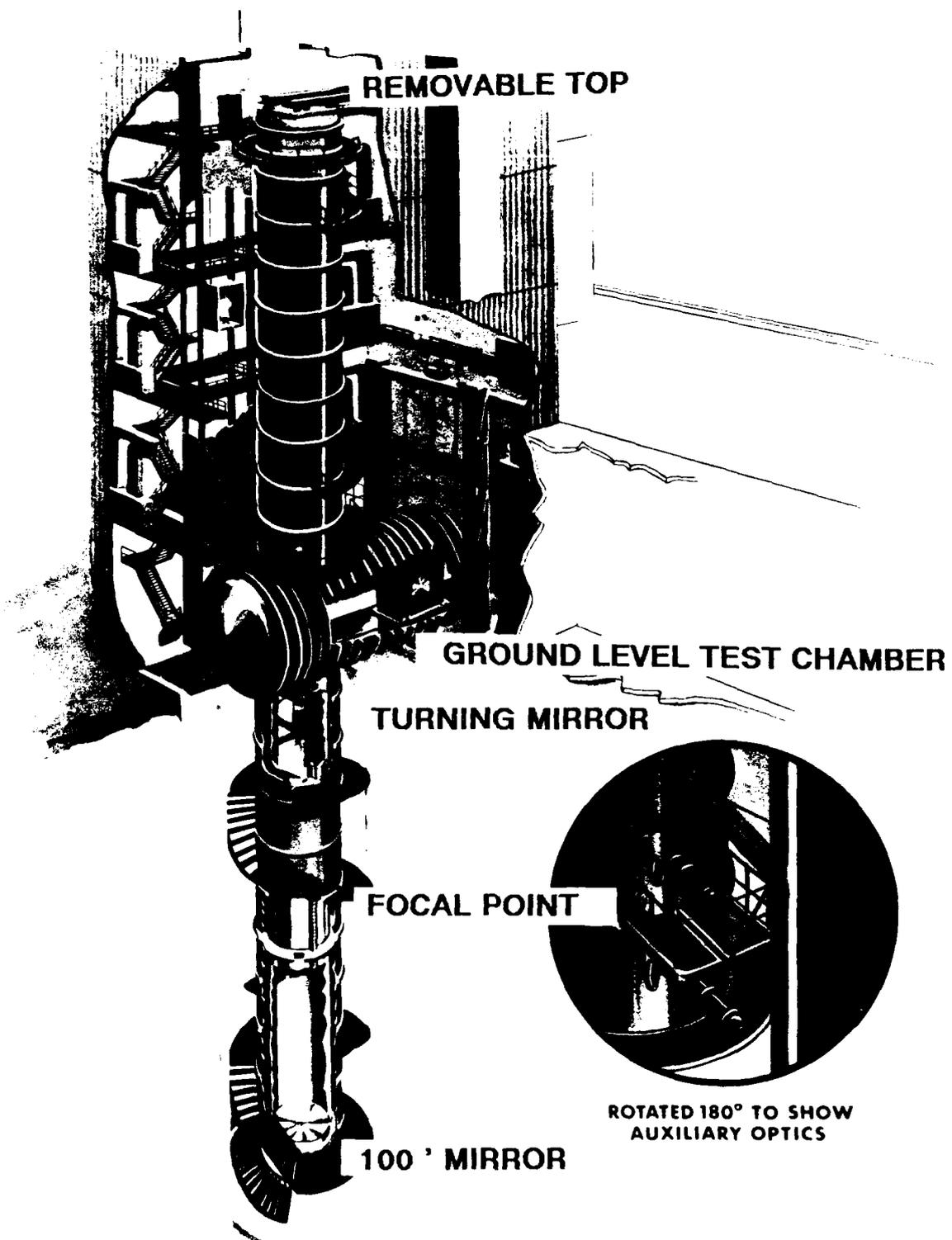
FIGURE 1. 100" COLLIMATOR FACILITY

Roof Return (9 June 1987)
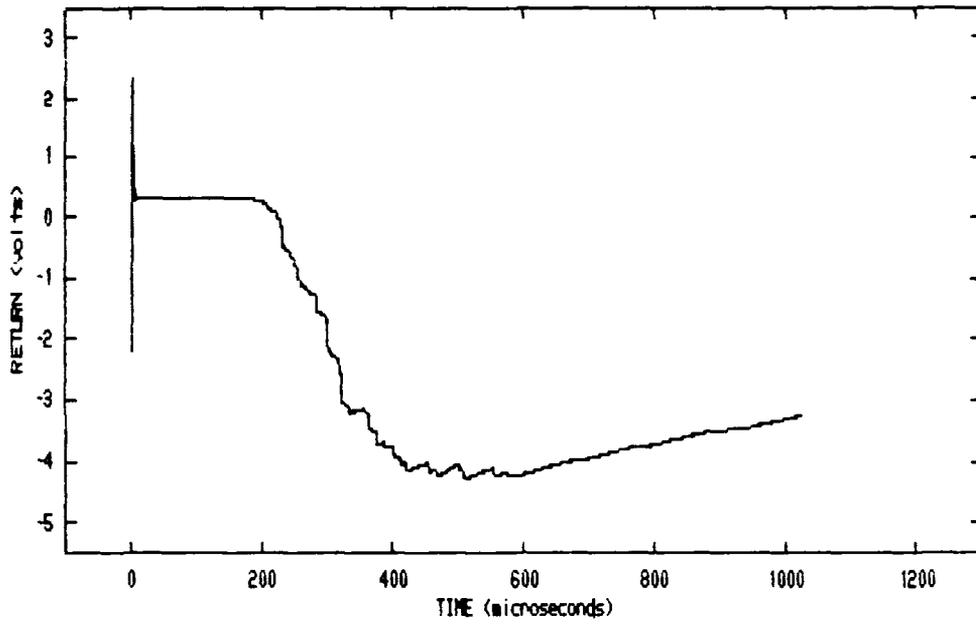
Sky Return (9 June 1987)
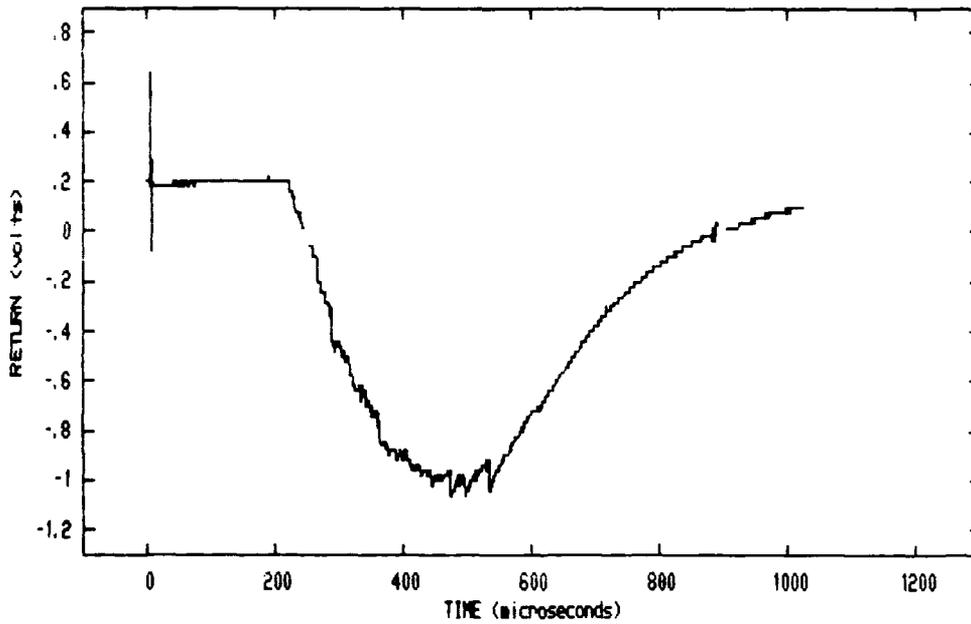
Figure 2: LIDAR Return Signals (No Q-switch)

400 Hz LINE CENTER STABILITY IN A GaAlAs DIODE LASER

by

T.M. Shay, J.D. Dobbins
Los Alamos National Laboratory
P.O. Box 1663, CLS-5 MS/E535
Los Alamos, NM 87545

Y.C. Chung
Utah State University
Dept. of Electrical Engineering
Logan, UT 84322

SUMMARY

Frequency-stabilized semiconductor lasers are practical sources for a wide variety of potential applications including remote sensing, laser spectroscopy, optical frequency standards, coherent optical communication, coherent optical sensors, laser gyroscopes, etc. In particular diode lasers are convenient sources for injection locking tunable solid state lasers. Solitary semiconductor lasers are essentially impervious to acoustical and mechanical disturbances since they have no external optics. On the other hand, the operating frequency of a semiconductor laser is very sensitive to temperature and current variations, therefore standard diode laser systems have very poor frequency stability. Thus the first step in frequency stabilizing a diode laser consists of stabilizing the temperature and injection current of the laser.

We have frequency-stabilized the line center of a semiconductor laser. We report a line center frequency-stability of 4 kHz open loop and 400 Hz closed loop for time periods of one hour. A commercial injection laser is stabilized to the Rb (D_2) transition. The stabilization electronics consist of two active control loops. First, a temperature control loop is utilized to maintain the diode laser heat sink temperature stable to within $\pm 3 \times 10^{-6}$ °C and thus compensate for environmental temperature changes. Second, a first-derivative frequency locking loop compensates for drift in the laser current source, short-term temperature changes, and maintains the laser frequency locked to the Rb transition.

Temperature stabilization is achieved by active stabilization of the diode-laser heat sink. A thermistor senses the laser heat sink temperature. When a temperature increase is sensed by the thermistor, the temperature-control circuit turns on the peltier cooler attached to the laser heat sink. Using only this heat sink stabilization we have been able to maintain our laser center frequency stable to within ± 44 kHz for over one hour.

The laser center frequency fluctuations were reduced to $\pm$ 1.5 kHz by adding the first derivative frequency-locking loop. The results of these frequency-stabilization experiments will be presented.

THURSDAY, OCTOBER 1, 1987

CONFERENCE ROOM 5

8:30 AM–10:15 AM

ThA1-5

SCATTERING AND TURBULENCE

Eugenio Zanzottera, CISE S.p.A., Italy, *Presider*

Nonlinear Optical Interaction of Laser Radiation with Water Droplets

Richard K. Chang

Yale University
Section of Applied Physics and Center for Laser Diagnostics
New Haven, Connecticut 06520, USA

In considering high-intensity laser propagation through the atmosphere, nonlinear optical effects such as stimulated Raman scattering (SRS), stimulated Brillouin scattering (SBS), superbroadening, self-focusing, and dielectric breakdown of the optically transparent air become even more important when the air contains water droplets. For transparent water droplets with large size parameter (defined as droplet circumference $2\pi a$ divided by wavelength of interest λ), the droplet can be envisioned as a lens to concentrate the incident intensity (I_0) at three main locations:[1] (1) outside the shadow face with $\cong 10^3 \times I_0$; (2) inside the shadow face with $\cong 10^2 \times I_0$; and (3) inside the illuminated face with less than $10^2 \times I_0$. The nonuniform internal-field distribution and internal intensity enhancement significantly affect the nonlinear optical effects. Furthermore, a large transparent droplet can be envisioned as an optical cavity for specific internal wavelengths which satisfy the droplet cavity resonance condition [commonly referred to as morphology-dependent resonances (MDR's)] associated with a sphere or spheroid.[2-4] An analogy to a Fabry-Perot interferometer can be made by associating the liquid-air interface with the reflector (via total internal reflection) and the droplet circumference with the round-trip distance. For spheres[5,6] and spheroids,[7] the Q-factor of the droplet and the precise wavelengths which satisfy the MDR's can be predicted by Lorenz-Mie and T-matrix formalism.

The combination of enhanced internal intensity at the input wavelength and high feedback for the internally generated Raman radiation (associated with the O-H stretching mode of water) greatly reduces the threshold for SRS in single micrometer-size water droplets.[8] A 1 GW/cm^2 pulse from the second-harmonic output of a Nd:YAG laser ($\lambda = 0.532$ μm) is below the SRS threshold of water in a 1-cm optical cell but exceeds the SRS threshold of a 30-μm radius water droplet.[9] Multiorder Stokes emission has been observed in the SRS spectra from water droplets.[9,10]

The threshold for SBS of water in a cell is known to be lower than that for SRS. Although SRS from water droplets has been observed,[9,11] SBS from water droplets has to date not been reported. Coherent anti-Stokes Raman scattering (CARS) from water droplets has been detected, and the effects of the phase-matching angles resulting from the localized internal-field distribution and the spread of the propagation vector within the droplet have been studied.[12,13] Time-dependent phase-modulation broadening (commonly referred to as superbroadening) of the elastically scattered linewidth as well as the SRS linewidth from a single CS$_2$ droplet has been reported.[14] CS$_2$ was chosen because of its large intensity-dependent index of refraction coefficient [i.e., $n = n_0 + n_2 I_0(t)$, where n_2 is large for CS$_2$]. Although similar experiments were conducted for water droplets irradiated with a 15-nsec, $\lambda = 0.532$ μm laser

beam, phase-modulation broadening was not observed for input intensities beyond the dielectric breakdown threshold. However, with subnanosecond and subpicosecond laser pulses, it may be possible to detect phase-modulation broadening in the elastic scattering and SRS spectra of water droplets before the onset of dielectric breakdown.

The presence of water droplets in the air greatly lowers the laser-induced breakdown (LIB) threshold and thus sets an upper limit on the laser intensity that can propagate through the atmosphere. Although the intensity distribution is largest in the region outside the droplet, the multiphoton ionization and avalanche multiplication processes favor the liquid. Whether LIB is initiated in air (just outside the shadow face) or in water (just inside the shadow face) is dependent on the droplet size and on the purity of the water.

The temporal sequence of LIB with droplets is summarized in Fig. 1 for a case in which LIB is first initiated in air during the rising portion of the input pulse (as the intensity reaches intensity level A), and the remaining portion of the laser pulse sustains the external plasma and the shock wave outside the droplet shadow face. When the rising portion of the input pulse reaches intensity level B, LIB of water occurs, and the remaining portion of the input pulse is then optically blocked from reaching the region outside the droplet. Furthermore, the remaining portion of the input pulse sustains the internal plasma and the shock or detonation wave (depending on I_0). For water droplets with $a \cong 30$ μm, LIB of water is initiated inside the droplet. For larger droplets (e.g., $a > 60$ μm), LIB of air is initiated outside the droplet.

Experimental determination of the location of LIB, i.e., within or outside the droplet shadow face, relies on spatially resolving the plasma emission spectra (both the continuum and discrete atomic lines) associated with LIB within the liquid droplet and/or in the surrounding air. The presence of discrete atomic hydrogen emission and the absence of discrete ionized nitrogen emission outside the droplet imply that LIB has occurred only inside the droplet. The atomic hydrogen results from the plasma-induced decomposition of water within the droplet and is expelled from the droplet during the explosive vaporization stage. The lack of ionized nitrogen implies that neither LIB of air nor shock wave induced ionization of air has occurred.[15] The time-averaged, spatially resolved plasma density and atomic temperature have been deduced from the Stark broadened linewidth and the intensity ratio of atomic emission lines.[16]

The temporal evolution of the plasma front associated with LIB has been investigated using a streak camera. When LIB is initiated within the water droplet, the plasma fronts propagate in the following directions: (1) in air, away from the droplet shadow face; (2) in liquid, toward the illuminated face; and (3) in air, away from the the illuminated face and toward the laser.

The creation of plasma within the water droplet transforms a normally transparent droplet into a highly absorbing droplet. During the laser pulse duration in the 10-nsec range, the droplet volume and shape remain nearly unchanged. However, during and after the laser pulse, the internal temperature is greatly increased (superheated) and the temperature distribution is highly nonuniform.[1] As the internal temperature and therefore the internal pressure rise, convection becomes the dominant mechanism causing mass transport

away from the droplet. Because the internal heating is greatest just within the shadow face, it is expected that the explosive vaporization will be asymmetrical relative to the droplet interface and mass transport will occur mainly away from the shadow face.

Using a time-resolved shadowgraph technique, we recorded the temporal evolution of the hot vapor transport and the remaining superheated droplet, after a high intensity laser pulse ($\lambda = 0.532$ μm) irradiated a large transparent water droplet ($a \cong 35$ μm). From these shadowgraphs, the propagation velocities of the following were deduced: (1) the contact surface normal to and transverse to the laser direction; (2) the deformation rate of the remaining superheated droplet; and (3) the recoil of the remaining droplet propelled by the hot water vapor streaming from the droplet shadow face. When the hot vapor front intercepts the neighboring droplets, vaporization occurs on those interfaces which face the laser-vaporized droplet.[17]

In conclusion, experiments involving high intensity ($\lambda = 0.532$ μm, 10-nsec pulse duration) laser beam interaction with single water droplets (with $a \cong 30$ μm) have demonstrated that nonlinear optical effects are important. The thresholds for coherent scattering processes, such as SRS, and for LIB are greatly lowered because of the droplet morphology. Experimental studies on the location of LIB, propagation velocity of the plasma front, plasma density and atomic temperature,[16,18] and evolution of the contact surfaces after explosive vaporization have provided the data needed for theoretical calculations associated with laser-induced heating of droplets.

REFERENCES

1. D. S. Benincasa, P. W. Barber, J.-Z. Zhang, W.-F. Hsieh, and R. K. Chang, Appl. Opt. 26, 1348 (1987).
2. S.-X. Qian, J. B. Snow, H.-M. Tzeng, and R. K. Chang, Science 231, 486 (1986).
3. J. B. Snow, S.-X. Cian, and R.K. Chang, Opt. News 12 (5), 5 (1986).
4. P. Chýlek, J. D. Pendleton, and R. G. Pinnick, Appl. Opt. 24, 3490 (1985).
5. S.-X. Qian, J. B. Snow, and R. K. Chang, in Laser Spectroscopy VII, T. W. Hansch and Y. R. Shen, eds. (Springer-Verlag, Berlin, 1985), p. 204.
6. S. C. Hill and R. E. Benner, J. Opt. Soc. Am. B 3, 1509 (1986).
7. P. W. Barber, private communication.
8. J. B. Snow, S.-X. Qian, and R. K. Chang, Opt. Lett. 10, 37 (1985).
9. J. H. Eickmans and R. K. Chang, in Proceedings of the Tenth International Conference on Raman Spectroscopy, W. L. Peticolas and B. Hudson, eds. (University of Oregon, Eugene, 1986), p. 8-7.

10. J. Eickmans, S.-X. Qian, and R. K. Chang, in 1. World Congress Particle Technology, Part I, Particle Characterization, K Leschonski, ed. (NMA, Nuremberg, 1986), p. 125.

11. P. Chýlek, M. A. Jarzembski, V. Srivastava, R. G. Pinnick, J. D. Pendleton, and J. P. Cruncleton, Appl. Opt. 26, 760 (1987).

12. S.-X. Qian, J. B. Snow, and R. K. Chang, Opt. Lett. 10, 499 (1985).

13. R. K. Chang, S.-X. Qian, and J. Eickmans, in Methods of Laser Spectroscopy, Y. Prior, A. Ben-Reuven, and M. Rosenbluh, eds. (Plenum Press, New York, 1986), p. 249.

14. S.-X. Qian and R. K. Chang, Opt. Lett. 11, 371 (1986).

15. J. H. Eickmans, W.-F. Hsieh, and R. K. Chang, Opt. Lett. 12, 22 (1987).

16. J. H. Eickmans, W.-F. Hsieh, and R. K. Chang, "Plasma Spectroscopy of H, Li, and Na in Plumes Resulting from Laser-Induced Droplet Explosion," submitted to Appl. Opt.

17. J.-Z. Zhang, J. K. Lam, C. F. Wood, B. T. Chu, and R. K. Chang, "Explosive Vaporization of a Large Transparent Droplet Irradiated by a High Intensity Laser," submitted to Appl. Opt.

18. A. Biswas, H. Latifi, P. Shah, L. J. Radziemski, and R. L. Armstrong, Opt. Lett. 12, 313 (1987).

Fig. 1. Schematic of LIB locations and processes of a high LIB threshold liquid droplet in a low LIB threshold gas at low I_0 (a), medium I_0 (b), and high I_0 (c). The shaded areas of the laser pulse represent the energy absorbed by the plasma produced by LIB in the gas (a), in the liquid (b), and by the laser-supported detonation wave (c).
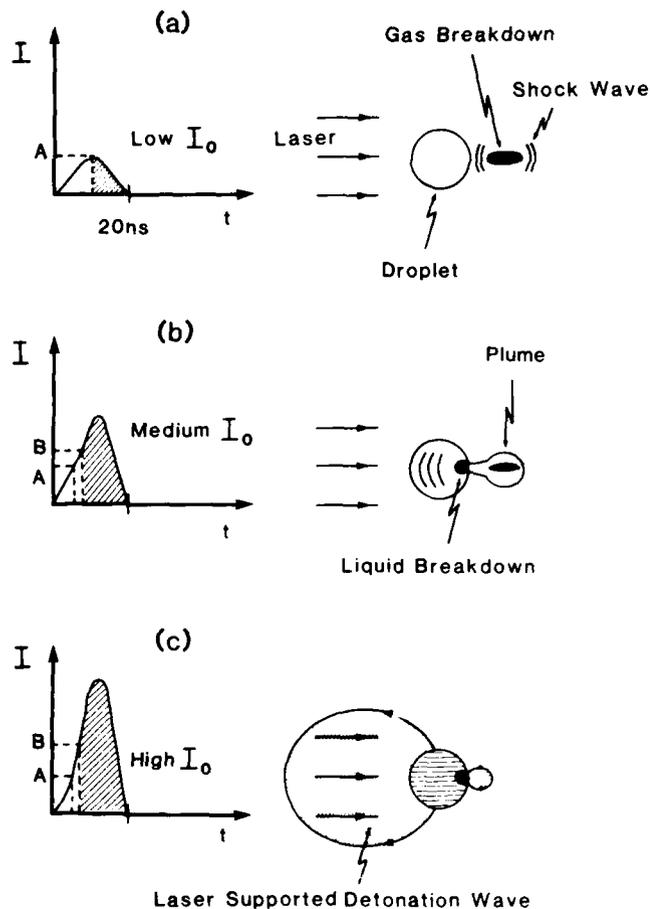
REMOTE SENSING OF REFRACTIVE TURBULENCE WITH OPTICAL SPATIAL FILTERS

James H. Churnside

NOAA Wave Propagation Laboratory

325 Broadway

Boulder, Colorado 80303

If a point source of light is allowed to propagate some distance through atmospheric turbulence, it will generate a random pattern of irradiance containing a wide range of spatial scales. Similarly, if an extended light source is viewed through atmospheric turbulence by a point detector, the irradiance at the detector will vary as if the extended source was a random pattern containing a wide range of spatial scales. These phenomena can be analyzed by assuming that light scattered by each scale size of refractive fluctuations in the atmosphere at each position along the propagation path reaches the observation plane with no perturbations from refractive fluctuations at other scale sizes or path positions. This analysis will be valid as long as the path-integrated turbulence is low and saturation of scintillation can be neglected.

From this type of analysis, one can show[1] that the strength of refractive turbulence in the atmosphere can be remotely measured using incoherent optical spatial filtering. We assume a source of incoherent light in the x-y plane whose irradiance is proportional to $\cos(K_T x)$, where K_T is the wavenumber of the transmitter and x is one component of position in the transmitter. Negative irradiances can be implemented by coding the positive and negative regions with different polarizations, as an example, and adding the sign at the receiver; they should not be a cause for concern. Similarly, the receiver, located some distance L away along the z axis, collects light through a filter whose transmission is proportional to $\cos(K_R x)$. The light transmitted by the receiver filter is collected by a detector and the variance of the photocurrent is measured.

The variance of the photocurrent is proportional to the value of the power spectral density of the refractive index fluctuations at a single wavenumber at a single path position. The wavenumber being sampled is

$$K = K_T + K_R \qquad (1)$$

and is in the same direction as the transmitter and receiver filters. The turbulence is being sampled at a path position of

$$z = \frac{K_R}{K_T + K_R} L \qquad (2)$$

where z is the distance from the transmitter.

As long as K is within the inertial subrange of turbulence, a measurement of the power spectral density can be converted into a measurement of turbulence strength using

$$C_n^2 = 30 \ K^{11/3} \ \phi_n(K) \qquad (3)$$

where C_n^2 is the refractive index structure parameter and $\phi_n(K)$ is the measured power spectral density of refractive turbulence fluctuations. If the power spectrum is simultaneously measured at a wavenumber higher than the inertial subrange, the inner scale can also be inferred. It can be approximated by[2]

$$\ell_o = \frac{5.92}{K_2} \ \ell n^{1/2} \ [\frac{C_n^2}{30 \ \phi_n(K_2)K_2^{11/3}}] \qquad (4)$$

where K_2 is the second wavenumber and C_n^2 is found using Eq. (3) and the first wavenumber.

The spatial resolution that can be achieved depends on the number of cycles of the spatial filters. For equal transmitter and receiver apertures, it can be approximated by

$$\Delta z = \frac{2L}{\pi(N_T + N_R)} \qquad (5)$$

where N_T and N_R are the number of cycles in the transmitter and receiver apertures, respectively.

An experiment was performed to measure the spatial resolution of the technique in the center of a 110 m path. The light source was a light emitting

diode with a wavelength of 0.93 μm. This was placed at the focus of a 26.7-cm-square Fresnel lens. The spatial filter consisted of 1.27-cm-wide strips of tape separated by 1.27 cm on the front of the Fresnel lens. At the receiver, an identical spatial filter was used in front of a 22.2-cm-diameter lens that collected the light onto a photodetector. The detector photocurrent was amplified, digitized, and recorded for later processing.

The spatial filters that were used more nearly approximate $1/2 + 1/2 \cos(Kx)$ than the desired $\cos Kx$ transmission function. However, the signal fluctuations due to the constant term tend to occur at much lower frequencies than those due to the desired term. These were eliminated by digitally filtering the recorded time series.

The spatial resolution was measured by moving a 44 kW kerosene heater along the optical beam and measuring the relative response of the system. Since we had 10.5 cycles across the transmitter and 8.7 cycles across the receiver, Eq. (5) would predict a spatial resolution of 3.6 m. The value actually measured was about 4 m, in close agreement with this prediction.

In a variation on this technique, one can imagine the transmitter to consist of a point source moving at some velocity v in the x direction.[3] If we look at the received signal fluctuations in some frequency range near ω, the effective wavenumber of the transmitter is given by ω/v. By measuring the power spectral density of the received signal, one is simultaneously measuring a different wavenumber at a different path position for each frequency resolution element. The specific values are found by replacing K_T with ω/v in Eqs. (1) and (2).

Near the center of the path, the spatial resolution of this synthetic aperture spatial filtering system can be approximated by

$$\Delta z = \frac{L}{2\pi N_R} \, . \tag{6}$$

Another interesting application is to put the source in low-earth orbit and measure vertical profiles of turbulence from the ground. In this case, the height resolution is given by

$$\Delta h = \frac{2h}{\pi N_R} \qquad\qquad (7)$$

where h is the height of the measurement.

References

1. R. W. Lee, "Remote probing using spatially filtered apertures," J. Opt. Soc. Am. 64, 1295-1303 (1974).

2. S. F. Clifford, "The classical theory of wave propagation in a turbulent medium," in Laser Beam Propagation in the Atmosphere edited by J. W. Strohbehn (Springer-Verlag, New York, 1978) p. 20.

3. S. F. Clifford and J. H. Churnside, "Refractive turbulence profiling using synthetic aperture spatial filtering of scintillation," Appl. Opt. 26, 1295-1303 (1987).

Minilidar for pollution monitoring and multiple scattering studies

Christian Werner
Institute for Optoelectronics
German Aerospace Research Establishment (DFVLR)
D-8031 Wessling, Fed. Rep. of Germany

1. Introduction

A simple backscatter lidar was developed to measure aerosol and cloud backscatter and extinction values. It can be used as ground based instrument as well as airborne unit. For different research goals different modules are available.

The main reason for development was the multiple scattering lidar experiment (MUSCLE), a joint DFVLR - Hebrew University experiment.

The system can also be used as an unit, which gives auxiliary data to other remote sensing instruments, for example cloud top height for the stereo imager.

2. Multiple Scattering Lidar Experiment (MUSCLE)

High optical depth values giving rise to multiple scattering effects are very common in measuring lidar echo from clouds. In order to investigate the cloud albedo, the cloud thickness for non-cirrus-clouds, and the liquid and ice water content, multiple scattering calculations must be included. The multiple scattering theory is based on single particle scattering theory assuming spherizity and the probability for the occurance of more than one scattering event between the lidar-transmitter and -receiver. Since the probability depends on the special geometry of the lidar involved, the theory will be developed for the Minilidar system.

In many cases the assumption that the single scattering originates from spherical particles introduces an additional inaccuracy. Ice crystal particles and desert durst particles are examples for the need of more sophisticated theory.

Lidar measurements can detect such non-spherical particles by analyzing the two first parameters of the Stoke scattering vector: Spherical particles will not affect the polarization of the incident linearly polarized light whereas nonspherical particles will give rise to a depolarization effect. This is true for single scattering events (optical thickness less than 0,1).

Multiple scatter effects involve several different scattering angles and therefore when present depolarization effects will also be measured for spherical particle of high optical depth.

In order to distinguish between depolarization caused by non-spherical particles and depolarization caused by multiple scattering from optical dense spherical particle layers the theory will be developed based on the delayer increasing de-polarization concept.

The hardware, the minilidar must have the possibility to measure the different polarized backscatter components and measure these components with different field of views. To vary the polarization direction of the transmitted radiation, two concepts are under construction.

The system was developed for proxy operation too. A trained technician can handle the system.
It is possible to add the minilidar to an existing sensor package to give range resolved backscatter information from clouds or aerosol layers which may be of interest for a passive sensor to increase its range resolution.

3. Technical desciription of the system minilidar

Laser:
Nd:YAG, linear polarized, Spectrum GmbH
Wavelength   1064 nm
pulse length   10 ns
pulse energy   10 mJ
pulse repetition rate   1/3 Hz
beam divergence   3 mrad
power   24 - 30 V, 1.5 A

receiver optic   modul 1

effective receiver area   62 cm^2
field of view   3, 6, 10 mrad
detector   YAG 444 PIN photodiode
polarizer with second detector as option

                modul 2

effective receiver area   896 cm^2
field of view   3, 6, 10 mrad
detector   YAG 444 PIN photodiode
polarizer with second detector as option

                modul 3
combination of modules 1 and 2, modul 1 without depolarization optic.

Signal processing:

2 channel A/D converter
10 Bit, 20 MHz as option
IBM-PC-AT via GRIB.

Option: laser energy monitor

Figure 1 shows the three possible modifications of the system minilidar.
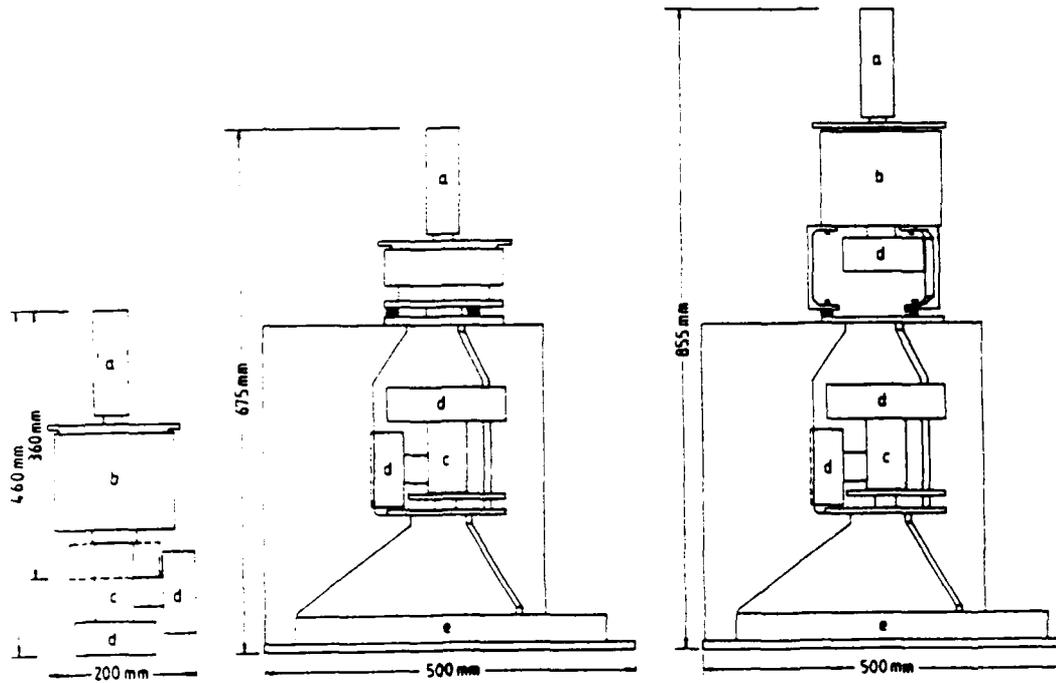
Figure 1.   System Minilidar   a. Laser
                                 b. receiver
                                 c. beamsplitter for polarization
                                    separation
                                 d. detector
                                 e. receiver

4. New concepts

There is a second unit under development for measuring the backscatter with circular polarized light. Figure 2 shows the concept.
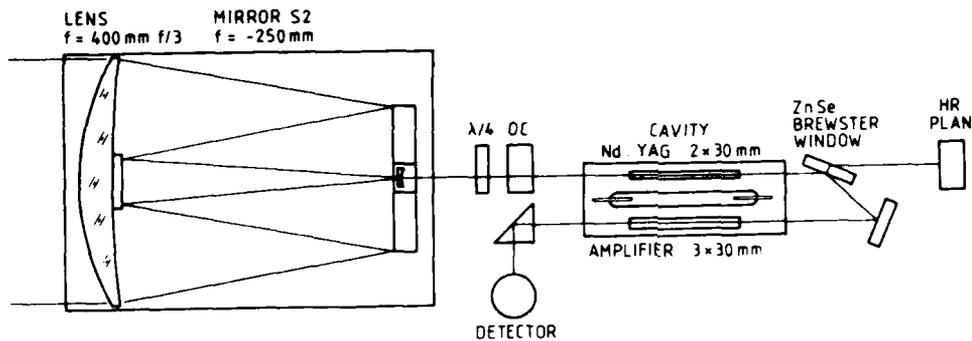
Figure 2.   Concept of the backscatter microlidar witn circular
            polarized transmitted light and optical detector
            preamplifiers.

The laser is used as transmitter and signal amplifier. The
quarter-wave-plate and the Brewster window are used to separate
the transmitted laser radiation from the received backscatter
signal.

A second Nd:YAG rod is installed in the cavity to amplify the
signal. Tests with laser diode pumped Nd:YAG amplifiers will
be reported.

IMPROVED DIODE-LASER
RANDOM-MODULATION CW LIDAR

Hiroshi BABA, Katsumi SAKURAI,
The University of Tokyo, Dept. of Pure and Applied Science,
Komaba, Meguro, Tokyo 153, Japan

Nobuo TAKEUCHI,
The National Institute for Environmental Studies,
Yatabe, Tsukuba, Ibaraki 305, Japan

and
Toshiyuki UENO
Chiba University, Faculty of Engineering,
Yayoi-cho, Chiba 260, Japan

Diode laser (DL) has the advantages such as compact size, small weight, small consumption power, low driving voltage, high power efficiency, easy handling of power and frequency modulation, long lifetime and low cost. Although the peak power is much smaller than that of the giant pulse solid-state laser (more than eight orders of magnitude), the average power is not so small. So the use of a cw-DL realizes a compact, reliable, practical, portable lidar system. Introducing the pseudo-random-modulation technique, we already reported the construction of a DL random-modulation cw (RM-CW) lidar and the successful operation of the nighttime aerosol measurement[1],[2]. In this paper, we report the outline of the RM-CW lidar, the improvement of the DL RM-CW lidar, and the measurement of the daytime aerosol profile measurement as well as the nighttime one.

[FUNDAMENTAL of the RM-CW LIDAR] The principle of the RM-CW lidar is already mentioned in the Ref. 1. For a square-shape M-sequence, a_i ($i=1,...,N$) ($a_i=1$ or 0), the cross-correlation with the corresponding $(1,-1)$ M-sequence a'_i gives the delta function-like result. Random-code modulated power is written as $P_\theta a_i$. Receiving signal y_i is the convolution of $P_\theta a_i$ with the response function of the aerosol spatial profile G_i. The signal z_i integrated over M periods is written as

$$z_i = \sum_{k=1}^{M} y_{i+(k-1)N} = \sum_{k=1,j=1}^{M\ N} \{P_0 a_{i+(k-1)N-j} G_j + b_i\}$$

Expectation value $\bar{S}_l$ of the cross-correlation of z_i with a'_i recovers the function corresponding to the A-scope of a pulsed lidar:

$$\bar{S}_l = E[S_l] = M\{P_0(N+1)G_l/2+b\}.$$

In a case of using a cw DL as the light source, the receiving signal intensity is in the photon counting region, and the signal-to-noise ratio is written as

$$SNR= S_1/\sqrt{V[S_1]}=\sqrt{M\xi}P_0(N+1)G_1/2\sqrt{\{P_0(N+1)G/2+b\}}.$$

Here $\xi=\eta_0\varepsilon\Delta t/h\nu$ (η_0 is the PMT quantum efficiency, ε is the constant relating to the discrimination level of the ADC, Δt is the sampling time) is the conversion coefficient from the detected power to the digitized count number.

[IMPROVED DL RM-CW LIDAR SYSTEM] The target of DL RM-CW lidar is to realize a portable, practical system for the measurement of atmospheric phenomena at short distance. Since currently commercial DL has the power level of less than 100 mW, the detection range is roughly 1 km for a thin medium (ex. aerosol), and several km for a dense target(ex. topographic targets, and cloud).

The specification of the improved system, which is similar to the previous[1], is shown in Table 1. The points of significant improvement are the use of a narrow-band optical filter, and the removal of electric noise and amplifier distortion. Other points of difference are :
1. the size of the telescope from 15 cm to 20cm in diameter,
2. the use of a DL in the single mode operation,
3. the removal of accumulation limit for the digitized count of 2^{16},
4. the flexibility of M-sequence code selection (12th-order or lower),
5. the addition of scanning function.

Table 1. Specification of the improved DL RM-CW Lidar.

LASER: GaAlAs-DL (Hitachi)

Wavelength	780 nm
Output	30 mW
Driving current	40mA(bias. + 40mA(mod.)
Bean Divergence	0.4mrad.

MODULATION: M-seq. random code

Clock Time	60ns
M-seq.order 12th, 10th or under	
(Number of elements 4095, 1023 or under)	
Range resolution	9m

RECEIVING OPTICS

Telescope	Cassegrainian (reflection)
Aperture	200mm
Focal length	2000mm
FOV	0.5 - 3mrad
Opt. Filter Bandwidth	0.3nm(FW)

DETECTOR

PMT	Hamamatsu R928

SIGNAL PROCESSOR

ADC	3 bit (clock time 60ns)
Accumulation	up to 2^{32}

The picture of the optical head is shown in Fig. 1. The lock of the single-mode DL frequency to the center of the narrow-band optical filter was pursued by giving the feedback to the DL drivingcurrent, so as to maximumize the doubly-modulated receiving signal, which was detected through the opt.cal filter. However, in most cases, the frequency stabilization of the DL was simply carried out by keeping the temperature constant. The adjustment of optics was carefully done, after estimating the complicated behavior of the geometrical form factor (cross-over function)[3] due to the tilted angle incidence to the narrow-band optical filter. The use of the filter makes possible the photon counting operation even at daytime.
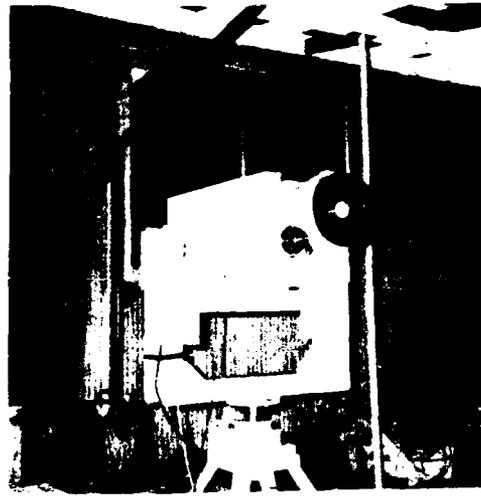
Fig. 1. Optical head of the improved LD RM-CW lidar. The transmitter is located down-left of the receiving telescope. The head is handled by a single person after decomposed into three parts.

[DAYTIME AEROSOL MONITORING] The distance-square corrected A-scope for the aerosol distribution is shown in Fig. 2. The data was taken at 2 pm. The elevation angle was 10°. The sky was partially covered by cloud. The aerosol profile was measured up to 500 m with the SN ratio of 10. Although the spatial resolution was 9 m, the rapid variation of the aerosol spatial profile was smoothened by the integration of 160 sec. The data shows the boundary layer is almost homogeneously mixed by the convection in the early afternoon. The addition of scan-
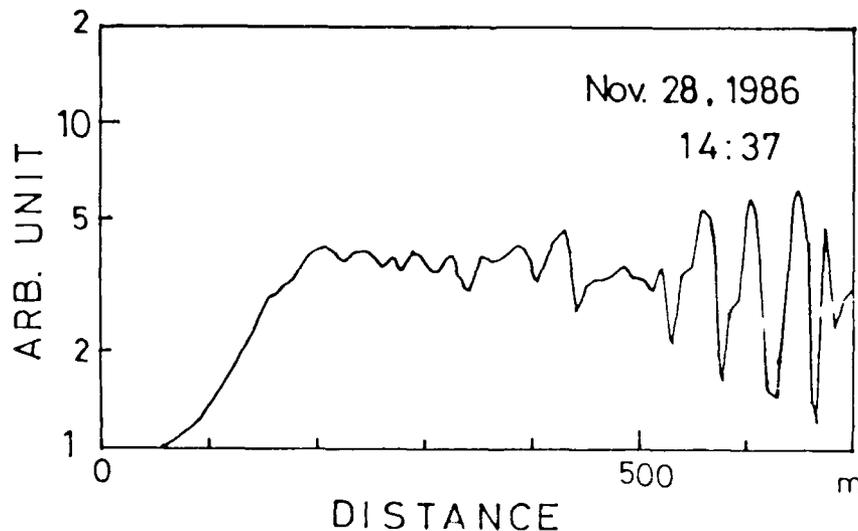
Fig. 2. Range-square corrected A-scope of the daytime measured aerosol profile. The integration time is 160 sec. The data was taken at 2 pm. The sky was slightly covered by cloud.

SAITAMA   1986.7.4-5

● LIDAR
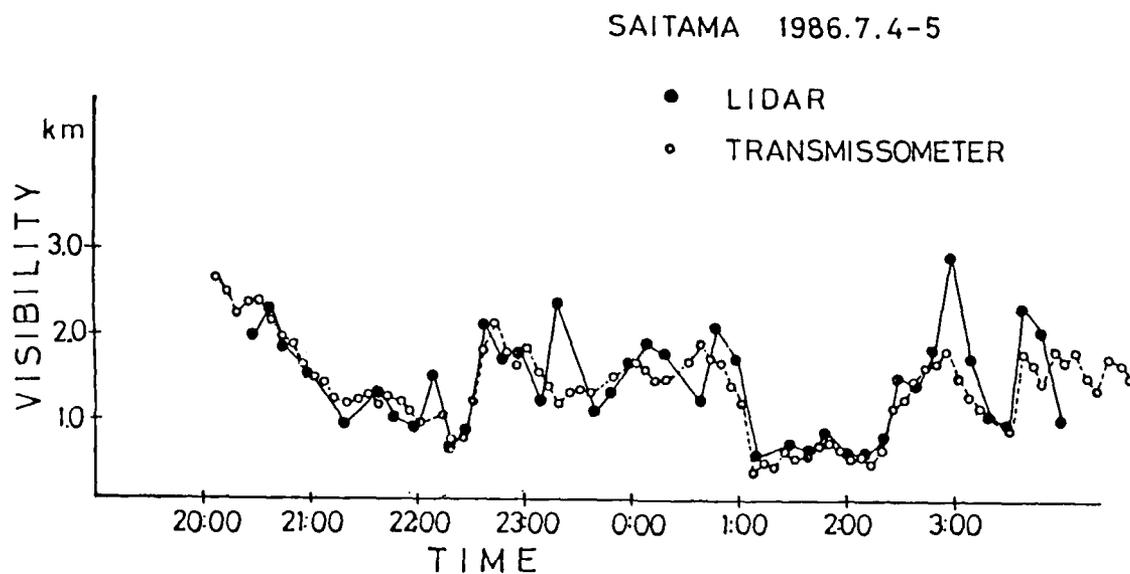
○ TRANSMISSOMETER

Fig. 3. Visibility measurement by a DL-RM-CW lidar. The data was
compared with a transmissometer data.

ning function will make possible the crosssection measurement of air
pollution phenomena such as plume dispersion.

[APPLICATION TO THE VISIBILITY MONITORING]   One of the most promising
application of the DL RM-CW lidar is the visibility measurement. Al-
though the real field test of the improved system is just to ready,
the prototype has been used to seek the possibility of the field use
of the DL RM-CM lidar. After the careful adjustment, the prototype
system was compared with a transmissometer. The region of the compar-
ison was taken almost the same. The visibility data obtained by the
slope method from the lidar measurement was compared with the trans-
missometer data in Fig. 3. The agreement of the both data is complete
if we take into account the wind condition and the difference of the
measurement site of 300 m. The dispersion of the automobile-stirring
dust was also monitored in addition to the boundary layer structure.

We would like to thank Meisei Electric Co. Limited for the coope
ration to the development of the system.

1) N.Takeuchi, H.Baba, K.Sakurai, T.Ueno:Appl. Opt. 25 (1986) 63-67.
2) N.Takeuchi, H.Baba, K.Sakurai, T.Ueno, N.Ishikawa:Proc. 13th ILRC B-10, Toronto. (1986) 41-44.
3) N.Takeuchi, and T.Satc: submitted to Review of Laser Engineering(in Japanese).

TURBULENCE MEASUREMENTS IN THE CONVECTIVE BOUNDARY LAYER
WITH A SHORT-PULSE CO$_2$ DOPPLER LIDAR

Wynn L. Eberhard and R. Michael Hardesty
NOAA Wave Propagation Laboratory
325 Broadway
Boulder, CO 80303

Tzvi Gal-Chen
School of Meteorology
University of Oklahoma
Norman, OK 73019

INTRODUCTION

A pulsed, coherent CO$_2$ Doppler lidar (Hardesty et al., 1983, 1987) will attempt a conical scan technique to measure turbulence and momentum fluxes in the convective boundary layer. Kropfli (1986) has shown success with this method using a Doppler radar in the convective boundary layer, but the lidar has an advantage in relying on the ubiquitous aerosol particles as tracers of air motion in a variety of meteorological conditions. We describe the data acquisition and processing methodology, progress in optimizing the lidar's spatial resolution, and the planned field measurement program.

METHOD TO OBTAIN TURBULENCE AND MOMENTUM FLUX

The lidar measures the radial component of air velocity at each range R while repeatedly performing conical scans through 360° azimuth (θ) at an elevation angle (ϕ).

The conventional VAD (velocity-azimuth display) method is first applied in data processing to obtain the wind averaged over each circle swept out by the range gate. A least-squares fit of

$$V_R(\theta,i) = A_{0i} + A_{1i} \sin\theta + A_{2i} \cos\theta \qquad (1)$$

to data at each range gate of the ith scan yields the wind components $u = A_{1i}/\cos\phi$ toward $\theta = 90°$ and $v = A_{2i}/\cos\phi$ toward $\theta = 0°$ at each height $z = R\sin\phi$. The offset term A_{0i} includes contributions from the vertical velocity and the horizontal divergence over the domain of the VAD circle. The mean wind for the period is determined by averaging over the scans to obtain A_0, A_1, and A_2. (If more complicated flow deformations occur, they can be determined by averaging the radial velocity over i and fitting a sinusoidal series of higher order in θ.) The result of this procedure is the period-mean fit $V_R(\theta)$.

The momentum fluxes are calculated from the deviation $V_R'(\theta,i)$ of the individual wind measurements from $V_R(\theta)$. The average variance over N scans is

$$\text{var}[V_R] = \frac{1}{N} \sum_{i=1}^{N} V_R'(\theta,i)^2 \qquad (2)$$

where var[V_R] is a function of θ. The var[V_R] is related to the turbulence variances and covariances (Wilson, 1970; Kropfli, 1986) by

$$\text{var}[V_R] = \text{var}[u] \cos^2\phi \sin^2\theta + \text{var}[v] \cos^2\phi \cos^2\theta \qquad (3)$$

$$+ \text{var}[w] \sin^2\phi$$

$$+ \text{cov}[uw] \sin2\phi \sin\theta + \text{cov}[vw] \sin2\phi \cos\theta$$

$$+ \text{cov}[uv] \cos^2\phi \sin2\theta ,$$

where cov(uw) signifies $\overline{u'w'}$, var(u) signifies $\overline{u'u'}$, and ($\overline{}$) represents a temporal average. If the variances and covariances are homogeneous, a Fourier decomposition of (3) extracts the covariance terms, for example

$$\text{cov}[uw] = \frac{1}{180 \sin2\phi} \int_{0}^{360} \text{var}[V_R] \sin\theta \, d\theta . \qquad (4)$$

Other Fourier coefficients yield var[u] + var[v], var[u] - var[v], var[w], cov[vw], and cov[uv].

When cov[uw] and cov[vw] are of primary interest, a ϕ of roughly 45° gives the best results. An elevation angle close to 0° is better for obtaining var[u] and var[v], whereas ϕ near 90° is better for measuring var[w]. A measurement period should continue long enough to sample a number of advecting eddies at the largest scale of interest in the turbulence spectrum. In convective conditions, a period roughly 1 h long should suffice.

LIDAR OPERATION WITH SHORT PULSES

Hardesty et al. (1983) gave a general description of the lidar, although it now uses a laser transmitter with higher performance (Hardesty, Lawrence, and Cupp, 1987). We have routinely operated this injection-locked TEA laser with a 7:2:1 mixture of He:CO_2:N_2 to produce 1 J pulses at 10 Hz repetition rate. The pulse energy extends (Fig. 1) over about 6 microseconds or 900 m range interval.

The outgoing pulse is directed through an off-axis paraboloid telescope with 28 cm diameter primary mirror and through a computer-controlled scanner to any specified direction in the upper hemisphere. The same telescope collects radiation backscattered from aerosol particles and directs it to the signal detector. A polarizing element in combination with a wedged plate
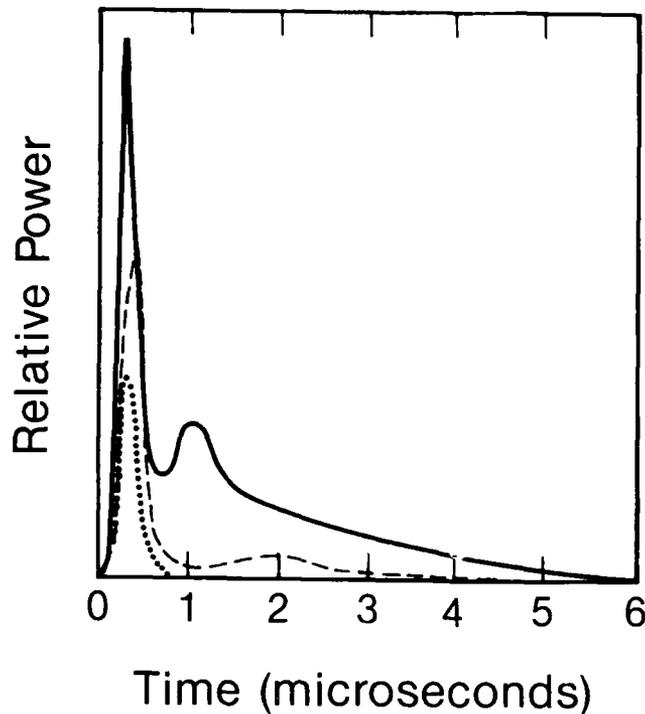
Fig. 1. Pulse shapes for three gas mixtures ($He:CO_2:N_2$).
Solid line is 7:2:1 mixture and 1 J pulse energy. Dashed
line is 7:2:0.3 and 0.4 J. Dotted line is 7:2:0 and 0.2 J.

near the Brewster angle act as a transmit/receive switch. The backscatter
signal mixes coherently with a CW local oscillator laser, whose frequency is
offset 22 MHz from the injection laser to obtain the sense as well as the
magnitude of the radial velocity.

A small fraction of the transmitted energy mixes with the local oscilla-
tor on a separate detector to monitor the energy and frequency of the
transmitted pulse. The data acquisition system switches from the pulse moni-
tor to the signal detector after an operator-selectable delay.

A real-time processor estimates the mean Doppler frequency at each range
gate for a selectable number of averaged pulses. A computer writes the
results to digital magnetic tape and generates a color display.

For the turbulence measurements we desire a shorter pulse compatible with
the processor's smallest range gate (150 m) to resolve as much of the energy-
containing turbulence as possible. We also need to eliminate the long tail
of the pulse to to reduce the minimum range to 500 m. A faster pulse rate of
20 Hz is preferred. Pulse energy as low as 0.1 J can be tolerated and still
attain adequate maximum range of about 10 km. By eliminating N_2 from the gas
mixture, we obtained a narrow pulse (Fig. 1) with 0.2 J energy. Unfor-
tunately, this mixture degraded rapidly, producing only about 10,000 pulses
before the laser discharge began arcing. The pulse shape (Fig. 1) from a

7:2:0.3 mix is marginally satisfactory, and the lifetime is barely acceptable. We are experimenting with gas mixtures and also constant flow replenishment in a further search for shorter pulses and a minimum of one hour of continuous operation. The conclusions from these trials will be presented at the meeting.

LIDAR AT FIFE

Measurements will be performed as part of the First ISLSCP Field Experiment (FIFE), where ISLSCP is the International Satellite Land Surface Climatology Project. FIFE will supply satellite and ground truth data to help validate algorithms to yield quantitative information concerning land surface climatological conditions from satellite-observed radiance data. The characterization of the planetary boundary layer is an important component of FIFE.

FIFE will take place in a region of grass-covered, moderately rolling terrain near Manhattan, Kansas, during four separate phases in 1987. The lidar will participate in the most extensive experimental phase June 25 - July 15. Surface stations and instrumented aircraft will measure, among other parameters, the turbulence and the vertical flux of horizontal momentum, which will be compared with the lidar results. A case study of preliminary results from this new application of lidar will be presented at the meeting.

REFERENCES

Hardesty, R. M., T. R. Lawrence, and R. L. Cupp, 1987: Performance of a 2-J/pulse injection-locked TEA laser for atmospheric wind measurements. Technical Digest, Conf. on Lasers and Electro-optics, Baltimore, Optical Soc. of Amer., Washington DC, 128.

Hardesty, R. M., T. R. Lawrence, R. A. Richter, M. J. Post, F. F. Hall, Jr., and R. M. Huffaker, 1983: Ground-based coherent lidar measurement of tropospheric and stratospheric parameters. SPIE Vol. 415--Coherent Infrared Radar Systems and Applications II, Soc. of Photo-Optical Instrumentation Eng., Bellingham WA, pp. 85-91.

Kropfli, R. A., 1986: Single Doppler radar measurements of turbulence profiles in the convective boundary layer. J. Atmos. Ocean. Tech., 3, 305-314.

Wilson, D. A., 1970: Doppler radar studies of boundary layer wind profiles and turbulence in snow conditions. Proc. 14th Conf. on Radar Meteorology, Tucson, Amer. Meteor. Soc., Boston MA, 191-196.

THURSDAY, OCTOBER 1, 1987

CONFERENCE ROOM 5

10:45 AM-12:30 PM

ThB1-5

TROPOSPHERIC REMOTE SENSING

James Hawley, SAIC, *Presider*

THE LEANDRE PROJECT : A FRENCH AIRBORNE LIDAR SYSTEM
FOR METEOROLOGICAL STUDIES

J. PELON
Service d'Aéronomie du CNRS Université Pierre et Marie Curie
75230 Paris Cédex 05, FRANCE

Introduction

An airborne lidar system for meteorological studies is beeing developed in France by the CNRS (Service d'Aéronomie, Laboratoire de Météorologie Dynamique -J. Pelon and P. Flamant principal investigators-, and Institut National des Sciences de l'Univers -M. Bourdet project manager-) and the CNES. It will be implemented on board the French Research Airplane, a Fokker F27, which will be also instrumented with numerous in situ sensors.

This project is the natural development of the previous studies performed at the Service d'Aéronomie and the Laboratoire de Météorologie Dynamique with ground based lidars. The LEANDRE systems use state of the art technology and are conceived compact modular and automatized. The LEANDRE project constitutes a very important step for meteorological studies at small and middle scale toward the future implementation of lidar systems on space platforms.

I. The LEANDRE programme

The scientific objectives of the LEANDRE project are related to the study of the lower atmosphere with specific emphasis on planetary boundary layer and low troposphere meteorology.
The airborne lidar development will be conducted in three phases for aerosol and cloud, water vapour, pressure and temperature and wind measurements. These objectives are summarized in table 1.

In the first two phases a backscatter lidar and a Differential Absorption Lidar (DIAL) with solid state laser technology and similar optical and electronic detection systems will be developed. In the third phase a backscatter lidar using CO_2 laser technology and specific heterodyne detection systems will be conceived. The first flights of the LEANDRE systems are scheduled from the end of 1988 for phase Ia to 1992 for phase III.

II. Description of the LEANDRE lidar systems

The concept of the LEANDRE system is modular to facilitate its evolution and adaption between phases. It is driven by the choice of lowest human intervention and compactness connected to a low power consumption.

The lidar system is composed of subsystems organized as shown on fig. 1.

Compatibility will be the most important between the first two phases. In these phases it is planned to perform nadir and zenith measurements as the maximum flight altitude of the Fokker is about 8 km. Ability to switch from nadir to zenith viewing during flight is foreseen. A mobile mirror will be used for the nadir viewing to allow horizontal structures to be studied perpendicularly to the flight track. The control by a central computer of the experiment with delocalized self control of each subsystem allows to make real time data processing to display the measurement parameters as a function of height and time. The development of all

Phase	Measured Parameters (technique)	Altitude range	Scientific Objectives	Schedule
Ia	aerosols clouds depolarization ratio (backscatter lidar)	0-30 km	- small and middle scale dynamics - fluxes and convection in the planetary boundary layer - exchanges PBL/free troposphere - cloud radiative budget - exchanges stratosphere-troposphere	1988
Ib	id. + water (DIAL)	0-8 km		1989
II	temperature pressure (DIAL)	0-20 km	- meteorology	1990
III	aerosols winds (Doppler lidar)	0-8 km	- synoptic scale dynamics	1992

Table 1 : Objectives of the LEANDRE Project
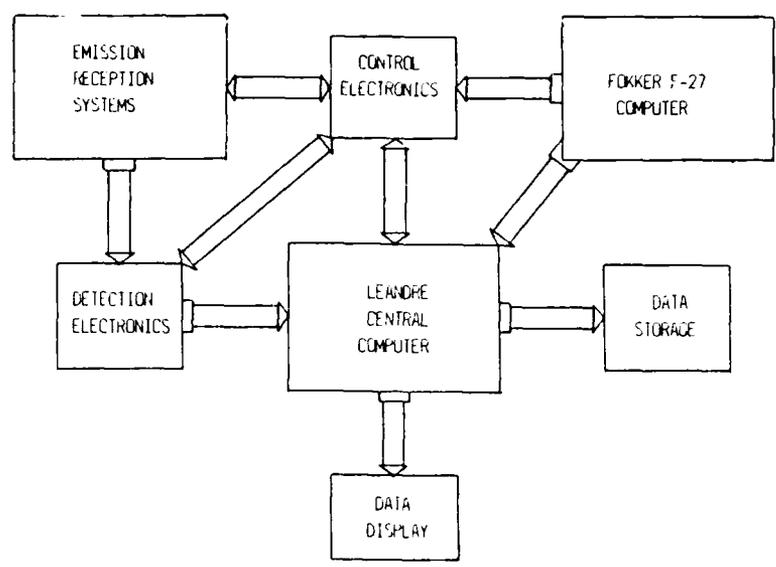
Fig. 1 : Schematic of the LEANDRE lidar

357

systems for implementation on board the plane has begun for phases I and II whereas for phase III only laboratory developments are presently performed. Phase III will not be discussed here.

II.a Emitter

As mentioned before all phases will have a specific emitters :

. In phase Ia the emitter is a pulsed Nd-Yag laser emitting in the infrared at 1.06 μm and in the green at 0.53 μm, with respective energies of 250 and 150 mJ in 10 ns pulses at a 10 Hz repetition frequency. Polarization is linear and beam divergence can be adjusted by means of a beam expander. A local minicomputer controls the operating mode of the laser (emitted energies, securities), and addresses parameters of importance such as energies to the central computer through the control electronics (cf. fig. 1).

. In phase Ia and II, the laser source will be an alexandrite oscillator emitting two pulses separated by about 70 μs at two frequencies on and off an absorption line of water vapour or oxygen, for humidity or pressure and temperature measurements by the DIAL technique (1,2,3). A prototype of this laser oscillator is presently developed at the Service d'Aéronomie (1). The ruggedized industrial version developed for the airplane should be capable of emitting twice 50 mJ monomode at 10 Hz for phase II experiment. The computer checking the laser operation should furthermore control the emitted wavelengths. This will be performed through a wavemeter using multibeam Fizeau interferometers similar to the one developed by CNRS and CNES in the frame of the LASE II project.

II.b Receiver

In the first two phases a compact 30 cm Ritchey-Chretien telescope has been chosen. In phase Ia, the detection optical system is designed to separate the two wavelengths and the two polarizations received. In phase Ib, II, only the two polarizations are separated, the two wavelengths beeing detected in sequence on the same channel. Narrow bandwith filters (0.2 nm) are used to limit background noise for day measurements. Temperature of the receiving optical box is controlled to avoid wavelength drifts of the filters. As much as four photomultiplier tubes or photodiodes can be used simultaneously to detect the backscattered signals.

IIIc. Detection electronics

As mentioned before up to four detectors can be used at the same time. In phase Ia they will be adapted for detection at 0.53 μm and 1.06 μm on both polarizations. In a first step three photomultipliers will be used and one photodiode for ground echo detection. All photomultipliers will be gated to reduce their gain by a factor of 100 during the laser emission and in case of high signal detection (clouds, ground echo). High dynamics, fast recovery preamplifiers are mounted in the sockets of the PM tubes. They are followed by gain switched amplifiers : the gain automatically increases by a factor of 100 for low detected signals.

The signals issued from the three PMT channels will be fed into three 12 bits 10 MHz analogical digitizers. A complementary 100 MHz 8 bits digitizer will be used in parallel on one channel to analyse a selectable region of the atmosphere with a ten times higher resolution.

II.d <u>Data acquisition and storage</u>

The acquisition system is based on a Hewlett Packard micro 1000 computer. The data stored in the internal memories of the transient digitizers are transfered to the computer by Direct Memory Access. The computer controls the data compression (1 to 5 shots can be averaged depending on flight configuration) and data storage on a 1600 bpi tape recorder through a 40 Mo Winchester disk. The computer is also in charge of the real time data display implying background substraction, solid angle compensation and also inversion of lidar data to physical parameters (scattering ratio, depolarization, humidity, temperature...).

The data are displayed on a 8 level color scale as a function of height and time every 2 seconds corresponding to a 200 m horizontal resolution, with a vertical resolution of 50 to 300 m depending of altitude range. This can be saved on a printer.
Data from in situ sensors (pressure, temperature, dew point,...) and the navigation system (speed, yaw, pitch...) and other systems (visible and IR radiometers) can be stored with the lidar data.

Conclusion

This lidar system will be one of the new instrument for meteorological research implemented a board the French atmospheric research aircraft. It is conceived as an evolutive system with complementary measurement ability and should give an new insight in synoptic scale meteorology.

References
(1) C. Cahen, G. Mégie, P. Flamant, J. Appl. Meteor. 22, 1136, 1983.
(2) G. Mégie, Appl. Opt. 19, 34, 1980.
(3) L. Korb, C.Y. Weng, J. Appl. Meteor., 21, 1346, 1982.
(4) J. Pelon, G. Mégie, C. Loth, P. Flamant, Opt. Comm., 59, 213, 1986.

Lidar Measurement of Boundary Layer Parameters

Edwin W. Eloranta
Department of Meteorology
University of Wisconsin
1225 W. Dayton
Madison,Wis 53706

(608)-262-7327

Atmospheric boundary layer air flows are organized by a variety of circulation patterns such as thermals, longitudinal roll vortices, and gravity waves. Studies of these structures are made difficult by the large range of spatial and temporal scales represented in these structures. Spatial scales vary from a centimeter for the smallest turbulent eddy to tens of kilometers for a cloud street circulation. Early morning thermals have typical dimensions which are smaller than 100 meters; during the the day these cells grow to sizes on the order of 2 kilometers. The lifetime of a typical cell ranges from a few minutes to the order of an hour. The overall structure of the boundary layer evolves with the diurnal cycle while the structures inside are swept rapidly along by the wind. While much has been learned about these circulations with aircraft and other traditional measurement techniques, active remote sensors such as radar and lidar are required to provide complete description of the evolving three dimensional structure.

It is possible to study boundary layer flow structures with lidar by mapping the distribution of aerosol optical backscattering. Circulation patterns are often marked by inhomogeneities in aerosol content. These inhomogeneities make the circulation patterns visible to lidar. One mechanism for the creation of aerosol inhomogeneities arises from surface aerosol sources. These aerosols are carried aloft into cleaner air by surface based thermals while air entrained into the boundary layer to replace the rising air of the thermal is cleaner than its surroundings. Pictures of lidar observed structures will be presented.

It is nearly always possible to observe a change in aerosol backscatter at the top of the convective boundary layer. This makes lidar an ideal tool for the measurement of boundary layer depth. The top of the boundary layer is frequently contorted by thermals pushing from below interspaced with downdrafts of clear air. Additional contortions are generated by shear disturbances. Conventional measurements of boundary layer depth suffer from sampling errors because they provide only single point measurements of the depth. Lidar is able to measure boundary layer depth in a region containing many thermals thereby providing an accurate mean depth measurement.

Inhomogeneities in the aerosol content are swept along with the wind; this makes it possible to measure wind speed and direction by observing the motion of the aerosol structures. Wind measurements are derived from two-dimensional spatial cross correlations of the aerosol structure observed at a small time separations. Inside the convective boundary layer sufficient structure is usually avaliable to allow remote wind measurements with non-Doppler lidars. Comparison of these wind measurements with conventional tower, pilot balloon and kytoon measured winds show differences which are limited only by the differences in the spatial averaging involved in the measurement techniques.

The cross correlations used for wind measurements also allow remote measurement of turbulent intensities. As the time separation is increased the maximum value of the cross correlation decreases. This decrease occurs as result of turbulence which distorts the aerosol pattern as it moves. Observations of the rate of correlation decay provide turbulence measurements.

The correlation measurements also provide direct measurements of typical shapes and orientations of boundary layer structures. The organizing effects of the wind direction are clearly evident in these measurements.

We have recently completed construction of a new lidar for the study of atmospheric structures. This system has been optimized to study three-dimensional structures in the boundary layer.

Lidar scans of the volume included in a 30 degree azimuth sector between 0 and 15 degrees can be obtained in approximately 3 minutes. Such a scan includes 5400 separate lidar profiles with as many as 2048 data points per profile. This provides a detailed three-dimensional picture of the convective structures inside the scan sector. Under favorable conditions clear air convective structures are visible at ranges up to 15km from the lidar. Examples of data obtained with this system will be presented.

LIDAR MEASUREMENTS OF THE TROPOSPHERE

A.I. Carswell, S.R. Pal and A.G. Cunningham

Dept. of Physics and CRESS, York University, 4700 Keele St.

North York, Ontario, Canada, M3J 1P3

This paper reports on an extended program of measurements of tropospheric properties using lidar remote sensing techniques. Two lidar systems have been employed. One is a dual frequency ruby lidar operating at low pulse repetition frequency ($\sim$0.2 Hz) and high energy output ($\sim$ 3 J @ 694 nm and $\sim$450 mJ @ 347 nm) and the other is a Xe Cl excimer lidar operating at a single ultraviolet wavelength (308 nm) with prfs of up to 50 Hz at energy levels of the order of 50 mJ. Both systems are equipped with high speed digitizers (100 MHz) and are coupled to IBM PC's for data capture and analysis. The excimer lidar data system also includes a high speed signal averaging system. The ruby system has a multichannel receiver so that several return signals (at different wavelengths or polarizations) can be recorded simultaneously but the Xe Cl lidar has only a single receiving channel.

During the last year many thousands of soundings of the troposphere have been made with these systems and on a number of occasions the lidar measurements were done in conjunction with in-situ airborne measurements of the troposphere conducted by the Canadian Atmospheric Environment Service. On these occasions the aircraft instrumentation included a variety of sensors to monitor the microphysical and chemical properties of the boundary layer aerosol and cloud formations. In particular, aerosol and cloud particle sizes and concentrations were recorded as well as the cloud liquid water content. In these collaborative measurement programs the objectives were to compare the lidar data on the aerosol and clouds to the

in-situ measurements. An overall objective of this lidar program is to investigate the extent to which lidar is capable of providing useful quantitative information on the troposphere.

To date the study tasks have been divided into two broad areas (1) Lidar Methodology Development and (2) Atmospheric Properties Measurement. (1) Lidar Methodology: Although lidar has been used for many years as an atmospheric probe there are still many unanswered questions relating to its optimal application for this task. One particularly useful capacity of a lidar is its ability to provide information on the 3-dimensional distribution of atmospheric contituents (both gaseous and particulate). However the lidar observable, the backscattered signal intensity as a function of space and time, is not simply related to the atmospheric optical properties (volume backscattering coefficient and volume extinction coefficient). The relation of the lidar signal strength to the physical and chemical properties of the atmosphere is even more complex. In this program activity we have been examining the acquisition, analysis and presentation of lidar data in a variety of ways in an effort to ascertain the value of the information which can be derived.

The approach has been to gather a time series of lidar returns for a range of atmospheric conditions of interest. The primary measurement is the range-dependent backscattered signal $P(R)$ where R is the distance to the scattering volume. Most data are collected in the vertical direction. Rayleigh/Mie (elastic scattering) returns at 694 and 308 nm and Raman returns at the first Stokes vibration-rotation frequencies for nitrogen, water vapour and liquid water using principally the Xe Cl 308 nm source have been recorded. These traces are digitized with a 10 to 20 rsec time resolution to provide the basic raw data set. Single shot traces are

recorded for all strong signal cases whereas often only multipulse averages are recorded for the weaker signals - generally Raman returns. Data have been collected using both linear and logarithmic amplifiers to examine the signal dynamic range considerations in a number of instances.

The time series is first presented as a ten-level intensity modulated plot of the range-squared corrected signal $S = \ln[R^2 P(R)]$ where S is shown as an altitude-time display. Both colour and black and white displays are available and the intensity contrast limits can be varied to enhance details for either the high signal levels (clouds) or low levels (aerosols). This display has been found to be very useful for demonstrating the time dependence of the atmospheric properties and for indicating regions with interesting or unusual features which merit more detailed analysis. The trace-to-trace correlations and the overall features of the returns can quite readily be identified in this format in addition to the integrated spatial and temporal behavior of the atmosphere.

For more detailed analysis the individual traces are used to determine both the extiction coefficient σ and the volume backscattering coefficient β_π by inverting the single scattering lidar equation using the analysis described by Klett (Appl. Opt. 24 1638 (1985)). In this inversion, the affects of the real input data and the theoretical assumptions on the derived values of σ and β_π are being investigated. Where possible these lidar-derived values are compared with the in-situ measurements either directly or with the aid of relationships determined from laboratory measurements. (R.N. Dubinsky, A.I. Carswell and S.R. Pal, Appl. Opt. 24 1614, (1985).

(2). Atmospheric Properties: The measurements to date have been mainly centred on the lower 3 km of the atmosphere. Both aerosols and clouds have been investigated and the spatial and temporal variabilities of these have

been recorded to investigate both seasonal and meteorological effects. The
interactions between aerosols and clouds have been observed on several
occasions and a number of interesting features are presented. The
simultaneous monitoring of the atmosphere with normal Mie backsattering and
the nitrogen and water Raman radiation has proven to be very useful. A
great deal of new information is obtainable from these multi-signal
analyses particularly in the case of low density aerosol layers, and
examples of this behavior are described. In this regard, work is in
progress to investigate the inversion of the Raman lidar equation by
extending the normal Mie inversion algorithms. The Raman signals provide
additional information on the volume backscattering coefficient,
independent of the atmospheric extinction since these two parameters can be
separated by the simultaneous Raman and Mie analysis. Progress in this
direction is described along with comparisons of the lidar data with
theoretical Mie calculations based on the in-situ measured atmospheric
properties.

Lidar Moisture Measurements During COHMEX

S. H. Melfi
NASA/Goddard Space Flight Center
Code 617
Greenbelt, MD 20771

David Whiteman
NASA/Goddard Space Flight Center
Code 674
Greenbelt, MD 20771

Richard Ferrare
University of Maryland
and
NASA/Goddard Space Flight Center
Code 613
Greenbelt, MD 20771

Water vapor is one of the most important state variables of the atmosphere. Its concentration and distribution with height influences atmospheric circulation and dynamics, and figures prominently in a number of atmospheric processes including: 1) atmospheric stability, 2) cloud formation, 3) radiative transfer, 4) storm development, to mention only a few.

High vertical (150 m) and temporal (2 min) resolution profiles of water vapor have been obtained using a Raman lidar and have shown structure which is unobtainable using standard techniques[1]. This paper will present recent results using the Raman lidar in a meteorological experiment conducted in northern Alabama during July 1986. The experiment, referred to as COHMEX for Cooperative Huntsville Meteorological Experiment, had as one of its objectives the investigation of the role of tropospheric moisture on convective storm development.

A block diagram of the lidar system is shown in figure 1. It consists of an Nd-YAG tripled (355 nm) laser firing at 10 pps and a 60-inch diameter telescope. The output of the telescope is divided by a dichroic beamsplitter into two channels, one located on the Raman band due to water vapor (407 nm) and the other due to nitrogen (387 nm). The signal from each photomultiplier is fed into both an Analog-to-Digital converter (ADC) and into a photon counter (PC). The ratio of the water vapor to nitrogen Raman signals has been shown to be proportional, to first order, to water vapor mixing ratio.[2] The signals are normally accumulated for typically 1000 shots thus providing an independent atmospheric profile of water vapor mixing ratio every 2 minutes. A comparison of a lidar-derived profile with a balloonsonde measurement of water vapor is shown in figure 2.

During the COHMEX experiment, lidar measurements of atmospheric moisture were made each night during the week of July 16 to 23, 1986, with the exception of the night of July 19-20. Each observation period lasted an hour or more during which moisture profiles were acquired every 2 minutes. All the

profiles from each observation period were formatted together to provide an image of the spatial and temporal variation of the moisture field over the lidar. An example of one image acquired during the early morning of July 22, 1986, is shown in figure 3. The figure indicates variations in water vapor mixing ratio shown in shades of grey as a function of both altitude (0 to 7 km) and time (3:00 a.m. to 5:10 a.m. CDT). The scale shown on the figure indicates the assigned relationship between atmospheric moisture and shades of grey, ranging from black at 0 g/kg to white at 20 g/kg. Figure 3 was constructed using data from both the ADC and PC. The transition is at a constant mixing ratio value and is barely noticeable in the image at around 2.5 km. Below this altitude the mixing ratio is derived from ADC data, and above this altitude it comes from PC data. The higher altitude resolution of the ADC which approaches 15 m gives a grainy appearance to the image below the transition level.

A number of interesting moisture features are obvious in the image of figure 3. They include: 1) the height of the previous day's boundary layer at about 1.8 km which is identified by the relatively constant high moisture within the layer, with rapid drying above, 2) the undulations at the top of the boundary layer which indicate turbulent fluctuations, and 3) the moisture reversal with altitude between 4 and 5 km (dry-moist-dry). This data along with other examples will be discussed in more detail during the presentation of the paper.

References

1. S. H. Melfi, D. Whiteman, "Observation of Lower-Atmospheric Moisture Structure and Its Evolution Using A Raman Lidar," Bull. Am. Meteor. Soc., 66, 1288 (1985).

2. S. H. Melfi, "Remote Measurements of the Atmosphere Using Raman Scattering," Appl. Opt., 11, 1605 (1972).
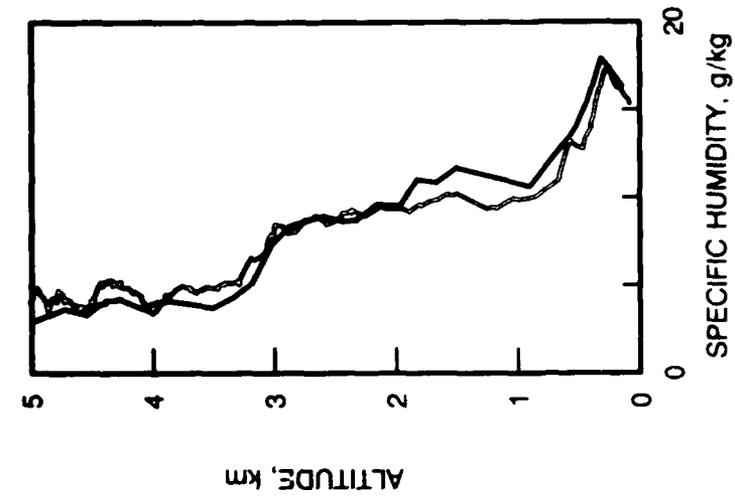
Figure 2. A comparison of lidar-derived water vapor mixing ratio, ≡, with an independent balloon-sonde, ▬
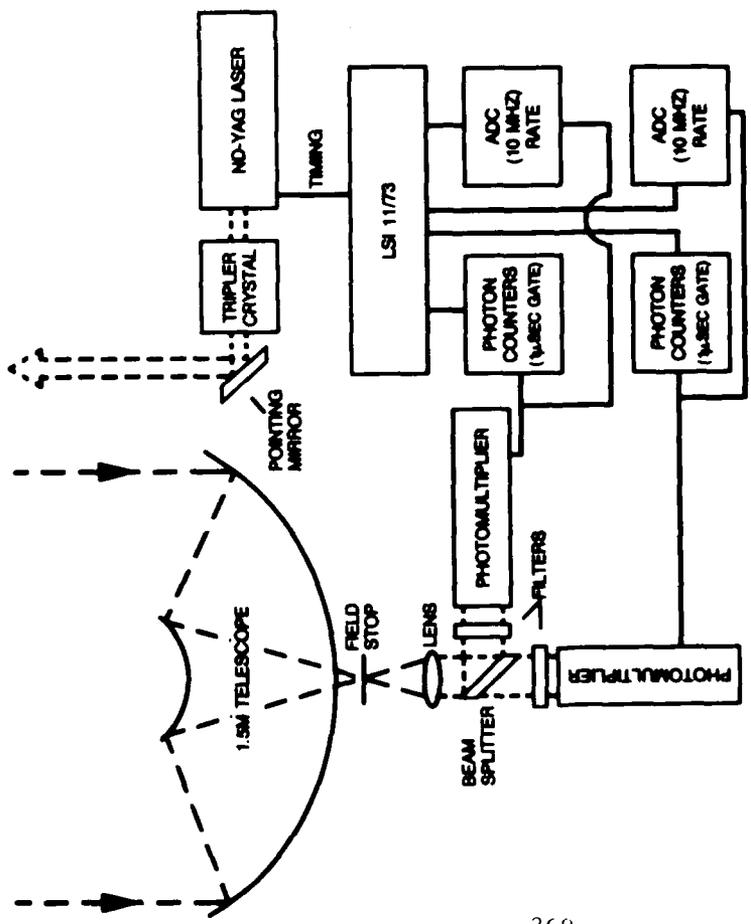
Figure 1. Equipment Block Diagram
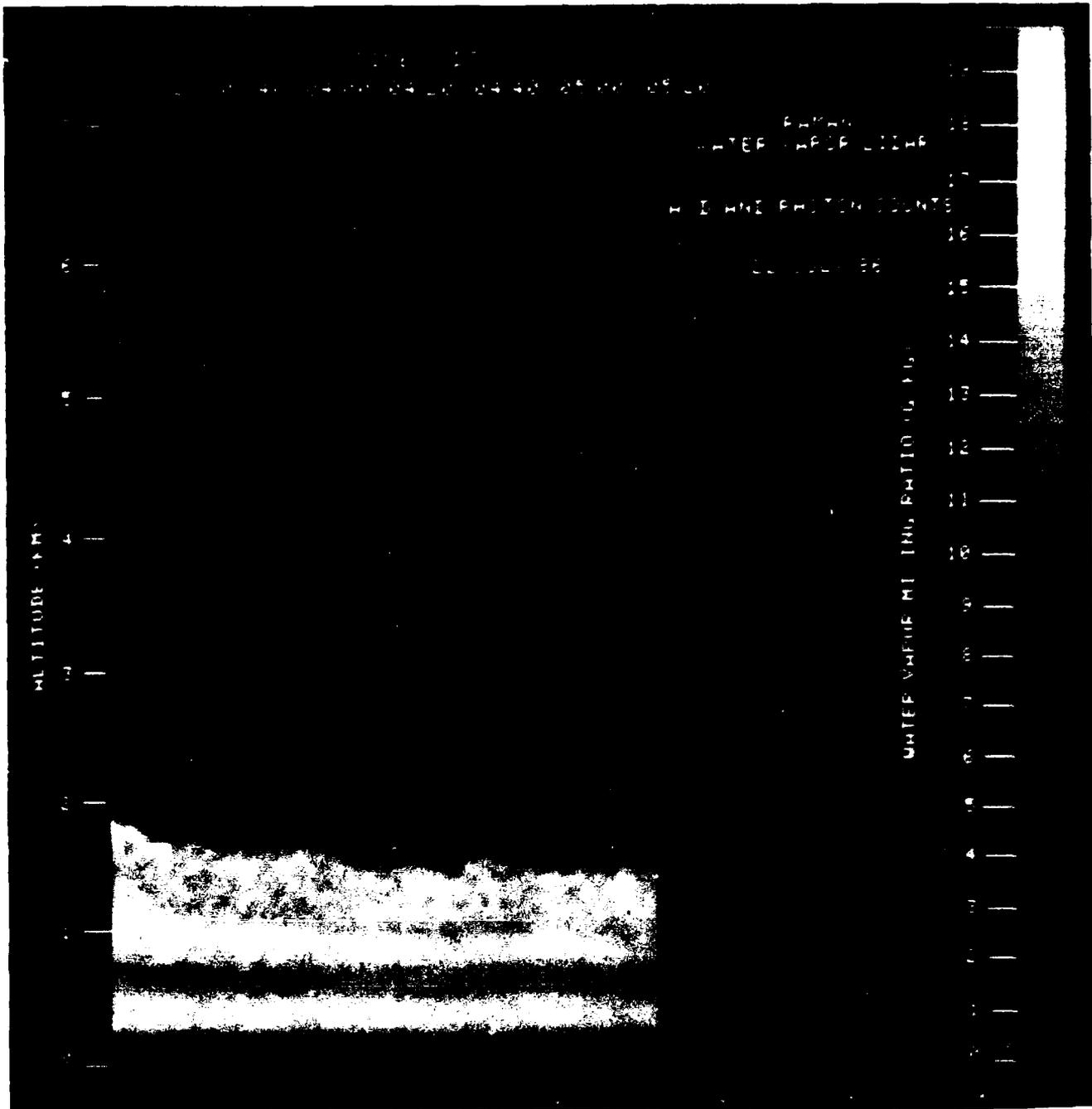
Figure 3. The moisture field over the lidar site during the early morning hours of July 22, 1986

Accuracy of Temperature Measurements Using

High Spectral Resolution Lidar

by

David A. Krueger and C Y. She
Department of Physics
Colorado State University
Fort Collins, Colorado 80523

The High Spectral Resolution LIDAR (HSRL) technique has been proposed (1,2) to measure the temperature profile in the atmosphere with a resolution of 1°K in real time with a spatial resolution of 15 to 30 m. A 10-nanosecond pulse centered on frequency, ν_L, is sent into the atmosphere. The returning light is split and each beam is passed through one of two very narrow atomic vapor filters centered on ν_F, but with slightly different band widths corresponding to different vapor temperatures. Tuning the laser frequency to coincide with the center of the filter will remove the strong central aerosol scattering peak. The transmitted light is that scattered by the air molecules at a range determined by the time delay. The ratio of these two signals is then compared to that calculated from kinetic theory (3,4) for different temperatures. The signal through the two filters will be given by

$$N_i = \int_{-\infty}^{\infty} F_i(\nu - \nu_F) \, R(\nu - \nu_L) \, A_i(\nu) \, d\nu; \quad i = 1 \text{ or } 2$$

where R is the calculated intensity of the scattered light, F is the transmission profile of the atomic vapor filter, A is the amplification factor of the electronics, and ν is the frequency of the returning light. F will be a function of the temperature of the atomic vapor.

Computer simulations of the line shape of the scattered light have been used to determine the sensitivities of the measured quantities, N_1 and N_2 to variations in the atmospheric properties (e.g. temperature, pressure, ratio of

the bulk viscosity to the shear viscosity, ratio of the thermal conductivity to the shear viscosity, internal specific heat, or the effective mass of an "air molecule"). We have also investigated the effects of a frequency mismatch of the laser with the absorption peak of the atomic vapor filter. In the actual experiment, one uses ratios of the intensities of the scattered light after filtering through two filters, N_1/N_2. This will eliminate the fluctuations in the overall intensity of the scattered light. Ultimately the filters will be optimized by varying their temperatures. For the present analysis, we have used the three ratios from Ba filters with vapor temperatures equal to 650°K, 725°K, and 800°K all centered at 553.7 nm. The filter line shape is the theoretical one given by Shimizu et al. (1). Comparisons are with a base case that corresponds to parameters given in Table I. For small variations of the parameters, the sensitivities of the measured ratios of intensities is given as a range of the percentage changes. An atmospheric temperature variation of 1°K changes the measured ratio by less than 0.5% which is over an order of magnitude more than a pressure variation of 1 mbar. Uncertainties of 10% in the air viscosities, thermal conductivities, and internal specific heat lead to less than 0.09% change in the measured ratios. A frequency mismatch of 100 MHz between the laser and the atomic vapor filter will be reflected in a large (1.4%) change in measured ratios. This highlights the importance of accurate tuning of the dye laser. The available theory for the lineshape is for a gas of a single diatomic molecular species. To account for the mixture of nitrogen, oxygen, and carbon dioxide we have used two averaging techniques. In the base case we simply use the average mass of a molecule in the atmosphere. Alternatively we have calculated the separate line shapes corresponding to atmospheres of nitrogen, oxygen, or carbon dioxide. These were then weighted according to their Rayleigh cross-sections and abundances in the atmosphere. The difference in these two averaging techniques is roughly 1.4%.

Because R is a function of the dimensionless x and y (3,4), the variations of N with wavelength, molecular mass, pressure, and temperature are not independent but depend upon only two parameters, $\langle \frac{\delta N}{\delta x} x \rangle$ and $\langle \frac{\delta N}{\delta y} y \rangle$

$$\delta N = \frac{\delta \lambda}{\lambda} \left[\langle \frac{\delta N}{\delta x} x \rangle + \langle \frac{\delta N}{\delta y} y \rangle \right] + \frac{\delta M}{M} \langle \frac{\delta N}{\delta x} x \rangle + \frac{\delta P}{P} \langle \frac{\delta N}{\delta y} y \rangle$$

$$- \frac{\delta T}{T} \left[\frac{1}{2} \langle \frac{\delta N}{\delta x} x \rangle + \langle \frac{\delta N}{\delta y} y \rangle \left\{ \frac{T + 220.8}{T + 110.4} \right\} \right]$$

For the three pairs of filters used above we find

$$\left\langle \frac{\delta N}{\delta x}x \right\rangle \simeq -0.42, \ -0.54, \ \text{and} \ -0.44$$

and

$$\left\langle \frac{\delta N}{\delta y}y \right\rangle \simeq 0.025, \ 0.017, \ \text{and} \ -0.0083$$

The insensitivity to pressure changes as compared to temperature changes is a reflection of the small value of $\left\langle \frac{\delta N}{\delta y}y \right\rangle / \left\langle \frac{\delta N}{\delta x}x \right\rangle$ for the three pairs of filters.

In addition to uncertainties in the properties of the air, the measured values will fluctuate due to noise in the incoming signal, due to variations in the width of the filter transmission corresponding to temperature fluctuations in the atomic vapor, and due to noise in the electronic amplifier circuit. Because of the small time slice (approximately 10 nanoseconds) the dark current will be insignificant, but the shot noise will be significant.

In summary, a temperature variation of 1°K will change the measured ratio, N_1/N_2 by about 0.2 to 0.5%, whereas a pressure variation of 1 mbar produces less than 0.02% change. Ten percent variations in viscosities, thermal conductivities, or internal specific heats produce changes of about 0.1%. Mismatch of the laser line and the atomic filter frequency by 100 MHz can give variations of up to 1.5%. Different methods of averaging over the main molecular constituents of air give variations of up to 1.5% also. Of course some of these uncertainties can be minimized by calibrating using scattering from air at known temperatures and pressures. Thus temperature determinations of 1°K and pressure variations of 20 mb are presently feasible. In fact, experimental verification of this temperature measurement technique has been carried out recently in the laboratory with a cw signal-frequency tunable dye laser (5).

(1) H. Shimizu, S. A. Lee, and C. Y. She, "High Spectral Resolution Lidar System with Atomic Blocking Filters for Measuring Atmospheric Parameters," Appl. Opt. 22, 1373 (1983).

(2) H. Shimizu, K. Noguchi, and C. Y. She, "Atmospheric Temperature Measurement by a High Spectral Resolution Lidar," Appl. Opt. 25, 1460-6 (1986).

(3)   G. Tenti and R. C. Desai, "Kinetic Theory of Molecular Gases.   I: Models
      of the Linear Waldmann-Snider Collision Operator," Can. J. Phys. 53,
      1266-1278 (1975).

(4)   G. Tenti and R. C. Desai, "Calculation of Time Dependent Correlation
      Functions," Can. J. Phys. 53, 1279-1291 (1975).

(5)   F. J. Lehmann, S. A. Lee, and C. Y. She, "Laboratory Measurements of
      Atmospheric Temperature and Backscatter-Ratio Using a High-Spectral-
      Resolution Lidar Technique," Opt. Lett. 11, 563-565 (1986).

TABLE I

Quantity		Range of Change of N_1/N_2
Base Case	Change	
$T = 294°K$	$-1°K$	0.23% to 0.47%
$P = 830$ mbar	1 mbar	0.002% to 0.015%
$\dfrac{\eta_{bulk}}{\eta_{shear}} = 0.76$	10%	0.008% to 0.069%
$\dfrac{\eta_{bulk}}{\kappa_{therm}} \dfrac{k_B}{M} = 0.198$	10%	0.010% to 0.083%
$c_{int}/k_B = 1$	10%	0.010% to 0.083%
$\Delta\nu = \nu_{laser} - \nu_{filter}$	100 MHz	-0.68% to -1.44%
$M_{avg} = 28.966$ amu	Averaged line shapes	0.32% to 1.4%

375

Mazzinghi, P. — MC17, MC19
McCleese, Daniel J. — TuA2, TuC22
McCormick, M. Patrick — MA2
McGarry, Jan F. — TuB4, TuC21
McLellan, E. J. — WC14
Megie, Gerard — WC17
Melfi, S. Harvey — WC, WC17, ThB4
Menyuk, Norman — MB5
Menzies, Robert T. — MB4
Michelson, Elizabeth — MB3
Milton, Martin J. T. — WC5
Moody, Stephen E. — TuC18
Mooradian, Aram — WB1
Moore, J. — MC11
Moosmuller, H. — WC18
Morrow, W. H. — TuC9
Moskowitz, W. P. — TuA3

Nelms, Richard R. — MA2
Newcomb, A. L. — TuC4
Nicholis, R. W. — TuC9
Nosov, V. V. — TuC2

Ochs, G. R. — TuC6
Orloff, Jon — WB3
Osborn, M. — MC11

Pagano, Thomas S. — TuC13
Pal, S. R. — ThB3
Palm, Stephen P. — MC7
Pantani, L. — MC16, MC17, MC18, MC19
Park, Jinwoo — TuC3
Partridge, Roger H. — WC5
Peacock, John — WC6
Pelon, J. — ThB1
Petheram, John — WA
Philbrick, C. R. — TuA3
Pippi, I. — MC16
Pizzolati, P. L. — TuB3
Ponomarev, Yu. N. — WC12
Poon, Ting-Chung — TuC3
Prasad, Coorg R. — WC11
Puretz, Joseph — WB3

Quenzel, H. — MA3

Radicati, B. — MC17, MC18, MC19
Renger, W. — MA3
Reuter, Dennis — TuC20
Richmond, Richard — WC21
Rider, David M. — TuC22
Rodger, M. O. — WC20
Romanovskii, O. A. — TuC1
Romoli, M. — MC17
Rosenberg, A. — WC19
Rossey, C. E. — TuC21
Rowe, H. E. — TuC21
Rowland, Carroll W. — MA2

Sakurai, K. — ThA4
Sambasivan, R. — TuC24
Samokhvalov, I. V. — WC1
Schofield, John T. — TuC22
Schwemmer, Geary K. — WC10, WC11, WC16, WC17
Senft, Daniel C. — MC14, MC15
Servaites, Jan — WC21
Shamanaev, V. I. — WC1
Sharma, R. D. — TuC10
Shay, T. M. — TuC17, WB4, WC22
She, C. Y. — WC18, ThB5
Shubin, S. F. — TuC1
Shumskii, V. K. — MC2
Singh, Upendra N. — WC2
Sinitsa, L. N. — WC12
Sipler, D. P. — TuA3
Sivertson, W. E. — TuC15
Siviter, J. H. — MC4
Spinhirne, James D. — MC7, MC13, TuB5
Sroga, J. — WC19
Stickel, R. E. — WC20
Strow, L. Larrabee — TuC19, TuC20
Swann, Nigel R. — MB3
Swirbalus, Robert A. — TuC23

Takeuchi, N. — WC, ThA4
Targ, Russell — TuC18
Tratt, David M. — MB4
Tyryshkin, I. S. — WC12

Uccellini, Louis — WC17
Ueno, T. — ThA4

Vaughn, Michael — WB2
Voevodin, V. G. — WC13
Volkov, S. M. — MC2
Vujkovic,Cvijin — MC16
Vvan der Laan, Jan E. — WC4

Warren, Russell E. — MC6
Welsh, Byron — TuA5
Weng, Chi Y. — MC5
Werner, Christian — ThA3
Whiteman, David — ThB4
Wilkerson, Thomas D. — WC2
Winker, D. M. — TuC12
Woods, Peter T. — MB3, WC5
Woody, Loren M. — TuC13

Zachor, A. S. — TuC10
Zanzottera, Eugenio — TuB3, ThA
Zhukov, A. F. — TuC2
Zuev, V. V. — TuC1, WC13
Zuev, Vladimir E. — MB1, MC1, MC2, TuC1, WC1,
   WC12, WC13

TECHNICAL PROGRAM COMMITTEE

END

DATE

FILMED

12-88

DTIC